

Wrocław University of Technology  
Centre of Advanced Materials and Nanotechnology

---

# Materials Science Poland

Sol-Gel Materials  
Research, Technology, Applications  
SGM '04

6-11 June 2004

Guest Editors:  
Krzysztof Maruszewski, Wiesław Stręk

Vol. 23

•

No. 1

•

2005

---



Oficyna Wydawnicza Politechniki Wrocławskiej

**Materials Science** is an interdisciplinary journal devoted to experimental and theoretical research into the synthesis, structure, properties and applications of materials.

**Among the materials of interest are:**

- glasses and ceramics
- sol-gel materials
- photoactive materials (including materials for nonlinear optics)
- laser materials
- photonic crystals
- semiconductor micro- and nanostructures
- piezo-, pyro- and ferroelectric materials
- high- $T_c$  superconductors
- magnetic materials
- molecular materials (including polymers) for use in electronics and photonics
- novel solid phases
- other novel and unconventional materials

The broad spectrum of the areas of interest reflects the interdisciplinary nature of materials research. Papers covering the modelling of materials, their synthesis and characterisation, physicochemical aspects of their fabrication, properties and applications are welcome. In addition to regular papers, the journal features issues containing conference papers, as well as special issues on key topics in materials science.

Materials Science is published under the auspices of the Centre of Advanced Materials and Nanotechnology of the Wrocław University of Technology, in collaboration with the Institute of Low Temperatures and Structural Research of the Polish Academy of Sciences and the Wrocław University of Economics.

All accepted papers are placed on the Web page of the journal and are available at the address:  
<http://MaterialsScience.pwr.wroc.pl>

### **Editor-in-Chief**

Juliusz Sworakowski

Institute of Physical and Theoretical Chemistry  
Wrocław University of Technology  
Wybrzeże Wyspiańskiego 27  
50-370 Wrocław, Poland  
[sworakowski@pwr.wroc.pl](mailto:sworakowski@pwr.wroc.pl)

### **Associate Editors**

Wiesław Stręk

Institute of Low Temperature  
and Structure Research  
Polish Academy of Sciences  
P.O. Box 1410  
50-950 Wrocław 2, Poland  
[strek@int.pan.wroc.pl](mailto:strek@int.pan.wroc.pl)

Jerzy Hanuza

Department of Bioorganic Chemistry  
Faculty of Industry and Economics  
Wrocław University of Economics  
Komandorska 118/120  
53-345 Wrocław, Poland  
[hanuza@credit.ae.wroc.pl](mailto:hanuza@credit.ae.wroc.pl)

### **Scientific Secretary**

Krzysztof Maruszewski

Institute of Materials Science and Applied Mechanics  
Wrocław University of Technology  
Wybrzeże Wyspiańskiego 27  
50-370 Wrocław, Poland  
[maruszewski@pwr.wroc.pl](mailto:maruszewski@pwr.wroc.pl)

### **Advisory Editorial Board**

Michel A. Aegerter, Saarbrücken, Germany  
Ludwig J. Balk, Wuppertal, Germany  
Victor E. Borisenko, Minsk, Belarus  
Mikheylo S. Brodyn, Kyiv, Ukraine  
Maciej Bugajski, Warszawa, Poland  
Alexander Bulinski, Ottawa, Canada  
Roberto M. Faria, São Carlos, Brazil  
Reimund Gerhard-Multhaupt, Potsdam, Germany  
Paweł Hawrylak, Ottawa, Canada  
Jorma Hölsä, Turku, Finland  
Alexander A. Kaminskii, Moscow, Russia  
Wacław Kasprzak, Wrocław, Poland  
Andrzej Kłonkowski, Gdańsk, Poland  
Seiji Kojima, Tsukuba, Japan  
Shin-ya Koshihara, Tokyo, Japan  
Marian Kryszewski, Łódź, Poland  
Krzysztof J. Kurzydłowski, Warsaw, Poland  
Jerzy M. Langer, Warsaw, Poland  
Janina Legendziewicz, Wrocław, Poland  
Benedykt Licznarski, Wrocław, Poland

Tadeusz Luty, Wrocław, Poland  
Joop H. van der Maas, Utrecht, The Netherlands  
Bolesław Mazurek, Wrocław, Poland  
Gerd Meyer, Cologne, Germany  
Jan Misiewicz, Wrocław, Poland  
Jerzy Mroziński, Wrocław, Poland  
Robert W. Munn, Manchester, U.K.  
Krzysztof Nauka, Palo Alto, CA, U.S.A.  
Stanislav Nešpůrek, Prague, Czech Republic  
Romek Nowak, Santa Clara, CA, U.S.A.  
Tetsuo Ogawa, Osaka, Japan  
Renata Reisfeld, Jerusalem, Israel  
Marek Samoć, Canberra, Australia  
Jan Stankowski, Poznań, Poland  
Leszek Stoch, Cracow, Poland  
Jan van Turnhout, Delft, The Netherlands  
Jacek Ulański, Łódź, Poland  
Walter Wojciechowski, Wrocław, Poland  
Vladislav Zolin, Moscow, Russia

The Journal is supported by the State Committee for Scientific Research

Editorial Office

Karol Langner  
Łukasz Maciejewski

Printed in Poland

© Copyright by Oficyna Wydawnicza Politechniki Wrocławskiej, Wrocław 2005

# Contents

## Conference papers

From the Guest Editors.....	5
S. Kundu, S. Jana, P.K. Biswas, Quantum confinement effect of in-situ-generated Cu <sub>2</sub> O in a nanostructured zirconia matrix.....	7
Y. Djaoued, J. Robichaud, R. Brüning, A.S. Albert, P.V. Ashrit, The effect of poly(ethylene glycol) on the crystallisation and phase transitions of nanocrystalline TiO <sub>2</sub> thin films.....	15
M.Gnyba, M. Keränen, M. Kozanecki, B.B. Kosmowski, Raman investigation of hybrid polymer thin films.....	29
M. Gnyba, M. Keränen, Raman system for monitoring dye doping to hybrid polymer network . . . . .	41
V. S. Gurin, A.A. Alexeenko, K.N. Kasparov, E.A. Tyavlovskaya, incorporation of zirconia and germania and ternary compounds of ZrO <sub>2</sub> -GeO <sub>2</sub> into silica sol-gel matrices.....	49
T. Hübert, A. Shimamura, A. Klyszcz, Carbon-silica sol-gel derived nanomaterials . . . . .	61
V. G. Kessler, G.A. Seisenbaeva, P. Werndrup, S. Parola, G.I. Spijksma, Design of molecular structure and synthetic approaches to single-source precursors in the sol-gel technology. . . . .	69
J. Michalski, T. Wejrzanowski, R. Pielaszek, K. Konopka, W. Łojkowski, K.J. Kurzydłowski, Application of image analysis for the characterization of powders.....	79
R. Kornak, D. Nižňansky, K. Haimann, W. Tylus, K. Maruszewski, Synthesis of magnetic nanoparticles via the sol-gel technique.....	87
B. Kościelska, L. Murawski, L. Wicikowski, Electrical and mechanical properties of nitrated sol-gel derived TiO <sub>2</sub> and SiO <sub>2</sub> -TiO <sub>2</sub> films.....	93
J. C. Pivin, Formation of nanostructures with a controlled size distribution in Si-based gels by ion irradiation.....	101
A. Ulatowska-Jarża, U. Bindig, H. Podbielska, I. Hołowacz, W. Stręk, G. Müller, HJ. Eichler, Spectroscopic properties of chlorophyll-based photosensitive dye entrapped in sol-gel fibre-optic applicators.....	111
R. Sindut, K. Cholewa-Kowalska, J. Najman, M. Łączka, M. Karpov, A.M. Osyczka, P. Leboy, Bioactive glass coatings.....	123
E. Szałkowska, J. Masalski, B. Kucharska, J. Głuszek, The effect of heat treatment of TiO <sub>2</sub> coatings obtained by the sol-gel method on the corrosion resistance of chromium steel.....	137
I. Zaręba-Grodź, W. Mišta, A. Sikora, T. Gotszalk, W. Stręk, K. Hermanowicz, K. Maruszewski, Textural properties of silica-based organic-inorganic polymer hybrid xerogels . . . . .	147
A. Zarycka, R. Zachariasz, J. Ilczuk, A. Chrobak, Internal friction related to the mobility of domain walls in sol-gel derived PZT ceramics.....	159
A. Zarycka, A. Lisińska-Czekaj, J. Czuber, T. Orkisz, J. Ilczuk, D. Czekaj, The sol-gel synthesis of bismuth titanate electroceramic thin films.....	167
E. Żelazowska, E. Rysiakiewicz-Pasek, M. Borczuch-Łączka, Sol-gel derived Li-ion conducting polymer electrolytes.....	177

## Regular papers

A. Mirończyk, A. Jankowski, A. Chyla, A. Ożyhar, P. Dobryszycki, The influence of ammonia, acetic acid and water vapour on the fluorescence of a 2-naphthol derivative in the Langmuir-Blodgett films.....	195
G. Paściak, J. Chmielowiec, P. Bujło, New ceramic superionic materials for IT-SOFC applications.....	209
M. Górską, H. Wrzeńska, A. Szerling, K. Hejduk, J.M. Łysko, HBV deep mesa etching in InGaAs/InAlAs/AlAs heterostructures on InP substrate.....	221
S. Gopakumar, C.J. Paul, M.R. Gopinathan Nair, Segmented block copolymers of natural rubber and 1,4-butanediol-toluene diisocyanate oligomers.....	227

A. N. Trefilova, LV. Korionov, A.N. Babushkin, W. Łojkowski, A. Opalińska, Correlation between high-pressure electrical properties of $ZrO_2$ and its crystallite size	247
A. M. Kłonkowski, I. Szałkowska, Functions of $Eu^{3+}$ ions in materials with CdS nanoparticles and oxide matrices	253
P. Mazur, D. Hreniak, J. Niittykoski, W. Stręk, J. Hölsä, Formation of nanostructured $Tb^{3+}$ -doped yttrium aluminium garnets by the glycol route	261
V. K. Sachdev, N.K. Srivastava, K. Kumar, R.M. Mehra, Pre-localized graphite/polyvinyl chloride composites for electromagnetic interference shielding in the X-band frequency range	269
M. Lewandowska, H. Garbacz, W. Pachla, A. Mazur, K.J. Kurzydłowski, Grain refinement in aluminium and the aluminium Al-Cu-Mg-Mn alloy by hydrostatic extrusion	279
V. N. Kokozay, D.V. Shevchenko, Direct synthesis as a new approach to heteropolynuclear complexes	287

## From the Guest Editors

It was our great pleasure to co-organize the Third International Conference on Sol-Gel Materials *Research, Technology, Applications* SGM '04. The Conference took place on 6-11 June 2004 in Wrocław, the capital of the Lower Silesia district of south-west Poland. It was organized by the Center of Excellence *Sol-Gel Materials and Nanotechnology* (SGM&N) at the Wrocław University of Technology. This event gathered more than 100 participants from: Belarus, Belgium, the Czech Republic, Finland, France, Germany, Great Britain, Israel, Italy, Japan, Lithuania, Poland, Portugal, South Korea, Spain, Sweden, and Vietnam. Most of the participants presented either oral communications or posters.

The Conference has covered a wide field of topics related to various aspects of theory and practice of the sol-gel technology - from biological sensors to fractal geometry of aerogel structures. We have finally accepted 28 full articles after customary peer reviews. The scope of the Conference is, by definition, a broad and interdisciplinary one. Thus, it has been decided to divide the contributions into two general classes, i.e. (1) articles concerned with optical materials and (2) with other issues. The first group of papers can be found in this issue of *Materials Science* while the others have been accepted by *Optical Materials*. We would like to express our warm thanks to the authors who contributed their works and to the reviewers for their prompt and thorough reviews.

The Conference was possible thanks to support of the European Commission which is gratefully acknowledged. The contribution of the Wrocław University of Technology is also acknowledged.

*Krzysztof Maruszewski*

*Wiesław Stręk*

# Quantum confinement effect of in-situ generated Cu<sub>2</sub>O in a nanostructured zirconia matrix

SUSMITA KUNDU, SUNIRMAL JANA\*, PRASANTA KUMAR BISWAS\*\*

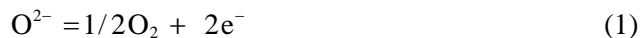
Sol-Gel Division, Central Glass and Ceramic Research Institute, Kolkata-700032, India

The incorporation of Cu<sup>2+</sup> in zirconyl chloride octahydrate sol or solution was used as a precursor for dip coating. This resulted in the in-situ formation of nanostructured Cu<sub>2</sub>O quantum particles in the zirconia matrix. The size-dependent properties of the Cu<sub>2</sub>O quantum particles were observed when the films were annealed in the range of 200–600 °C. A red shift of the UV band, ascribed to the transition from the copper d-shells to higher sublevels of the conduction band, was observed in the range of 260–315 nm due to an increase in the nanocrystallite size with increasing annealing temperature. Three types of emissions, blue, green, and yellow, were observed in films of relatively high thickness (around 120–130 nm) due to Wannier-like excitonic transitions. For films of relatively low thickness (50–70 nm) only green emission was observed. From lifetime measurements of samples annealed at 450 °C it may be concluded that the short decay time is bi-exponential in character from ns to ps with the chi-square value of 1.005, which is due to the confinement of Cu<sub>2</sub>O quantum particles.

Key words: *sol-gel; nanostructured Cu<sub>2</sub>O; quantum confinement; exciton; short-life emission*

## 1. Introduction

Nano-sized zirconia films can be prepared on silica glass substrates by the sol-gel technique [1]. When the size of the zirconia particles (grains) is in the nano-range (below 250Å), the meta-stable cubic or tetragonal state of zirconia becomes more stabilized [1]. As a result, the surface area and surface energy increases, facilitating in-situ generation of Zr<sup>3+</sup> along with oxygen deficiencies in the zirconia system [2, 3]. The generation of trivalent zirconium is possibly due to the formation of oxygen deficient centres in the film in accordance to the following sequence of reactions:



---

\*Presently in Glass-Technology Section, CGCRI, Kolkata, India.

\*\*Corresponding author, e-mail: pkb@cgcri.res.in.

Incorporation of transition metal ions into the precursor leads also to the formation of a reduced state of the metal ion [4, 5] due to the partial reduction of the metal ion by electrons trapped in oxygen deficient centres.

In the case of the  $\text{Cu}^{2+}$  system, incorporation leads to the generation of  $\text{Cu}_2\text{O}$  clusters in the zirconia film,  $\text{Cu}_2\text{O}$  exhibiting excitonic behaviour. Excitation-dependent emission spectra of  $\text{Cu}_2\text{O}$  clusters of a particular size have been examined but their size-dependence on excitation wavelengths has not been reported so far. Lifetime measurements of the fluorescence spectra of nano clusters, usually exhibiting a short lifetime, imply excitonic behaviour. In view of the above facts, an attempt was made to synthesize and characterize the size-dependent emission spectra and fluorescence lifetime of  $\text{Cu}_2\text{O}$  microcrystallites in nano zirconia, where both host and dopants are nanosized.

## 2. Experimental

### 2.1. Preparation of precursor solution

The precursor solution for films of zirconium oxide-copper oxide was prepared maintaining the atomic ratio, Zr:Cu at 1:1. The starting materials were: recrystallised zirconyl chloride octahydrate (ZOO) and copper(II) nitrate trihydrate in an acidic solvent mixture containing glacial acetic acid (a complexing or polymeric agent). The solvent mixture contained dehydrated ethanol and 2-butanol. The wt. % equivalent of  $\text{ZrO}_2$  in the solution was 2.0. The solution was prepared by mixing the requisite amounts of ZOO and Cu(II) salt in the required amount of the acidic solvent mixture while stirring for 2 h. The final solution was green in colour. The sol was aged for five days.

### 2.2. Preparation of films

The resulting solution was used for the deposition of layers on cleaned Heraeus (Germany) make suprasil grade pure silica glass, adopting a dipping technique with two different withdrawal speeds, namely (i) 4 cm/min (ii) 18 cm/min, to attain films of two different thicknesses. After dipping, the solution layer was formed on both sides of the glass substrate. The coated samples were placed in an air oven and heated at 100 °C for 30 min and then put into a furnace and heated at various temperatures (200°, 300°, 450°, and 600°±5°C) for 30 min in an air atmosphere.

### 2.3. Characterization

UV-visible absorption spectra of films prepared at various temperatures were recorded at room temperature using a Shimadzu UV-VIS-NIR spectrophotometer (photometric accuracy: ±0.002 Abs in the range of 0.0–0.5 Abs, ±0.004 in the range 0.5–1.0, ±0.3% *T* in transmittance). The thicknesses of the films were measured ellip-

sometrically (Gaertner, L116B). Room temperature fluorescence (lamp-corrected for emission excitation) spectra of the samples were recorded with a Perkin-Elmer Fluorimeter. The fluorescence lifetimes of the multilayer films annealed at 450 °C were measured. For this measurement, a coherent CW mode locked Nd:YAG (Antavs 76 s) synchronously pumped cavity dumped hybrid mode locked Rhodamine 6G dye laser light at 600 nm was used. The fundamental 600 nm laser light was frequency doubled to produce then exciting 300 nm light. The emission was detected at a magic angle (54–74) polarization using a Hamamtsu MCP photomultiplier tube (2809 U) in a time correlated single photon counting set-up. The lifetime of the set-up was 50–60 ps. Microstructure and crystal symmetry (electron diffraction, ED) of the films were analysed by a transmission electron microscope (TEM) (JEOL, JEM-200CX). The accelerating voltage and camera length were 160 kV and 55 cm, respectively.

### 3. Results and Discussion

#### 3.1. Absorption spectra

It was observed that the precursor solution containing zirconium oxychloride octahydrate and Cu(II) nitrate trihydrate yielded in-situ Cu<sub>2</sub>O microcrystallites by the partial reduction of Cu<sup>2+</sup> caused by trapped electrons in the oxygen deficient nano-zirconia film matrix [3]. These Cu<sub>2</sub>O microcrystallites exhibited excitonic transitions in the UV (260–315 nm) (Fig. 1a) and visible (Fig. 1b) regions at room temperature. The absorption bands (UV) of Cu<sub>2</sub>O excitons shifted towards longer wavelengths with increasing microcrystallite size, due to the increase in annealing temperature. Microcrystallite sizes can be determined [6, 7] from the excitonic transitions in bulk crystal and microcrystallites. We observed absorption peak shifting due to annealing the film at 200°, 300°, 450°, and 600°C. As the nature of absorption was shoulder-like, we took the 2nd derivative of each absorption and confirmed the absorption peak positions. These were 261 nm, 268 nm, 285 nm, and 288 nm for the above respective annealing temperatures. The microcrystallite size of Cu<sub>2</sub>O in the nano zirconia films was evaluated from the shift of the absorption band:

$$E_{\text{QD}} = E_{\text{bulk}} + \frac{h^2}{8MR^2} \quad (3)$$

$E_{\text{QD}}$  and  $E_{\text{bulk}}$  are the exciton energies in the quantum well and bulk, respectively. The simplified form of Equation (3) in terms of the peak wavelength  $\lambda$  and  $R$  (the average radius of a microcrystallite) is

$$R = 1.7396 \left( \lambda_{\text{QD}}^{-1} \lambda_{\text{bulk}}^{-1} \right)^{-1/2} \quad (4)$$

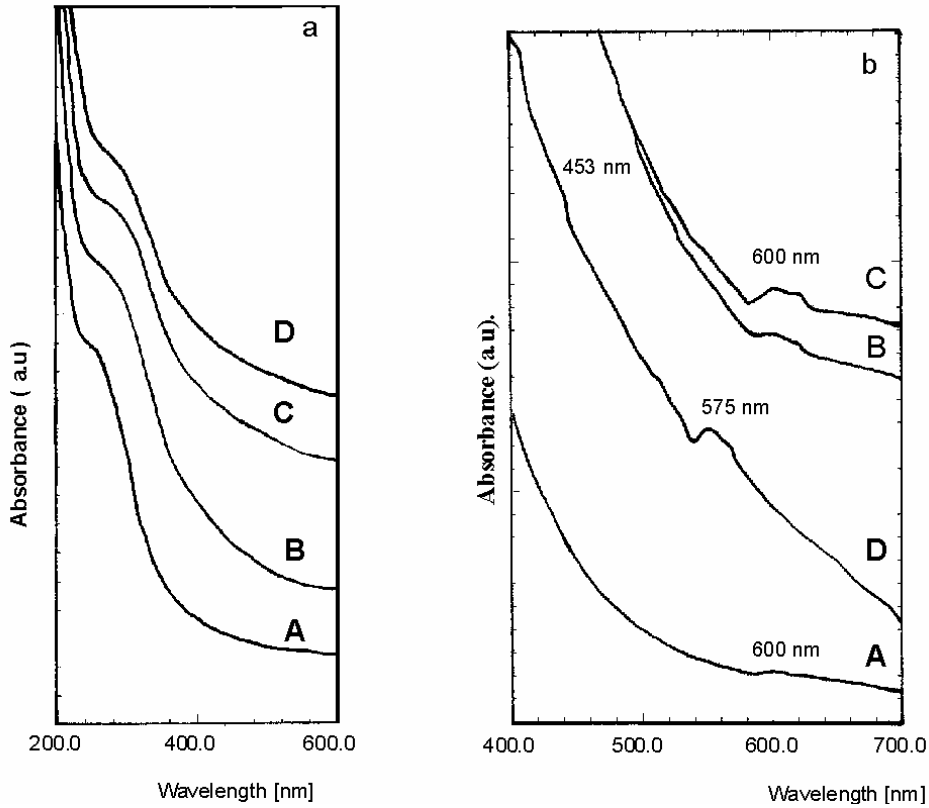


Fig. 1. UV (a) and visible (b) absorption spectra of Cu<sub>2</sub>O excitons embedded in a nano zirconia film matrix deposited on a pure silica glass substrate and annealed at: A) 200 °C, B) 300 °C, C) 450 °C, D) 600 °C

We assume the translational reduced mass  $M$  of excitons to be  $3m_0$ , where  $m_0$  is the mass of the electron in vacuum.  $R$  and  $\lambda$  are expressed in Å and nm, respectively. The excitonic transition for the bulk was chosen at 371 nm after Jana and Biswas [5]. They observed that the peak at 371 nm does not shift with increasing temperature, i.e., increasing size. The evaluated sizes of the Cu<sub>2</sub>O microcrystallites in the corresponding annealing films were 51 Å, 54 Å, 61 Å, 62 Å. We have taken TEM pictures of a typical film annealed at 450 °C (Fig. 2), which indicates that the microcrystallite sizes are in the range of 80–120 Å. The appearance of diffraction rings in the electron diffraction also reveals its crystalline feature, although we did not observe any identifiable  $2\theta$  lines in the XRD (not shown here).

The UV bands may be assigned to the transition from the copper d-shells to higher sublevels of the conduction band, as described in the plausible scheme in Fig. 3. In addition to the UV absorption band, a few more absorption bands are observed in the blue, green, and yellow regions. These are expected to be due to Wannier-like excitonic transitions. We did not observe any shifting of these bands due to increasing annealing temperature. They are hydrogen-like, generated from Cu<sub>2</sub>O excitons, and

their tentative assignments are shown in the scheme proposed. The absorption band at 600 nm is possibly due to  $\lambda_1^y$  (first line in the yellow series), but  $\lambda_1^G$  (first line in the

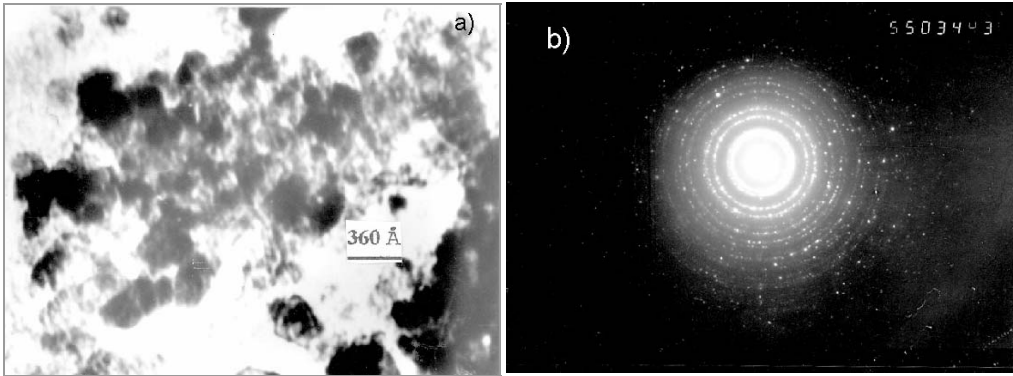


Fig. 2. Transmission electron micrograph (a) and electron diffraction pattern (b) of the film heated at 450 °C

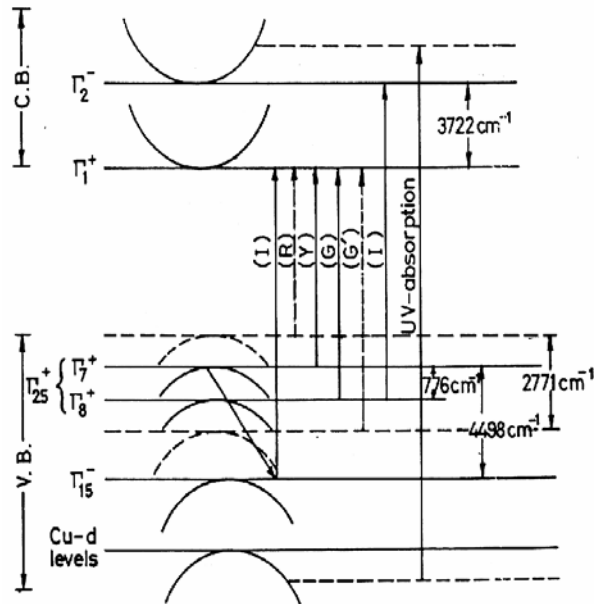


Fig. 3. A plausible path of excitonic transitions in Cu<sub>2</sub>O microcrystallites deduced from the absorption bands. The symbols I, Y, and G indicate the indigo, yellow, and green series of excitonic transitions, respectively. G and R represent transitions (dotted lines) from possible sublevels (dotted curves) for green and red, respectively

green series) is not unlikely. Therefore, the band at 555 nm may be assigned to  $\lambda_2^G$  (2nd line in the green series). The transitions of the yellow and green series are partially forbidden direct transitions from  $\Gamma_7^+$  to  $\Gamma_1^+$  and  $\Gamma_8^+$  to  $\Gamma_1^+$ , respectively, as the valence band

$\Gamma_{25}^+$  with the degenerate states  $\Gamma_7^+$  and  $\Gamma_8^+$  will split under spin orbit coupling into  $\Gamma_7^+$  (higher energy state) and  $\Gamma_8^+$  (lower energy state). Valence band splitting may be obtained from the difference in energy between the yellow ( $n = 1$ ) and green ( $n = 1$ ) series, which is very close to the values reported by other authors [8–13]. In addition, the appearance of a band (Indigo, at 453 nm) in the blue series is possibly due to the transition from  $\Gamma_8^+$  to an excited conduction band  $\Gamma_2^-$  or to the transition from  $\Gamma_{15}^-$  to  $\Gamma_1^+$ .

### 3.2. Luminescence spectra

Excitonic transitions were also evidenced from the fluorescence spectra of the films. We have developed films of two different thicknesses, namely (i) 70 nm and

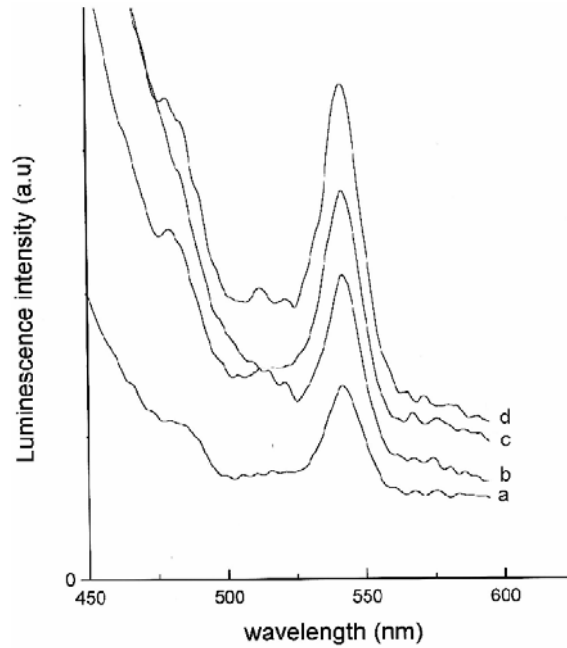


Fig. 4. Emission spectra of films of small thickness, annealed at: a) 200 °C, b) 300 °C, c) 450 °C, d) 600 °C with fixed excitation at 400 nm

(ii) 130 nm. The films of relatively low thickness exhibited a prominent emission peak at ~540 nm (green region) with two shoulders in the blue and yellow regions (Fig. 4). On the other hand, films 130 nm thick exhibited prominent emission peaks in the blue, green, and yellow regions (Fig. 5), which correspond to the emissions of Wannier-like transitions. It is interesting to note that films of the sample annealed at 200 °C, characterized by very small microcrystallite sizes, exhibits only blue and green emissions, although it is relatively thick. The intensity of this green emission decreases with increasing microcrystallite sizes, and the intensity of yellow emission

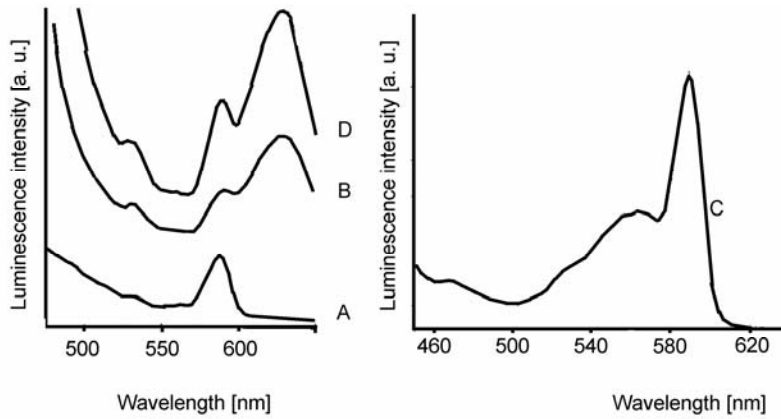


Fig. 5. Emission spectra of films of large thickness, annealed at: A) 200°C, B) 300°C, C) 450°C, D) 600 °C, with fixed excitation at 400 nm

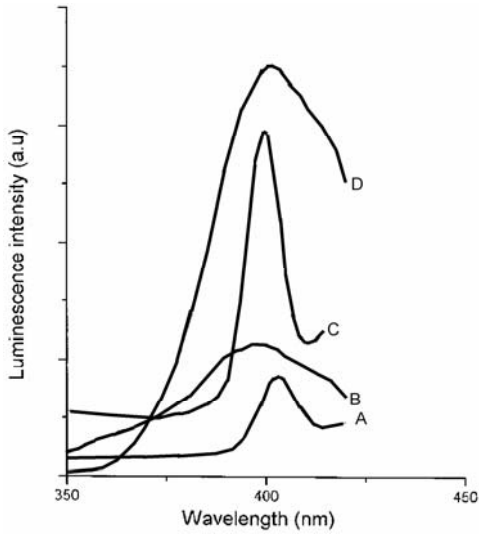


Fig. 6. Excitation spectra of films annealed at: A) 200 °C, B) 300 °C, C) 450 °C, D) 600 °C, with fixed emission at 580 nm

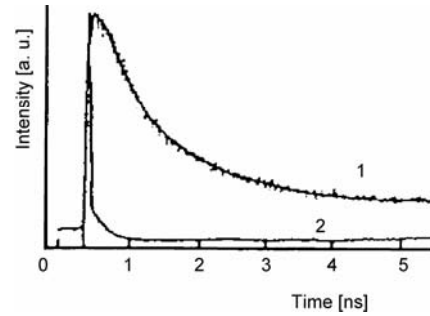


Fig. 7. Experimental fluorescence ( $\lambda_{\text{ex}} = 300$  nm) decay curve (1) of a film annealed at 450 °C and the fluorescence decay curve (2) of the lamp used

gradually increases. The above observation was monitored by fixing the excitation wavelength at 400 nm because excitonic transition at 400 nm was observed (Fig. 6) in each case if the excitation wavelength be fixed at the emission peak for yellow region. Although we did not observe any significant excitonic transition in the yellow region of the emission spectra, we observed prominent absorption in that region. It may hence be stated that the yellow emission is possibly due to a 1s excitonic band at ~600 nm. The emissions are expected for the radiation energy from  $\Gamma_1^+$  to  $\Gamma_7^+/\Gamma_8^+$  sublevels, as shown in the Scheme (Fig. 3).

The quantum confinement of Cu<sub>2</sub>O microcrystallites was confirmed by the measurement of fluorescence lifetime (Fig. 7) excited with a 300 nm pulsed dye laser. The fluorescence decay was of bi-exponential character with a chi square value of 1.005. The response times were 275 ps and 1318 ps. The short decay corresponded to the existence of quantum confinement [14]. We expect the bi-exponential character is due to the formation of mono-excitons and bi-excitons at the excited state.

## 4. Conclusion

Cu<sub>2</sub>O microcrystallites in nanozirconia film matrix were developed by the sol-gel in-situ method. Films of relatively low and high thicknesses were deposited on pure silica glass to observe the effect of film thickness on excitonic transitions. The quantum confinement effect of the microcrystallites was also observed by the measurement of the fluorescence lifetime.

### Acknowledgements

Authors are thankful to Dr. H. S. Maiti, Director, CG & CRI, Kolkata for his constant encouragement to carry out this work. One of the authors (SK) thanks CSIR, India for offering her a research internship. She also thanks the Director for allowing her to work in the CTSM programme (CMM 0022 (1)).

### References

- [1] GARVIE R.C., J. Phys. Chem., 82 (1978), 218.
- [2] LIU H., FENG L., ZHANG X., XUE Q., J. Phys. Chem., 99 (1995), 335.
- [3] JANA S., BISWAS P.K., Mater. Lett., 30 (1997), 53.
- [4] JANA S., BISWAS P.K., Bull. Mater. Sci., 23 (2000), 263.
- [5] JANA S., BISWAS P.K., Mater. Letts., 32 (1997), 263.
- [6] RULLER J.A., WILLIAMS G.M., FRIEBELE E.J., [in:] *Ceramic Transitions*, Solid State Optical Materials, Vol. 28, A.J. Bruce, B.V. Hiremath (Eds.), The American Ceramic Society, Ohio, 1992, p. 499.
- [7] EKIMOV A.I., ONUSHCHENKO A.A., Sov. Phys. Semicond., 16 (1982), 775.
- [8] NIKITINE S., [in:] S. Nudelman, S.S. Mitra (Eds.), *Optical Properties of Solids*, Plenum Press, New York, 1969, p. 197.
- [9] GRUN J.B., SIESKIND M., NIKITINE S., J. Phys. Chem. Solids, 21 (1961), 119.
- [10] DAHL J. P., SWITENDICK A. C., J. Phys. Chem. Solids, 27 (1966), 931.
- [11] ELLIOTT R.J., Phys. Rev., 124 (1961), 340.
- [12] GROSS E.F., Sov. Phys. Usp., 5 (1962), 195.
- [13] NIKITINE S., [in:] *Progress in Semiconductors*, Vol. 6, A.F. Gibson (Ed.), Wiley, New York, 1962, p. 253.
- [14] BOL A.A., MEIJERINK A., Phys. Rev. B, 58 (1998), R15997.

Received 6 June 2004  
Revised 8 September 2004

# The effect of poly(ethylene glycol) on the crystallisation and phase transitions of nanocrystalline TiO<sub>2</sub> thin films

YAHIA DJAOUED<sup>1\*</sup>, JACQUES ROBICHAUD<sup>1</sup>, RALF BRÜNING<sup>2</sup>,  
ANDRE-SEBASTIEN ALBERT<sup>1</sup>, PANDURANG V. ASHRIT<sup>3</sup>

<sup>1</sup>Université de Moncton - Campus de Shippagan, 218, J.-D. Gauthier, Shippagan, N.-B., Canada, E8S 1P6

<sup>2</sup>Physics Department, Mount Allison University, Sackville, N.B., Canada E4L 1E6

<sup>3</sup>Département de physique et d'astronomie, Université de Moncton, Moncton, N.-B., Canada E1A 3E9

Titanium dioxide (TiO<sub>2</sub>) films, composed mainly of anatase nanocrystallites, have been obtained from a low temperature poly(ethylene glycol) (PEG) modified sol-gel method. The maximum process temperature in this method is around 90 °C. An addition of PEG in the films accelerates the formation of anatase nanocrystallites. In order to better understand the nature of the influence of PEG on film crystallization, sol-gel solutions were prepared with PEG of different molecular weights (200, 400 and 600). The reference solution without PEG was also prepared. In addition, the influence of different PEG chain lengths on the films' phase transition from anatase to rutile was studied by means of Raman spectroscopy and XRD. Anatase was found to be stable up to 900–1000 °C, depending on the molecular weight of the PEG used in the films.

Key words: *nanocrystalline titania films; sol-gel, poly(ethylene glycol) (PEG); phase transition; Raman; XRD*

## 1. Introduction

Titanium dioxide films are used in technological applications such as optical filters, optical wave-guides, chemical sensors, solar cells, thin film capacitors, and electrochromic materials [1–10]. Especially, the nanostructured (NS) form of these films has attracted the attention of researchers, because their porous nature and large internal surface enhances their performance compared to traditional coarse-grained (CG) films [11]. Thin films of titania (TiO<sub>2</sub>) composed of nanosized particles in the anatase form show a very high photocatalytic activity due to their large internal surface [12].

---

\* Corresponding author, e-mail: djaoued@umcs.ca

Both the optical properties and the photocatalytic activity of TiO<sub>2</sub> coatings depend on the crystallite size, the phase, and porosity of the coatings. Hence, the micro- or nanostructure of the TiO<sub>2</sub> films and their strict control through the preparation methodology is of paramount importance. Recently, significant effort has been directed towards the low-temperature transformation of TiO<sub>2</sub> by using the sol-gel process. In a previous work, we have found that nanostructured anatase phase TiO<sub>2</sub> thin films can be fabricated by a sol-gel method at temperatures as low as 100 °C [7]. These films, with nanometric (5 nm) grain size, were obtained by using a structure-directing agent such as poly(ethylene glycol) (PEG).

We report on the synthesis of TiO<sub>2</sub> nanocrystalline thin films with a low-temperature method by treating the sol-gel deposited TiO<sub>2</sub> films in hot water. Nanoscale anatase films have been obtained by using PEG as a templating agent. In order to better understand the nature of the influence of PEG on film crystallization, sol-gel solutions were prepared in the presence of PEG of different molecular weights (200, 400 and 600). In addition, the influence of the PEG chain lengths on the film's phase transition from anatase to rutile was studied using Raman and XRD.

## 2. Experimental

In the preparation of PEG-containing TiO<sub>2</sub> films, titanium tetra-*n*-butoxide (TTB) obtained from Aldrich Chem Co. was used as the starting material. The concentration of TTB in the solution was 0.5 mol/L. TTB was first mixed with a small amount of ethanol in a container and stirred for 30 min. A mixture of water containing 3 wt. % HCl and ethanol was poured under stirring into the transparent solution to promote hydrolysis; the molar ratio of H<sub>2</sub>O to TTB was 1:1. Finally, an organic polymer (PEG) was added slowly to this solution and stirred for one hour. The resulting solution was used for the TiO<sub>2</sub> film coating. The sol-gel solutions were prepared in the presence of PEG of various molecular weights (200, 400 and 600). The molar ratio of PEG to TTB was 1. A reference solution without PEG was prepared as well.

Films annealed at 400 °C and below were coated on corning glass substrates, whereas films annealed at temperatures from 500 to 1000 °C were deposited on vitreous silica. A dip-coating apparatus constructed in our laboratory was used for the depositions. The substrate was lowered into the coating solution and then withdrawn at a regulated speed of 4 mm/s. After each coating, the films were first dried at 60 °C for 2 minutes and then heat-treated at 90 °C for 1 hour in air inside an oven. These samples were then treated in hot water at 90 °C for 1 hour. Thereafter, the films were heated at a rate of 0.5 °C to annealing temperatures ranging between 100 to 1000 °C in order to study their evolution. The samples were held at the peak temperature for one hour and then cooled to room temperature.

Raman spectra were collected at room temperature with a Jobin-Yvon Labram HR combined Raman-IR microanalytical spectrometer equipped with a motorized *xy* stage and autofocus. The spectra were generated with excitation at 632.8 nm and were dis-

persed with an 1800 gr/mm grating across the 0.8 m length of the spectrograph. The laser power was kept low in order to avoid undesired heating effects on the samples. The spectral resolution of this apparatus is approximately 0.5 cm<sup>-1</sup>.

X-ray diffraction measurements were carried out with a custom-built diffractometer equipped with a graphite monochromator and analyser crystals. The data were taken in reflection mode with Cu<sub>Kα</sub> radiation ( $\lambda = 0.1542$  nm). The signal measured from the glass and quartz substrates was subtracted from the data. The data are shown in Figs. 7–10 as a function of the length of the scattering vector,  $q = 4\pi\lambda^{-1}\sin\theta$ , where  $2\theta$  is the scattering angle. The crystalline phases were identified using the ICDD/JCPDS database [13]. Crystal sizes were determined based on the anatase (101) and (200) peaks using the Scherrer formula [14].

### 3. Results and discussion

#### 3.1. FTIR and Raman microspectroscopy

Figure 1 shows the Raman (1a – IR) and FTIR (1a – IR) spectra of the as-deposited TiO<sub>2</sub> film containing PEG on a glass substrate (the molecular weight of PEG was 600 in this film). Raman and IR spectra were recorded at the same point of the sample, by using the SameSpot technology. The a-IR infrared absorption spectrum shows a  $\nu_{\text{OH}}$  at 3457 cm<sup>-1</sup>, assigned by us to PEG hydrogen bonded to TiO<sub>2</sub> [15]. It is known that PEG molecules adsorb exothermically onto TiO<sub>2</sub> oligomers by forming hydrogen bonds between oxygen atoms in the PEG and hydroxyl groups on the TiO<sub>2</sub> oligomers [16]. The bands at 2862, 1462, and 1347 cm<sup>-1</sup> correspond to C–H vibrations, while the bands centred at 1093 and 1246 cm<sup>-1</sup> originate in the C–O–C bonds of PEG. The Raman spectrum (1a – IR), measured at the same spot, shows only the PEG bands. The O–H stretching band seen in the FTIR spectra at 3457 cm<sup>-1</sup> is not observed in Raman spectrum.

Figure 2 shows spectral changes occurring in the film when heated to 90 °C in hot water for an hour. Once again, the Raman (a-R) and FTIR (a-IR) spectra were recorded at the same point. The most significant Raman bands appear at 150, 399, 522, and 646 cm<sup>-1</sup>. They correspond to TiO<sub>2</sub> modes in the anatase phase [17]. The main anatase band is shifted to a higher frequency (150 cm<sup>-1</sup>) compared to that of the bulk (144 cm<sup>-1</sup>). The FTIR spectrum changes entirely (Fig. 2a-IR) when the film is immersed in boiling water for one hour. The bands corresponding to PEG disappear almost entirely with hot water treatment, indicating that the PEG molecules leach out of the film. Matsuda [18] showed that during heat treatment in air PEG starts to decompose only around 250 °C and that the temperature of at least 300 °C is necessary to completely remove PEG from the film.

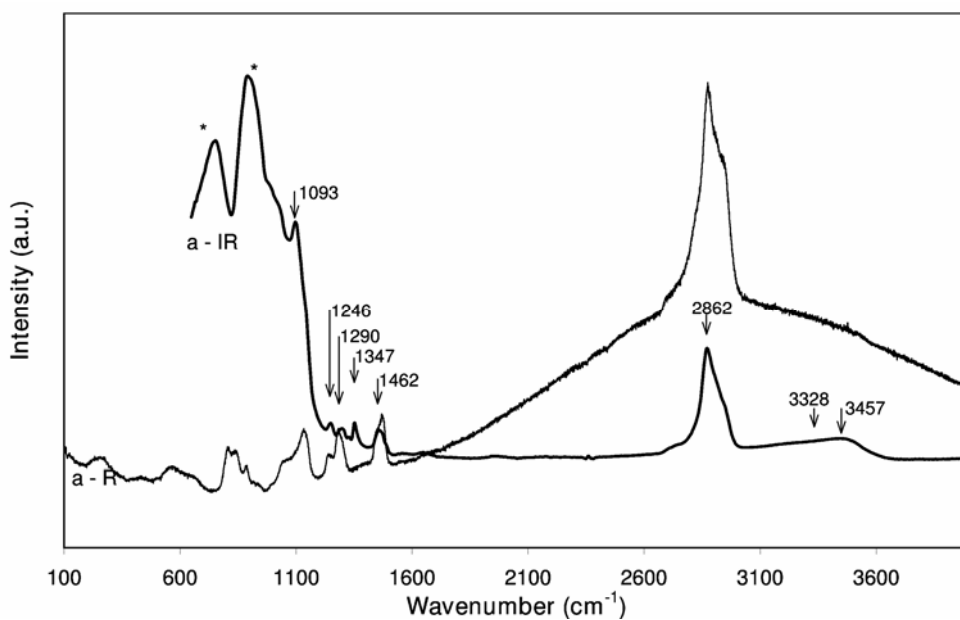


Fig. 1. Raman and FTIR spectra recorded at the same point of the as-deposited TiO<sub>2</sub>-PEG 600 (TiO<sub>2</sub>:PEG molar ratio of 1:1) composite film on a glass substrate. The peaks of the glass substrate are marked by asterisks

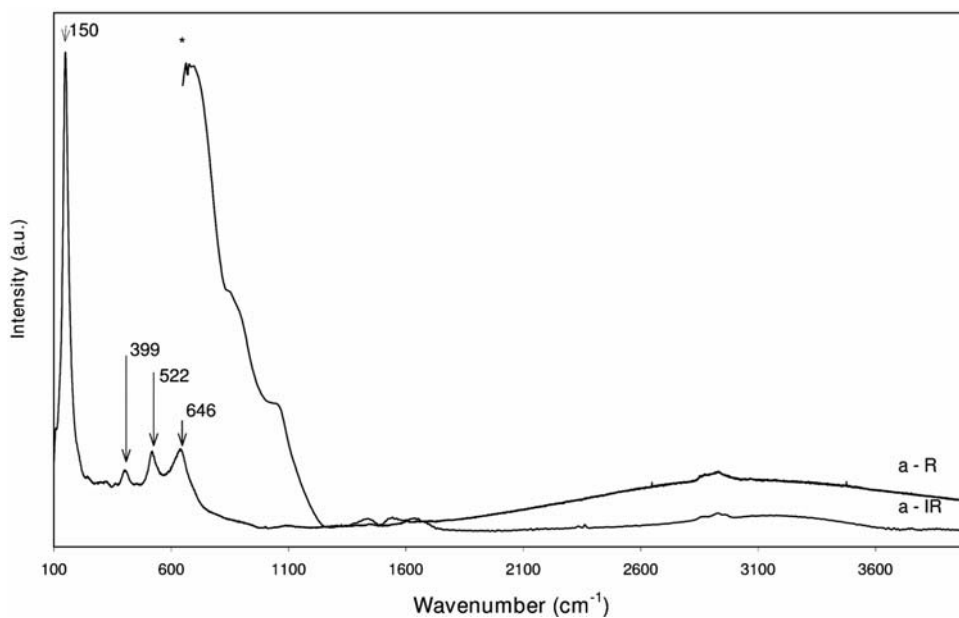


Fig. 2. Raman and FTIR spectra recorded at a single point of a TiO<sub>2</sub>-PEG 600 composite film on a glass substrate, treated at 90 °C in hot water for 1 hour. The peaks of the glass substrate are marked by an asterisk

### 3.2. Raman spectroscopy

Figure 3 shows the Raman spectra of samples prepared from PEG-free dipping solution and treated at 90 °C in hot water. After that, the films were annealed at the temperature ranging from 100 to 1000 °C. The Raman spectra of the films annealed up to 300 °C showed they were quasi-amorphous. The TiO<sub>2</sub> started to be transformed to anatase at 400 °C, and the transition was completed at 500 °C. Only typical features of anatase are present in the spectra until the temperature of the film reaches 1000 °C. At this temperature, a mixed anatase-rutile phase is seen. The formation of anatase nanocrystals was not observed in PEG-free TiO<sub>2</sub> even when the films were treated in hot water for more than 5 hours. Thus, it is evident that the formation of anatase nanocrystals with hot water treatment is initiated and accelerated by the addition of PEG to the dipping solution.

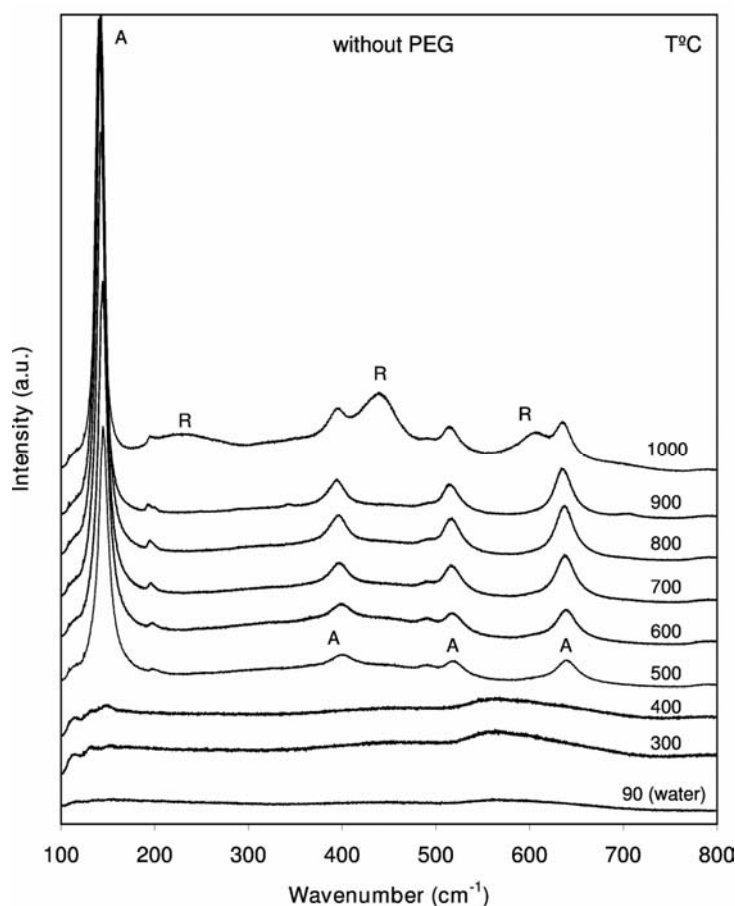


Fig. 3. Raman spectra of TiO<sub>2</sub> films prepared without PEG as a function of temperature; A and R indicate anatase and rutile, respectively

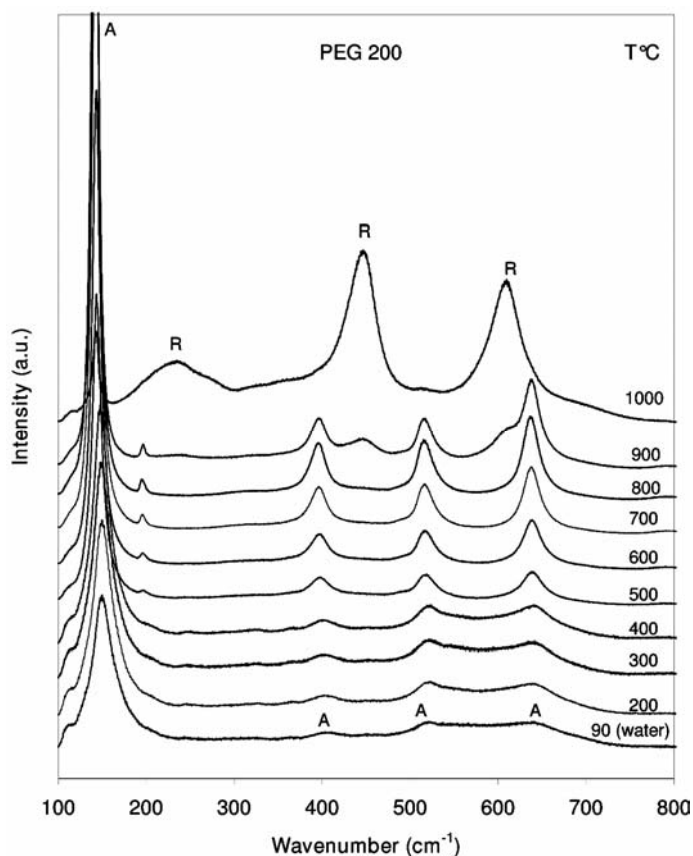


Fig. 4. Raman spectra of TiO<sub>2</sub> films prepared with PEG 200 as a function of temperature; A and R indicate anatase and rutile, respectively

Figures 4–6 show the Raman spectra of samples prepared in the presence of PEG of various molecular weights (200, 400 and 600) and treated at 90 °C in hot water. Subsequently, films were annealed at the temperatures ranging from 100 °C to 1000 °C. The crystallization to anatase was complete when the film was treated in hot water at 90 °C for 1 hour (Figs. 4–6). Only small differences are observed between the spectra. This indicates that there is no systematic effect of PEG molecular weight on the TiO<sub>2</sub> film. In films prepared with PEG 200 and 600, the anatase phase is stable up to 800 °C, followed by a partial transformation to rutile at 900 °C. This transformation is almost complete after annealing at 1000 °C (Figs. 4 and 6). Figure 5 shows that only a partial anatase-to-rutile transformation occurs at 1000 °C for samples prepared with PEG 400.

For samples containing PEG and annealed at low temperatures, the anatase Raman bands are blue-shifted and broadened with respect to the single-crystal spectrum. With increasing temperature, the frequency and width of the peaks tend towards single-crystal values. Using a phonon confinement model [19], it is possible to obtain

a rough estimate of the crystal size from the width and position of the main anatase Raman peak. In the sample prepared with PEG 200 and treated in hot water for 1 h, the anatase main Raman peak is centred at 151.5 cm<sup>-1</sup> (the bulk value being 144 cm<sup>-1</sup>), with a full width at half maximum (FWHM) of 23 cm<sup>-1</sup> (7 cm<sup>-1</sup> being the bulk value). This corresponds to the crystal size of 6.2 nm. For the films prepared with PEG 400 and PEG 600 and treated in the same way, the peak frequency is centred at 151 and 150.5 cm<sup>-1</sup> with the FWHM of 21.5 and 22 cm<sup>-1</sup>, corresponding to the crystal size of 8 and 7.4 nm, respectively. We can attribute such large shifts and broadening of the main Raman bands of the anatase phase mainly to the particle size effect [17, 20–23].

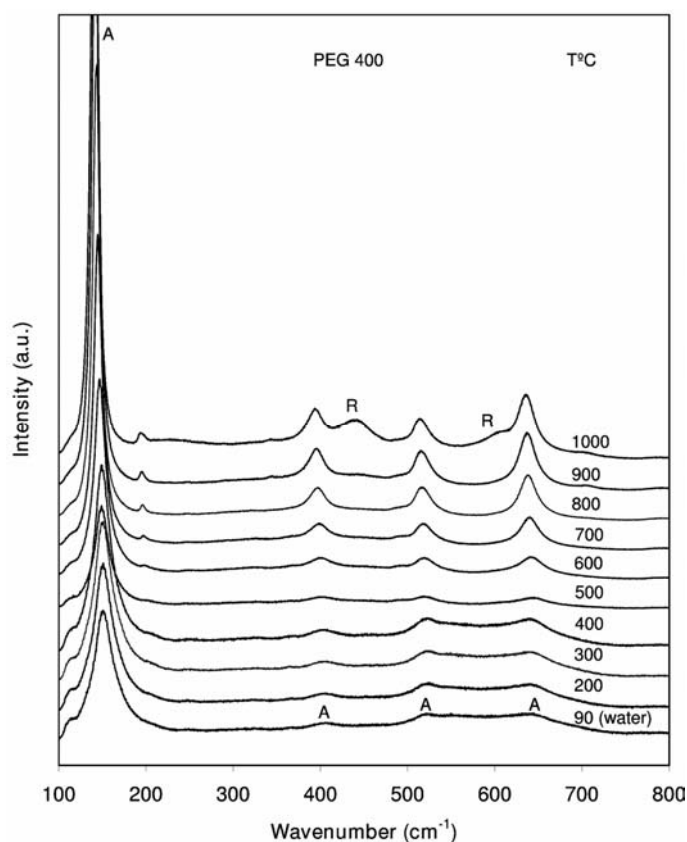


Fig. 5. Raman spectra of TiO<sub>2</sub> films prepared with PEG 400 as a function of temperature; A and R indicate anatase and rutile, respectively

However, the non-stoichiometry of anatase, which is likely to contain defects such as hydroxyl groups or oxygen vacancies as a result of the low temperature of synthesis (90 °C in hot water), is known to produce significant broadening and frequency shifts of the main anatase band [17]. Again, the evolution of the crystallite size is largely independent of the molecular weight of the PEG used in sample preparation.

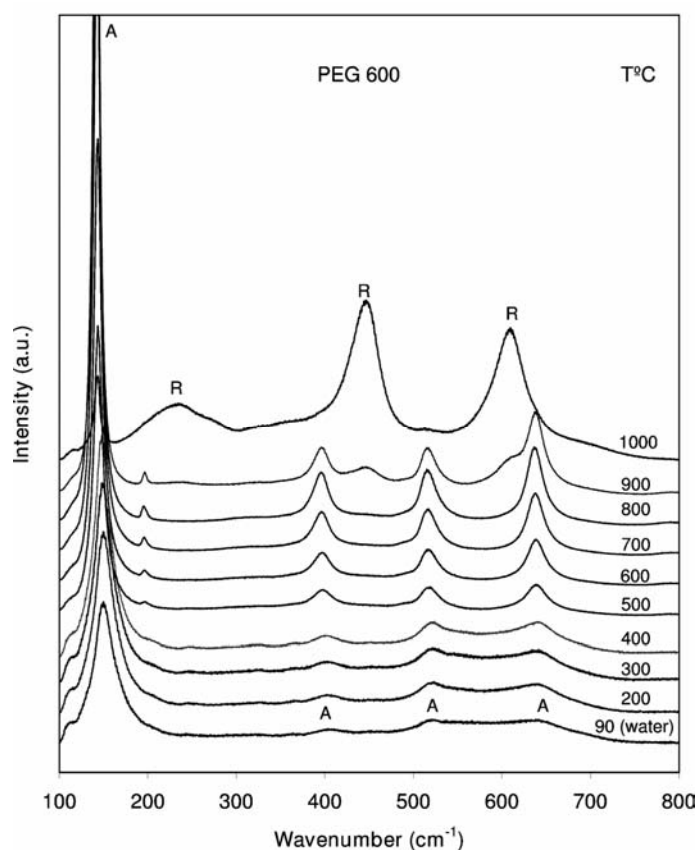


Fig. 6. Raman spectra of  $\text{TiO}_2$  films prepared with PEG 600 as a function of temperature; A and R indicate anatase and rutile, respectively

### 3.3. X-Ray Diffraction

Samples without PEG, prepared on glass slides at annealing temperatures not higher than 400 °C, show no signs of crystallization (Fig. 7). Samples without PEG prepared on vitreous silica substrates show anatase crystals. After annealing at 1000 °C, anatase crystals coexist with rutile. Enhancement of the (110), (220), and (330) peaks, at 19.35, 38.70 and 58.03 nm, indicates the preferred orientation of the rutile crystallites. A rocking centre measurement shows that these crystallites are aligned to within 6.5° FWHM with the substrate surface.

Samples prepared with PEG 200, PEG 400, and PEG 600 evolve in nearly identical ways upon heating (Figs. 8–10). The as-deposited films scatter X-rays below  $5 \text{ nm}^{-1}$ , as well as between 11 and  $18 \text{ nm}^{-1}$ . Treatment in water at 90°C eliminates most of this diffuse scattering, and leads to nanoscale anatase crystals. Annealing

after treatment in hot water leads to a sharper anatase (101) peak at  $17.85 \text{ nm}^{-1}$ . The anatase (200) peak at  $33.21 \text{ nm}^{-1}$  is the second prominent peak of this phase. The absence of the brookite (121) peak at  $21.67 \text{ nm}^{-1}$  indicates that brookite does not form. The XRD data are in good agreement with the Raman results discussed above. For the film prepared from PEG-free dipping solution, however, no anatase phase can be seen in the XRD pattern (Fig. 7) corresponding to  $400 \text{ }^\circ\text{C}$ . Generally, Raman scattering is more sensitive than X-ray diffraction to small quantities of anatase [24].

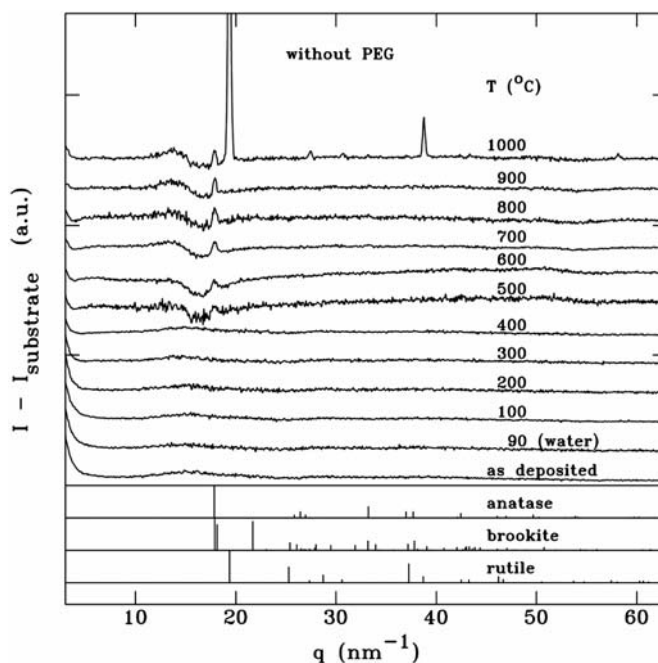


Fig. 7. X-ray scattering intensities of films without PEG as a function of the scattering vector. The scattering originating from an empty substrate was subtracted. The films were annealed at the indicated temperatures ( $100 \text{ }^\circ\text{C}$  and above). The powder scattering intensities for anatase, brookite, and rutile are shown at the bottom of the diagram

The evolution of crystal size is shown in Fig. 11. After treatment in hot water, the crystallite size is about  $5 \text{ nm}$ . Upon annealing at temperatures not higher than  $400 \text{ }^\circ\text{C}$ , crystallite size remains unchanged, increasing continuously to about  $19 \text{ nm}$  as the annealing temperature is raised to  $900 \text{ }^\circ\text{C}$ , followed by a (partial) transformation to rutile at  $1000 \text{ }^\circ\text{C}$ . The width of the anatase (101) peaks are, within experimental error, equal to the width of the anatase (200) peaks. This indicates that the peak width is indeed caused by small crystal size rather than strain. Considering the additional broadening effects in the Raman spectra, the crystallite sizes calculated from XRD and Raman are consistent. Furthermore, the evolution of the crystallite sizes is largely independent of the molecular weight of the PEG used in sample preparation.

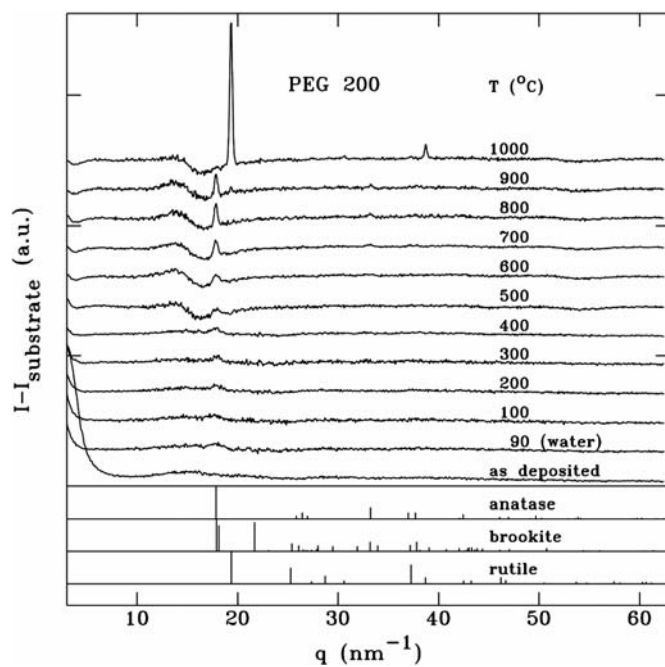


Fig. 8. X-ray scattering intensities of films with PEG 200 as a function of the the scattering vector

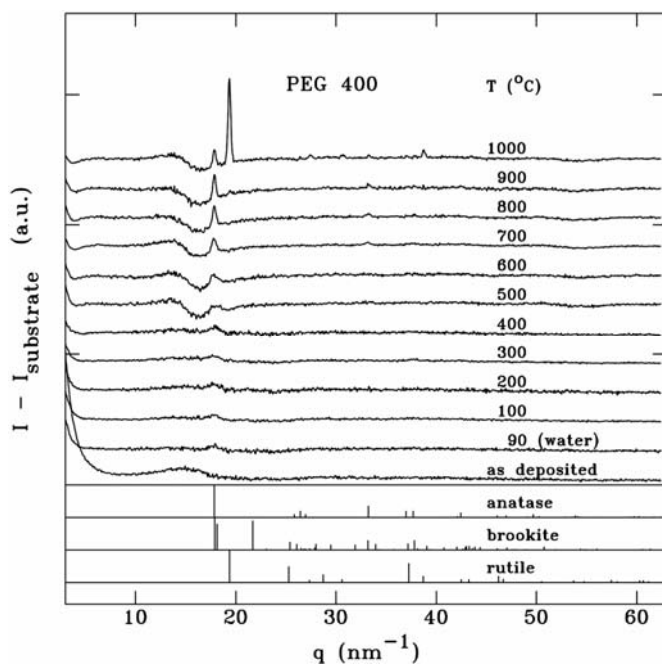


Fig. 9. X-ray scattering intensities of films with PEG 400 as a function of the scattering the vector

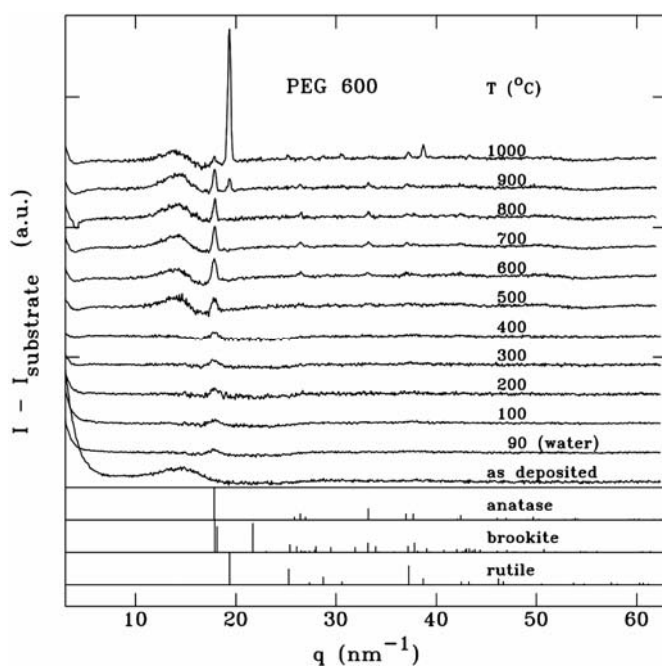


Fig. 10. X-ray scattering intensities of films with PEG 600 as a function of the scattering vector

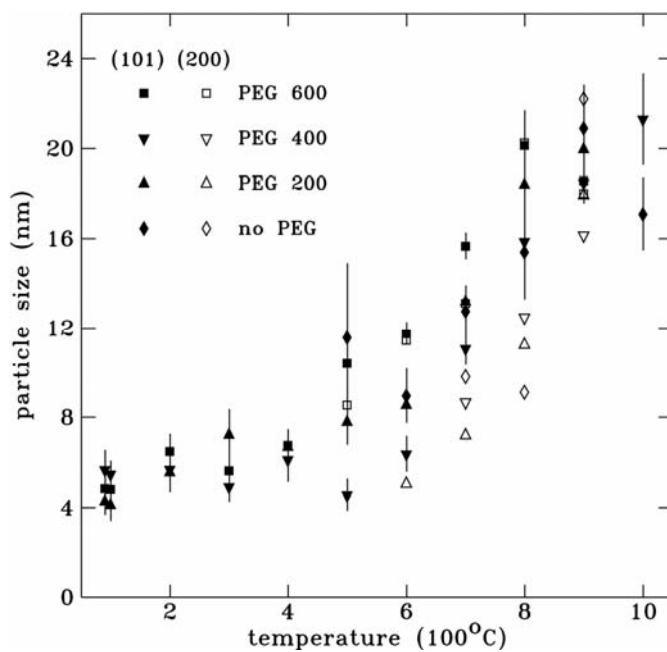


Fig. 11. The size of the anatase particles as a function of annealing temperature. For clarity, error bars are only shown for anatase (101) peaks

## 4. Conclusion

Transparent nanocrystalline anatase films have been synthesised by treating sol-gel TiO<sub>2</sub> samples containing PEG of different molecular weights in hot water. The maximum process temperature in this method was around 90 °C. The effect of PEG of different molecular weights on the crystallization of TiO<sub>2</sub> films and the anatase-to-rutile phase transition has been studied by Raman spectroscopy and XRD. The results indicate that crystallization was complete when PEG-containing films were treated in hot water at 90 °C for 1 hour. The films are composed of anatase crystallites with dimensions of about 5 nm. Upon annealing at temperatures not higher than 400 °C, the crystallite size remains unchanged. The anatase-to-rutile phase transition and crystallite sizes are independent of the molecular weight of the PEG used in sample preparation. The anatase phase was found to be stable up to 900–1000 °C, beyond which it transforms to highly oriented rutile crystallites. A film of nanometric anatase particles on a transparent substrate, stable against crystal growth at temperatures up to 400 °C, is a promising candidate for use in photocatalytic or photovoltaic devices at high temperatures.

### Acknowledgements

The financial support of New-Brunswick Innovation Foundation – Research Innovation Fund Innovation Capacity Development and Atlantic Innovation Fund (FIA) – in carrying out this work is gratefully acknowledged.

### References

- [1] BENNETT J.M., PELLETIER E., ALBRAND G., BORGOGNO J.-P., LAZARIDES B., CARNIGLIA C.K., SCHMELL R.A., ALLEN T.H., TUTTLE-HART T., GUENTHER K.H., SAXER A., *Appl. Opt.*, 28 (1989), 3303.
- [2] DESU S. B., *Mater. Sci. Eng.*, B13 (1992), 299.
- [3] GRATZEL M., *Comment. Inorg. Chem.*, 12 (1991), 93.
- [4] LOBL P., HUPPERTZ M., MERGEL D., *Thin Solid Films*, 251 (1994), 72.
- [5] HA H.K., YOSIMOTO M., KOINUMA H., MOON B., ISHIWARA H., *Appl. Phys. Lett.*, 68 (1996), 2965.
- [6] NATARAJAN C., NOGAMI G., *J. Electrochem. Soc.*, 143 (1996), 1547.
- [7] DJAOUED Y., BADILESCU S., ASHRIT P.V., BERSANI D., LOTTICI P. P., BRÜNING R., *J. Sol-Gel Sci. Tech.*, 24 (2002), 247.
- [8] GAO L., LI Q., SONG Z., WANG J., *Sensors and Actuators*, B71 (2000), 179.
- [9] TAKAO Y., IWANAGA Y., SHIMIZU Y., EGASHIRA M., *Sensors and Actuators*, B10 (1993), 229.
- [10] KIMER U., SCHIERBAUM K. D., GÖPEL W., LEIBOLD B., NICOLOSO N., WEPPNER W., FISHER D., CHU F., *Sensors and Actuators*, B1 (1990), 103.
- [11] SBERVEGLIERI G., DEPERO L. E., FERRONI M., GUIDI V., MARTINELLI G., NELLI P., PEREGO C., SANGALLETI L., *Adv. Mater.*, 8 (1996), 334.
- [12] MATSUDA A., KOTANI Y., KOGURE T., TATSUMISAGO M., MINAMI T., *J. Am. Ceram. Soc.*, 83 (2000), 229.
- [13] Powder Diffraction File, ICDD, JCPDS, Swarthmore, PA, 1988 (Card Nos. 21-1272, 21-1276 and 29-1360).

- [14] BERTAUD E., *International Tables for X-ray Crystallography*, Kynoch Press, Birmingham, England, 1968, p. 318.
- [15] DJAOUED Y., BRÜNING R., BERSANI D., LOTTICI P.P., BADILESCU S., *Mater. Lett.* in print.
- [16] SIFFERT B., LI J.F., *Colloid. Surf.*, 40 (1989), 207.
- [17] PARKER J.C., SIEGEL R.W., *J. Mater. Res.*, 5 (1990), 1246.
- [18] MATSUDA A., KATAYARNA S., TSUNO T., TOHGE N., MINAMI T., *J. Am. Ceram. Soc.*, 75 (1990), 2217.
- [19] BERSANI D., LOTTICI P.P., XING-ZHAO D., *Appl. Phys. Lett.*, 72 (1998), 73.
- [20] IIDA Y., FURUKAWA M., KATO K., MORIKAWA H., *Appl. Spectr.*, 51 (1997), 673.
- [21] BERSANI D., ANTONIOLI G., LOTTICI P.P., LOPEZ T., *J. Non-Cryst. Solids*, 232–234 (1998), 175.
- [22] POTTIER A., CASSAIGNON S., CHANÉAC C., VILLAIN F., TRONC E., AND. JOLIVET J.-P., *J. Mater. Chem.*, 13 (2003), 877.
- [23] BOBOVICH Y.S., TSENER M.Y., *Opt. Spectrosc.*, 53 (1982), 332.
- [24] GAYNOR A.G., GONZALEZ R.J., DAVIS R.M., ZALLEN R., *J. Matter. Res.*, 12 (1997), 1755.

*Received 6 June 2004*

*Revised 11 June 2004*

## **Raman investigation of hybrid polymer thin films**

MARCIN GNYBA<sup>1\*</sup>, MIKKO KERÄNEN<sup>2</sup>,  
MARCIN KOZANECKI<sup>3</sup>, BOGDAN B. KOSMOWSKI<sup>1</sup>

<sup>1</sup>Gdańsk University of Technology, Department of Optoelectronics,  
ul. Narutowicza 11/12, 80-952 Gdańsk, Poland

<sup>2</sup>VTT Electronics, Kaitoväylä 1, P.O. Box 1100, FIN-90571 Oulu, Finland

<sup>3</sup>Technical University of Łódź, Department of Molecular Physics,  
ul. Żeromskiego 116, 90-924 Łódź, Poland

Raman spectroscopic studies were carried out for hybrid polymer thin films prepared for photonic applications by the sol-gel technology. Our aims were to analyse the ability of the Raman method to estimate the efficiency of the main reactions of the sol-gel process and to provide information about the chemical composition of the films as well as their thickness, profile, and quality. The difficulties in measurement such as low level of Raman signals, difficulties in data analysis caused by the complex structure of the materials, and the influence of interfering signals, are discussed. The application of Raman microscopy for characterising films based on 3-glycidoxypropyl-trimethoxysilane (GPTS), methacryloxypropyl-trimethoxysilane (MPTS), and 3-aminopropyl-trimethoxysilane (APTES) is presented. The efficiencies of reactions of inorganic and organic polymerisation were measured and their products have been identified. The influence of the excitation beam wavelength as well as the type of substrate on the Raman spectra was investigated. Moreover, two-dimensional Raman mapping enabled us to record the thickness profiles of the deposited structures and to detect their defects.

*Key words: Raman spectroscopy; optical materials; hybrid polymers; thin films*

### **1. Introduction**

A group of inorganic-organic hybrid polymers known as Organically Modified Silanes (ORMOSILs) has been recently developed for photonic applications. These materials are prepared with a sol-gel technology and deposited as thin-film structures. The main reason for developing hybrid polymers is their wide variety of controllable

---

\*Corresponding author, e-mail: mgnyba@eti.pg.gda.pl.

optical, mechanical, and electrical properties, which can be regulated by proper molecular design of the precursors used. Hybrids have better thermal stability, scratch resistance, and higher hardness than organic materials [1, 2]. In comparison to inorganic materials, they have better flexibility and a very good workability.

Hybrids can be used in photonics to manufacture planar waveguides, lenses, Bragg gratings, and components for integrated optics. Moreover, dielectric layers, coatings, and packaging are produced from these materials. Research on applying them in optical fibre sensors (including bio-sensors) and solid-state lasers is underway [1]–[7].

Sol-gel manufacturing of hybrid polymer thin films for photonic applications requires high precision, which stimulates the search for effective diagnostic tools. One of them is Raman spectroscopy, which enables the measurement of important chemical and physical properties, including chemical composition, molecular orientation, crystallinity, temperature, and the thickness profile. It also allows the detection of defects. In the case of complex materials such as ORMOSILs, however, Raman investigation of thin transparent films is a difficult task. The applications of Raman microscopy in the investigation of hybrid polymer thin films that have been presented so far include: characterising coatings [4], recording the depth profiles of coatings [5, 6], investigating thin-film materials for waveguide applications [7], and two-dimensional mapping of Bragg gratings produced from dye-doped ORMOSIL thin films [8]. Raman spectroscopic investigation of a sol-gel process covering all steps, from precursors through gelation to thin-film structure deposition and development, has also been reported [6, 7].

In spite of the intensive research conducted in this field, not all ORMOSIL materials and devices have been investigated in a sufficient depth. Moreover, the number of reported Raman optics configurations used in the studies of hybrid polymer thin films [4]–[9] is limited. In this paper, the most important problems of Raman investigations of sol-gel-derived thin films are outlined and the results of selected hybrid polymer film investigations are presented. The main metrological aims of the presented research were to set up an optical system providing a high collection efficiency of the Raman signal from thin transparent films and to select the excitation wavelength and power level of the laser that minimizes interfering signals and does not damage the samples.

## 2. Raman systems for thin film investigations

Raman spectroscopy is based on the recording and spectral analysis of radiation scattered inelastically by the molecules of the investigated object [9]. As a result of the interaction between monochromatic light and dipoles induced in oscillating molecules, the spectrum of scattered light may contain wavelengths different than those of the incident beam ( $\lambda_0$ ). The difference, referred to as Raman shift, is related to the characteristic oscillation frequencies of the molecule, i.e. the vibrations of a single

molecular bond or larger fragment of a polymer network. For a given excitation wavelength  $\lambda_0$ , the Raman intensity can be expressed as [9]:

$$I_R = I_L \sigma K P C \quad (1)$$

where:  $I_R$  – measured Raman intensity [photons per second],  $I_L$  – laser excitation intensity [photons per second],  $\sigma$  – absolute Raman cross-section [ $\text{cm}^2$  per molecule],  $K$  – a constant accounting for the measurement parameters,  $P$  – sample path length [cm],  $C$  – concentration [molecules per  $\text{cm}^3$ ].

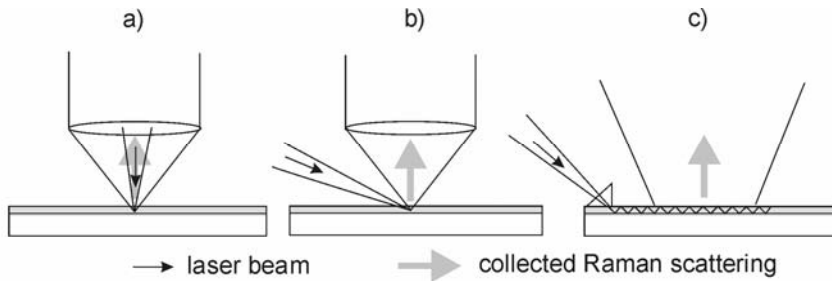


Fig. 1. Optical setups for Raman investigations of thin transparent films: a) the backscattering configuration, b) glancing-incidence configuration, c) waveguide configuration

One of the important problems encountered in Raman investigations of sol-gel derived thin films is a low level of useful Raman signals, which is the result of a small path length  $P$  in the sample. Optical setups used in the studies of thin films are presented in Fig. 1. In the most common one – the backscattering configuration shown in Fig. 1a – the angle between the excitation beam, incident on the investigated object, and the collected Raman beam is equal to  $180^\circ$ . However, a typical optical backscattering configuration does not provide sufficient sensitivity when the film thickness is below  $10 \mu\text{m}$  [10]. One solution that can increase the sensitivity of the measurement system is to modify the backscattering setup by using microscope optics. Microscopic systems enable much thinner films to be investigated and provide better spatial resolution ( $\sim 1 \mu\text{m}$ ) than the typical backscattering configuration ( $\sim 40 \mu\text{m}$ ) [10]. Moreover, the use of additional pinholes creates a truly confocal system, in which Raman spectra can be recorded as a function of depth [5, 6]. The main disadvantage of microscopic setups is a small distance between the optics and sample (usually a few millimetres), which limits the applications of the setup mainly to *ex-situ* measurements.

The glancing-incidence configuration (Fig. 1b), can be used to increase the effective path length  $P$ . This setup, however, is more difficult to adjust as the laser beam must be precisely focused on the sample at the focal point of the collecting optics. Moreover, the efficiency of Raman signal collection depends on the angle between the laser beam and collecting direction [10].

The Raman setup shown in Fig. 1c, referred to as a waveguide configuration, is based on a significant increase of the effective path length  $P$  by internal reflection of

the laser beam inside the investigated thin-film structure. The intensity of the Raman signal in the waveguide configuration can be even  $3 \cdot 10^3$  times higher than in the typical backscattering configuration [10]. The main drawbacks of the waveguide setup are: moderate spatial resolution and strict requirements of repeatability for launching the excitation laser beam into the thin film structure.

The level of the Raman scattering signal depends on the excitation wavelength. For  $\lambda_0$  far from the molecule absorption band, the intensity of the Raman signal is inversely proportional to  $\lambda_0^4$ . Therefore, the application of a VIS or UV laser as the excitation source should be more effective than an IR one in terms of Raman scattering. The practical efficiency of Raman scattering versus excitation wavelength, however, may also depend on the dimensions and crystallinity of the investigated structures. Moreover, strong interfering signals originating from laser-induced fluorescence in the organic part of the polymer, Raman scattering in the substrate, and external illumination must also be taken into account. The fluorescence is the strongest for the excitation wavelength from 270 to 700 nm [11] but its level can be different for various materials. As a result, the power and wavelength of the excitation beam as well as the type of substrate must be selected experimentally for each set of the samples.

### 3. Experimental

#### 3.1. Thin film preparation

Hybrid polymer thin films based on commercially available precursors (3-glycidoxypropyl-trimethoxysilane (GPTS), methacryloxy-propyltrimethoxysilane (MPTS), and 3-aminopropyl-trimethoxysilane (APTES)) were synthesised and investigated. The precursors were mixed with solvents and water and, after distillation and filtering, the obtained gels were deposited and stirred on substrates. Two types of substrates were used for tests: silicon and borosilicate glass (BSG). Films were subsequently baked and hardened. Reflection spectroscopy as well white-light profilometry and prism-coupling refractometry were used to measure the thickness and refractive index of the deposited films. Detailed parameters of the films are presented in Table 1.

Table 1. Investigated thin films

System of silane precursors	Refractive index $n$	Film thickness range [ $\mu\text{m}$ ]	Thickness determination method	Type of substrate
GPTS/MPTS	1.50–1.54	3.070–4.195	spectroscopic reflectometry	borosilicate glass
GPTS/APTES	1.48–1.50	3–4	white-light profilometry	borosilicate glass
GPTS/APTES	1.48–1.50	3–4	white-light profilometry	silicon

### 3.2. The Raman system

During the experimental part of the research presented in this paper, thin film samples were measured using a microscopic Raman system, which is shown in Fig. 2.

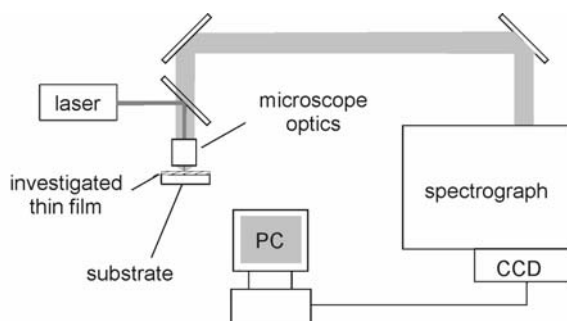


Fig. 2. Micro-Raman system using backscattering configuration

Preliminary investigations were conducted in order to select a suitable excitation wavelength  $\lambda_0$ . Three laser beams were tested on GPTS/MPTS-based thin films: 632.8 nm from a He-Ne laser and 488 nm and 514.5 nm from an Argon-Ion laser. A Raman microscope (Jobin Yvon T64000), equipped with a 100 $\times$  objective, was used for these wavelengths. Additional tests were carried out on hybrid polymer thin films using an excitation wavelength of 785 nm (dispersive Kaiser Raman Hololab 5000 spectrometer, equipped with an Olympus microscope) and 257 nm (Renishaw spectrometer 1000 UV, equipped with a microscope). The power on samples was a few mW. Beams were focused on the surface of the films. The samples were inspected by optical microscopy after measurements. No trace of damage was observed for excitation in the VIS and NIR ranges, while the application of a UV beam caused photochemical reactions and consequential damage to the samples, which was detected by optical means.

The Raman scattering signal from the substrate was the only one recorded when  $\lambda_0$  was 632.8 nm or 785 nm, although a power level of a few mW should be sufficient for polymer films [11]. Therefore, an absence of a signal from the film for these excitation wavelengths was probably caused by the insufficient efficiency of Raman signal generation in the polymer structures (as thin as 3–4  $\mu\text{m}$ ) and by problems with focusing the beam on the sample.

Raman spectra of ORMOSIL films were recorded for a  $\lambda_0$  of 488 nm but the sensitivity of the measurements was limited by fluorescence. The spectra of GPTS/MPTS-based films deposited on BSG, recorded by a Raman microscope with  $\lambda_0$  equal to 488 nm and 514.5 nm are shown in Fig. 3.

A wide band between 2850 and 2980  $\text{cm}^{-1}$ , assigned to the stretching vibrations  $\nu(\text{CH})$ ,  $\nu(\text{CH}_2)$ , and  $\nu(\text{CH}_3)$ , can be observed in both spectra. Other strong peak at 456  $\text{cm}^{-1}$  originates from  $\delta(\text{Si-O-Si})$  bending mode in the substrate and inorganic

network of polymers [12]. The intensity ratio of the bands at 2850–2980  $\text{cm}^{-1}$  and 456  $\text{cm}^{-1}$  is higher for the excitation of 488 nm than 514.5 nm. We think that the

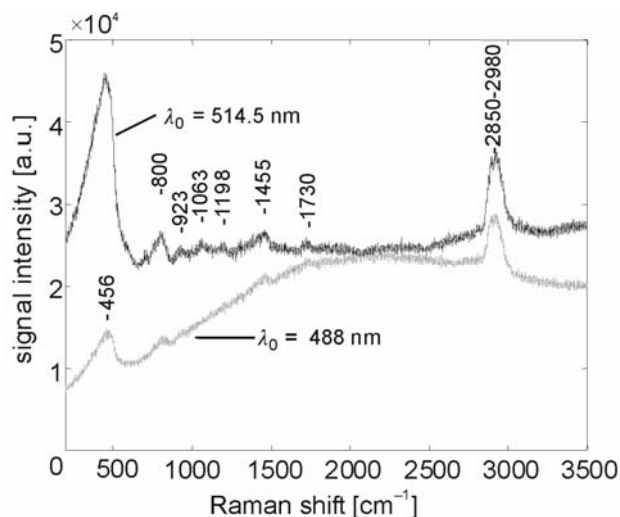


Fig. 3. Raman spectra of samples based on systems of GPTS and MPTS, recorded at various excitation wavelengths  $\lambda_0$

488 nm beam is slightly better focused on the film than the 514.5 nm one, since it has a smaller diffraction-limited spot size. Due to fluorescence, however, more Raman peaks were recorded for  $\lambda_0$  equal to 514.5 nm (see Fig. 3), and this wavelength was assumed to be optimal for ORMOSIL film investigations. Measurements were made in the range of 200–3500  $\text{cm}^{-1}$  with a spectral resolution of 4  $\text{cm}^{-1}$ . A 100 $\times$  objective was used during investigation of the chemical composition, while a confocal system with a 50 $\times$  objective and a pinhole with a diameter of 100  $\mu\text{m}$  were sufficient for Raman mapping.

## 4. Results

### 4.1. Chemical composition of the films

One of main objectives of the micro-Raman measurements presented in this paper was to determine the chemical composition of sol-gel derived thin films after deposition and subsequent procedures, i.e. heating, hardening, and structure development.

Micro-Raman spectra of GPTS/MPTS thin film samples deposited on BSG are shown in Fig. 4. The strongest bands, at 2850–2980  $\text{cm}^{-1}$  and 456  $\text{cm}^{-1}$ , are assigned to stretching vibrations ( $\nu(\text{CH})$ ,  $\nu(\text{CH}_2)$ , and  $\nu(\text{CH}_3)$ ) and  $\delta(\text{Si-O-Si})$  bending, respectively. The weaker band at 1455  $\text{cm}^{-1}$  is probably due to asymmetric bending

( $\delta(\text{CH})$ ,  $\delta(\text{CH}_2)$ , or  $\delta(\text{CH}_3)$ ), but deformations of  $\text{O}-\text{CH}_2$  bonds or scissoring of hydrogen atoms in  $\text{CH}_2$  may also contribute to its intensity. The bands at  $923\text{ cm}^{-1}$ ,  $1063\text{ cm}^{-1}$ , and  $1198\text{ cm}^{-1}$  are due to the  $\text{C}-\text{C}$  skeletal vibration,  $\text{CH}_2$  vibrations, or  $\nu(\text{Si}-\text{O})$  stretching in the inorganic network. The peak at  $1299\text{ cm}^{-1}$  is due to  $\nu_w((-\text{CH}_2)_n-)$  wagging [12].

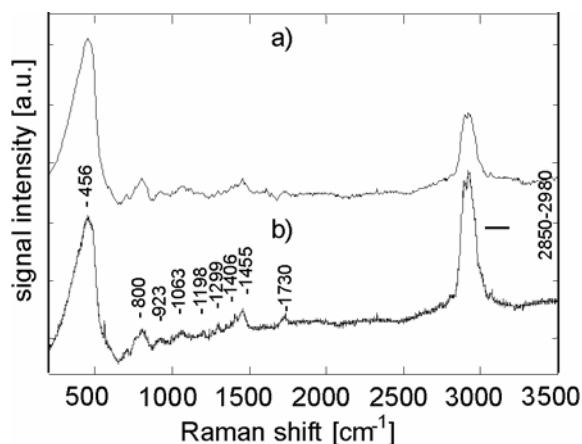


Fig. 4. Micro-Raman spectra of thin films based on systems of GPTS and MPTS; thickness: a)  $3\text{ }\mu\text{m}$ , b)  $4\text{ }\mu\text{m}$

In the spectra of investigated GPTS/MPTS-based thin films, the peaks assigned to epoxy ring breathing ( $1256\text{ cm}^{-1}$ ) and  $\nu(\text{C}=\text{C})$  stretching ( $1635\text{ cm}^{-1}$ ) were observed as weak shoulders. The peak at  $1730\text{ cm}^{-1}$  is assigned to  $\nu(\text{C}=\text{O})$  stretching. Contrary to that observed in MPTS and sol spectra [7], the intensity of this peak is much higher than the band assigned to  $\nu(\text{C}=\text{C})$ . This means that most of the epoxy rings of GPTS and double  $\text{C}=\text{C}$  bonds of MPTS were opened and replaced by single bonds, allowing an organic network to be formed. Moieties originating from both precursors behave like a *network former*. The  $\text{C}=\text{O}$  double bonds of MPTS were not opened and did not participate in network formation.

Regarding other basic reactions in the organic part of various sol-gel derived materials, the following Raman peaks can be important in their studies:  $1640\text{--}1650\text{ cm}^{-1}$ , assigned to  $\text{C}=\text{N}$  bonds and the doublet at  $3310\text{--}3370\text{ cm}^{-1}$ , which is due to  $\text{N}-\text{H}$  bonds stretching [12].

#### 4.2. Influence of the substrate

As was shown before, the spectra of thin films may contain peaks originating from the substrate, which may introduce ambiguity in data analysis. One example is the assignment of the peak at  $456\text{ cm}^{-1}$  ( $\text{Si}-\text{O}-\text{Si}$  network vibrations) in the spectrum of hybrid polymers deposited on a glass substrate. Due to this, the influence of the substrate on Raman measurements was studied by the comparison of the spectra of GPTS/APTES-based thin films deposited on a BSG and silicon substrate.

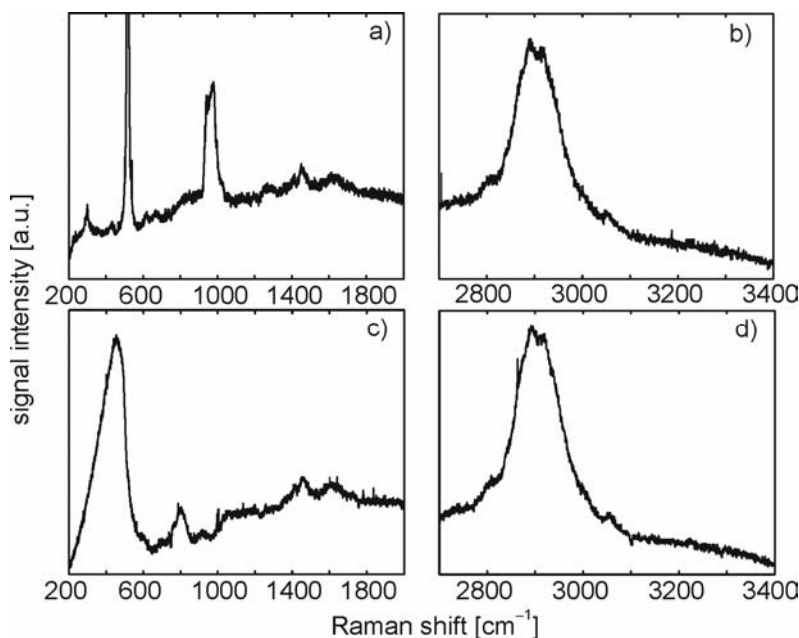


Fig. 5. Micro-Raman spectra of thin films based on systems of APTES and GPTS deposited on: a), b) silicon substrate, c), d) borosilicate glass substrate

The comparison of spectra in Fig. 5 enables the proper assignment of the band at  $456\text{ cm}^{-1}$  in the spectra of films deposited on BSG. It can be seen that the  $\text{SiO}_2$  network in the substrate is the main origin of this peak for the investigated samples. A small peak at  $456\text{ cm}^{-1}$  for films deposited on silicon shows the intensity of the Raman signal originating from the inorganic part of the sol-gel material.

### 4.3. Profile of thickness

Equation (1) enables thin film thickness to be estimated. For hybrid polymers, this information can be obtained from the ratio of the intensities of the two strongest peaks:  $2850\text{--}2980\text{ cm}^{-1}$  (assigned to the organic part of the film) and  $456\text{ cm}^{-1}$  (assigned mostly to the substrate and partially to the inorganic part of the film). For the example shown in Fig. 4, the ratio is lowest for the thinnest sample (b) and highest for the thickest one (a). Good agreement was obtained with results of thickness measurements made by the spectroscopic system Filmetrics F20. Due to their relative nature, however, Raman measurements can be used to complement profilometry measurements or to monitor changes of the film thickness during manufacturing rather than for absolute thickness measurements. For Raman measurements of thickness, an additional pre-calibration procedure conducted by another method, e.g. spectroscopic reflectometry, is required. Moreover, in practice the dependence of the Raman signal on the thickness may be not linear due to changes in the excitation laser focal tube. In

general, additional calculation must be carried out to take into account the influence of changes of the refractive index at air/film and film/substrate interfaces on the dimensions of the focal tube [5]. In the case of the investigated hybrids deposited on BSG, the difference between the refractive indices of the film and substrate are so low (see Table 1) that despite differences between film thicknesses for various samples, the focal tubes can be assumed to be the same. Consequently, additional calculations are not required.

Additional studies were conducted on using micro-Raman mapping to investigate the thickness profiles of thin films. These measurements could be particularly useful in investigation of integrated optics components. Within the frame of research presented in this paper, Raman images were recorded for planar waveguide structures made from hybrid material based on a system of GPTS/APTES deposited on BSG substrate. Thickness profiles were recorded as two-dimensional distributions of the intensity of the band at  $2850\text{--}2890\text{ cm}^{-1}$  (assigned to  $\nu(\text{CH})$ ,  $\nu(\text{CH}_2)$ , and  $\nu(\text{CH}_3)$  stretching vibrations). The following investigations were made by Raman microscopy in the mapping mode: structure shape, edge quality, and detection of structural defects.

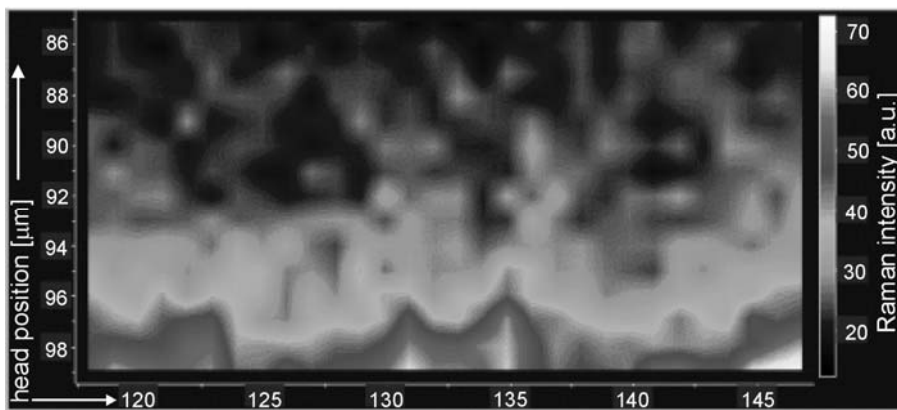


Fig. 6. The image of the edge of an investigated thin-film structure recorded using Raman mapping of the line assigned to C–H bonds

A Raman image of the edge of the investigated waveguide structure is presented in Fig. 6. In the image, the shape of the structure and the thickness distribution are presented by a grey colour scale related to the amount of C–H bonds originating from the organic part of the material. It can be noticed that the edge of the waveguide structure is not sharp and that there are small amounts of sol-gel material outside the predicted area of the waveguide. For photonic applications, the quality of edges may significantly determine the acceptable distance between neighbouring waveguides and cross talks between them.

A Raman image of a waveguide cross-section is shown in Fig. 7. Such a map of the intensity of the Raman band assigned to C–H bonds enables the dimensions and thickness profile of thickness of the path to be determined. Moreover, a defect in the waveguide path

with a diameter of about  $2\ \mu\text{m}$  was detected. The results of waveguide dimensions and profile thickness measurements obtained by microscopic Raman 2-D mapping were confirmed by optical microscopy (c.f. Fig. 7) and white-light profilometry. As Raman micro-

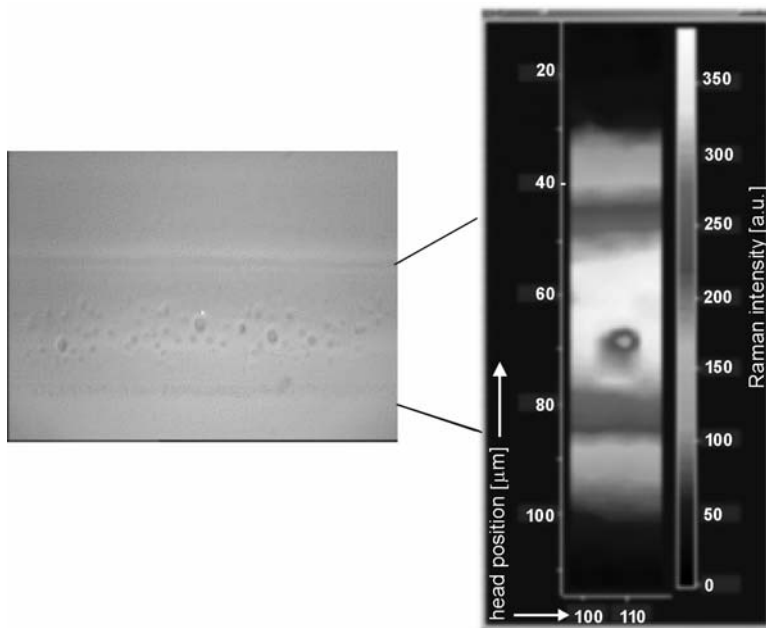


Fig. 7. Microscopic (left) and micro-Raman (right) images of the cross-section of a sol-gel derived waveguide structure

imaging is based on the detection of chemical bonds (C–H in this particular case), it can be treated as a complementary technique to optical microscopy, spectroscopic reflectometry, and white-light profilometry, which are all methods that are based on the investigation of optical properties, e.g. transparency, reflectance, and refractive index.

## 5. Conclusions

Raman spectroscopy proved to be a useful tool in the diagnostics of hybrid polymer thin films. The following Raman measurements were made for thin-film materials based on GPTS/MPTS and GPTS/APTES systems and sol-gel-derived planar waveguide structures: molecular composition and homogeneity, thickness distribution, device shape, structure profile, and edge quality. Moreover, the detection of defects was demonstrated. Good agreement between Raman and other methods of imaging was obtained.

The problems concerning the application of Raman spectroscopy to sol-gel derived hybrid polymer thin films were discussed in this paper. They include: configur-

ing the excitation and collecting optics, selecting the excitation power and wavelength, the influence of the substrate, and data analysis. The comparison of the spectra recorded in various conditions shows that the Raman microscopic measurement system with the excitation laser beam of 514.5 nm and a few mW is an effective tool in investigating sol-gel-derived hybrid polymer thin films thicker than 0.5  $\mu\text{m}$ . *Ex-situ* microscopic investigations presented herein will be the basis for further research. Selecting the optimal wavelength and sufficient power of the excitation beam (subchapter 3.2), studies on the influence of the type of substrate (subchapter 4.2), and analysing optical systems for Raman spectroscopy (chapter 2) will be used during the development of a Raman system for monitoring film deposition and following steps *in-situ*. On-line measurements performed with this system will enable the process to be optimised in real time.

#### Acknowledgements

This research was supported by the Gdańsk University of Technology (Faculty of Electronics, Telecommunication and Informatics), Łódź University of Technology, VTT Technical Research Centre of Finland and State Committee for Scientific Research (Polish KBN- project No. 4 T11B 062 25 conducted in years 2003–2005).

#### References

- [1] POPALL M., DABEK A., ROBERTSSON M., GUSTAFSSON G., HAGEL O.-J., OLSOWSKI B., BUESTRICH R., CERGEL L., LEBBY M., KIELY P., JOLY J., LAMBERT D., SCHAUB M., REICHL H., 48th IEEE Electronic Components and Technology Conference, 1998, 1018.
- [2] SEDDON A., IEE Colloquium on Sol-Gel Materials for Device Applications, 5 (1998), 6/1.
- [3] RANTALA J., PENNER R., HONKANEN S., NORDMAN N., NORDMAN O., VÄHÄKANGAS J., FALLAHI M., PEYGHAMBARIAN N., Proc. SPIE Conference on Organic-Inorganic Hybrid Materials for Photonics 3469, (1998), 30.
- [4] QUE W., SUN Z., ZHOU Y., LAM Y., CHENG S., CHAN Y., KAM C., Mater. Lett., 42 (2000), 326.
- [5] BAIA L., GIGANT K., POSSET U., PETRY R., SCHOTTNER G., KIEFER W., POPP J., Vib. Spectrosc., 29 (2002), 245.
- [6] POSSET U., GIGANT K., SCHOTTNER G., BAIA L., POPP J., Opt. Mater., 26 (2004), 173.
- [7] GNYBA M., KERÄNEN M., KOZANECKI M., BOGDANOWICZ R., KOSMOWSKI B., WROCYŃSKI P., Optoelectron. Rev., 10 (2002), 137.
- [8] MARINO I.G., BERSANI D., LOTTICI P.P., Optical Materials, 15 (2001), 279.
- [9] PELLETIER M., *Analytical Applications of a Raman Spectroscopy*, Blackwell Science, Oxford, 1999.
- [10] GARDINER D., GRAVES P., *Practical Raman Spectroscopy*, Springer-Verlag, Berlin, 1991.
- [11] KOENIG J.L., *Spectroscopy of Polymers*, Elsevier, New York, 1999.
- [12] LIN-VIEN D., COLTHRUP N., FATELEY W., GRASSELLI J., *The Handbook of Infrared and Raman Characteristic Frequencies of Organic Molecules*, Academic Press Inc., San Diego, 1991.

Received 23 July 2004

Revised 3 December 2004

## Raman system for monitoring dye doping to hybrid polymer network

MARCIN GNYBA<sup>1\*</sup>, MIKKO KERÄNEN<sup>2</sup>

<sup>1</sup>Gdańsk University of Technology, Department of Optoelectronics,  
ul. Narutowicza 11/12, 80-952 Gdańsk, Poland

<sup>2</sup>VTT Electronics, Kaitoväylä 1, P.O. Box 1100, FIN-90571 Oulu, Finland

Being a relatively low-temperature technique, the sol-gel technology enables the synthesis of hybrid polymers doped by organic dyes. In order to ensure the required properties of the final product, however, the mixing of sol and dye must be strictly controlled to avoid unwanted chemical reactions between them. Raman spectroscopic *in-situ* monitoring of the process was used to address this problem. Problems encountered in spectroscopic studies of non-transparent dye-doped sols, arising from intensive scattering, attenuation of the Raman signal inside the investigated material, and fluorescence induced by the laser beam, are discussed. The Raman measuring system constructed for the research presented in this paper uses a diode laser and a compact spectrometer connected to a reaction glass vessel by a fibre optic probe. Proper selection of the excitation beam wavelength and suitable design of the opto-mechanical setup results in an increase of the Raman signal and improved rejection of interfering signals. The system presented does not require access inside the vessel. *In-situ* monitoring was carried out for the process conducted at room temperature and up to 87 °C. As the intensity of the Raman bands assigned to the dye did not change during the process, it can be concluded that dye does not decompose.

Key words: *Raman monitoring; dye doped materials; sol-gel*

### 1. Introduction

Due to its relatively low temperature, the sol-gel process enables the inclusion of large organic particles, i.e. dyes or antigens, into a hybrid organic-inorganic polymer network. The doping procedure of sol by the functional particles, however, must be strictly controlled to avoid unwanted chemical reactions and, consequently, their decomposition. This requirement stimulates the search for effective diagnostic tools for *in-situ* monitoring of the synthesis process of doped materials.

---

\*Corresponding author, e-mail: mgnyba@eti.pg.gda.pl.

The main aim of the research presented in this paper was to apply Raman spectroscopy to studies of doping hybrid polymers with dye particles. The procedure of mixing the dye, dissolved in acetone, with the sol was the subject of real-time Raman monitoring. The main objective of this investigation was to make sure that no chemical reaction takes place between the sol and dye and that the latter is not being decomposed during the mixing. The investigation of dye-doped sols, usually non-transparent, is a difficult metrological task due to scattering and attenuation of the Raman signal inside the material investigated. Moreover, a strong fluorescence signal induced in the organic part of the material by the laser beam must be taken into account [1].

## 2. Experimental

### 2.1. Investigated sol-gel process

The sol was prepared using the following precursors: glycidyloxypropyltrimethoxysilane (GPTS), methacryloxypropyltrimethoxysilane (MPTS), 2-hydroxyethyl-methacrylate (HEMA), tetramethoxysilane (TMOS), and aluminium-tri-sec-butoxide ( $\text{AlOBU}_3$ ). The dye – commercially available NIR-absorbing IR165 – was dissolved in acetone and subsequently mixed with the sol. A two-neck 50 ml glass vessel and a smaller, one-neck 10 ml vessel were used in the experiments. The sol-gel reaction vessels were equipped with a magnetic stirrer as well as an oil bath system for reactions requiring heating.

### 2.2. Raman monitoring system

In order to perform real-time monitoring of sol and dye mixing, a dedicated Raman scattering measurement system was built and coupled with a glass reaction vessel by a fibre optic probe. The measurement set-up is presented in Fig. 1a. The Raman system consists of an excitation diode laser, emitting an 830 nm beam and providing power on sample that can be varied from 0 to 200 mW. The application of a NIR laser reduces the interfering fluorescence signal [2]. An axial transmissive spectrograph with a transmission holographic grating (wavelength from 850 to 1000 nm), developed at VTT Electronics, and an Oriel InstaSpec IV Spectroscopy CCD camera, TE-cooled to  $-30\text{ }^\circ\text{C}$ , were used in the detection part. Comparative measurements were made using CCD-Raman system Ramstas, developed at VTT Electronics [2]. The Raman ranges of both systems extend from  $200\text{ cm}^{-1}$  to  $2000\text{ cm}^{-1}$ , with a resolution of  $8\text{ cm}^{-1}$ .

The fibre optic probe used in the investigation of dye-doped sol-gel materials works in a backscattering configuration of Raman optics, which is especially useful in the study of highly absorbing samples [3]. The setup of the probe as well as its con-

nection with the reaction vessel is presented in Fig. 1b. In comparison to typical, commercially available Raman spectrometers equipped with fibre optic probes, e.g. systems made by Ocean Optics [4] and standard configurations of Ramstas developed by VTT [2], the system presented in this paper is equipped with a more sophisticated, dedicated focusing lens system. Moreover, this system uses a dedicated opto-mechanical setup based on a micrometric-grade 3-D positioning system of the Raman probe, which enables a precise adjustment of the measurement optics and effective optical coupling between the reaction vessel and the probe.

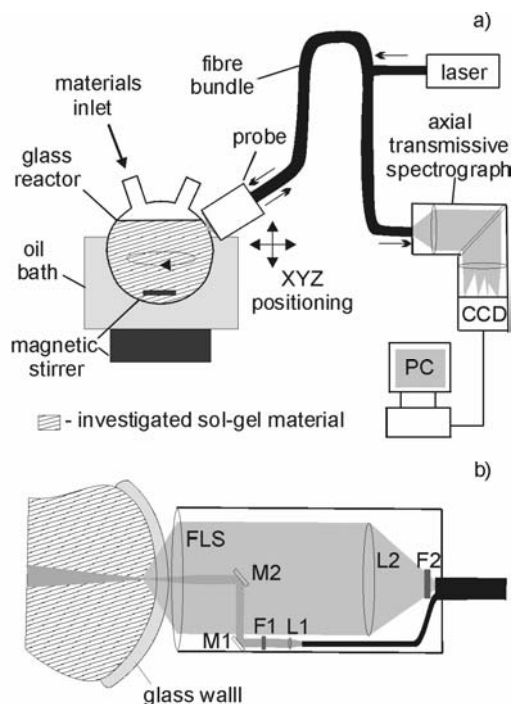


Fig. 1. Schematic diagram of: a) Raman system for in-situ monitoring of dye and sol mixing, b) optical rays inside the probe coupled with the reaction vessel

Laser radiation is transmitted through a single fibre and collimated by the lens (L1). A band pass filter (F1) cuts off fluorescence while two mirrors (M1 and M2) and a dedicated focusing lens system (FLS) enable transmission and focusing the laser beam inside the glass vessel. Having a focal length variable in the range of 12.5–25 mm, the FLS is used for focusing the laser beam inside the vessel and collecting the scattering signal. Part of the scattering signal collected by the FLS is transmitted by an edge filter (F2) that cuts off the Rayleigh scattering signal, while the Raman signal in the Stokes band is transmitted. The lens L2 focuses the scattering radiation into a fibre bundle that transmits it to the spectrometer [2].

As a result of careful optimisation of the FLS design, it is possible to avoid the excitation of interfering Raman scattering in the glass wall of the reaction vessel for

a broad range of wall thicknesses and vessel diameters. The location of the focal point can be adjusted, using the micrometric 3-D positioning system and FLS, in order to reduce the intensity of the Raman band at  $450\text{ cm}^{-1}$  originating from the glass wall and to obtain intensive Raman peaks originating from the investigated materials. The peak at  $1144\text{ cm}^{-1}$ , observed in the spectrum of IR165, can be used for adjusting the measurement system when Raman monitoring is started after inserting the dye inside the vessel. For experiments in which Raman monitoring is to be started before adding the dye, a peak at  $1448\text{ cm}^{-1}$ , assigned to  $\delta(\text{CH}_3)$  bending in the sol, can be used for preliminary Raman system adjustment. As the liquid inside the flask is stirred with high velocity (from 100 to 700 rev./min.), it can be assumed that measurements carried out for one point are representative of the whole volume.

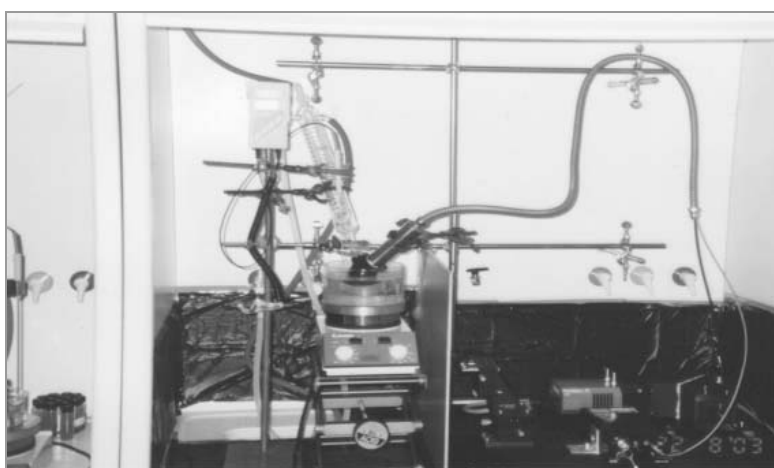


Fig. 2. Raman system coupled with a reaction glass vessel equipped with a magnetic stirrer and oil bath heating system

Measurements were carried out in a remote way. The Raman system was used for monitoring the doping process *in-situ*, carried out at room temperature and up to  $87\text{ }^\circ\text{C}$  in an oil bath during mixing (Fig. 2). Contrary to Raman systems presented elsewhere [5, 6], a reaction vessel dedicated to Raman monitoring is not required. Moreover, any part of the spectroscopic fibre optic system presented in this paper does not need to be placed inside the vessel and consequently does not interfere with the investigated process. Furthermore, continuous stirring of the solution reduces the risk of thermal damage to the sol-gel material by the focused laser beam [3].

### 3. Results and discussion

Raman spectra of the following materials were recorded: GPTS, MPTS, HEMA, TMOS,  $\text{AlOBu}_3$ , and sols based on them, as well as the dye, acetone, and the dye dis-

solved in acetone. Moreover, the mixing of the dye with the sol was monitored in real time. The spectra of the dye dissolved in acetone, pure acetone, and the sol are presented in Figures 3–5, respectively. The spectra of the solid dye (not shown) and the dye dissolved in acetone are identical. In the spectrum of the dye dissolved in acetone, peaks originating from acetone were not recorded, although visual observation suggested that acetone did not evaporate from the closed flask. An absence of a signal originating from acetone in the spectrum of dye/acetone solution was probably caused

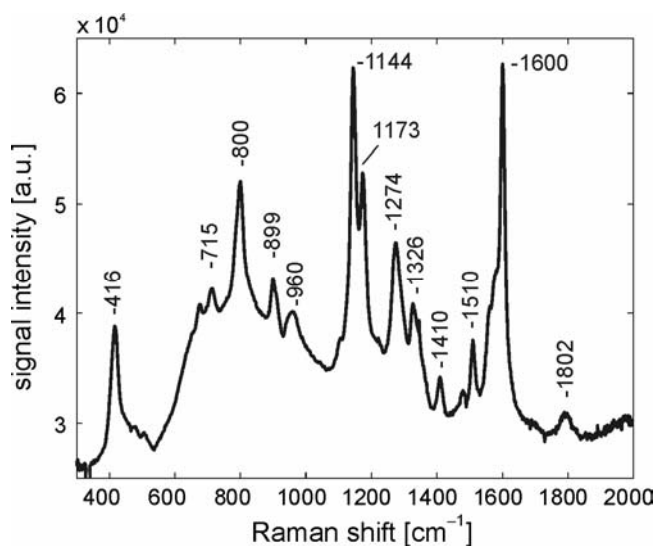


Fig. 3. Raman spectrum of the dye dissolved in acetone

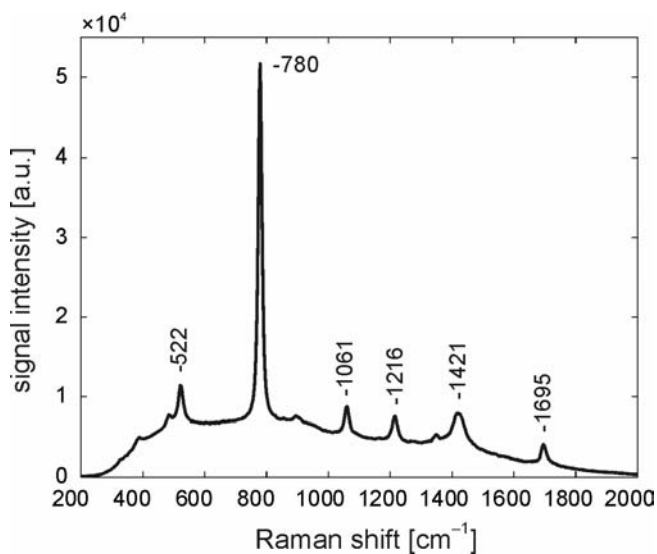


Fig. 4. Raman spectrum of pure acetone

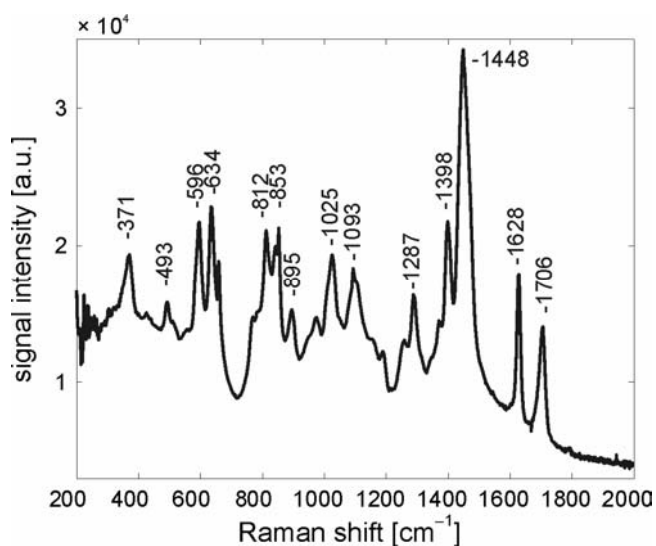


Fig. 5. Raman spectrum of the sol

by the reduced penetration length of the excitation beam in the mixture and by a modification of the acquisition cone, which results from significant differences in the refractive index and optical density of the solution containing particles of the dye as compared to pure transparent materials (e.g. acetone).

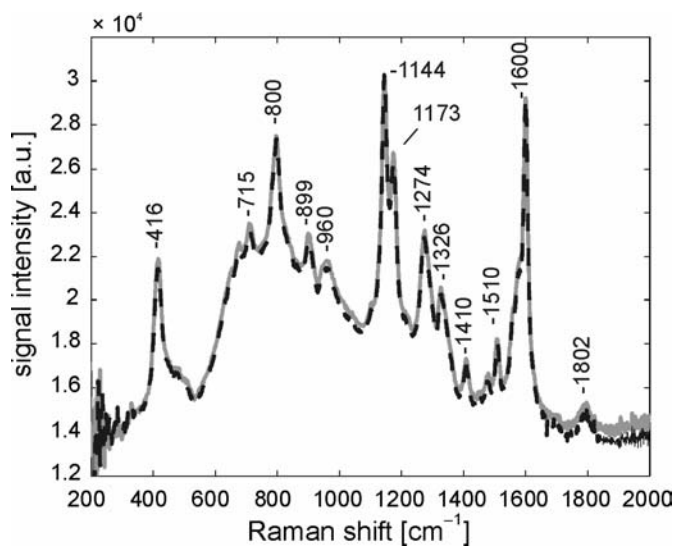


Fig. 6. Raman spectra recorded after adding the dye to the sol (solid grey line) and after subsequent 16 hour-and-20 minute of mixing (black dashed curve)

Changes in the Raman spectrum of sol and dye during mixing, conducted at room temperature, are shown in Fig. 6. Based on a comparison between the Raman spectra

of the components (Figs. 3–5) and the spectrum of the full system, the origin of peaks can be determined. Similarly to the spectrum of the dye dissolved in acetone, it can be noted that peaks assigned to the dye also dominate in the spectrum of the dye–sol mixture. It can be therefore concluded that also in the case of the investigated dye–sol systems, the dye determines optical properties of the material. As a result, peaks originating from the sol cannot be recorded. However, an investigation dye decomposition can be carried out if the Raman spectrum is monitored in a sufficiently wide range of the Raman wave numbers.

During 16 hours and 20 minutes of mixing, the Raman spectrum monitored in the range of 200–2000  $\text{cm}^{-1}$  did not change and all the peaks assigned to the dye maintained their intensities and relative ratios, which confirms that the sol did not react with the dye and that the dye did not decompose.

Confirming experiments were conducted and similar Raman monitoring was carried out for the dye–sol system mixed at a 87 °C (the temperature was maintained by an oil bath system). During some of the experiments, the level of optical background increased, but the ratios of the Raman peaks remained constant, which confirms that the dye did not decompose during any of the experiments.

## 4. Conclusions

An optical system for the Raman investigation of highly scattering and attenuating materials was built and successfully applied. On-line monitoring was performed for the mixing process of the dye and sol as a diagnostic tool, which can be the basis for controlling the dye-sol system.

The Raman system, which can be precisely adjusted for background and fluorescence reduction, does not require any components to be placed inside the reaction vessel. Therefore, it can be attached to standard glass reaction vessels and reactors with glass windows in such a way that eliminates the risk of material pollution by airborne contaminants and prevents the uncontrolled evaporation of some reagents.

The developed Raman system is fully compatible with clean-room conditions. The small sizes of the components (see Fig. 2) and fibre optic probe enable the system to be attached to even complex chemical reactors and *in-situ* process monitoring to be conducted in an industrial environment.

### Acknowledgements

This research was supported by the VTT – Technical Research Centre of Finland, Gdańsk University of Technology (Faculty of Electronics, Telecommunication and Informatics) and State Committee for Scientific Research (pol. KBN research project No. 4 T11B 062 25 conducted between 2003 and 2005).

### References

- [1] KOENIG J.L., *Spectroscopy of Polymers*, Elsevier, New York, 1999.
- [2] NIEMELÄ P., SUHONEN J., SUMEN J., AIKIO J., Proceedings of Finnish Optics Days, Oulu, 1998, 35.

- [3] GARDINER D.J., GRAVES P.R., *Practical Raman Spectroscopy*, Springer-Verlag, Berlin, 1991.
- [4] [www.oceanoptics.com](http://www.oceanoptics.com)
- [5] RIEGEL B., BLITTERSDORF S., KIEFER W., HOFACKER S., MÜLLER M., SCHOTTNER S., *J. Non-Crystalline Sol.*, 226, (1998), 76.
- [6] LEE M., KIM H., RHEE H., CHOO J., *Bull. Korean Chem. Soc.*, 24, (2003), 205.

*Received 23 July 2004*  
*Revised 28 September 2004*

# **Incorporation of zirconia and germania and ternary compounds of $ZrO_2-GeO_2$ into silica sol-gel matrices**

VALERIJ S. GURIN<sup>1\*</sup>, ALEXANDER A. ALEXEENKO<sup>2</sup>,  
KONSTANTIN N. KASPAROV<sup>3</sup>, ELENA A. TYAVLOVSKAYA<sup>3</sup>

<sup>1</sup>Physico-Chemical Research Institute, BSU, Minsk, Belarus

<sup>2</sup>Institute of Electronics, National Academy of Sciences of Belarus, Minsk, Belarus

<sup>3</sup>Gomel State Technical University, Belarus

Silica sol-gel glasses were doped with zirconia and germania. Nanoparticles composed from these oxides and the binary oxides Zr-Ge-O were produced within the matrices. XRD, TEM, and XPS studies were used to determine the phase composition and energy of the electronic states of the elements. The optical features of the materials were characterized by UV/Visible absorption and photoluminescence. Nanoparticles of  $ZrGeO_4$  and  $Zr_3GeO_8$  within the solid matrices were fabricated for the first time.

Key words: *zirconia; germania; nanoparticles; sol-gel glasses*

## **1. Introduction**

The most extensively studied nanoparticles are the elemental ones (e.g. Si, Ge, Ag, Cu, Au, etc) and binary compounds like CdS, ZnS, CdSe, etc. [1, 2]. The theory of the size dependence of nanoparticle properties based on the quantum confinement of charge carriers describes observations quite well in many cases, but more complex species which do not belong to direct-band semiconductors or s-metals frequently reveal rather challenging size-dependent features [3–5]. Oxide nanophases (most often studied are: ZnO, TiO<sub>2</sub>, SnO<sub>2</sub>, etc.) fit much worse into the theory of quantum confinement, and in each case special studies are required to investigate the features of small particles of these compounds. The expansion of chemistry of nanoparticles to new compounds is rarely simple. It requires not only the synthesis of nanoparticles,

---

\*Corresponding author, e-mail: gurin@bsu.by.

but also the fabrication materials to stabilize them for proper characterization. The sol-gel technique possesses powerful potential to expand the chemistry of nanoparticles. In the present work, we address a binary oxide system (and consequently ternary chemical compounds) with zirconium and germanium oxides and report the first results on the synthesis of Zr–Ge–O nanoparticles within the silica matrix.

A great interest exists in the studies of IV-group oxides in composition with silica for the fabrication of nanocomposites doped by isovalent compounds. A number of studies of the binary oxides of silica–germania (e.g., for the waveguide technique [6]) and silica–zirconia (for unique ceramics [7]) have been performed. A combination of both  $ZrO_2$  and  $GeO_2$  [8–10] has rarely been studied. However, it is of interest due to the following reasons: (i) the polymorphism of both compounds with a strong size dependence, in particular  $ZrO_2$  (see, e.g. [11] and Refs.); (ii) various glass-forming abilities, much more  $GeO_2$  than  $ZrO_2$  [12]; (iii) variable coordination numbers of the elements with oxygen in different phases; Zr atoms can have the coordination number of 6–8, while for Ge atoms it can be 4–6; in the latter case this provides easy feasibility of complicated network structures with germanates and polygermanates, which are well known for Ge(IV) chemistry [13]. On the other hand, silica sol-gel matrices open the possibility of controlling the concentration of components, stabilizing nanoparticles and metastable phases, and can be the basis for producing materials with a wide range of applications (optical, catalytic, sensoric, etc.) [14].

Germania is rather rarely used as a dopant in zirconia-based systems, but it works not only due to the effect of the great difference in ionic radii ( $R(Zr^{4+})/R(Ge^{4+}) \approx 2$ ) in solid solutions but also due to the formation of stable chemical compounds [8–10] rather than a compensation of oxygen deficiency with usual dopants in  $ZrO_2$  like M(II) and M(III). Zirconia–germania nanocomposites have also been recently synthesized without any matrix [15, 16]. They reveal rather challenging properties, and the formation of new phases was found. Below, we describe nanoparticles of this system within a  $SiO_2$  matrix and investigate them with X-ray diffraction (XRD) and transmission electron microscopy (TEM). The electronic state of the elements has been analysed with X-ray photoelectron spectroscopy (XPS), optical UV/Vis absorption, and photoluminescence, demonstrating that the nanoparticles behave like semiconductors, the band structure of which is affected by their chemical composition and oxygen deficiency rather than their size.

## 2. Experimental

The samples studied were silica-based glasses with incorporated Zr–Ge–O. The sol-gel derived silica matrix for glass fabrication was obtained by the conventional sol-gel technique [14] with the acid hydrolysis of tetraethoxysilane slightly modified to speed up gelation without strong volume contraction [17], as applied successfully by us for the incorporation of semiconductor nanoparticles into silica glasses [18]. This method resulted in aqueous-alcoholic silica sols mixed with a solid silica filler

(pyrogenic SiO<sub>2</sub>, aerosil, with particle size ~10–20 nm) in a mole ratio TEOS/aerosil = 1/1. The sols were neutralized by aqueous ammonia (0.1 M) up to pH≈6, and the gels were produced. Drying in air at 60 °C and annealing at 800 °C lead to porous SiO<sub>2</sub>-matrices, usually named ‘xerogels’, which are able to incorporate various species by simple impregnation and absorption. Zirconium and 4 germanium were introduced into these xerogels by impregnation in solutions of ZrO(NO<sub>3</sub>)<sub>2</sub> in acetic acid (concentrations varied from saturated down to a 1/10 dilution), in solutions of germania in water, and in ammonia (both saturated at 20 °C). These solutions (as sources of Zr and Ge) were used to provide a high amount of incorporated species. The solutions penetrated the matrices for a few minutes, and were kept in this state for about 8 h. In order to get samples containing both Zr and Ge, the impregnation procedures were performed with both solutions, the second element being introduced after drying the sample. The samples were dried and annealed in air by a special temperature–time profile up to a maximum of 1200 °C, resulting in the formation of transparent glasses. The samples studied in present paper differ in the sequence of Zr and Ge incorporation and in the concentrations of the precursor solutions. Samples with co-incorporated Zr and Ge are labelled as N11 and N13: for N11 the incorporation of zirconium preceded the incorporation of germanium from an ammonia solution of GeO<sub>2</sub>; for N13 the first step was the incorporation of zirconium from a doubly diluted saturated acetic acid solution of ZrO(NO<sub>3</sub>)<sub>2</sub> after which germanium was introduced from a saturated aqueous solution.

XRD measurements were done for both powders and glassy samples with a DRON-3 device using CoK<sub>α</sub> radiation and a MnO<sub>2</sub> filter. XPS studies were performed with an ES2401 spectrometer (Russia) with MgK<sub>α</sub> radiation, and C1s line calibration at 284.6 eV was used.

In order to visualize nanoparticles in the glassy samples with TEM, a ‘replica with extraction’ method was used. This method consisted of the deposition of a thin carbon film (10–20 nm) onto the surface of the freshly etched glasses, followed by stripping the carbon film upon contact with water. Micrographs were obtained with a UEM-100LM microscope (Russia) in the medium magnification range.

UV/Vis absorption spectra were recorded with a Specord M40 (Carl Zeiss) device in air, and photoluminescence spectra were obtained with a fluorimeter Fluoromax-2 (Jobin-Yvon) under monochromatic excitation from a Xenon lamp.

### **3. Results and discussion**

#### **3.1. TEM**

The TEM data presented in Fig. 1 display the structures of a series of glasses prepared with different compositions: glasses doped with ZrO<sub>2</sub>, GeO<sub>2</sub>, and co-doped ones (the two samples described above, N11 and N13). The formation of particles is ob-

served within all types of glasses, however, the morphology of particles is different. The size of particles enters the range of 20–100 nm, but the particles are aggregated in co-doped glasses. Particle concentration cannot be determined unambiguously with the TEM sample preparation method used here. One can state, however, that the order of magnitude is comparable with materials with individual oxides, and rises for binary oxides. Thus, these TEM data in general allow us to consider the synthesized glasses to be nanoparticles-in-matrix systems, and the silica matrix looks like an inert support in a first approximation.

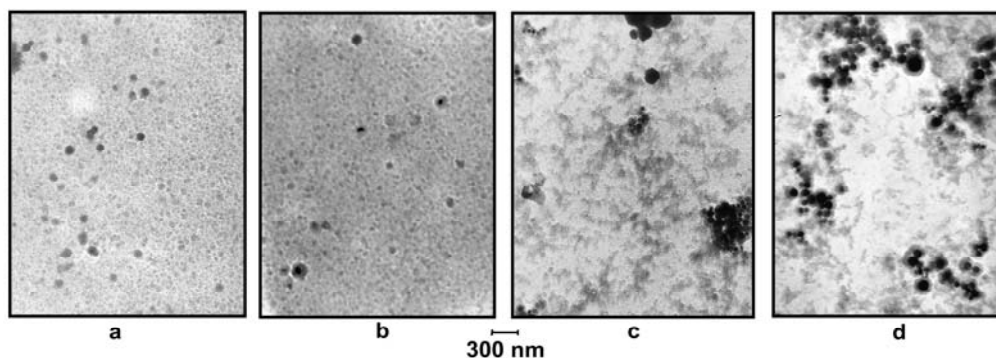


Fig. 1. TEM images of nanoparticles produced in silica glasses by the incorporation of  $\text{ZrO}_2$  and  $\text{GeO}_2$ : a)  $\text{ZrO}_2$ ; b)  $\text{GeO}_2$ ; c)  $\text{ZrO}_2$  and  $\text{GeO}_2$  (N11); d)  $\text{ZrO}_2$  and  $\text{GeO}_2$  (N13)

This appearance can be explained by nanoparticle formation accompanied by simultaneous matrix annealing. The initial content of zirconia–germania precursors can be rather high in pores within the silica xerogel, and after pore contraction they may form aggregates rather than separated particles. It should be expected that lowering of the amount of precursors would result in the same final products with particles placed separately in the matrix.

### 3.2. XRD

The XRD patterns presented in Fig. 2 (besides the  $\text{GeO}_2$ -doped ones, showing only simple amorphous-type patterns) evidence that the nanoparticles observed by TEM are nanocrystalline phases and that the patterns can be decoded. The picture contains the reference data for three phases suggested: monoclinic zirconia and two compounds common to this binary oxide system, namely the scheelite phase  $\text{ZrGeO}_4$  (JCPDS 34-0407) and the compound  $\text{Zr}_3\text{GeO}_8$  (JCPDS 16-0800). They appear within the annealed glassy silica matrix (the broad halo in the range  $2\theta = 15\text{--}30$  deg). The peaks observed are comparatively weak. Keeping in mind that these inclusions are present in the matrix at low concentrations, however, this observation seems to be sufficient for documenting the preparation of this type of material for the first time. The broadening of

the peaks also occurs, and the particle size of both binary oxide phases can be estimated to be 10–30 nm.

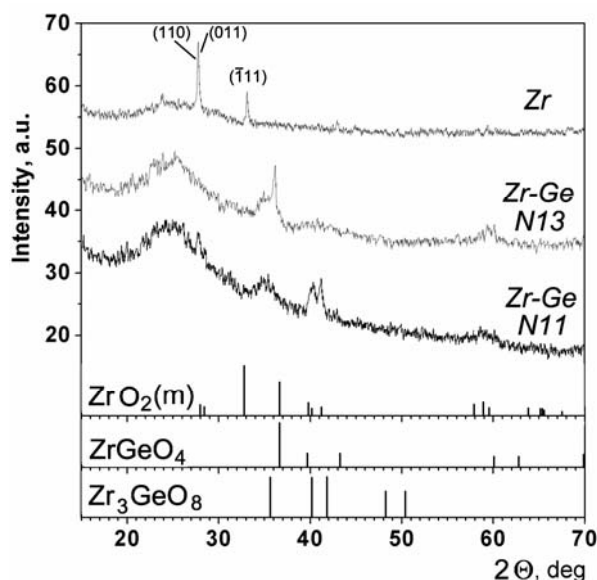


Fig. 2. XRD patterns of silica glasses doped with  $ZrO_2$  and co-doped with  $ZrO_2$  and  $GeO_2$ , referenced to bulk  $ZrGeO_4$  (JCPDS 34-0407), and  $Zr_3GeO_8$  (JCPDS 16-0800)

This range does not contradict the TEM data (Fig. 1). The TEM images also indicate, however, some coarser particles with sizes up to 100 nm. This can be explained by a tendency to aggregate. Possibly, the coarser particles are the products of secondary processes rather than single particles originally formed within the glass. The XRD pattern for the sample doped with only  $ZrO_2$ , in which the monoclinic zirconia phase has been detected, essentially exhibits less broadened peaks, although the size range in TEM is close to that of the binary oxides. Hence, the broadening effect in the latter case is not only due to size. It could be due to structural disorders, which are known to be specific for these types of compounds [19]. Some authors consider both  $ZrGeO_4$  and  $Zr_3GeO_8$  as solid solutions based on the tetragonal zirconia lattice [10], and a solid solution can possess various degrees of disorder.

On the other hand, a comparison of the reference peaks of zirconia, shown at the bottom axis of Fig. 2, reveals that the case of zirconia is also not simple: the reflexes (111) (shown) and (111) (not shown, since they are absent in the experimental pattern) have much smaller intensity than the (110) and (011) reflexes, and the ratio of intensities is strongly altered from the ones referenced by JCPDS data. We may suppose that the zirconia particles observed in the glasses are oriented nanocrystals as long as the assignment of XRD patterns in the case of glass doped with zirconia is not complicated by any binary phases and compounds from the  $Zr$ – $Si$ – $O$  system and other

ZrO<sub>2</sub> patterns are far from the pattern of monoclinic zirconia. A preferred direction is manifested in the glasses investigated by XRD, since flat samples were fabricated in this case. The preparation of samples for TEM includes the removal of particles from the matrix (see Experimental) and any orientational effects are therefore lost. The possibility of orientation of zirconia nanoparticles will be investigated in future studies and is of interest in the context of optical polarization effects.

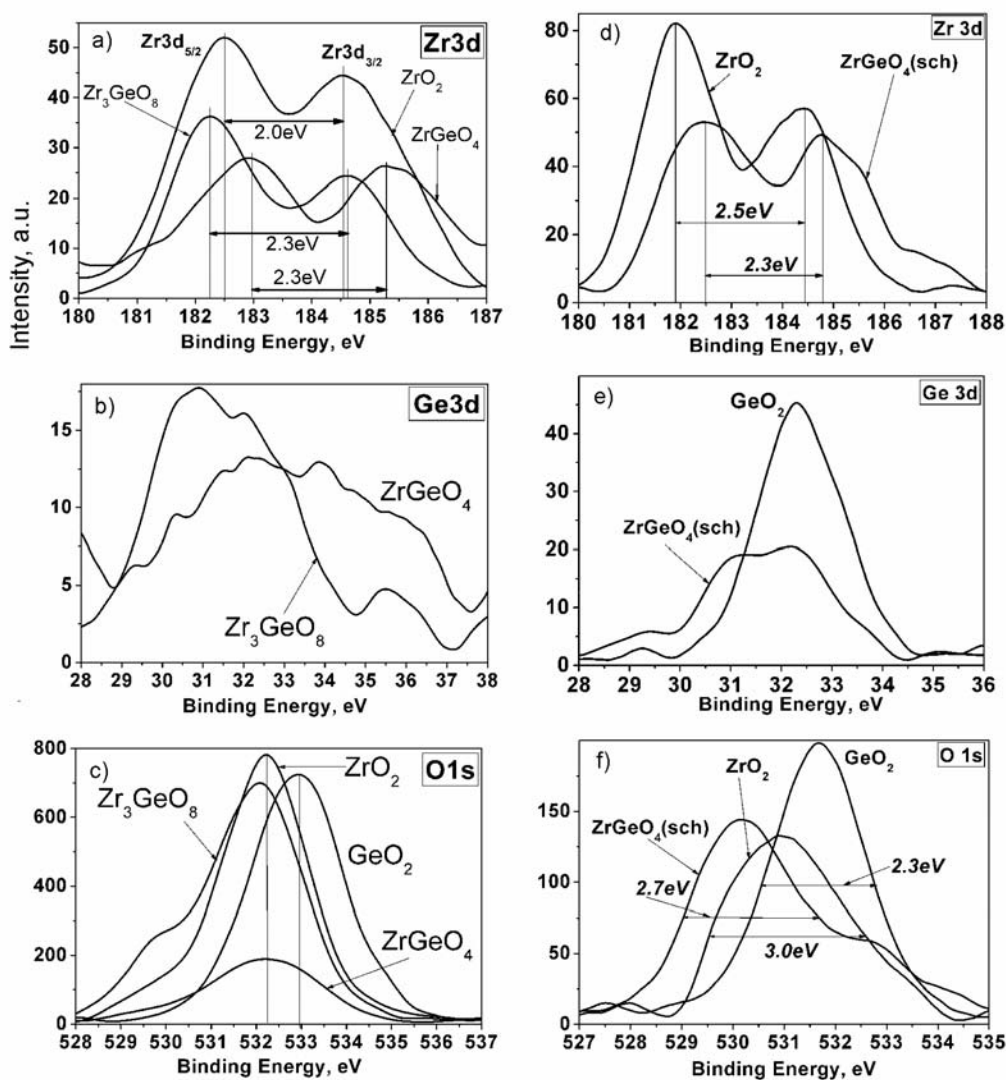


Fig. 3. XPS data for silica glasses doped with ZrO<sub>2</sub> and co-doped with ZrO<sub>2</sub> and GeO<sub>2</sub> in comparison to the data for ZrO<sub>2</sub>, GeO<sub>2</sub> (commercial pure chemicals), and ZrGeO<sub>4</sub> prepared by high-temperature sintering of ZrO<sub>2</sub> and GeO<sub>2</sub>

The silica glasses fabricated with zirconia- and zirconia–germania dopants exhibit nanoparticles of mono-oxides or binary oxides from the two known compounds of the Zr–Ge–O system. The phase composition depends on the sequence of zirconia and germania incorporation. The electronic state of the elements in the samples of different composition was studied with XPS and compared to the data available for the corresponding compounds without matrix (Fig. 3).

### 3.3. XPS

The XPS spectra of four types of glasses doped with zirconia and germania and two co-doped versions are presented in Figs. 3a–c. The elements in all the compounds considered in the system present formally the same oxidation degrees for the series of samples of  $Zr^{4+}$  and  $Ge^{4+}$ . The XPS data, however, reveal strong differences in the positions of the photoemission lines and in the intensities for the same compounds in the corresponding samples. Variations in intensity can be associated with the inhomogeneous localization of nanoparticles throughout the sample volume. A noticeable range of binding energy of the core electrons of all elements under consideration also exists for the reference samples (Figs. 3d–f). We have used a commercial zirconia (a monoclinic modification stable at room temperature) and polycrystalline  $ZrGeO_4$  synthesized from  $ZrO_2$  and  $GeO_2$  by the high-temperature sintering in a sealed ampoule followed by the XRD confirmation.  $ZrO_2$  formed within glasses gives the Zr doublet signal (the usual 5/2 and 3/2 components) shifted to higher energies by about 0.6 eV with respect to the reference  $ZrO_2$ .  $ZrGeO_4$  has a much larger shift, while the shift for the glass with  $Zr_3GeO_8$  is, in contrast, less than for  $ZrO_2$ , but still positive (Fig. 3a).

A positive shift in the binding energy of the  $Zr_{3d}$  doublet also occurs for  $ZrGeO_4$  in glass as compared to the bulk polycrystalline compound. The interval between the doublet components is observed in the range of 2.3–2.5 eV for all except  $ZrO_2$  nanoparticles in glass, for which it equals 2.0 eV. The general width of the latter is larger, however, and it could possibly be deconvoluted into two components with close binding energies. These may be, for example, contributions due to surface and interior atoms. For these reasons, we can draw some conclusions from the above variations in the interval between the 5/2 and 3/2 components of the  $Zr_{3d}$  core levels.

Thus, two main observations can be established from the XPS data of Zr: (i) a pronounced difference between  $ZrGeO_4$  and  $Zr_3GeO_8$ , the first showing a more positive position, 0.7–0.8 eV; (ii) significant positive shifts for compounds within the glasses as compared to those in a matrix-free polycrystalline form, amounting to about 0.5 eV for both  $ZrGeO_4$  and  $ZrO_2$ . The latter conclusion indicates that nanocrystallines formed (being close to their macroscopic counterparts in the long-range ordering as shown the XRD patterns) are essentially different in their local structures. We expect, that one of the factors in this difference can be the oxygen deficiency effect, which can get stronger at the nanoscale level due to larger surface contribution and due to

effects of the silica matrix. Naturally, the oxygen deficiencies of  $\text{ZrGeO}_4$  and  $\text{Zr}_3\text{GeO}_8$  can be different, since the Zr/O ratio is different for these compounds, and the coordination number of Zr atoms for oxygen in the structure of  $\text{Zr}_3\text{GeO}_8$  is larger than that for  $\text{ZrGeO}_4$ . Oxygen deficiency should diminish the positive shift in the binding energy with respect to the zero-valent state of Zr. Thus, in the glasses studied the compounds include less oxygen vacancies than their bulk counterparts. The matrix can be a stabilizing factor, keeping the structures closer to the stoichiometric ones.

The XPS data for the germanium core level are shown only for the binary oxides, and have low intensity. Ge levels used in this analysis display weaker photoemission signals. Moreover, conclusions concerning the shifts in this case are rather disputable due to the possible contribution of  $\text{Zr}_{4p}$  states to these signals (they also appear at 30 eV [20]). By comparing the data in Fig. 3b with that in Fig. 3e, we may see that the germanium state is different from that of  $\text{GeO}_2$ , and is very smooth both in bulk and nanoparticles. There is a clear tendency for a lower binding energy than in the stoichiometric oxide  $\text{GeO}_2$ . The spectra for  $\text{O}_{1s}$  core levels (Figs. 3c, f) in the glasses based on silica have a big contribution from the oxygen in the matrix. We have observed, however, that a noticeable difference exists for glasses with the oxide phases studied. Without the matrix we attain reasonable differences both in the maxima position and width of the lines (Fig. 3f). The less ionic oxide,  $\text{GeO}_2$ , has the most positive position, and  $\text{ZrGeO}_4$  looks like a sum of two or more components. The complicated profiles of the lines, in particular that of  $\text{ZrO}_2$  and  $\text{ZrGeO}_4$ , can be explained by the contribution of adsorbed oxygen and hydroxyl from air. The spectra of  $\text{O}_{1s}$  levels of the compounds in the glass appeared to be closer one to another, which can be explained by the dominance of oxygen in the silica matrix of the same composition, and a noticeable difference exists nevertheless. It corresponds to the reference samples without the matrix. The spectrum for  $\text{Zr}_3\text{GeO}_8$  is similar to that of  $\text{ZrO}_2$  with an additional shoulder on the lower-energy side (probably the adsorbed or non-bridging oxygen). Thus, the data for oxygen photoemission confirms the formation of different nanophases within glasses.

### 3.4. Optical studies

Figure 4 presents the optical absorption spectra and photoluminescence spectra of a series of glasses. Absorption spectra show that binary Zr–Ge oxides reveal semiconductor-like behaviour with rather sharp edges, 5.0 eV and 4.6 eV for  $\text{ZrGeO}_4$  and  $\text{Zr}_3\text{GeO}_8$ , respectively. The features at  $\sim 220$  nm in the spectra are not discussed here since the silica matrix begins to absorb in this range. The spectra of glasses with  $\text{ZrO}_2$  and  $\text{GeO}_2$  nanoparticles display similar behaviour, but have larger slopes. According to the known values of the band gaps for these oxides, namely  $\sim 5.2$  eV [21, 22] and  $\sim 5.6$  eV [23, 24], respectively, and to the referenced view of spectra, we would expect more pronounced absorption edges. The broad rise for  $\text{ZrO}_2$  at  $\lambda < 400$  nm and the feature at  $\lambda = 270$  nm for  $\text{GeO}_2$  can be due to structure defects developing as a result

of high-temperature treatment in contact with the silica matrix during the annealing of the glasses with nanoparticles. The range of absorption of both oxides is in accordance with the above reference data, but details (including the minor features observed) depend strongly on the history of the oxides (heating, storage, atmosphere, impurities).

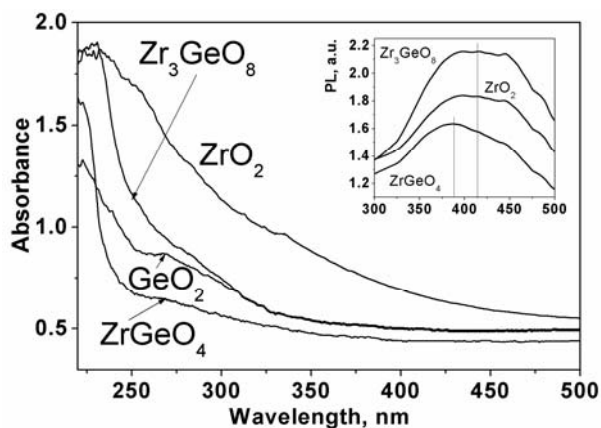


Fig. 4. UV/Vis absorption spectra of silica glasses with nanoparticles of different compositions (indicated). The inset contains photoluminescence spectra obtained with a 280 nm excitation

The optics of glassy  $GeO_2$  has been studied [25], and the absorption features, like those presented by us in Fig. 4 for  $GeO_2$ , have been reported for the heated glasses. They are associated to paramagnetic defect centres observed simultaneously by ESR. The nanoparticles of binary oxides show sharper edges in the absorption spectra. This suggests that they are more stable with respect to structure defect formation, which in oxides like  $ZrO_2$  and  $GeO_2$  occurs easily due to the high mobility of oxygen ions. Taking into account the above XPS data, we may not propose that higher oxygen deficiency provides additional absorption. Hence, oxygen defects can take the form of some absorption positions at the particle–matrix interface or uneven nanocrystal sites.

Preliminary electron spin resonance data were obtained for these samples and no ESR signals for the nanoparticles of  $ZrGeO_4$  and  $Zr_3GeO_8$  were detected (to be published elsewhere). The photoluminescence spectra presented in the inset of Fig. 4 show significant signals for the glasses containing nanoparticles of  $ZrGeO_4$ ,  $Zr_3GeO_8$ , and  $ZrO_2$ . The glass with  $GeO_2$  showed no photoluminescence above the background. An observable intensity cannot be considered to be an essential factor, since it varies in the range of double enhancement for one sample with respect to another due to little differences in size and thickness. The positions of the band maxima, however, are shifted about 50 nm to the right for glasses with  $ZrO_2$  and  $Zr_3GeO_8$  as compared to  $ZrGeO_4$ . Note that the absorption of the first pair also enters higher wavelengths. The excitation wavelength was chosen to get the most intense spectrum without contribution from matrix luminescence (a relatively low concentration of nanoparticles in the samples

necessitates the separation of background from the matrix also showing a luminescence signal, though this is much weaker than for glasses with Zr-containing particles).

Similar emission spectra and Stock's shifts of the photoluminescence signal, about 100 nm for  $\text{ZrGeO}_4$  and 150 nm for  $\text{ZrO}_2$  and  $\text{Zr}_3\text{GeO}_8$ , can point to a similar photoluminescence mechanism: light with  $\lambda=280$  nm only partially corresponds to the inter-band excitation of the semiconductors. The emission bands are rather broad and multiple centres can be responsible for their appearance. It should be noticed that the detailed nature of photoluminescence in materials of this type can be rather complicated. A formation of various oxygen-deficient centres is strongly inherent to metal oxides with high oxygen content like  $\text{ZrO}_2$  and  $\text{GeO}_2$  (and compounds derived from them), without a reduction in the oxidation degrees of the elements.

At deeper steps, this process can lead to some amount of low valence states ( $\text{Zr}^{3+}$  [26] and  $\text{Ge}^{2+}$ , Ge–Ge–bonds [27]), which appear usually as active luminescence centres. The latter phenomenon is probably not of great importance in our case, since we do not observe these states in the XPS analysis. As long as the glasses with  $\text{GeO}_2$  do not show luminescence signals and only Zr-containing compounds have visible bands, it is worthwhile to associate the nature of luminescence centres with zirconia. Moreover, the intensity of the band is higher when the atomic ratio of  $\text{Zr}/\text{Ge} = 3$ , and for  $\text{Zr}/\text{Ge} = 1$  the band is weaker (Fig. 4, inset). The luminescence band in the range of 380–450 nm is typical of  $\text{ZrO}_2$ . The centres responsible for the emission can be oxygen vacancies, F-centres, surface defects, or impurities of foreign ions [28, 29]. They have been extensively studied from the point of view of the thermoluminescent behaviour of zirconia [30, 31].

Our interpretation of the luminescence bands is based on the most common item that can be expected in both Zr–Ge compounds studied and in  $\text{ZrO}_2$  created in an oxidative environment (air, 1200 °C) and in contact with silica matrix. The latter is not an active oxygen-transferable medium and is chemically active at high temperatures with respect to many metal oxides that could be present as uncontrollable impurities. On the other hand, silica is inert with respect to zirconia under these conditions, since we did not detect any zirconia silicate phase. We suppose that a small amount of oxygen vacancies are formed, and their concentration is variable depending on the type of compound, but is too small to shift any XPS lines or change lattice parameters in the XRD data within experimental error. A large tendency to produce oxygen vacancies occurs in zirconia synthesized from hydrous forms [32, 33] by heat treatment in air or vacuum. The silica matrix in our case, however, can be a stabilizing agent. A more detailed study of the nanoparticles in the materials fabricated will be presented in future publications, after more data is obtained.

## 4. Conclusions

A novel approach to the fabrication of composite optical materials containing nanoparticles of binary oxide semiconductors is offered in this work. The selection of

dopants has been motivated by a search for oxide compounds that exhibit polymorphic transformation at ambient pressure and interesting features in their optics, catalysis, ionic conduction, etc. In contrast to chalcogenide compounds, which are the most frequently studied among semiconductor nanoparticles, oxides are more compatible with the silica matrix and more stable under heating in air. Zirconia and germania (oxides from the IV group) and silica can exist in several crystalline forms. Furthermore, germania is capable of amorphisation. The compounds in the system,  $ZrO_2$  and  $GeO_2$ , have been studied rather scarcely. We have produced them within a solid matrix by a simple method of co-impregnating porous silica, followed by thermal treatment with simultaneous annealing at the silica matrix to the glass state. The composition of the final products is determined by several factors that are easily controlled during the developed procedure: (i) the concentration of dopants and solvent used for impregnation; (ii) the order of the sequential introduction of Zr- and Ge-containing precursors; (iii) the properties of the silica matrix used (porosity, hydroxyl groups, etc). Other ways to control the final state will be elaborated with further research.

$ZrO_2$  and  $GeO_2$  possess a limited homogeneity region to form solid solutions with a structure based on one of the components. Three known compounds have been reported in this system to date. In our materials, however, we have detected only two, with the compositions  $ZrGeO_4$  and  $Zr_3GeO_8$  (a third phase has been reported recently [34] and has a zircon-like structure). Their features have been revealed by TEM, XRD, XPS, UV/Vis absorption, and photoluminescence measurements. The nanoparticles are aggregated within the matrix, and the mean size range is tens of nanometers. XPS data have shown a chemical shift for zirconium (with respect to the bulk counterparts) probably due to diminishing oxygen deficiencies stabilized by the matrix. The optical data correspond to the formation of a wide-gap semiconductor with blue luminescence.

Promising applications of glasses with Zr–Ge-oxide nanoparticles offer silica-based optical materials with a low content of wide-band gap semiconductors ( $ZrO_2$ ,  $ZrGeO_4$ , and  $Zr_3GeO_8$ ) and media with lower valence states of germanium (including Ge nanoparticles and clusters) that are tuneable by reducing the chemical treatment of the glasses presented above. Preliminary results have been obtained, showing the appearance of new and intense luminescence bands.

#### Acknowledgements

The work was performed with the support of the Belarusian Fundamental Research Foundation (project X03-318) and the NANOTEX program under the Ministry of Education of Belarus. The authors thank G. Tuchkovsky for technical assistance in XRD measurements and Dr. K. Kaparikha for TEM experiments.

#### References

- [1] *Nanoparticles: From Theory to Application*, G. Schmid (Ed.), Wiley, Weinheim, 2004.
- [2] PILENI M.P., *Semiconductor Nanocrystals*, [in:] *Nanoscale Materials in Chemistry*, K.J. Klabunde (Ed.), Wiley, New York, 2001, 61–84.

- [3] MAIER J., *Nanoionics and Soft Materials Science*, [in:] *Nanocrystalline Metals and Oxides. Selected Properties and Applications*, Ph. Knauth and J. Schoonman (Eds.), Kluwer Acad. Publ., Boston, 2002, 81–110.
- [4] *Fine Particles. Synthesis, Characterization, and Mechanisms of Growth*, T. Sugimoto (Ed.), Marcel Dekker, New York, 2000.
- [5] AYYUB P., PALKAR V.R., CHATTOPADHYAY S., MULTANI M., Phys. Rev. B, 51 (1995), 6135.
- [6] NEUSTRUEV V.B., J. Phys. Cond. Matter, 6 (1994), 6901.
- [7] WINTERER M., *Nanocrystalline ceramics: Synthesis and structure*, Springer-Verlag, Berlin, 2002.
- [8] LEFEVRE L., Ann. Chim., 8 (1963), 117.
- [9] LI P., CHEN I.W., J. Am. Ceram. Soc., 77 (1994), 1281.
- [10] KARLIN S., COLOMBAN P., J. Am. Ceram. Soc., 82 (1999), 735.
- [11] STICHERT W., SCHUTH F., Chem. Mater., 10 (1998), 2020.
- [12] RAWSON H., *Inorganic Glass-forming Systems*, Academic Press, London, 1967.
- [13] INGRI N., Acta Chem. Scand., 17 (1963), 597.
- [14] HENCH L.L., WEST J.K., Chem. Rev., 90 (1990), 33.
- [15] FROLOVA E.V., GURIN V.S., IVASHKEVICH L.S., SVIRIDOV V.V., *Investigation of zirconiagermania glasses and solids prepared by sol-gel technique* [in:] *Sol-Gel Optics VI*, E.J.A.Pope, H.K. Schmidt, B.S. Dunn and Sh. Shibata (Eds.). Proc. SPIE, 4804 (2002), 81.
- [16] FROLOVA E., Mater. Sci. Eng. C, 23 (2003), 1093.
- [17] PODDENEZHNYI E.N., BOIKO A.A., *Sol-gel synthesis of optical quartz glass*, GGTU, Gomel, 2002 (in Russian).
- [18] GURIN V.S., ALEXEENKO A.A., PRAKAPENKA V.B., KOVALENKO D.L., YUMASHEV K.V., PROKOSHIN P.V., Mater. Sci., 20 (2002), 30.
- [19] SMYTH D.M., *The Defect Chemistry of Metal Oxides*, Oxford University Press, New York, 2000.
- [20] SARMA D.D., RAO C.N.R., J. Electron Spectr. Rel. Phenom. 20 (1980), 25.
- [21] SARVER J., Ceram. Bull., 46 (1967), 837.
- [22] AITA C.R., HOPPE E.E., SORBELLO R.S., Appl. Phys. Lett., 82 (2003), 677.
- [23] PAJASOVA L., Czech. J. Phys. B, 19 (1969), 265.
- [24] CHRISTIE D.M., J.R. CHELIKOWSKY, Phys. Rev. B, 62 (2000), 14703.
- [25] WEEKS R.A., PURCELL T., J. Chem. Phys., 43 (1965), 483.
- [26] MOCHNIAK J., WRZESIŃSKA A., Acta Phys. Polon. A, 41 (1972), 165.
- [27] LI J., WU X.L., YANG Y.M., YANG X., BAO X.M., Phys. Lett. A, 314 (2003), 299.
- [28] LI Q., AI D., DAI X., WANG J., Powder Technol., 137 (2003), 34.
- [29] DE LA ROSA-CRUZ E., DIAZ-TORRES L.A., SALAS P., CASTANO V.M., HERNANDEZ J.M., J. Phys. D, 34 (2001), L83.
- [30] BETTINALI C., FERRARESO G., MANCONI J.W., J. Chem. Phys., 50 (1969), 3957.
- [31] SARVER J.F., J. Electrochem. Soc., 113 (1966), 124.
- [32] LIVAE J., DOI K., MAZIERES, J. Am. Ceram. Soc., 51 (1968), 349.
- [33] GOMEZ P., LOPEZ T., BOKHIMI X., MUNOZ E., BOLDU J.L., NOVARO O., J. Sol-Gel Sci. Technol., 11 (1998), 309.
- [34] HIRANO M., MORIKAWA H., INAGAKI M., TOYODA M., J. Am. Ceram. Soc., 85 (2002), 1915.

Received 19 August 2004  
Revised 10 December 2004

# Carbon–silica sol-gel derived nanomaterials

THOMAS HÜBERT\*, AKI SHIMAMURA, ANDREAS KLYSZCZ

Bundesanstalt für Materialforschung und -prüfung (BAM), D-12203 Berlin, Germany

The preparation of sol-gel derived silica-based nanomaterials containing electrical conductive carbon fillers in an extensive composition range is described and their electrical properties are presented. Nanomaterials of carbon filler concentrations up to 60% (v/v) were obtained by dip coating or screen-printing from precursors of hydrolysed alkoxysilanes. Nanostructured morphology could be identified to consist of homogeneously dispersed carbon black particles or carbon fibres of 30 to 500 nm in size in a modified silica matrix. The electrical resistivity of the films changes drastically from  $10^{10}$  to  $10^{-1}$   $\Omega$ -cm, according to the amount of dispersed conductive particles. A threshold between 5 and 50% (v/v), at which the resistance abruptly decreases, was determined. A geometrical model related to percolation theory explains this non-linear dependence on the filler composition in the materials. Moreover the temperature dependence of resistance and the current-voltage characteristics of the nanomaterials can also be illustrated using this geometric model.

Key words: *sol-gel, nanomaterials; carbon black; electrical resistivity; percolation*

## 1. Introduction

Silica materials prepared by the sol-gel route combine excellent chemical and temperature stabilities with a high electrical resistance (above  $10^{15}$   $\Omega$ -cm) [1]. The addition of conductive fillers into the insulating matrix may result in a change of its properties and reduction of the resistance, which can offer new applications. The synthesis of sol-gel films containing fine noble metal particles such as gold or platinum is already known to optical applications [2]. The addition of silver or copper oxide is proposed for optical or antibacterial use [3–5]. The formation of other metals in a glass matrix, like nickel or cobalt, demands an additional reduction process employing hydrogen gas at higher temperatures [6]. We chose carbon black as a cost-effective material, which should be introduced into the sol-gel matrix at high concentrations. Carbon black shows a low resistivity (about  $10^{-5}$   $\Omega$ -cm) and is stable under

---

\*Corresponding author, e-mail: thomas.huebert@bam.de.

the oxidizing conditions of film preparation. Various kinds of carbon black are industrially produced for several applications. The single particles are mostly nanosized, but as in many other nanopowders they tend to agglomerate and form larger aggregates.

Carbon organic polymer composite materials, such as films or compact materials, have been widely studied and applied, for example, in rubber material or duro plastics for electronic units, conductive glue, anti-electrical charging, and electrical shielding. The dependence of electrical properties on carbon black concentration have already been well studied [7–9]. Inorganic or hybrid sol-gel derived materials containing carbon black in a silica matrix are already used in applications such as biosensors and electrodes for electrochemical and analytical procedures as so-called carbon containing electrodes (CCE) [10–12]. The resistance of the composite materials is related to the formation of a network of contacting filler particles within the matrix. It decreases sharply at a characteristic conducting particle concentration, known as the percolation threshold [13]. On the other hand, systematic investigations of materials containing carbon embedded in an inorganic or hybride matrix prepared by wet synthesis are still incomplete [13]. Therefore, in this study, modified silica nanomaterials containing different kinds of carbon black or carbon nanofibres were synthesised via the sol-gel process and their morphology and electrical properties were characterised. Films in a wide range of filler concentrations were prepared and examined. Preparation includes a traditional dip-coating process, so that crack-free films with a thickness smaller than 10  $\mu\text{m}$  can be obtained. In order to obtain thicker films, silk screen printing was applied, which demands an increased viscosity of the usual liquid precursor. Therefore, other compositions had to be considered and further additives were necessary.

## 2. Experimental

### 2.1. Synthesis of films

Precursor solutions for thin films were obtained from a mixture of tetraethoxysilane (TEOS), methyltriethoxysilane (MTES), water, and ethanol, in a molar ratio of 0.67:1:0.9:2.6, which was heated at 40 °C for 4 h. Hydrolysis was catalysed by 0.01 M  $\text{HNO}_3$ . An alcoholic solution of 20% graphite was added in order to obtain 5–60% (v/v) carbon in the completed films. Silicon wafers, fused silica, and silicate glass were used as substrate materials. Employing a dip-coater, the substrates were dipped into the precursor solution mixture and withdrawn at rates between 3 and 25  $\text{cm}\cdot\text{min}^{-1}$ . The films were dried for an hour at 50 °C and for 4 hours at 100 °C, followed by heat treatment at 450 °C for 20 min. The heating rate was 1  $\text{K}\cdot\text{min}^{-1}$ . The basic solution was stable for more than 90 days without any relevant increase in particle size and viscosity, which was tested by light scattering experiments and viscosity measurements.

Thick films were obtained from a mixture of tetraethoxysilane (TEOS), glycidyoxypropyltrimethoxysilane (GPTS), 3-methacryloxypropyltrimethoxysilane (MPTS), diphenylsilandiol (DPS), and water in the molar ratio 1: 9.75:9.75:4.5:13.38. In order to increase the viscosity of the precursor, up to 10% silica (Degussa, Aerosil® R972) or a modified silicate (Southern Clay Prod. Inc., Cloisite B30) was added. Four different carbon black powders (Degussa, XE-2B and L6, and RUF IN-1, IN-2) and carbon nanofibres (Applied Sciences INC., Pyrograf III) were added in concentrations up to 20% to the paste and homogenised using an ultrasound stick or bath (Bandelin). The paste was printed on alumina and glass substrates and heat-treated up to 200 °C for 15 min.

## 2.2. Material characterization

The thickness of the films was determined by a mechanical stylus system (Tencor Instr., Alpha-Step 200). SEM investigations (Hitachi S4100) were performed for characterising the morphology of the carbon and of the prepared filled nanomaterials on cuts perpendicular to the coated substrate. The electrical resistance of the films was measured by an I–V measurement system (Material Development Corp.), which uses electrodes consisting of a mercury dot (760 µm in diameter) surrounded by a mercury ring. Samples of different filler content were investigated with d.c. and a.c. up to the frequency of 1 MHz. The specific resistance was calculated from the measured sheet resistance and film thickness. The temperature dependence of resistance was investigated within the range from –30 to 150 °C. The temperature coefficient of resistance (TCR) was calculated from the slope of the least-squares regression line.

## 3. Results and discussion

The SEM investigation shows that the carbon black fillers vary in their grain sizes from 30 to 500 nm. The carbon fibres have diameters of 70–300 nm and lengths of 30–150 µm (Fig. 1). The micrographs indicate that the most carbon black particles are homogeneously dispersed in the sol-gel derived modified silica matrix. Although the sol was treated by ultra sound for homogenisation, carbon black forms aggregates with a diameter of 200–800 nm in the SiO<sub>2</sub> matrix. The thickness of the films prepared by dip coating was 0.3–3 µm, depending on the filler concentration and rate of withdrawal. The layers prepared by screen-printing have the thickness of 10–30 µm. Both types of films exhibit good mechanical stability and adhesion on the substrate.

The films with high filler content show linear current–voltage characteristics in d.c. measurements, whereas in the case of low carbon black filler concentrations a non-linear behaviour was observed, which is typical of semiconductive materials (Fig. 2). For interpreting this behaviour, a model of two kinds of geometrical arrangements of adjacent conductive particles in the insulating matrix is used [15]. In the first type of arrangement, the particles contact each other directly while in the

other one the particles are separated by a very thin insulating layer and form a metal–insulator–metal unit. At low filler concentrations, most clusters form the latter type of arrangement, so that conductivity occurs via a tunnelling effect, which can explain the non-ohmic behaviour. At high filler concentrations contacting particles prevail and an ohmic-type of conductive mechanism dominates.

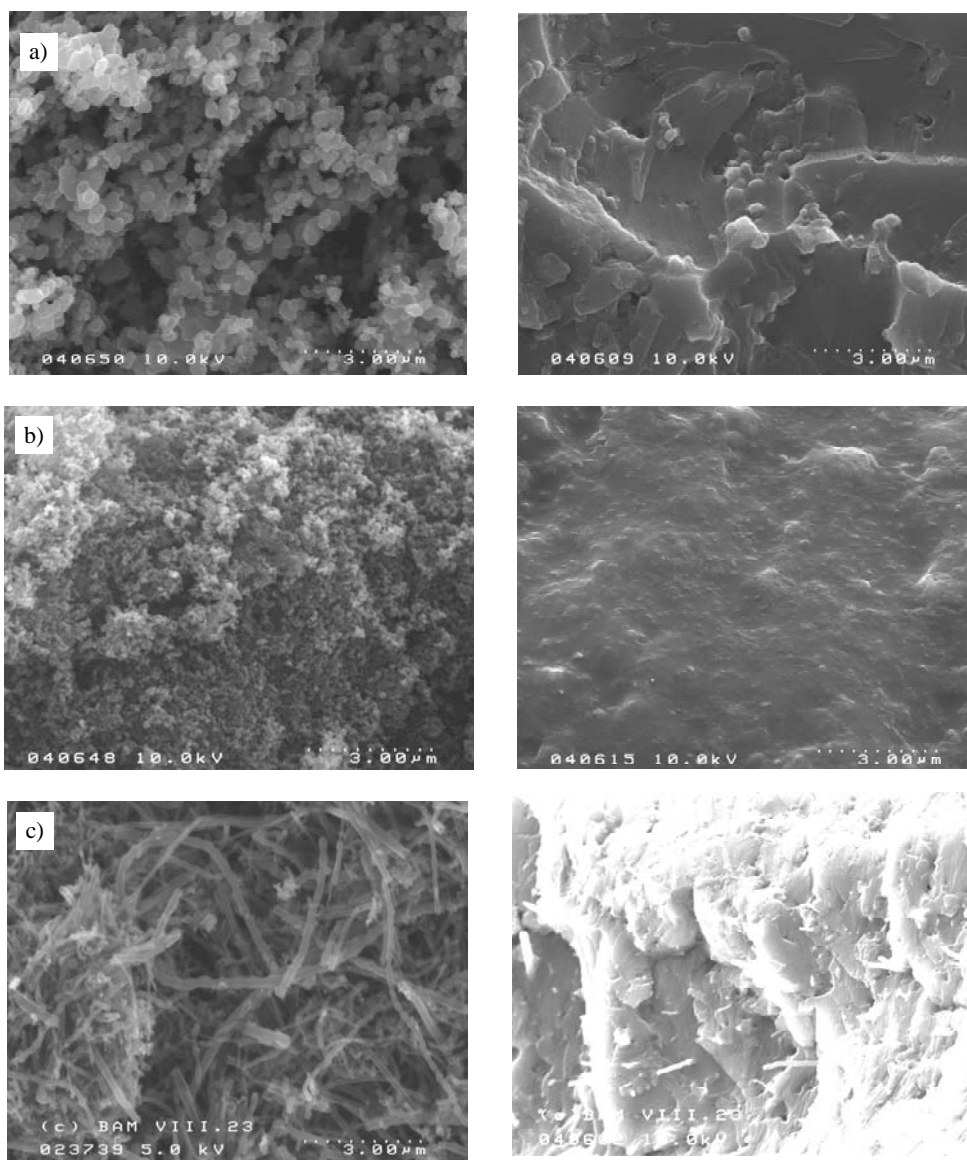


Fig. 1. SEM photomicrographs of various carbon fillers (left side) and the corresponding sol-gel derived thick films (right side), containing 5% (v/v) C: a) IN-1, b) 2B, c) Pyrograf III

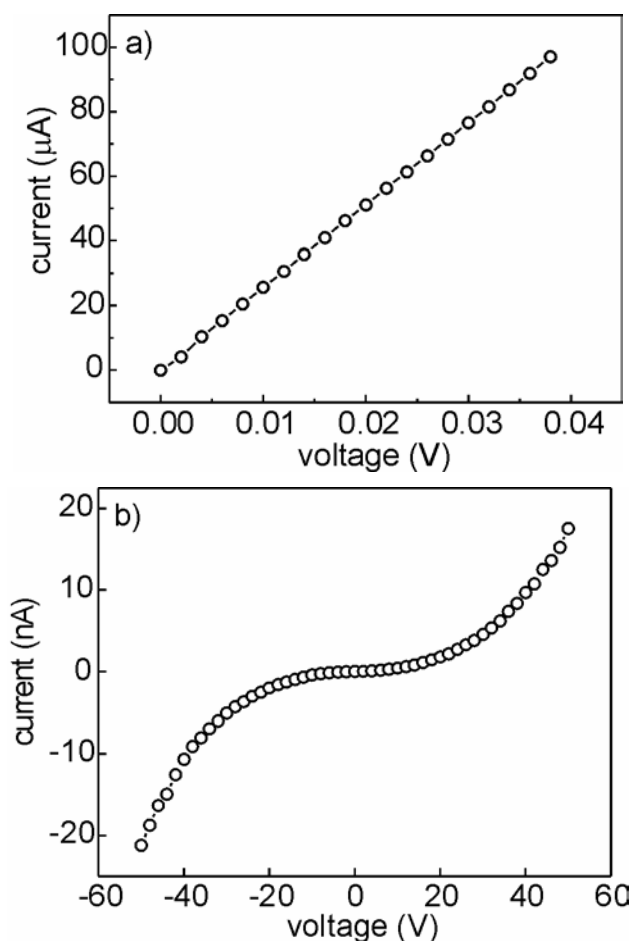


Fig. 2. Current–voltage characteristics of thin modified silica films containing carbon black: a) SiO<sub>2</sub> 50% (v/v) C, b) SiO<sub>2</sub> 60% (v/v) C

The resistivity of the films depends on the filler concentration in a characteristic manner. Although the carbon black concentration increases, the films have a high resistivity up to a critical filler concentration. Around the critical concentration, the resistivity drops drastically and reaches a minimum value. The resistance of thin films prepared by dip-coating remains nearly unaffected up to a carbon black concentration of about 50% (v/v), and then decreases abruptly. A detailed investigation of the influence of the amount of carbon black amount on resistivity gives the results shown in Fig. 3 [16].

This non-linear behaviour can be explained by the percolation theory. Fine conductive particles are dispersed in an insulating matrix and build agglomerates, so-called clusters. It is assumed that electric current can flow between particles being nearest neighbours. When a cluster spans the system from one side to the other (from one electrode to the other) at a concentration  $v_c$ , the so-called percolation threshold,

then the properties of the system change drastically from insulating to semi-conducting and conducting. The percolation transition is a critical phenomenon and implies that physical quantities related to the transition can be characterised by power laws of  $(v - v_c)$ :

$$R = K(v - v_c)^{-\beta} \quad (1)$$

Here  $R$  is resistivity,  $K$  and  $\beta$  are constants,  $v$  is the concentration of the conducting particles, and  $v_c$  the critical concentration. For thin films prepared by dip-coating, the most appropriate curve can be obtained for  $K = 0.03$ ,  $\beta = 1.75$ , and  $v_c = 0.50$ . This means that the electrical path of clusters is built at a filler concentration of 50% (v/v). The percolation threshold is strongly influenced by particle size and morphology. Typically values of 4–12 % (v/v) [17], but also up to 35 % (v/v) [9] and even below 0.2 % (v/v) [7] have been reported. The estimated relatively high value of  $v_c = 0.50$  indicates particle aggregation. The value of the critical exponent  $\beta$  between 1.3 and 1.75 was observed for a two-dimensional percolation network, which is supposed from the theory, and 2 for a three-dimensional model [18, 19].

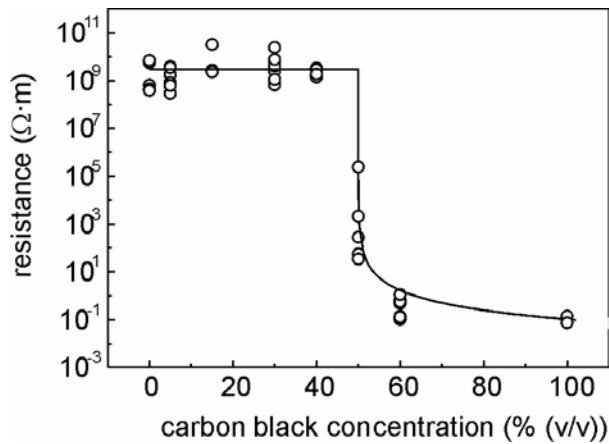


Fig. 3. The percolation threshold of a thin film material

The resistivity of films prepared by screen-printing changes from  $10^9$  to  $1.0 \Omega \cdot cm$  at a critical concentration of about 5% (v/v). The influence of grain size can be observed. Films containing various kinds of carbon fillers differ in the minimum resistivity. Those including carbon black with particle diameter of about 500 nm, carbon fibre, and carbon black of finer grain size exhibit a minimum resistivity of  $10^8$ ,  $10^4$  and  $1.0 \Omega \cdot cm$ , respectively (Fig. 1). Although the carbon particles in the graphite paste used to prepare thin films are smaller than most of those in the solution used to prepare thick films, they built aggregates and behave similarly to larger particles in the sol. These secondary particles make the percolation threshold of dip-coating films produced by graphite solution higher than of screen-printed films.

The dependence of the film resistance on frequency was determined in the range from 20 Hz to 1 MHz. The resistivity of the films showing high resistivity (above  $10^3 \Omega\text{-cm}$ ) at 20 Hz decreases with increasing frequency linearly in a logarithmic scale, whereas films of low resistivity (below  $10^2 \Omega\text{-cm}$ ) at 20 Hz are nearly independent on frequency until 1MHz. This behaviour could be illustrated by the tunnel effect. It is assumed that the current between clusters (agglomerations of conducting particles), which are separated by a very thin insulating silica layer, occurs by means of the tunnelling effect. The resistivity of a film can then be found from the tunnelling current using the following equation

$$\rho_{AC} \propto \frac{1}{\sigma_0 + 2\pi f \epsilon_0 \epsilon''} \quad (2)$$

Here  $\sigma_0$  is the part of the conductivity that is not influenced by the frequency  $f$ ,  $\epsilon_0$  is the permittivity of vacuum and  $\epsilon_r''$  the loss index. At low carbon filler amounts, the films show higher resistivity and the term  $2\pi f \epsilon_0 \epsilon_r''$  is significant, which results in a strong frequency dependence of the resistance for highly resistant films. Above the percolation threshold,  $\sigma_0$  dominates and the impedance values are less influenced by the frequency.

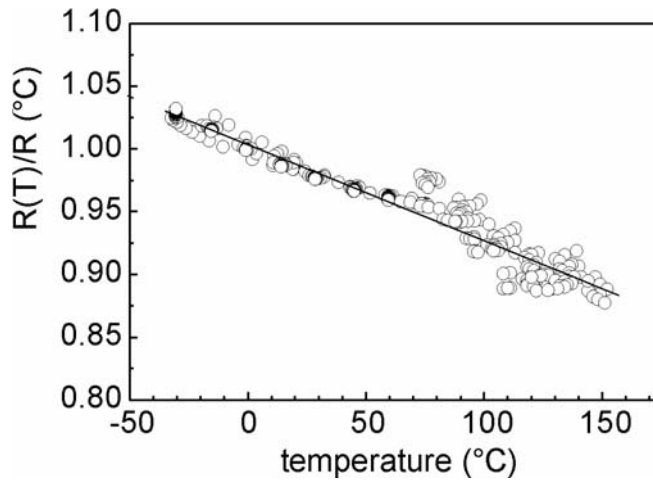


Fig. 4. The temperature dependence of the resistance of modified silica films containing 60% (v/v) carbon black at 1 kHz;  
TCR =  $-760 \times 10^{-6} \text{ K}^{-1}$ , uncertainty  $\pm 10 \times 10^{-6} \text{ K}^{-1}$

Measurements of the temperature dependence of resistance between  $-30$  and  $150 \text{ }^\circ\text{C}$  give a negative temperature coefficient of resistance (TCR) for both types of films. An example for a thin film is given in Fig. 4. Depending on the film composition, the TCR varies from  $-200$  to  $-1300 \times 10^{-6} \text{ K}^{-1}$ , which is comparable to values of carbon-based resistors.

## 4. Conclusions

Nanocomposites containing carbon fillers in a wide composition range can be prepared via the sol-gel process. The variation of filler concentration and grain size results in changes in resistance and its dependence on voltage and temperature. This behaviour is not immediately related to the concentration of the components and their mixture, but can be illustrated using the percolation model and a specific conductive mechanism of two kinds of adjacent small conductive particles. These nanomaterials can be considered to be promising new functional materials for miniaturized resistor units, electrodes, and sensors, combining interesting electrical and improved mechanical and thermal properties.

### Acknowledgements

The authors are grateful to Mrs. K. Keil for experimental support and Mrs. E. Strauss for SEM investigations.

### References

- [1] WARREN W.L., LENAHAN P.M., BRINKER C.J., SHAFFER R.G., ASHLEY C.S., REED S.T., *Sol-Gel Thin Film Electronic Properties*, Mat. Res. Soc. Symp. Proc., 180 (1990), 413.
- [2] SAKKAS S., KOZUKA H., *J. Sol-Gel Sci. Technol.*, 13 (1998), 701.
- [3] INNOCENCI P., KOZUKA H., *J. Sol-Gel Sci. Technol.*, 3 (1994), 229.
- [4] MENNING M., SCHMITT M., SCHMIDT H., *J. Sol-Gel Sci. Technol.*, 13 (1998), 701.
- [5] TRAPALIS C.C., KOKKORIS M., PEDIKADIS G., KORDAS G., *J. Sol-Gel Sci. Technol.*, 26 (2003), 1213.
- [6] LUTZ T., ESTOURNES C., GUILLE J. L., *J. Sol-Gel Sci. Technol.*, 13 (1998), 929.
- [7] FLADIN L., PRASSE T., SCHUELER R., SCHULTE K., BAUHOFFER W., CAVAILLE J.-Y., *Phys. Rev. B* 59 (1999), 14349.
- [8] NAKAMURA S., SAITO K., SAWA G., KITAGAWA K., *Jpn. J. Appl. Phys.*, 36 (1997), 5163.
- [9] ORLIKOWSKI J., *J. Corr. Measurement*, 2 (2002), <http://www.korozja.pl/4-01-02.pdf>.
- [10] TSIONSKY M., GUN G., GLEZER V., LEV O., *Anal. Chem.* 66 (1994), 1747.
- [11] OPALLO M., SACZEK-MAJ M., *Chem. Comm.* (2002) 448.
- [12] PRODROMIDIS M., KARAYANNIS M., *Electroanalysis* 14 (2002), 241.
- [13] BUNDEA., HAVLIN S., *Fractals and Disordered Systems*, Springer-Verlag, Berlin, 1996.
- [14] FUJIKI K., OGASAWARA T., TSUBOKAWA N., *J. Mater. Sci.*, 33 (1988), 1871.
- [15] KUSY A., LISTKIEWICZ E., *Solid State Electronics*, 31 (1988), 821.
- [16] SHIMAMURA A., Thesis, Technical University of Ilmenau, 2003.
- [17] JÄGER K.-M., McQUEEN D.H., TCHMUTIN I.A., RYVKINA N.G., KLÜPPEL M., *J. Phys. D: Appl. Phys.* 34 (2001), 2699.
- [18] HIDDEN G. et al., *J. Optoelectronics and Advanced Materials*, 6 (2004), 1065.
- [19] CARLBERG C., BLACHEN S., GUBBELS F., BROUERS F., DELTOUR R., JÉRÔME R., *J. Phys. D: Appl. Phys.*, 32 (1999), 1517.

*Received 12 August 2004*

*Revised 1 December 2004*

## **Design of molecular structure and synthetic approaches to single-source precursors in the sol-gel technology**

VADIM G. KESSLER<sup>1\*</sup>, GULAIM A. SEISENBAEVA<sup>1</sup>, PIA WERNDRUP<sup>1</sup>,  
STEPHANE PAROLA<sup>2</sup>, GERALD I. SPIJKSMA<sup>3</sup>

<sup>1</sup>Department of Chemistry, SLU, Box 7015, 75007 Uppsala, Sweden

<sup>2</sup>Laboratoire des Multimatériaux et Interfaces, UMR 5615, Université Claude Bernard,  
Lyon 1, 43 Bd 11 Novembre 1918, 69622 Villeurbanne, France

<sup>3</sup>Inorganic Materials Science, Faculty of Science & Technology, and Mesa<sup>+</sup> Research Institute  
for Nanotechnology, University of Twente, P.O. Box 217, 7500 AE, Enschede, The Netherlands

Metal alkoxide and  $\beta$ -diketonate complexes are broadly recognized as versatile precursors of high-purity glass and ceramic materials in the sol-gel technology. By applying reactants containing various metal atoms in the proper ratio and assuring their conservation through sol-gel treatment, single-source precursors (SSP) provide an efficient approach to complex materials. Simple and cost-efficient routes to SSP can be developed by applying the concept of geometrical molecular structure design, which is based on the choice of a type proper of molecular structure and its completion with ligands, providing the necessary number of donor atoms for the chosen core as well as sterical protection.

*Key words: precursor chemistry, single-source precursor, geometric design, solution stability, reactivity control*

### **1. Introduction**

Development of synthetic approaches to new complex materials urges the search for new routes to design and synthesise precursors. The requirements normally put on these compounds, belonging usually to the family of metal alkoxides [1–4], are high solubility in organic solvents, stability in solution, possibility of controlled hydrolysis (most often simply by water without any catalyst), limited sensitivity to moisture (requiring only reasonable precautions in treatment), and last, but far not the least, the accessibility and commercial availability. All these properties are directly determined

---

\*Corresponding author, e-mail: Vadim.Kessler@kemi.slu.se.

or, like the last one, strongly influenced by the molecular structure of these species. The ability to predict the molecular structure is the key to design the approaches to new precursors. The need in purpose design becomes crucial in approaches to the single source precursors (SSP) – the species permitting to specifically facilitate the formation of the desired material in such aspects as chemical and phase composition, morphology or domain structure via preservation of the chemical composition or structure features of the building blocks from precursor molecule to material. In literature, before recently, one could find two approaches to design of the alkoxide species: the concept of “alkoxosalts” of Meerwein for heterometallic and Bradley’s structure theory for homometallic ones. The former considered the heterometallic alkoxides as salts of “ansolvoacids”,  $\text{H}[\text{Al}(\text{OR})_4]$ ,  $\text{H}[\text{Zr}_2(\text{OR})_9]$  and  $\text{H}[\text{Nb}(\text{OR})_6]$ , respectively [4, 5]. It predicted successfully the compositions of some of the derivatives of alkali and alkaline earth metals, but failed already in application to derivatives of lanthanides:  $\text{La}_2\text{Zr}_3\text{O}(\text{O}^i\text{Pr})_{16}$  [3] was found instead of  $\text{La}[\text{Zr}_2(\text{O}^i\text{Pr})_9]_3$  [6],  $\text{LaNb}_2(\text{O}^i\text{Pr})_{13}$  [7] instead of  $\text{LaNb}_3(\text{O}^i\text{Pr})_{18}$  [8] etc. Bradley’s theory predicted the structure of stable oligomeric aggregates to be containing the minimal number of metal atoms providing possibility of formation of stable coordination polyhedra for all of them and turned efficient in prediction of molecular structures for a number of compounds but gave no approach to species with desired size or desired structure.

Having carried out the analysis of available structural data on Ba–Ti system [9–12], we were able to trace the trend to formation of molecules belonging to a limited number of stable structure types, requiring the presence of well-defined number of donor atoms in the ligands. Completing a chosen structure type with additional donor atoms via use of  $\beta$ -diketonate ligands, we were able to prepare a principally new solution-stable precursor of  $\text{BaTiO}_3$ ,  $\text{Ba}_2\text{Ti}_2(\text{thd})_4(\text{OEt})_8(\text{EtOH})_2$  [13], belonging to a very common and stable  $\text{M}_2\text{M}'_2\text{X}_{16}$  structure type, and formulated a new principle in approach to the complex precursors, the molecular structure design concept (MSDC): to design a new heterometallic alkoxide complex one should choose a desired structure type and complete it with ligands, providing both the necessary number of donor atoms and the sterical protection of the chosen core [14].

We report the successful application of this concept to design and synthesis of new classes of precursors for such materials as spinels, barium and strontium zirconates, zirconia and titania–zirconia.

## 2. Experimental

All manipulations were carried out in a dry nitrogen atmosphere using Schlenk technique or a glove box. Waterfree  $\text{M}^{\text{II}}(\text{acac})_2$ ,  $\text{M} = \text{Co}, \text{Ni}$ , was obtained by sublimation of  $\text{M}^{\text{II}}(\text{acac})_2 \cdot x\text{H}_2\text{O}$  (Aldrich Chemical Company Inc.) at 110–145 °C and 1 mm Hg. Water-free  $\text{Zn}(\text{acac})_2$  was obtained by refluxing  $\text{Zn}(\text{acac})_2 \cdot x\text{H}_2\text{O}$  (Aldrich Chemical Company Inc.) with dry toluene with subsequent evaporation, repeated twice.  $\text{Mg}(\text{acac})_2$

was prepared by refluxing magnesium metal with acetylacetone. The slurry and solvent were transferred to a new flask, the solvent was removed by decantation and the crystals were washed with boiling toluene and evaporated to dryness, repeated twice. Titanium and zirconium alkoxides were purchased from Aldrich and used without further purification.  $\text{Ta}(\text{O}^i\text{Pr})_5$  and  $\text{Nb}(\text{O}^i\text{Pr})_5$  were prepared by anodic oxidation of the metals in methanol and purified according to conventional techniques [7, 8].  $\text{Al}(\text{O}^i\text{Pr})_3$  was obtained by reaction of aluminium foil with isopropanol and purified by recrystallization from toluene. Isopropanol (Merck, p.a.) was purified by distillation over  $\text{Al}(\text{O}^i\text{Pr})_3$  and hexane and toluene (Merck, p.a.) by distillation over  $\text{LiAlH}_4$ . The metal ratio in the bimetallic complexes was determined, exploiting the facilities of the Arrhenius Laboratory, Stockholm University, Sweden, on JEOL-820 scanning electron microscope (SEM), supplied with Link AN-10000 energy dispersive spectrometer (EDS). Mass-spectra were recorded using JEOL JMS-SX/SX-102A mass-spectrometer applying electron beam ionization ( $U = 70$  eV) with direct probe introduction. UV-Vis spectra were registered for 0.025–0.05 M solutions in toluene using Hitachi U-2001 spectrophotometer. IR spectra of nujol mulls were registered with a Perkin Elmer FT-IR spectrometer 1720 X.  $^1\text{H}$  NMR spectra were recorded for the  $\text{CDCl}_3$  solutions on a Bruker 400 MHz spectrometer. The results of microanalysis (C, H) were obtained for all the reported compounds in the Laboratory of Organic Microanalysis of Moscow State University, Russia and Mikrokemi AB, Uppsala, Sweden using the combustion technique.

X-ray single crystal studies were made on SMART CCD 1k diffractometer using SHELXTL-NT program package for computations. X-ray powder diffraction (XRD) patterns of the obtained phases were recorded with a Philips PW 3710 diffractometer with  $\text{CuK}\alpha_1$  radiation ( $\lambda = 1.54056$  Å). The morphology of the films and the particles was investigated with a Hitachi S800 15 kV scanning electron microscope (SEM). The roughness of the film surface was studied with a Picoscan-5 Molecular Imaging atomic force microscopy (AFM). A Topcon EM-002 B Ultrahigh resolution analytical electron microscope was used for the Transmission Electron Microscopy images. Analysis of the composition of the gas phase after thermal decomposition of the precursors was performed using a HP 5973 mass spectrometer coupled with a HP 6890 gas chromatography.

### 3. Results

In this work, we have carried out a study of structure and stability of the products of modification of zirconium alkoxides  $\text{Zr}(\text{OR})_4$ ,  $\text{R} = {}^n\text{Pr}$ ,  ${}^i\text{Pr}$  with chelating ligands such as acetylacetone, Hacac, and diethanolamine,  $(\text{HOC}_2\text{H}_4)_2\text{NH}$ . It turned out that in case of Hacac in the absence of hydrolysis only two types of compounds characterized as  $[\text{Zr}(\text{OR})_3(\text{acac})]_2$  and  $\text{Zr}(\text{acac})_3(\text{OR})$  could be formed, none of them being stable in

solution for a long time according to NMR investigation – all of them rearranged slowly yielding  $Zr(acac)_4$  as the final product (see Fig. 1).

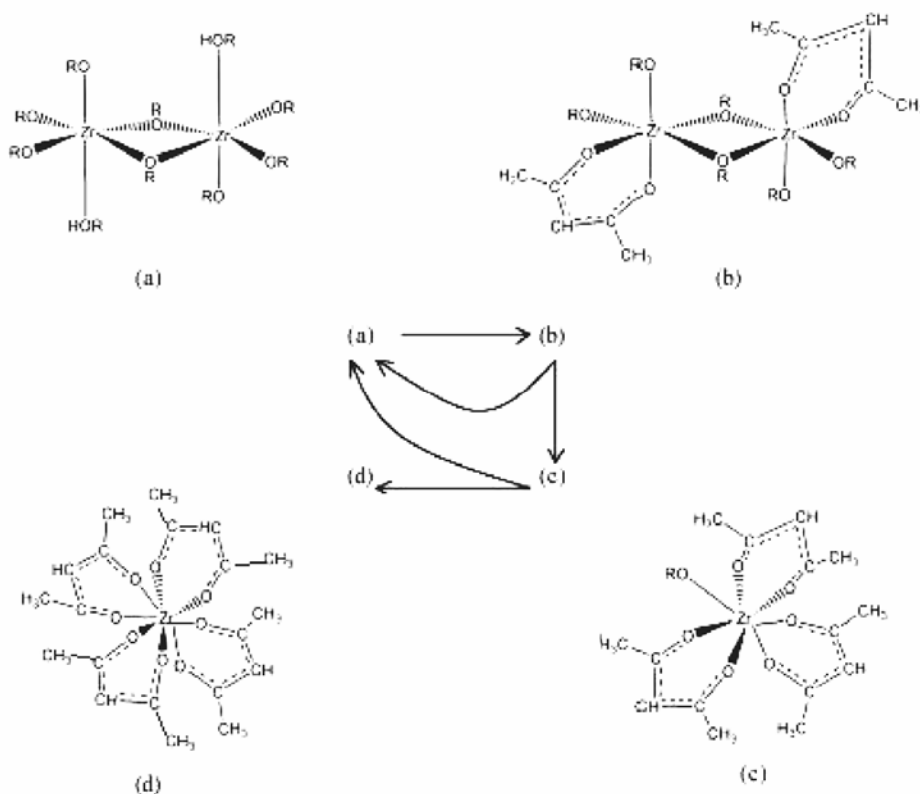


Fig. 1. The proposed mechanism and structures for the stabilization of zirconium propoxide in propanol. Addition of up to 1 mol equivalent Hacac to the initial precursor (a) leads to (b). Addition of more than 1 mol equivalent leads to a reaction of (b) to (a) and (c). Spontaneous rearrangement of (c) gives (d) and (a)

Solution-stable modified species,  $Zr_3(dea)_3(O^iPr)_6(^iPrOH)_2$  (Fig 2a), were obtained by the reaction of  $[Zr(O^iPr)_4(^iPrOH)]_2$  with diethanolamine (up to 1 eq per mol Zr). This structure contained two types of metal atom positions – nona-coordinated  $Zr(\mu_2\mu_2\eta^3\text{-dea})_3$  in the middle and hexacoordinated  $Zr(\mu_2\text{-dea})_3(O^iPr)_3$  at the ends. It was evident that these could host a different, smaller metal atom and we succeeded in the preparation of a solution-stable bimetallic Zr–Ti analog,  $ZrTi_2(dea)_3(O^iPr)_6$  (Fig. 2b) by modification of a Zr : Ti = 1 : 2 mixture with 3 equivalents of  $H_2dea$ .

Application of these compounds to prepare mesoporous oxides will be reported separately, but it is important to mention that the Zr–Ti complex with only one type of alkoxide groups (at Zr atoms) opens prospects for approach to oxides from  $TiO_2$ – $ZrO_2$  systems with uniform distribution of cations in them.

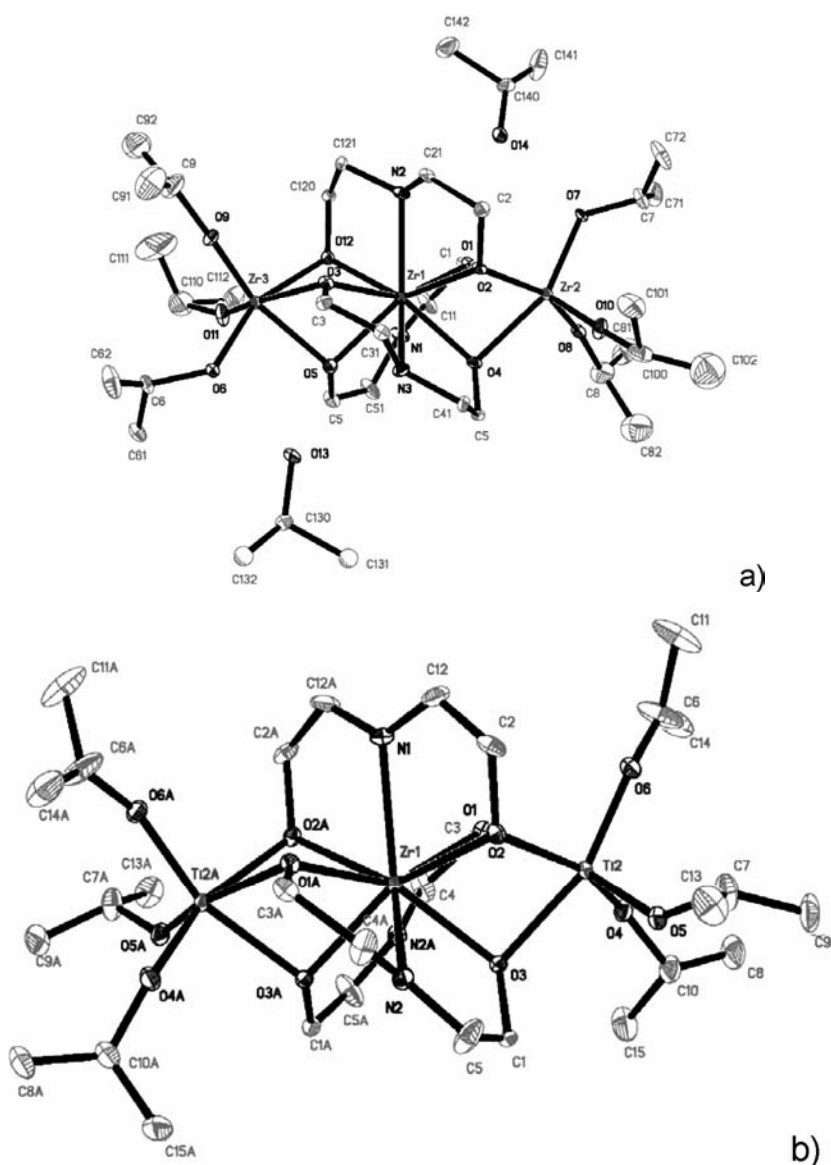


Fig. 2. Molecular structures of  $Zr_3(dea)_3(O^iPr)_6(iPrOH)_2$  (a) and  $ZrTi_2(dea)_3(O^iPr)_6$  (b)

Application of MSDC to the synthesis of precursors of ferroelectric materials,  $M^{II}ZrO_3$ ,  $M^{II} = Sr, Ba$  permitted to develop simple one-batch approaches to hydroxide isopropoxide species (Fig. 3) via partial hydrolysis of solutions of  $M^{II}(O^iPr)_2$  and  $Zr(O^iPr)_4$  (1:1 ratio) with 1 eq. of water in isopropanol. The Veith et al. idea [1] about the kinetic control in formation of these species was shown to be erroneous and leading to irrationally complicated synthetic approaches.

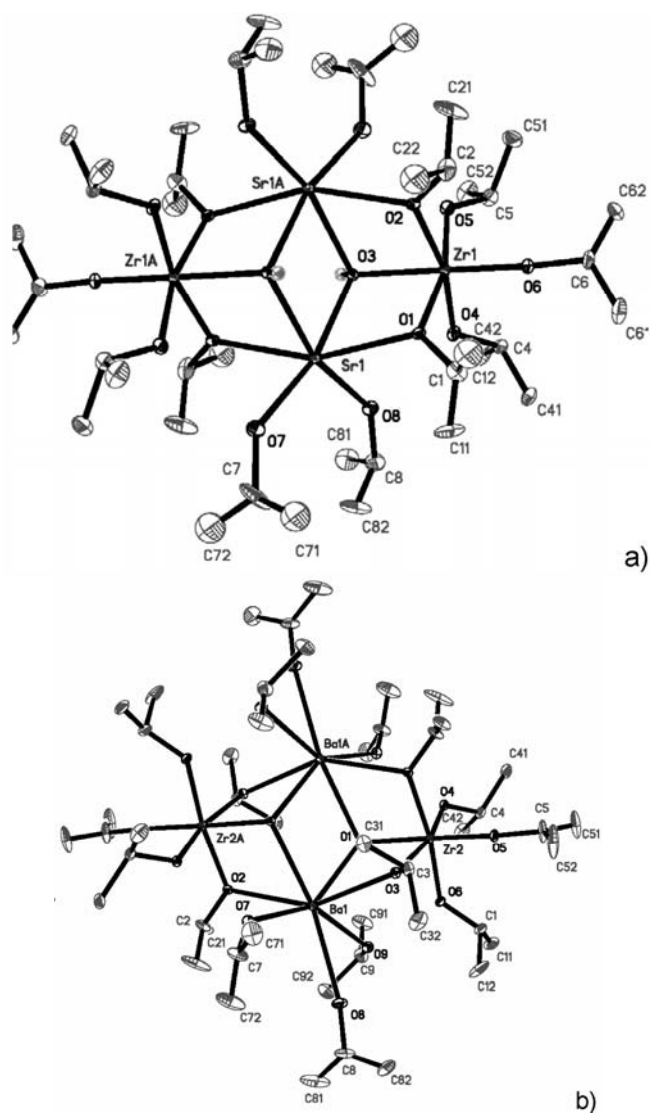


Fig. 3. Molecular structures of  $\text{Sr}_2\text{Zr}_2(\text{OH})_2(\text{O}^i\text{Pr})_{10}(\text{}^i\text{PrOH})_4$  (a) and  $\text{Ba}_2\text{Zr}_2(\text{OH})_2(\text{O}^i\text{Pr})_{10}(\text{}^i\text{PrOH})_6$  (b)

Both these compounds turn out to be unstable in solution, displaying irreproducible solubility in alcohols and decomposition with precipitation of solvated hydroxides,  $\text{M}^{\text{II}}(\text{OH})_2(\text{ROH})_x$ , on dissolution in hydrocarbons. Highly soluble solution-stable species were obtained following the same logic as for Ba–Ti precursors, i.e. applying  $\beta$ -diketonate ligands such as 2,2,6,6,-tetramethylheptanedion (Hthd) as modifier (1 eq. for 1:1 mixtures of  $\text{M}^{\text{II}}(\text{O}^i\text{Pr})_2$  and  $\text{Zr}(\text{OR})_4$ ,  $\text{R} = {}^n\text{Pr}$ ,  ${}^i\text{Pr}$ ) in toluene (see fig. 4).

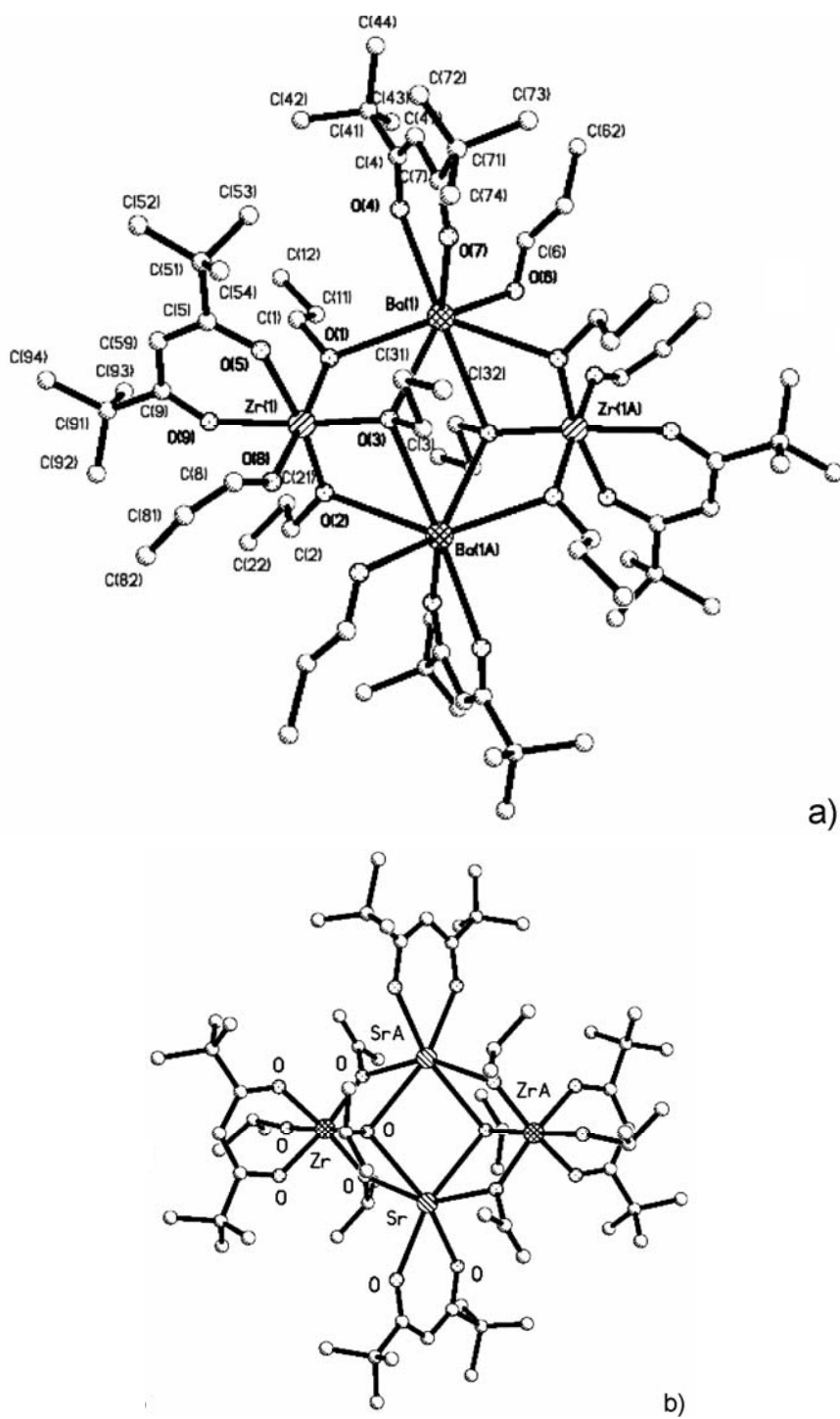


Fig. 4. Molecular structures of  $\text{Ba}_2\text{Zr}_2(\text{thd})_4(\text{O}^i\text{Pr})_8(\text{PrOH})_2$  (a) and  $\text{Sr}_2\text{Zr}_2(\text{thd})_4(\text{O}^i\text{Pr})_8$  (b)

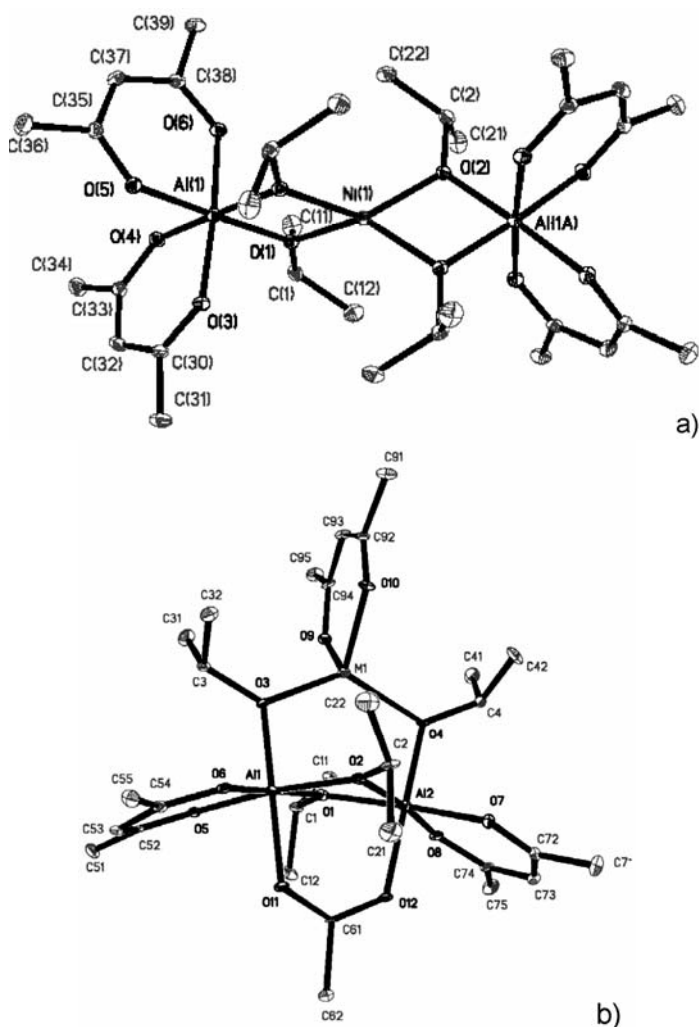


Fig. 5. Molecular structures of  $M^{II}Al_2(O^iPr)_4(acac)_4$  (a) and  $M^{II}Al_2(O^iPr)_4(acac)_3(OAc)$  (b)

Formation of the  $M_2M'_2X_{16}$  structure type is characteristic of the complexes of comparably small cations, such as those of late transition metals and Mg, with normal chain structure ligands (methoxides, ethoxides, *n*-propoxides) or bigger cations, such as Sr or Ba, with iso- or sec-alkoxide derivatives. Complexes of smaller cations and iso- or sec-alkoxide ligands have usually chain structures with two or three alkoxide bridges between the metal atoms [3, 14]. We have applied this knowledge for development of approaches to two new families of spinel precursors,  $M^{II}Al_2(acac)_4(O^iPr)_4$ ,  $M^{II} = Mg, Mn, Co, Ni$ , [15] and  $M^{II}Al_2(acac)_3(OAc)(O^iPr)_4$ ,  $M^{II} = Mg, Mn, Co, Zn$ , [16] by simple one-batch synthetic techniques:





The molecular structures of these two new families of precursors (Fig. 5) demonstrate two structure types with analogous formal composition,  $MM'_2X_{12}$ , but different geometries: the linear chain one giving easier hydrolysis and less solution stability and the ring-type one with higher solution stability and higher resistance to hydrolysis (due to higher Lewis acidity of Al-fragment involving more ionically bonded acetate ligand).

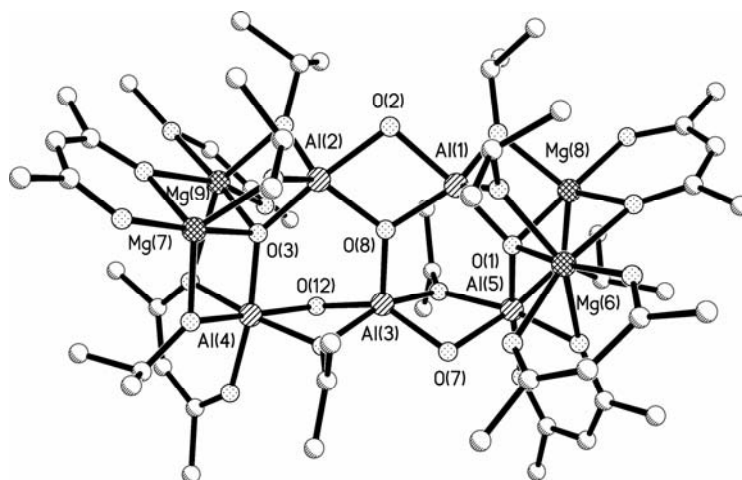


Fig. 6 Molecular structure of  $\text{Al}_5\text{Mg}_4\text{O}_3(\text{OH})_3(\text{O}^i\text{Pr})_8(\text{acac})_6$  formed on microhydrolysis of  $\text{MgAl}_2(\text{O}^i\text{Pr})_4(\text{acac})_4$

In sol-gel application of the first of these classes it is important to avoid partial hydrolysis as the solution equilibria for metal alkoxide complexes are leading usually to redistribution of cations in the partially hydrolyzed species [9]. We have carried out a study of partial hydrolysis on  $\text{MgAl}_2(\text{O}^i\text{Pr})_4(\text{acac})_4$  and observed also in this case the formation of a complex with changed stoichiometry,  $\text{Al}_5\text{Mg}_4\text{O}_3(\text{OH})_3(\text{O}^i\text{Pr})_8(\text{acac})_6$  (Fig. 6).

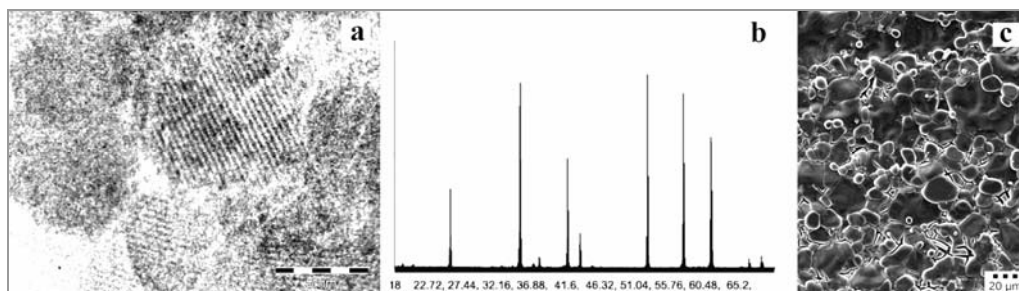


Fig. 7. HREM image of the  $\text{CoAl}_2\text{O}_4$  nanoparticles obtained from  $\text{CoAl}_2(\text{O}^i\text{Pr})_4(\text{acac})_3(\text{OAc})$  by sol-gel (a), X-ray powder pattern (b) and SEM image (c) of the  $\text{NiAl}_2\text{O}_4$  film obtained by dip-coating from solution of  $\text{NiAl}_2(\text{O}^i\text{Pr})_4(\text{acac})_4$  in toluene on melted alumina support

Single-phase nanopowders of spinels could successfully be prepared from both classes of precursors by complete hydrolysis (Fig. 7). Single-phase coatings of spinels were obtained from  $M^{II}Al_2(O^iPr)_4(acac)_4$  by dip-coating technique in humid atmosphere with intermediate heat treatments at 100 °C and final annealing at 400 °C.

## 4. Discussion

The present work shows unambiguously that the formation of alkoxide complexes is a result of thermodynamically driven self-assembly and the nature of these compounds, being attractive molecular precursors of materials, including their composition and molecular geometry can be predicted using the molecular structure design concept. The conditions of hydrolysis and subsequent thermal treatment should be carefully investigated in order to support the single-source precursor effect – an erroneous treatment can lead to chemical and phase impurities in the material even when a complex with proper composition is applied as precursor.

## References

- [1] VEITH M., Dalton Trans., 2002 (2002), 2405.
- [2] HUBERT-PFALZGRAF L.G., Inorg. Chem. Commun., 6 (2003), 102.
- [3] TUROVA N.YA., TUREVSKAYA E.P., KESSLER V.G., YANOVSKAYA M.I., *The Chemistry of Metal Alkoxides*, Kluwer, Boston, 2002.
- [4] BRADLEY D.C., MEHROTRA R.C., ROTHWELL I.P., SINGH A., *Alkoxo and Aryloxo Derivatives of Metals*, Academic Press, San Diego, 2001.
- [5] MEERWEIN H., BERSIN T., Ann., 476 (1929), 113.
- [6] TRIPATHI U.M., SINGH A., MEHROTRA R.C., Polyhedron, 10, (1991), 949.
- [7] TUREVSKAYA E.P., TUROVA N.YA., A.V. KOROLEV, YANOVSKY A.I., YU.T. STRUCHKOV, Polyhedron, 14, (1995), 1531.
- [8] BRADLEY D.C., MEHROTRA R.C., GAUR D., *Metal Alkoxides*, Academic Press, London, 1978.
- [9] YANOVSKAYA M.I., TUREVSKAYA E.P., KESSLER V.G., OVBINTSEVA I.E., TUROVA N.YA., Integrated ferroelectrics, 1, (1992), 343.
- [10] YANOVSKY A.I., YANOVSKAYA M.I., LIMAR V.K., KESSLER V.G., TUROVA N.YA., STRUCHKOV YU.T., Chem. Commun., 1991, (1991), 1605.
- [11] TUROVA N.YA., TUREVSKAYA E.P., KESSLER V.G., YANOVSKAYA M.I., J. Sol-Gel Sci. Tech., 2, (1994), 17.
- [12] CAULTON K.G., HUBERT-PFALZGRAF L.G., Chem. Rev., 90, (1990), 969.
- [13] KESSLER V.G., HUBERT-PFALZGRAF L.G., DANIELE S., GLEIZES A., Chem. Mater., 6, (1994), 2236.
- [14] KESSLER V.G., Chem. Commun., 2003, (2003), 1213.
- [15] KESSLER V.G., GOHIL S., PAROLA S., Dalton Trans., 2003, (2003), 544.
- [16] SEISENBAEVA G.A., SUSLOVA E.V., KRITIKOS M., KESSLER V.G., RAPENNE L., ANDRIEUX M., CHASSAGNEUX F., PAROLA S., J. Mater. Chem., 2004 (in press).

Received 16 July 2004  
Revised 4 November 2004

## **Application of image analysis for characterization of powders**

JAKUB MICHALSKI<sup>1\*</sup>, TOMASZ WEJRZANOWSKI<sup>1</sup>, ROMAN PIELASZEK<sup>2</sup>,  
KATARZYNA KONOPKA<sup>1</sup>, WITOLD ŁOJKOWSKI<sup>2</sup>, KRZYSZTOF JAN KURZYDŁOWSKI<sup>1</sup>

<sup>1</sup>Warsaw University of Technology, Faculty of Materials Science and Engineering,  
Wołoska 141, 02-507 Warsaw, Poland

<sup>2</sup>High Pressure Research Center of the Polish Academy of Science,  
Sokołowska 29, 01-142 Warsaw, Poland

A number of currently developed and produced modern multi-functional materials are to a large extent based on the use of powders. Powders with precisely characterized size, size distribution, shape and surface are used directly (e.g. catalysis) or to fabricate novel ceramics, metals and composites. Description of morphology of powders, both in micro- and nano-scale, could be obtained by the means of modern stereological methods supported by computerized image analysis. These methods can be used to describe size, shape, surface topography for both the aggregates and agglomerates and single crystallites. Stereological methods supported by computerized image analysis of high-resolution electron microscope images are becoming an important tool of modern powder-related materials science. The present work demonstrates the possibility of using such methods in determining the basic stereological parameters characterizing the morphology of the ceramic powders in micro- and nano-scale.

Key words: *nano-crystals; grain size and shape; image analysis; stereology*

### **1. Introduction**

Progress in development of modern materials, including so-called nanomaterials, is enhanced by advances in powder technologies and improvement in powder characterization methods. Production, processing and thorough characterization of ultra fine-grained powders in connection with novel techniques of their consolidation is an important segment of nanotechnologies. Currently nanopowders are used, for example, as filling materials for different kinds of polymers and ceramics to produce compos-

---

\*Corresponding author, e-mail: [jmichalski@inmat.pw.edu.pl](mailto:jmichalski@inmat.pw.edu.pl).

ites with better strength, hardness, corrosion and electrical resistance. They are also directly applied in medicine (drug delivery) and chemical industry (catalytic processes).

The efficiency of nanopowders is controlled by their chemistry but also by size and shape. The aim of the present paper is to demonstrate how size and shape can be characterized from images of powders particles correlated with methods of indirect size estimates.

## 2. Size and shape

Powders are usually mixtures of different sized grains, where the fine fraction, decisive on the properties of the particular powder, reveals desirable characteristics of the nanoscale, whilst larger grains might significantly weaken this effect. At the same time, most nanopowders have tendency to form agglomerates as a result of high surface energy related to their high specific surface. This is why nanopowders are usually composed of micrometric agglomerates of nanometrical crystallites.

Figure 1 shows the relation of intensity of a hypothetical size effect (e.g. luminescence) to the average powder grain size  $\langle \bar{d} \rangle$  (horizontal axis, [nm]) and relative grain size distribution (vertical axis,  $CV(d)/\langle R \rangle$ ) [2]. An assumption has been made that the effect is strongest for crystals of 5 nm size and weakens with the grain size as  $1/R$ . One contour line represents a decrease in the effect intensity by about 9%. It thus clear that not only the average grain size but also size distribution both influence the effects observed in nanoscale.

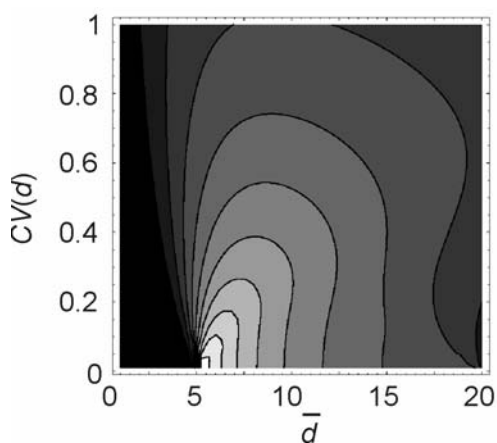


Fig. 1. Relation of intensity of the hypothetical size effect (e.g., luminescence) to the average powder grain size  $\langle \bar{d} \rangle$  (horizontal axis, [nm]) and relative grain size distribution (vertical axis,  $CV(d)$ )

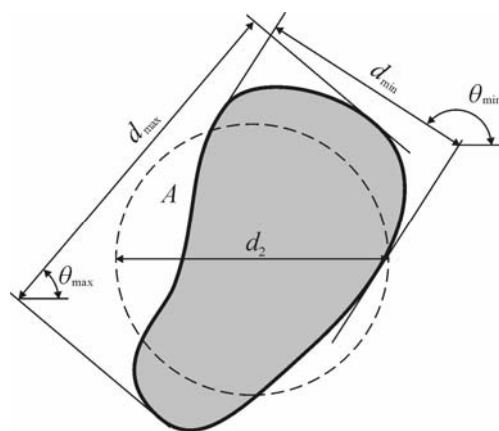
Therefore, in modern applications it is not sufficient to control only average grain size which can be obtained from standards methods of the specific surface or analysis of peak widths in X-ray diffraction. Thorough characterization is needed which requires description of individual grains and the agglomerates of grain powders. Size

and shape of individual crystallites relate to the first concept, yet the most complete description of the powder as a whole is its grain size distribution.

The methods used to measure the powder grain size, enabling the analysis of the grain size distribution, could be divided into two groups: direct and indirect. The direct methods map the geometry of individual grains via electron scanning and transmission microscopy. Indirect methods are based on physical effects, such as widening of X-ray diffraction reflexes in XRD methods or laser diffraction [1, 2]. The present paper concerns direct measurements of grain/particle size.

Stereological methods could be used for precise description of powders based on their planar images. Useful for powder characterization are parameters measured for individual “objects” such as: equivalent average  $d_2$ ,  $d_{\max}$ ,  $d_{\min}$  and shapes factors  $\alpha = d_{\max}/d_2$ ,  $\beta = p/\pi d_2$ ,  $\gamma = p/p_c$ . These parameters are relatively easy to determine with the planimetric methods and computer image analysis. The graphic illustration of the above-listed parameters is shown in Fig. 2.

Fig. 2. Graphical interpretation of parameters describing image of the grains: area ( $A$ ), calculated on planar section, conventional diameter ( $d_2$ ), diameter of a circle of the same surface as the surface of the analyzed grain, maximal projection ( $d_{\max}$ ), circumference ( $p$ ), shape coefficient ( $\alpha = d_{\max}/d_2$ ,  $\beta = p/d_2$  and  $\gamma = p/p_c$ ) [3]



The above parameters are determined for individual grains/particles. Statistical size distribution is described by the frequency function  $f(x)$  and usually characterized by means of statistical moments. The basic moment is the average value of the particular parameter  $E(x)$ . Also, the coefficient of variation, marked as  $CV(x)$  is used. It describes the relative extent of dispersion of measured values ( $CV(x) = SD(x)/E(x)$ , where  $SD(x)$  is the standard deviation [3]). Average values:  $A$  and  $d_2$ ,  $E(A)$  and  $E(d_2)$ , allow one to determine the average grain size. However, in order to fully characterize the structure, it is also necessary to determine the size distribution of the measured structure elements. This helps to prevent mistakes in interpretation of the results obtained with the use of parameters such as  $E(A)$  or  $E(d_2)$  for materials with diversified elements (Fig. 3). In some cases it is possible to establish weighted particle size distribution taking particle volume, as the weight. This enables presenting the real particle volume distribution in the analyzed powder (large particles even though less numerous take up a larger volume than smaller particles which there are usually more of).

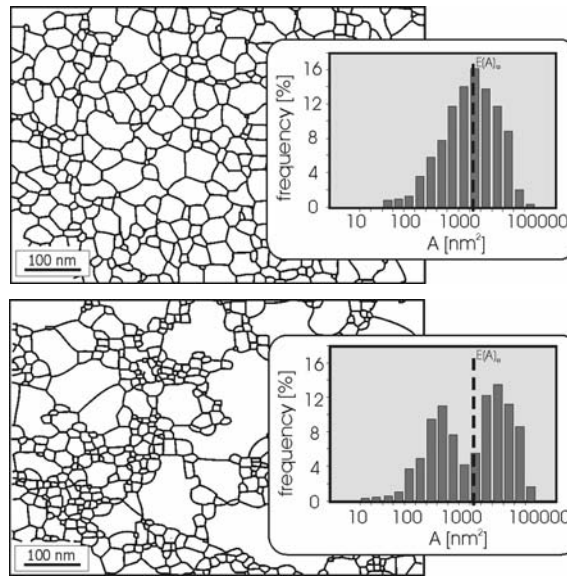


Fig. 3. Sample structures characterized by the same average grain surface value but with different grain size distribution

Average values of shape parameters  $E(d_{\max}/d_2)$ ,  $E(p/d_2)$ ,  $E(p/p_c)$  are used for quantitative description of grain elongation, curvature of grain boundary and convexity. Sample shapes of structural elements for different combinations of the shape coefficients are shown in Fig. 4.

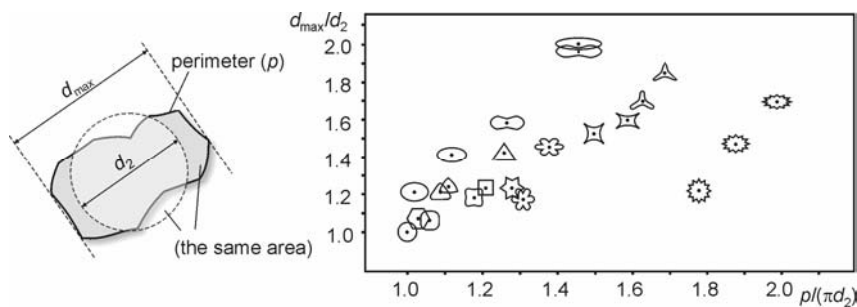


Fig. 4. Shapes of structure elements for different combinations of the shape coefficients

### 3. Image analysis and stereology

Stereological methods supported by computer image analysis make useful tools for quantitative powder characterization. Software MicroMeter developed at the Faculty of Materials Science and Engineering of the Warsaw University of Technology

was used in the present work [4] for the analysis of the size and shape of the nanopowders.

Procedure of qualitative powder analysis with the use of already mentioned methods could be divided into 3 stages: imaging, image analysis and determination of the stereological parameter.

The choice of imaging technique depends largely on the type of powder and especially its size. In the case of very fine-grained powders, it is necessary to use TEM, nevertheless even in such a case images under smaller magnifications (e.g. SEM) could reveal the degree of agglomeration.

For the purpose of qualitative analysis, microscopic images are transformed into binary ones which determine the powder grains. For the purpose of further analysis those grains are selected, which do not overlap with others (see Fig.5).

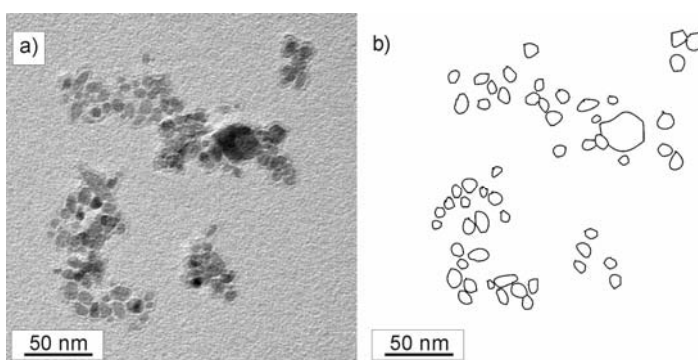


Fig. 5. TEM image of  $ZrO_2$  powder (a) and its binary representation (b)

Parameters obtained as a result of qualitative analysis and their distributions are then transformed into true distribution (3D) through stereological modelling. Such models focus mostly on the grain shape. When powder particles are spherical, their projections on microscopic images are circles, and the diameter of each of these circles could be regarded as the spatial diameter.

#### 4. Examples of applications

AKP-50 Sumimoto sub micron  $Al_2O_3$  powder was subject to laser diffraction (Fig. 6), computer image analysis of SEM (Fig. 7) and TEM (Fig. 8). Quantitative analysis of the ceramic  $Al_2O_3$  Sumimoto powder revealed that this powder is characterized by the average grain size of 120–130 nm. Also, the grain sizes are uniform (coefficient of variation – 30%) and the size distribution is a log-normal.

Powder grain shape analysis showed that the particular powder grains are spherical-like shaped ( $\alpha = 1.26$ – $1.33$ ). The low value of the variation coefficient obtained for the shape factor  $\alpha$  (Tables 1 and 2) proves a strong shape homogeneity of powder particles.

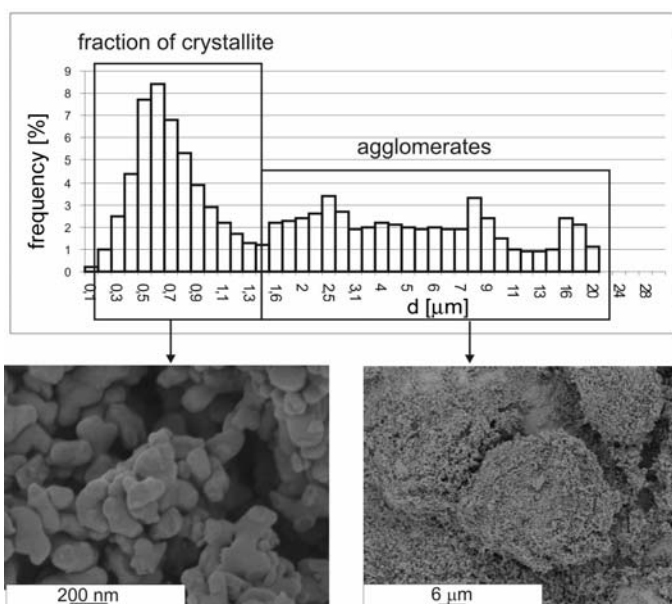


Fig. 6. Grain size distribution of sub micron powder AKP-50 measured by the laser diffraction

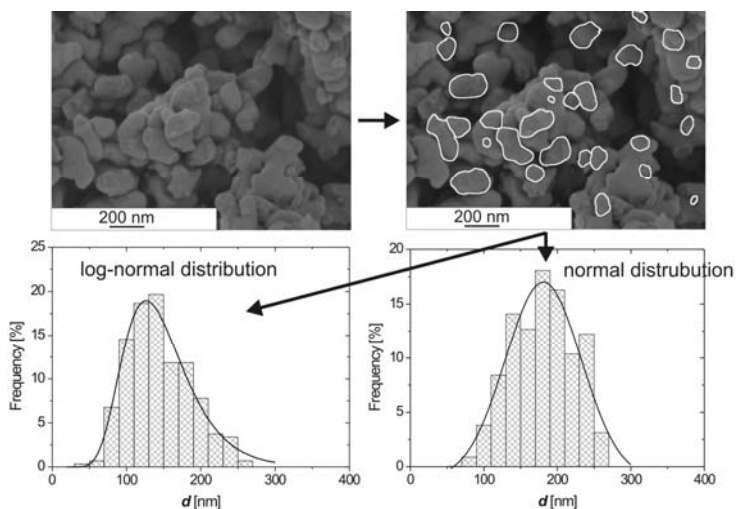


Fig. 7. Grain size distribution of the sub micron powder AKP-50 by computer analysis of SEM image, log-normal distribution (a), weight distribution (b)

When comparing the results obtained by laser diffraction with the results from quantitative analysis of images it is easy to notice the deviation caused in laser diffraction by powder agglomeration. The average grain size of  $3.16 \mu\text{m}$  is a combination of sizes of individual crystallites and agglomerations, whilst the results of quantitative analysis performed on SEM and TEM images result in true values of 120 to 130 nm.

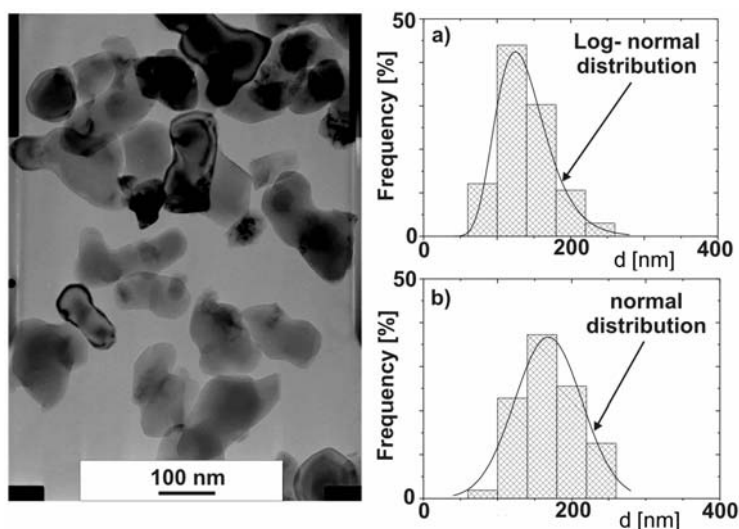


Fig. 8. The grain size distribution of sub micron powder AKP-50 by computer analysis of TEM image, log-normal distribution (a), weight distribution (b)

Table 1. The results of measurements shown in Fig. 7 for SEM

Value	$d$	Shape factor $\alpha$
Average	130 nm	1.26
Coefficient of variation	30%	9%

Table 2. The results of measurements shown in Fig. 8 for TEM

Value	$d$	Shape factor $\alpha$
Average	120 nm	1.33
Coefficient of variation	30%	9%

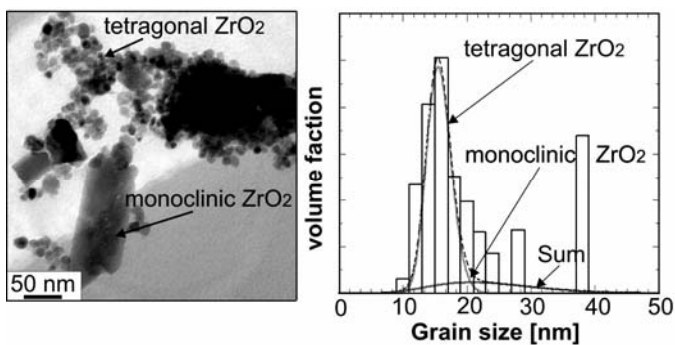


Fig. 9. The grain size distribution of  $ZrO_2$  nano-powder obtained from TEM image analyses and from XRD method

ZrO<sub>2</sub> powder, obtained by the hydrothermal method, was also subject to computer analysis of TEM images and a unique method of XRD experimental data analysis (Fig. 9).

The results obtained through two different methods (Fig. 9) show high degree of conformity in the crystallite size distribution. The qualitative TEM image analysis revealed the presence of large crystallites of about 40 nm in the tested powder. The XRD analysis has shown that the tested powder contains two phases, tetragonal ZrO<sub>2</sub> and monoclinic ZrO<sub>2</sub>, with larger crystallites of the latter.

#### 4. Summary

Computer quantitative SEM and TEM image analysis could be a very useful tool providing on a fast and precise analysis of powders both in micro and nano scales. It enables not only an accurate estimation of average grain size of the analyzed powder but also a characterization of its grain size distribution. This is important in order to process technologically the samples and also to forecast the properties of powders and materials obtained from the powder.

#### Acknowledgement

This research has been financially supported by the State Committee for Scientific Research (KBN) under contract No. 3 T08A 029 27.

#### References

- [1] PIELASZEK R., *Analytical expression for diffraction line profile for polydispersive powders*, Appl. Crystallography, Proceedings of the XIX Conference, Kraków, Poland, September 2003, pp. 43–50.
- [2] PIELASZEK R., *J. Alloys Comp.* 382 (2004), 128.
- [3] KURZYDŁOWSKI K.J., RALPH B., *Quantitative description of the microstructure of materials*, CRC Press, Baton Rouge, USA, 1995.
- [4] WEJRZANOWSKI T., *Computer assisted analysis of gradient materials microstructure*, Master Thesis, Warsaw University of Technology, 2000.

*Received 6 June 2004*

*Revised 11 June 2004*

## Synthesis of magnetic nanoparticles via the sol-gel technique

RÓŻA KORNAK<sup>1</sup>, DANIEL NIŽŇANSKÝ<sup>2</sup>, KRYSZYNA HAIMANN<sup>1</sup>  
WŁODZIMIERZ TYLUS<sup>3</sup>, KRZYSZTOF MARUSZEWSKI<sup>1\*</sup>

<sup>1</sup>Wrocław University of Technology, Institute of Materials Science  
and Applied Mechanics, 50-370 Wrocław, Poland

<sup>2</sup>Department of Inorganic Chemistry, Faculty of Natural Sciences of Charles University,  
128 43 Prague 2, Czech Republic

<sup>3</sup>Wrocław University of Technology, Institute of Inorganic Technology,  
Wybrzeże Wyspiańskiego 27, 50-370 Wrocław, Poland

Magnetic nanopowders have been prepared by the sol-gel method. The particles were characterized using nitrogen adsorption-desorption isotherms and SEM techniques. The properties of the magnetic nanopowders were characterized by <sup>57</sup>Fe Mössbauer absorption spectrometry and magnetization measurements.

Key words: *sol-gel; magnetic particles; ferromagnetic, superparamagnetic*

### 1. Introduction

The development of polymer and hybrid particles composed of polymeric and magnetic materials is of great interest due to their e.g. biological applications. For such purposes it is necessary that the materials – especially the surfaces of the particles – are biocompatible and non-toxic [1]. Studies of magnetic nanoparticles combine a broad range of synthetic and investigative techniques from physics, chemistry, and materials science [2]. In this paper, we report preliminary results of the structural and magnetic properties of silica powders doped with magnetic particles prepared by the sol-gel method. One of the most interesting aspects of this approach is the possibility of producing uniform silica spheres of submicron size. It needs to be stressed that these syntheses are carried out at room temperature in water solutions of the precursors.

---

\*Corresponding author, e-mail: maruszewski@pwr.wroc.pl.

Magnetic nanoparticles exhibit new phenomena such as superparamagnetism, high field irreversibility, high saturation field, extra anisotropy contributions, or shifted loops after field cooling. These phenomena arise from finite sizes and surface effects that dominate the magnetic behaviour of individual nanoparticles [3].

## 2. Experimental

Silica nanopowders were prepared by hydrolysis and polycondensation of tetraethyl orthosilicate in the systems  $\text{Si}(\text{C}_2\text{H}_5\text{O})_4/\text{NH}_3/\text{C}_2\text{H}_5\text{OH}$ . The sol-gel synthesis of spherical silica particles with a narrow size distribution is based on the Stöber method [4]. The final particle sizes depend on the silicon alkoxide precursors and the alcohol used. Sols were usually mixed for 2 h in an ultrasonic bath at room temperature. After gelation, the wet gels were dried slowly, starting from room temperature up to 80 °C (for 2, 3 days). The magnetic dopant solutions (FF6.2 dissolved in hexane) were added to the hydrolizates. Batches of the magnetic powders were obtained by adding 0,8 cm<sup>3</sup> of the dopant solutions to 56 cm<sup>3</sup> of the hydrolizates. The magnetic dopant FF6.2 is a molecular magnet containing particles of Fe<sup>2+</sup> and Fe<sup>3+</sup> belonging to a new group of EMC compounds (EMC – electromagnetic compatibility) capable of absorbing electromagnetic energy. FF6.2 was prepared by Kolodziej et. al. [5].

## 3. Results and discussion

Magnetic powders were obtained by encapsulating magnetic nanoparticles in SiO<sub>2</sub> spherical submicron grains (Fig. 1). The sizes and morphologies of the non-doped and dye-doped silica microspheres were determined from photographs obtained by scanning electron microscopy (JEOL JMS-5800LV I S-180 Cambridge).

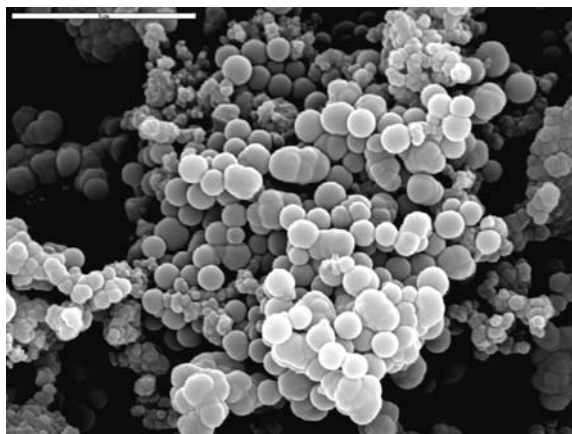


Fig. 1. A SEM photograph of SiO<sub>2</sub> powders doped with magnetic nanoparticles; magnification 8500×

The silica particles are biocompatible and non-toxic. Magnetic nanoparticles did not occur on the surfaces of the grains; they were entrapped in the grain bulk. XPS was performed using a SPES ESCA system equipped with a Phoibos 100 analyser and a Speclab software.

Measurements of the specific BET surface areas (and pore size distributions) were performed with a BET Surface Analyser (Coulter SA 3100) after the samples were outgassed (15 minutes) at 1200 °C. BET isotherms of the SiO<sub>2</sub> powders doped with the magnetic material have the form typical of the isotherm Type II for non-porous adsorbents (Fig. 2). The BET surface area of this powder was 6,33 m<sup>2</sup>/g.

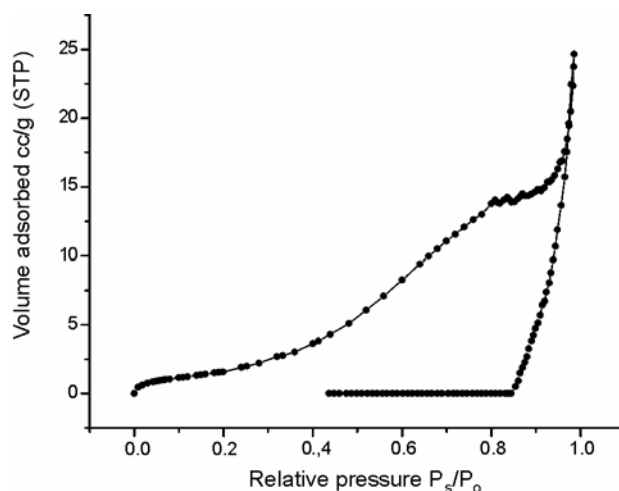


Fig. 2. BET isotherm of SiO<sub>2</sub> powder doped with magnetic nanoparticles

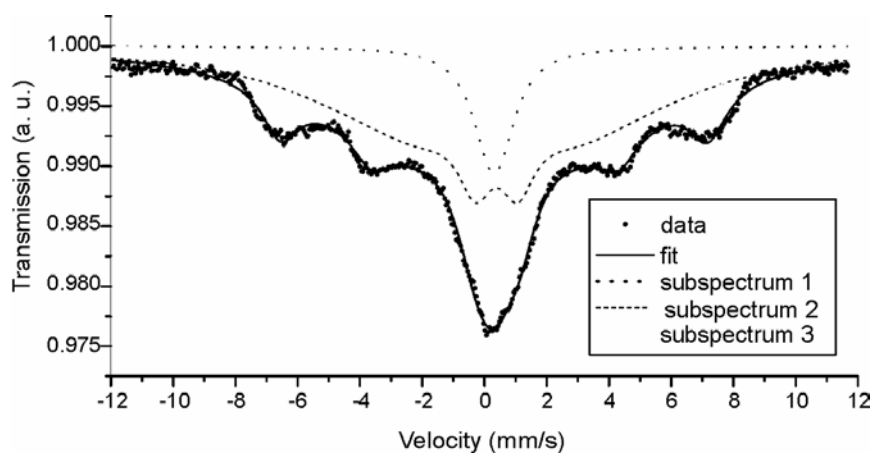


Fig. 3. Mössbauer spectra of magnetic particles in silica powders

Mössbauer spectra were obtained at room temperature (Fig. 3). Measurements were done in the transmission mode with <sup>57</sup>Co diffused into a Cr matrix as the source,

moving with a constant acceleration. The spectrometer was calibrated using a standard Fe foil and the isomer shift was expressed with respect to this standard at 293 K. The fitting of the spectra was performed with the help of the NORMOS program.

Table 1. The results of Mössbauer measurements of magnetic particles in silica powders

Parameter	Subspectrum 1	Subspectrum 2	Subspectrum 3
Isomer shift $\delta$	0.31 mm/s	0.39 mm/s	0.32 mm/s
Quadrupole splitting $\Delta E_Q$	0.00 mm/s	-0.01 mm/s	0.00 mm/s
Hyperfine field $B_{Hf}$	X	28.4 T	42.7 T
Full line width at the half height of the BHf distribution	1.9 mm/s	44 T	1.44 mm/s

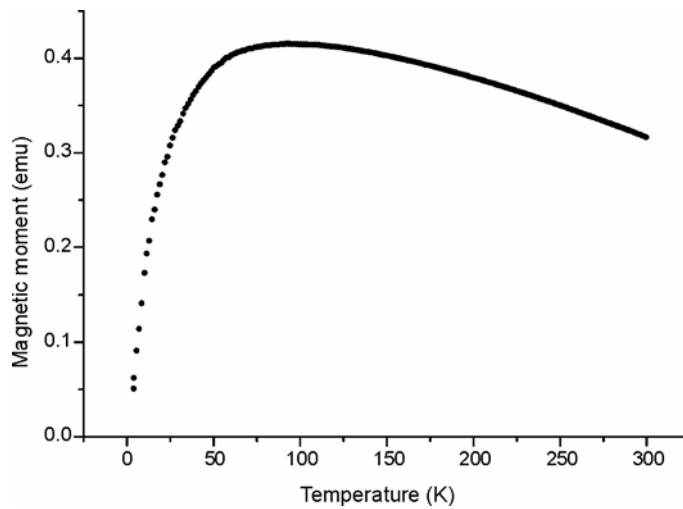


Fig. 4. The ZFC curve. Temperature dependence of the magnetic moment of doped powders

The spectrum contains: a singlet (subspectrum 1, isomer shift 0.31 mm/s) corresponding to the iron in the particles in the superparamagnetic state (the fraction of particles with a blocking temperature below the temperature of measurements), a broad sextet (subspectrum 2, isomer shift 0.39 mm/s, quadrupole splitting 0,01 mm/s, hyperfine field 28.4 T) corresponding to the iron in the particles with a blocking temperature very close to the temperature of measurement, a sextet (subspectrum 3, isomer shift 0.32 mm/s, quadrupole splitting 0.00 mm/s, hyperfine field 42.7 T) probably corresponding to ferrimagnetic magnetite  $\text{Fe}_3\text{O}_4$ . The most probable is maghemite ( $\gamma\text{-Fe}_2\text{O}_3$ ) due to an isomer shift of 0.32 mm/s, which is the characteristic value of three-valent iron.

Magnetization data were obtained with a DC magnetometer (PPMS 9T) in the temperature range of 2–350 K in fields up to 5 T. Low-field temperature scans of zero-field cooled (ZFC) DC magnetization were measured at the field of 0.01 T. The temperature dependence of the magnetic moment of the the samples is shown in Fig. 4.

The “frozen” positions of the magnetic moments of grains in the investigated powders were not random. They were opposite to the direction of the applied external magnetic field (100 Gauss, or 0.01 T). The established blocking temperature (i.e., the point at which the ZFC curve first derivative is zero)  $T_B = 96$  K. The magnetization behaviour of the investigated particles above the blocking temperature is identical to that of atomic paramagnets (superparamagnetism) [6]. The dependence of magnetic induction on the external magnetic field obtained at 4 K for doped silica powders is shown in Fig 5. We have observed a weak ferromagnetic character of the samples with a coercive field  $H_c = 80$  Oe at this temperature.

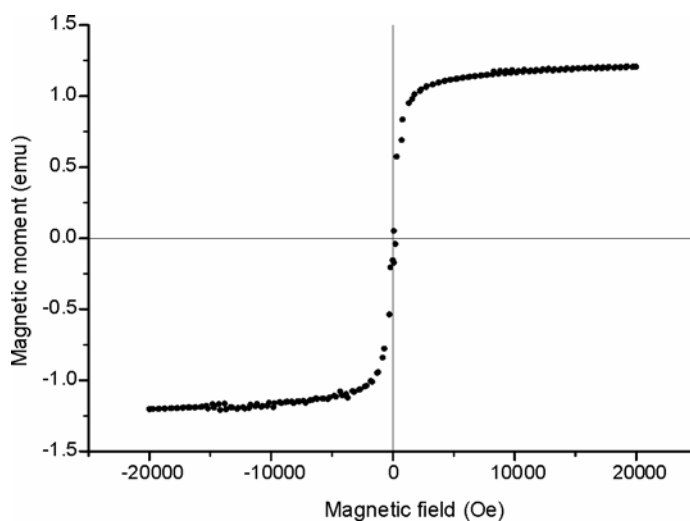


Fig. 5. Magnetic induction vs. external magnetic field dependence at 4 K for doped silica powders. Coercive field  $H_c = 80$  Oe

## 4. Conclusions

$\text{SiO}_2$  powders doped with magnetic nanoparticles (iron crystals of an average grain size of 5 nm) have been prepared via the sol-gel method. The obtained silica particles are bio-inert and non-toxic. The BET surface area of the magnetic powders is  $6,33 \text{ m}^2/\text{g}$ , their adsorption isotherms being of type II, typical of non-porous adsorbents. Very broad peaks observed at room temperature in the Mössbauer spectra show that the samples are in the superparamagnetic state. Doped silica powders display a weak ferromagnetic character at 4 K.

### Acknowledgements

The authors thank A. Kołodziej and A. Vogt for the magnetic dopant used to obtain silica powders displaying magnetic properties. The project has been partially funded by the Polish State Committee for Scientific Research (KBN) following Art. 3 of the Agreement between the Government of the Czech

Republic and the Government of the Republic of Poland on the Scientific and technological Cooperation  
(Grant KBN No. 14/2004/Cz.

### References

- [1] LANDFESTER K., RAMIREZ L., J. Phys. Condens. Matter., 15 (2003) S-1345.
- [2] DIANDRA L. LESLIE-PELECKY, REUBEN D., RIEKE., Chem. Mater., 8 (1996), 1770.
- [3] TARTAJ P., MORALES M.P., VEINYEMILLAS-VERDAGUER S., GONZALEZ-CARRENO T., SERNA C.J., J. Phys. D, Appl. Phys., 36 (2003), R182.
- [4] STÖBER W., FINK A., BOHN E., J. Colloid Interface Sci., 26 (1968), 62.
- [5] KOŁODZIEJ H.A., VOGT A.A., SOWA A.E., CICHY A., STRZELECKI S., *Electromagnetic energy absorbing material*, UK Patent., GB 2379331A (2001).
- [6] BEAN C.P., LIVINGSTON J.D., J. Appl. Phys., 30 (1959), 1205.

*Received 20 October 2004*

*Revised 6 December 2004*

## **Electrical and mechanical properties of nitrided sol-gel derived $\text{TiO}_2$ and $\text{SiO}_2\text{-TiO}_2$ films**

BARBARA KOŚCIELSKA\*, LEON MURAWSKI, LESZEK WICIKOWSKI

Faculty of Applied Physics and Mathematics, Gdańsk University of Technology,  
Narutowicza 11/12, 80-952 Gdańsk, Poland

The results of measurements of electrical conductivity for titanium–nitride films prepared by the amonolysis of sol-gel derived  $\text{TiO}_2$  and  $\text{SiO}_2\text{-TiO}_2$  coatings are presented. Sol-gel derived films on silicon and quartz substrates were nitrided by ammonia treatment in the temperature range from 500 to 1200 °C. The dc conductivity of nitrided films has been measured from 10 K to 900 K. It was found that conductivity is related to the amount of  $\text{TiO}_2$ , which is converted to TiN during ammonolysis. In this way it is possible to change the electrical conductivity of samples by many orders of magnitude. The observed activation energy of the samples containing large amounts of TiN is below 0.1 eV. This indicates that the conductivity mechanism may be interpreted as electrons tunnelling between metallic TiN granules. The mechanical properties were evaluated by a nanoidentometric technique. The results of nanoidentometric measurements confirm an increase in microhardness and Young's modulus for nitrided  $\text{SiO}_2\text{-TiO}_2$  films containing large amounts of TiN.

Key words: *sol-gel; nitridation; electrical conductivity; Young's modulus*

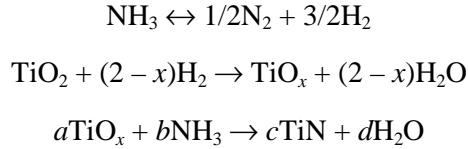
### **1. Introduction**

In recent years, much attention has been paid to nitride and oxynitride thin films. Nitride and oxynitride thin films are interesting because of their electrical, chemical, mechanical, and dielectric properties. In particular, TiN is a hard coating material with many commercial applications related to its high melting point, hardness, and resistance to corrosion. One common method of preparation of oxynitride films is the thermal nitridation of sol-gel derived films with ammonia (ammonolysis). The coatings obtained by sol-gel methods are especially suitable for amonolysis due to their porosity. The microporous structure allows both a significant incorporation of nitrogen and its distribution throughout the film [1, 2]. The incorporation of TiN in the

---

\* Corresponding author, e-mail: basia@mifgate.mif.pg.gda.pl.

layer may be explained by reactions between ammonia and reduced titanium oxide during ammonolysis. Kamiya et al. [3] proposed that nitridation may proceed via the following sequence of reactions:



where  $\text{TiO}_x$  may be  $\text{TiO}$ ,  $\text{Ti}_2\text{O}_3$ , or another reduced titanium oxide. On the basis of these reactions, it can be stated that the reduction of  $\text{TiO}_2$  to  $\text{TiO}_x$  facilitates the agglomeration of TiN on the surface.

This paper is devoted to the electrical and mechanical properties of titanium nitride films prepared by the ammonolysis of sol-gel derived  $\text{TiO}_2$  and  $\text{SiO}_2$ - $\text{TiO}_2$  coatings.

## 2. Experimental

The starting solution for obtaining  $x\text{SiO}_2$ -( $100-x$ ) $\text{TiO}_2$  films ( $x = 20, 40, 50, 60, 80$  mol%) was prepared by mixing tetraethylorthoxysilicate (TEOS) and titanium isopropoxide (TPOT) with ethanol (EtOH), water, and hydrochloric acid as a catalyst in the molar ratio  $\text{TEOS} + \text{TPOT}:\text{H}_2\text{O}:\text{EtOH} = 1:4:25$ . The layers were obtained by dropping (using a burette) this solution on a silicon and quartz substrate. A different preparation method was applied to obtain  $\text{TiO}_2$  films. The starting solution was prepared by mixing titanium butoxide with ethanol (EtOH) in the molar ratio 1:5 and acetylacetonone (AcAc) as the complexing agent. The films were deposited on a quartz substrate by spin coating. Finally, the resulting  $x\text{SiO}_2$ -( $100-x$ ) $\text{TiO}_2$  and  $\text{TiO}_2$  gel layers were dried and then heated at  $500^\circ\text{C}$  for 1 hour. The samples were subsequently nitrided by ammonia treatment in the temperature range from  $500$  to  $1200^\circ\text{C}$ . The measured thickness of the films amounted  $450$  nm.

The formation of TiN microcrystals was examined by X-ray diffraction (XRD) with a Philips X'Pert diffractometer system. XRD patterns were taken at room temperature using  $\text{CuK}_\alpha$  radiation.

dc conductivity measurements of samples containing large amounts of TiN metallic granules were carried out using a typical four-terminal configuration of electrodes. For measurements of films exhibiting high resistance, a pair of circular gold electrodes (electrode distance about  $0.25$  mm) was vacuum deposited. The dc conductivity from room temperature to  $900$  K was measured in nitrogen atmosphere.

The nanoindenter technique was applied to investigate mechanical properties (Nano Instruments Inc., Knoxville, TN, U.S.A.). The details of this technique are described elsewhere [4]. During the experiment, the apparatus continuously records the displacement and applied load in an ultra-low range ( $< 1$  mN). Hardness and Young's

modulus at the depth of 30 nm were calculated from the displacement dependence of the indenter load. Typical load and displacement resolutions were 75 nN and 0.04 nm, respectively. More than 10 indents were performed on each film and the average values of microhardness and modulus were calculated.

### 3. Results and discussion

It is well known that thin films of pure  $\text{TiO}_2$  crystallise in the anatase phase at about 350 °C and in the rutile phase at and above 600 °C [5]. The XRD patterns of a  $\text{TiO}_2$  film and a nitrated  $\text{TiO}_2$  film are presented in Fig. 1. The pure  $\text{TiO}_2$  film was annealed under the same thermal conditions as during ammonolysis. The XRD results for the  $\text{TiO}_2$  film indicate that only the rutile phase is present (curve a). The XRD peaks of the nitrated  $\text{TiO}_2$  film correspond mainly to the  $\text{TiN}$  phase, but the  $\text{Ti}_2\text{N}$  phase was also observed (curve b).

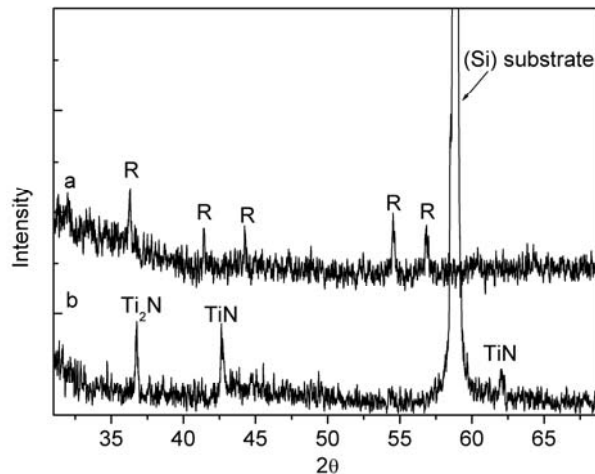


Fig. 1. XRD patterns of a pure  $\text{TiO}_2$  film (curve a) and nitrated  $\text{TiO}_2$  film (curve b). A pure  $\text{TiO}_2$  film was annealed in the same thermal conditions as during ammonolysis

#### 3.1. Electrical properties of poorly nitrated $\text{TiO}_2$ films

In Figure 2, the logarithm of the surface conductivity of the  $\text{TiO}_2$  film (annealed under the same thermal conditions as during ammonolysis) and a poorly nitrated  $\text{TiO}_2$  film versus the inverse of temperature is presented. Measurements were performed in the temperature range of 450–900 K. The activation energy  $E_a$ , calculated from the Arrhenius plot,  $\sigma = \sigma_0 \exp(-E_a/kT)$ , by the least squares method, was about 1.12 eV for the pure  $\text{TiO}_2$  sample and 1.14 eV for the nitrated one. The conduction band in crystalline  $\text{TiO}_2$  is composed of unoccupied titanium 3d orbitals, while the valence

band is formed by filled oxygen 2p orbitals. It is confirmed that oxygen vacancies can be treated as electron donors, which determine n-type conductivity. Measurements

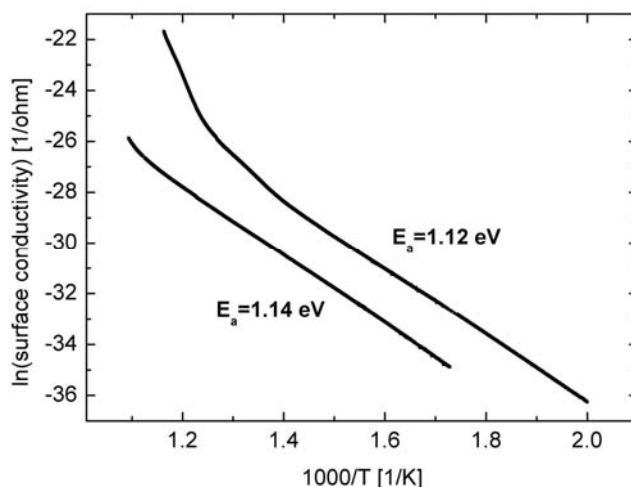


Fig. 2. The logarithm of surface conductivity for a pure TiO<sub>2</sub> film (annealed under the same thermal conditions as during ammonolysis) and a poorly nitrated TiO<sub>2</sub> film versus the inverse of temperature. Measurements were performed in nitrogen atmosphere

were performed in nitrogen atmosphere, and the large value of  $E_a$  suggests that bulk oxygen vacancies lying below the conduction band (0.75 eV and 1.18 eV) are responsible for dc transport [6]. A similar conductivity behaviour is observed in poorly nitrated TiO<sub>2</sub> films, for which conductivity is even lower. This may suggest that some oxygen vacancies disappeared during heat treatment in ammonia atmosphere.

### 3.2. Electrical properties of highly nitrated TiO<sub>2</sub> and SiO<sub>2</sub>-TiO<sub>2</sub> films

The results for  $x$ SiO<sub>2</sub>-(100 -  $x$ )TiO<sub>2</sub> films ( $x$  = 20, 40, 50, 60, 80 mol %) and a TiO<sub>2</sub> film containing large amounts of TiN are presented in Fig. 3. The increase in the amount of TiO<sub>2</sub> in the films corresponds to the increased amount of TiN in the nitrated sample. The activation energy of these films decreases from 0.1 eV (for the film containing 20 mol % of TiO<sub>2</sub>) to 0.003 eV (for the film containing 80 mol % TiO<sub>2</sub>), and the surface conductivity increases by several orders of magnitude. The surface conductivity of these samples varies very little in the entire temperature range. We have previously investigated AFM images of these films, which indicate that the granules of TiN are randomly distributed in the network [7]. This structure is similar to the discontinuous metal structures usually prepared by evaporating or sputtering metal onto a glass surface [8-10]. A commonly accepted theoretical model for electrical conductivity in discontinuous metal structures is based on the tunnelling process of electrons between metal granules [9, 10]. Creation of charge carriers is due

to thermal processes leading to the transfer of electrons from one metal granule to neighbouring ones. The energy  $E_a$  needed for the creation of two granules, one positively charged and the other negatively charged, is described by the equation

$$E_a = \frac{e^2 F(s,d)}{4\pi\epsilon\epsilon_0 d}$$

where  $d$  is the diameter of the granules,  $s$  is the distance between two granules,  $\epsilon$  is the dielectric constant of the matrix, and  $F(s,d)$  is a function depending on the distribution of sizes and distances between granules. Calculations of the activation energy for a typical discontinuous metal structure have shown that this value is small, generally below 0.1 eV [9, 10]. This is consistent with the present results of dc conductivity measurements for TiN-containing films with less than 40%  $\text{TiO}_2$  (Fig. 3 and Table 1).

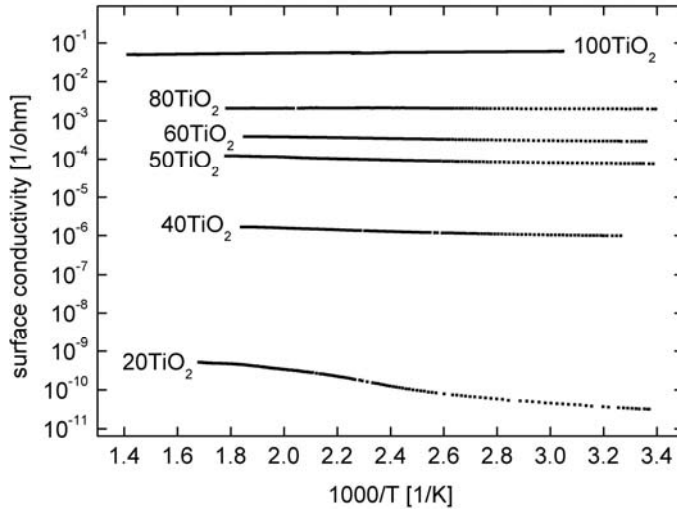


Fig. 3. The surface conductivity of  $x\text{SiO}_2\text{-(}100-x\text{)TiO}_2$  nitrated films ( $x = 20, 40, 50, 60, 80$  mol %) and a  $\text{TiO}_2$  film containing large amounts of TiN versus the inverse of temperature

Table 1. Conductivity parameters of  $(100-x)\text{SiO}_2\text{-}x\text{TiO}_2$  nitrated films ( $x = 20, 40, 50, 60, 80$  mol %). The accuracy of conductivity measurements was about 2%

$x$ [mol %]	Activation energy [eV]	$\sigma_{300\text{ K}}$ [ $\Omega^{-1}\cdot\text{cm}^{-1}$ ]	$\sigma_{540\text{ K}}$ [ $\Omega^{-1}\cdot\text{cm}^{-1}$ ]
20	$0.16\pm 0.002$	$3.2\times 10^{-11}$	$5.0\times 10^{-10}$
40	$0.031\pm 0.002$	$9.9\times 10^{-7}$	$1.7\times 10^{-6}$
50	$0.026\pm 0.002$	$7.3\times 10^{-5}$	$1.2\times 10^{-4}$
60	$0.016\pm 0.002$	$2.95\times 10^{-4}$	$3.9\times 10^{-4}$
80	$0.003\pm 0.001$	$2.05\times 10^{-3}$	$2.1\times 10^{-3}$

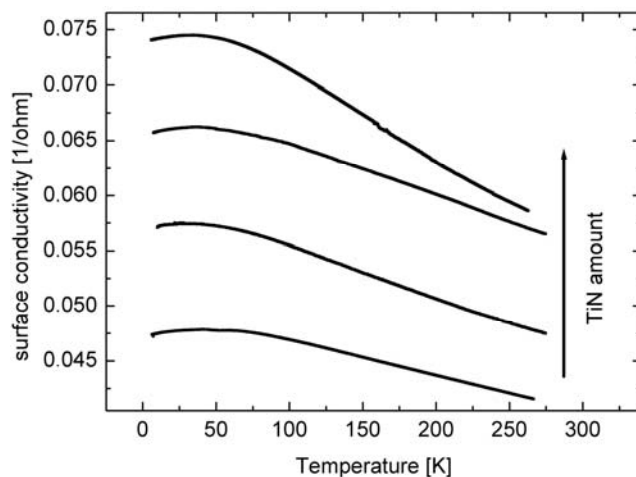


Fig. 4. Surface conductivity versus the inverse of temperature for  $\text{TiO}_2$  films with high amounts of TiN metallic granules

$\text{TiO}_2$  films with high amounts of TiN metallic granules exhibit typical metallic behaviour; their conductivity decreases with temperature (Fig. 4).

### 3.3. Elastic properties of $(100 - x)\text{SiO}_2 - x\text{TiO}_2$ nitrided films

The nanoindenter technique was applied to investigate the mechanical properties of films. Figure 5 presents typical load–unload plots for a sample containing 80 mol % of

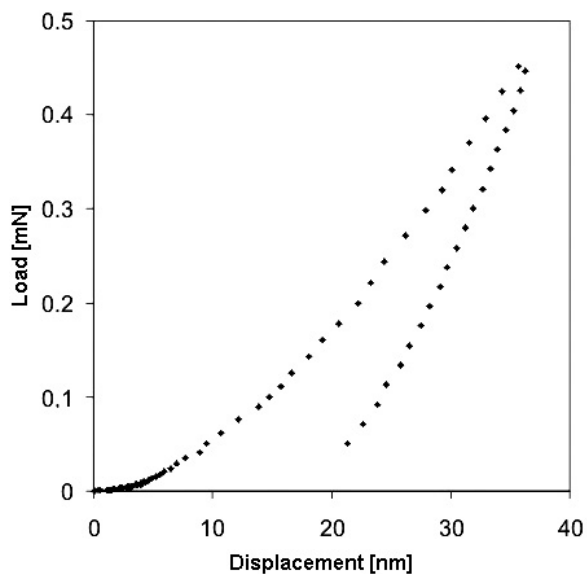


Fig. 5. Indentation load–displacement data for a nitrided  $\text{TiO}_2$  (80%)– $\text{SiO}_2$  (20%) film

TiO<sub>2</sub>. The elastic modulus  $E$  of the indented film is calculated from the slope of the unloading curve at the peak load. The hardness  $H$  is defined by the relationship  $H = P/A$ , where  $P$  is the load and  $A$  is the area of the indent calculated from its plastic depth. The results of calculations for all measured samples are presented in Table 2. The hardness and Young's moduli for these films are similar to those obtained for TiN layers by Oliver et al. [11]. It is found that Young's modulus and hardness increase with titania content and that these values are higher than for silica ( $E = 72$  GPa,  $H = 8$  GPa) [4]. This result appears to be consistent with AFM observations [7], which indicate that the surfaces of high-content titania films are almost completely covered by TiN. Therefore, the displacement of the indenter at a depth of 30 nm takes place in TiN and their elastic properties are not very different from pure TiN layers.

Table 2. Young modulus and hardness of the  $(100 - x)\text{SiO}_2-x\text{TiO}_2$  nitrided films ( $x = 20, 40, 50, 60, 80$  mol %).

mol% TiO <sub>2</sub>	80	60	50	40	20
Hardness [GPa]	18.6±1	14±1	13.7±1	13.8±1	15±1
Modulus [GPa]	240±20	180±20	180±20	180±20	140±20

#### 4. Conclusions

The conductivity of nitrided TiO<sub>2</sub> and SiO<sub>2</sub>-TiO<sub>2</sub> films is related to the amount of TiO<sub>2</sub> which is converted to TiN during ammonolysis. In this way, it is possible to change the electrical conductivity of these films by several orders of magnitude. The activation energy of nitrided samples is generally below 0.1 eV. This indicates that the conductivity mechanism may be interpreted as the tunnelling of electrons between metallic TiN granules. TiO<sub>2</sub> films with a high content of TiN metallic granules exhibit decreasing conductivity with temperature, typical of metallic behaviour. The mechanical properties of titania-silica films are improved after nitridation. The films exhibit improved hardness and resistance to scratching. This indicates that TiN nanocrystals are strongly bonded with the matrix.

#### References

- [1] BROW R.K., PANTANO C.G., J. Am. Ceram. Soc., 70 (1987), 9.
- [2] GUGLIELMI M., COLOMBO P., BATTAGLIN G., MAZZOLDI P., DE POLO A., BOSCOLO-BOSCOLETTO A., GRANOZZI G., J. Non-Cryst. Solids, 147, 148 (1992), 451.
- [3] KAMIYA K., NISHIJIMA T., TANAKA K., J. Am. Ceram. Soc., 73 (1990), 2750.
- [4] OLIVER W.C., PHARR G.M., J. Mater. Res., 7 (1992), 1564.
- [5] SANKUR H., W. GUNNING, J. Appl. Phys., 66 (1989), 4747.
- [6] CRONEMEYER D.C., Phys. Rev. 113 (1959), 1222.
- [7] WICKOWSKI L., KUSZ B., MURAWSKI L., SZANIAWSKA K., SUSŁA B., Vacuum, 54 (1999), 221.

- [8] NEUGEBAUER C.A., WEBB M.W., J. Appl. Phys., 33 (1962), 74.
- [9] HILL R.M., COUTTS T.J., Thin Solids Films, 42 (1977), 201.
- [10] ABELES B., SHENG P., COUTTS M.D., ARIE Y., Adv. Phys., 24 (1975), 407.
- [11] OLIVER W.C., MCHARGUE C.J., ZINCKLE S.J., Thin Solid Films, 153 (1985), 185.

*Received 16 July 2004*  
*Revised 10 September 2004*

# **Formation of nanostructures with a controlled size distribution in Si-based gels by ion irradiation**

JEAN-CLAUDE PIVIN\*

C.S.N.S.M., Bâtiment 108, 91405 Orsay Campus, France

Studies of irradiation effects in inorganic polymers and gels performed at CSNSM during the past 10 years are overviewed and examples of precipitations with interesting applications (C, Si, metals) occurring during the conversion into ceramics are presented. The precipitation yield, as a function of irradiation fluence or annealing conditions, and particle physical properties were investigated by means of various techniques, depending on their nature. The rates of gel-to-ceramics conversion and of precipitation are determined by the density of electronic excitations produced by ion irradiation (collision cascades slightly assisting the diffusion of metal atoms). Particles formed by ion irradiation show a narrower range of sizes and consequently more interesting characteristics for magnetic or optical applications than those formed in heat-treated gels.

Key words: *sol-gel; nanomaterial; ion irradiation*

## **1. Introduction**

Materials with nanometric structures not only have technological applications in various areas, but also are of fundamental interest for studying the changes of phase properties in this transition regime between the bulk and molecular scales. Sol-gel chemistry is a very convenient technique for producing nanomaterials with a wide range of compositions. The rate of reactions occurring during their thermal processing and the evolution of some components are, however, not well controlled. The ceramics obtained are often porous, heavily cracked, and the particles of the secondary nanophase tend to exhibit a wide range of sizes.

Studies of irradiation effects in inorganic polymers and gels performed during the past 10 years have demonstrated the interest in using this route instead of thermal processing for releasing only hydrogen and obtaining ceramic films fully densified and free of cracks (they are principally due to a mismatch in the expansion coeffi-

---

\*E-mail: pivin@csnsm.in2p3.fr.

cients of the film and substrate in the case of heat treatments) [1]. The out-of-equilibrium nature of ion irradiation chemistry also permits selective promotion of some reactions between gel components, because the formed radicals are able to migrate only at short range, among other reasons. This paper reports the control of the size of various types of particles formed in Si-based gels under ion irradiation and their optical or magnetic properties. The first type of precipitation studied is that of C or Si atoms in excess with respect to the equilibrium composition of glasses,  $\text{SiO}_x\text{C}_{1-x/2}$  (with  $1-x/2 \leq 1/4$ ). The second is the precipitation of transition metals in gels from triethoxysilane (hereafter labelled TH). Different physical quantities are used to assess the precipitation kinetics as a function of the fluence and mass of ions, depending on the nature of the particles.

## 2. Experimental

Silicon ethoxides (TEOS, MTES, PTES, and mixtures of these precursors) were hydrolysed as usual by adding 2 moles of water and  $10^{-2}$  moles of nitric acid for each mole of ethoxide in ethanolic solution and stirring for 1 h at room temperature, after which films with a thickness of 400–500 nm were deposited by spinning the filtered gel on Si wafers. Triethoxysilane mixed in equimolar proportion with pure ethanol was simply stirred for 5 min before adding salts of various metals M (M = Fe, Co, Ni, Cu). The TH:M filtered gels were used immediately for spinning films, in order to hamper the progressive hydrolysis of Si–H bonds and their possible reaction with metal ions before treatment (noticed only in the case of  $\text{Cu}^{2+}$ ). Analyses of films without salt, by means of ion beam techniques, show that a silicon suboxide  $\text{SiO}_{1.5}$  containing less than 2 at. % C is obtained with this simple procedure, followed by irradiation or heat treatment for removing H. The O/Si content increases a little (up to 1.7 times) in films from sols containing 10–20 mol %  $\text{MNO}_3 \cdot x\text{H}_2\text{O}$  (M=Fe, Ni, Co) or 20 %  $\text{CuCl}_2 \cdot 2\text{H}_2\text{O}$  (the addition of  $\text{CuNO}_3$  catalyses the precipitation of silica).

Ions of various masses and energies in the MeV range were used for varying the yields of electronic excitations and atomic displacements in the films. The electronic and nuclear stopping powers,  $S_e$  and  $S_n$ , of 3 MeV Au ions are of same order of magnitude (1.5 and 3.0 keV/nm, respectively), and the total  $S_e$  value obtained by adding the energy lost by recoil atoms and primary ions becomes equal to  $S_n$ . Si ions of 3 MeV were selected for producing a comparable linear density of electronic excitations ( $S_e = 1.8$  keV/nm) and much smaller atomic displacements ( $S_n = 100$  eV/nm). 1 MeV He ions also lose their energy essentially in electronic excitations with a lower density of 300 eV/nm. Ag ions of 100 MeV were also used in a limited number of experiments for increasing the  $S_e$  value up to 20 keV/nm while keeping  $S_n$  at a low level of 300 eV/nm. Note finally that all these ions stop at some micrometers in the substrate.

The composition of films was analysed by means of ion beam techniques: (i) by Rutherford Back-scattering Spectrometry (RBS), with 2.4 MeV He at normal incidence, for studying the depth profiles of heavy elements; (ii) by Elastic Recoil Detec-

tion Analysis (ERDA), with 3 MeV He ions for profiling H, and (iii) by  $^{16}\text{O}(\text{d}, \text{p})^{17}\text{O}$  and  $^{12}\text{C}(\text{d}, \text{p})^{13}\text{C}$  Nuclear Reactions Analysis (NRA), with deuterons of 920 keV, for determining the areal densities of these elements more accurately than with RBS. Their structure was studied by X-ray diffraction at grazing incidence and TEM observations of cross-sections, prepared by mechanical polishing followed by ion etching. Nanochemical investigations were carried out on TEM samples containing C clusters, using a high resolution Philips CM 20 FEG field emission electron microscope, run at 200 kV and equipped with a Gatan Imaging Filter (GIF 200). Besides electron energy loss spectroscopy at an energy resolution of 0.8 to 1 eV, this filter enables a specific element to be imaged with a spatial resolution better than 1 nm (energy filtered electron microscopy, EFTEM). Optical transmittance spectra in the wavelength range 200–800 nm were recorded with a CARY 5 VARIAN UV-VIS-NIR dual beam spectrometer. The formation of C and Si nanoparticles was characterized by measuring photoluminescence (PL) in the visible range, with excitation by a 488 nm line  $\text{Ar}^+$  ion laser at a power density below  $1 \text{ W}/\text{cm}^2$ , and analysing the emitted light by a double SPEX 1403 monochromator and an EMI 9863B photomultiplier. Electron spin resonance (ESR), with a Bruker spectrometer operating at 9.8 GHz (X-band) and equipped with 100 kHz modulation, was used for studying the precipitation kinetics of the magnetic phases and the magnetization anisotropy of the films at room temperature (RT). In addition, measurements of magnetization were performed as a function of the applied field  $H$  and temperature  $T$  with a SQUID magnetometer S600X from Cryogenic Ltd.

### 3. Study of H radiolysis and C or Si precipitation

Typical kinetics of hydrogen (H) evolution from Si-based gels with different C contents are presented in Figure 1, for example under He irradiation. The variation in H concentration is plotted versus the integrated amount of electronic excitations,  $S_e\phi$ , where  $\phi$  is the ion fluence ( $\text{ions}/\text{cm}^2$ ), because a comparison of the various ions effects shows that  $S_n$  plays no significant role in the process. A detailed analysis of the kinetics shows that the release of  $\text{H}_2$  molecules obeys an exponential law (the retained H concentration varies as  $\exp(-\sigma S_e\phi)$ ) up to a given fluence. Above this fluence, the radiolytic efficiency  $\sigma$  decreases and the evolution kinetics is limited by the combination rate of H radicals inside ion tracks to form molecules [2]. The  $\sigma$  value decreases markedly with increasing C content in the material, whose effect is attributed to the strength of C–H bonds with respect to O–H bonds (this strength also increases as  $\text{CH}_3$  groups are partially decomposed).

Energy-filtered TEM images of the C distribution in cross-sections of the irradiated films provides evidence that C atoms or  $\text{CH}_x$  radicals migrate in the structure to form clusters with a diameter of 3–7 nm, depending on the C content and irradiation conditions ( $S_e$  value). In the case of phenyl-substituted precursors (PTES and silsesquioxanes), clusters are also supposed to form on the spot of the radiolysis event [1].

Ions with a low energy per nucleon, such as 3 MeV Au ions, are scattered in random directions during nuclear collisions, while swift ions undergoing only electronic stopping have a straight path.

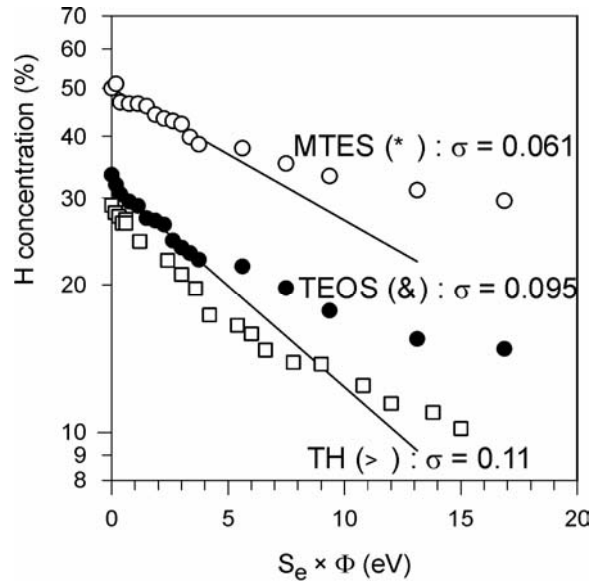


Fig. 1. Kinetics of H release in various gels (TEOS, TH, MTES) under He irradiation and a fit of the initial decrease of H concentration  $\rho$  with the simple exponential law  $\rho = \rho_0 \exp(-\sigma S_e \phi)$

Accordingly, one observes C clusters with a random or a linear distribution along ion tracks, as shown in Figure 2. It is known that regions with a perturbed structure in swift ion tracks may be spherical and isolated, oblong, or percolating in the form of cylinders, depending on  $S_e$  and on ion velocity [53]. The last geometry mentioned seems to be obtained in the case of 100 MeV Ag irradiation of MTES films, and this result may find applications in fabricating field-emitting fibres or electric contacts with a well defined and very small section. Whatever the shape of the C particles, Raman scattering analyses show that they exhibit a noticeable degree of tetragonal hybridisation [1]. These semiconducting particles emit a yellow-green luminescence, with a maximum yield for a defined amount of excitations  $S_e \phi$  of  $30 \text{ eV} \times 10^{23} \text{ ions/cm}^3$  [4]. The PL emission wavelength and intensity seem to be the same for spherical clusters and cylinders obtained for a given  $S_e \phi$  value [5]. On the other hand, the peak position shifts from 460 to 540 nm with irradiation fluence as the clusters grow under the cumulative effects of ions in same spot. It is worth noting that films of same nature annealed at  $1000^\circ \text{C}$  in a vacuum of  $10^{-7}$  torr (for not burning C) exhibit no excitonic luminescence [5]. Raman analyses indicate that this is due to the graphitic nature of the clusters [6]. The difference in the hybridisation states of annealed and irradiated films can be ascribed either to the known formation of  $sp^2$  rings upon a critical cluster size or to a tendency towards a more stable structure during annealing treatment [1, 6].

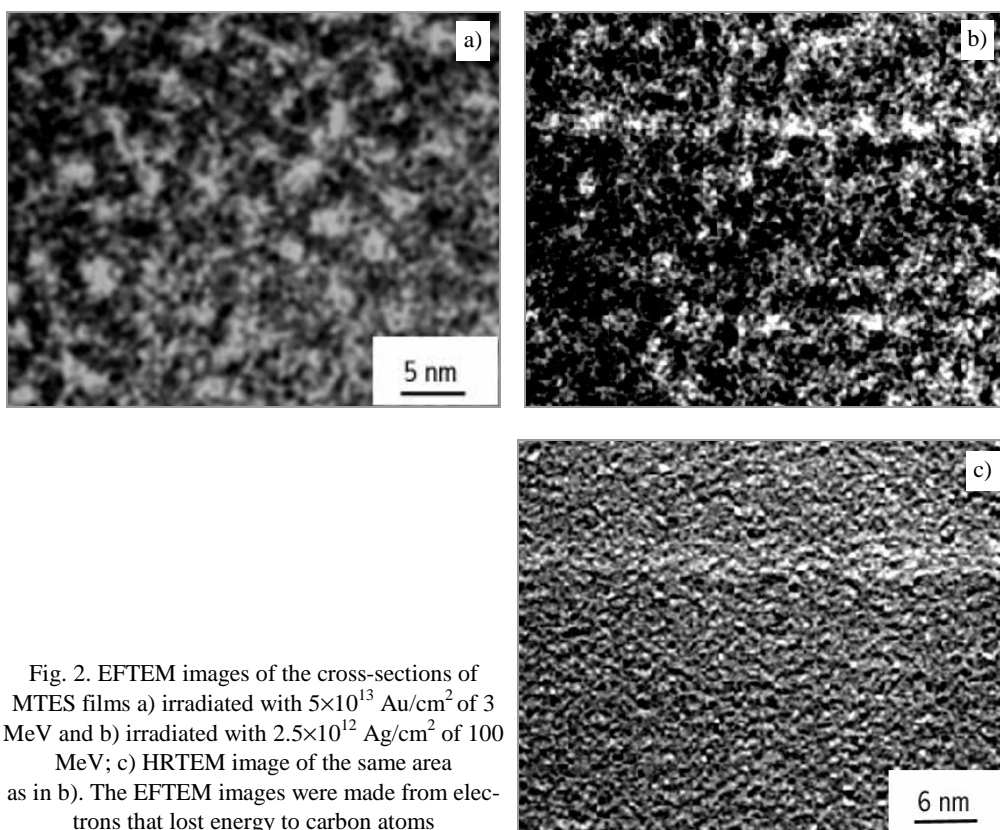


Fig. 2. EFTEM images of the cross-sections of MTES films a) irradiated with  $5 \times 10^{13}$  Au/cm<sup>2</sup> of 3 MeV and b) irradiated with  $2.5 \times 10^{12}$  Ag/cm<sup>2</sup> of 100 MeV; c) HRTEM image of the same area as in b). The EFTEM images were made from electrons that lost energy to carbon atoms

Similarly to C in MTES, PTES and silsesquioxanes, Si precipitates under irradiation in Si suboxide derived from TH, and the semiconducting clusters show a red luminescence with a wavelength correlated to the particle size ( $\sim 1$  nm) [7]. In the case of TH films, the small departure from SiO<sub>2</sub> stoichiometry makes particles formed during annealing treatments at 1000–1100 °C in vacuum have an optimum size of 2–3 nm for the luminescence of confined excitons [8].

#### 4. Studies of metallic precipitations in TH

Precipitations of Cu, Fe, Co, and Ni are observed by means of TEM in samples containing 10 to 25 mol % of salt and irradiated with 3 MeV Au ion fluences of  $5 \times 10^{14}$  to  $10^{15}$ /cm<sup>2</sup> [9]. Their range of size is relatively narrow (the distribution is of a gaussian type with a standard deviation/mean size ratio of 25%) and their spatial distribution is homogeneous. On the contrary, the size distribution of particles formed in films heat-treated at 600 °C in vacuum is of the lognormal type with a half-width/mean size ratio of 100%. In addition, ovoid porosities are systematically ob-

served in annealed TH:Ni and TH:Co samples, and the particles are segregated on pore walls and on some linear defects (which may be nanocracks, see Fig. 3).

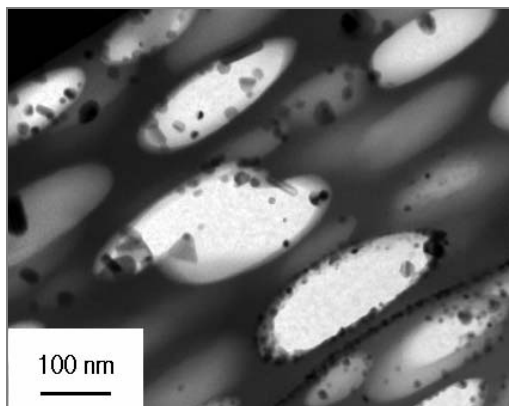


Fig. 3. TEM image of the cross section of a TH Ni film (3 at.% Ni) annealed at 600 °C. The large axes of porosities are parallel to the film surface

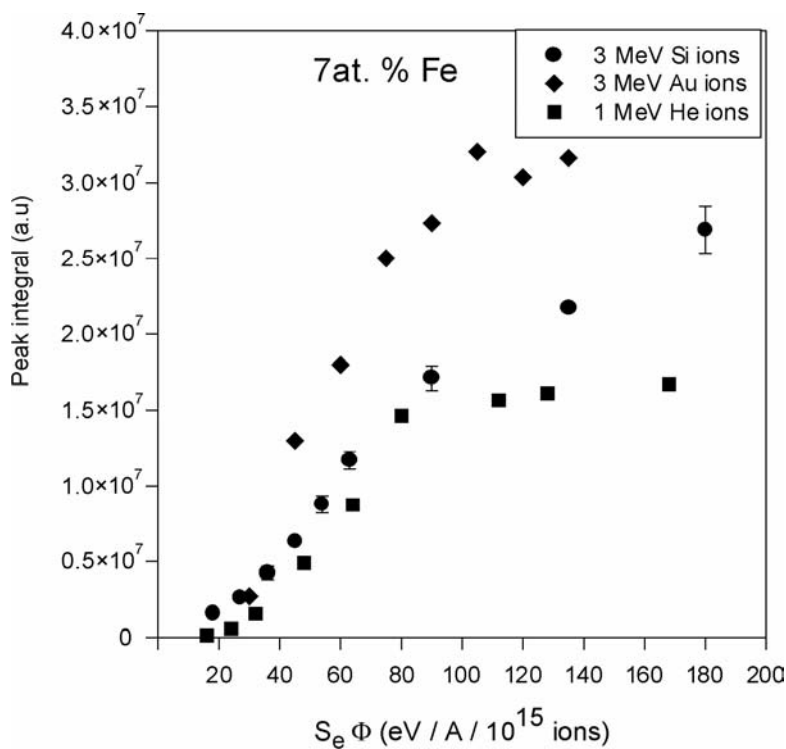


Fig. 4. Variation of the integral of the absorbed power measured in electron spin resonance from TH films doped with 20 mol %  $\text{FeNO}_3$  (7.5 at. % Fe in the glass) as a function of the energy deposited in electronic excitations under 1 MeV He, 3 MeV Si, and 3 MeV Au irradiation

X-ray diffraction spectra show that silicides form when the annealing temperature reaches 1000 °C. The formation of a ferromagnetic phase is detected by means of ESR for a threshold energy  $S_e\phi$  of  $40 \text{ eV} \times 10^{23} \text{ ions/cm}^3$ . The total volume  $V$  of the magnetic phase, estimated from the integral of absorbed power seems to obey the law typical of precipitation processes under irradiation for ions producing few displacements ( $1 - \exp(-\sigma S_e\phi)$ ), and to be linear function of the fluence under 3 MeV Au irradiation (Fig. 4). The rates  $V/S_e$  are, however, very close for the various types of ions. The different behaviour of Au irradiated films is ascribed to the occurrence of radiation-induced diffusion on short range, assisting the segregation of metal atoms. A similar change of kinetic law was observed previously for the formation of amorphous clusters in metallic alloys, according to the irradiation temperature [10]. Another effect of displacements, which can be observed in Fig. 4, is the occurrence of a magnetization maximum of the order of  $8 \times 10^{14} / \text{cm}^2$  for a fluence of 3 MeV Au ions. It is interpreted to be due to a re-dissolution of the clusters by cascade mixing. This dissolution is confirmed by the observation of a linear decrease in magnetization when submitting pre-annealed samples to irradiation [11]. A study of the resonance peak position,  $H_{\text{res}}$ , as a function of the direction  $\varphi$  of the applied static field with respect to the surface, shows that the internal field  $H_i$  is that of an homogenous ferromagnetic medium, which is given by the Kittel equation:

$$\frac{\omega_0^2}{\gamma^2} = H_0^2 = (H_{\text{res}} - H_i \cos 2\varphi) \times (H_{\text{res}} + H_i \sin^2 \varphi)$$

where  $\omega_0$  is the angular frequency of the cavity and  $\gamma$  the gyromagnetic ratio of the ferromagnetic electrons.  $H_i$  is equal to the demagnetising (Zeeman) field  $H_d$  when there is no other anisotropy factor than the sample shape and  $H_d$  is  $-4\pi M$  for a thin plate or  $2\pi M$  for a rod,  $M$  being the magnetization at saturation of the bulk metal multiplied by the volume fraction  $f$  of the metal. Annealed films behave as homogeneous plates, despite the porosities and segregation of particles on defects. The angular variation of  $H_{\text{res}}$  is of same type in irradiated samples (Fig. 5), but  $H_i$  exceeds  $-4\pi M$  when the effective precipitation yield  $f$  is taken into account. An interesting change in anisotropy is observed when submitting pre-annealed samples to irradiation with swift ions producing cylindrical tracks: the film anisotropy becomes similar to that of an assembly of rods, with the internal field  $H_i$  exactly equal to  $2\pi M$  (Fig. 5).

In fact, the apparent excess of magnetization in pristine films directly submitted to irradiation ( $H_a = |H_i| - 4\pi M$ ) and maybe also the tilt of the easy magnetization axis in annealed-irradiated films is due to magnetostriction. Nanoparticles of any type undergo a compression, increasing in inverse proportion to their size, under the effect of interfacial energy (Laplace's law), to which the stress induced by the athermal compaction of the matrix and by the limited diffusion of atoms (for accommodating the volume change due to metal precipitation) must be added in the present case. In annealed TH:Ni or TH:Co samples, these stresses are compensated by the formation of voids elongated parallel to the surface (Fig. 3). TEM observations show that the

change in the magnetic anisotropy of annealed films (including TH:Fe films free of voids) after irradiation with high-energy ions is not due to the rearrangement of particles in more or less continuous cylinders and that their size distribution remains the same. Thus, it is ascribed to changes in the stress state related to the creation of defects in the matrix, as already observed for single-phased magnetic materials [3].

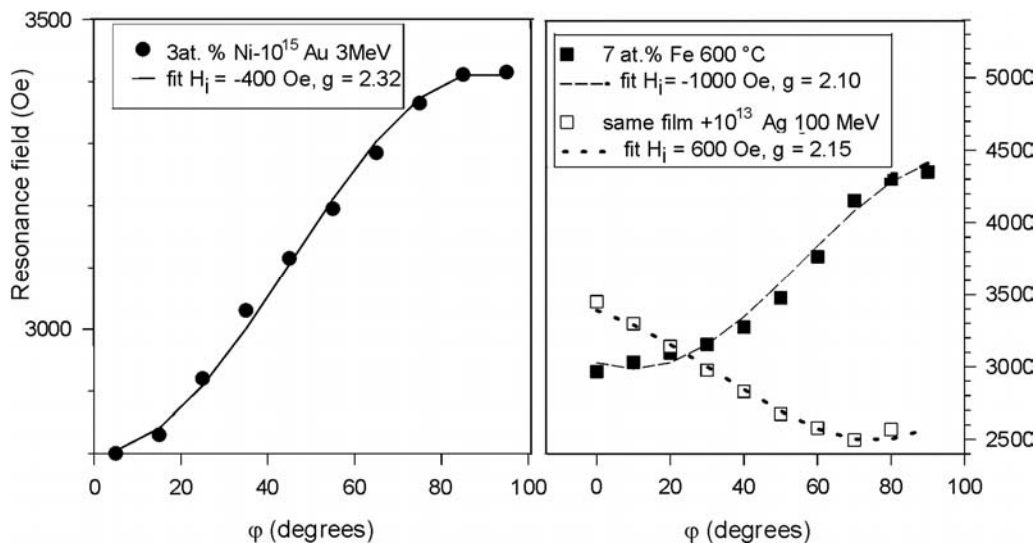


Fig. 5. Anisotropy of spin resonance in TH:M films irradiated with 3 MeV Au, and annealed at 600 °C or annealed then irradiated with 100 MeV Ag ions

There is no place here for a discussion of the superparamagnetic or ferromagnetic behaviour of samples as a function of temperature, metal content, and type of treatment. Interest in the triethoxysilane matrix being a host of metal particles is more worthwhile to emphasize. Films formed from tetraethoxysilane exhibit no magnetisation and X-ray diffraction provides evidence of the formation of antiferromagnetic oxides (annealed samples) or solid solutions (irradiated samples). The formation of fayalite, magnetite, or NiO was observed by other authors in TEOS monoliths that were heat-treated in hydrogen [12]. Irradiation chemistry may also differ noticeably from thermo-chemistry in some cases, since Cu particles with a plasmon resonance in the visible are observed exclusively in TH:Cu irradiated samples [13]. Respectively, the irradiation of TEOS:Ag films or exchanged glasses already containing clusters with very energetic ions (100 MeV Ag or Au) induces a re-dissolution of the clusters [14]. This effect is not yet elucidated nor the absence of detectable precipitation in TH:Fe or TH:Ni pristine films when irradiated with the same ions. Metallic nuclei may explode by Coulombic repulsion between ionised M atoms when the yield of secondary electrons expelled from the track core (always huge) exceeds a threshold value [3].

## 5. Conclusion

Ion irradiation of gel films leads to the formation of nanoclusters issued from the precursor backbone or from a reaction between precursor side groups and dissolved ions (TH). The driving process is essentially the formation of free radicals via electronic excitations. A defined value of the radiolytic cross section,  $\sigma_{S_e}$ , for a given ion species makes clusters exhibit an homogenous size, while they tend to grow by Ostwald ripening in the case of gels converted to ceramics by heat treatment. Changes in the track core dimension ( $\pi r^2 = \sigma_{S_e}$ ) and in the energy of the secondary electrons expelled from the core with increasing velocity of ions [15] seem to induce the gathering of C, Si, or M atoms into narrow cylinders. This new type of nanostructure is of great interest for applications such as magnetic memories perpendicular to the surface, nano-diodes, electric contacts, etc. The density and very good adhesion of irradiated films are also advantages with respect to thermal processing worth keeping in mind whatever the nature of the gel, especially when useful fluences are very low and their cost not prohibitive.

### Acknowledgement

Thanks are due to E. Pippel of Max-Planck Institute, Halle, for having performed the EFTEM observations shown in Figure 2.

### References

- [1] PIVIN J.C., COLOMBO P., SORARU G.D., *J. Am. Ceram. Soc.*, 83 (2000), 713.
- [2] SRIVASTAVA S.K., AVASTHI D.K., PIVIN J.C., *Nucl. Instr. Meth.*, B 191 (2002), 7185.
- [3] TOULEMONDE M., BOUFFARD S., STUDER F., *Nucl. Instr. Meth.*, B 91 (1994), 108.
- [4] PIVIN J.C., SENDOVA-VASSILEVA M., *Mater. Sci. Eng.*, B69 (2000), 574.
- [5] KUMAR A., SINGH F., AVASTHI D.K., PIVIN J.C., to be published
- [6] PIVIN J.C., COLOMBO P., *J. Mat. Sci.*, 32 (1997), 6163.
- [7] PIVIN J.C., COLOMBO P., MARTUCCI A., SORARU G.D., PIPPEL E., SENDOVA-VASSILEVA M., *J. Sol-Gel Sci. Technol.*, 26 (2003), 251.
- [8] JIMENEZ DE CASTRO M., PIVIN J.C., *J. Sol-Gel Sci. Technol.*, 28 (2003), 37
- [9] PIVIN J.C., VINCENT E., ESMOUF S., DUBUS M., *Eur. Phys. J. B.*, 37 (2004), 329.
- [10] COHEN C., BENYAGOUB A., BERNAS H., CHAUMONT J., THOME L., BERTI M., DRIGO A.V., *Phys. Rev.*, B31 (1985), 5.
- [11] PIVIN J.C., ESMOUF S., unpublished results.
- [12] ENNAS G., CASULA M.F., FALQUI A., GATTESHI D., MARONGUI G., PICCALUGA G., SANGREGORIO C., PINNA G., *J. Non-Cryst. Solids*, 293 (2001), 1.
- [13] PIVIN J.C., *Nucl. Instr. Meth.*, B216 (2004), 239.
- [14] PIVIN J.C., ROGER G., GARCIA M.A., SINGH F., AVASTHI D.K., *Nucl. Instr. Meth.*, B 215 (2004), 373.
- [15] CHADDERTON L.T., *Rad. Measurements*, 36 (2003), 13.

*Received 16 July 2004*

*Revised 25 July 2004*

## **Spectroscopic properties of a chlorophyll-based photosensitive dye entrapped in sol-gel fibre-optic applicators**

AGNIESZKA ULATOWSKA-JARŻA<sup>1,2\*</sup>, UWE BINDIG<sup>2</sup>,  
HALINA PODBIELSKA<sup>1,3</sup>, IWONA HOŁOWACZ<sup>1</sup>, WIESŁAW STREK<sup>4</sup>,  
GERHARD MÜLLER<sup>5</sup>, HANS JOACHIM EICHLER<sup>2,3</sup>

<sup>1</sup>Bio-Optics Group, Institute of Physics, Wrocław University of Technology,  
Wybrzeże Wyspiańskiego 27, 50-370 Wrocław, Poland

<sup>2</sup>Laser-und Medizin-Technologie GmbH, Berlin, Fabeckstr. 60-62, 14195 Berlin, Germany

<sup>3</sup>Institute of Optics, Technical University Berlin, Strasse des 17. Juni 135, 10623 Berlin, Germany

<sup>4</sup>Institute of Low Temperature and Structure Research, Polish Academy of Science,  
Okólna 2, 50-119 Wrocław, Poland

<sup>5</sup>Charité – Universitätsmedizin Berlin, Campus Benjamin Franklin, Institute of Laser Physics  
and Laser Medicine, Freie University Berlin, Fabeckstr. 60-62, 14195 Berlin, Germany

One of the promising modalities of modern medical treatment is interstitial laser therapy, where a special fibre-optic applicator is used to ensure a proper curing light distribution in the pathological lesion. Such an applicator can act as a light diffuser, and simultaneously it can serve as a carrier of the therapeutic medium, e.g. a photosensitive dye for photodynamic therapy in situ. For applicator construction, silica based sol-gels coatings are proposed in this paper. The sol-gel applicators were prepared from the silicate precursor TEOS (tetraethylorthosilicate) mixed with ethyl alcohol in acid-catalysed hydrolysis. A suitable amount of surfactant (Triton X-100) was used. The carrier matrices were produced with a solvent to precursor molar ratio of 20. In these studies, optical fibres from Laser Components were used (core diameter 400 nm, HCS, low OH). The external jacket was mechanically removed at a distance of 25 mm. The modified dip-coating method was exploited to cover the bare fibres with sol-gel material. Two types of applicators were produced, silica sol-gels with an addition of chlorophyll-derived sensitizer (Photolon) in two various concentrations. It was proved that the immobilization of Photolon in a silica sol-gel does not destroy its chemical activity and does not disturb contact with the external environment.

Key words: *sol-gel coatings; fibre optic applicator; chlorophyll-based photosensitizer*

---

\* Corresponding author, e-mail: Agnieszka.Ulatowska-Jarza@pwr.wroc.pl.

## 1. Introduction

Photodynamic therapy (PDT) of malignant tumours is a treatment method based on selective accumulation of light-absorbing agents (photosensitisers) in pathologic tissue, capable of stimulating photoreactions after irradiation by light of a certain wavelength, which destroy the targeted cells.

Various dyes have already been used in photodynamic therapy. This paper is focused on chlorin derivatives. A chlorin is a large heterocyclic aromatic molecule, consisting at the core of 3 pyrrole rings and one reduced pyrrole ring, all coupled by methine linkages. Magnesium-containing chlorins are called chlorophylls, and are the main photosensitive pigments in chloroplasts. A related compound, with 2 reduced pyrroles, is called bacteriochlorin. Due to their strong photosensitivity, chlorins are used as photosensitising agents in experimental PDT therapies.

Water-soluble derivatives of chlorophyll were first introduced as potential drugs by Snyder (USA) in 1942 [1]. The next important step was done by Allen [2]. He revealed that the major chemical compound of native chlorin mixtures is chlorin  $e_6$ , which under oral and intravenous administration possess low toxicity and demonstrates hypotensive, antisclerotic, spasmolytic, anaesthetic, and antirheumatoid activity. The first PDT usage of a chlorin concerns pheophorbide  $\alpha$ -derivatives. Some of them were patented as prospective photosensitizers for PDT in Japan in 1984 by Sakata et al. [3]. In 1986, an American group reported a photosensitizer meeting crucial PDT requirements: good tumour affinity and intensive absorption in the middle red part of the visible spectrum [4]. Their choice was mono-L-aspartyl-chlorin  $e_6$  (MACE). At present, this compound is at stage III of clinical trial studies in Japan. This group has even patented other functionally advanced chlorin and bacteriopheophorbide  $\alpha$ -derivatives as photosensitizers for PDT [5]. In the 1990s, a Byelorussian group at first headed by G. Gurinovich reported research on water-soluble chlorin-type photosensitizers derived from nettle [6]. Recently, their work was focused on the spectral-luminescent characteristics of chlorine  $e_6$  and the newly developed photosensitizer – Photolon – in whole blood [7].

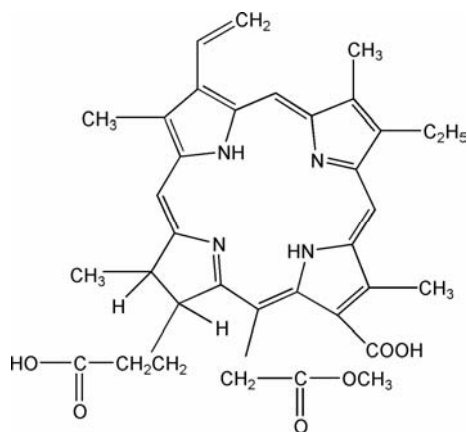


Fig. 1. Chemical structure of the Photolon according to [8]

Photolon – a chlorin derivative – belongs to the class of one-photon-based photosensitizers [8]. The dye is approved for cancer treatment in some countries [9]. Photolon is referred to a group of new sensitizers for treating cancer by means of photodynamic therapy. It can be administrated intravenously or topically. Recently, some non-oncologic applications have been reported as well [10]. The formula is shown in Fig. 1.

Interstitial laser thermotherapy is also a new method designed for minimally invasive therapy of pathologic lesions in environments difficult to access (e.g. the brain, liver). Fibre-optics laser applicators are used to perform interstitial therapy with laser light. The applicator is inserted into the pathologic lesion and curing laser light is guided through the fibre [11, 12]. We have already demonstrated that sol-gel coatings may improve the characteristics of applicators. Depending on the amount of compounds used for producing sol-gels, different optical and structural properties could be achieved [13–15].

Our idea was to combine interstitial therapy with photodynamic therapy. In this paper, we report on the development of a modified light delivery system – a sol-gel fibre-optic applicator doped with Photolon. The sol-gel was deposited on the optical fibre core and the influence of immobilized chlorophyll-derived dye on the applicator's spectral properties was investigated.

## 2. Preparation of sol-gel matrices

### 2.1. Materials

Solvents and reagents were obtained from commercial sources and used without further purification: a) solvents, methanol (Merck, UV-grade), ethanol (Merck), pyridine (Aldrich), b) chemicals, zinc acetate (Merck), Triton X-100 (Aldrich), tetraethylorthosilane (TEOS) (Fluka), hydrochloric acid (Merck), phosphate buffered saline (PBS) pH 7.2 (Biochrom). Photolon (Belmedpreparaty in cooperation with Haemato Ltd., Germany) was used as the active photosensitizer. Aqueous solutions were prepared with Millipore water (Milli-Q/USA). Phosphate buffered saline (PBS) pH 7.2 (Biochrom) was used to mimic physiological conditions, otherwise aqueous solutions were prepared with Millipore water.

The sol-gel films were produced from sol-gel hydrolyzate prepared from the silicate precursor TEOS mixed with solvent (ethanol, 96 % v/v). The sol-gel material was prepared with a solvent to precursor molar ratio  $R$  of 20. Hydrochloric acid (37%, w/w) was added as a catalyst in a proportion that ensured acidic hydrolysis (pH  $\approx$  2). The mixture was stirred at room temperature for 4 hours with a magnetic stirrer (speed 400 rev./min).

## 2.2. Preparation of sol-gel coatings on optical fibres

Hard Clad Silica (HCS) fibres of low OH (CFO 1493-12), originating from Laser Components, were used (fused silica core  $\phi_1 = 400 \mu\text{m}$ ; cladding  $\phi_2 = 430 \mu\text{m}$ ; ETFE buffer diameter  $730 \mu\text{m}$ ). They feature high transmission values from UV to IR (200–2400 nm). The fibres were cut into 200 cm sections. The external jacket was mechanically removed up to 2.5 cm from one end, then the cladding was treated with a hot torch. The residuals were removed with linen cloth and cleaned with ethanol. A modified dip-coating method was applied to cover the bare fibres with sol-gels. The fibres were placed vertically in a plastic container with a specially designed bottom, possessing an opening with a controlled diameter to ensure the required speed (1 cm/h) of hydrolyzate outflow. The container was filled with hydrolyzate up to the non-removed cladding. Just before the deposition procedure, the surfactant Triton X-100 (Aldrich) was added to the liquid hydrolyzate (20  $\mu\text{l}$  of Triton per 1 ml of hydrolyzate).

## 2.3. Photolon-doped coatings

Aqueous stock solutions ( $8.2 \times 10^{-4} \text{ M}$  and  $1.6 \times 10^{-4} \text{ M}$  Photolon) were prepared by dissolving the photosensitizer in water (Millipore grade). Aliquots of 50  $\mu\text{l}$  stock solution and 20  $\mu\text{l}$  of Triton X-100 were added to 1 ml of the freshly prepared hydrolyzate to get final Photolon concentrations of  $3.8 \times 10^{-5} \text{ M}$  and  $7.6 \times 10^{-6} \text{ M}$ , respectively. The newly prepared hydrolyzate was used to produce doped fibre-optic coatings according to the procedure described above. The stock solutions and the sol-gel modified fibres were stored at room temperature in darkness.

For metal insertion, zinc acetate was dissolved at room temperature in methanol (20 mg/ml) and the fibre was placed in the solution. The dopant sol-gel fibre was left there for 72 h. Then the fibre was removed, rinsed with ethanol, dried in air, and its luminescence and absorption spectra were recorded.

# 3. Spectroscopic measurements

## 3.1. Apparatus

Fluorescence spectra were obtained by means of a fluorescence spectrometer LS-50B (Perkin Elmer/UK). The spectra were recorded in the wavelength range from 350 to 750 nm (100 nm/min, excitation slit 3 nm, emission slit 5 nm) by using quartz micro-cuvettes (optical length 0.5 cm, Hellma, Germany). 10 scans were accumulated.

The absorption spectra of Photolon solutions were obtained by means of a Lambda 2 (Perkin Elmer, UK) spectrophotometer (optical length 1 cm, wavelength range

300–750 nm, 250 nm/min). A hand-held UV-lamp ( $\lambda_{\text{exc}} = 365 \text{ nm}$ ) was used for pre-detecting and controlling the luminescent sol-gel coating.

### 3.2. Spectroscopic examinations of Photolon in solvents

The Photolon molecule shows a partially reduced porphyrine moiety (Fig. 1). Its molecular structure is similar to the structure of chlorine  $e_6$  molecule, which can be isolated after hydrolysing the 5-membered exocyclic  $\beta$ -ketoester moiety of pheophorbide A. It is well known that the absorption and fluorescence of tetrapyrrolic macrocycles are sensitive to changes in their molecular environment.

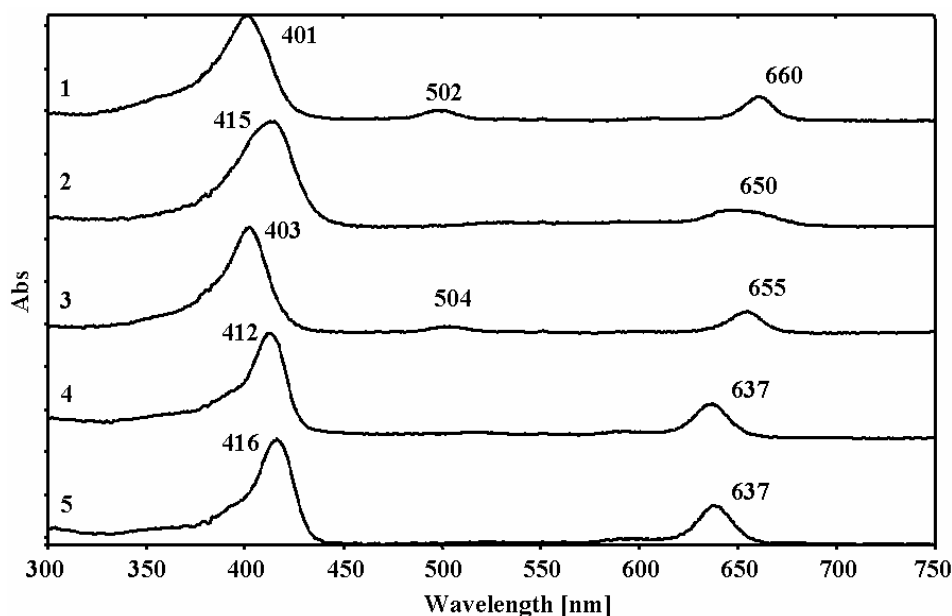


Fig. 2. Absorption spectra of Photolon in various solvents (from the top to the bottom): 1 – in methanol; 2 – in methanol acidified with hydrochloric acid; 3 – in phosphate-buffered saline (pH 7.2); 4 – after addition of zinc acetate in methanol; 5 – after addition of pyridine to 4

The absorption and fluorescence spectra of Photolon were recorded in various solvents. A stock solution of Photolon dissolved in methanol ( $1 \times 10^{-6} \text{ M}$ ) was prepared and visible spectra were recorded (Fig. 2). The Soret band and additional absorption bands in the wavelength range 500–700 nm (Q-bands) were observed. Two prominent absorptions, at 401 nm (Soret band) and at 660 nm (chlorine-type band), are visible. The addition of 0.1 ml of the concentrated hydrochloric acid to 2.5 ml of the methanolic dye solution leads to a bathochromic shift ( $\lambda_{\text{Soret}} = 415 \text{ nm}$ ). A second strong absorption band appears at 650 nm. The absorption intensity decreases and the bands become broader. In phosphate-buffered saline (PBS), the absorption of Photolon re-

mains essentially the same as in methanol (403 nm and 655 nm). After adding zinc acetate, a spectral change due to the insertion of zinc into the macrocycle is detected within minutes. The Soret band shifts towards 412 nm and the chlorine-type absorption band undergoes a hypsochromic shift to 637 nm. When pyridine is added to the zinc complex, a further shift of the Soret band ( $\lambda_{\max} = 416$  nm) is recorded.

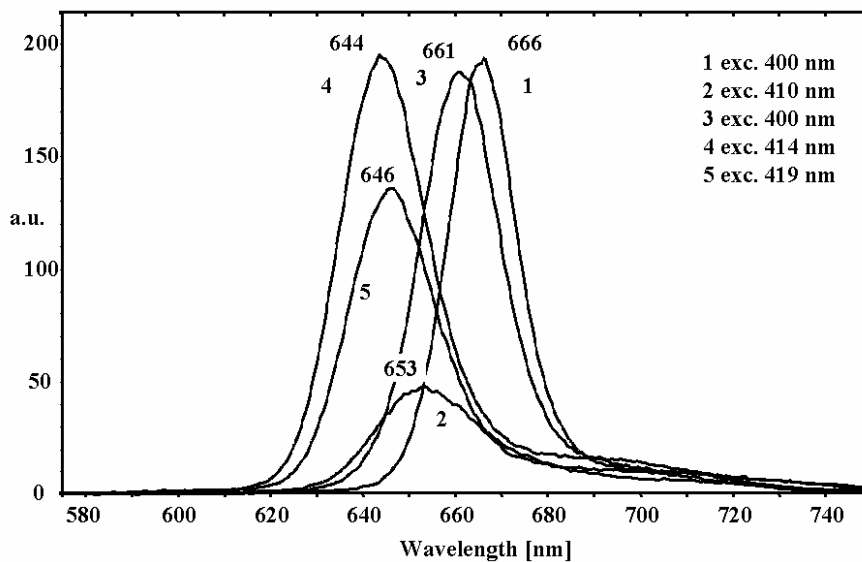


Fig. 3. Fluorescence spectra of Photolon in solutions: 1 – in methanol; 2 – in methanol acidified with hydrochloric acid; 3 – in PBS (pH 7.2); 4 – after addition of zinc acetate in methanol; 5 – after addition of pyridine to 4

The fluorescence spectra recorded in the wavelength range of 575–750 nm are shown in Fig. 3. In methanol, the fluorescence maximum of Photolon is observed at 666 nm ( $\lambda_{\text{exc}} = 400$  nm). In acidified methanol, the maximum is shifted towards 653 nm upon excitation at 410 nm. At the same time, the emission intensity decreased by a factor of approx. 4. In aqueous solution (PBS, pH = 7.2), the emission maximum is shifted to 661 nm ( $\lambda_{\text{exc}} = 400$  nm). Compared to the fluorescence spectrum of Photolon in methanol, the zinc complex in methanol shows strong fluorescence at 644 nm ( $\lambda_{\text{exc}} = 414$  nm). The coordination of pyridine to this metal complex, however, leads to the fluorescence signal at 646 nm.

### 3.3. Spectroscopic examinations of Photolon in sol-gel applicators

For fluorescence measurements, the sol-gel coated fibres were placed diagonally inside a cuvette. Spectra were recorded in air, in solvents, and after chemical altering. In order to avoid artifacts, the spectra were recorded at various positions on the same fibre.

First, the unmodified quartz fibre and sol-gel coated fibres without dopant were investigated in order to check their spectroscopic properties. Excitations from 395 up to 420 nm ( $\Delta\lambda = 5$  nm) using the pure core fibre as a target gave only a very weak fluorescence emissions in the range of 525–575 nm. A negligible fluorescence is also observed in air for the undoped sol-gel coated fibres. The addition of solvents leads to a further decrease in the fluorescence intensity.

Fibres with a sol-gel Photolon-doped coating were investigated in air and in the presence of solvent. Spectra were recorded for fibres doped with two concentrations of Photolon ( $3.8 \times 10^{-5}$  M and  $7.7 \times 10^{-6}$  M) (Fig. 4). Fluorescence and fluorescence excitation spectra were recorded in the wavelength range 550–775 nm and 350–625 nm, respectively.

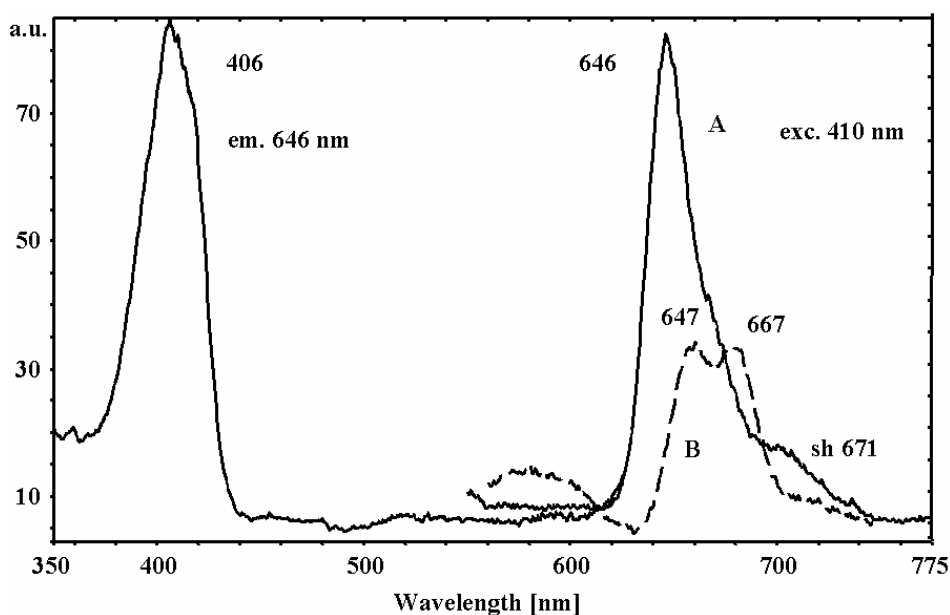


Fig. 4. Excitation and emission spectra in air, sol-gel applicator (A:  $3.8 \times 10^{-5}$  M; B:  $7.7 \times 10^{-6}$  M Photolon)

The fluorescence intensity of the sol-gel applicator was found to depend on the Photolon concentration (Fig. 4). A similar dependence (not shown here) was observed in absorption spectra. The fluorescence was determined in the range of 620–750 nm. The excitation spectra were recorded in a step-by-step mode ( $\Delta\lambda = 5$  nm) with  $\lambda_{\text{exc}}$  in the range of 395–420 nm. In Fig. 4, the fluorescence spectra ( $\lambda_{\text{exc}} = 410$  nm) are shown for fibres measured in air just after the coating procedure. For the fibre referred to as A ( $3.8 \times 10^{-5}$  M Photolon) in Fig. 4, the emission maximum at 646 nm and a shoulder at 671 nm were recorded. For the fibre with a lower dye concentration ( $7.7 \times 10^{-6}$  M Photolon), assigned to B, maxima at 647 nm and 667 nm were detected. The excitation spectrum shows a strong absorption at 406 nm ( $\lambda_{\text{em}} = 646$  nm).

Photolon dissolved in methanol shows the absorption maximum at 401 nm and a strong emission at 666 nm. The wavelengths of absorption and emission maxima in PBS (pH 7.2) are similar – 403 nm and 646 nm, respectively (Figs. 2 and 3). Both in methanol and PBS only the free base of Photolon is present. Adding hydrochloric acid to the methanolic solution, however, leads to a protonated form of the dye (emission,  $\lambda_{\text{max}} = 646$  nm). The addition of acid is crucial for sol-gel preparation, in order to initiate polymerisation, hence this will also lead to a protonation of the chromophore. Therefore, as indicated by the emissions at 647 and 667 nm, two different species – the neutral and a protonated form – seem to be present in the sol-gel matrix.

### 3.4. Spectroscopic examinations of Photolon-doped sol-gel applicators in various environments

Due to a high solubility of Photolon in organic solvents, fluorescence measurements were done in order to check whether the dopant leaks from the coating and to detect changes in the spectral properties of the applicator. The release of Photolon from the sol-gel matrix was also checked for aqueous solutions of PBS and Millipore water as described above, but no fluorescence could be detected. Therefore, after the measurement was completed, the modified fibre was removed and the remaining solvent was examined again.

Figure 5 shows the spectra for a doped fibre ( $R = 20$ ,  $3.8 \times 10^{-5}$  M Photolon) placed in methanol. Compared to the measurement in air, the overall intensities are slightly lower. The fluorescence is recorded in the wavelength range of 620–750 nm. The emission spectra ( $\lambda_{\text{exc}} = 395, 407, \text{ and } 420$  nm) do not differ from the spectra in air (Fig. 4). Emission maxima appear at 647 and 668 nm. Excitation at 395 nm leads to strong fluorescence at 668 nm. Upon excitation at 420 nm, the intensity decreases by up to 50%. Emission at 647 nm leads to a Soret band at 408 nm, whereas emission at 667 nm leads to a Soret band at 404 nm. A minor absorption in the Q-band range at 500 nm ( $\lambda_{\text{em}} = 667$  nm) is also observed.

An example of the protonation of a Photolon-doped fibre is shown in Fig. 6. In order to determine the protonated species of Photolon encapsulated in the sol-gel matrix, 100  $\mu\text{l}$  conc. hydrochloric acid was added. After 10 minutes, the spectra were measured (Fig. 6), then the solvent was replaced by a PSB-buffer. The emission spectra were immediately recorded and the process of neutralization was monitored. An excitation spectrum was recorded before and after protonation.

The emission spectrum of Photolon cations shows strong fluorescence at  $\lambda_{\text{max}} = 649$  nm ( $\lambda_{\text{exc}} = 410$  nm) and a Soret band at 407 nm ( $\lambda_{\text{em}} = 50$  nm). In PBS, the fluorescence is shifted toward 667 nm ( $\lambda_{\text{exc}} = 405$  nm) and the Soret band is determined to be at 405 nm ( $\lambda_{\text{em}} = 666$  nm). In accordance to the absorption spectrum of Photolon in PBS (Fig. 2), the excitation spectrum in PBS shows an additional absorbance at approximately 506 nm.

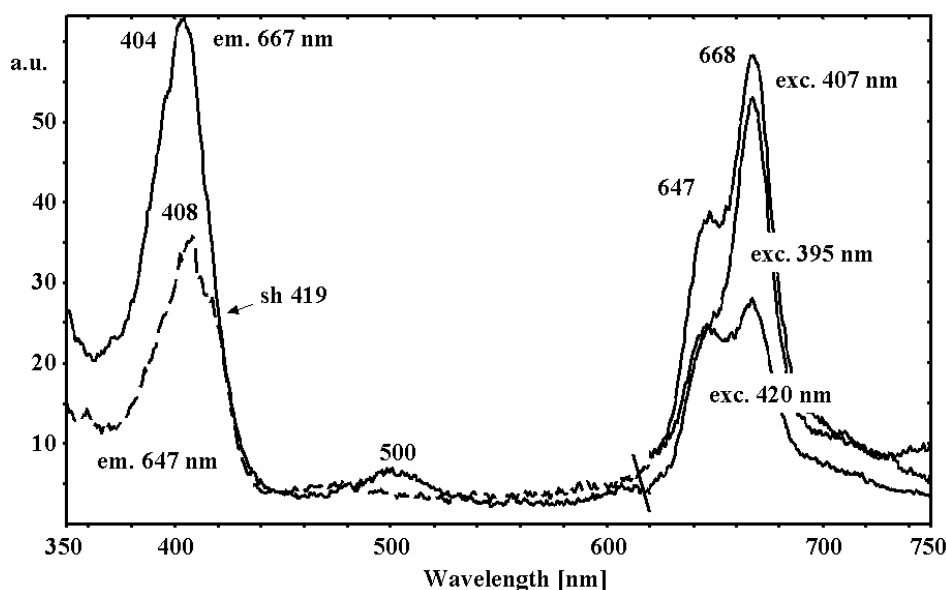


Fig. 5. Fluorescence excitation and emission spectra of a fibre  $R = 20$  ( $3.8 \times 10^{-5}$  M Photolon) placed in methanol

To monitor the chemical reactivity of the embedded Photolon, the fibre was left in a solution of zinc acetate (20 mg/ml) in methanol for 12 h at room temperature. Prior to this, it was placed in PBS to ensure the presence of the neutral species. After 12 h the fibre was removed and the solution, as well as the fibre in the dry state, were examined. No fluorescence was detected in the organic solution.

In result, there is another strong fluorescence at 667 nm ( $\lambda_{\text{exc}} = 395$  nm), which is assigned to the free base of Photolon. Another emission band is observed at 646 nm ( $\lambda_{\text{exc}} = 415$  nm) – this may be caused by the partial protonation of Photolon. The emission at 646 nm, however, leads to an excitation spectrum with a broad Soret-band at 407 nm and a shoulder at 416 nm (not shown).

We conclude that no metal insertion takes place. Neither a longer reaction time, gentle heating of the reaction solution, nor high concentrations of zinc acetate enforced metal insertion.

Due to the initial preparation conditions and to sol-gel polymerisation, the neutral and the cationic species of Photolon are present in different amounts. The ratio can be changed with protonation and by using different solvents. While the insertion of zinc into the dye is observed within minutes when Photolon is dissolved in methanol, the doped fibre remains unchanged. It is well known [16] that porphyrin monomers exist only at very low dye concentrations or in a strong acidic medium. Usually, at normal conditions, porphyrins as well as chlorin will dimerise. Therefore, we conclude that besides the limitation due to the pore diameter of the sol-gel, the embedded Photolon molecules (preferred species: dimer) cannot be reached by the zinc cations in the sol-gel matrix. Also, no phenomenon of dye aggregation (which happens through a self-

enforced process that builds up supramolecular structures, namely H- (stacked) or J- (side by side) complexes [17], was not observed during spectroscopic examinations.

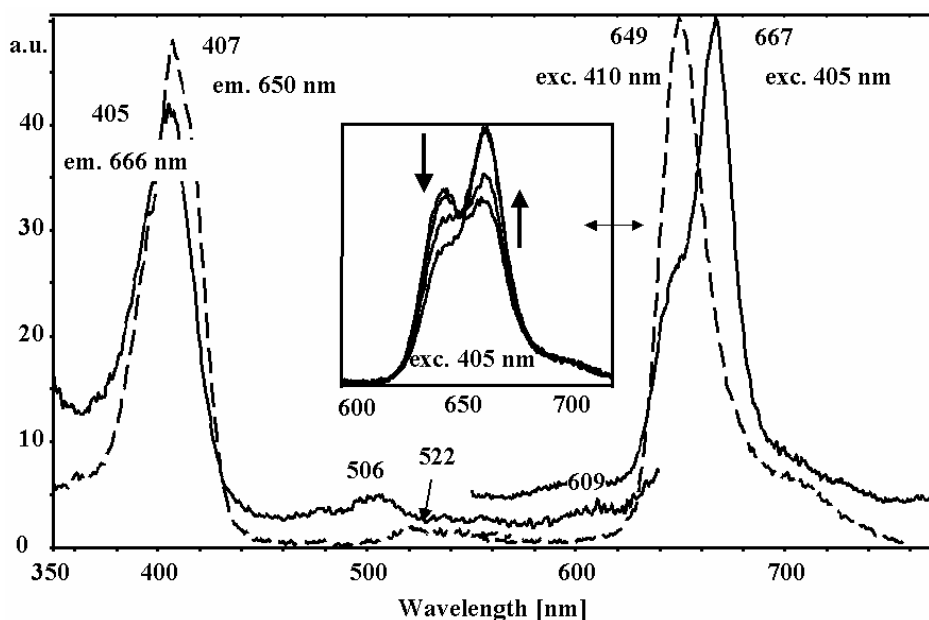


Fig. 6. Excitation and emission spectra from applicator ( $3.8 \times 10^{-5}$  M Photolon) placed in 0.5 M HCl (dashed line) and PBS-buffer (pH 7.2). Inset: fluorescence spectral evolution by time ( $\lambda_{\text{exc}} = 405$  nm) during reaction in PBS

#### 4. Conclusions

Our work was focused on the examination of the optical properties of doped silica sol-gel coatings, which may be used for photodynamic therapy in situ. It has already been proved [18] that Protoporphyrine IX-doped sol-gel coatings deposited on the fibre core changes the light propagation conditions, depending on the sol-gel  $R$  factor (solvent to precursor molar ratio) and on the coating technology as well. These observations should be considered in the construction of sol-gel based applicators.

In this paper, we have shown that Photolon entrapped in sol-gel preserves its chemical activity and may contact with the external environment. Chemical reactions like protonation occurred quite fast. This indicates that the interconnected porous network could be easily penetrated by relatively small molecules. On the other hand, reactions with zinc cations cannot be clearly observed by spectroscopic examination. The silica sol-gel structure was modified by adding Photolon in such a way that pores are too small or there is a kinetic effect. The insertion of zinc ions into the sol-gel matrix might take more time than the duration of our experiments, 72 h at room temperature, and 6 h at 50 °C. The diameter of the zinc ion is about 83 pm, and a solva-

tion sphere has to be taken into account. Solvation phenomena make necessary preparation of the silica sol-gel matrix with a diameter of pores much larger than that of the introduced molecule.

The absorption peak of zinc-Protoporphyrin is 12 times higher and shifted as compared the absorption peak of Protoporphyrin IX [18]. We did not observe a similar phenomenon in the case of Photolon with and without Zn ions – the intensity of absorption is approximately the same. This could explain lack of a clean signature of metallation of the chlorin derivative. The Zn-Photolon complex is not so easy distinguishable in absorption spectrum.

Photolon molecules did not leave the pores of the silica sol-gel coating and no aggregation was observed. The protonation of Photolon occurred slowly when the concentration of  $H^+$  ions was low. The higher the concentration of  $H^+$  ions, the faster appeared the protonated form of Photolon. The deprotonation of the dye, conducted in a PBS environment (pH~7.2), occurred after 15 min.

Structural changes caused by the addition of Photolon to the sol-gel matrix influence not only the optical properties, but also the durability of the coatings. During the examinations described in this paper, lasting a few days in various conditions (various solvents, drying in air), no changes in the stability of coatings were observed. We did not notice any alterations in the Photolon-doped silica sol-gel coatings.

Further investigations will involve studies on dye metallation (the insertion of Zn ions) and oxidation (under  $O_3$  and  $H_2O_2$  conditions). We are going to prepare Photolon-doped silica sol-gel coatings with various values of  $R$ , not only  $R = 20$  (chosen because of the quality of the coating, stability, and optical properties).

#### Acknowledgements

This work was partially financed by the Polish State Committee for Scientific Research (KBN), Grant No. 4T11E01124. A. Ulatowska-Jarza is an Alexander von Humboldt Foundation research fellow.

#### References

- [1] SNYDER E.G., *Preparation of chlorin e*, Patent 2,274,101 USA, (02/1942).
- [2] ALLEN E.A. *New porphyrinic and chlorophyllic compositions and process therefore*, Patent 3,102,891 USA, (1963).
- [3] SAKATA I., NAKAJIMA S., *Pheophorbide derivatives and alkaline salts thereof*, Patent 4,709,022 USA, (11/1987), C.A., 103 (15), 123271s, (1985).
- [4] BOMMER J.C., SVEIDA Z.J., BURNHAM B.F., *Proceedings of 1st International Conference of Clinical Applications of Photosensitization for Diagnosis and Treatment*, Tokyo, 1986, p.129.
- [5] BOMMER J.C., BURNHAM B.F., *Tetrapyrrol therapeutic agents*, Patent 4,656,186 USA (04/1987), C.A. 106, 85048b, 1987.
- [6] KOSTENICH G.A., ZHURAVKIN I.N., ZHAVRID E.A., *J. Photochem. Photobiol.*, 22 (1994), 211.
- [7] PARKHOTS M.V., KNYUKSHTO V.N., ISAKOV G.A., PETROV P.T., LEPESHKEVICH S.V., KHAIRULLINA A.YA., DZHAGAROV B.A., *J. Appl. Spectr.*, 70 (2003), 921.
- [8] KAROTKI A., *Simultaneous two-photon absorption of tetrapyrrolic molecules: from femtosecond coherence experiments to photodynamic therapy*, Ph.D. Dissertation, Montana State University, Bozeman, MT, 2003.

- [9] Web site: [www.belmedpreparaty.com](http://www.belmedpreparaty.com).
- [10] PODBIELSKA H., STREK W., DEREN P., BEDNARKIEWICZ A., *Physica Medica*, 20, Suppl. I (2004), 61.
- [11] *Laser-Induced Interstitial Thermotherapy*, G. Muller, A. Rogan (Eds.), SPIE Optical Engineering Press, Bellingham, Washington, USA, 1995.
- [12] ROHDE E., MESECKE I. VON RHEINBABEN, PODBIELSKA H., HOPF M., MUELLER G., *Med. Laser Appl.*, 16 (2001), 81.
- [13] LECHNA M., HOLOWACZ I., ULATOWSKA A., PODBIELSKA H., *J. Surf. Coat. Technol.*, 151&152 (2001), 299.
- [14] JELEŃ Ł., CEGIELSKI M., ULATOWSKA-JARŻA A., PODBIELSKA H., *Opt. Appl.*, 32 (2002), 759.
- [15] KOBEL J., SUCHWAŁKO A., PODBIELSKA H., ULATOWSKA-JARŻA A., *Opt. Eng.*, 42 (2003), 1137.
- [16] *The Porphyrins*, Volume VII: *Biochemistry*, Part B, D. Dolphin (Ed.), Academic Press, New York, 1979.
- [17] FUHRHOP J.-H., *Irreversible Reactions on the Porphyrin Periphery*, [in:] *The Porphyrins*, Vol. 2, D. Dolphin (Ed.), Academic Press, New York, 1978, p. 255–287.
- [18] ULATOWSKA-JARŻA A., BINDIG U., PODBIELSKA H., ANDRZEJEWSKI D., MÜLLER G., EICHLER H.J., *SPIE Proc. on Light & Optics in Biomedicine*, in press.

*Received 24 July 2004*  
*Revised 24 November 2004*

## Bioactive glass coatings

RAFAL SINDUT<sup>1</sup>, KATARZYNA CHOLEWA-KOWALSKA<sup>1</sup>, JELENA NAJMAN<sup>2</sup>,  
MARIA ŁACZKA<sup>1\*</sup>, MARIA KARPOV<sup>3</sup>, ANNA MARIA OSYCZKA<sup>3</sup>, PHOEBE LEBOY<sup>3</sup>

<sup>1</sup>AGH-University of Science and Technology, Faculty of Materials Science and Ceramics,  
Department of Glass Technology and Amorphous Coating, 30-059 Cracow, Poland

<sup>2</sup>Cracow University of Technology, Faculty of Chemical Engineering  
and Technology, 31-155 Cracow, Poland

<sup>3</sup>University of Pennsylvania, Philadelphia, 19104 PA, USA

Four kinds of gel-derived materials of the CaO–P<sub>2</sub>O<sub>5</sub>–SiO<sub>2</sub> (S2, II, I, A2) system were obtained in the form of thin coatings on microscope slides. The obtained materials differed from each other in the ratio of the basic components (CaO and SiO<sub>2</sub>). The coatings were characterised with regard to the state of the surface as well as to the phase composition of the materials. In order to determine any bioactive properties of the gel-derived coatings *in vitro*, tests in simulated body fluid (SBF) were made and biochemical examinations using cultured human marrow stromal cells (hMSC) were conducted. It was found that surface crystallisation of hydroxyapatite (HAp) indicating the bioactivity of the material occurred in SBF only in the case of A2 coatings, which are characterised by the highest ratio of CaO:SiO<sub>2</sub>. Tests with hMSC showed that the A2 biomaterial promotes both the osteogenesis and remodelling of bone (osteoclastogenesis).

Key words: *biomaterials; bioactivity; sol-gel method*

### 1. Introduction

Bioactive ceramic materials are based on the CaO–P<sub>2</sub>O<sub>5</sub>–SiO<sub>2</sub> system [1, 2]. They comprise both glasses and glass-ceramic materials with hydroxyapatite and wollastonite as the main crystal phases. They are assumed to satisfy the following requirements:

- biocompatibility,
- suitability for clinical applications,
- ability to form a stable connection with the bone as well as to promote bone regeneration.

---

\* Corresponding author, e-mail: mlaczka@poczta.fm.

When in contact with body fluid, these materials form layers of hydroxyapatite (HAp) on their surfaces, through which the implant materials form permanent bonds with the bone in a living organism. The ability to form HAp on the surface of biomaterials is usually indicated by results of simulated body fluid (SBF) tests, which allow *in vitro* character of changes on the biomaterial surface to be estimated after contact with SBF [3]; biomaterials are preliminarily defined by this basic bioactive property.

In recent years, great interest has arisen for a new generation of bioactive materials with increased bioactivity, interpreted mainly as the ability to stimulate faster regeneration of natural tissues [4, 5]. In order to obtain such materials, the sol-gel method is used, which enables biomaterials with a high degree of both chemical and biological surface activities to be produced [6]. This method allows the production of biomaterials in the form of powders and granules, dense and porous sinters, thin coatings, on bioinert substrates. So far, however, it has not been fully recognized which material parameters, such as the state of the surface, pore structure, chemical and phase composition, etc. affect the bioactive properties of these biomaterials. The lack of this knowledge does not permit fully controlled production processes to be carried out.

The aim of this study was to obtain bioactive gel-derived coatings with various characteristics (chemical properties, phase composition, surface roughness) and to evaluate their bioactive properties under *in vitro* conditions from the point of view of material parameters.

## 2. Materials and methods

Biomaterials from the system  $\text{CaO-P}_2\text{O}_5\text{-SiO}_2$  have been chosen for the investigations. Their chemical compositions are given in Table 1.

Table 1. The chemical composition of the investigated materials

Chemical composition	Symbol			
	S2	II	I	A2
$\text{SiO}_2$	80	72	64	40
$\text{CaO}$	16	24	30	54
$\text{P}_2\text{O}_5$	4	4	6	6
$\text{CaO/SiO}_2$	0.2	0.33	0.47	1.35

Such a choice of chemical compositions allowed materials to be obtained with various molar ratios of the components having considerable influence on the bioactive properties, i.e.  $\text{CaO}$  and  $\text{SiO}_2$ .

To prepare the starting solutions, the following reagents were used:  $\text{Si}(\text{OC}_2\text{H}_5)_4$  (TEOS) (Merck),  $\text{OP}(\text{OC}_2\text{H}_5)_3$  (Merck), and  $\text{Ca}(\text{NO}_3)_2 \cdot 4\text{H}_2\text{O}$  (POCh). In addition to

distilled water, ethanol was used as a solvent and hydrochloric acid (HCl) as a catalytic agent. The scheme of preparing the starting solutions is given in Fig. 1.

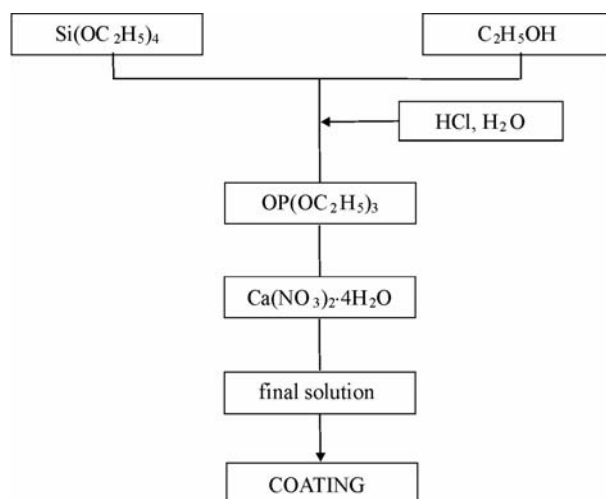


Fig. 1. A scheme for the preparation of coatings

The solutions were used to deposit coatings on bioinert substrates (microscopic glass slides). Thin coatings were deposited by dip coating, using a specially designed apparatus. The glasses with the deposited coatings were dried at ambient temperature and subsequently heated in an electric furnace at the temperature of 450 °C. The coatings obtained were either opaque or transparent. Coatings prepared in this way were subject to the following observations and investigations:

- evaluation of the quality of the coatings by visual and microscopic methods,
- determination of the phase composition of the coating materials by X-ray diffraction analysis (XRD), using a Seifert diffractometer and applying  $\text{CuK}\alpha$  radiation;
- determination of layers roughness according to ISO (DIS H287/1), using a profilometer (Hammel Tester T500, Mommelwerke GmbH, Berlin),
- testing bioactivity *in vitro* (the simulated body fluid (SBF) test) comprising:
  - investigation of the solubility of the coating materials in SBF within a period of 1–21 days; to this end, the concentrations of Ca ions in SBF were measured by the complexometric method (applying a solution of disodium versenate in the presence of calcein as an indicator),
  - evaluation of the changes on the surfaces of the coatings after 1–21 days of contact with SBF by means of SEM observations (JEOL 5400, Tokyo, Japan), EDAX analysis (LINK ISIS 300), and XRD diffraction phase analysis (Seifert diffractometer),
  - *in vitro* tests of the A2 material with cultured human marrow stromal cells (hMSC); the aim of this test was to check if the obtained gel-derived material promotes both osteogenesis and bone remodelling (osteoclasogenesis). Three independ-

ent samples of human marrow cells, isolated from the femurs of individuals undergoing total hip replacement, were cultured in a medium ( $\alpha$ -MEM + 15% bovine serum FBS). When confluent, the adherent layer of hMSC was re-plated on either the A-2 gel-derived coating or on a tissue-cultured plastic. Cells were harvested for mRNA assays after 7 days with either ascorbate-2-P (Asc), Asc with bone morphogenetic protein BMP2 or dexamethasone (a synthetic glucocorticoid) Dex, or with both BMP2 and Dex. Alkaline phosphatase (ALP) and RANK-L were localised with immunocytochemistry. ALP was treated as a marker of osteogenesis and RANK-L as a marker of the promotion of bone remodelling (osteoclastogenesis) [7–9].

### 3. Results

#### 3.1. Characteristics of the coatings

The coatings deposited on the microscope slides tightly covered the substrate and were characterized by very good adhesion. Coatings S2, I, and II were translucent, while coatings made from the A2 material were opaque (Fig. 2).

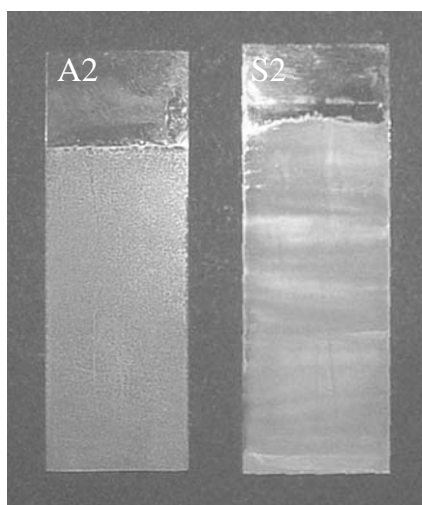


Fig. 2. Thin coatings of the A2 and S2 materials on microscopic glass slides

It can be inferred from SEM observations (Figs. 3, 5) that the quality of the obtained coatings was good. At some places a few cracks, typically in the boundary area, were visible. In the case of the A2 coating, spherical micro areas could be observed, uniformly distributed on the entire surface, evidence of liquation and/or crystallization. The chemical compositions of the coatings were in agreement with the expected compositions of the gel-derived materials (results of EDAX analysis – Figs. 4, 6).

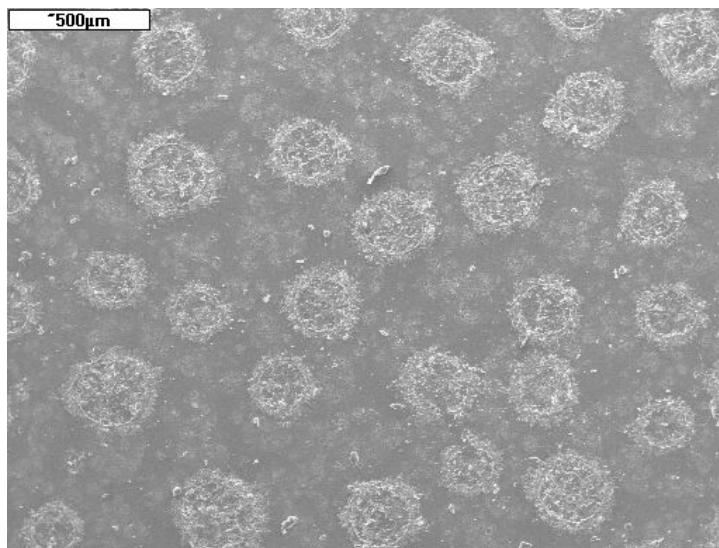


Fig. 3. SEM image of the surface of a gel-derived A2 coating

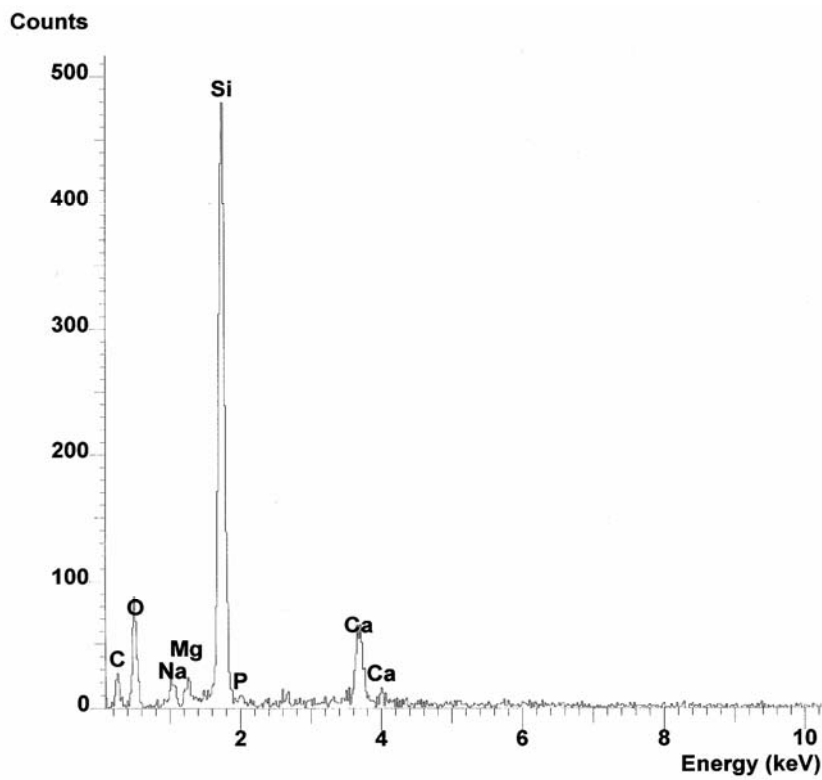


Fig. 4. Results of EDAX analysis for the surface of a gel-derived A2 coating

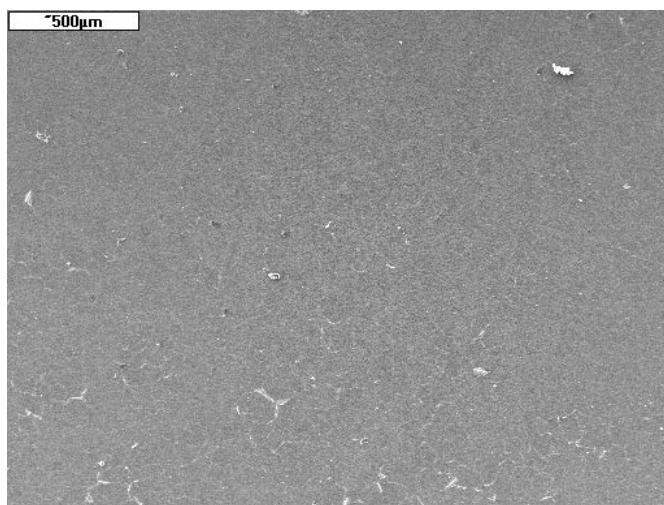


Fig. 5. SEM image of the surface of a gel-derived S2 coating

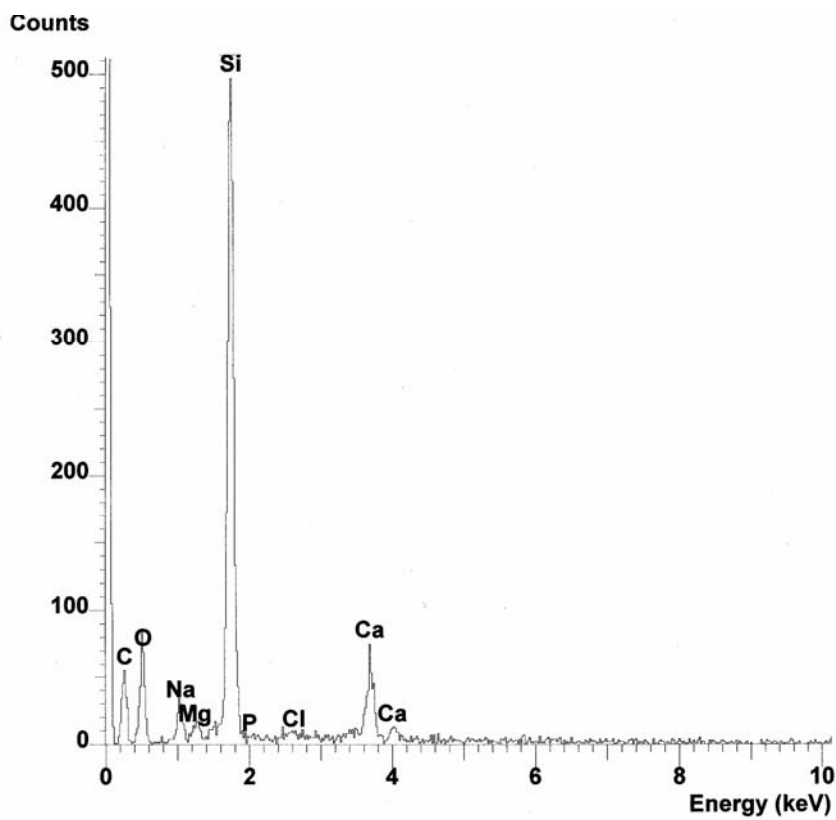


Fig. 6. Results of EDAX analysis for the surface of a gel-derived S2 coating

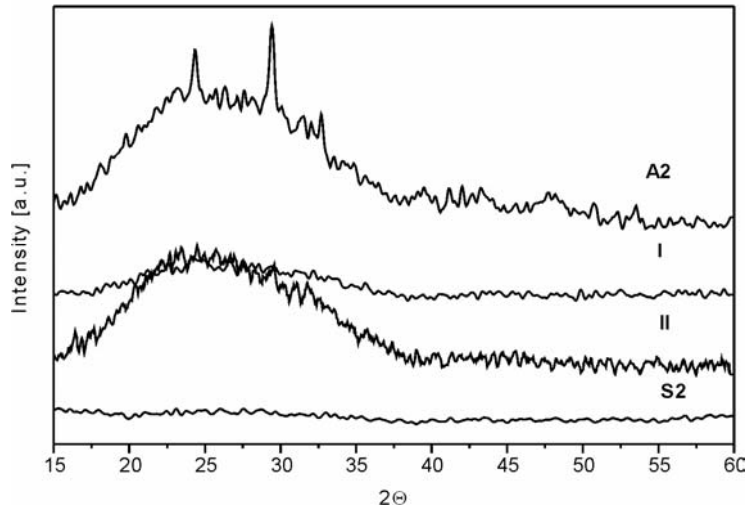


Fig. 7. XRD patterns of gel-derived A2, II, I, and S2 coatings

X-ray diffraction analysis showed (Fig. 7) that the coatings S2, I, and II are completely amorphous, while the coating made of the A2 material contains a crystal phase (phases) with calcium. On account of the low intensity of the reflexes, however, it is difficult to identify the character of these phases (phase).

Table 2. The surface properties of the investigated materials

Coefficient	Gel-derived layer			
	S2	A2	I	II
$R_a$	0.06	0.96	0.06	0.12
$R_z$	0.59	10.19	0.80	1.83
$R_t$	1.72	11.71	1.10	4.17

Three parameters defining the state of the surface coatings (roughness and topography) have been measured (Table 2):

- $R_a$  – the arithmetic mean of the deviation of the filtered roughness profile from the centre line within the measured length;
- $R_t$  – the vertical distance between the maximum and the highest points in the filtered roughness profile within the reference length;
- $R_z$  – the height of ten points (upper level of the absolute values of the five highest peaks and five lowest valleys within the measured length 1m).

From the data given in Table 2, it appears that the A2 coating, in which crystallization occurred, was characterized by the largest roughness. In the case of the amorphous coatings S2 and I, the roughness was considerably smaller, whereas the amor-

phous coating II exhibited a roughness that could be defined as intermediate between that of A2 and the materials S2 and I.

### 3.2. Test in SBF

Treatment of the gel-derived coatings with simulated body fluid (SBF) induced some changes in the chemical composition of the fluid (Fig. 8) as well as on the surface of the coatings (results of EDAX analysis – Figs. 10, 12).

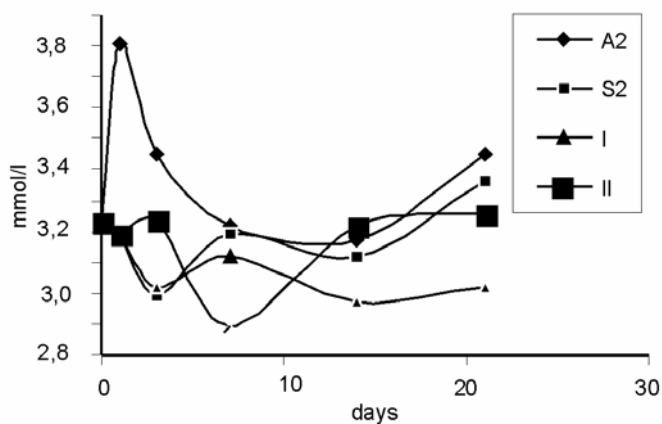


Fig. 8. Ca concentration of glass slides covered with the gel-derived A2, II, I, and S2 materials after various immersion times in SBF

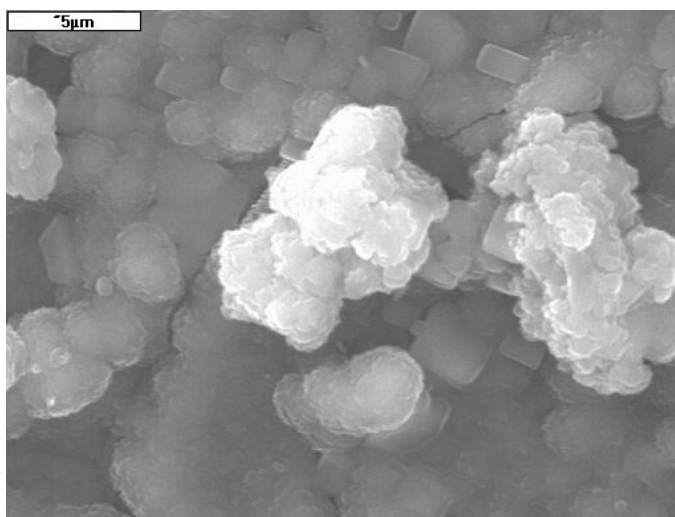


Fig. 9. SEM image of the surface of a gel-derived A2 coating after 7 days contact with SBF

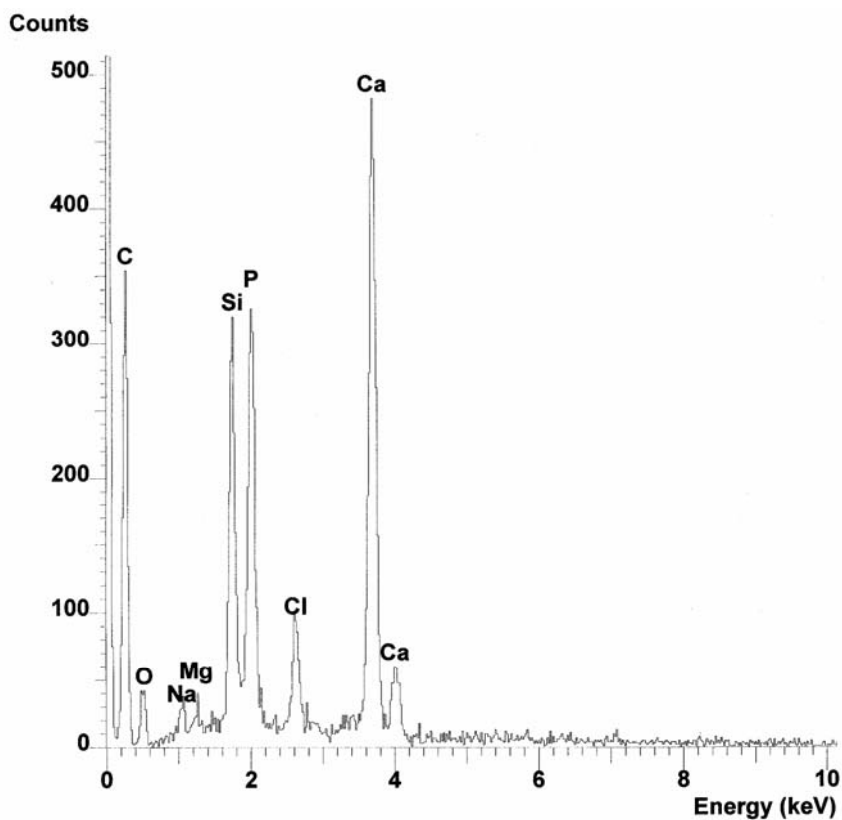


Fig. 10. Results of EDAX analysis for the surface of a gel-derived A2 coating after 7 days contact with SBF

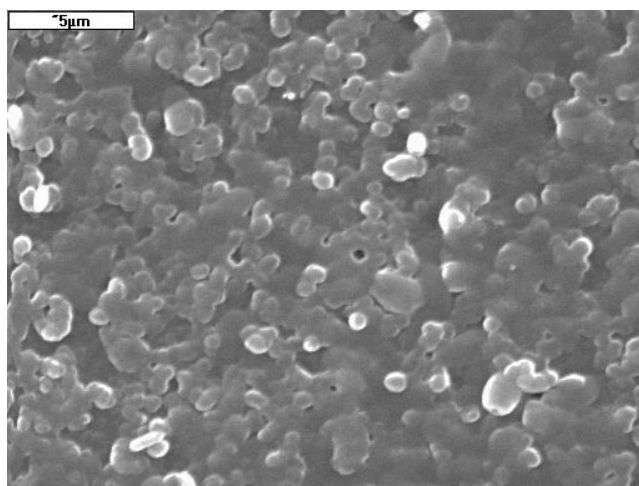


Fig. 11. SEM image of the surface of a gel-derived S2 coating after 7 days contact with SBF

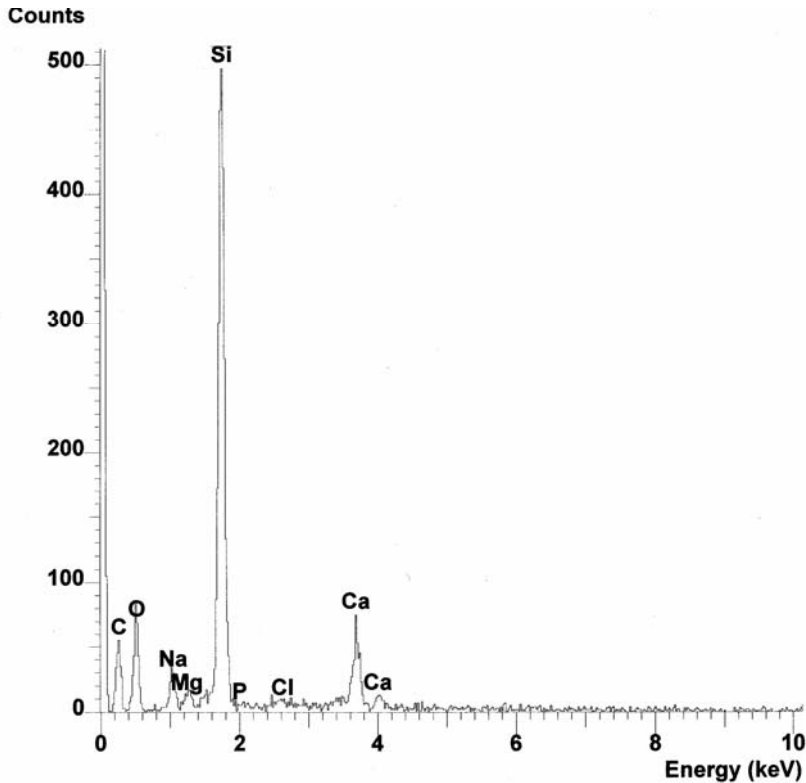


Fig. 12. Results of EDAX analysis for the surface of a gel-derived S2 coating after 7 days contact with SBF

Changes in SBF composition were caused by the solubility of the coating materials. This solubility was evaluated only with respect to the calcium content in SBF. In the case of other components of the coatings, no measurable solubilities have been observed. From among the four examined gel-derived materials, only the A2 coating, for which the  $\text{CaO}:\text{SiO}_2$  ratio is the highest, exhibited a considerable loss of calcium already 1 day after contact with SBF. The consequence of this was an increase in the Ca concentration in the SBF. With further contact, the content of Ca in SBF showed a tendency to fall, which might be connected to the surface crystallization of hydroxyapatite. In the case of other coatings, the Ca concentration in SBF, independently of the duration of contact with the biomaterial, was close to the starting concentration.

Changes in chemical composition and SEM images (resulting from contact with SBF) were observed only in the case of the A2 material (Figs. 9, 10). From EDAX analysis (Fig. 10) it appears that already after 7 days after immersion, the concentration of calcium and phosphorus in the surface layer of the material increased. This is an indication of the surface crystallization of calcium phosphates. With prolonged contact time with SBF (up to 21 days), the content of Ca and P on the surface increased, while the content of silicon decreased.

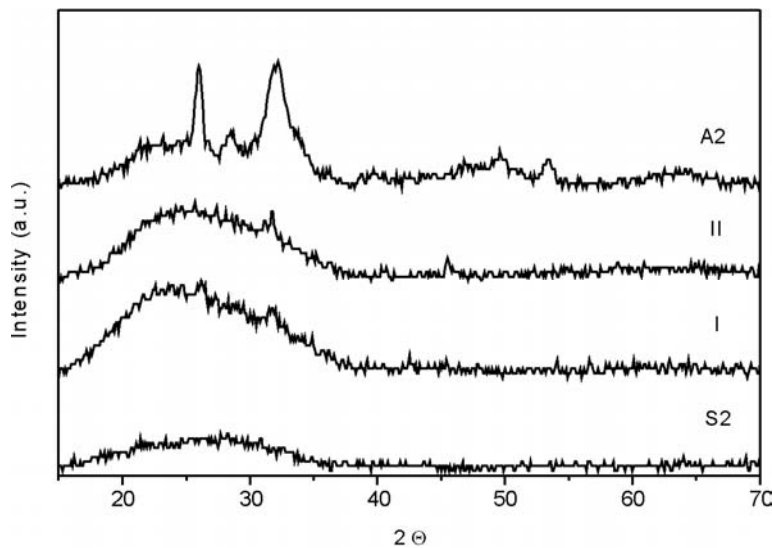


Fig. 13. XRD patterns of gel-derived A2, II, I, and S2 coatings after 7 days contact with SBF

Changes in the chemical composition were accompanied by a distinct change in the morphology of the layer surface. The surface became covered with spherical forms (Fig. 9), which after 21 days completely covered the primary layer. XRD investigations (Fig. 13) showed that the spherical forms appearing on the surface were composed of hydroxyapatite. The described phenomenon was observed for layers characterized by a lower ratio of CaO to SiO<sub>2</sub> (Figs. 11–13). Since the results of the tests with SBF show that only the A2 material is able to produce hydroxyapatite on its surface, it was chosen for *in vitro* tests with human marrow cells.

### 3.3. In vitro test with human marrow stromal cells

Cells cultured directly on the A2 surface showed a stimulation pattern for alkaline phosphates (ALP) similar to that of cells cultured on plastic, though the levels on A2 were slightly lower (Fig. 14a). The A2 glass, however, had a far more profound effect on the expression of osteopontin and RANK-L (Fig. 14b). MSC cultured on a A2 surface had osteopontin and RANK-L mRNA levels 5–10 times higher than those of cells on plastic, and addition of BPM caused a further increase in the mRNA levels.

## 4. Discussion

The sol-gel process enabled coatings with various chemical compositions to be obtained in a relatively simple way on glass plates. The phase composition of the layers depended on the molar ratio CaO:SiO<sub>2</sub>. At the highest value of this ratio (ca. 12), the

liquation and crystallization of the phase enriched with calcium probably took place. The effect of crystallization was the deterioration of surface smoothness, resulting in an increase of the parameters  $R_a$ ,  $R_z$ , and  $R_t$ .

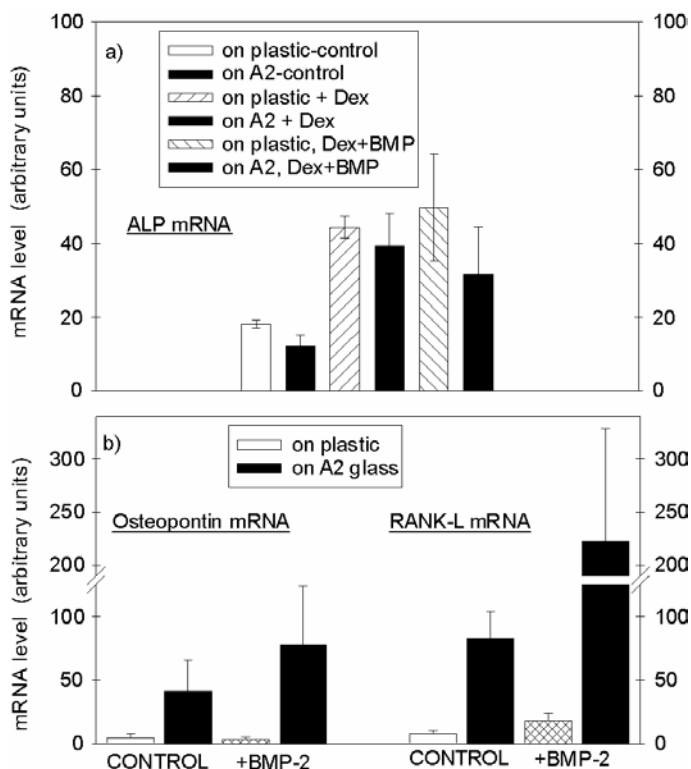


Fig. 14. Expression of mRNA in hMSC, cultured for 7 days on a tissue culture plastic (plastic) and on A2 gel-derived coating (A2 glass, black bars). Cells were cultured with a media containing 100  $\mu$ g/ml ascorbate (control), a control media with 100 nM Dex, a control media with 100  $\mu$ g/ml BMP-2, or with Dex + BMP. Comparison of ALP mRNA in cells on plastic or A2 glass with various inducers (A). The effect of A2 glass, with and without BMP treatment, on the expression of mRNA for steopontin and RANK-L (B)

When considering the chemical composition of the examined layers from the point of view of its influence on the bioactive properties of the materials, it should be expected that increasing the  $\text{SiO}_2$  concentration would favour HAp crystallization due to an increase of the number of active nucleation centres in the form of Si-OH groups [10, 11]. On the other hand, HAp crystallization can occur at an appropriate concentration of calcium in SBF, exceeding the solubility HAp. Thus, the increased concentration of calcium in the material should be a factor promoting HAp crystallization in this case.

As a result of the test in SBF, it has been found that within the investigated period of 21 days HAp was formed due to contact with SBF only on the surface of the A2

material, which is characterized by the highest CaO:SiO<sub>2</sub> ratio. At the same time, only in A2 layers a considerable solubility of Ca in SBF was observed. Thus, it can be assumed that an appropriate level of calcium solubility, determined by the value of the CaO:SiO<sub>2</sub> ratio in CaO–P<sub>2</sub>O<sub>5</sub>–SiO<sub>2</sub> gel-derived coatings, is the factor that determines the ability of HAp to form on the surface. Accordingly, it can be expected that coatings with appropriately high CaO:SiO<sub>2</sub> ratios can be bioactive. This statement, however, needs to be verified in *in vitro* conditions.

At the same time, our *in vitro* study identifies the bioactive gel-derived A2 material to potentially support the growth and osteoblast differentiation of human bone marrow stromal cells. Surfaces coated with the A2 sol-gel glass were found to permit the adherence, proliferation, and differentiation of hMSC at levels comparable to those seen for tissue culture plastics. Furthermore, the A2 glass induces the expression of both osteopontin, which promotes the migration of osteoblast precursors, and RANK-L, which induces the differentiation of osteoclast precursors. Our data indicate that those MSC that exhibit increased ALP levels are the same cells that show elevated RANK-L levels. There may be, however, an inverse relationship between the levels of ALP and RANK-L. The ability to promote both osteogenesis and osteoclastogenesis may facilitate not only new bone formation, but also the subsequent remodelling of the new bone. Since hMSC are believed to be stem cells that play a key role in providing new osteoblasts for bone repair and remodelling, A2 gel-derived glass is significantly promising as a coating for orthopaedic and dental implants.

## 5. Conclusions

The bioactive properties of CaO–P<sub>2</sub>O<sub>5</sub>–SiO<sub>2</sub> gel-derived coatings, determined on the basis of HAp surface crystallization capability caused by contact with simulated body fluid (SBF), are determined for different CaO:SiO<sub>2</sub> ratios. The increase of CaO content at the expense of SiO<sub>2</sub> leads to a higher solubility of Ca in SBF and promotes the surface crystallization of HAp.

The material for which the surface crystallization of HAp occurs as a result of contact with SBF, promotes both osteogenesis and osteoclastogenesis, which may facilitate the formation and remodelling of the newly formed bone.

### Acknowledgements

The research was financially supported by the Polish State Committee for Scientific Research, project No. PBZ-KBN-082-T08.

### References

- [1] HENCH L.L., Am. Ceram. Soc. Bull., 77 (1998), 67.
- [2] HENCH LL., J. Am. Ceram. Soc., 74 (1991), 1487.
- [3] KOKUBO T., KUSHITANI H., OHTSUKI C., SAKKA K., YAMAMURO T., J. Mater. Sci. Mater. Med., 3, (1992), 78.

- [4] LI R., CLARK A.E., HENCH LL. *J. Appl. Biomat.*, 2 (1991), 231.
- [5] LACZKA M., CHOLEWA-KOWALSKA K., LACZKA-OSYCZKA A.M., TWORZYDLO M., TURZYNA B., *J. Biomed. Mat. Res.*, 52 (2000), 601.
- [6] DISLICH H., *J. Noncryst. Sol.*, 73 (1985), 599.
- [7] SAKOU T., *Bone*, 22 (1998), 591.
- [8] LACZKA-OSYCZKA A.M., LACZKA M., KASUGAI S., OHYA K., *J. Biomed. Mat. Res.*, 42 (1998), 433.
- [9] SANTOS E.M., RADIN S., SHENKER B.J., SHAPIRO I.M., DUCHEYNE P., *J. Biomed. Mat. Res.*, 41 (1998), 87.
- [10] KOKUBO T., *J. Noncryst. Sol.*, 120 (1990), 138.
- [11] DUCHEYNE P., QIU Q., *Biomaterials*, 20 (1999), 2287.

*Received 13 August 2004*

*Revised 6 December 2004*

# The effect of heat treatment of TiO<sub>2</sub> coatings obtained by the sol-gel method on the corrosion resistance of chromium steel

EWA SZAŁKOWSKA<sup>1\*</sup>, JAN MASALSKI<sup>2</sup>, BARBARA KUCHARSKA<sup>3</sup>, JÓZEF GŁUSZEK<sup>2</sup>

<sup>1</sup>Department of Chemistry, Częstochowa University of Technology,  
al. Armii Krajowej 19, 42-200 Częstochowa, Poland

<sup>2</sup>Institute of Inorganic Technology and Mineral Fertilizers, Wrocław University of Technology,  
Wybrzeże Wyspiańskiego 27, 50-370 Wrocław, Poland

<sup>3</sup>Institute of Materials Engineering, Częstochowa University of Technology,  
al. Armii Krajowej 19, 42-200 Częstochowa, Poland

The corrosion resistance of chromium steel without coating and with a four-layer one-component TiO<sub>2</sub> coating has been examined in acidic sulphatic solution at pH 3.0 and the temperature of 25±0.2 °C. TiO<sub>2</sub> coatings were obtained by the sol-gel method. Ti(C<sub>3</sub>H<sub>7</sub>O)<sub>4</sub> (tetrakisopropyl orthotitanate) was used as the titanium precursor. Chromium steel was coated with the dip coating method. The structure and phase composition of the TiO<sub>2</sub> coatings were determined from X-ray diffraction data. The topography of TiO<sub>2</sub> coatings before and after corrosion tests was examined by scanning electron microscopy. The protective effect of one-component coatings was evaluated based on polarization curves. The heat-treating of the coatings influences their protective properties. In the solution examined, the best protective properties exhibited TiO<sub>2</sub> coating (4 layers) heat-treated at 500 °C for 10 minutes.

Key words: *sol-gel method; potentiodynamic curves; X-ray diffraction; TiO<sub>2</sub>; stainless steel*

## 1. Introduction

TiO<sub>2</sub> is a ceramic material that can be deposited in layers on different metallic substrates. TiO<sub>2</sub> layers are hard and chemically resistant and also possess a high dielectric constant and a high index of refraction. Thus, they are widely applied in electronics and optics [1–4]. They are also used in the form of coatings as corrosion protection and wear-resistant materials. The most common methods of TiO<sub>2</sub> deposition are CVD and PVD [5-7]. The sol-gel method, however, is also used to obtain TiO<sub>2</sub> layers [8–12].

---

\*Corresponding author, e-mail: ewas@mim.pcz.czest.pl.

Grain boundaries have crucial influence on the final properties of ceramic systems, regardless of the method by which they are obtained. Grain boundary properties are in turn defined by the porosity and segregation of impurities. The structure and composition of grain boundaries have great influence on surface properties. This is directly connected to surface functional properties such as corrosion and wear resistance. Porosity as well as pores size depend on many mutually dependent factors, i.e. the precursor used, the pH of the solution, the catalyst used, the solvent, time and temperature, reactor type, and finally component concentration in solution. One of the ways to achieve smaller pore size is to mix reactants by means of ultrasounds [13]. The pore volume (porosity) of coatings obtained by the sol-gel method may vary between 0 and 65%, pores size between 0.4 and 5 nm, and the specific surface between 1 and 250 m<sup>2</sup>/g [14, 15]. The sol-gel method enables precise control of the microstructure of the deposited layer, i.e. the control over pore size and volume as well as specific surface.

Research conducted to date by the authors [16–19] has shown that a considerable improvement of the corrosion resistance of chromium steel can be achieved by using a protective oxide coating produced by the sol-gel method.

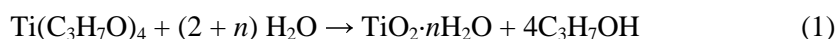
## 2. Experimental

One of the steps of the sol-gel method is high-temperature treatment of oxide coatings. The steel substrate might show a phase transition during this operation if iron steel is used. To avoid it, chromium steel (a modification of AISI 403) was chosen. The additional elements – molybdenum and vanadium (absent in AISI 403) – stabilize the precipitated carbides, making the steel more temperature-resistant. The chemical composition is given in Table 1. Samples were in the form of discs 12.0 mm in diameter and 1.0 mm thick. Before coating, the surfaces were ground with emery paper #1000, rinsed with distilled water, and degreased with tetrachloromethane in an ultrasonic washer.

Table 1. Chemical composition of the stainless steel used (% w/w)

C	Mn	Si	P	S	Cr	Ni	Mo	V	W	Cu
0.12	0.51	0.35	0.026	0.029	12.4	0.43	0.11	0.04	0.13	0.12

To obtain the TiO<sub>2</sub> sol, a solution containing 6.0 cm<sup>3</sup> of tetraisopropyl orthotitanate Ti(C<sub>3</sub>H<sub>7</sub>O)<sub>4</sub> and 45.0 cm<sup>3</sup> of anhydrous ethanol was used, to which a solution containing 6.0 cm<sup>3</sup> 30% (m/m) of hydrous acetic acid and 45.0 cm<sup>3</sup> of anhydrous ethanol was added during stirring. The solution obtained was left in a closed vessel to age. After 3 to 5 hours, the solution became turbid, yielding 2.0% (m/m) of TiO<sub>2</sub> sol. The hydrolysis of tetraisopropyl orthotitanate proceeds as follows:



The viscosity of the solution at 20 °C was 3.4–3.5 cP, as measured with a Hoppler viscosimeter.

Films were deposited on the samples by dip coating. First, the sol was homogenized for 45 minutes in an ultrasonic washer, then the samples were dipped in the sol for 2 minutes in order to establish the equilibrium at the boundary of the substrate/solution phases. The dipping and withdrawing of samples was performed at a constant rate of 1.0 mm/s. The samples were then kept at  $t = 25$  °C for 24 hours and heat-treated in an electric furnace, heated to a maximum temperature of 300 °C, 400 °C, 500 °C, or 750 °C at a rate of 2.0 °C/min and kept at that temperature for 10 minutes. The process was repeated 4 times. Each following layer was deposited on a previous one heat-treated at the same temperature. For comparison, uncoated steel was examined in the same conditions.

X-ray diffraction of TiO<sub>2</sub> coatings was performed with MRD-Philips equipment (Materials Research Diffractometer), with a parallel Cu<sub>K $\alpha$</sub>  beam falling on the layer at a constant angle ( $\theta = 4^\circ$ ). The intensity of the diffracted beam was measured within the angle range  $2\theta = 20$ – $100^\circ$ . In the analysis of the experimental data, the PC-Identify program was used. The program was linked to the crystallographic database “Database – PDF1”. Phase identification was done by comparing the  $2\theta$  diffraction angle values and the reflex intensity (I) provided by the X-ray diagrams with the table data included in the „PC-Identify” program.

Electrochemical examinations were also performed. Polarization curves were measured in a conventional three-electrode thermostated system at  $25 \pm 0.2$  °C. In the potentiodynamic tests, a platinum electrode was used as an auxiliary one and a saturated calomel electrode (SCE) as a reference one. An analysis of the dependence of current density on the potential applied in acidic sulphate solution (pH 3.0) was performed by means of an automated measuring system consisting of an EP-20 potentiostat, an EC 20B generator, a 5D logarithmic amplifier (ELPAN, Poland), and a system for signal recording (AMBEX, Poland) connected to a PC. The potential was changed from cathodic to anodic values with respect to SCE at a small rate (1.0 mV/s), since the passivation process is typically slow.

For the polarization curves of uncoated and untreated chromium steel, 10 repetition scans were carried out, while 3 repetitions were performed for uncoated and heat-treated as well as for coated and heat-treated chromium steel. Differences between repetitions for the same type of samples did not exceed 5%. In some cases, when differences were bigger, additional repetitions were carried out.

The surface topographies of coatings deposited on chromium steel were obtained using a JEOL JSM-5400 scanning microscope before and after the experiment.

### 3. Results and discussion

The main objective of the X-ray analysis was to determine the structure and phase composition of TiO<sub>2</sub> coatings. X-ray diagrams are shown in Fig. 1. Significant re-

flexes are visible. Those due to the steel substrate are marked with asterisks and those caused by the  $\text{TiO}_2$  layer with arrows.

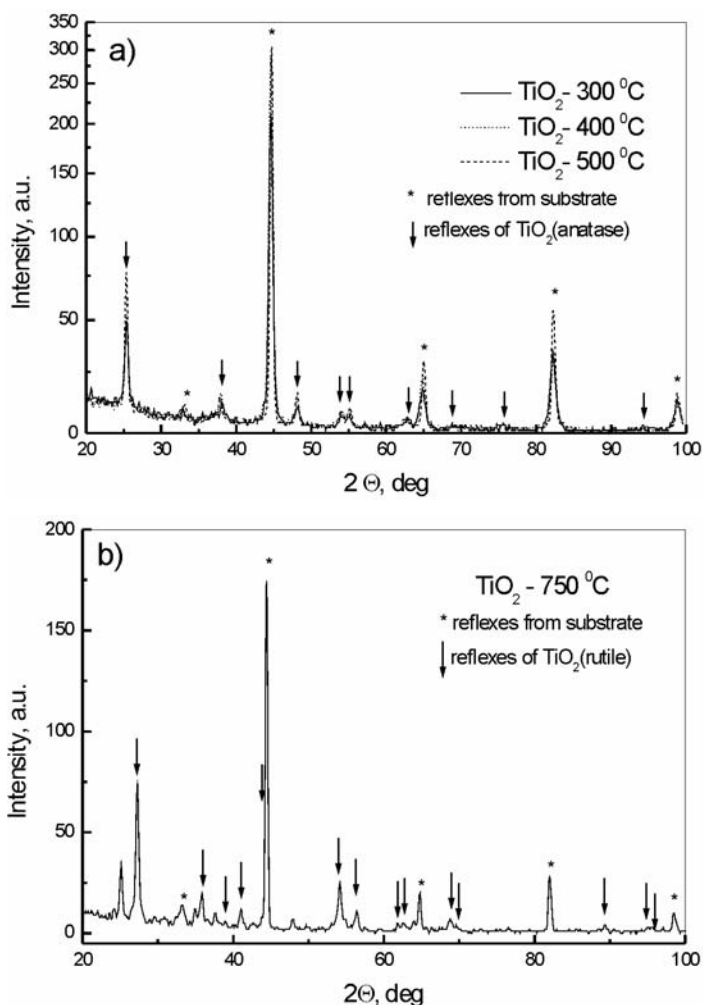


Fig. 1. X-ray diffraction of  $\text{TiO}_2$  coatings on chromium steel coatings heat-treated at: 300 °C, 400 °C, and 500 °C a coating heat-treated at 750 °C

As far as the the phase structure is concerned, the coatings heat-treated at 300 °C, 400 °C, and 500 °C (Fig. 1a) are identical, i.e. they all possess the crystallographic structure of anatase (ASTM identification card 21-1272). As the heat-treatment temperature rises, however, an increase of the reflex intensities can be observed (Fig. 1a). The  $\text{TiO}_2$  coating heat-treated at 750 °C (Fig. 1b) exhibits the crystallographic structure of rutile (ASTM identification card 21-1276) as well as weak reflexes originating from another phase, which cannot be identified due to their low intensity.

In order to determine the anticorrosion effectiveness of coatings, potentiodynamic polarization curves in an acidic sulphuric solution with pH 3.0 were measured (Figs. 2–5).

The analysis of the curves for uncoated steel indicates that the cathodic oxygen reduction takes place at a slower rate on heat-treated than untreated steel. During the

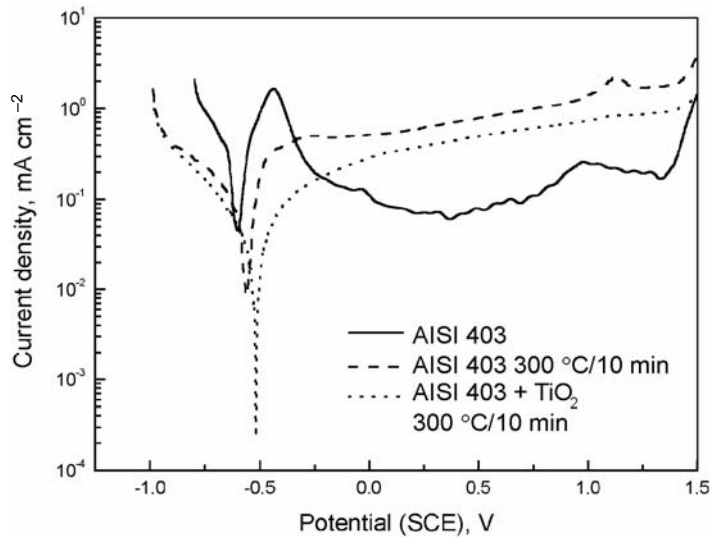


Fig. 2. Polarization curves recorded for chromium steel (uncoated and untreated, uncoated and heat-treated at 300 °C,  $\text{TiO}_2$ -coated and heat-treated at 300 °C) in a sulphuric solution with pH 3.0

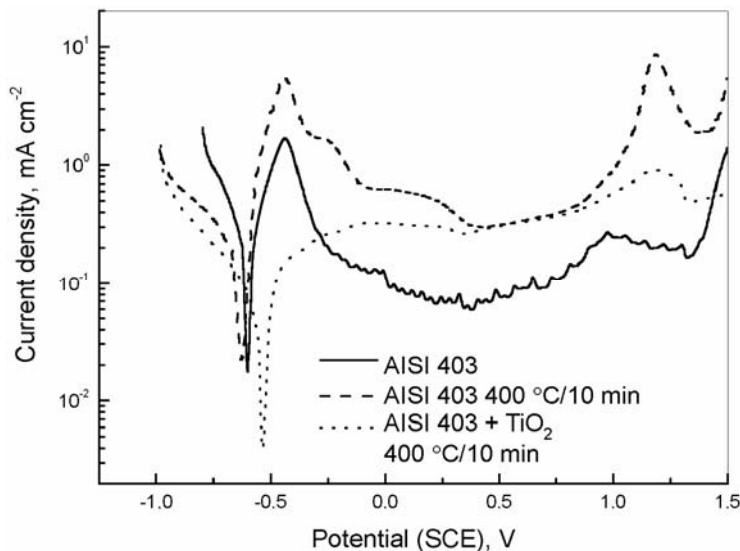


Fig. 3. Polarization curves recorded for chromium steel (uncoated and untreated, uncoated and heat-treated at 400 °C,  $\text{TiO}_2$ -coated and heat-treated at 400 °C) in a sulphuric solution with pH 3.0

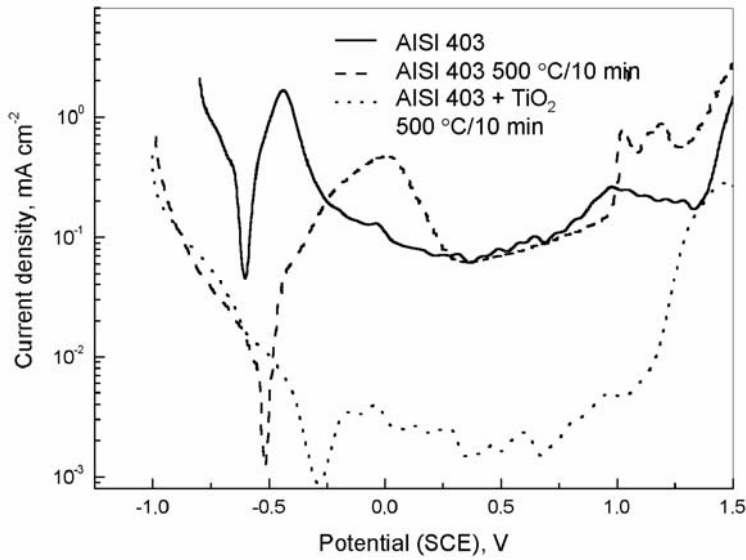


Fig. 4. Polarization curves recorded for chromium steel (uncoated and untreated, uncoated and heat-treated at 500 °C, TiO<sub>2</sub>-coated and heat-treated at 500 °C) in a sulphatic solution with pH 3.0

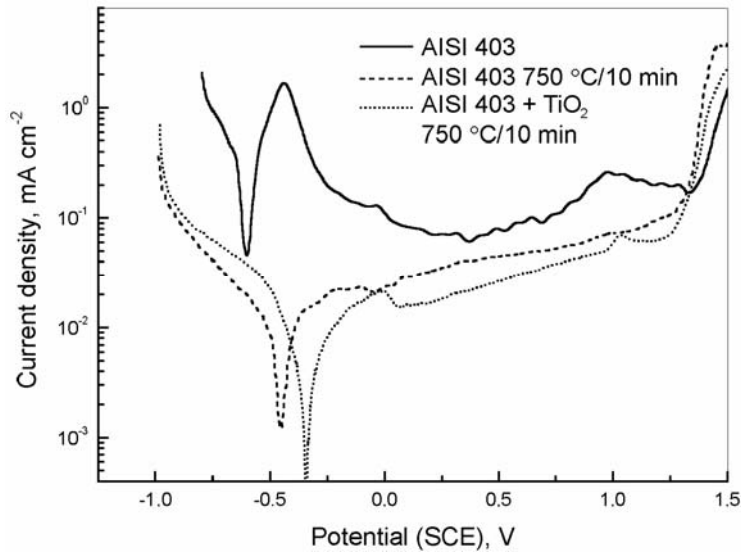


Fig. 5. Polarization curves recorded for chromium steel (uncoated and untreated, uncoated and heat-treated at 750 °C, TiO<sub>2</sub>-coated and heat-treated at 750 °C) in a sulphatic solution with pH 3.0

steel heat-treatment in air, chromium spinel appears on its surface. Its general formula is  $\text{FeFe}_{2-x}\text{Cr}_x\text{O}_4$ , where  $x$  represents values close to 2 [20]. It is therefore highly probable that the chromium–iron spinel on the steel surface slows down cathodic reduction. Heat-treatment temperature has an influence on steel behaviour in the corrosion

solution. A decrease in the cathodic and anodic current density is observed when the steel is heat-treated at 500 °C or 750 °C. The best corrosion resistance was shown by steel heat-treated at 750 °C and the worst by steel heat-treated at 400 °C. As can be seen in Figures 2–5,  $\text{TiO}_2$  coatings also slow down the cathodic processes, the most effective being observed for the layer heat-treated at 500 °C. For coatings heat-treated at 300 °C or 400 °C (Figs. 2 and 3), deterioration in the passive state properties is observed. On the other hand, a considerable decrease in both cathodic and anodic current density could be achieved for coatings heat-treated at 500 °C or 750 °C, and the speed of the anodic process decreased by a factor two at the cathodic-anodic transition potential as compared to the steel substrate.

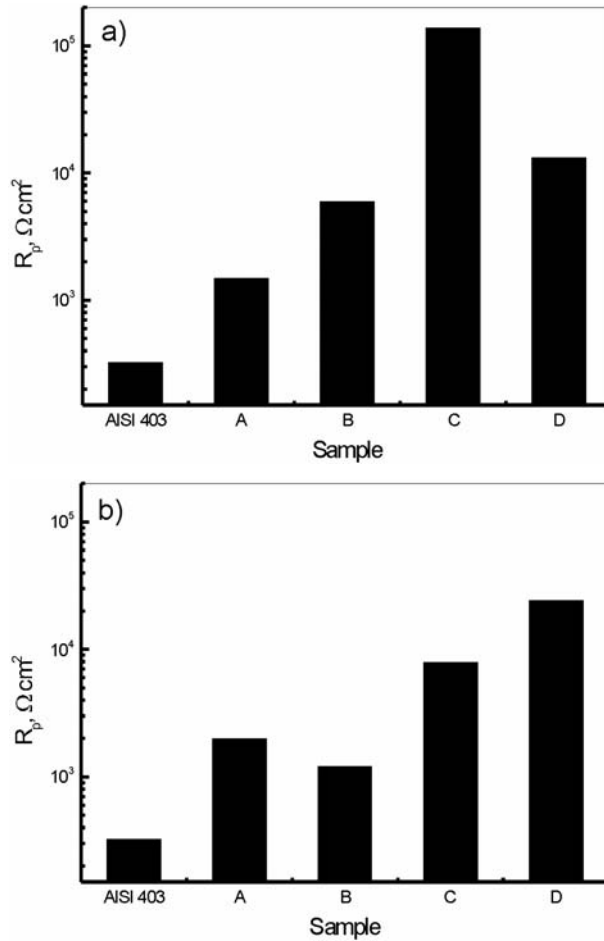


Fig. 6. Comparison of the polarization resistance  $R_p$  of a) coated and uncoated AISI 403: A) coating heat-treated at 300 °C, B) coating heat-treated at 400 °C, C) coating heat-treated at 500 °C, D) coating heat-treated at 750 °C; b) treated and untreated AISI 403 steel: A) steel heat-treated at 300 °C, B) steel heat-treated at 400 °C, C) steel heat-treated at 500 °C, D) steel heat-treated at 750 °C

A larger decrease in  $\text{TiO}_2$  coating corrosion speed when heat-treated at  $750\text{ }^\circ\text{C}$  is difficult to obtain since the coatings are porous. When higher heat-treatment temperatures are applied, an increase in the  $\text{Cr}_2\text{O}_3$  crystalline layer on the border of steel/coating phases was observed, increasing the number of cracks produced at lower temperatures.

To evaluate the quality of the coatings, the polarization resistance  $R_p$  was determined. Experimental points close to the cathodic-anodic transition potential were used. In an  $E-i$  plot, they form a straight line, whose slope is directly connected to the polarization resistance. Values of  $R_p$  were determined using linear regression (Fig. 6). A change in the heat-treatment temperature of the coatings causes alterations in the polarization resistance of AISI 403 steel with coatings. From Fig. 6 it can be concluded that the heat-treatment temperature of  $\text{TiO}_2$  coating influences its protective properties. This is due to the removal of  $\text{H}_2\text{O}$  and  $\text{ROH}$ , as well as to the densification of the gel structure. The best protective properties were shown by coatings heat-treated at  $500\text{ }^\circ\text{C}$  and the worst by coatings heat-treated at  $300\text{ }^\circ\text{C}$ .

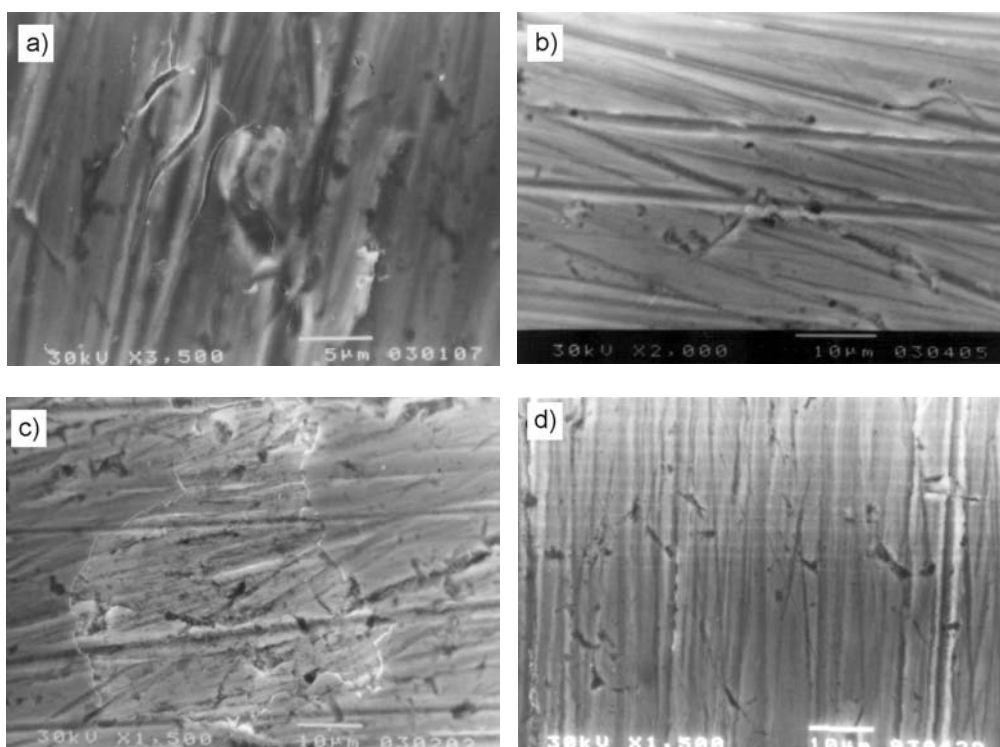


Fig. 7. The microstructure of  $\text{TiO}_2$  coating on chromium steel: a) heat-treated at  $300\text{ }^\circ\text{C}$ , b) heat-treated at  $500\text{ }^\circ\text{C}$ , c) heat-treated at  $300\text{ }^\circ\text{C}$  after corrosion tests in a sulphatic solution with pH 3.0, d) heat-treated at  $500\text{ }^\circ\text{C}$  after corrosion tests in a sulphatic solution with pH 3.0

Coatings heat-treated at  $300\text{ }^\circ\text{C}$  or  $500\text{ }^\circ\text{C}$  were subject to microscopic examination before and after corrosion tests. Due to their relatively small thickness, the coat-

ings reflect irregularities and scratches on the substrate resulting from the use of sandpaper (Figures 7a and b). The coating heat-treated at 500 °C showed the same thickness on the entire substrate surface (Fig. 7b). After the corrosion test performed in a sulphatic solution with pH 3.0, the coating partially dissolved but preserved its continuity. The coating heat-treated at 300 °C shows local discontinuities (cracks) (Fig. 7a), which may be due to the heat-treatment process. After the corrosion tests, considerable losses were observed (Fig. 7c) due to a fast dissolution of the coating at the cracks. The coated substrate heat-treated at 300 °C shows a significantly higher level of corrosion than that heat-treated at 500 °C (Figs. 7c and d).

It is therefore necessary to improve or to modify the sol-gel method used to obtain TiO<sub>2</sub> coatings. Such coatings are porous and do not protect the metallic substrate from water and oxygen penetration, although thermal treatment leads to a certain decrease in porosity.

## 4. Conclusion

TiO<sub>2</sub> coatings have been deposited on chromium steel by means of the sol-gel method. These coatings improve the corrosion resistance of steel in acidic sulphatic solution with pH 3.0, but the protective properties of the coatings depend on the heat-treatment temperature. This is due to the vaporization of H<sub>2</sub>O and ROH and to the densification of the gel structure. The best protective properties were shown by a four-layer TiO<sub>2</sub> coating heat-treated at 500 °C for 10 minutes. The temperature of heat-treatment of steel also influences its behaviour in the corrosion solution. The best corrosion resistance was found for AISI 403 steel heat-treated at 750 °C for 10 minutes. On the basis of X-ray diffraction, the structures and phase compositions of the investigated oxide coatings were obtained. TiO<sub>2</sub> coating produced at 750 °C exhibits a rutile crystallographic structure. Coatings heat-treated at lower temperatures, on the other hand, show an anatase crystallographic structure.

## References

- [1] YOKO T., KAMIYA K., YUASA A., TANAKA K., SAKKA S., *J. Non-Cryst. Solids*, 100 (1988), 483.
- [2] ATTA A.K., BISWAS P.K., GANGULI D., *Mater. Lett.*, 15 (1992), 99.
- [3] YEH Y.C., TSENG T.Y., CHANG D.A., *J. Am. Ceram. Soc.*, 73 (1990), 1992.
- [4] YOKO T., YUASA A., KAMIYA K., SAKKA S., *J. Electrochem. Soc.*, 138 (1991), 2279.
- [5] GŁUSZEK J., MASALSKI J., FURMAN P., NITSCH K., *Biomaterials*, 18 (1997), 789.
- [6] FURMAN P., GŁUSZEK J., MASALSKI J., *J. Mat. Sci. Lett.*, 16 (1997), 471.
- [7] BATTISTON A., GERBASI R., PORCHIA M., MARIGO A., *Thin Solid Films*, 239 (1994), 186.
- [8] KAJIHARA K., NAKANISHI K., TANAKA K., HIRAO K., SOGA N., *J. Am. Ceram. Soc.*, 81 (1998), 2670.
- [9] IMAI H., HIRASHIMA H., *J. Am. Ceram. Soc.*, 82 (1999), 2301.
- [10] WANG M. CH., LIN M.H., *J. Mater. Res.*, 14 (1999), 196.
- [11] VORKAPIC D., MATSOUKAS T., *J. Am. Ceram. Soc.*, 81 (1998), 2815.
- [12] SZAŁKOWSKA E., GŁUSZEK J., MASALSKI J., TYLUS W., *J. Mat. Sci. Letters*, 20 (2001), 495.

- [13] MACKENZIE J.D., *Science of Ceramic Chemical Processing*, Wiley, New York, 1986.
- [14] ILER R.K., *The Chemistry of Silica*, Wiley, New York, 1982.
- [15] BRINKER C.J., SCHERER G.W., *Sol-Gel: The Physics and Chemistry of Sol-Gel Processing*, Academic Press, San Diego, 1990.
- [16] SZAŁKOWSKA E., GŁUSZEK J., MASALSKI J., *Inż. Powierzchni*, 1 (2000), 36.
- [17] SZAŁKOWSKA E., GŁUSZEK J., MASALSKI J., *Inż. Mat.*, (2000), No. 6, 453.
- [18] SZAŁKOWSKA E., MASALSKI J., GŁUSZEK J., *Inż. Mat.*, (2002), No. 5, 503.
- [19] SZAŁKOWSKA E., MASALSKI J., GŁUSZEK J., *Mater. Sci.-Poland*, 21 (2003), 397.
- [20] SEDRIKS A.J., *Corrosion of stainless steels*, Wiley, New York, 1996.

*Received 6 June 2004*

*Revised 12 June 2004*

## Textural properties of silica-based organic-inorganic polymer hybrid xerogels

IWONA ZARĘBA-GRODŹ<sup>1</sup>, WŁODZIMIERZ MIŚTA<sup>2</sup>, ANDRZEJ SIKORA<sup>3</sup>,  
TEODOR GOTSZALK<sup>3</sup>, WIESŁAW STRĘK<sup>2</sup>,  
KRZYSZTOF HERMANOWICZ<sup>2</sup>, KRZYSZTOF MARUSZEWSKI<sup>1\*</sup>

<sup>1</sup>Institute of Materials Science and Applied Mechanics, Wrocław University of Technology,  
Smoluchowskiego 25, 50-370 Wrocław, Poland

<sup>2</sup>Institute for Low Temperature and Structure Research, Polish Academy of Sciences,  
Okólna 2, 50-950 Wrocław, Poland

<sup>3</sup>Laboratory of Near Field Microscopy, Nanometrics and Nanostructures,  
Wrocław University of Technology, Janiszewskiego 11/17, 50-372 Wrocław, Poland

Samples of xerogels containing organic polymers were prepared by the sol-gel method via the reaction of tetraethoxysilane (TEOS) and organic monomers with an acidic catalyst. These materials were obtained as transparent and homogeneous bulk materials. The samples were characterized by Raman and IR spectroscopies, N<sub>2</sub>-adsorption (77 K), and atomic force microscopy (AFM). Specific surface areas and porosities of the samples were estimated from nitrogen adsorption-desorption isotherms at 77 K. Textural properties such as specific surface areas ( $S_{\text{BET}}$ ), pore volume ( $V_p$ ), average pore sizes ( $R_p$ ), and micropore volume ( $V_{\text{DR}}$ ) were obtained. The complete adsorption-desorption isotherms and pore size distributions were analysed following the Dollimore-Heal method. Atomic force microscopy was used to investigate the morphology and roughness of the samples.

*Key words: organic-inorganic polymer hybrid materials, sol-gel process, photo-polymerisation, organically modified silicates, porosity, roughness*

### 1. Introduction

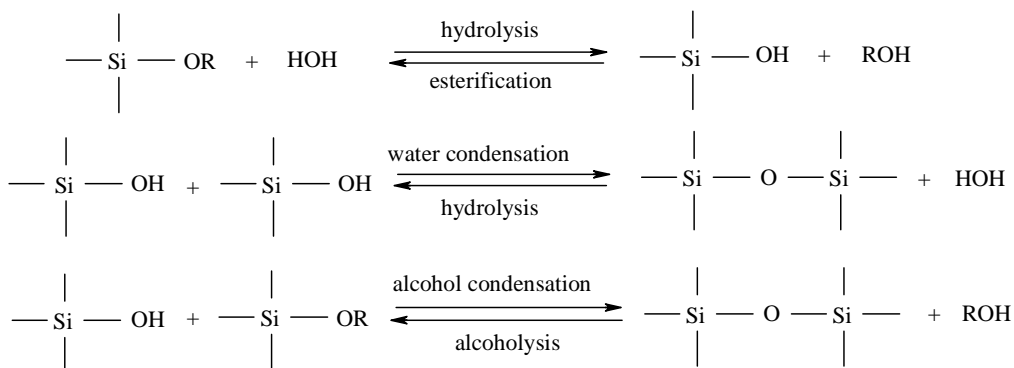
Organic-inorganic polymer hybrids are a new type of composite materials, in which the organic and inorganic components are combined at the molecular level [1]. There has been much research on the applications of these hybrid materials as functional coatings on glass, ITO (indium-tin oxide), and polymer substrates (bulks, pow-

---

\*Corresponding author, e-mail: krzysztof.maruszewski@pwr.wroc.pl.

ders, and fibres). In particular, these organic-inorganic polymer hybrids could potentially yield transparent, abrasion-resistant materials. They possess interesting properties such as molecular homogeneity, transparency, flexibility, and durability. Such materials could be employed in various applications, e.g. solid state lasers (optical components), replacements for silicon dioxide as an insulating material in the micro-electronic industry, anti-corrosion coatings, scratch resistant coatings, contact lenses, host materials for chemical sensors, and membrane materials [2–7].

In these organic-inorganic polymer networks, formation of an inorganic network occurs through sol-gel processes [8]. The organic phase of the organic-inorganic polymer hybrid is synthesized “in situ” in liquid hydrolysed silica. The sol-gel method is widely used to prepare hybrid materials, since it has the advantage of being a low-temperature process and potentially giving highly homogeneous nanomaterials. The chemical reactions involved in the sol-gel process are as follows:



During these reactions, the hydrolysis and condensation of metal alkoxides (based on, e.g., Si, Ti, V, or Zr) such as tetraethoxysilane (TEOS) takes place and a network is formed in the process. During the build-up of the inorganic network, appropriately functionalised organic (or organic-inorganic) moieties can also be incorporated. This method can lead to either an alloy-like material (if a molecular dispersion is obtained) or a system with a morphology defined by the presence of several microphases [1].

Mechanical durability and reliability belong to the most important features of these materials. Thus, it is practically important to characterize and, if possible, control and improve these properties. The relevant mechanical parameters are: hardness, elastic modulus, residual stress, fracture toughness, and interfacial fracture toughness (or adhesion energy) [9]. For certain materials it is also possible to measure such properties as surface roughness and porosity.

Surface roughness is of crucial importance for applications in many fields [10–12]. Multilayer coatings prepared from sol-gel films over polymeric substrates have found use in areas such as photography, radiography, holography, reprography (materials for printers and photocopiers), and optical or protective coatings [8]. Most of these materials must have a specific surface roughness in order to guarantee optimal adherence for retaining various active agents (e.g., inks) [13].

Porous materials with controlled porosity in the micropore (<2 nm) and mesopore (2–50 nm) ranges have received great attention due to their potential use as filters and sorbents in separation systems, catalytic supports in full cell electrodes, as well as double layer supercapacitors for energy storage. Numerous techniques for preparing micro- and mesoporous materials can be found in literature [14–18]. The preparation of micro- and mesoporous silica using organic agents as templates is a good example. By means of this technique, it is possible to obtain porous materials with large surface areas, high porosities, and controlled narrow pore size distributions (PSDs) in the micro- and mesopore ranges.

The preparation of these materials consists of three stages: (1) the infiltration of the porous structure of inorganic materials (templates) by organic components, (2) the polymerisation of the infiltrated materials, (3) the elimination of templates [19]. The procedure of core/template removal by calcinations was first introduced by Kawahashi and Mitijevi during their search to produce hollow spheres from yttrium compounds [20]. There exist many examples of templates employed in inorganic materials, which are usually SiO<sub>2</sub>, TiO<sub>2</sub>, or other common oxides. Synthetic polymers, surfactants, organogels, carbon nanotubes, or organic crystals and biomaterials have been used successfully as templates [21].

In this work, following our preliminary reports [22], we present hybrid organic-inorganic materials of the interpenetrated network (IPN) character. The relationships between the synthetic process and the textural properties of the sol-gel materials are discussed as well. The obtained materials have been investigated by spectroscopic (IR, Raman), microscopic (AFM), and nitrogen adsorption-desorption techniques.

## 2. Experimental

### 2.1. Synthesis

The syntheses of silica-based organic-inorganic polymer hybrid xerogels were carried out in ethanol solutions by combining the sol-gel [8] and organic photopolymerisation [24] methods [22]. TEOS (tetraethoxysilane, Si(OC<sub>2</sub>H<sub>5</sub>)<sub>4</sub>, Sigma-Aldrich) was mixed with distilled water with hydrochloric acid (HCl<sub>aq</sub>, Polish Chemical Reagents) as a catalyst. The reagent molar ratio TEOS:H<sub>2</sub>O was 1:16. The solution was stirred for 1 hour at room temperature. The organic monomers, acrylamide (C<sub>3</sub>H<sub>5</sub>NO) or 2-hydroxy-ethylmethacrylate (C<sub>6</sub>H<sub>10</sub>O<sub>3</sub>, HEMA), and the photo-initiator, benzil (C<sub>14</sub>H<sub>10</sub>O<sub>2</sub>), were purchased from Sigma-Aldrich. The monomers and the initiator were introduced to the liquid hydrolysed silicate solutions. The molar ratios of the components are presented in Table 1. The compositions of silica/organic monomers were irradiated by UV light (a Hg lamp, OPTEL Opole, Poland) at room temperature for 5 h [24].

Table 1. Molar ratios of the components

No.	Molar ratio			
	TEOS	Acrylamide	HEMA	Benzil
1	1	–	–	–
2	1	–	0.3	0.0025
3	1	0.3	–	0.0025
4	1	0.15	0.15	0.0025

## 2.2. Characterisation

Raman spectra were measured on a Bruker RFS100/S FT-Raman spectrophotometer. IR spectra were measured on a FT IR Biorad FTS 575C spectrophotometer. The morphologies and structures of the materials were characterized by an Atomic Force Microscope (DME Rasterscope 3000). The roughness of the organic-inorganic polymer hybrid samples were calculated using the European/Polish Norm ISO 4287:1997 [25]. The roughness scaling characteristics were determined by statistical analysis of the AFM surface images using homemade scaling analysis software. The specific surface areas and porosities of the samples were obtained from nitrogen adsorption-desorption isotherms measured on a Sorptomatic 1900 FISONs system at 77 K. The samples were evacuated at 200 °C (using a rotary pump) in order to remove the liquid from the pores. The pore size distributions were analysed following the Dollimore–Heal method [26]. For microporous materials, the specific surface areas and micropore volumes ( $V_{DR}$ ) were calculated by the Dubinin method [27]. Pore volume ( $V_p$ ) was calculated from the adsorbed volumes at  $p/p_0 = 0.95$ . Pyrolysis of the organic-inorganic polymer hybrid samples was performed at 600 °C under oxygen flow (heating rate = 5 °C/min). In order to remove residual water, alcohol and all organic components from the silica glass, the inorganic silica sol-gel polymers were heat-treated at 600 °C, 750 °C, 900 °C, or 1050 °C under oxygen flow (heating rate was 5 °C/1min). The porosities of all the organic-inorganic polymer hybrid samples and the inorganic silica polymer were also measured before and after calcinations.

## 3. Results and discussion

FT-IR and FT-Raman spectra of the SiO<sub>2</sub>/acrylamide polymer hybrid (a), the SiO<sub>2</sub>/HEMA polymer hybrid (b), and the SiO<sub>2</sub>/acrylamide–HEMA copolymer hybrid (c) are presented in Figs. 1 and 2, respectively. FT-IR and FT-Raman spectra (not shown) were obtained and compared for the pure SiO<sub>2</sub> sample and the independently made organic polymers and copolymers as well as for the free organic monomers. The analysis of these spectra is described in [22].

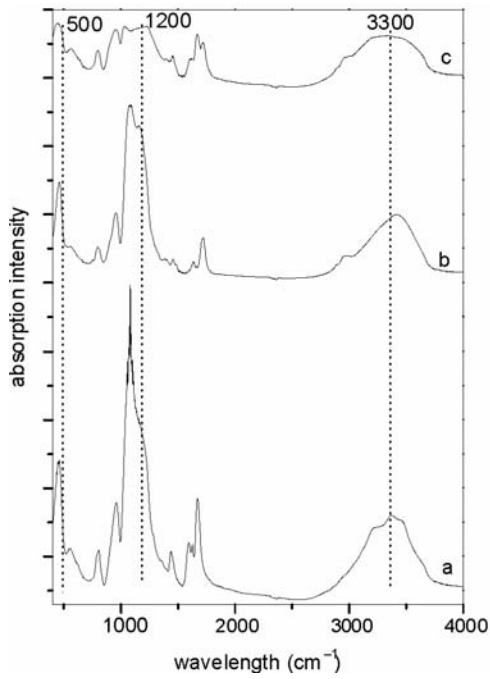


Fig. 1. FT-IR spectra of SiO<sub>2</sub>/acrylamide polymer hybrid (a), SiO<sub>2</sub>/HEMA polymer hybrid (b), and SiO<sub>2</sub>/acrylamide-HEMA copolymer hybrid (c)

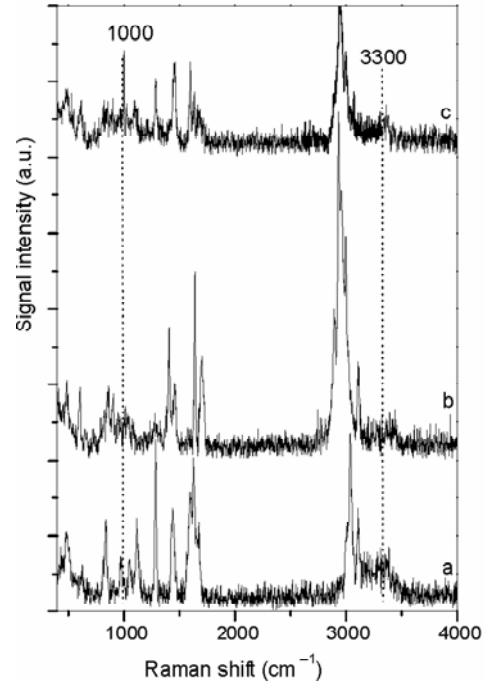


Fig. 2. FT-Raman spectra of SiO<sub>2</sub>/acrylamide polymer hybrid (a), SiO<sub>2</sub>/HEMA polymer hybrid (b), and SiO<sub>2</sub>/acrylamide-HEMA copolymer hybrid (c)

The surface texture is defined as the local deviation of a surface from its ideal shape. The deviations may be repetitive or random and may result from roughness, waviness, lay, and defects. Roughness comes from the finer irregularities of the surface, usually including those that result from the inherent action of the production process [28, 29]. Porosity is defined as the ratio of the void space volume to the bulk volume of a sample (expressed as a fraction or percentage) [27].

AFM was used to measure the surface roughness of the organic-inorganic polymer hybrid samples. Parameters such as the roughness average ( $R_a$ ), root mean square roughness ( $R_q$ ), maximum profile peak height ( $R_p$ ), maximum profile valley depth ( $R_v$ ), and average maximum height of the profile ( $R_z$ ), obtained from these images, are listed in Table 2.  $R_a$  and  $R_q$  are two of the most often used parameters concerning surface roughness [30, 31].

The average roughness  $R_a$  is defined as:

$$R_a = \frac{1}{L} \int_0^L |Y(x)| dx \quad (1)$$

where:  $R_a$  is the arithmetic average deviation from the mean line,  $L$  – the sampling length,  $Y$  – the ordinate of the profile curve.

Table 2. Roughness parameters

Name	SiO <sub>2</sub> /polyacrylamide	SiO <sub>2</sub> /polyHEMA	SiO <sub>2</sub> /poly(acrylamide -co-HEMA)
Average roughness, $R_a$ (nm)	0.707	4.002	4.442
Root mean square roughness, $R_q$ (nm)	0.956	5.122	5.555
Maximum profile peak height, $R_p$ (nm)	4.649	17.055	22.235
Maximum profile valley depth, $R_v$ (nm)	3.335	14.858	13.329
Average maximum height of the profile, $R_z$ (nm)	7.984	31.914	35.564
Percentage distribution of the height, $P$ (%)	38.2	26.2	26.4
Material ratio of the profile $R_{m(cr)}$ (%)	100	100	100

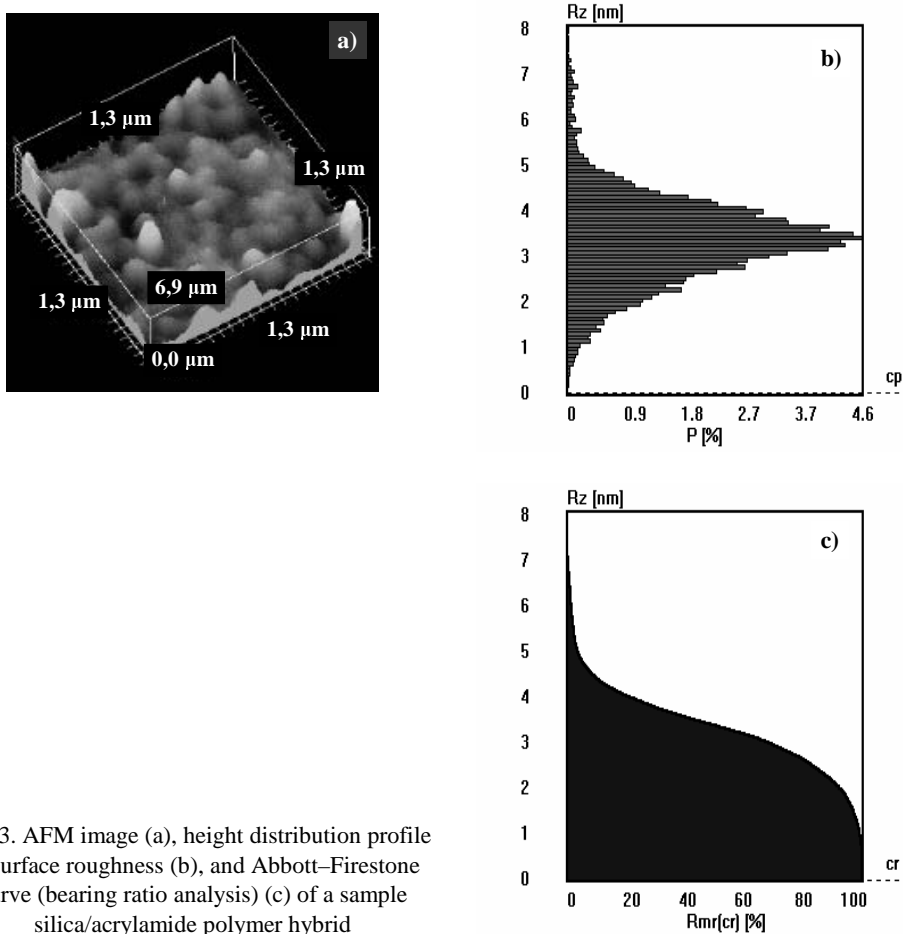


Fig. 3. AFM image (a), height distribution profile of surface roughness (b), and Abbott–Firestone curve (bearing ratio analysis) (c) of a sample silica/acrylamide polymer hybrid

The parameter  $R_q$  is defined as:

$$R_q = \sqrt{\frac{1}{L} \int_0^L Y(x)^2 dx} \quad (2)$$

$R_q$  is the root mean square average of the measured height deviations, taken within the evaluation length or area and measured from the mean linear surface.  $R_q$  represents the standard deviation of the profile heights and is used in the computation of skew and kurtosis.

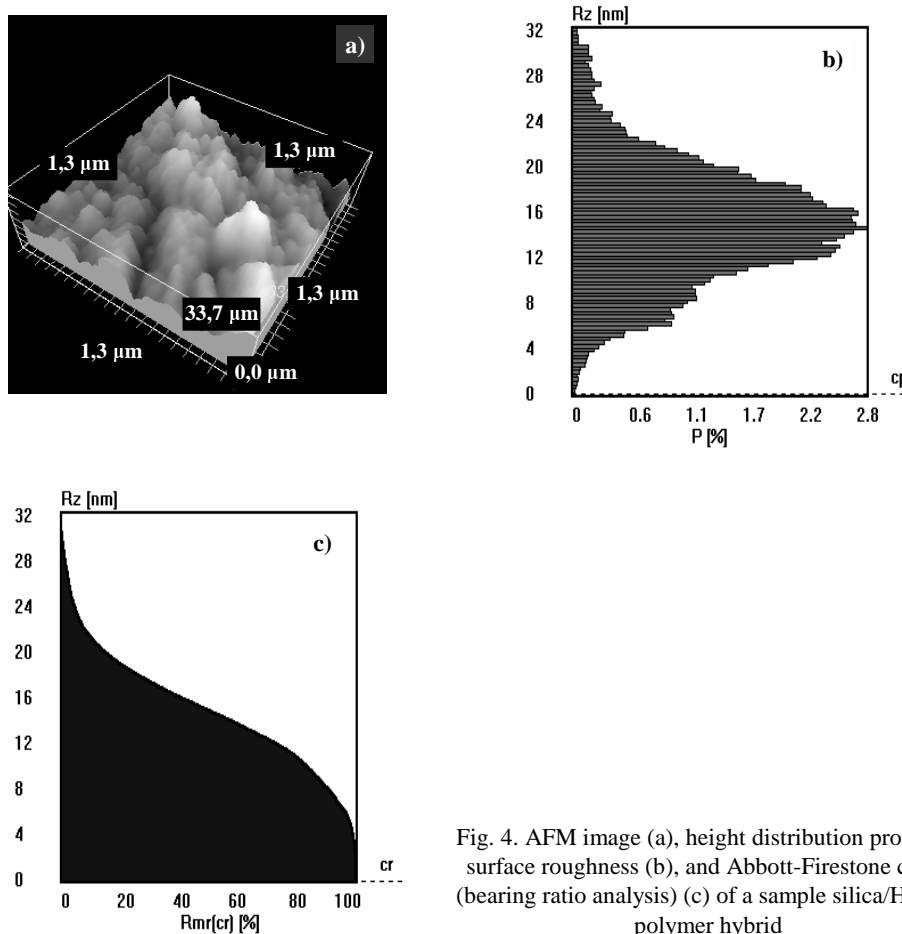


Fig. 4. AFM image (a), height distribution profile of surface roughness (b), and Abbott-Firestone curve (bearing ratio analysis) (c) of a sample silica/HEMA polymer hybrid

Figures 3a–5a show the topographies of synthetic organic-inorganic polymer hybrids obtained by the sol-gel method. It can be seen that the AFM images of polysilica/polyHEMA and polysilica/poly(acrylamide-co-HEMA) are a little different from that of polysilica/polyacrylamide. The AFM pictures demonstrate that the creation of polyacrylamide “in situ” in the silica matrix results in a surface less rough than that obtained by adding other organic polymers.

Figures 3b–5b show the height distribution profiles of surfaces roughness. The histograms of the surface height distribution profiles, obtained from AFM images, show that all of the organic-inorganic polymer hybrid samples have surfaces with irregularities of quite small height. In the cases of polysilica/polyHEMA and polysilica/poly(acrylamide-co-HEMA), the largest observed heights were 15 nm and 11 nm, respectively. The sample of polysilica/acrylamide displays an even smaller amplitude of the irregularities – 3,5 nm. This trend is also followed by the widths of irregularity height distribution peaks. The sample of polysilica/acrylamide displays a distribution peak much narrower than that of polysilica/polyHEMA and polysilica/poly(acrylamide-co-HEMA) samples.

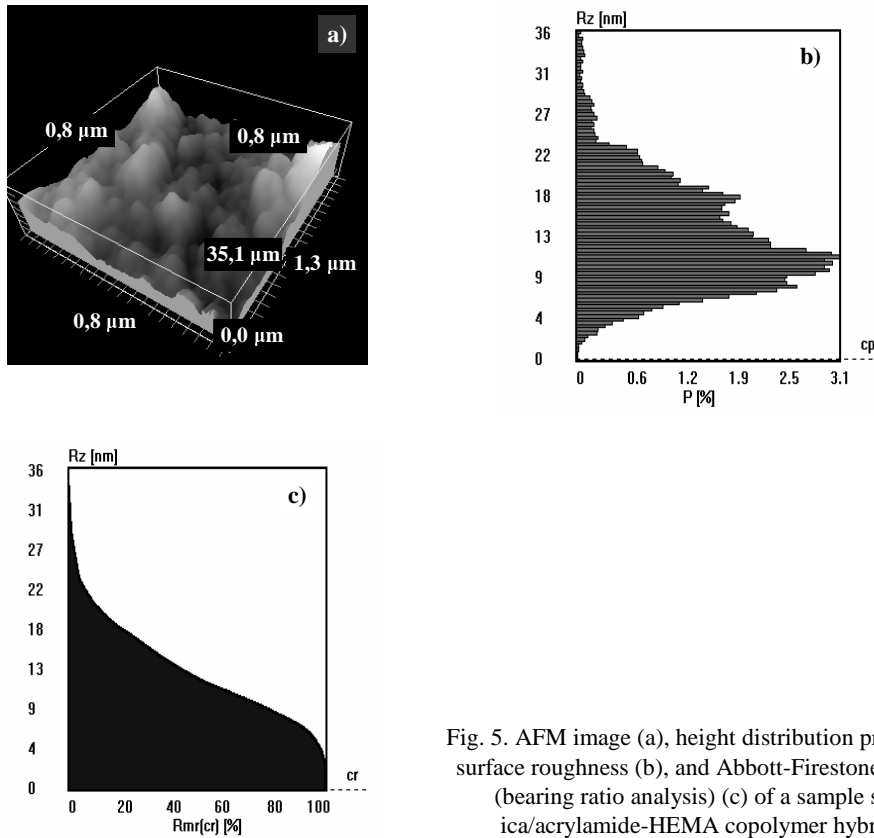


Fig. 5. AFM image (a), height distribution profile of surface roughness (b), and Abbott-Firestone curve (bearing ratio analysis) (c) of a sample silica/acrylamide-HEMA copolymer hybrid

Figures 3c–5c show bearing ratio analyses. A bearing ratio analysis indicates the percentage of a surface that falls above/below a particular depth. The material ratio  $R_{mr[cr]}$  is the ratio expressed in percent of the material-filled length to the evaluation length  $l_m$  at the profile section level  $c$ :

$$R_{mr[cr]} = \frac{1}{l_m} (L_1 + L_2 + \dots + L_n) \times 100\% \quad (3)$$

The material ratio curve (the Abbott–Firestone curve – AFC) shows  $R_{mr}[cr]$  as a function of the profile section level  $c$ . The Abbott–Firestone curve plays an important role in contact mechanics and wet friction applications. Based on Figs. 3c–5c, it has been found that about 50% of the material in each sample resides in medium-sized surface irregularities.

Table 3. Analysis of porosity

Sample (obtained by the sol-gel method)	$S_{BET}$ [m <sup>2</sup> /g]	$V_p$ [ml/g]	$R_p$ [nm]	$V_{DR}$ [ml/g]	Class of the pores
SiO <sub>2</sub>	190	1.32	8.5	0.08	meso
SiO <sub>2</sub> (600 °C)	196	1.02	19	0.08	meso
SiO <sub>2</sub> (750 °C)	74	0.24	23	0.03	meso
SiO <sub>2</sub> (900 °C)	83	0.27	22	0.03	meso
SiO <sub>2</sub> (1050 °C)	118	0.69	15	0.045	meso&macro
SiO <sub>2</sub> /polyacrylamide	17	0.02	–	–	–
SiO <sub>2</sub> /polyacrylamide (600 °C)	534*	0.27	<2	0.19	micro
SiO <sub>2</sub> /polyHEMA	7	0.01	–	–	–
SiO <sub>2</sub> /polyHEMA (600 °C)	682*	0.29	<2	0.24	micro
SiO <sub>2</sub> /poly(acrylamide-co-HEMA)	<1	–	–	–	–
SiO <sub>2</sub> /poly(acrylamide-co-HEMA) (600°C)	805*	0.34	<2	0.29	micro

Table 3 and Figures 6, 7 summarize the porosity-related data for silica heated at different temperatures and the organic-inorganic polymer hybrid. As can be seen, the sol-gel SiO<sub>2</sub> sample, heated at all temperatures, is mesoporous and the isotherm resembles the IUPAC type IV [26] classification with a closed and well-defined hysteresis loop. On the other hand, the hybrid sample is not porous before calcination. After the burnout of the organic components, however, the sample becomes microporous with an average  $R_p$  value smaller than 2 nm and a high specific surface area. The isotherm curve (Figure 7) obtained for the calcinated hybrid sample follows the IUPAC type I curve [26], indicating the microporous character of the sample.

The porosities of the polysilica samples as a function of temperature are shown in Fig. 6 and Table 3. It has been found that the porosity remains constant up to 600 °C. This may be due to the reversible dehydroxylation. Further increase in temperature within the range 600–900 °C lead to a decrease in porosity. This may be due to irreversible dehydroxylation. Above 900 °C, the densification process begins. It is enhanced by three mechanisms: condensation, structural relaxation, and viscous sintering. The effect of temperature on the pore size distribution (PSD) of xerogels for five different temperatures is shown in the insert of Figure 6. It is clearly seen from this figure that the pore size distribution for fresh silica (dried at room temperature) and silica heated at 600 °C is narrow and uniform. This may be due to the elimination of physically adsorbed species of water and organic compounds through gel without affecting the silica network. The figure shows that pores are uniform for particles

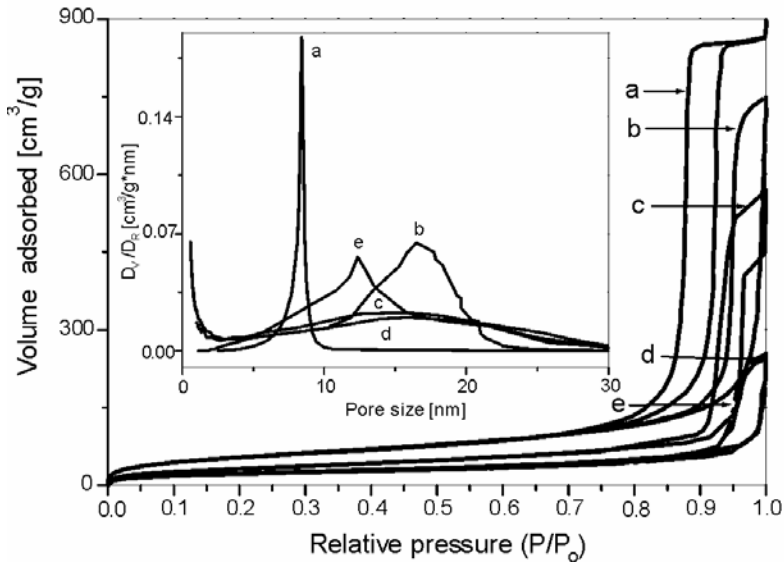


Fig. 6. Nitrogen adsorption-desorption isotherms for sol-gel  $\text{SiO}_2$  samples: fresh bulk (a),  $\text{SiO}_2$  after pyrolysis in oxygen at 600 °C (b), at 750 °C (c), at 900 °C (d), and 1050 °C (e).  
Inset: pore size distributions of the samples

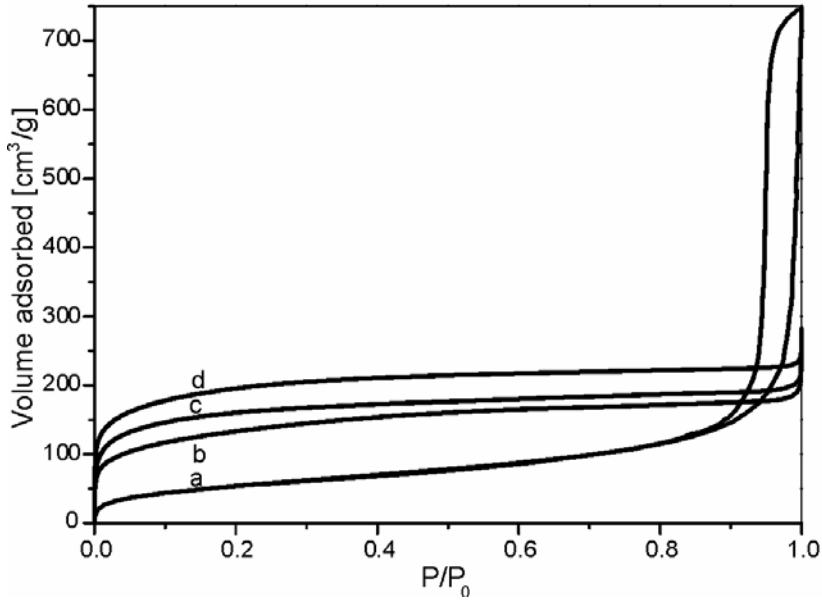


Fig. 7. Nitrogen adsorption-desorption isotherms after pyrolysis in oxygen at 600 °C for sol-gel  $\text{SiO}_2$  bulk (a),  $\text{SiO}_2$ /acrylamide polymer hybrid (b),  $\text{SiO}_2$ /HEMA polymer hybrid (c), and  $\text{SiO}_2$ /acrylamide-HEMA copolymer hybrid (d)

heated at both temperatures. At medium temperatures (750 °C and 900 °C), the pore size distributions are wide and shifted towards larger pore sizes. At a higher temperature (1050 °C), the PSD is uniform and narrow compared to the PSD at a lower temperature (600 °C). It is interesting to note that the narrow PSD at the higher temperature is shifted towards smaller pore sizes. This is due to the formation of a continuous network, attributed to the condensation of the silanol groups and leading to a complete formation of Si–O–Si bonds. Heating xerogels above 1050 °C led to the formation of a continuous SiO<sub>2</sub> network without any porosity.

## 4. Conclusions

Organic-inorganic polymer hybrids were investigated by FT-IR, FT-Raman, AFM, and N<sub>2</sub>-adsorption (77K) methods. AFM micrographs of the organic-inorganic polymer hybrid samples show that the obtained materials are homogenous. Based on the AFM micrographs and the Polish Standards definitions [25], it has been established that the sample surfaces are randomly isotropic and do not exhibit periodicity or any other regularity. The height distribution profile of surface roughness indicates that the greatest contribution to roughness comes from profiles with medium heights. The pore size of the inorganic silica polymers can be controlled by varying the heating temperatures. The template method can be used to prepare microporous silica of various specific surface areas and pore sizes.

### Acknowledgements

This work has been partially funded by the Polish State Committee for Scientific Research (grant KBN 3 T09 008 26).

## References

- [1] SPERLING L.H., *Interpenetrating Polymer Networks and Related Materials*, Plenum Press, New York, 1981, Ch. 1.
- [2] JUDEINSTEIN P., SANCHEZ C., *J. Mater. Chem.*, 6 (1996), 511.
- [3] MACKENZIE J.D., BESCHER E.P., *J. Sol-Gel Sci. Tech.*, 13 (1998), 371.
- [4] KLUKOWSKA A., POSSET U., SCHOTTNER G., WIS M.L., SALEMI-DELVAUX C., MALATESTA V., *Mat. Sci.*, 20 (2001), 95.
- [5] GIGANT K., POSSET U., SCHOTTNER G., *Appl. Spectr.*, 56 (2002), 762.
- [6] SANCHEZ C., LEBEAU B., CHAPUT F., BOILOT J-P., *Adv. Mater.*, 15, (2003), 1969.
- [7] CASTELVETRO V., DE VITA C., *Adv. Colloid Interface Sci.*, 108-109 (2004).
- [8] BRINKER C.J., SCHERER G.W., *Sol-Gel Science*, Academic Press, San Diego, 1990.
- [9] MALZBENDER J., DEN TOONDER J.M.J., BALKENENDE A.R., DE WITH G., *Mater. Sci. Eng.*, R36 (2002), 47.
- [10] HERMANN H., PITSCHE W., MATTERN N., *Phys. Stat. Sol. (a)* 132 (1992), 103.
- [11] SMITH P.F., CHUN I., LIU G., DIMITRIEVICH D., RASBURN J., VACSO G.J., *Polym. Eng. Sci.*, 36 (1996), 2129.
- [12] CASTRO-RODRIGUEZ R., OLIVA A.I., SOSA V., CABALLERO-BRIONES F., PEÑA J.L., *Appl. Surf. Sci.*, 161 (2000), 340.

- [13] LARENA A., MILLAN F., VERDU M., PINTO G., *Appl. Surf. Sci.* 174 (2001), 217.
- [14] FUERTES A.B., *Mater. Lett.* 58 (2004), 1494.
- [15] WANG X., LI W., ZHU G., QIU S., ZHAO D., ZHONG B., *Microporous and Mesoporous Mater.*, 71 (2004), 87.
- [16] ALVAREZ S., FUERTES A.B., *Carbon*, 42 (2004), 423.
- [17] CHOMA J., KLOSKE M., JARONIEC M., *J. Colloid Interface Sci.*, 266 (2003), 168.
- [18] OGAWA M., *J. Photochem. Photobiol., C: Photochem. Rew.*, 3 (2002), 129.
- [19] FUERTES A.B., NEVSKAIA D.M., *Microporous and Mesoporous Mater.*, 62 (2003), 177.
- [20] KAWAHASHI N., MATIJEVIĆ E., *J. Colloid Interface Sci.*, 143 (1991), 103.
- [21] KJELD VAN BOMMEL J.C., FRIGGERI A., SHINKAI S., *Angew. Chem. Int. Ed.*, 9 (2003), 42.
- [22] ZARĘBA-GRODŹ I., MIŚTA W., STRĘK W., BUKOWSKA E., HERMANOWICZ K., MARUSZEWSKI K., *Opt. Mater.*, 26 (2004), 207.
- [23] NOVIKOVA E., KOLENDO A., SYROMYATNIKOV V., AVRAMENKO L., PROT T., GOLEC K., *Polimery* 46 (2001), 6 (in Polish).
- [24] MATSUURA Y., MATSUKAWA K., KAWABATA R., HIGASHI N., NIWA M., INOUE H., *Polymer*, 43 (2002), 1549.
- [25] Polish Norm ISO 4287:1998.
- [26] SING K.S. (Ed.), *Pure & Appl. Chem.*, 57, (1985), 603.
- [27] GREGG S.J., SING K.S.W., *Adsorption, Surface Area and Porosity*, Academic Press, second Ed., London, 1982.
- [28] LOU M.S., CHEN J.C., LI C.M., *J. Ind. Technol.*, 15 (1999), No. 1.
- [29] SUNG J.N., HU Y., FRIEZE W.E., CHEN W., GIDLEY D.W., *J. Electrochem. Soc.*, 150 (2003), F97–F101.
- [30] YANG J.L., CHEN J.C., *J. Ind. Technol.*, 17 (1999), No. 2.
- [31] OCZOŚ K.E., LIUBIMOV V., Geometrical surface structure, OWPRz, Rzeszów, 2003 (in Polish).

*Received 20 October 2004*

*Revised 8 December 2004*

## Internal friction related to the mobility of domain walls in sol-gel derived PZT ceramics

ALDONA ZARYCKA\*, RADOSŁAW ZACHARIASZ, JAN ILCZUK, ARTUR CHROBAK

University of Silesia, Faculty of Computer and Materials Sciences, Department of Materials Science,  
ul. Źeromskiego 3, 41-200 Sosnowiec, Poland

Internal friction  $Q^{-1}$  and Young's modulus  $E$  were measured as functions of temperature for undoped  $\text{Pb}(\text{Zr}_{0.65}\text{Ti}_{0.35})\text{O}_3$  ceramics obtained by the sol-gel technique. Experiments were performed with a RAK-3 resonant mechanical spectrometer. The  $E(T)$  curves show two anomalies associated with two peaks,  $P_R$  and  $P_F$ , in the  $Q^{-1}(T)$  dependence. Moreover,  $Q^{-1}(T)$  curves recorded for two different frequencies show that the  $P_R$  peak has a relaxation character. It was found that its activation energy and relaxation time should be attributed to the interaction of domains with point defects.

Key words: *sol-gel method; ferroelectric ceramics; PZT; internal friction; domain structure*

### 1. Introduction

Lead zirconate titanate  $\text{Pb}(\text{Zr}_x\text{Ti}_{1-x})\text{O}_3$  ceramics (PZT) are one of the most common industrial piezoelectric materials: they are used as transducers between electrical and mechanical energy in phonograph pickups, air transducers, underwater sound and ultrasonic generators, delay-line transducers, wave filters, etc. [1–3]. Generally, all such applications require a high piezoelectric constant as well as low electrical and mechanical loss. Variations of internal friction and the elastic modulus as functions of temperature and excitation frequency can provide direct information on energy dissipation in the material. For example, Postnikov et al. [4] have shown that the internal friction in PZT is not only associated with domain walls, but also with point defects.

The chemical composition and structure of piezoceramics, which can essentially influence the stability of their parameters, play an important role in the application of piezoceramics. Changes in their real structure, texture, and properties are possible, for

---

\*Corresponding author, e-mail: azarycka@us.edu.pl.

example, by inserting point structural defects. These defects can be the result of mechanical treatment of the ceramics, irradiation with molecules or photons with high energy, or annealing in vacuum.

With their many applications and controlling factors, PZT materials have been subject to continuous research over the past few decades. In the present study, the temperature dependencies of the internal friction  $Q^{-1}$  and dynamic Young's modulus  $E$  of PZT 65/35 ceramics obtained by the sol-gel method were measured.

## 2. Experimental

The technological process of fabricating PZT ceramics consists of two basic stages. The first is the preparation of amorphous nanopowders of the solid solution  $\text{Pb}(\text{Zr}_{0.65}\text{Ti}_{0.35})\text{O}_3$  by the sol-gel method, and the other is the consolidation of these nanopowders and preparing fine-grained PZT ceramics by conventional ceramic sintering (CCS). The powder was obtained by introducing lead in the form of trihydrate lead acetate into the environment of the chemical reaction during the sol-gel process. Titanium and zirconium were introduced in the form of aloxides, namely  $\text{Ti}(\text{OCH}_2\text{CH}_2\text{CH}_3)_4$ -titanium(IV) propoxide, and  $\text{Zr}(\text{OCH}_2\text{CH}_2\text{CH}_3)_4$ -zirconium(IV) propoxide. To dissolve all compounds and form a solution, *n*-propanol was used. Synthesis was carried out in an argon atmosphere by heating the solution for 2 hours below the solvent boiling point, forming alkoxide complexes. The by-product obtained (propyl acetate ester) was removed from the solution by distillation. After cooling the reaction mixture to room temperature, *n*-propanol and acetyloacetone were added. The mixture was then hydrolysed (to activate the hydrolysis reaction, distilled water was used) and a colloid solution was formed. After a few minutes, the sol-gel system was formed. The sol-gel derived powder obtained in this way was ground in a mortar with the addition of a softening agent, and annealed at 573 K for 2 hours. The powder obtained after disintegrating the annealed pallets was mixed with liquid paraffin and finally used for preparing the ceramic samples [5, 6]. Ceramic bodies were fabricated by conventional ceramics sintering (CCS) [7], after which samples in rectangular bars (80×10×1) mm<sup>3</sup> were received. The samples were annealed at  $T = 873$  K for  $t = 4$  h and then ground and polished. Electrodes were deposited on their surface by the silver paste burning method.

The temperature dependencies of  $Q^{-1}(T)$  and  $E(T)$  were determined while heating at a constant rate of 3 K/min. Additionally, the temperature dependencies  $Q^{-1}(T)$  and  $E(T)$  were determined at two different frequencies: 524 Hz and 555 Hz (at a constant heating rate of 3 K/min.).

All measurements were done with a RAK-3 resonance mechanical spectrometer controlled by a computer [8]. In order to quantify internal friction, a logarithmic decrement of suppression was used:

$$\delta = \frac{1}{N} \ln \frac{A_0}{A_N} \quad (1)$$

where:  $A_0$  – the initial amplitude of deformation,  $A_N$  – the amplitude after  $N$  vibrations.

Young's moduli  $E$  were calculated from the resonance frequency  $f$  vibration of the sample, measured simultaneously with the internal friction measurements, from the dependence:  $f$

$$E = 94,68 \left( \frac{l_r}{h} \right)^3 \frac{m_d}{b} f^2 \quad (2)$$

where:  $l_r$ ,  $h$ ,  $b$ , and  $m_d$  – respectively: length, thickness, width, and mass of the vibrating part of the sample.

### 3. Results and discussion

The crystal structure of PZT 65/35 samples was investigated by XRD using a Philips PW 3710 diffractometer. Diffraction data (Table 1) were collected for  $2\theta$  between  $20^\circ$  and  $65^\circ$  and  $\text{CuK}_\alpha$  radiation was used. Figure 1 shows the XRD pattern recorded for a PZT 65/35 sample. PZT 65/35 piezoceramics shows an XRD pattern typical of the perovskite-type structure. No pyrochlore-type phase was observed. In general, the activation energy of nucleation for perovskite PZT decreases with increasing Ti content [9]. Therefore, the crystalline structure depends strongly on the composition ratio of Zr/Ti. The structure was identified as a rhombohedral  $R3m$  phase (space group number 160), with the following parameters of the elementary cell:  $a_h = 0.5756$  nm,  $c_h = 0.7058$  nm. It can be seen that PZT materials with the perovskite structure were formed (a good correspondence with the PZT phase diagram was found).

Figure 2 presents  $Q^{-1}(T)$  and  $E(T)$  curves obtained for PZT 65/35 ceramics for five heating cycles, with a temperature ramp of 3 K/min in vacuum. The  $E(T)$  curves show two anomalies, called  $M_R$  and  $M_F$ . The minimum  $M_R$  is located at 385, 391, 395, 383, and 379 K for the 1st, 2nd, 3rd, 5th, and 8th heating cycle, respectively. It is correlated to a sharp internal friction peak called  $P_R$ . The  $M_F$  anomaly in Young's modulus  $E$  and the  $P_F$  peak are due to the phase transition from the rhombohedral to the cubic (ferroelectric to paraelectric) phase.

In the  $Q^{-1}(T)$  curve shown in Fig. 2, it is possible to divide the temperature range according to the level of internal friction. From 293 K to 355 K,  $Q^{-1}$  remains constant. Above 355 K,  $Q^{-1}$  increases and the  $P_R$  peak is formed. Above 450 K,  $Q^{-1}$  increases strongly up to a maximum at the  $P_F$  peak (at the Curie temperature). In the paraelectric region, the drastic decrease in  $Q^{-1}$  reminds us that the mechanisms of energy dissipation in the ferroelectric state are obviously linked to the motion of domain walls.

The same shapes of the  $Q^{-1}(T)$  and  $E(T)$  curves are obtained for all five heating processes.

Table. 1. The Miller indices, positions of diffraction peaks, and interplanar distances for PZT 65/35 sol-gel ceramics

Indices $hkl$	$2\theta$ [deg]	$d_{hkl}$ [Å]
101	21.810	4.07176
012	31.023	2.88032
110	31.049	2.87802
003	38.223	2.35271
021	38.265	2.35271
202	44.464	2.03588
113	50.034	1.82153
211	50.068	1.82037
104	55.173	1.66340
122	55.221	1.66207
300	55.237	1.66163
024	66.670	1.44016
220	64.728	1.43901

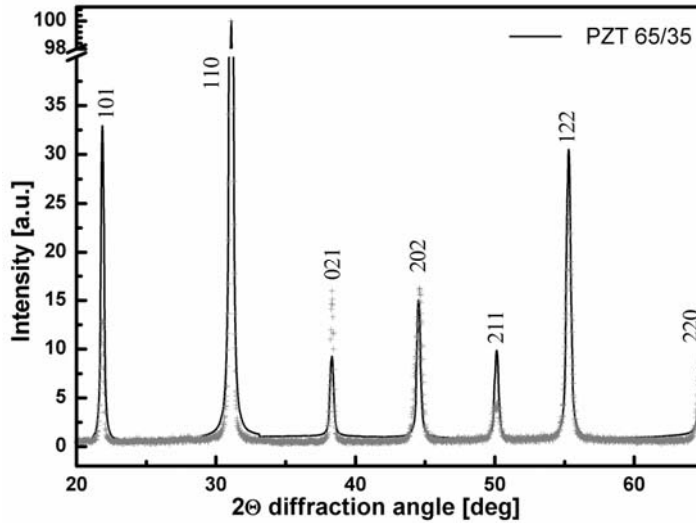


Fig. 1. X-ray diffraction pattern of PZT 65/35

Around the  $P_R$  peak, a decrease in the background value of internal friction  $Q^{-1}$  and a displacement of the temperature of the  $P_R$  peak towards higher temperatures were observed for the 1st, 2nd, and 3rd cycles of heating. In the 5th and 8th heating cycles, the  $P_R$  peak moved towards lower temperatures.

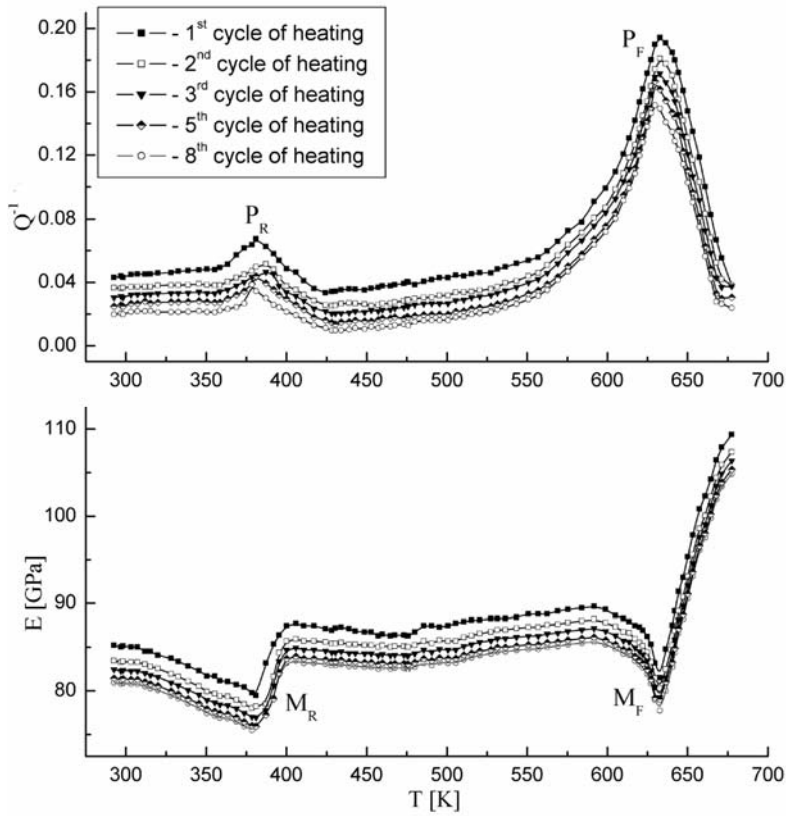


Fig. 2. Temperature dependences of the internal friction  $Q^{-1}(T)$  and Young's modulus  $E(T)$  obtained during five heating cycles, with a temperature ramp rate of 3 K/min in vacuum

From the above results concerning the peak temperature, the activation energy  $H$  and relaxation time  $\tau_0$  of the  $P_R$  peak are determined and shown in Table 2. According to the Arrhenius equation, the relaxation time can be written as [10]:

$$\tau = \tau_0 \exp\left(\frac{H}{kT}\right) \quad (3)$$

where:  $\tau_0$  – the inverse of the frequency factor,  $H$  – the activation energy,  $k$  – the Boltzmann constant,  $T$  – absolute temperature.

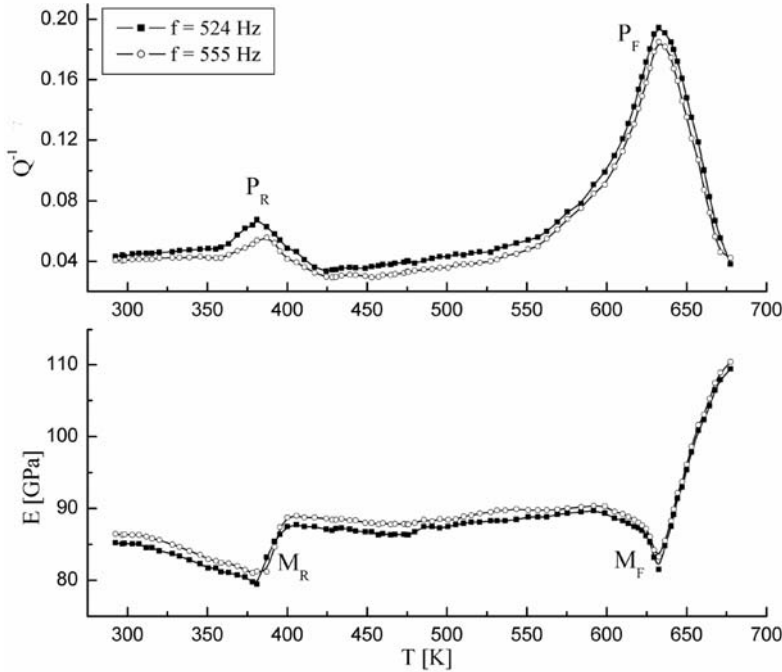
The activation energy was obtained on the basis of the half width of the  $Q^{-1}(T)$  curve:

$$H = \frac{2.63kT_1T_2}{T_2 - T_1} \quad (4)$$

where  $T_1$  and  $T_2$  are the temperatures for  $(1/2)Q_{\max}^{-1}$ , respectively.

Table 2. Activation energy and relaxation time of the  $P_R$  relaxation peak

Cycle of heating	$T_{PR}$ [K]	$H$ [eV]	$\tau_0 \times 10^{14}$ [s]
First	385	$1.05 \pm 0.03$	$(0.10 \pm 0.06)$
Second	391	$0.93 \pm 0.03$	$(1.22 \pm 0.06)$
Third	395	$0.90 \pm 0.03$	$(4.28 \pm 0.06)$
Fifth	383	$0.85 \pm 0.03$	$(8.13 \pm 0.06)$
Eights	379	$0.82 \pm 0.03$	$(9.94 \pm 0.06)$

Fig. 3. Temperature dependences of the internal friction  $Q^{-1}(T)$  and Young's modulus  $E(T)$  obtained for two different frequencies while heating with a temperature ramp rate of 3 K/min

For the  $P_R$  peak, the magnitude of the relaxation time ( $\tau_0 = (0.1-9.94)10^{-14}$  s) is coherent with a point defect relaxation and the  $P_R$  peak could be due to interaction between domain walls and oxygen vacancies, because the activation energy ( $H = 0.82-1.05$  eV) for the diffusion of oxygen vacancies in PZT materials is about 0.9 eV. The displacement of the temperature of the  $P_R$  peak towards higher temperatures, observed for the 1st, 2nd, and 3rd cycles of heating and subsequent displacement towards lower temperatures for the 5th and 8th heating cycles is caused by the interaction of the domain walls with point defects (oxygen vacancies), anchoring them. It is confirmed that the  $P_R$  peak originates from a thermally activated relaxation process, and we think that the motion of domain walls should have a dominant role in the mechanism of the  $P_R$  peak in PZT 65/35 ceramics [11].

To attain more evidence of the dependence of the  $P_R$  peak on oxygen vacancies, internal friction  $Q^{-1}$  was measured at two frequencies: 524 Hz and 555 Hz. The results obtained with PZT 65/35 ceramic samples are shown in Fig. 3. The  $E(T)$  curves show the  $M_R$  and  $M_F$  anomalies in the Young's modulus due to two peaks,  $P_R$  and  $P_F$ , in the  $Q^{-1}(T)$  curves. During measurements at various frequencies, changes in the temperature position of the  $P_R$  peak were observed – a displacement of this peak from 385 K (524 Hz) to 393 K (555 Hz). Therefore, the  $P_R$  peak has a relaxation behaviour, because it is frequency-dependent and related to oxygen vacancies and domain walls [12]. The nature of the  $P_R$  peak can be explained in terms of Postnikov's model, which involves interaction between mobile point defects and stationary 90° domain walls [4].

The  $P_F$  peak originates from a ferroelectric–paraelectric phase transformation, because no change in its position was observed with changes in the measurement frequency. Only a rise in the  $P_F$  peak height with decreasing resonance frequency of the sample's vibrations were observed [13].

#### 4. Conclusions

Two maxima of the internal friction were observed in the temperature dependences obtained for PZT 65/35 ceramics:  $P_F$ , connected with the transformation phase and the relaxation maximum in the ferroelectric phase  $P_R$ . The temperature displacement of the  $P_R$  peak's position towards higher temperatures with an increasing resonance frequency of the sample's vibrations suggest a relaxation character of the peak. The  $P_R$  peak could be attributed to the interaction of domain walls and oxygen vacancies, induced during temperature annealing in vacuum.

#### References

- [1] JAFFE B., COOK W.R. Jr., JAFFE H., *Piezoelectric Ceramics*, Academic Press, London, 1971.
- [2] SHEPPARD L.M., *Silicates Industriels (Belgium)*, 58 (1993), 118.
- [3] ARLT G., DEDERICHS H., *Ferroelectrics*, 29 (1980), 47.
- [4] POSTNIKOV P.V., PAVLOV V.S., GRIDNEV S.A., TURKOV S.K., *Soviet Phys.-Solid State*, 10 (1968), 1267.
- [5] ZARYCKA A., ILCZUK J., CZEKAJ D., *Mat. Sci.-Poland*, 21, (2003), 439.
- [6] SUROWIAK Z., KUPRIANOV M.F., CZEKAJ D., *J. Europ. Ceramic Soc.*, 17 (2001), 1377.
- [7] ZARYCKA A., ZACHARIASZ R., BRUŚ B., ILCZUK J., *Mol. Quant. Acoustics*, 24 (2003), 255.
- [8] ZACHARIASZ R., ILCZUK J., CHROBAK A., *Ceramics*, 66 (2001), 710.
- [9] WILLEMS G.J., WOUTERS D.J., MAES H.E., *Integr. Ferroelectrics*, 15 (1997), 19.
- [10] NOWICK A.S., BERRY B.S., *Anelastic Relaxation in Crystalline Solids*, Academic Press, Chap. 3, New York, 1972.
- [11] CHENG B.L., GABBAY M., MAGLIONE M., JORAND Y., FANTOZZI G., *J. Physique IV*, 6 (1996), 647.
- [12] BRUŚ B., ZACHARIASZ R., ILCZUK J., *Phys. Stat. Sol. (a)*, 201, (2004), 798.
- [13] BOURIM E.M., TANAKA H., GABBAY M., FANTOZZI G., *Jpn. J. Appl. Phys.*, 39 (2000), 5542.

*Received 16 July 2004*  
*Revised 28 September 2004*



## The sol-gel synthesis of bismuth titanate electroceramic thin films

ALDONA ZARYCKA\*, AGATA LISIŃSKA-CZEKAJ, JUSTYNA CZUBER,  
TOMASZ ORKISZ, JAN ILCZUK, DIONIZY CZEKAJ

University of Silesia, Department of Materials Science, ul. Śnieżna 2, 41-200 Sosnowiec, Poland

The present study reports results of the synthesis of randomly oriented  $\text{Bi}_4\text{Ti}_3\text{O}_{12}$  (BTO) thin films by a modified hybrid sol-gel process. Bismuth nitrate and titanium(IV) butoxide were used as the starting materials. Crystalline films were deposited on silicon and stainless steel substrates by spin coating and subsequently annealed at 650 °C. The structure of the films was investigated by X-ray diffraction. The formation of a layered perovskite-like structure with orthorhombic symmetry was confirmed. Scanning electron microscopy showed that the surfaces of the films were smooth, dense, and crack free. Conservation of the chemical composition was confirmed by energy dispersive spectroscopy.

*Key words:*  $\text{Bi}_4\text{Ti}_3\text{O}_{12}$ ; ferroelectric thin films; sol-gel method; X-ray studies

### 1. Introduction

In recent years, considerable attention has been devoted to the development of thin film technologies for perovskitic materials due to their technically important properties [1]. Depending on the stoichiometry used, such materials exhibit ferro-, piezo- and pyroelectric, or electrostrictive properties. Their composition can also be adjusted to attain electronically conductive materials.

We will concentrate on thin films of materials from the Aurivillius family. Attention to the Aurivillius phases, which constitute a wide family of layered compounds, has increased due to their potential use in electrooptic devices. They are generically described as intergrowth structures of fluorite-like  $(\text{Bi}_2\text{O}_2)^{2+}$  units and perovskite-like  $(\text{A}_{n-1}\text{B}_n\text{O}_{3n+1})^{2-}$  slabs, where  $n = 1-5$  or 8 [2]. The 12-fold perovskite A sites can be occupied by mono-, di-, or trivalent cations like  $\text{Na}^+$ ,  $\text{Ba}^{2+}$ ,  $\text{Ca}^{2+}$ ,  $\text{Sr}^{2+}$ ,  $\text{Bi}^{3+}$ , and rare-earth cations. The 6-fold B sites are usually occupied by smaller cations like  $\text{Ti}^{4+}$ ,  $\text{Ta}^{5+}$ ,  $\text{Nb}^{5+}$ , and  $\text{W}^{6+}$ , leading to  $\text{BO}_6$  octahedra [3].

---

\* Corresponding author, e-mail: azarycka@us.edu.pl.

Bismuth titanate  $\text{Bi}_4\text{Ti}_3\text{O}_{12}$  (BTO) was synthesized by Aurivillius in 1949 [4]. Due to its structural characteristics, BTO single crystals are strongly anisotropic in terms of ferroelectric properties such as polarization and coercive field. The polarization direction of BIT is 4.50 of its cell structure base plane, thus giving rise to a much larger  $a$ -axis polarization ( $P_s = 45\text{--}50 \mu\text{C}/\text{cm}^2$ ) than  $c$ -axis polarization ( $P_s = 4.5 \mu\text{C}/\text{cm}^2$ ) [5]. If bismuth-layered perovskite films are to be used in ferroelectric thin film capacitors with plane electrodes on the top and bottom (as in the geometry used for dynamic random access memories), however, a polarization component oriented normally to the electrode plane is essential. The preparation of randomly oriented thin films of this family has thus become a challenging issue, since the anisotropy phenomenon is expected to be critical for high-density devices [6]. Therefore, we concentrate on the growth of randomly oriented BTO thin films in the present study.

The idealized structure (space group (SG)  $I4/mmm$ ;  $a_T \approx 3.86 \text{ \AA}$  and  $c_T \approx 32.8 \text{ \AA}$ ) of the  $n = 3$  Aurivillius compound  $\text{Bi}_4\text{Ti}_3\text{O}_{12}$  is shown in Fig. 1.

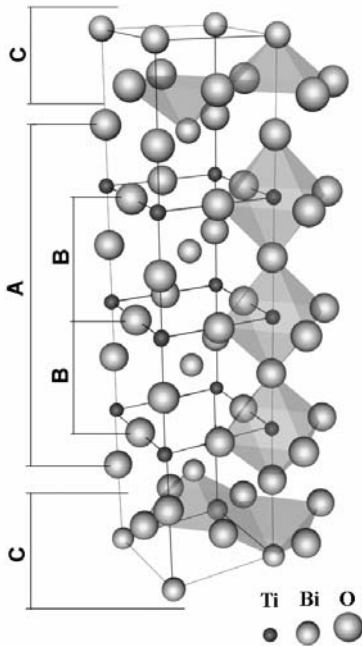


Fig. 1. Half of the pseudotetragonal unit cell of  $\text{Bi}_4\text{Ti}_3\text{O}_{12}$  (for  $z = 0.25\text{--}0.75$ ): A – the perovskite layer  $\text{Bi}_2\text{Ti}_3\text{O}_{12}^{2-}$ , C – the  $\text{Bi}_2\text{O}_2^{2+}$  layers, B – the unit cell of the hypothetical perovskite structure  $\text{BiTiO}_2$  (after [4])

Quite different chemical and physical methods have been used to deposit  $\text{Bi}_4\text{Ti}_3\text{O}_{12}$  thin films, e.g., RF sputtering, sol-gel processing, laser ablation, and metal-organic chemical vapour deposition [7]. These methods are competitive and each of them has advantages and disadvantages in terms of homogeneity, processing temperatures, and processing costs.

Processing high-quality thin films requires low-temperature synthesis, high reproducibility, simplicity in all processing steps, and low cost. Due to these requirements, the search for new routes of films preparation remains an interesting and open subject,

in order to improve the stability of complex solutions, enhance stoichiometry control in film composition, or reduce the cost of the process.

In the presented research, we succeeded, using a hybrid sol-gel spin coating method, in growing randomly oriented  $\text{Bi}_4\text{Ti}_3\text{O}_{12}$  thin films on silicon and stainless steel substrates. Their microstructures, structures, and chemical compositions were studied.

## 2. Experimental

A modified sol-gel process was employed to prepare  $\text{Bi}_4\text{Ti}_3\text{O}_{12}$  thin films. Bismuth nitrate  $\text{Bi}(\text{NO}_3)_3 \cdot 5\text{H}_2\text{O}$ , instead of bismuth acetate, and titanium(IV) butoxide  $\text{Ti}(\text{OC}_4\text{H}_9)_4$  were used as the starting materials [8]. Bismuth nitrate was dissolved in 2-methoxyethanol to form bismuth solution, while titanium(IV) butoxide was stabilized by acetylacetone to form titanium solution. An excess of 10% Bi was used to compensate the evaporation of bismuth during annealing.  $\text{Bi}_4\text{Ti}_3\text{O}_{12}$  precursor solution was then obtained by mixing the two solutions. After that deionised water was added to this mixture while stirring. The advantage of using 2-methoxyethanol as the solvent of bismuth nitrate in the present study (over the generally used acetic acid) is that it dissolves bismuth nitrate at room temperature. After thorough mixing, the precursor solution was used to deposit  $\text{Bi}_4\text{Ti}_3\text{O}_{12}$  thin films on silicon, glass, and stainless steel substrates by spin coating at 3500 rpm for 30 s.

Amorphous films were kept in a preheated furnace at 350 °C for 5 minutes to remove the volatile organic components. The coating process (i.e., spinning – drying – pyrolysis) was repeated up to 10 times. The as-deposited films were then heat-treated at 650 °C for 2 hours to form a good crystal structure [9].

The crystalline structures of the annealed thin films were examined by X-ray diffraction (XRD) analysis, using a Philips PW 3710 X-ray diffractometer with  $\text{CoK}_{\alpha 1,2}$  radiation. Scanning electron microscopy (HITACHI S-4700-type microscope) was used to study the surface morphology of the films. The stoichiometry of the films was investigated using a chemical composition analysis system (EDS) of the VANTAGE type. All characterizations were carried out at room temperature.

## 3. Results and discussion

The surface morphologies of the thin films grown on stainless steel and silicon substrates are given in Fig. 2. Although the temperature of crystallization of the BTO thin films was the same for both types of substrates ( $T = 650$  °C for 2h), one can see influence of the substrate on the crystallization conditions. We can conclude, however, that our modified sol-gel technique can prevent the formation of cracks and yields homogeneous dense nanocrystalline microstructures, similar to those arising from films prepared by the sol-gel technique elsewhere [10, 11].

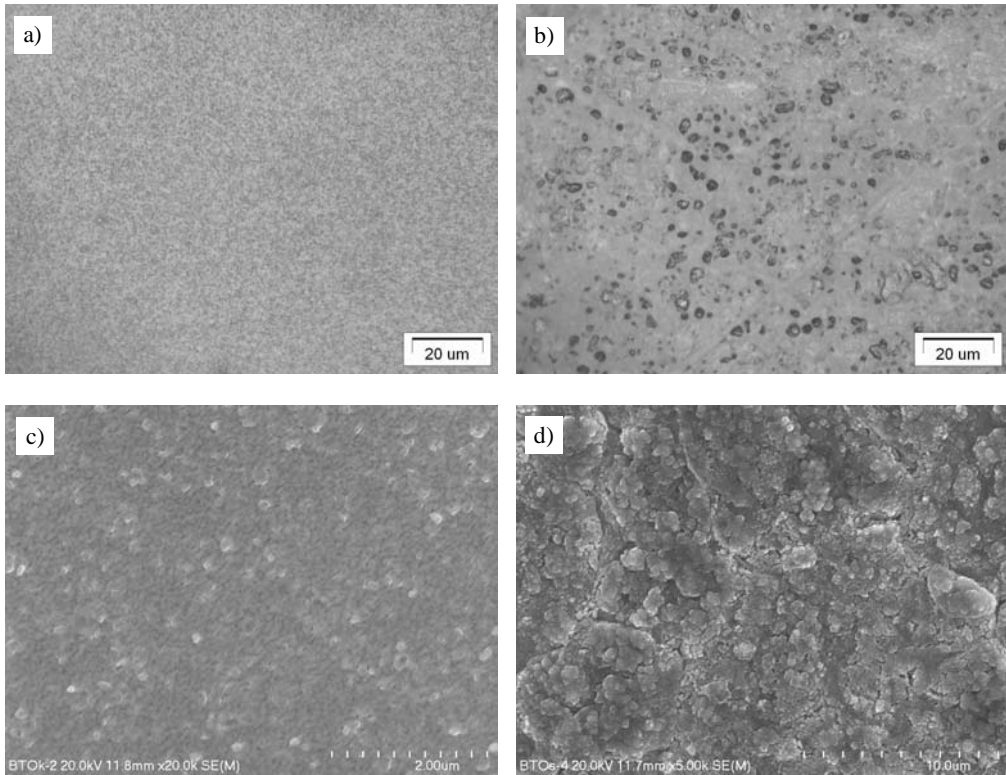


Fig. 2. Optical (a, b) and SEM images (c, d) of the surfaces of BTO thin films deposited on silicon substrates (a, c) and stainless steel substrates (b, d)

Point analysis of the chemical composition in micro-areas for BTO on stainless steel substrates was done by EDS. The results of these measurements give the following compositions of the thin films: Ti – 11.70 wt. %, Bi – 72.20 wt. %, O – 16.10 wt. %. On the other hand, the results of theoretical calculations for stoichiometric  $\text{Bi}_4\text{Ti}_3\text{O}_{12}$  give: Ti – 12.26 wt. %, Bi – 71.35 wt. %, O – 16.39 wt. %.

The actual crystal structure of BTO was determined by Rae et al. [12] from single-crystal XRD data. It was described as a commensurate modulation of an orthorhombic average structure (SG  $Fmmm$  No. 69;  $a_{\text{orth}} \approx b_{\text{orth}} \approx a_{\text{tet}}\sqrt{2}$  and  $c_{\text{orth}} = c_{\text{tet}}$ ) that leads to a monoclinic system (SG  $B1a1$  No. 7, non-standard setting of  $P1c1$ ) with  $a_{\text{mon}} = 5:450(1)\text{\AA}$ ,  $b_{\text{mon}} = 5.4059(6)\text{\AA}$ ,  $c_{\text{mon}} = 32.832(3)\text{\AA}$ , and  $\beta = 90.00^\circ$  (the non-conventional B centering is used for easy comparison with the parent  $I4/mmm$  prototype and the  $a$ - and  $b$ -axis corresponding to the diagonals  $a_{\text{tet}}\pm b_{\text{tet}}$  of the parent structure) [13].

The XRD patterns of the produced BTO films revealed that good crystalline  $\text{Bi}_4\text{Ti}_3\text{O}_{12}$  films were obtained (Figs. 3, 4). Careful examination of the XRD patterns indicates that there is no preferred orientation for any sample. The lattice parameters for  $\text{Bi}_4\text{Ti}_3\text{O}_{12}$  were calculated for the orthorhombic phase of bismuth titanate using the Rietveld refinement [14] built into the computer program PowderCell 2.4 [15].

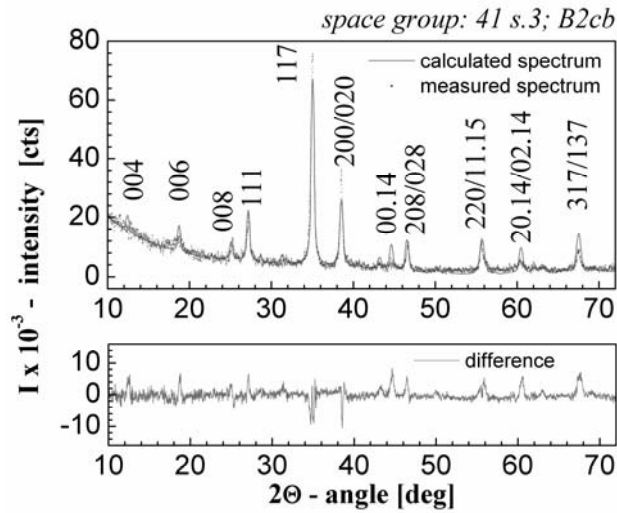


Fig. 3. Results of X-ray pattern fitting for BTO thin films on silicon substrates (circles – raw data points, the solid line – the best calculated profile according to the *B2cb* space group). The trace at the bottom is a plot of the difference between the calculated and observed intensities

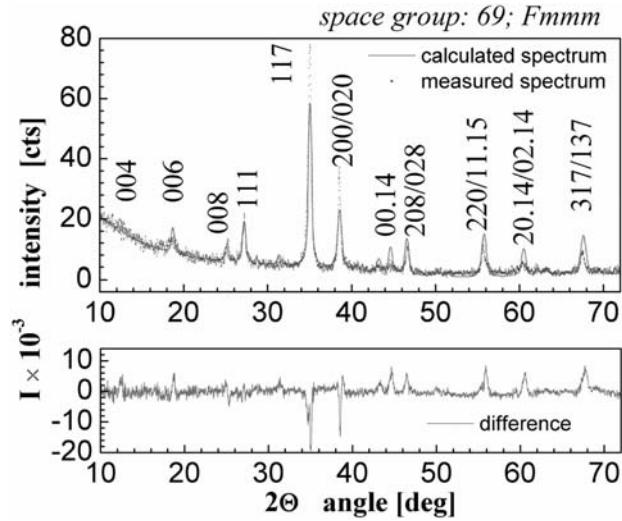


Fig. 4. Results of X-ray pattern fitting for the BTO thin film on silicon substrates (circles – the observed pattern, solid line – the calculated pattern according to the *Fmmm* space group). The trace at the bottom is a plot of the difference between the calculated and observed intensities

Two model structures were used, both of the orthorhombic symmetry, namely *B2cb* (ICSD, data file No. 16488 [16]) (Fig. 3), and *Fmmm* (ICSD, data file No. 24735 [4]) (Fig. 4). Detailed information about the model structures is given in Tables 1 and 2, whereas the details of the calculated X-ray spectra are given in Tables 3 and 4.

Table 1. Parameters of the model structure used for XRD pattern fitting (see Fig.3)

Space group number		41						
Space group		<i>B2cb</i>						
Cell choice		3						
Lattice parameters		5.4162 Å, 5.4132 Å, 32.9200 Å						
Angles		90.00°, 90.00°, 90.00°						
Atoms in asymmetric unit		10						
Atoms in unit cell		76.0, 76 generated position						
Volume of cell		965.18 Å <sup>3</sup>						
Relative mass of unit cell		4686.47						
X-ray density		8.0628 g/cm <sup>3</sup>						
Mass absorption coefficient		287.41 cm <sup>-1</sup> /g						
Name	P. No.	Ion	Wyck.	<i>x</i>	<i>y</i>	<i>z</i>	SOF	<i>B</i>
Bi1	83	Bi <sup>3+</sup>	8b	0.0000	0.9978	0.0668	1.00	1.00
Bi2	83	Bi <sup>3+</sup>	8b	0.9991	0.0199	0.2113	1.00	1.00
Ti1	22	Ti <sup>4+</sup>	4a	0.5452	0.0000	0.0000	1.00	1.00
Ti2	22	Ti <sup>4+</sup>	8b	0.0533	0.9990	0.3714	1.00	1.00
O1	8	O <sup>2-</sup>	8b	0.2070	0.2220	0.9967	1.00	1.00
O2	8	O <sup>2-</sup>	8b	0.2640	0.2520	0.2507	1.00	1.00
O3	8	O <sup>2-</sup>	8b	0.0730	0.9750	0.4404	1.00	1.00
O4	8	O <sup>2-</sup>	8b	0.9600	0.9260	0.3185	1.00	1.00
O5	8	O <sup>2-</sup>	8b	0.2940	0.2850	0.1215	1.00	1.00
O6	8	O <sup>2-</sup>	8b	0.1590	0.2000	0.8690	1.00	1.00

Table 2. Parameters of the model structure used for XRD pattern fitting (see Fig. 4).

Space group number		69						
Space group		<i>Fmmm</i>						
Cell choice		1						
Lattice parameters		5.4238 Å, 5.3941 Å, 32.9400 Å						
Angles		90.00°, 90.00°, 90.00°						
Atoms in asymmetric unit		9						
Atoms in unit cell		76.0, 76 generated position						
Volume of the cell		967.92 Å <sup>3</sup>						
Relative mass of unit cell		4686.46						
X-ray density		8.0400 g/cm <sup>3</sup>						
Mass absorption coefficient		287.41 cm <sup>-1</sup> /g						
Name	P. No.	Ion	Wyck.	<i>x</i>	<i>y</i>	<i>z</i>	SOF	<i>B</i>
Bi1	83	Bi3+	8i	0.000	0.000	0.933	1.0	0.00
Bi2	83	Bi3+	8i	0.000	0.000	0.789	1.0	0.00
O1	8	O2-	8e	0.250	0.250	0.000	1.0	0.00
O2	8	O2-	8f	0.250	0.250	0.250	1.0	0.00
O3	8	O2-	8i	0.000	0.000	0.564	1.0	0.00
O4	8	O2-	8i	0.000	0.000	0.692	1.0	0.00
O5	8	O2-	16j	0.250	0.250	0.128	1.0	0.00
Ti1	22	Ti4+	4b	0.000	0.000	0.500	1.00	0.00
Ti2	22	Ti4+	8i	0.000	0.000	0.628	1.00	0.00

Table 3. Details of the calculated X-ray spectrum (see Fig. 3)

<i>hkl</i>	$2\theta$ [deg]	$d_{hkl}$ [Å]	<i>I</i> [rel.]	$ F(hkl) $	<i>Mu</i>	FWHM
004	12.447	8.25150	6.32	212.07	2	0.4226
006	18.717	5.50100	13.10	463.21	2	0.4316
008	25.043	4.12575	7.84	485.16	2	0.4442
111	27.177	3.80728	26.20	483.32	8	0.4493
117	35.006	2.97418	100.00	1239.75	8	0.4716
020	38.533	2.71090	19.08	1203.63	2	0.4835
200	38.553	2.70959	19.59	1220.35	2	0.4836
0014	44.595	2.35757	12.10	1128.25	2	0.5067
028	46.510	2.26559	10.69	786.51	4	0.5148
208	46.526	2.26483	11.32	809.82	4	0.5149
220	55.648	1.91643	20.14	1323.89	4	0.5585
1115	55.906	1.90829	8.65	616.86	8	0.5599
0214	60.374	1.77895	10.15	1030.01	4	0.5847
2014	60.388	1.77858	10.14	1030.05	4	0.5848
137	67.444	1.61124	16.98	1062.95	8	0.6288
317	67.470	1.61069	16.78	1057.03	8	0.6290

Table 4. Details of the calculated X-ray spectrum (see Fig. 4).

<i>hkl</i>	$2\theta$ [deg]	$d_{hkl}$ [Å]	<i>I</i> [rel.]	$ F(hkl) $	<i>Mu</i>	FWHM
004	12.472	8.23500	6.67	215.89	2	0.4941
006	18.754	5.49000	14.32	479.77	2	0.5018
008	25.094	4.11750	8.15	490.06	2	0.5128
111	27.236	3.79912	23.66	455.16	8	0.5172
117	35.082	2.96797	100.00	1228.71	8	0.5368
200	38.519	2.71189	20.31	1227.22	2	0.5470
020	38.739	2.69703	20.10	1228.61	2	0.5477
0014	44.689	2.35286	13.46	1179.69	2	0.5680
208	46.527	2.26480	12.39	837.43	4	0.5750
028	46.716	2.25612	12.32	839.18	4	0.5757
220	55.778	1.91232	24.60	1450.54	4	0.6150
1115	56.030	1.90441	7.55	571.01	8	0.6162
2014	60.440	1.77720	10.57	1040.81	4	0.6386
0214	60.598	1.77300	10.53	1041.89	4	0.6395
317	67.471	1.61066	17.15	1056.69	8	0.6791
137	67.770	1.60442	17.06	1058.57	8	0.6810

The  $R$ -values of the Rietveld analysis obtained assuming the  $B2cb$  space group are:  $R_p = 27\%$ ,  $R_{wp} = 42.95\%$ ,  $R_e = 5\%$ , whereas, the  $R$ -values for the assumed SG  $Fmmm$  are  $R_p = 26.82\%$ ,  $R_{wp} = 41.44\%$ ,  $R_{exp} = 5\%$ . Although the numerical criteria of the goodness of fit (i.e. the  $R$ -values) are very important, it is necessary to point out that they do not fully reflect the quality of fitting. Graphical criteria such as plots of the calculated and observed intensities and plots of their differences are also necessary. From the traces on the bottom of Figs. 3 and 4, one can see that there are no gross errors of fitting, which might originate in bad scaling parameters, an incorrect crystalline structure used for simulation, or incorrect elementary cell parameters. However, one can see the “negative” lines at the diffraction angle  $2\theta = 35.0^\circ$  and  $2\theta = 38.5^\circ$ . These “negative” lines may arise from the difference between the supposed, pure stoichiometric chemical composition  $\text{Bi}_4\text{Ti}_3\text{O}_{12}$  (see Tables 1 and 2, column SOF) and the actual chemical composition of the grown BTO thin film (our BTO films depart by 6% from the theoretical Bi/Ti ratio).

For the films crystallized on Si substrates at  $650^\circ\text{C}$  for 2h, the calculated parameters were (for the expected SG  $B2cb$ ):  $a = 5.416(2)\text{\AA}$ ,  $b = 5.413(2)\text{\AA}$ , and  $c = 32.920(0)\text{\AA}$  (Table 1), or (for the expected SG  $Fmmm$ ):  $a = 5.423(8)\text{\AA}$ ,  $b = 5.394(1)\text{\AA}$ , and  $c = 32.940(0)\text{\AA}$  (Table 2). These parameters slightly differ from the values given in the JCPDS 12-213 data input for the single crystal ( $a = 5.41\text{\AA}$ ,  $b = 5.45\text{\AA}$  and  $c = 32.84\text{\AA}$ ). These differences may be attributed to the influence of several parameters, such as the substrate, crystallization conditions, grain size, and others. Depending on the substrate and growth conditions, undesired phases such as  $\text{Bi}_4\text{Ti}_8\text{O}_{12}$ ,  $\text{Bi}_2\text{Ti}_2\text{O}_7$ , or  $\text{Bi}_2\text{O}_3$  sometimes occur [7]. It is important that for the films studied in this work, only the single phase of  $\text{Bi}_4\text{Ti}_3\text{O}_{12}$ , grown at  $650^\circ\text{C}$ , was been observed.

The structural determinations presented above prove that the compound crystallizes with the orthorhombic symmetry, as shown in Figs. 3 and 4. On the other hand, the crystallization of BTO thin films in the SG  $B1a1$  system (ICSD data file 70000 [12]) has not been observed.

## 4. Conclusions

Randomly oriented  $\text{Bi}_4\text{Ti}_3\text{O}_{12}$  thin films were grown on silicon and stainless steel substrates by sol-gel spin coating. Chemical composition microanalyses carried out by EDS showed the following stoichiometric errors: for Ti – 4.6%, for Bi – 1.2%, and for O – 1.8%. It can be concluded that the processing route used for thin film fabrication preserves the stoichiometry (a 6% departure from the theoretical Bi/Ti ratio). X-ray diffraction analysis proved the formation of bismuth layer-structured BTO thin films with orthorhombic structure. Preference is given to the  $Fmmm$  space group, due to the smaller  $R$ -values obtained in simulations. No evidence of monoclinic  $B1a1$  phases was found.

The results of these investigations suggest that our modified sol-gel technique can prevent the formation of cracks and yields dense micro-structured perovskite-type films on metal and single crystal substrates.

### References

- [1] CZEKAJ D., *Technology Properties and Applications of PZT Thin Films*, Wyd. Uniw. Śl., Katowice, 2002.
- [2] SUROWIAK Z., GEGUZINA G., FESENKO E., LISIŃSKA A., SHUVAEVA E., *Polish J. Appl. Chem.*, 38 (1994), 3.
- [3] SUBBARAO E.C., *Phys.Rev.*, 122 (1961), 804.
- [4] AURIVILLIUS B., *Arkiv Kemi*, 1 (1950), 499.
- [5] CUMMINS S. E., CROSS L. E. *J. Appl. Phys.*, 39 (1968), 2268.
- [6] JIN SOO KIM, SANG SU KIM, JONG KUK KIM, TAE KWON SONG, *Jpn. J. Appl. Phys.*, 41 (2002), 6451.
- [7] ARAUJO E.B., NUNES V.B., ZANETTE S.I., EIRAS J.A., *Mat. Lett.*, 49 (2001) 108.
- [8] KONG L.B., MA J., *Thin Solid Films*, 379 (2000), 89.
- [9] MOROZOV M. I., MEZENTSEVA L. P., GUSAROV V. V., *Russian J. Gen. Chem.*, 72, (2002), 1038.
- [10] ARAUJO E. B., EIRAS J. A., *J. Eur. Ceram. Soc.*, 19 (1999), 1453.
- [11] SEDLAR M., SAYER M., *Ceramics Int.*, 22 (1996), 241.
- [12] RAE A.D., THOMPSON, J.G., WITHERS R.L., WILLIS A.C., *Acta Cryst.*, B46 (1990), 474.
- [13] CHU M.-W., CALDES M.T., PIFFARD Y., MARIE A.-M., GAUTIER E., JOUBERT O., GANNE M., BROHAN L., *J. Sol. State Chem.*, 172 (2003), 389.
- [14] *The Rietveld Method*, R.A. Young (Ed)., Oxford University Press, Oxford, 1995.
- [15] NOLZE G., KRAUS W., *Powder Diffraction*, 13, (1998), 256.
- [16] DORRIAN J.I., NEWHAM R.E., SMITH D.K., *Ferroelectrics*, 3 (1971), 17.

*Received 12 August 2004*

*Revised 8 December 2004*

## Sol-gel derived Li-ion conducting polymer electrolytes

ELŻBIETA ŻELAZOWSKA<sup>1\*</sup>, EWA RYSIAKIEWICZ-PASEK<sup>2</sup>, MARIA BORCZUCH-ŁACZKA<sup>3</sup>

<sup>1</sup>Institute of Glass and Ceramics, Cracow Branch, ul. Lipowa 3, 30-702 Cracow, Poland

<sup>2</sup>Institute of Physics, Wrocław University of Technology,  
Wybrzeże Wyspiańskiego 27, 50-370 Wrocław, Poland

<sup>3</sup>Faculty of Materials Science and Ceramics, AGH University of Science and Technology,  
al. Mickiewicza 30, 30-059 Cracow, Poland

Organic-inorganic hybrids have recently become a remarkable family of amorphous polymer materials with promising potential applications. In the present study, sol-gel derived organic-inorganic hybrid electrolytes doped with lithium salts (LiCl, LiClO<sub>4</sub>) were produced from inorganic and organic precursors such as tetraethyl orthosilicate, poly(ethylene oxide), poly(ethylene glycol), propylene oxide, propylene carbonate, ethylene glycol, and 1,2-propylene glycol. The hybrid electrolytes were obtained in the form of flexible or glassy materials depending on the composition and heat treatment temperature (ranging from 80 to 125 °C). The morphology, structure and elemental chemical composition of the electrolytes obtained were examined by scanning electron microscopy equipped with energy dispersive X-ray spectroscopy (SEM/EDS), FTIR spectroscopy, and X-ray diffraction (XRD). Infrared spectroscopy and SEM observation results indicate that the structural properties of the synthesized materials are significantly influenced by organic additives and the sol-gel preparation procedure. The formation of organic group –O–Si linkages was confirmed by infrared spectra in all of the electrolytes obtained. The results of FTIR analysis are in a good agreement with <sup>13</sup>C and <sup>1</sup>H MAS NMR spectroscopy measurements performed for the hydrolysed sols immediately before the gel transformation process and at early gel stages. These results have revealed an enhanced duration of the cross-linking process in the species prepared with low molecular mass glycols. Cells in an electrochromic window arrangement were prepared in order to observe the photometric and cyclic voltammetry characteristics of thin-film electrochromic systems with the investigated hybrid materials employed as electrolytes. The results indicate that the inorganic-organic hybrids synthesized in this work are promising electrolytes for thin film electrochromic systems based on WO<sub>3</sub>.

Key words: *organic-inorganic hybrid; sol-gel; ionic conductivity; Li<sup>+</sup>-conductive electrolytes*

---

\* Corresponding author, e-mail: ezelazowska@isic.krakow.pl.

## 1. Introduction

The development of high conductive solid electrolytes for applications in advanced electrochemical and optoelectronic devices such as lithium rechargeable batteries and electrochromic windows and displays, have recently focused extensive research efforts on materials with high ionic conductivity at low temperatures [1–4].

Polymer electrolytes based on complexes of poly-ethers with alkali metal salts and especially poly(ethylene oxide) (PEO) which act as host matrices for lithium salts have been extensively studied for such applications in light of their advantageous chemical and mechanical resistance and excellent contact with electrode materials. The main disadvantage of using polymer electrolytes in electronic and optoelectronic devices is their relatively high content of crystalline phases resulting in low room-temperature ionic conductivity. Low-temperature ionic conductivity in polymers is known to be almost exclusively dependent on the mobility of ionic charge carriers in the amorphous regions and due to this, much research effort has been directed towards the possible enlargement of amorphous phase content in polymer electrolytes [5–7]. In recent years, there have been reports on so-called composite polymer electrolytes with ionic conductivity improved due to the addition of liquid plasticisers and/or application of solid fillers, advantageously in the form of fine ceramic particles [8–10]. Such modifications of polymer electrolytes morphology have proved to be an effective way to suppress the tendency for crystallization. It seems to be more suitable, however, for rechargeable fuel cells rather than electrochromic window systems, which are required to be transparent and highly colourless in the bleached state [1–4, 11].

On the other hand, transparent amorphous materials, both in monolithic and thin film forms, can be relatively easily obtained by using a sol-gel method [12–14]. The organic modification of glasses and the other sol-gel derived materials is possible, as sol preparation and the sol-gel process proceed at ambient and negligibly increased temperatures, respectively. Due to, a great number of organic additives were successfully incorporated into gels from the solutions containing gel precursors in mixtures with the organic compounds [15–22]. Sol-gel process have proved to be a useful tool for obtaining new families of organically modified ceramics (ormocers) and silicate materials (ormosils), as well as organically modified electrolytes (ormolytes) in which organic groups can be included either by the co-polymerisation of organic monomers with metal alkoxides or by the co-condensation of modified alkoxides [17–22]. Among others, Malzbender et al. [15] have reported on organic-inorganic hybrid coatings for float glass, where the coating fluid contained methyltrimethoxysilane (MTMS). Georgi et al. [16] have studied the influence of glutardialdehyde, 3,4-dimethoxybenzaldehyde, and aminocaproic acid additives on the properties of sol-gel layers derived from tetraethoxysilane (TEOS).

The sol-gel method has also proved to be an excellent process for preparation of silica- or silica-based gels. Silica gels contain a large number of micro-pores, which

makes them useful in many various applications [23–25]. In addition, the pore structure and size can be controlled by the parameters of the sol-gel process, such as the atmosphere and rate of solvent evaporation during the first stages of drying and parameters during subsequent heat treatment.

Porous gel materials can trap or be easily filled and/or processed with liquids and gases. Matsuda et al. [26] have studied the proton conductivity of sol-gel derived porous silica gels impregnated with sulphuric acid. On the other hand, it is known that polymers with incorporated liquid electrolytes, i.e. containing plasticisers or porous gelled polymer electrolytes, generally exhibit ionic conductivity at room temperature being about  $10^{-3} \text{ S}\cdot\text{cm}^{-1}$  higher than that of “dry” polymer electrolytes (such as PEO-lithium salt solid complexes). Matrices of hybrid electrolytes or those derived from porous silica gels can be expected to trap a liquid phase with dissolved lithium salt. Due to this, such systems can be considered to consist of a liquid electrolyte dispersed in a solid matrix, with the lithium and counter ions migrating throughout the solvent [27].

Many kinds of polymers have been proposed as components of gel polymers and sol-gel derived hybrid electrolytes, including polyacrylonitrile (PAN), poly(ethylene oxide) (PEO), poly(tetramethylene oxide) (PTMO), poly(methyl methacrylate) (PMMA), polyethylene glycol (PEG), polypropylene glycol (PPG), poly(vinylidene fluoride) (PVDF), some network polymers prepared by cross-linking reactions, and mixtures of polymers from these two groups [28–31]. Among those organic compounds, polyether polymers have a favourable feature of being miscible with many kinds of liquid electrolytes used in Li batteries [29, 31]. In addition, the preparation of hybrid gel electrolytes with polyethers as organic parts is relatively easy. Dahmouche et al. [32, 33] have investigated two families of  $\text{Li}^+$ -conducting electrolytes. The first family, with ionic conductivity higher than  $10^{-4} \text{ S}\cdot\text{m}^{-1}$  at room temperature and exhibiting chemical bonds between the organic and inorganic phase, was obtained from a mixture of 3-isocyanatopropyltriethoxysilane, O,O'-bis-(2-aminopropyl)-polyethylene glycol (or O,O'-bis-(2-aminopropyl)-polypropylene glycol, and lithium salt. In the other family, prepared by ultrasonic or traditional sol-gel processes from the mixture of tetraethyl orthosilicate (TEOS), polyethylene glycol (PEG), and lithium salt ( $\text{LiClO}_4$ ), the organic and inorganic parts were not chemically bonded and ionic conductivities of up to  $10^{-2} \text{ S}\cdot\text{m}^{-1}$  were obtained at room temperature with a silica-PEG<sub>300</sub> system (PEG/TEOS = 40% in weight). Chaker et al. [34] have reported on siloxane-poly(propylene oxide) (PPO, with 2000 and 4000 g/mol molecular weight) hybrid electrolytes doped with sodium perchlorate ( $\text{NaClO}_4$ ), obtained by the sol-gel method and exhibiting the ionic conductivity of  $8,9 \times 10^{-4} \text{ S}\cdot\text{cm}^{-1}$  at room temperature. Poly(ethylene oxide)-based gel-type polymer electrolytes doped with lithium perchlorate ( $\text{LiClO}_4$ ), containing nanoscale-fumed  $\text{SiO}_2$  dispersed in acetonitrile and showing ionic conductivity higher than  $10^{-3} \text{ S}\cdot\text{cm}^{-1}$  at room temperature have been obtained by Aihara et al. [35].

In general, organic-inorganic hybrids have proved to be a remarkable family of amorphous polymeric materials with promising potential applications.

The goal of this work was to obtain sol-gel derived organic-inorganic hybrid electrolytes doped with lithium salt (LiCl, LiClO<sub>4</sub>). The electrolytes were produced from solutions containing tetraethyl orthosilicate (TEOS) as an inorganic precursor of SiO<sub>2</sub> gels and poly(ethylene oxide) (PEO) or poly(ethylene glycol) (PEG), together with propylene oxide (PO), propylene carbonate (PC), ethylene glycol (EG), and 1,2-propylene glycol (PG) as low-molecular-weight organic additives. The structural properties of the organic-inorganic hybrids were compared with those of lithium doped or pure (without lithium salt doping) silica gels prepared under the same conditions and using the same sol-gel procedure employed for obtaining the inorganic parts of hybrid electrolytes.

## 2. Experimental

Based on earlier results for the same sol-gel procedures [28], the sols for preparing silica gels were produced by mixing TEOS Si(OC<sub>2</sub>H<sub>5</sub>)<sub>4</sub> (Merck), distilled water, and 36.6% HCl as a catalyst. HCl was added drop by drop until pH = 2 was reached. Two receipts were used: the first, for PEO-containing sols, with the volume ratio of TEOS :distilled water:ethanol being 1:1:2.5, and the other, for sols with glycols, with the molar ratio of TEOS:distilled water being 1:4. Solutions of PEO-(CH<sub>2</sub>CH<sub>2</sub>O)<sub>n</sub> (nominal molar weight  $M_w = 600\ 000$ , Aldrich) in organic solvents (dichloromethane, ethanol, or acetonitrile C<sub>2</sub>H<sub>3</sub>N), and aqueous or ethanol solutions of poly(ethylene glycol) (nominal molar weight  $M_w = 6000$  or  $15\ 000$ , Fluka, Aldrich, respectively) with appropriate additives (Table 1) of propylene carbonate PC C<sub>4</sub>H<sub>6</sub>O (Merck), propylene oxide PO C<sub>3</sub>H<sub>6</sub>O ( $M_w = 58.08$ , Merck), ethylene glycol EG HO(C<sub>2</sub>H<sub>4</sub>O)<sub>n</sub>H ( $M_w = 62.08$ , Merck), 1,2-propylene glycol PG CH<sub>3</sub>·CH(OH)·CH<sub>2</sub>OH ( $M_w = 76.10$ , Fluka), and lithium salts (LiClO<sub>4</sub> or LiCl, Merck) with a weight ratio of about 0.02 and 0.03 with respect to the mass of fresh gels were used.

The chemical components and solvents employed were of at least reagent grade. The salts for doping, before being added to the solution of TEOS or to the mixtures of TEOS with other components, were dissolved in the entire calculated amount of water, ethanol, or PC. The sols containing TEOS were vigorously stirred for about one hour before being mixed with the polymer solution, and the resulting sols were stirred for the next 2.5–3.0 hours at the temperatures in the range of 50–55 °C, until the end of the hydrolysis reaction, namely after about 30 minutes. The mass fractions of the organic additions were calculated with respect to the resulting content of organic part in the gels of about 20 wt. %, with weight concentration of PEO or PEG to low-molecular-weight organic additives equal to 1, and molar ratio of low-molecular-weight monomers equal to 1.

The solutions of TEOS and polymers with appropriate solvents, before being used, were first stirred for 2 days and then baked and degassed by vacuum heating at 50 °C for 3–4 hours.

Table 1. Components of the starting solutions (quality composition) of the investigated gels

Sample	Components/solvents	Salt/fraction	Appearance, remarks
R	TEOS	LiClO <sub>4</sub> /PC/0.03	silica glass, colourless, completely transparent
O	TEOS, 1,2-PG, PC	LiCl/H <sub>2</sub> O/0.02	organic glass, colourless, completely transparent
S	TEOS, PEO/CH <sub>3</sub> CN, PC, PO	LiClO <sub>4</sub> /PC/0.03	organic glass, slightly opalescent, colourless
Y	TEOS, PEG (6000)/H <sub>2</sub> O	LiClO <sub>4</sub> /PC/0.02	organic glass, slightly opalescent, colourless
T	TEOS, PEG(15000)/CH <sub>2</sub> Cl <sub>2</sub> , 1,2-PG, PO, PC	LiCl/H <sub>2</sub> O/0.03	organic glass, colourless, transparent
X	TEOS, EG, 1,2-PG	LiClO <sub>4</sub> /PC/0.03	organic glass, colourless, completely transparent
Z	TEOS, PEG (15000), PEO/CH <sub>2</sub> Cl <sub>2</sub> , 1,2-PG	LiCl/H <sub>2</sub> O/0.02	organic glass, slightly opalescent, colourless

No precipitations or liquid remains were observed in the organic-inorganic materials after gelation was complete. All the gels obtained were kept in closed containers for two weeks and then dried for a week at ambient temperature and for three hours in an electric drier at 80–125 °C. The same treatment was applied to gels prepared as thin layers, by casting immediately onto glass sheets coated with thin films of SnO<sub>2</sub>F and WO<sub>3</sub> or NiO. They were then used as transparent electrolytes in the electrochemical cells of an electrochromic window, and their suitability for such applications was examined. Thin electrochromic films of WO<sub>3</sub> and NiO on glass were obtained by pyrolysis at the temperatures in the range of 750–800 °C, using acetylacetonates of the appropriate metals as precursors. The detailed procedures of metal oxide film preparation have been described earlier [36].

The morphology, elemental chemical composition, and crystalline character of the hybrid electrolytes and silica gels obtained in this work were examined by SEM/EDS using scanning electron microscopy (JEOL JSM 5400) equipped with energy dispersive X-ray spectroscopy (LINK An 10/5) and X-ray diffraction (XRD 7, Seiffert diffractometer). Structural properties were investigated with FTIR spectroscopy (BIORAD FTS 60 VM, on samples prepared by the KBr pellet technique). <sup>13</sup>C, <sup>1</sup>H MAS NMR (Bruker AMX 500 spectrometer) measurements were made for sols at three stages (two days after preparing the mixtures, and subsequently a week and two weeks later). Spectral transmittance (UV/VIS/NIR, Jasco-570 spectrometer) and current-voltage (CV) characteristics were recorded in systems consisting of two glass sheet-coated with metal oxides and layers of the hybrid electrolytes under investigation in an electrochromic window arrangement. The WO<sub>3</sub> and NiO thin metal films and electrolyte layers, as measured with a “Talystep” (Taylor Hobson) stylus microprofilometer, were about 140 nm and 170 nm thick, respectively, while the layers of electrolytes were about 6 μm thick. Transparent electrodes were prepared with their conductive paths coated with Ag-paste on the face side. The electrodes were placed along one edge of the sample, but opposite to each other and with platinum wires fixed to the paths with Ag-paste. When sandwiched with an examined electrolyte, all the cells under investigation were sealed around the edges with silicon sealant. Low voltage

( $\pm$ ) polarized d.c. potential was applied to the cells through a potentiostat/galvanostat as the power source. A rectangular pulse of current was supplied using a galvanostat and a pulse generator. The d.c. electrical conductivity was measured by using domestically set equipment, with a potentiostat and four-point probe included. The current and potential differences for each pair of contacts between the probe and examined sample were monitored with a high impedance (larger than 1000 M $\Omega$ ) ammeter and voltmeter. Specific surface area and porosity were measured by N<sub>2</sub> adsorption at 77 K, using the BET and BJH equations, respectively).

### 3. Results and discussion

The names and appearance of the hybrid gel materials obtained are given in Table 1. The hybrid gels and silica gels prepared in order to compare their properties with those of hybrids were obtained in the form of the monolithic, colourless transparent discs with various thicknesses and diameters in the range of 20–50 mm. The hybrid materials were also obtained in the form of thin layers, immediately cast on glass coated with electrochromic thin metal oxide films. All the obtained hybrid electrolytes proved to be amorphous under XRD examination. The XRD patterns of typical hybrid electrolytes obtained in this work, named O, X and Y, are shown in Fig. 1.

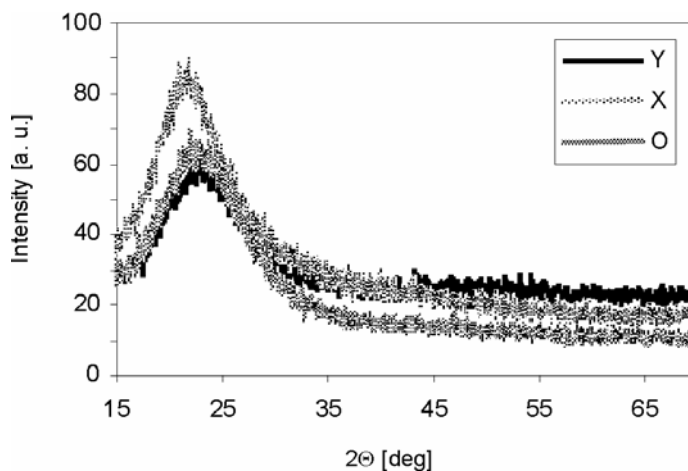


Fig. 1. X-ray diffraction patterns for sol-gel derived hybrid materials: O, X and Y

The morphologies of the hybrids and silica gels under investigation were observed using SEM/EDX. In Figure 2, planar-view SEM images of the hybrid gels (a–e) and silica gel doped with LiClO<sub>4</sub>/PC (f) are shown.

FTIR spectra of silica-gel-derived hybrid materials, as well as silica gels, are shown in Fig. 3, and the assignments of the characteristic absorption bands are given in Table 2.

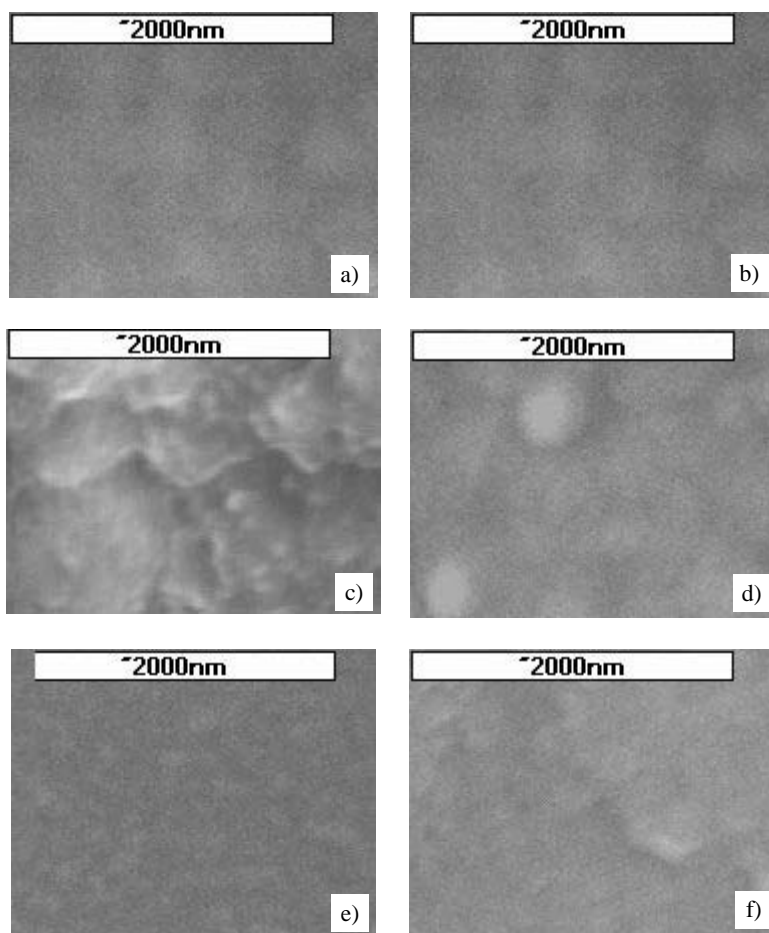


Fig. 2. SEM planar view images of hybrid organic-inorganic electrolytes: a) S, b) T, c) X, d) Y, e) Z and f) R: silica gel doped with  $\text{LiClO}_4$  dissolved in PC ( $x = 0.03$ )

Spectroscopic FTIR investigations (Fig. 3, Table 2) have revealed the presence of absorption bands characteristic of silicon–oxygen bonds, organic groups, and structural species connected to lithium bonding. Bands characteristic of water, both in the molecular (at about  $3400\text{ cm}^{-1}$ ) and adsorbed form (at about  $1620\text{ cm}^{-1}$ ) are also observed. Absorption bands in the wave number range  $624\text{--}778$  can be assumed to originate from organic structures ordered in molecular groups and in the presence of lithium atoms, but without phase separation or crystallization. Absorption bands at about  $630\text{ cm}^{-1}$  can be ascribed to  $\text{ClO}_4^-$ . The propylene oxide absorption band is also localized around that wave number [37]. The absorption band at about  $782\text{ cm}^{-1}$  is characteristic for hybrid gels and, according to Gunzler and Gremlich [38], can be ascribed to vibrations of the  $\text{O-Si-C}_n\text{H}_m$  species. It can therefore be considered as evidence of hybrid structure formation in the gels under investigation, with the organic and inorganic parts being connected to each other by oxygen bridges. In the spectra of all the

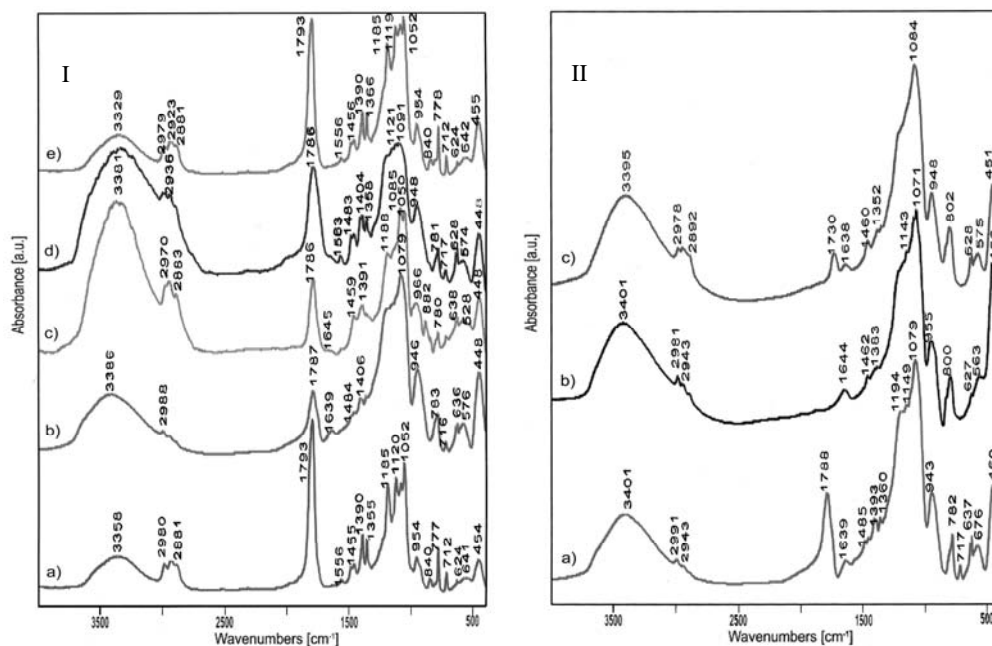


Fig. 3. FTIR spectra of organic-inorganic hybrid gels (heated for 3 hours at 125 °C): T (Ia), S (Ib), Y (Id), Z (Ie); (heated at 80 °C for 3 hours): X (Ic), O (II a); and R (II b, heated for 3 hours at 125 °C); (IIc-S heated for 5 hours at 210 °C). The main components used to obtain the gels and the gel names correspond to those in Table 1

gels obtained, absorption bands originating from Si-O-Si groups are present (the bending vibration of O-Si-O bridges is at about 450  $\text{cm}^{-1}$ , the stretching vibration of Si-O-Si bridges at about 1080  $\text{cm}^{-1}$ , and the asymmetric stretching vibrations of Si-OH groups at about 950  $\text{cm}^{-1}$ ).

In the case of the hybrid gels named X, Z and T, the fine structure of the main absorption band, located at about 1050–1100  $\text{cm}^{-1}$ , is clearly seen in their FTIR spectra. The observed splitting of this absorption band is probably connected to the vibrations of  $\text{R}_x\text{-Si-O}^-$  bridges. It can be concluded from its absolute intensity and width that the structure of the hybrid gel becomes more ordered in molecular groups in the presence of glycols as organic additives. It also implies less defected bonding states in the molecular groups, although without long distance ordering. The bands originating from the organic parts are found at 2880–2980  $\text{cm}^{-1}$  (C-H bonds), 1785  $\text{cm}^{-1}$ , and 1185 (C=O, C-O, respectively), and in the range 1330–1480  $\text{cm}^{-1}$  ( $\text{CH}_2\text{-O}$  and also likely  $\text{CH}_3$  groups). The observed increase in the intensity as well as the shifts in these bands are clearly connected to the addition of glycol species.

Table 3 shows typical results of a porous structure examination for the hybrid materials (S,T) and, for comparison, of silica gels (pure and doped with  $\text{LiClO}_4$  dissolved in PC, which were heated for 5 hours at 230 °C and 210 °C, respectively), together with results of d.c. conductivity measurements for the S and T hybrid electrolytes.

Table 2. Assignments of the characteristic bands in FTIR spectra [37–41]

Location of IR band about wave numbers, [cm <sup>-1</sup> ]							
Hybrid gels				Silica gels			
T	S	X	Y	Z	O	R	Origin
454	448	448	448	455	450	459	$\rho$ Si–O–Si
541	576	528	574	542	574	563	Li in LiClO <sub>4</sub> , Li with organics, Si–O ring (4)
624	636	638	628	624	637	628	ClO <sub>4</sub> <sup>-</sup> , Li–organics (PO)
712	719	716	717	712	717		$\nu$ SiO–C <sub>2</sub> H <sub>5</sub> , organics
777	783	780	781	778	782	800	$\nu_s$ Si–O–Si, $\nu_{as}$ Si–C, $\rho_{as}$ Si–CH <sub>2</sub> , Si–O–Si–C <sub>n</sub> H <sub>m</sub>
840		882		840			$\rho_s$ Si–CH <sub>2</sub>
954	946	966	948	954	943	955	$\nu_{as}$ Si–OH
1052	1079	1050 1085	1091	1052	1079	1071	$\nu_{as}$ Si–O–Si, $\nu_s$ Si–O–Si
1120			1121	1119	1149	1143	$\nu$ Si–O–R $\nu$ Si–O–Si,
1185	1185	1188	1199	1185	over- lapped		$\nu$ C–C, –OR (C <sub>2</sub> H <sub>5</sub> ), C–O, organics
1355 1390	1406	1391	1358, 1404	1355, 1390	1360, 1408	1383	organics, $\nu$ CH <sub>3</sub> , $\nu$ CH <sub>2</sub> –O
1455	1484	1459	1483	1456	1485	1462	$\nu$ C–O–C, organics
1556	1639	1645	1563	1556	1639	1644	H–O–H, molecular
1793	1787	1786	1785	1793	1788		organics, C=O
2881 –2980	2900 –2988	2883 –2970	2800 –2970	2881 –2979	2881 –2979	2943 –2981	$\nu_{as}$ CH <sub>2</sub> , $\nu$ C–H <sub>x</sub> of aliphatic organic groups
3358	3360 –3386	3381 (around)	3329 (around)	3340 (around)	3401	3401	$\nu$ OH, adsorbed H–O–H, LiOH

Table 3. Results of texture and conductivity examinations

Material	Silica gel pure	Silica gel doped with LiClO <sub>4</sub> /PC ( $x = 0.03$ )	$S$	$T$
Single point surface area [m <sup>2</sup> /g]	737.77	235.27	1.938	–
BET surface area [m <sup>2</sup> /g]	752.69	248.96	3.854	1,881
Langmuir surface area [m <sup>2</sup> /g]	1030.1	347.87	2.453	–
Micropore volume [cm <sup>3</sup> /g]	0.0943	–0.004	–	–
Micro-pore area [cm <sup>3</sup> /g]	219.3	2.6048	–	–
Single point total micro-pore volume, $V_{sing}$ [cm <sup>3</sup> /g]	0.3699	0.4177	0.00185	–
BJH adsorption meso-pores volume, $V_{meso}$ [cm <sup>3</sup> /g]	0.0928	0.4311	0.00293	–
Average micro-pore diameter (4V/A by BET) [nm]	1.9657	6.7103	1.9219	–
BJH adsorption average pore diameter [nm]	2.5623	5.6562	4.7708	–
Conductivity $\sigma_{25}$ [S·cm <sup>-1</sup> ]	–	$5.6 \times 10^{-5}$	$1.32 \times 10^{-3}$	$1.05 \times 10^{-3}$

The conductivities of the other hybrid electrolytes, not listed in Table 2, were all of the order  $10^{-3} \text{ S}\cdot\text{cm}^{-1}$ , and specifically 7.26, 6.54, 5.63, 2.14, and  $1.39\cdot 10^{-3} \text{ S}\cdot\text{cm}^{-1}$  for samples O, P, X, Y and Z, respectively. The examination of porous structure of hybrid materials containing glycols, especially those of low molecular weight, has proved to be practically aimless due to very low values of BET surface area. In the sol-gel process, the formation of sol particles occurs due to the hydrolysis of alkoxides and subsequent polycondensation of the hydrolysate and gelation of the sol particles. Murakata et al. [42] have investigated the influence of inorganic salts and some surfactants on the pore size distribution in silica gels and have found that the addition of any inorganic salt decreases the gel surface area and depresses the formation of mesopores. Such effects can be considered to be connected with a compression of the dielectric double layer around ions and with a reduction in coagulation stability, which are both effects of the pore size distribution of the gel being altered. They also have observed through SEM examination that the surfaces of gels with low concentrations of inorganic salt, especially those of univalent metals, become flat and smooth, practically without macropores. A similar effect has been obtained with non-ionic surfactants containing alkyl chains, especially PEG additives. Generally, the effect of such additives on the size distribution of the pores in silica gels has been found to be strongly dependent on alkyl chain length. Such results seem to be in good agreement with those obtained in this work from SEM observations and  $\text{N}_2$  adsorption measurements for hybrid electrolytes. In addition, polyethylene glycols are known for their hydrophilic properties, and organic low-molecular-weight additives of the hybrid materials obtained in this work can also act as solvents for lithium salts and the other organic components.

The influence of polyethylene glycol (PEG) on the nanostructure of sol-gel derived  $\text{TiO}_2$  coatings was studied by Kato and Hiihara [43] with the aim of obtaining nano-sized pores. They established that a temperature as high as  $400^\circ\text{C}$  was not enough to thermally decompose the PEG incorporated into titanium oxide.

In this work, SEM images show smooth and homogeneous surfaces of the samples under examination, and XRD patterns a wide broadening of the background for diffraction angles  $2\theta$  in the range  $15\text{--}35^\circ$ , which is characteristic of glassy amorphous materials. In addition, the room temperature conductivities obtained for all the hybrid electrolytes investigated were as high as  $10^{-3} \text{ S}\cdot\text{cm}^{-1}$ . These results can be attributed to suitable conditions, which enable the fast transportation of ionic charge carriers through hybrid electrolytes. Such a condition is a high amorphous phases content, which creates structural paths large enough to accommodate and allow hopping movements of lithium ion, as well as allow for the segmental motion of the polymer chains fragments involved in the structure of the hybrid materials. It is known that polymer electrolytes based on PEO that conduct lithium ions should be in an amorphous state for the effective transport of lithium and counter ions through the polymer.  $\text{Li}^+$  is thought to move by a hopping mechanism, which requires a segmental motion of the polymer host. Another model – a free volume model – suggests a corre-

lation of the ionic conductivity of  $\text{Li}^+$  with chain segment motion, in which ions move when a local void opens that can accommodate the ion, as is thought to occur in liquids [44].

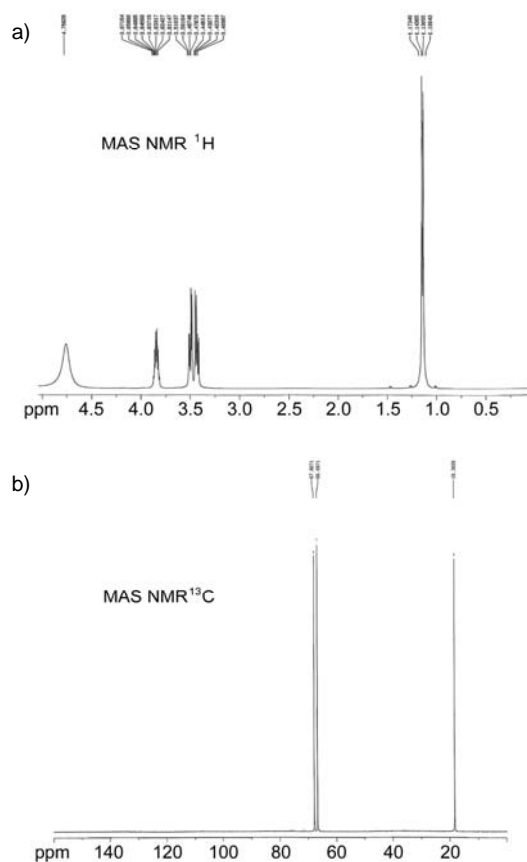


Fig. 4.  $^1\text{H}$  (a) and  $^{13}\text{C}$  (b) MAS NMR spectra for 1,2-propylene glycol (references for NMR measurements of the hybrid electrolytes O and X)

The addition of propylene carbonate and some other low molecular weight organic compounds to the PEO improves ionic transport by reducing the glass transition temperature of the polymer [7, 45, 46]. Ito et al. [45] have studied the influence of low-molecular-weight glycols on the ionic conductivity of the  $\text{PEO-LiCF}_3\text{SO}_3$  complex electrolyte and have established that the conductivity increases with the decreasing molecular weight of PEG and with increasing PEG content. Significant conductivity enhancement at room temperature can be attributed to an increase in the content of amorphous regions, which are responsible for ionic conduction. In alkali ion-conducting glasses, mobile ion conduction is also thought to proceed by means of free volume, i.e. voids, and at a given alkali content the ionic conductivity can be enhanced by increasing the free volume. Nevertheless, ionic conductivity is first of all

dependent on the number of mobile ions and on the ion–ion distance in conduction paths. The structural changes in silica bonding states due to organic additions and doping with lithium were expected to change the coordination of oxygen atoms, result in the partial dissociation of immobile species from non-bridging oxygen atoms, and enlarge the pathways available for migration of lithium ions in the frame of the silica host [47]. The characteristic structural properties of the hybrid materials obtained in this work, as revealed by infrared spectroscopy, can be considered to correspond well with such assumptions.

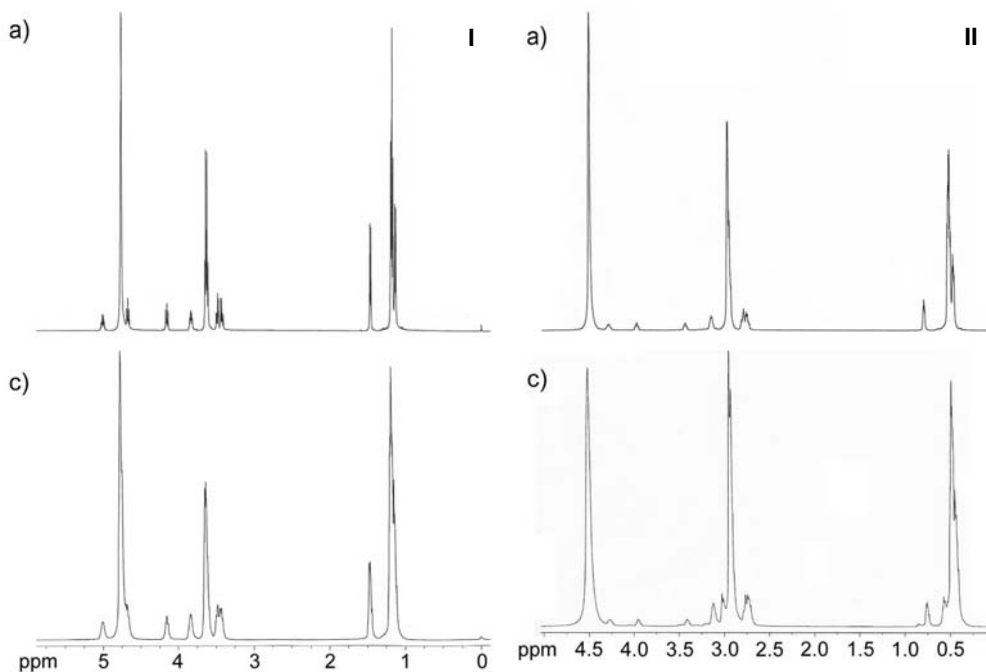


Fig. 5.  $^1\text{H}$  MAS NMR spectra for hybrid materials: O (I, stages a and c) and X (II, stages a and c)

The sharp diminishing of porous structures, which are significantly developed and clearly connected with the silica gel parts in hybrid materials containing other additives (PEO, PO), is especially pronounced for the O and X hybrid materials (which have low-molecular-weight glycols as organic additives). Samples of these two materials were examined additionally by MAS NMR ( $^{13}\text{C}$ ,  $^1\text{H}$ ) spectroscopy. The NMR spectra of samples of each material were recorded three times with a waiting time of about a week between each observation. The first time spectra were taken two days after the reaction of hydrolysis in the sols, and the following spectra were recorded 7 and 14 days later. The final MMR measurements were conducted a few hours before the complete sol to gel transformation had occurred. The NMR spectra of the hybrid materials O and X were referenced to those recorded for 1,2- propylene glycol.

The  $^1\text{H}$  and  $^{13}\text{C}$  NMR spectra for 1,2-propylene glycol are shown in Figs. 4a, b, respectively, and the spectra for the hybrid electrolytes O and X are given in Figs. 5–7.

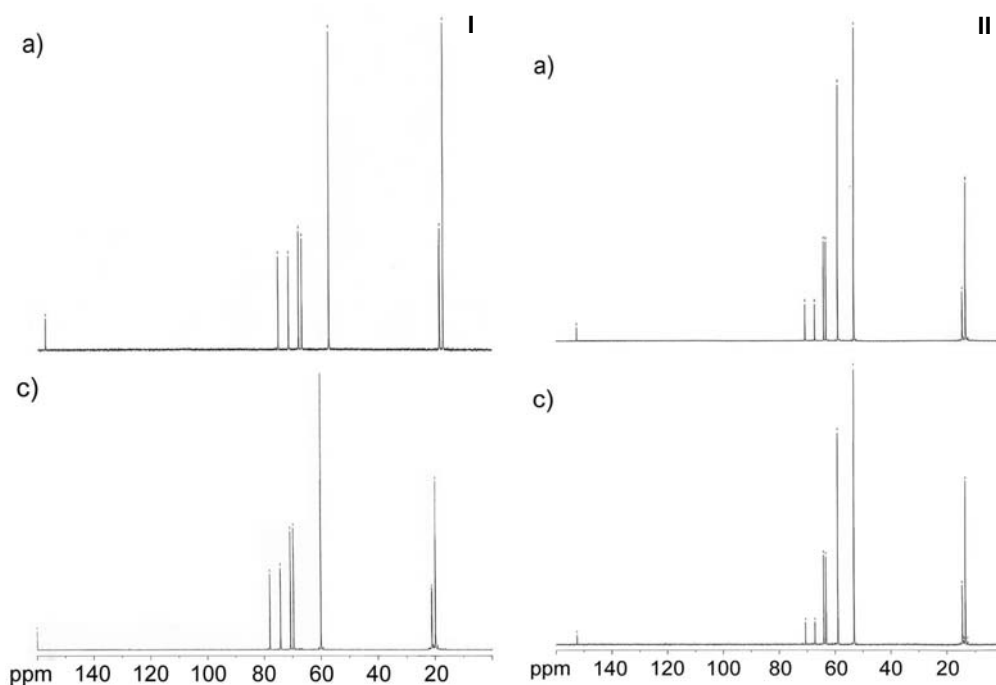


Fig. 6.  $^{13}\text{C}$  MAS NMR spectra for hybrid materials: O (I, stages a and c) and X (II, stages a and c)

No  $^1\text{H}$  or  $^{13}\text{C}$  MAS NMR spectra of hybrid gels obtained from mixtures of similar components to those under investigation here have been previously reported in the available literature. The chemical shifts and intensity changes of the signals originating from the starting components of the sols, as well as the appearance of new bands and disappearance of  $\text{D}_2\text{O}$  bands, which was used as a solvent for the O samples, can be ascribed to structural reordering due to the formation of the hybrid cross-linked structure between the organic and inorganic parts of the materials under investigation. In the spectra registered during the first two stages of the gelation process, only relatively small differences were observed, mainly intensity changes, which indicate that low-molecular-weight glycol species delay the waiting time for the resulting structural order, perhaps due to the cage effect. An example in which such an effect occurs has been described by Matějka et al. [48], where the sol-gel polymerisation of a hybrid material resulted in the growth of a polysilsesquioxane structure when glycidylpropyltrimethoxysilane was used. On the other hand, the reactivity of the O material, containing 1,2-propylene glycol and PC as organic additives, has proved to be high enough to incorporate all the  $\text{D}_2\text{O}$  applied as a solvent in the preparation of the sample for final NMR measurements (Fig. 7). In the region of silanol signals (dominated at 3.83–3.41 ppm, Fig. 7), there is a significant split, decrease in intensity,

as well as a chemical shift in signal localization, which is clearly connected with a cross-linked bonding process that develops between the organic and inorganic parts of the starting sols [49]. NMR studies of the hybrids synthesized in this work, among others, will be continued with the aim to explain the vanishing of porous structures (or capturing).

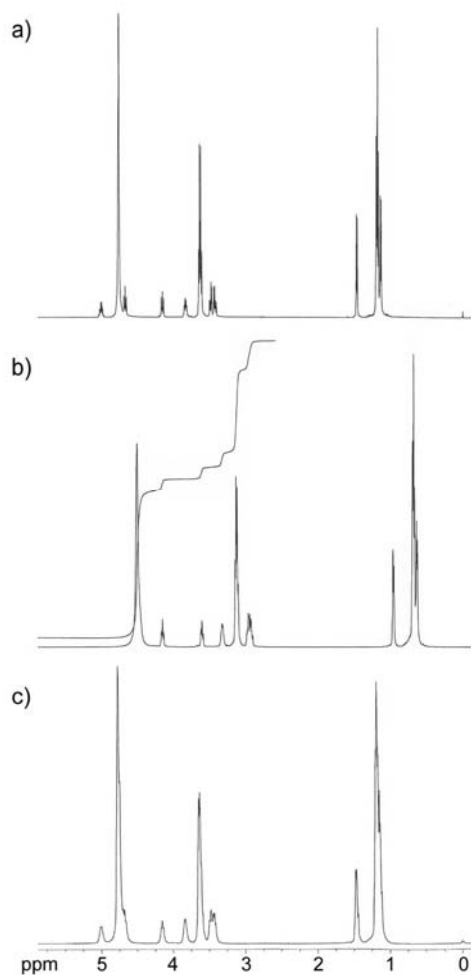


Fig. 7.  $^1\text{H}$  MAS NMR spectra for the hybrid material O (stages a–c)

The organic-inorganic hybrid materials obtained in this work were examined as electrolytes for cells based on the  $\text{WO}_3$  thin film with an electrochromic window arrangement. A typical response to a rectangular shaped current signal and a cyclic voltammogram (CV) taken for the electrochromic cell under ( $\pm$ ) polarized low d.c. voltage are shown in Fig. 8 (a, b), respectively. The transmission photometric charac-

teristics of  $\text{WO}_3$ -based electrochromic systems with a NiO film as the counter-electrode material are given in Fig. 9.

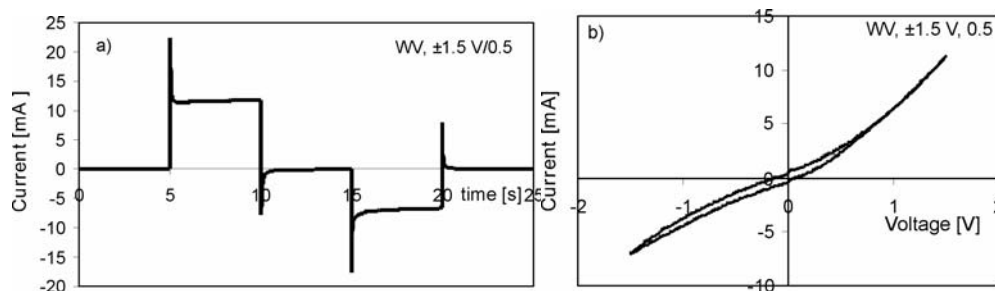


Fig. 8. Current response (a, plane line) and cyclic voltammogram (b, dashed line) for thin film tungsten oxide/organic-inorganic hybrid electrolyte Y (TEOS, PEG (6000)/ $\text{H}_2\text{O}$ ,  $\text{LiClO}_4/\text{PC}/0.02$ )/vanadium oxide electrochromic cell, cycled with a voltage of  $\pm 1.5$  V (cycled area  $3 \text{ cm}^2$ , scan rate  $50 \text{ mV/s}$ )

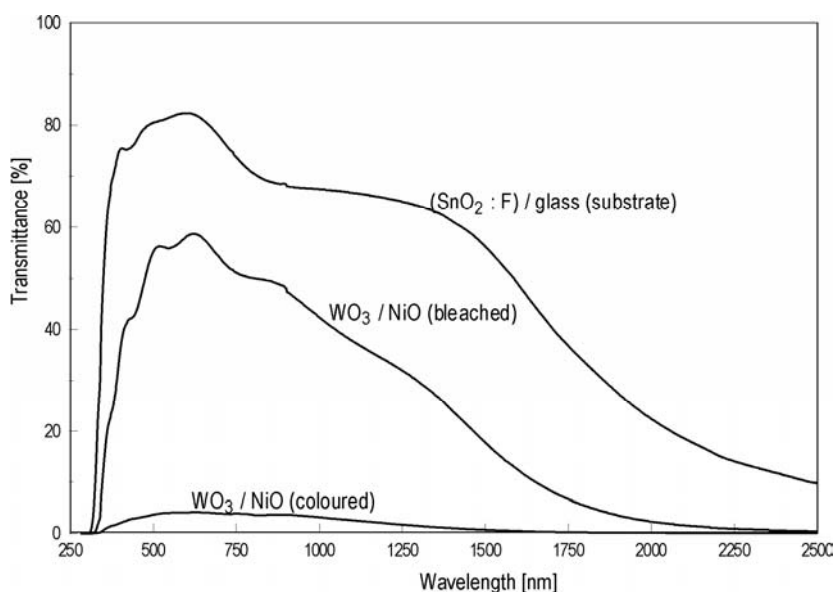


Fig. 9. Typical transmission characteristics as a function of the wavelength for a thin metal oxide electrochromic coating system:  $\text{WO}_3$ /organic-inorganic hybrid electrolyte Z (TEOS, PEO-PEG (15000)/ $\text{CH}_2\text{Cl}_2$ , 1,2-PG,  $\text{LiCl}/\text{H}_2\text{O}/0.02$ )/NiO, with electrochromic metal oxide materials coated by spray pyrolysis onto a glass substrate with  $(\text{SnO}_2:\text{F})$  layers, (presented in the coloured and bleached states, with lithium ions inserted/extracted into the  $\text{WO}_3$  structure under a d.c. voltage range of  $(\pm) 2.5$  V)

All the sol-gel derived hybrid materials obtained in this work were able to take part in electrochromic reactions, which depend on the insertion/extraction of lithium ions and injection/extraction of electrons, and which result in reversible dark blue or colourless states of the tungsten oxide layer. The d.c. conductivity values for the hybrid electrolytes under investigation were of the order of magnitude  $10^{-3} \text{ S}\cdot\text{cm}^{-1}$  when

measured at room temperature. They have proved to be dependent on composition and morphological properties, and connected with structural modifications due to organic additives. The values of ionic conductivity reported there, are improved by about one order of magnitude in comparison to those obtained by the authors previously for electrolytes of mixed silica–PEO systems (with and without chemical bonds between the organic and inorganic parts) [50], and similarly in comparison to the results reported by Dahmouche et al. [32] for hybrid electrolytes of silica–PEG<sub>300</sub> systems doped with lithium salt and without chemical bonds between the organic and inorganic phases. Generally, the ionic conductivity of sol-gel derived hybrid electrolytes is higher for those that are lithium ion and/or proton conductors [29]. The conductivity values of hybrid electrolytes obtained in this work with lithium salt doping are about two to three orders of magnitude higher than those described by Chaker et al. [35] for siloxane–PPO hybrid electrolytes doped with sodium perchlorate.

#### 4. Summary

Sol-gel derived, lithium ion conducting, amorphous, organic-inorganic hybrid materials, containing about 20% of organic additives, were obtained from TEOS, PEO, PO, PC, PEG, EG, and 1,2-PG with the aim to be used as solid electrolytes for electrochemical and optoelectronic applications.

All of the synthesized hybrid materials have proved to be amorphous and homogeneous, with morphology and textural properties significantly differing between each other, corresponding with the variety of compositions of the starting solutions. They were all stable at temperatures as high as 125 °C.

The organic-inorganic hybrid character of the gels obtained in this work has been confirmed by the results of infrared spectroscopy investigations.

All the hybrid sol-gel derived materials obtained have proved to be suitable as transparent and colourless lithium ion conducting electrolytes when examined in electrochemical cells with a thin film electrochromic window arrangement based on WO<sub>3</sub>, with a d.c. conductivity of the order of 10<sup>-3</sup> S·cm<sup>-1</sup>.

Additional studies are required and will be carried out with the aim of explaining the suppression of porous structures, as measured by nitrogen adsorption in hybrid materials with low molecular weight glycols as organic additives. The reason for this phenomenon, which is most intensively observed for the O and X hybrid materials, seems to be caused by liquid phase addition due to the cage effect and/or trapping.

#### Acknowledgement

Financial support of this work provided by the Ministry of Scientific Research and Information Technology, Department of Scientific Research, Poland, Grant No. 4 T08D 001 25 is gratefully acknowledged. The authors wish to thank Dr. Edward Szneler from the Department of Chemistry of the Jagiellonian University in Cracow, for NMR measurements.

## References

- [1] GRANQVIST C.G., AZENS A., ISIDORSSON J., KHARRAZI M., KULLMANN L., LINDSTRÖM T., NIKLASSON G.A., ROBBING C.-G., RÖNNOW D., MATSSON M.S., VESZELEI M., *J. Non-Cryst. Solids.*, 218 (1997), 273.
- [2] MATHEW J.G.H., SAPERS S.P., CUMBO M.J., O'BRIEN N.A., SARGENT R.S., RAKSHA V.P., LAHADERNE R.B., HICHWA B.P., *J. Non-Cryst. Solids.*, 218 (1997), 342.
- [3] BAUCKE F.G.K., *Mater. Sci. Eng.*, B10 (1991), 285.
- [4] KUWABARA K., ICHIKAWA S., SUGIYAMA K., *J. Mater. Sci.*, 22 (1987), 4499.
- [5] HUNT A., *J. Non-Cryst. Solids.*, 175 (1994), 59.
- [6] FAN J., MARZKE R.F., SANCHEZ E., ANGELL C.A., *J. Non Cryst. Solids.*, 172–174 (1994), 1178.
- [7] WALKER CH.W. Jr., SALOMON M., *J. Electrochem. Soc.*, 140 (1993), 3409.
- [8] J. FAN, P.S. FEDKIW, *J. Electrochem. Soc.*, 144 (1997), 399.
- [9] KUMAR B., RODRIGUES S.J., SCANLON L.G., *J. Electrochem. Soc.*, 148 (2001), A1191.
- [10] SUN H.Y., TAKEDA Y., IMANISHI N., YAMAMOTO O., SOHN H.-J., *J. Electrochem. Soc.*, 147 (2000), 2462.
- [11] ŻELAZOWSKA E., RYSIAKIEWICZ-PASEK E., *Mol. Phys. Reports.*, 35 (2002), 71.
- [12] DISLICH H., *J. Non-Cryst. Solids*, 73 (1985), 599.
- [13] PARASHAR V.K., RAMAN V., BAHL O.P., *J. Non-Cryst. Solids*, 201 (1996), 150.
- [14] VROON Z.A.E.P., SPEE C.I.M.A., *J. Non-Cryst. Solids*, 218 (1997), 189.
- [15] MALZBENDER J., DE WITH G., TOONDER J.M.J., *Thin Solid Films*, 366 (2000), 139.
- [16] GEORGI U., SCHLOTTING F., GRAEBNER H., VAN STEENSEL L., WOLF G., ROEWER G., *J. Non-Cryst. Solids*, 277 (2000), 173.
- [17] ŁĄCZKA M., CHOLEWA-KOWALSKA K., OLEJNICZAK Z., *Phys. Chem. of Glasses*, 43C (2002), 409.
- [18] PARK M., KOMARNENI S., CHOI J., *J. Mater. Sci.*, 33 (1998), 3817.
- [19] LI H.R., ZHANG H.J., LIN J., WANG S.B., YANG K.Y., *J. Non-Cryst. Solids*, 278 (2000), 218.
- [20] OH E.O., CHAKRABARTI K., JUNG H.Y., WHANG C.M., *Mater. Sci. Eng.*, B90 (2002), 60.
- [21] HAAS K.-H., AMBERG-SCHWAB S., ROSE C., *Thin Solid Films*, 351 (1999), 198.
- [22] PROSPITO P., CASALBONI M., DE MATTEIS F., PIZZOFRATTO R., *Thin Solid Films*, 373 (2000), 150.
- [23] HRUBESH L.W., *J. Non-Cryst. Solids*, 225 (1998), 335.
- [24] LAND D.V., HARRIS T.M., TEETERS D.C., *J. Non-Cryst. Solids*, 283 (2001), 11.
- [25] EINARSRUT M.-A., *J. Non-Cryst. Solids*, 225 (1998), 1.
- [26] MATSUDA A., KANZAKI T., TADANADA K., KOGURE T., TATSUMISAGO M., MINAMI T., *J. Electrochem. Soc.*, 149 (2002), E292.
- [27] HUANG H., WUNDER S.L., *J. Electrochem. Soc.*, 148 (2001), A279.
- [28] KONO M., HAYASHI E., NISHIURA M., WATANABE M., *J. Electrochem. Soc.*, 146 (1999), 1626.
- [29] NAKAJIMA H., NOMURA S., SUGIMOTO T., NISHIKAWA S., HONNA I., *Electrochem. Soc.*, 149 (2002), A953.
- [30] SONG J.Y., WANG Y.Y., WAN C.C., *J. Electrochem. Soc.*, 147 (2000), 3219.
- [31] POINSIGNON C., *Mater. Sci. Eng.*, B3 (1989), 31.
- [32] DAHMOUCHE K., ATIK M., MELLO N.C., BONAGAMBA T.J., PANEPUCCI H., AEGERTER A., JUDEINSTEIN P., *J. Sol-Gel Sci. Technol.*, 8 (1997), 711.
- [33] DAHMOUCHE K., SANTILLI C.V., DA SILVA M.A., RIBEIRO C.A., PULCINELLI S.H., CRAIEVICH A.F., *J. Non-Cryst. Solids*, 247 (1999), 108.
- [34] CHAKER J.A., DAHMOUCHE K., SANTILLI C.V., DA SILVA M.A., PULCINELLI S.H., BRIOIS V., FLANK A.-M., JUDEINSTEIN P., *J. Non-Cryst. Solids*, 304 (2002), 109.
- [35] AIHARA Y., APPETECCHI G.B., SCROSATI B., *J. Electrochem. Soc.*, 149 (2002), A849.
- [36] ŻELAZOWSKA E., ZIEMBA B., LACHMAN W., *Opt. Appl.*, 30 (2000), 663.
- [37] OGUMI Z., UCHIMOTO Y., TAKEHARA Z., *J. Electrochem. Soc.*, 136 (1989), 625.
- [38] GUNZLER H., GREMLICH H.-U., *IR Spectroscopy. An Introduction*, Wiley-VCH, Weinheim, 2002.
- [39] MARAGE P., LANGLET M., JOUBERT J.C., *Thin Solid Films*, 238 (1994), 218.

- [40] YING J.Y., BENZIGER J.B., NAVROTSKY A., J. Am. Ceram. Soc., 76 (1993), 2571.
- [41] MUNRO B., Glastech. Ber. Glass Sci. Technol., 68 (1995), 123.
- [42] MURAKATA T., SATO S., OHGAWARA T., WATANABE T., SUZUKI T., J. Mater. Sci., 27 (1992), 1567.
- [43] KATO K., KO-ICH HIIHARA, Thin Solid Films, 298 (1997), 76.
- [44] YOFFE A.D., Sol. State Ionics, 39 (1990), 1.
- [45] ITO Y., KANEHORI K., MIYAUCHI K., KUDO T., J. Mater. Sci., 22 (1987), 1845.
- [46] KUUTTI L.M.A., SEPPÄLÄ J.V., PASSINIEMI P., Sol. State Ionics, 39 (1990), 151.
- [47] DOI A., J. Non-Cryst. Solids, 246 (1999), 155.
- [48] MATĚJKA L., DUKH O., BRUS J., SIMONSICK W.J. Jr., MEISSNER B., J. Non Cryst. Solids, 270 (2000), 34.
- [49] BRUS J., ŠKRDLANTOVÁ M., J. Non Cryst. Solids, 281 (2001), 61.
- [50] ŽELAZOWSKA E., RYSIAKIEWICZ-PASEK E., Ceramics. Polish Ceramic Bull., 66/2 (2001), 637.

*Received 16 July 2004*  
*Revised 3 December 2004*

# The influence of ammonia, acetic acid and water vapour on the fluorescence of a 2-naphthol derivative in the Langmuir–Blodgett films

AGNIESZKA MIROŃCZYK<sup>1</sup>, ANDRZEJ JANKOWSKI<sup>1\*</sup>, ANTONI CHYLA<sup>2</sup>,  
ANDRZEJ OŻYHAR<sup>3</sup>, PIOTR DOBRYSZYCKI<sup>3</sup>

<sup>1</sup>University of Zielona Góra, Institute of Biotechnology and Environmental Science,  
ul. Monte Cassino 21b, 65-561 Zielona Góra, Poland

<sup>2</sup>Wrocław University of Technology, Institute of Physical and Theoretical Chemistry,  
Wybrzeże Wyspiańskiego 27, 50-370 Wrocław, Poland

<sup>3</sup>Wrocław University of Technology, Institute of Organic Chemistry, Biochemistry and Biotechnology,  
Wybrzeże Wyspiańskiego 27, 50-370 Wrocław, Poland

2-naphtholo-6-sulfonamide (NSDA) undergoes an excited state proton transfer to the environment when incorporated into Langmuir–Blodgett (LB) films. We present the effect of acetic and hydrochloric acids, as well as ammonia and water vapour, on the fluorescence and absorption spectra of LB films. Acetic acid inhibits deprotonation of the excited state (ESDP), enormously (by up to 2 orders of magnitude) increases the fluorescence quantum yield ( $\Phi$ ) of NSDA, blue-shifting its fluorescence band. The influence of hydrochloric acid on the fluorescence of NSDA is similar, although the enhancement of  $\Phi$  is lower in this case. Ammonia leads to the promotion of ESDP and an increase in  $\Phi$ . Water vapour does not change the fluorescence intensity markedly but it increases the probability of ESDP. These observations can be explained by the formation of a complex between acetic acid and NSDA, and by limited penetration of ammonia and water into the film.

Key words: 2-naphthol; fluorescence; Langmuir–Blodgett films

## 1. Introduction

The fluorescence of some dyes and aromatic compounds included into Langmuir–Blodgett (LB) films has been extensively studied [1–6]. Only scarce information is available in the literature, however, on the spectroscopy of compounds in LB films undergoing excited state proton transfer [1, 7]. The fluorescence spectra of such com-

---

\*Corresponding author, e.mail: jjj@wchuwr.chem.uni.wroc.pl.

pounds are very sensitive to the presence of acid and base vapours, due to varying proportions of the protonated ( $\text{ROH}^*$ ) and ionic ( $\text{RO}^-*$ ) forms of the fluorophore taking part in deprotonation of the excited state (ESDP) (Fig. 1). Therefore, one may expect that these substances, incorporated in LB films, may find application as chemical sensors [8] and signal processors [9]. On the other hand, investigations of the response of these substances to changes in atmosphere composition may throw a light onto the structure and physicochemical properties of LB films. We have shown [1] that 2-naphtholo-6-sulfonamide of dodecylamine (NSDA) included in a LB film can undergo ESDP to the environment. The scope of the present work is to explore the influence of gases on the electronic spectra of 2-naphthol derivatives in LB films.

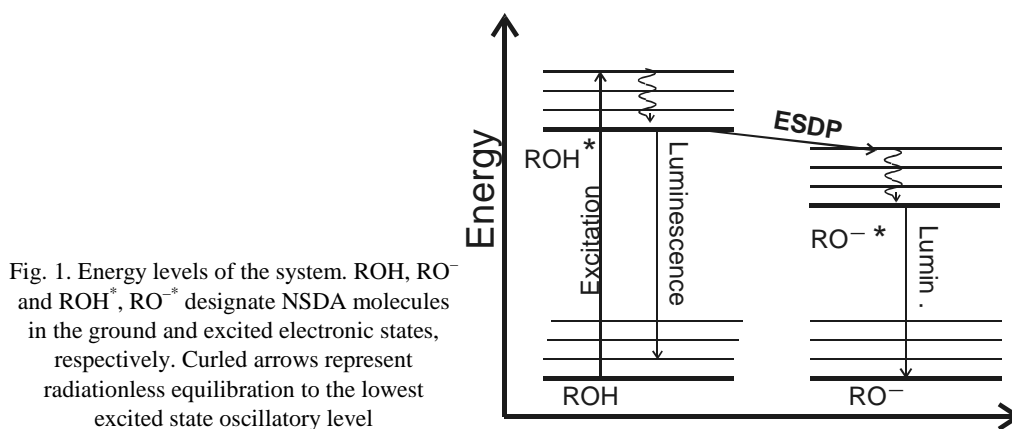


Fig. 1. Energy levels of the system. ROH,  $\text{RO}^-$  and  $\text{ROH}^*$ ,  $\text{RO}^-*$  designate NSDA molecules in the ground and excited electronic states, respectively. Curled arrows represent radiationless equilibration to the lowest excited state oscillatory level

The results are explained in terms of changes in the film structure under the influence of absorbed gases, penetrating into the layers and creating complexes with NSDA. The influence of modifying of the film composition by adding hydrophobic peptides (gramicidin A) on the film properties has also been studied.

## 2. Materials and methods

The synthesis of 2-naphtholo-6-sulfonamide of dodecylamine (NSDA), its chemical structure, and absorption, fluorescence, and phosphorescence properties are described elsewhere [1]. Gramicidin A from *Bacillus brevis* was purchased from Fluka and kept in 4 °C.

LB films containing NSDA were deposited onto quartz plates using a KSV-5000 trough (KSV, Finland) by means of a vertical dipping procedure. LB films of pure NSDA, as well as binary systems of NSDA with stearic acid or octadecylamine (0.05–0.2 mol fraction) were used. In some cases, gramicidin (G) was added to the system. The surface tension, transfer ratio, barrier speed, and diving and lifting speed were controlled during deposition. The average area per one molecule estimated for

pure NSDA films was  $0,323 \text{ nm}^2$ . Transfer isotherms of NSDA and NSDA diluted with stearic acid are shown in Figs. 2 and 3, respectively.

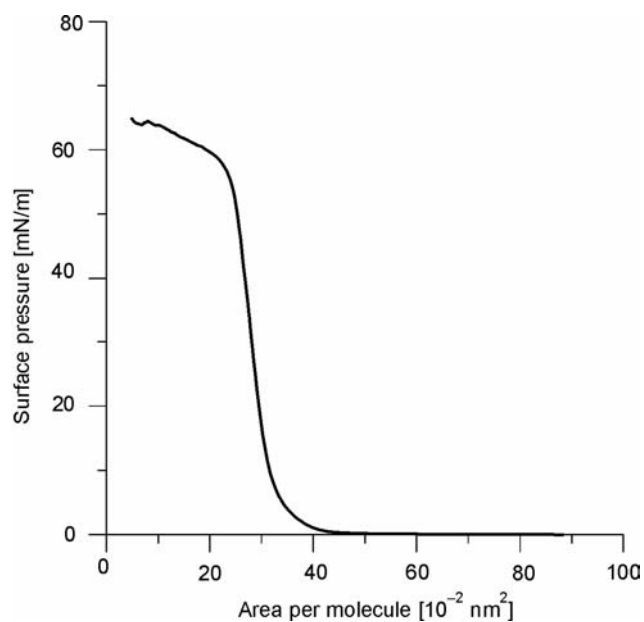


Fig. 2. The transfer isotherm of NSDA

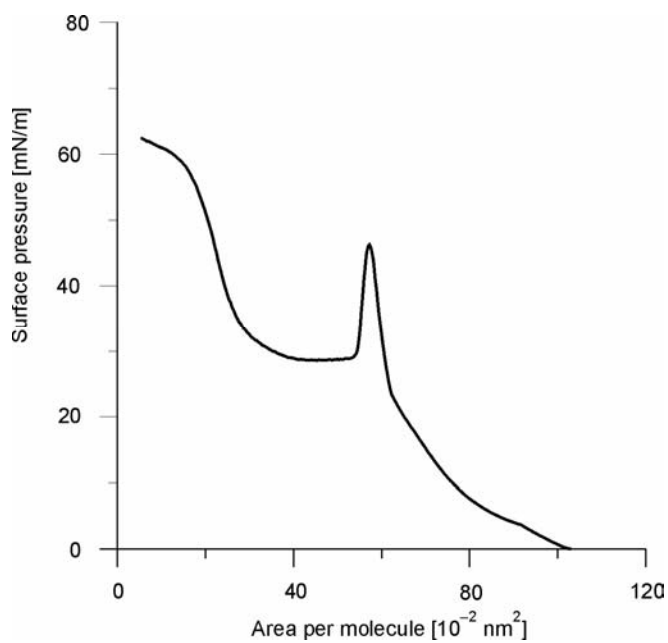


Fig. 3. The transfer isotherm of NSDA (0.1 molar fraction) diluted with stearic acid

To improve the anchoring of NSDA, the substrates (quartz plates) were covered prior to its deposition with a monomolecular layer of stearic or tricosanoic acid, with hydrophilic groups directed to the plate. The remaining procedure of LB film deposition depends on the type of layout required. The head to tail (○—○—) layout was obtained by upstroke movements of the substrate, initially placed under water. Before consecutive dippings, the films were left to dry and the water surface was cleaned. Repeating this procedure gave the layout required. In most cases, the transfer ratio was close to 1.

### 3. Results and discussion

#### 3.1. The absorption and fluorescence spectra of NSDA in LB films

Two characteristic bands can be discerned in the absorption spectra of LB films of NSDA at 210 nm (the absorbance of a 3-layer film being 0.073) and 320 nm (absorbance being 0.020). A low noise-to-signal ratio of about 5% and good reproducibility of the spectra confirms fair stability of the structures investigated.

Table 1. Absorption characteristics of NSDA in organic solvents and LB films (3 layers of NSDA)

System	Absorption maxima <sup>a</sup> [nm]		
	Band 1 ( $L_a$ )	Band 2 ( $L_b$ )	Band 3 ( $L_b$ )
NSDA in hexane	288	317	332
NSDA in CHCl <sub>3</sub>	286	320	337
NSDA in CH <sub>3</sub> OH	286	318	335
NSDA in LB film	300	320	337

<sup>a</sup> $L_a$  and  $L_b$  are the electronically excited levels of aromatic molecules according to Platt's notation.

The wavelengths of absorption band maxima for NSDA in organic solvents and in LB films are presented in Table 1. The absorbance at 320 nm was used to determine the fluorescence quantum yield.

In the fluorescence spectra of NSDA in LB films, two bands can usually be distinguished, centred at 370–393 nm (LM1) and 430–468 nm (LM2) [1]. The first one may be attributed to the protonated (ROH<sup>\*</sup>) form of NSDA and the other to its ionic (RO<sup>-\*</sup>) form. The positions of LM1 and LM2, as follows from the band separation procedure [1], depend on the degree of aggregation of NSDA molecules in the LB film. The fluorescence quantum yield  $\Phi$ , defined as a sum of the band heights at LM1 and LM2, and the excited state lifetime ( $\tau$ ) of selected layers of NSDA in LB films and of the analogous compound 2-naphtholo-6-sufonamide of glycine (2-NSGly) in methanol solution are given in Table 2. Both the fluorescence quantum yields and lifetimes for all LB films are greatly reduced, and that the positions of the absorption and emission bands are red shifted with respect to those of solutions.

Table 2. Fluorescence quantum yields ( $\Phi_n$ ), excited state lifetimes ( $\tau$ ), and ROH\* band positions (LM1<sub>n</sub>) in a neutral atmosphere

Sample Label <sup>a</sup>	Film layout	$\Phi_n$	LM1 <sub>n</sub> [nm]	LM2 [nm]	$\tau$ [ns]
2-NSGly <sup>b</sup>	—	0.18	363	454	4.76
1) TN.a	○—○— T:N	$1.9 \times 10^{-3}$	370	430	0.16
2) TNN.c	○—○—○ T : N : N	$7.5 \times 10^{-4}$	393	468	
3) TNN.b	○—○—○ T : N : N	$4.3 \times 10^{-3}$	384	456	
4) TNN.y	○—○—○—○— T : N : N	$1.9 \times 10^{-3}$	400	485	
5) NN.c	○—○—○ N:N	$8.8 \times 10^{-3}$	373	433	
6) NNN.1	○—○—○—○ N : N : N	$1.7 \times 10^{-4}$	380	440	
7) TNS.1 $x = 0.123$	○—○— T : N+S	$7.4 \times 10^{-3}$	391	447	0.268
8) TNS.1w $x = 0.100$	○—○— T : N+S	$1.0 \times 10^{-2}$	366	422	
9) TNS.3 $x = 0.050$	○—○— T : N+S	$3.3 \times 10^{-2}$	369	423	0.319
10) TNSNS.5 $x = 0.120$	○—○—○ T:N+S:N+S	$3.7 \times 10^{-3}$	389	468	0.438
11) TNSNS.z $x = 0.050$	○—○—○ T:N+S:N+S	$1.1 \times 10^{-2}$	379	442	0.621

<sup>a</sup> $x$  is the molar fraction of NSDA in the mixture, N – NSDA, T – tricosanoic acid, S – stearic acid.

<sup>b</sup>The data for 2-naphtholo-6-sulfonamide of glycine are taken from Ref. [10]

A similar effect was observed for organic chromophores incorporated into LB films [6]. Exploiting this analogy, the observed effects may be contributed to collective excitations (exciton effects) and energy transfer from fluorescent (F) to nonfluorescent (N) centres in the film [11, 12]. It can be noticed (Table 2) that NSDA films diluted with stearic acid (7–11) have much higher fluorescence quantum yields ( $\Phi$ ) than undiluted ones (1–6). Also, the films with higher molar fractions of NSDA and with chromophores closely located (3, 4) usually have lower values of  $\Phi$  than others. Octadecylamine as a diluter acts more or less similarly to stearic acid. This may be caused by hindering the aggregation of NSDA in films via dilution with nonfluorescent compounds.

### 3.2. The impact of acetic acid and HCl vapours on the fluorescence quantum yield, lifetime, and position of the ROH\* band maximum (LM1) of undiluted NSDA in LB films

When non-diluted LB films of NSDA are exposed to an atmosphere saturated with acetic acid, the dual fluorescence is converted into a one-band spectrum, centred at about 360 nm (LM1) (Fig. 4). A dramatic increase in the fluorescence quantum yield can also be observed. The values of  $\Phi$  and LM1 for selected layers are presented in Table 3.

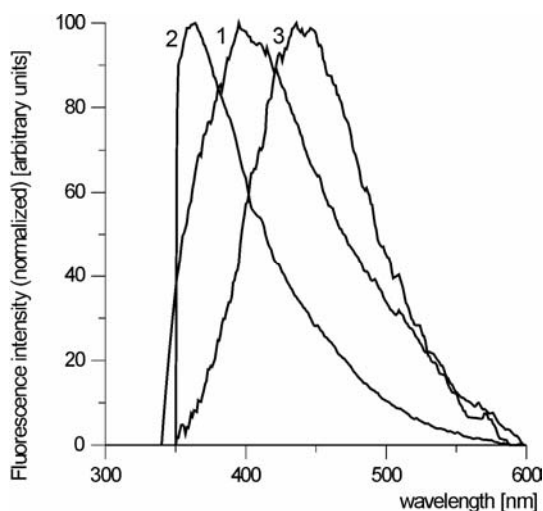


Fig. 4. Fluorescence spectra of the sample T:N:N.c (○—○) in a neutral atmosphere (1) and under the influence of acetic acid (2) and ammonia (3)

The impact of HCl vapours is similar; the dual fluorescence spectrum is replaced by a one-band spectrum. The effect on the fluorescence quantum yield, however, is much weaker. For instance, the fluorescence quantum yield of sample 4 in Table 3 after adding HCl is  $4 \times 10^{-3}$ .

Table 3. The fluorescence quantum yields ( $\Phi$ ) and positions of ROH\* band maxima for samples 1–6<sup>a</sup> in acetic acid ( $\Phi_{AA}$ , LM1<sub>AA</sub>)

Sample Label <sup>b</sup>	$\Phi_{AA}$	LM1 <sub>AA</sub> [nm]	$\Delta\%$ <sup>c</sup>
1) TN.a	$7.7 \times 10^{-3}$	367	75.3
2) TNN.b	$1.7 \times 10^{-2}$	360	74.7
3) TNN.c	$1.9 \times 10^{-3}$	375	60.5
4) TNN.y	$1.5 \times 10^{-2}$	368	87.3
5) NN.c	$1.5 \times 10^{-2}$	360	41.3
6) NNN.1	$3.7 \times 10^{-4}$	360	54.0

<sup>a</sup>The samples are labelled in the same way as in Table 2.

<sup>b</sup>Abbreviations are the same as in Table 2.

<sup>c</sup> $\Delta\% = 100(\Phi_{AA} - \Phi_0)/\Phi_{AA}$ .

The increase in fluorescence quantum yield in the presence of acetic acid vapour is accompanied by a blue shift of the ROH\* band (LM1). Both these spectral changes are accomplished within 10–15 min. These effects in acidic environment are opposite in direction to the changes in  $\Phi$  and LM1 ascribed to the aggregation process of fluorophore molecules [1]. A possible interpretation is that acetic acid decreases aggregation. This effect may be contributed to the formation of complexes of organic

acid and NSDA [10], which may substantially decrease the interaction between fluorophore molecules. The equilibrium constant of the formation of such complexes cannot not be high, since the fluorescence changes are rapidly reverted (5 min) after removing the acid from the environment.

### 3.3. The impact of ammonia on the fluorescence quantum yield, lifetime, and position of the RO<sup>-\*</sup> (LM2) band maximum of undiluted NSDA in LB films

The enhancement of the fluorescence quantum yield of the RO<sup>-\*</sup> form of NSDA in ammonia (AM) vapour, estimated with respect to a neutral atmosphere ( $\Phi'_{AM} - \Phi'_n$ ) (Table 4) is lower than the analogous change in acetic acid ( $\Phi_{AA} - \Phi_n$ ).

Table 4. The fluorescence quantum yields and positions of the RO<sup>-\*</sup> band maxima for samples 1–3<sup>a</sup> in ammonia vapour ( $\Phi_{AM}$ , LM2<sub>AM</sub>)

Sample Label <sup>b</sup>	$\Phi_{AM}$	LM2 <sub>AM</sub> [nm]	$\Delta\%$ <sup>c</sup>
1) TN.a	$2.0 \times 10^{-3}$	430	5.0
2) TNN.b	$9.0 \times 10^{-3}$	447	52.7
3) TNN.c	$1.9 \times 10^{-3}$	450	3.8

<sup>a</sup>Sample numbers are the same as in Tables 2, 3.

<sup>b</sup>See comments to Table 3.

<sup>c</sup> $\Delta\% = 100(\Phi_{AM} - \Phi_n)/\Phi_{AM}$ .

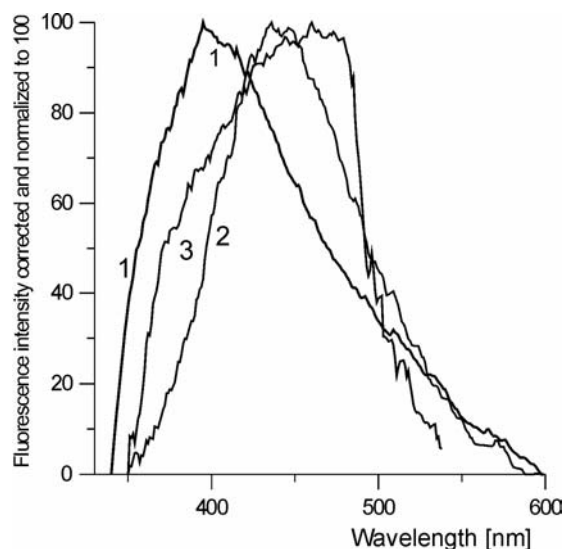


Fig. 5. Fluorescence spectra of the sample TNN.d (○—○—○) in a neutral atmosphere (1), in ammonia (2), and after removing NH<sub>3</sub> (3)

The penetration of  $\text{NH}_3$  into the film seems to be faster than that of acetic acid, since the changes in the fluorescence spectra are accomplished usually within 1 min after the admission of ammonia, while in acetic acid vapour gradual changes in the fluorescence spectra can be observed for 20 min. Moreover, the changes induced by ammonia are in most cases irreversible after equilibration in ambient atmosphere (Fig. 5), while those in acetic acid are usually reversible under the same conditions. Similarly, the absorption spectra of NSDA in LB films show irreversible changes under  $\text{NH}_3$ , though the variation is smaller than that of the fluorescence.

One can draw the conclusion that  $\text{NH}_3$  interacts with NSDA in the film, but that its penetration is limited to the outer sphere of the fluorophore aggregates, therefore its impact on fluorescence is less marked than that of acetic acid and is achieved faster.

### 3.4. The influence of acetic acid and ammonia vapour on the fluorescence quantum yield, lifetime, and position of the $\text{ROH}^*$ band maximum of NSDA in LB films diluted with nonfluorescent compounds

The increase of the fluorescence quantum yield in acetic acid vapour is higher for pure (undiluted) NSDA films (Table 3) than that for films diluted with stearic acid (Table 5) or octadecylamine. Moreover, the diluted samples, in contrast to undiluted ones, do not show a single emission from  $\text{ROH}^*$ , but always exhibit dual fluorescence in acetic acid (Fig. 6).

Table 5. The fluorescence quantum yields and positions of the  $\text{ROH}^*$  and  $\text{RO}^*$  band maxima for NSDA diluted by nonfluorescent compounds in acetic acid ( $\Phi_{\text{AA}}$ ,  $\text{LM1}_{\text{AA}}$ ) and ammonia vapour ( $\Phi_{\text{AM}}$ ,  $\text{LM2}_{\text{AM}}$ )

Sample <sup>a</sup>	$\Phi_{\text{AA}}$	$\text{LM1}_{\text{AA}}$ <sup>b</sup> [nm]	$\Phi_{\text{AM}}$	$\text{LM2}_{\text{AM}}$ [nm]	$\Delta\%$ <sup>c</sup>
1) TNS.1	$1.7 \times 10^{-2}$	387	–	–	56.4
2) TNS.1w	$2.5 \times 10^{-2}$	360	$2.1 \times 10^{-2}$	443	60.0
3) TNS.3	$1.8 \times 10^{-1}$	360	–	–	81.6
4) TNSNS.5	$8.7 \times 10^{-3}$	381	–	–	57.4
5) TNSNS.z	$2.9 \times 10^{-2}$	369	–	–	62.0

<sup>a</sup>Sample numbers correspond to No. 7–11 of Table 2, respectively.

<sup>b</sup>Abbreviations the same as in Table 2.

<sup>c</sup> $\Delta\% = 100(\Phi_{\text{AA}} - \Phi_{\text{n}})/\Phi_{\text{n}}$ .

The increase of  $\Phi'$  in AM ( $\Phi'_{\text{AM}} - \Phi'_{\text{n}}$ ) is also higher for the undiluted samples than that for the diluted ones. Such results suggest that aliphatic acid or octadecylamine, used for dilution, are included into the molecular aggregates of the fluorophores in the film. In some cases, acetic acid or ammonia can replace long-chain analogues in the aggregates. This would explain a less marked influence of the gases on the spectra compared to the undiluted samples. Similar to undiluted samples, the impact of  $\text{NH}_3$  is also irreversible for the diluted ones.

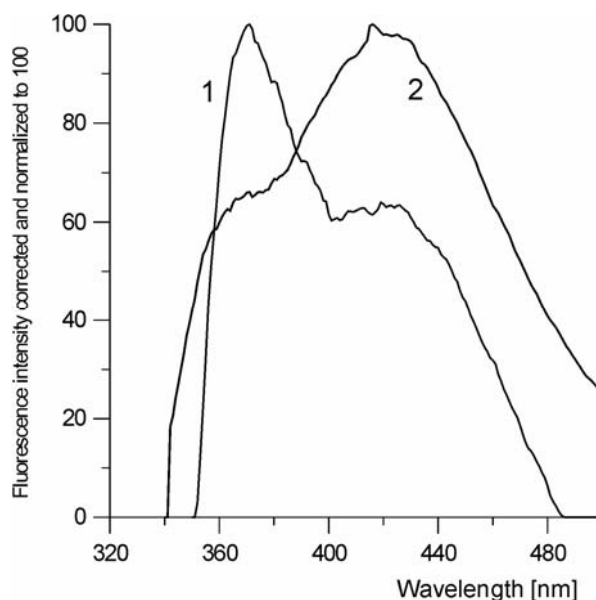


Fig. 6. Fluorescence spectrum of two samples of NSDA diluted with octadecylamine or stearic acid in acetic acid vapour after 30 min: curve 1 – film layout S:N+S,  $x = 0.098$ , curve 2 – film layout  $\circ - \circ - \circ$  S:N+O:N+O,  $x = 0.098$  (S – stearic acid, N – NSDA, O – octadecylamine,  $x$  – molar fraction of NSDA)

We have found the ratio  $\Phi_{AA}/\Phi_n$  to be between 2 and 10, and  $\Phi'_{AM}/\Phi'_n$  in most cases between 1 and 2 (Tables 2 and 4). At the same time, the ratios of the lifetimes of the excited states,  $\tau_{AA}/\tau_n$  and  $\tau_{AM}/\tau_n$ , are lower (eg. for sample 11 in Table 2,  $\tau_n = 0.621$  ns and  $\tau_{AA} = 0.810$  ns). The lack of proportionality between changes in  $\Phi$  and  $\tau$  may be explained by various influence of the organic acid on NSDA molecules in the fluorescent (F) and nonfluorescent (N) domains of the film.

### 3.5. Correlation between the position of the ROH\* band maximum (LM1) and fluorescence quantum yield and lifetime

As mentioned above, the reduction of the fluorescence quantum yield of NSDA in LB films with respect to that of the analogous compound in methanol is caused by the aggregation of chromophores and by the excitonic interaction of their electronic transition moments. For the same reason, we observe a spectral shift toward the red. Therefore, the decrease in  $\Phi$  should correlate with the red shift of the band maxima (LM1 and LM2). The dependence of  $\Phi$  on LM1 for NSDA diluted with stearic acid is shown in Fig. 7.

The data in Table 3 suggest that the limiting value of the ROH\* band position, which should be observed if acetic acid induces complete dissociation of aggregated NSDA molecules, is close to 360 nm.

This fact, together with the correlation of  $\Phi$  with LM1 (Fig. 7), suggests that at 360 nm the fluorescence quantum yield in the absence of ESDP and exciton effects ( $\Phi_{00}$ ) should be close to 0.04. This value is much lower than that for the analogous compounds in methanol (0.18) [6] which means that, even if NSDA molecules in the fluorescent centres (F) of a LB film do not interact with each other, there must be a certain number of NSDA molecules in the nonfluorescent (N) centres that contribute to the strong reduction of the fluorescence quantum yield. A correlation of the mean lifetime  $\tau$  of the excited state with LM1 by linear regression ( $r = 0.86$ ) yields the limiting value,  $\tau_{00}$ , near 1 ns. Correlations of  $\Phi$  and  $\tau$  with LM1 were obtained only for the samples in which NSDA was diluted with stearic acid. For undiluted NSDA in LB films, the correlation is worse.

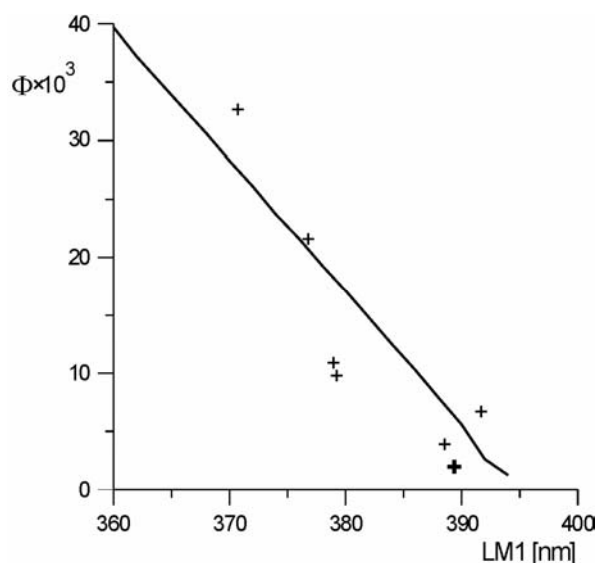


Fig. 7. The correlation of the  $\text{ROH}^{\oplus}$  band maximum position (LM1) with the fluorescence quantum yield for NSDA diluted with stearic acid. Correlation coefficient  $r = 0.81$

### 3.6. The influence of water on the fluorescence spectra of NSDA in LB films

It has been found that for NSDA in organic solvents and their mixtures with water the rate and efficiency of ESDP depends critically on the content of water [10]. It may be concluded by analogy to ESDP in solutions, that water molecules penetrating into the layer probably play the role of proton acceptors in LB films.

NSDA films diluted with aliphatic acid or octadecylamine and equilibrated in a laboratory atmosphere (humidity ca. 55%) show slight blue shift after injecting water to bottom of the measuring cuvette. The changes are subtle, but well reproducible for the diluted samples. In contrast to this, the fluorescence spectra of undiluted samples are much more sensitive to water (Fig. 8).

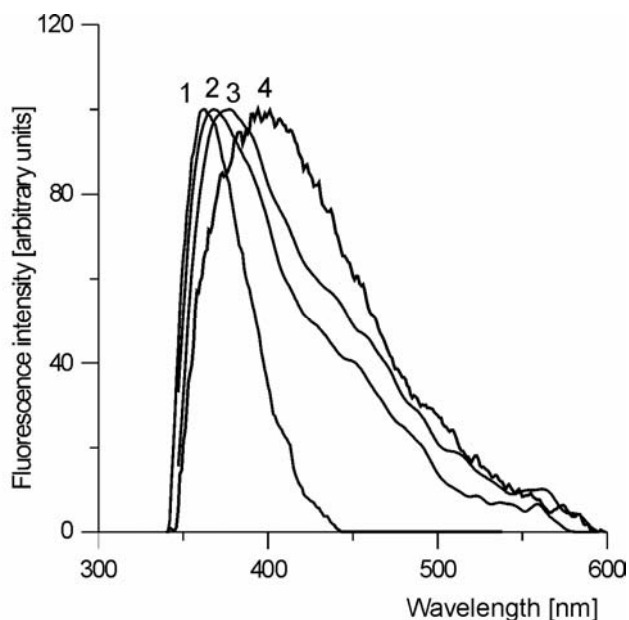


Fig. 8. Changes in the fluorescence spectrum of the sample T:N:N.d (—○—○—○) under the influence of water and acetic acid: in acetic acid (1), in H<sub>2</sub>O 10 min (2), in H<sub>2</sub>O 20 min (3), in a neutral atmosphere (4) (see also Fig. 5 of [1])

The spectrum obtained immediately after drying the sample in a vacuum desiccator differs significantly from the spectrum of the same sample equilibrated at ambient atmosphere (Fig. 5 of ref. [1]). Even the spectrum recorded in a laboratory atmosphere (humidity 55%) is considerably changed by the addition of 0.05 cm<sup>3</sup> of water to the bottom of measuring cuvette. The changes are markedly dependent on time (Fig. 8). After increasing humidity, the fluorescence band is blue-shifted within 10 minutes to almost its position in the spectrum in acetic acid. This effect may be caused by partial dissociation of the aggregates of NSDA in water. After some time (a further 10 min), the emission band is red-shifted, approaching its position in a neutral atmosphere, and the intensity of the other band at about 450 nm, attributed to the RO<sup>\*</sup> form, increases. This last process may occur as an answer to the increasing rate of ESDP by the formation of hydrogen bonds with water molecules.

### 3.7. The influence of gramicidin A on the penetration of gases into LB films containing NSDA

Gramicidin (G) is a peptide antibiotic that increases the permeability of cell membranes to protons, thus uncoupling the energy transforming mechanism of the cell. G forms channels in cell membranes, with hydrophobic residues directed outside and hydrophilic CO and NH groups oriented inside the channel and forming intramolecular hydrogen bonds [13].

The effect of G on the permeation of acetic acid into the LB film is depicted in Fig. 9. As stated above (section 3.4), the dilution of NSDA by stearic acid (S) in LB film inhibits the penetration of acetic acid into the specimen, which is concluded from the fact that the acid does not influence the shape of the fluorescence spectrum as it does in undiluted films.

The impact of acetic acid in the case of undiluted samples is contributed (section 3.2) to the formation of complexes with NSDA. If gramicidin A is added to a layer of NSDA, the change in the spectrum is characteristic of undiluted samples and consists of band narrowing and a blue spectral shift after the admission of acetic acid (Fig. 9, curve 4). It follows that G promotes the penetration of acetic acid into films diluted with S. The addition of G to the nonfluorescent layer of S gives no such effect (curve 3). Gramicidin also gives an increase to the permeation of water and ammonia into the film.

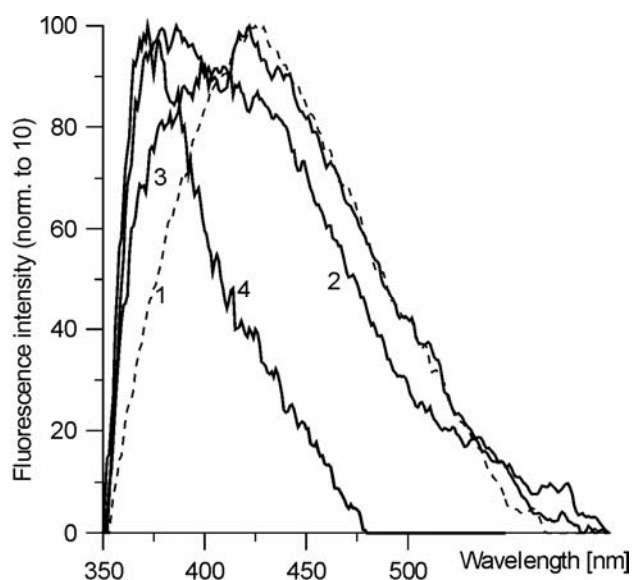


Fig. 9. The influence of gramicidin A on the penetration of acetic acid into LB films.

Fluorescence spectra of LB films containing NSDA (N) diluted with stearic acid (S) and gramicidin (G): 1 – in a neutral atmosphere, film layout:  $\circ$ — $\circ$  N+S+G: S+G, 2 – sample as in (1) in acetic acid vapour after 2 min, 3 – similar sample with the film layout:  $\circ$ — $\circ$  N+S : S+G in acetic acid vapour after 60 min, 4 – sample as in (1) in acetic acid vapour after 20 min

## 4. Conclusions

The absorption of acetic acid, HCl, NH<sub>3</sub>, and water into a LB film strongly affects the fluorescence of NSDA. The observed changes consist in an increase in the fluorescence intensity and a blue shift of the band maximum, probably caused by the intercalation of gas molecules into the layer of NSDA. A small quantity of water is

probably present even in samples dried in a desiccator. Water molecules penetrating the film would approach only the phenolic groups of NSDA, but not the aromatic chromophore. Therefore, increasing the content of water does not greatly influence the structure of NSDA aggregates in LB films. In consequence, the fluorescence quantum yield remains practically unchanged.

Ammonia, on the other hand, promotes excited state deprotonation (ESDP) and enhances, to a limited degree, the quantum yield. It may be therefore assumed that  $\text{NH}_3$  also does not interact directly with the fluorophore, but only with water molecules, inducing the polarization of the aggregate as a whole and an irreversible change in the molecular arrangement of the film.

Acetic acid can form complexes with NSDA molecules in LB films, which probably leads to the dissociation of aggregates. The formation of complexes between acetic acid and 2-naphthol analogues has already been postulated for an environment with low polarity (see [10] and references therein). The arising of such complexes can lead to an increase of  $\Phi$  greater than that in ammonia, due to the dissociation of fluorophore aggregates in the film. Moreover, the binding of acetic acid may also cause the apparent inhibition of ESDP by the rapid reprotonation of the excited phenolate.

The effects described here may be used in molecular switches [9] due to the dependence of the response of samples on atmosphere composition. The possibility of modifying this response by specific additives is another advantageous property of such systems.

## References

- [1] MIROŃCZYK A., JANKOWSKI A., CHYLA A., OŻYHAR A., DOBRYSZYCKI P., *J. Phys. Chem. A*, 108 (2004), 5308.
- [2] KAJIWARA T., CHAMBERS R., KAERNS D., *Chem. Phys. Lett.*, 22 (1973), 38.
- [3] VIEIRA FERREIRA L., ROSARIO M., GARCIA A., *J. Chem. Soc. Faraday Trans.*, 88 (1992), 15.
- [4] KESTI T., VEHMANEN V., MÖRSKY S., TKACHENKO T., EFIMOV A., LEMMETYINEN H., *J. Mater. Chem.*, 10 (2000), 2283.
- [5] ORBULESCU J., MELLO S., QUN HUO G., SUI P., KELE R., LEBLANC R., *Langmuir*, 17 (2001), 1525.
- [6] RAY K., NAKAHARA H., *J. Phys. Chem. B*, 106 (2002), 92.
- [7] ILICHEV Y., SOLNTSEV K., DEMYASHKEVICH A., KUZMIN M., *Chem. Phys. Lett.*, 193 (1992), 128.
- [8] KANG K., KIM J., KIM D., JUNG S., CHANG J., KWON Y., *Sensors and Actuators B*, 77 (2001), 293.
- [9] DE SILVA A., GUNARATNE H., GUNNLAUGSON TH., HUXLEY A., MC COY C., RADEMACHER J., RICE T., *Chem. Reviews*, 97 (1997), 1515.
- [10] MIROŃCZYK A., JANKOWSKI A., *J. Photochem. Photobiol. A*, 153 (2002), 89.
- [11] LAGUITTON-PASQUIER H., PEVENAGE D., BALLEST P., VUORIMAA E., LEMMETYINEN H., JEURIS K., DE SCHRYVER F., VAN DER AUWERER M., [in:] B. Valeur, J. Brochon (Eds.), *New Trends in Fluorescence Spectroscopy*, Springer-Verlag, Berlin, 2001, pp. 100–124.
- [12] KASHA M., RAWLS H., EL-BAYOUMI A., *Pure Applied Chem.*, 11 (1965), 371.
- [13] OVCHINNIKOV Y.A., *Bioorganic Chemistry* (in Russian), Prosvesheniye, Moscow, 1988, p. 599.

Received 26 July 2004

Revised 6 September 2004

## **New ceramic superionic materials for IT-SOFC applications**

GRZEGORZ PAŚCIAK<sup>\*</sup>, JACEK CHMIELOWIEC, PIOTR BUJŁO

Electrotechnical Institute Division of Electrotechnology and Materials Science  
ul. M. Skłodowskiej Curie 55/61, 50-369 Wrocław, Poland

The syntheses of new ceramic superionic materials based on  $\text{Bi}_2\text{O}_3$  (BIMEVOX and  $\delta\text{-Bi}_2\text{O}_3$ ), their elemental analyses, thermodynamical stability, and electrical properties are presented. The materials show high ionic conductivities (ca. 0.1 S/cm) at a relatively low temperature (600 °C), which makes them applicable as electrolytes in IT-SOFC fuel cells. Ionic conductivity measurements of these materials were performed with the DC (four probe configuration) and IS (impedance spectroscopy) methods, whereas structural research was performed using X-ray spectroscopy. Investigations of the thermodynamic stability of the elaborated materials in oxygen-free atmosphere were also performed. Based on the results of the investigations, the most suitable superionic conductors for fuel cell were selected.

*Key words: impedance; ionic conductivity; fuel cells; membranes*

### **1. Introduction**

In recent years, continuous development and an increase in the amount of energy produced from alternative sources is observed. Among others, special attention is paid to intermediate temperature solid oxide fuel cells (IT-SOFC) due to their high efficiency of conversion of chemical energy stored in a fuel into electricity (ca. 60%) [1], quiet and pollution-free operation, the possibility of supplying energy from different kinds of fuels, high resistance to unfavourable atmospheric phenomena and natural disasters, making them very attractive in terms of their application. High working temperature enables easy recovery of waste heat in combined heat and power systems.

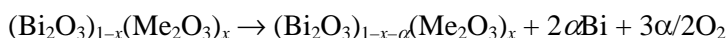
The element of the cell having the greatest impact on the fuel cell efficiency, production cost, and stable operation is the electrolyte. It should be characterised by high ionic conductivity (at least 0.1 S/cm) at relatively low temperature, impermeability to

---

<sup>\*</sup>Corresponding author, e-mail: pasciak@iel.wroc.pl.

gases, high mechanical strength, good resistance to thermal shock, and thermodynamic stability (especially in a reducing atmosphere).

Until now, stabilized  $ZrO_2$  was the most often used electrolyte in SOFC. It has satisfactory mechanical and electrical parameters, but a very high working temperature (ca. 1000 °C), limiting its commercial applications. The present authors investigated the possibility of applying  $Bi_2O_3$ -based solid solutions and the BIMEVOX family of electrolytes, being good ionic conductors ( $O^{2-}$ ) at relatively low temperatures (ca. 600 °C). A high-temperature and highly ionically conductive ( $O^{2-}$ ) modification of  $\delta$  bismuth oxide could be stabilized at lower temperatures by adding rare earth oxides ( $L_2O_3$ , where  $L = Gd, Er, Dy, Y, Ho, Nd, Sm$ ) [2]. No sudden decrease in the ionic conductivity of doped  $\delta$ - $Bi_2O_3$  is observed, which takes place during the phase transitions  $\delta \rightarrow \gamma$  and  $\delta \rightarrow \alpha$  when a sample of pure  $Bi_2O_3$  is cooled. The doped samples, however, are reactive in oxygen-free atmosphere or at a very low oxygen concentration in atmosphere; the reduction of oxide to metallic Bi takes place [3–5]:



Thus the use of  $Bi_2O_3$ -based oxide-doped electrolytes requires that a “safe” oxide concentration range be known precisely.

The BIMEVOX (BI – bismuth, ME – additive metal, V – vanadium, OX – oxygen) family of electrolytes belongs to the newest generation of electrolytes based on  $Bi_2O_3$ . The basic compound of the BIMEVOX family is  $\gamma$ - $Bi_2VO_{5.5}$ . A high-temperature, highly ionically conductive modification of  $\gamma$ - $Bi_2VO_{5.5}$  is stabilized to lower temperatures by adding an oxide of another metal (e.g. Cu, Ni, Zn, Fe, Co, Mg) [6–10]. Moreover, these electrolytes have the ability to dynamically self-transform into electrode materials under polarization [11], so a BIMEVOX membrane could be used without other electrode materials.

In order to select the most appropriate electrolyte for IT-SOFC applications:

- 18 electrolyte bulks were synthesized and samples in the form of beams, tablets, and screen-printed layers were prepared;
- X-ray investigations of the composition and thermodynamic stability of the synthesized bulks were performed;
- the ionic conductivities of the electrolyte samples were measured using the DC and IS methods.

## 2. Experiments

*Sample preparation.* Electrolyte samples were prepared in the form of beams, pellets, and screen-printed layers (Fig. 1). Pellets and beams were pressed at 500 kG/cm<sup>2</sup> and then sintered. Thin layers were applied on an alundum base with a plotted Pt heater and Pt electrode (Fig. 2). This method is suitable for making relatively thin

layers of electrolyte, ca. 0.1 mm thick. The composition of the electrolyte bulks and the preparation method are presented in Table 1.

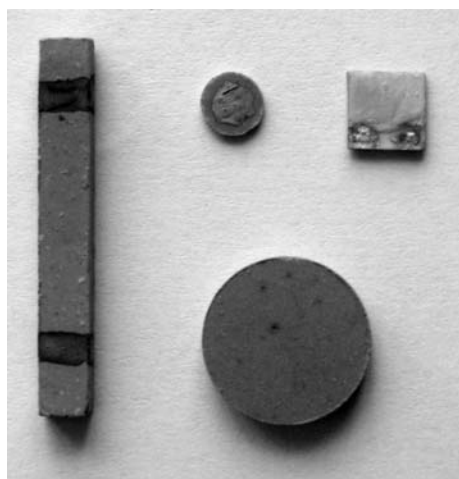


Fig. 1. Electrolyte samples: beam, tablet, and printed electrolyte layer

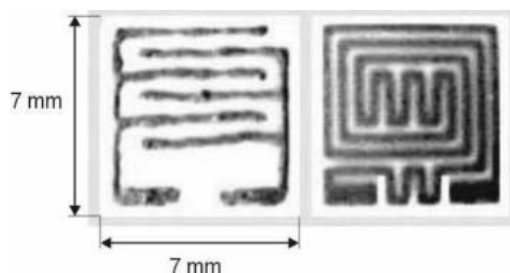


Fig. 2. Comb electrode and a heater, applied on an alumina base by using the screen-printing method (averse and reverse)

Table 1. Compound formulas and synthesis conditions of the investigated masses

No.	Compound formula	Name	Synthesis condition
1	$\text{Bi}_2\text{V}_{0.75}\text{Cr}_{0.25}\text{O}_{5.25}$	$\alpha$ -BIMEVOX	sintering 800 °C, 12 h
2	$\text{Bi}_2\text{V}_{0.9}\text{Sb}_{0.1}\text{O}_{5.4}$	$\gamma$ -BIMEVOX	
3	$\text{Bi}_2\text{V}_{0.9}\text{Co}_{0.1}\text{O}_{5.4}$	BICOVOX	
4	$\text{Bi}_2\text{V}_{0.875}\text{Ti}_{0.125}\text{O}_{5.4375}$	BIMEVOX	
5	$\text{Bi}_2\text{V}_{0.86}\text{Zn}_{0.1}\text{O}_{5.25}$	BIMEVOX	
6	$\text{Bi}_2\text{V}_{0.73}\text{Zn}_{0.27}\text{O}_{5.095}$	BIZNVOX.27	
7	$\text{Bi}_2\text{V}_{0.9}\text{Cu}_{0.1}\text{O}_{5.35}$	BICUVOX.10	
8	$\text{Bi}_4\text{V}_2\text{O}_{11}$	BIVOX	sintering 830 °C, 12 h
9	$\text{Bi}_4\text{V}_{1.9}\text{Co}_{0.1}\text{O}_{10.85}$	BICOVOX	
10	$\text{Bi}_4\text{V}_{1.8}\text{Co}_{0.2}\text{O}_{10.7}$	BICOVOX	
11	$\text{Bi}_2\text{Co}_{0.1}\text{V}_{0.9}\text{O}_{5.35}$	BICOVOX	calcination 610 °C, sintering 800 °C, 12 h
12	$(\text{Bi}_{0.95}\text{Zr}_{0.05}\text{O}_{1.525})_{0.8}(\text{YO}_{1.5})_{0.2}$	stabilized $\delta$ - $\text{Bi}_2\text{O}_3$	830 °C, 12 h
13	$\text{Bi}_4\text{V}_{1.95}\text{Fe}_{0.05}\text{O}_{10.95}$	BIMEVOX	sintering 850 °C, 24 h, slowly cooled to room temperature
14	$\text{Bi}_4\text{V}_{1.9}\text{Fe}_{0.1}\text{O}_{10.9}$	BIMEVOX	
15	$\text{Bi}_4\text{V}_{1.8}\text{Fe}_{0.2}\text{O}_{10.8}$	BIMEVOX	
16	$\text{Bi}_4\text{V}_{1.5}\text{Fe}_{0.5}\text{O}_{10.5}$	BIMEVOX	
17	$\text{Bi}_4\text{V}_{1.75}\text{Fe}_{0.25}\text{O}_{10.75}$	BIMEVOX	
18	$\text{Bi}_4\text{V}_{1.7}\text{Fe}_{0.3}\text{O}_{10.7}$	BIMEVOX	

*X-ray stability investigations.* X-ray measurements of the phase composition of the electrolyte bulks and investigations of the thermodynamic stability in reducing atmos-

phere were performed with an X-ray diffractometer DRON-2 with Co radiation filtered with Fe. XRD was measured in the  $2\theta$  range from 10 to  $95^\circ$ .

*Four-probe DC measurements of ionic conductivity.* A scheme of the four-probe configuration for ionic conductivity measurements using Wagner's method is presented in Fig. 3. The measurements were made with the samples prepared from the synthesized material in the form of beams with platinum electrodes. Ionic conductivities were measured during the heating and cooling of the samples (the current – 0.1 and 1 mA).

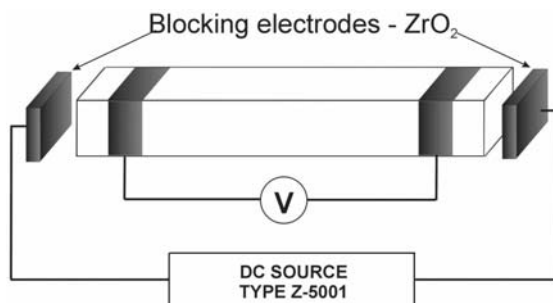


Fig. 3. Scheme of the system used for measurements of ionic conductivity, DC four-probe Wagner method

*IS measurements of ionic conductivity.* Impedance measurements of ionic conductivity [12] were performed for electrolyte layers applied on an alumina base using the screen-printing method. The real and imaginary part of the impedance (impedance spectra) were measured at frequencies from 20 Hz to 1 MHz and in the temperature range from 20 to 700 °C. The amplitude of the sinusoidal sampling signal was 20 mV. An RLC meter (HP 4284A) was used. The samples were heated with a platinum heater, placed on the reverse side of the alumina base. Temperature was determined based on the measured linear dependence of the heater resistance on temperature. A schematic diagram of the test stand is presented in Fig. 4.

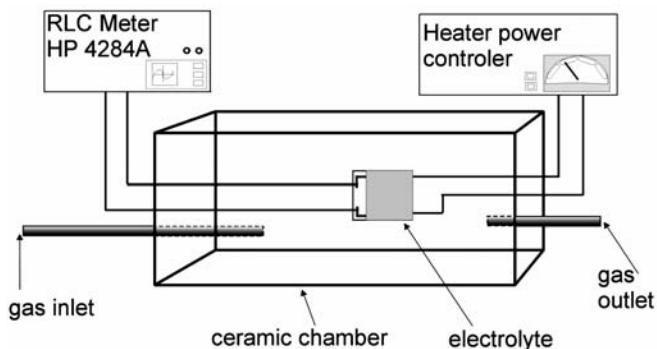


Fig. 4. Scheme of the test stand used for measurement of ionic conductivity, IS impedance spectroscopy method

### 3. Results and dicussion

#### 3.1. X-ray investigations of the composition and thermodynamic stability of selected electrolytes

X-ray spectra of selected electrolytes are presented in Figs. 5–8.

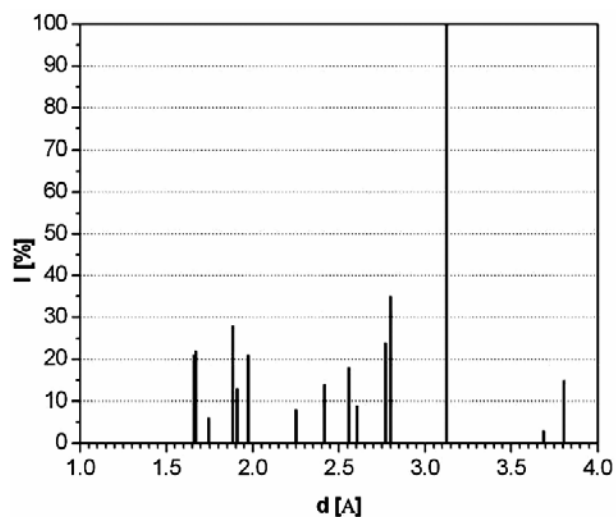


Fig. 5. X-ray spectra of the sample made of mass No. 8, identified as  $\text{Bi}_4\text{V}_2\text{O}_{11}$

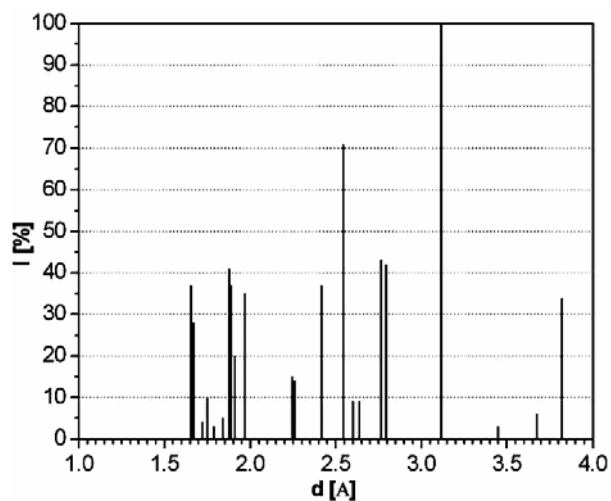


Fig. 6. X-ray spectra of the sample made of mass No. 8 after curing in a reducing atmosphere, identified as  $\text{Bi}_4\text{V}_2\text{O}_{11}$

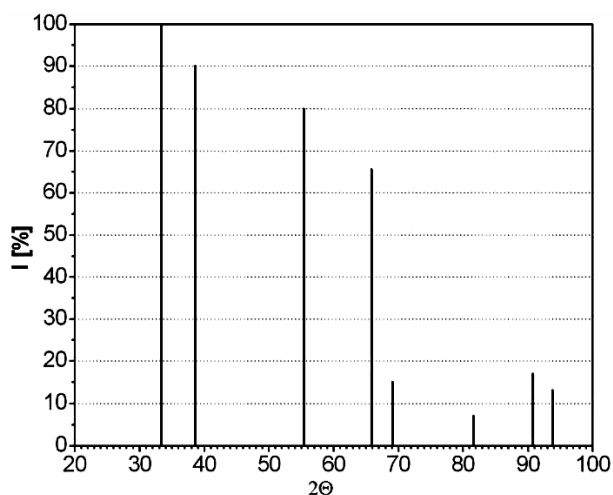


Fig. 7. X-ray spectra of the sample made of mass No. 12, identified as  $\text{Bi}_{1.5}\text{Y}_{0.5}\text{O}_3$  or  $\delta\text{-Bi}_2\text{O}_3$

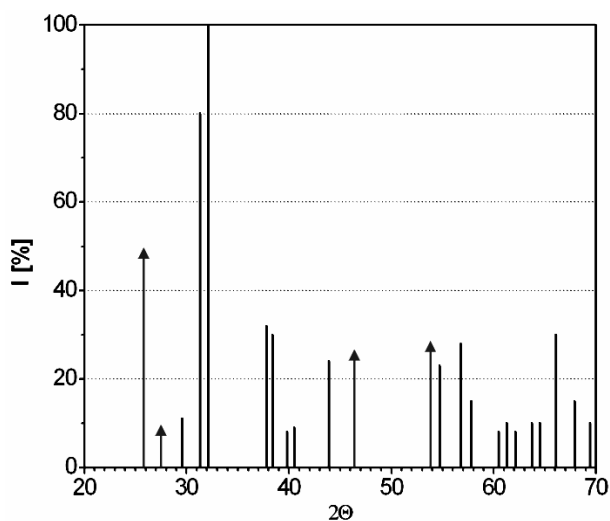


Fig. 8. X-ray spectra of the sample made of mass No. 12 after curing in a reducing atmosphere, identified as  $\alpha\text{-Bi}_2\text{O}_3$  and Bi (▲)

Basing on the analysis of the spectra, it was established that:

- Electrolytes of the BIVOX and BIMEVOX families are generally thermodynamically stable in the presence of reducing gases (oxygen-free atmosphere), although in some cases the samples of BIMEVOX electrolytes decomposed (Fig. 9).

- The electrolyte based on stabilized bismuth oxide  $\delta\text{-Bi}_2\text{O}_3$  (mass No. 12) is unstable thermodynamically and decomposes to  $\alpha\text{-Bi}_2\text{O}_3$  and finally to pure Bi (Fig. 10).



Fig. 9. Decomposed tablet made of mass No. 5 after a hazard in a reducing atmosphere

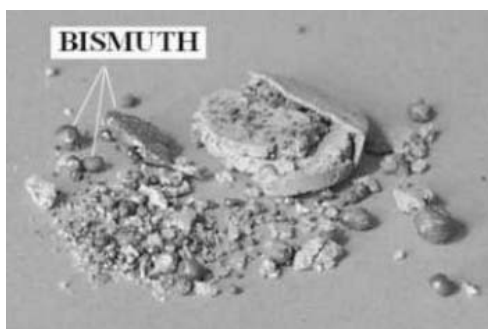


Fig. 10. Decomposed tablet made of mass No. 12 after a hazard in a reducing atmosphere

### 3.2. DC measurements of ionic conductivity

The temperature dependences of the ionic conductivities of selected electrolytes (mass No. 8, 12 and  $ZrO_2$ ) are presented in Fig. 11. Measurements were performed during the heating and cooling of the samples. The ionic conductivities for all electrolytes investigated are presented in Table 2.

Table 2. Ionic conductivities of the electrolyte bulks

No.	$\sigma$ [ $1/(\Omega \cdot \text{cm})$ ]	
	400 °C	660 °C
1	–	0.006
2	0.0397	0.084
3	0.0062	0.079
4	0.0010	0.095
5	0.0008	0.054
7	0.0003	0.047
8	–	0.536
9	0.0020	0.322
10	0.0016	0.118
12	0.0009	0.694
13	–	0.510
14	0.0011	0.328
15	0.0010	0.255
16	0.0001	0.016
17	0.0013	0.088
18	0.0007	0.065
$ZrO_2$	–	0.005

Basing on the results obtained it was affirmed that:

- In the temperature range from 200 °C to 700 °C, ionic conductivities of electrolytes based on  $\text{Bi}_2\text{O}_3$  are ca. 3 orders of magnitude higher than the conductivity of the traditional electrolyte  $\text{ZrO}_2$ .

- In the temperature range of 400–700 °C (the range of operation of fuel cells), the highest ionic conductivity measured was for the electrolyte bulks No. 8, 9, 12, 13.

- The most linear Arrhenius characteristic, without any hysteresis, was exhibited by the mass No. 12. This confirms that no phase transformations take place during its heating in air.

- The lowest value of ionic conductivity was measured for mass No. 1, in which X-ray composition analysis showed the presence of the poorly ionically conductive phase  $\alpha\text{-Bi}_2\text{O}_3$ .

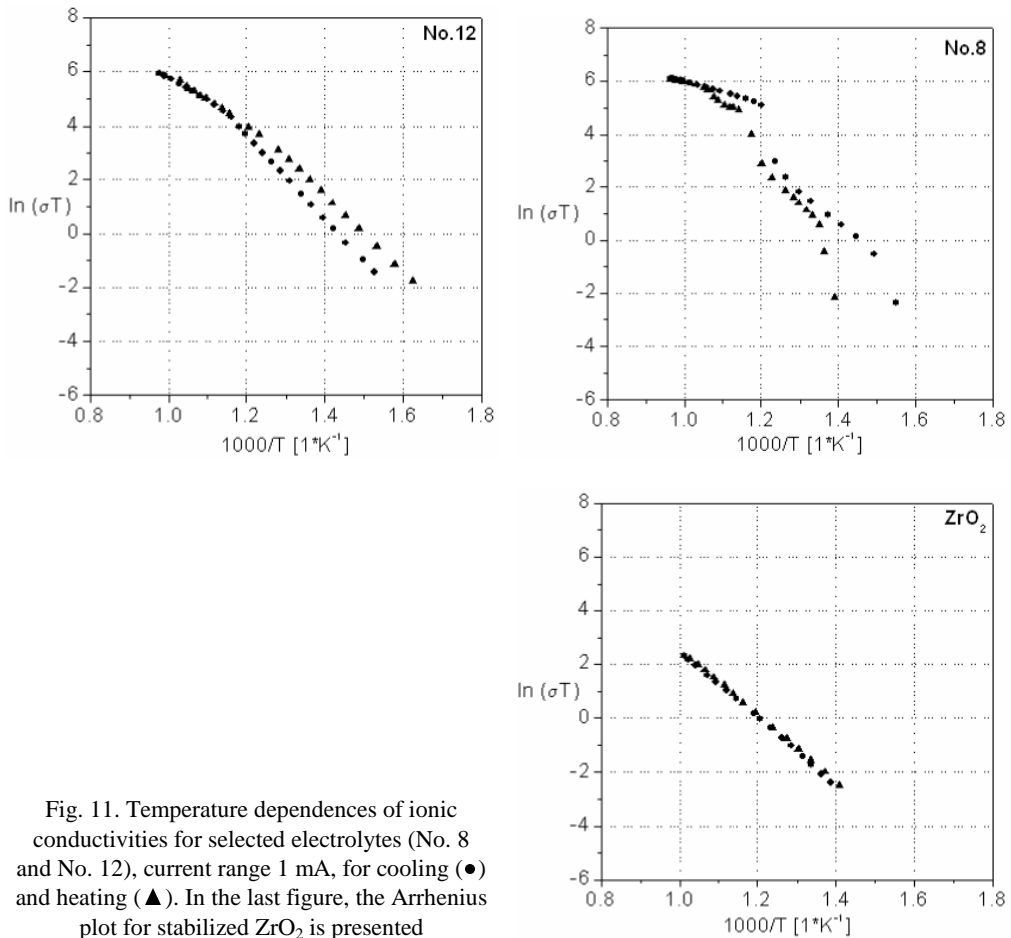


Fig. 11. Temperature dependences of ionic conductivities for selected electrolytes (No. 8 and No. 12), current range 1 mA, for cooling (●) and heating (▲). In the last figure, the Arrhenius plot for stabilized  $\text{ZrO}_2$  is presented

### 3.3. IS measurements of ionic conductivity

Using the DC method it is impossible to determine the ionic conductivity of electrolyte layers prepared with the screen-printing method, it was thus decided to apply the AC method for ionic conductivity measurements. Examples of impedance spectra measured in function of temperature (350–600 °C) for the mass No. 5 are presented in Fig. 12.

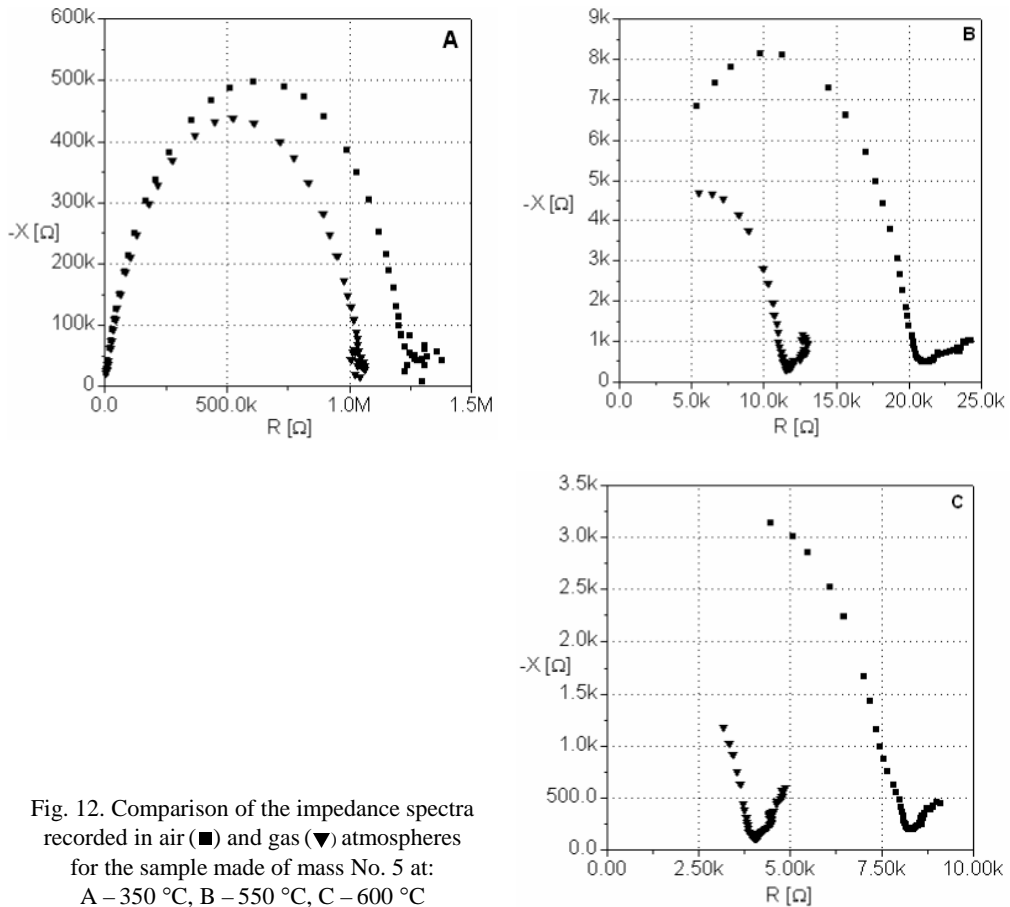


Fig. 12. Comparison of the impedance spectra recorded in air (■) and gas (▼) atmospheres for the sample made of mass No. 5 at: A – 350 °C, B – 550 °C, C – 600 °C

In order to determine the influence of a reducing atmosphere on the ionic conductivity of the electrolytes, impedance spectra measurements were performed in both air and gas (propane butane atmospheres). The results of these measurements are presented in Fig. 13 and Table 3.

Basing on impedance spectra analysis, it was confirmed that the ionic conductivity of all electrolyte bulks measured in air is higher than that measured in a reducing atmosphere. It was also proved (similar to the DC method) that the highest ionic conductivity were exhibited by samples No. 8 and 12. The reason for the differences in

the ionic conductivities measured by the DC and IS methods is probably the different densities of the samples, prepared using pressing and screen-printing methods. Screen-printed layers have an ionic conductivity two order of magnitude lower than traditionally pressed samples.

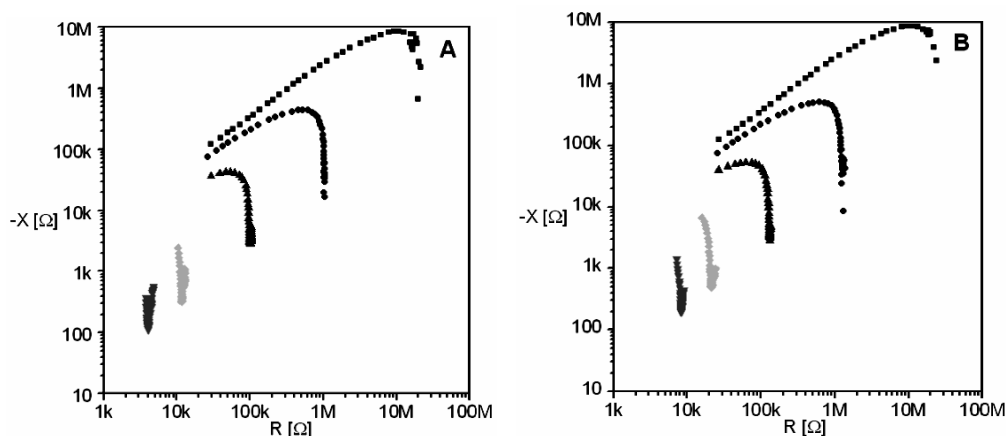


Fig. 13. Impedance spectra of mass No. 5 measured in air (A) and in a reducing atmosphere (B) at: ■ – 250 °C, ● – 350 °C, ▲ – 450 °C, ◆ – 550 °C, ▼ – 600 °C

Table 3. Ionic conductivities of the electrolytes (flow of air and reducing gas)

No.	$\sigma$ [ $1/(\Omega \cdot \text{cm})$ ]			
	In air		In gas	
	450 °C	600 °C	450 °C	600 °C
5	$2.35 \times 10^{-6}$	$5.9 \times 10^{-5}$	$1.21 \times 10^{-6}$	$2.87 \times 10^{-5}$
6	$1.44 \times 10^{-15}$	$3.48 \times 10^{-14}$	$1.24 \times 10^{-15}$	$3.29 \times 10^{-14}$
7	$2.88 \times 10^{-5}$	$2.19 \times 10^{-3}$	$5.00 \times 10^{-7}$	$1.21 \times 10^{-3}$
8	$1.17 \times 10^{-5}$	$2.41 \times 10^{-3}$	$2.74 \times 10^{-5}$	$2.92 \times 10^{-3}$
10	$9.25 \times 10^{-5}$	–	$7.66 \times 10^{-5}$	$1.59 \times 10^{-3}$
12	$3.26 \times 10^{-4}$	–	$3.26 \times 10^{-4}$	$9.65 \times 10^{-3}$
17	$1.59 \times 10^{-4}$	$1.90 \times 10^{-3}$	$2.22 \times 10^{-4}$	$2.85 \times 10^{-3}$

## 4. Conclusions

It is possible to operate SOFC fuel cells based on BIMEVOX or  $\delta\text{-Bi}_2\text{O}_3$  electrolyte, with a relatively low working temperature (ca. 600 °C). In the range of 200–700 °C, the ionic conductivity of electrolytes based on  $\text{Bi}_2\text{O}_3$  is quite higher (ca. 3 orders) than for the conventional electrolyte  $\text{ZrO}_2$ .

Compounds from the BIVOX and BIMEVOX families (bulk No. 8) have suitable properties for fuel cell applications, since their ionic conductivity is high (ca. 0.,5 S/cm) at

a relatively low temperature (650 °C) and they are thermodynamically stable in reducing atmospheres.

The material based on stabilized  $\delta$ -Bi<sub>2</sub>O<sub>3</sub> (bulk No. 12) is not thermodynamically stable in a reducing atmosphere, thus its application as an electrolyte in fuel cells is impossible.

#### Acknowledgements

The project was realized within the frame of the grant *New Electrolytes for Solid Oxide Fuel Cells*, financially supported by the Polish Ministry of Scientific Research and Information Technology, under the contract No. 4 T10A 013 24.

#### References

- [1] BERG N., WILLE A., ALSTOM T&D Review, 1999.
- [2] TAKAHASHI T., IWARA H., ESAKA, T., J. Electrochem. Soc., 124 (1977), 1563.
- [3] YAREMCHENKO A.A., KHARTON V.V., NAUMOVICH E.N., TONOVAN A.A., Mat. Res. Bull., 35 (2000), 515.
- [4] VERKERK M. J., BURGGRAAF, A.J., J. Electrochem. Soc., 128 (1981), 75.
- [5] TAKAHASHI T., ESAKA T., IWAHARA, H., J. Appl. Electrochem., 7 (1977), 299.
- [6] SHUK P., WIEMHOFER H.-D., GUTH U., GOPEL W., GREENBLATT M., Solid State Ionics, 89 (1996), 179.
- [7] PAŚCIAK G., PROCIÓW K., MIELCAREK W., GÓRNICKA B., MAZUREK B., J. Eur. Cer. Soc., 21 (2001), 1867.
- [8] LAZURE S., VERNOCHECH CH., VANNIER R. N., NOWOGROCKI G., MAIRESSE G., Solid State Ionics, 90 (1996), 117.
- [9] ABRAHAM F., BOIVING J.C., MAIRESSE G., NOWOGROCKI G., Solid State Ionics, 40–41 (1990), 934.
- [10] KROK F., ABRAHAMS I., MALYS M., BOGUSZ W., DYGAS J.R., NELSTROP J.A.G., BUSH A.J., Solid State Ionics, 136–137 (2000), 119.
- [11] PIROVANO C., VANNIER R.N., CAPOEN E., NOWOGROCKI G., BOIVIN J.C., MAIRESSE G., ANNE M., DOORYHEE E., STROBEL P., Solid State Ionics, 159 (2003), 167.
- [12] BOGUSZ W., KROK F., *Solid Electrolytes, Their Electrical Properties and Methods of Their Measurement* (in Polish), WNT, Warszawa, 1995.

Received 29 July 2004

Revised 8 September 2004

## **HBV deep mesa etching in InGaAs/InAlAs/AlAs heterostructures on InP substrate**

MARIANNA GÓRSKA\*, HANNA WRZESIŃSKA, ANNA SZERLING,  
KRZYSZTOF HEJDUK, JACEK RATAJCZAK, JAN MAREK ŁYSKO

Institute of Electron Technology, al. Lotników 32/46, 02-668 Warsaw, Poland

The chemical composition of newly developed anisotropic etching solution and several experimental results obtained with heterostructure barrier varactor (HBV) deep mesa formation are presented. The novel solution enables the deep etching of the InGaAs/InAlAs/AlAs heterostructure over InP substrate, up to 5  $\mu\text{m}$  in the [100] crystal direction. It ensures etch-stop at the InP substrate and gives almost perfect surface quality, with mesa profiles meeting device design requirements. The etching solution is a mixture of two components: A ( $\text{H}_2\text{SO}_4:\text{H}_2\text{O}_2:\text{H}_2\text{O} = 1:1:8$ ) and B ( $\text{C}_6\text{H}_8\text{O}_7:\text{H}_2\text{O} = 1:1$ ), in the proportion B:( $\text{H}_2\text{O}_2$  content in A) =1:1.

Key words: *heterostructure; anisotropic; wet etching; mesa*

### **1. Introduction**

In recent years, new varactor structures (Heterostructure Barrier Varactor, HBV) [1] with characteristics with even symmetry have been proposed. The importance of optoelectronic and other high-speed devices on InP bases is recognized today in modern technology. Nevertheless, there are critical technological steps in the processing of such devices that have not been optimally solved. In this publication, we present the HBV diode technology, especially the fragment related to mesa etching in InGaAs/InAlAs/AlAs heterostructures deposited with the MBE method on (100) InP substrates. The technology of HBV structure fabrication, which consists of two mesa formation steps – a big and a small one – is shown in Fig. 1.

The technological flow chart starts with the deposition of a 300 nm thick PECVD dielectric. After the first photolithography and mesa shape patterning in the dielectric layers, a 4.5  $\mu\text{m}$  thick heterostructure is anisotropically etched in the newly developed

---

\*Corresponding author, e-mail: gorska@ite.waw.pl.

solution. Dielectric layers, still remaining at the top of the first mesa, are used again in a second lithography step to define the second mesa shapes. Etching the second mesa is performed with a standard  $\text{H}_2\text{SO}_4:\text{H}_2\text{O}_2:\text{H}_2\text{O} = 1:8:40$  solution. It is very important that the InP substrate is not affected by this solution. The technological sequence is completed by the photolithography and lift-off technique of a metal sandwich, which forms electrical paths, contacts, and bonding pads.

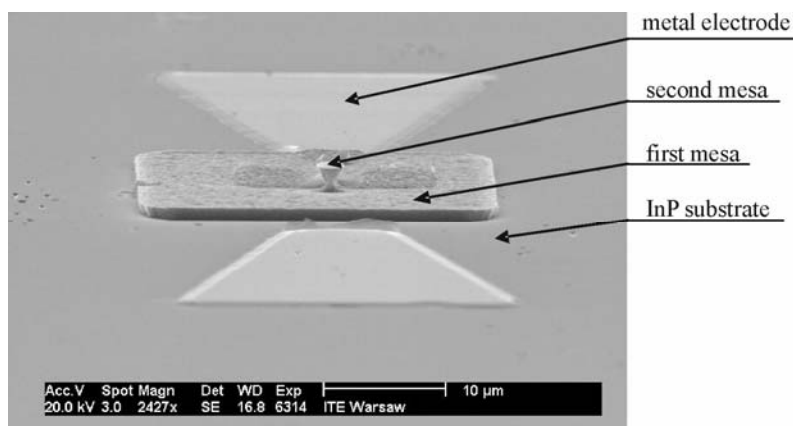


Fig. 1. Top view of the chip after the first metal level step

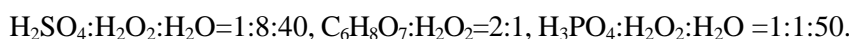
The main problem with the technology presented in this paper is a deep (ca.  $4.5\ \mu\text{m}$ ) etching of the first mesa. According to the design requirements of the HBV diode, two mesa mask edges parallel to the  $[01\bar{1}]$  crystal orientation should give a soft transition after the etching step which ensures the continuity of the metal paths. The other two mesa sidewalls, oriented along the  $[0\bar{1}\bar{1}]$  crystal direction, should form sharp edges for the self-aligned cut-off of the metal paths. A negative angle between the crystal plane (100) of the substrate surface and the mesa sidewall crystal plane (332) is highly advantageous.

The solution presented in this work makes the deep etching of InGaAs/InAlAs/AlAs heterostructures on InP substrates possible up to  $5\ \mu\text{m}$  in the  $[100]$  crystal direction. It enables the etching zone to stop at the InP substrate and gives the almost perfect surface quality of the samples, with the mesa profiles meeting the design requirements of the device.

## 2. Experimental

Experiments were focused on the development of deep mesa etching technology (first mesa indicated in Fig. 1) in InGaAs/InAlAs/AlAs heterostructures, according to the requirements presented in Fig. 2. On the basis of published data [2, 3], three mixtures were selected. They selectively etch InGaAs and InAlAs against the InP sub-

strate with the etching rate of several  $\mu\text{m}/\text{min}$ . These mixtures were prepared using sulphuric, citric, and phosphoric acids in the following proportions:



### 3. Results

SEM microphotographs of mesas etched in InGaAs/InAlAs/AlAs heterostructures over (100) InP substrates using the above mixtures are shown in Figs. 3–7.

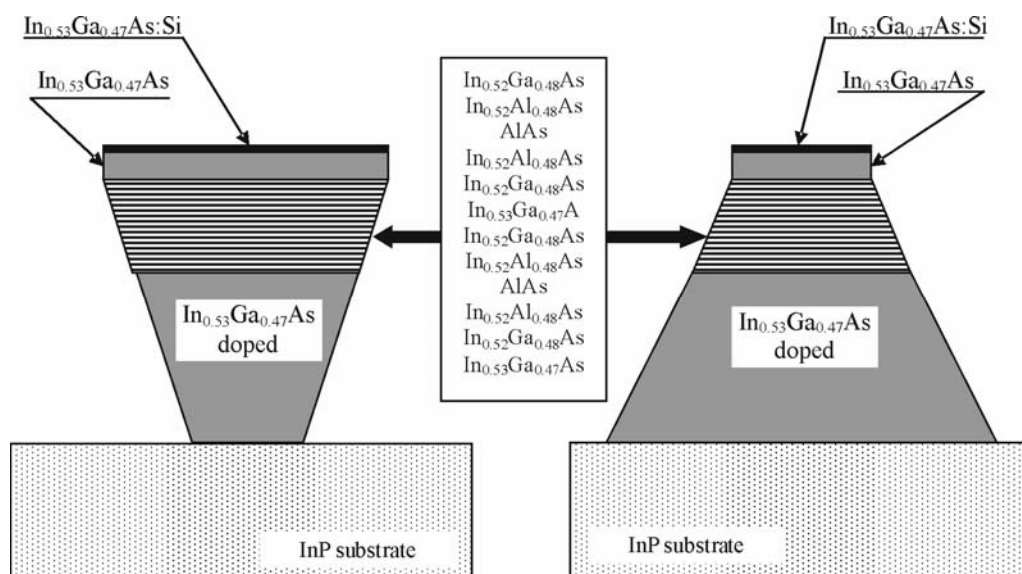


Fig. 2. Scheme of the two cross-sections of the required mesa profile (in the  $[01\bar{1}]$  and  $[0\bar{1}1]$  crystal directions, not in scale)

Experiments performed with the etching solution  $\text{H}_2\text{SO}_4:\text{H}_2\text{O}_2:\text{H}_2\text{O} = 1:8:40$  gave the sample profiles as shown in Figs. 3, 4. Good results were obtained with shallow mesa etching only. Unfortunately, it was impossible to reach a sufficient etch depth, good (100) surface quality, and proper mesa profile. Longer etch times gave deformed dovetail profiles.

Other experiments were done applying citric acid with hydrogen peroxide mixtures. Figures 5, 6 show two sample profiles, obtained after etching with  $\text{C}_6\text{H}_8\text{O}_7:\text{H}_2\text{O}_2 = 2:1$ . It was expected, based on the published data, that after 480 sec the etch zone would reach the depth of at least  $3\ \mu\text{m}$ . The depth of only  $1.05\ \mu\text{m}$  was obtained. A longer etching time (1200 sec) caused forming of triple-stepped mesa profiles about  $2\ \mu\text{m}$  deep disqualifying this mixture.

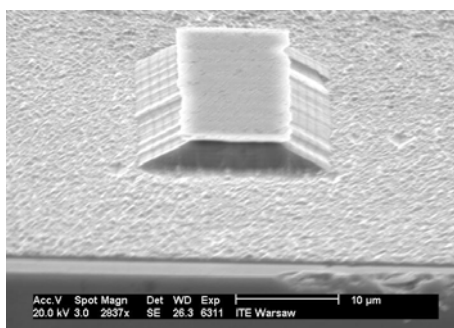


Fig. 3. Top view of the sample etched in  $\text{H}_2\text{SO}_4:\text{H}_2\text{O}_2:\text{H}_2\text{O} = 1:8:40$ , time 180 sec, etch depth 3.5 μm, poor (100) surface quality

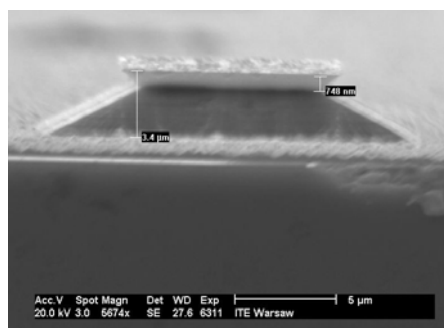


Fig. 4. Profile view of the sample etched in  $\text{H}_2\text{SO}_4:\text{H}_2\text{O}_2:\text{H}_2\text{O} = 1:8:40$ , time 240 sec, etch depth 3.4 μm, dovetail effect

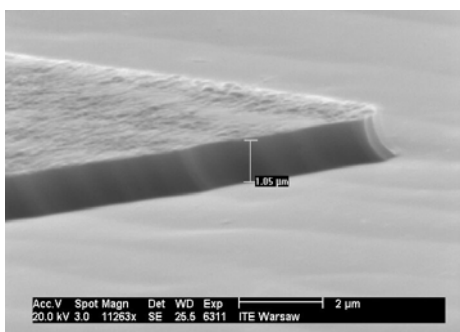


Fig. 5. Top view of the sample etched in  $\text{C}_6\text{H}_8\text{O}_7:\text{H}_2\text{O}_2 = 2:1$ , time 480 sec, etch depth 1.05 μm

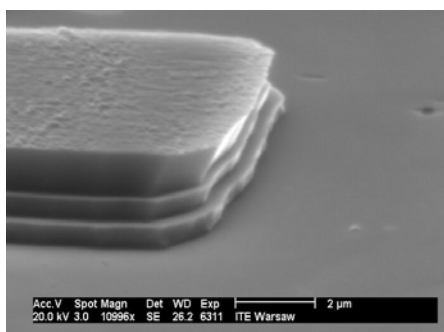


Fig. 6. Top view of the sample etched in  $\text{C}_6\text{H}_8\text{O}_7:\text{H}_2\text{O}_2 = 2:1$ , time 1200 sec, undesired three-step mesa profile

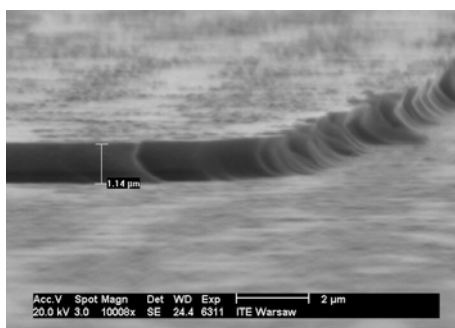


Fig. 7.  $\text{H}_3\text{PO}_4:\text{H}_2\text{O}_2:\text{H}_2\text{O} = 1:1:50$ , time 900 sec, etch depth 1.14 μm, uneven mesa edge

Phosphoric acid was also taken into consideration and tested, with the composition  $\text{H}_3\text{PO}_4:\text{H}_2\text{O}_2:\text{H}_2\text{O} = 1:1:50$ . After 900 sec, the etch depth was only 1.14 μm, and the masking edge and surface quality were not satisfactory.

The results presented suggest that heterostructures consisting of several very thin layers (individual layer thickness from 3 nm to 40 nm) of InGaAs and InAlAs are etched with significantly lower rates than the solids presented in literature. The mixture proposed in this publication, designed for HBV diode etching, consists of sulphuric and citric acid, mixed together with hydrogen peroxide and water [4]. Its chemical composition is as follows: component A =  $\text{H}_2\text{SO}_4:\text{H}_2\text{O}_2:\text{H}_2\text{O} = 1:1:8$ , component B =  $\text{C}_6\text{H}_8\text{O}_7:\text{H}_2\text{O} = 1:1$ , mixed in the following proportion  $k$  (in volume), prepared just before use, at room temperature, where:

$$k = \frac{V_B}{V_{\text{H}_2\text{O}_2 \text{ in A}}} = 1 \quad (1)$$

This newly proposed anisotropic etching solution matches all technological requirements of the device. The samples were etched at room temperature. The chemical reaction was of the redox type. Sulphuric acid and hydrogen peroxide act as the oxidizing agents of the sample surface, forming the oxide layer. Citric acid and water

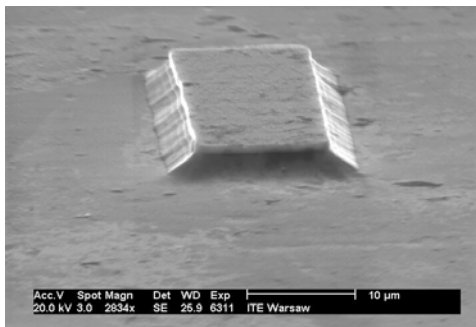


Fig. 8. Proper mesa shape, obtained with the newly developed solution. Two sidewalls (left and right) have soft slopes and the two other (upper and lower) have abrupt edges with negative angle of inclination; a residual dielectric layers still covers the mesa surface and reveals moderate lateral undercuts of the mask edges

dissolve this layer and discover semiconductor new surfaces for chemical oxidation. It is well known that even small changes in the etchant chemical composition influence the etch rate. The etch rate depends on the etchant and semiconductor chemical activity, as well as on the transport mechanism from/to the sample interface of the substrates and products. Diffusion is dependent on the stirring or agitation of the etching solution. The etchant composition proposed and optimum process parameters (temperature, agitation, liquid volume) give the required anisotropy of the mesa profile with respect to the crystal lattice orientation. Finally, good results obtained with the newly developed solution are shown in Fig. 8 and were confirmed by a number of other experiments not presented here.

#### 4. Conclusions

An anisotropic etching solution that enables deep etching in heterostructures, with almost perfect surface quality, anisotropy effect, and etch-stop at the InP interface,

was developed for the HBV (Heterostructure Barrier Varactor) mesa formation technology. An etchant composed of  $\text{H}_2\text{SO}_4$ ,  $\text{C}_6\text{H}_8\text{O}_7$ ,  $\text{H}_2\text{O}_2$ , and  $\text{H}_2\text{O}$  fulfils the device design and technological requirements, which is confirmed by several SEM microphotographs of the etched samples.

### References

- [1] KOLLBERG E.L., RYDBERG A., *Electronics Lett.*, 25 (1989), 1696.
- [2] STANO A., *J. Electrochem. Soc.*, 134 (1987), 448.
- [3] HOWES M.J., MORGAN D.V., *Gallium Arsenide. Materials, Devices and Circuits*, Wiley, Chichester, 1985.
- [4] GÓRSKA M., WRZESIŃSKA H., ŁYSKO J.M., patent pending No. P-360860, Poland.

*Received 9 September 2004*

# **Segmented block copolymers of natural rubber and 1,4-butanediol-toluene diisocyanate oligomers**

S. GOPAKUMAR, C. J. PAUL, M. R. GOPINATHAN NAIR\*

School of Chemical Sciences, Mahatma Gandhi University,  
Priyadarshini Hills, Kottayam – 686 560, Kerala, India

Segmented block copolymers were synthesized from hydroxyl terminated liquid natural rubber (HTNR) and polyurethane oligomers (PU), formed from 1,4-butanediol (1,4-BDO) and toluene diisocyanate (TDI). The samples were synthesized in solution in two series by the one-step and two-step methods. They were characterized by spectral analysis, thermal analysis, etching studies, microscopy and mechanical testing. IR and NMR spectral data, along with etching studies, support the notion that a chemical reaction leads to block copolymerization. Differential scanning calorimetric (DSC) analysis showed a soft segment glass transition temperature between  $-62\text{ }^{\circ}\text{C}$  and  $-63\text{ }^{\circ}\text{C}$  and a hard segment glass transition temperature between  $87\text{ }^{\circ}\text{C}$  and  $100\text{ }^{\circ}\text{C}$  for different samples. This observation and two-stage thermal decomposition of the samples in thermogravimetric analysis (TGA) clearly indicate that the block copolymers are completely phase-segregated systems. The amorphous heterophase morphology of the samples is indicated by SEM, which shows well-defined beads of hard phase dispersed in a matrix. SEM results, along with the etching studies, revealed that the samples are systems consisting of block copolymers and some quantity of uncoupled polyurethane homopolymers in the form of beads. The homopolymer beads suggest that the efficiency of the chain extension in the present method of synthesis is slightly lower than expected. Tensile properties improved with the hard segment content in the samples. Low hard segment content leads to a flexible elastomer, while at the high one rigid plastics are formed. Intermediate compositions yielded rigid elastomers. Two-step samples showed slightly better properties compared to the one-step samples. This may be due to the systematic way by which the reaction progresses in two-step synthesis. The overall properties are found to be lower than that of the conventional polyurethane elastomers. This is attributed to the absence of phase mixing and the inability of the soft segments to crystallise under strain due to their short segments.

Key words: *segmented block copolymer; liquid natural rubber; polyurethane*

## **1. Introduction**

The chemical modification of natural rubber has been studied for many years and a great number of derivatives have been prepared from this naturally occurring poly-

---

\*Corresponding author, e-mail: mgusc@rediffmail.com.

mer. As a result of these studies, many of the physical and mechanical properties of NR, such as glass transition temperature, compatibility, gas permeability, vulcanising properties, adhesive strength, oil resistance, tensile strength etc. can be modified to a great extent.

Modification involves the liquefaction of NR by photochemical degradation and subsequent block copolymerization with thermoplastic segments such as polyurethanes [1–4] or polyethylene glycols [5]. These block copolymers were found to be completely phase-separated systems with properties ranging from soft elastomers to rubber-toughened plastics as the hard segment content increases. This variation of mechanical properties could be caused by a change in sample morphology as is discernible in studies of block copolymers of natural rubber with polyethylene glycol hard segments of higher molecular weight (4000 and 6000), being crystalline solids [5]. At low hard segment content, the NR soft segment is a continuous phase, in which the hard segment domains act as physical crosslinks and reinforcing fillers. At higher hard segment content, the block copolymers appear to be bicontinuous in nature.

Of all the diols used for chain extension in the synthesis of polyurethane-based block copolymer, 1,4-butanediol yielded the best results in terms of material properties. The present work is an attempt to synthesise and characterise a series of block copolymers of NR and polyurethane using 1,4-butanediol as a chain extender. A small part of this work has already been presented as a symposia paper [1]. This contribution is an attempt to report findings after carrying out more work on the subject involving different routes of synthesis and elaborate studies on product characterisation.

## 2. Experimental

### 2.1. Materials

Natural rubber (ISNR-5) with viscosity average molecular weight – 820,000, intrinsic viscosity in benzene at 30 °C = 44.5 cm<sup>3</sup>/g, Wallace plasticity,  $P_0 = 39.0$  was obtained from Rubber Research Institute of India, Kottayam. Hydrogen peroxide (30%) was supplied by Merck, India. Toluene (reagent grade, Merck, India), ethanol (reagent grade, BDH, India), toluene diisocyanate (TDI) (80/20 mixture of 2,4- and 2,6-isomers, Fluka, Switzerland), were used without further purification. 1,4-Butanediol (1,4-BDO, Fluka, Switzerland) was dehydrated with anhydrous calcium oxide and then distilled under reduced pressure. Tetrahydrofuran (THF, BDH, India) was dried using sodium wire and distilled before use. Dibutyltin dilaurate (DBTDL, Merck, Germany), was used as the catalyst without further purification. N,N'-dimethyl formamide (DMF, Merck, India), was dried by phosphorous pentoxide and distilled before use.

Hydroxyl-terminated liquid natural rubber (HTNR) of number average molecular weight 3000 was prepared in the laboratory by the photochemical degradation of natu-

ral rubber as per a reported procedure [6]. It was reprecipitated three times from toluene using methanol and dried at 70–80 °C in vacuum.

## 2.2. Synthesis

Segmented block copolymers with varying compositions were synthesized in solution by the one-step and two-step processes. The overall compositions of the reactants used are given in Table 1.

Table 1. The overall compositions of the one-step and two-step block copolymers

Sample	Molar composition HTNR/TDI/1,4-BDO	Per cent of hard segment
NR/1,4-BDO(70/30)-1&2	1.0/5.97/4.86	33.0
NR/1,4-BDO(60/40)-1&2	1.0/8.74/7.57	42.3
NR/1,4-BDO(50/50)-1&2	1.0/12.60/11.35	51.2
NR/1,4-BDO(40/60)-1&2	1.0/18.39/17.03	61.2
NR/1,4-BDO(30/70)-1&2	1.0/27.04/26.49	70.3

*The two-step process.* The stoichiometric amount of HTNR dissolved in THF (30% w/v) was placed in a flat-bottomed flask equipped with a magnetic stirrer, a reflux condenser, and a dropping funnel. The catalyst, DBTDL (0.03 wt. % of HTNR) was added and the solution was brought to reflux at a temperature between 70 and 80 °C. The final stoichiometric amount of TDI dissolved in THF was dropped into it over a period of 30 min followed by 90 min of reaction time to ensure the complete end-capping of HTNR. The required amount of 1,4-BDO (30% w/v) was then added and stirring was continued for 3 hours. The product was poured into a tray treated with silicon release agent and kept overnight for casting into a sheet. The sheet was then subjected to heat treatment at 70 °C for 24 hours to remove residual solvent followed by one week of aging at room temperature in a dry atmosphere.

*The one-step process.* The required stoichiometric amounts of HTNR and 1,4-BDO in THF (30% w/v) were placed in a flat-bottomed flask. DBTDL catalyst (0.03 wt. % of HTNR) was added and the solution was brought to reflux at a temperature between 70 and 80 °C. The final stoichiometric amount of TDI was dropped into it over a period of 45 min. Stirring and refluxing were continued for 4 hours. The viscous liquid was then cast, cured, and aged, as described in the case of two-step samples.

## 2.3. Extraction study

Etching studies on the block copolymer were done by keeping a known weight of the NR/1,4-BDO(50/50)-2 as a film in N,N'-dimethyl formamide for two days. The insoluble part (gel fraction) was separated by filtration. This etching process was repeated three times on the same gel fraction. It was finally dried to a constant weight.

## 2.4. Polymer designation

The samples were designated as follows. As an example, NR/1,4-BDO (70/30)-1 means that the sample contained around 70 wt. % of HTNR and 30 wt. % of polyurethane hard segment, based on 1,4-BDO and toluene diisocyanate. The exact compositions are given in Table 1. The number 1 given at the end indicates that the sample was made by the one-step process. The number 2 is given for samples made with the two-step process.

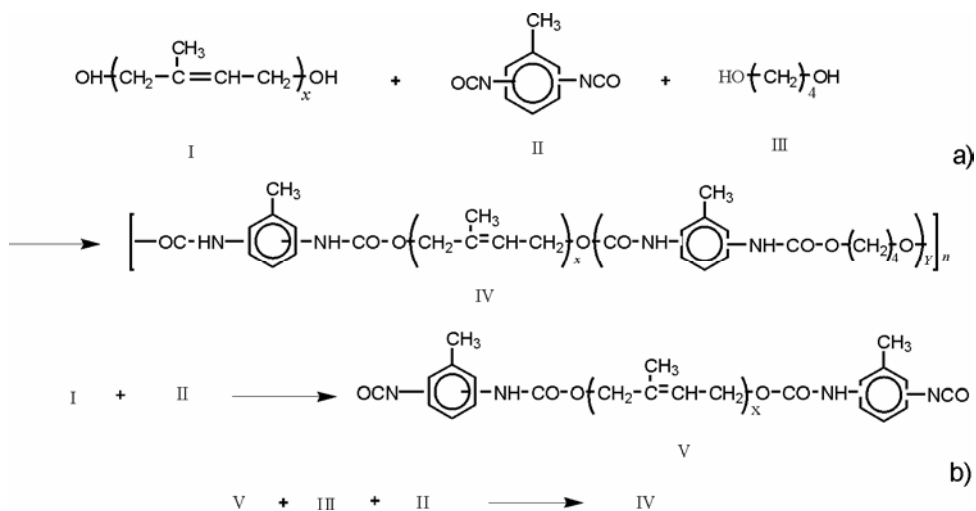
## 2.5. Measurements

Infrared spectra of the samples were recorded on a Shimadzu FTIR-8400S spectrometer (Japan). The  $^1\text{H}$  NMR spectra were recorded on a Bruker AC 200 MHz NMR spectrometer and  $^{13}\text{C}$  NMR spectra on a Bruker AC 50 MHz NMR spectrometer (USA). Differential scanning calorimetry (DSC) was performed with a Mettler Inc (TA 300) microcalorimeter (USA) and with a Perkin Elmer Delta Series DSC 7 calorimeter (USA) at a heating rate of 10 K/min. All DSC scans were first scans. Glass transition temperature was noted as the temperature corresponding to one half of the increases in heat capacity at the transition. Thermogravimetric analysis (TGA) was carried out using a Perkin Elmer TGA 7 analyser (USA) at a scanning rate of 10 K/min. The peak temperature in the DTG curve is taken as the decomposition temperature. Stress-strain behaviour was studied on a Zwick 1474 Universal Testing Machine (Germany) as per the ASTM D 412-80 test method at a constant cross head speed of 500 mm/min. The fracture surfaces of the samples from tensile tests were sputter coated with approximately 300 Å of gold and examined on a JEOL JSM-35C scanning electron microscope (Japan) at 15 kV using magnifications of 400 to 1000 $\times$  to study the morphology of the materials.

## 3. Results and discussion

The test samples were prepared in two series basing on different routes of synthesis – one-step and two-step processes. All syntheses were done in solution and the samples were made in sheet form by casting the reaction mixture and subsequent heat treatment and ageing as described in the previous section. The sheets do not dissolve but swell to a great extent in suitable solvents which is characteristic of a crosslinked product. This indicates that the chemical reactions continue through the casting stage, resulting in the crosslinking of the product. The probable reactions leading to the formation of the one-step and two-step products are presented in Scheme I. Reactions leading to the end-capping of HTNR, formation of polyurethane, and chain extension occur simultaneously in the case of the one-step products, whereas for two-step prod-

ucts end-capping occurs in the first stage, followed by chain extension with polyurethane in the second stage.



Scheme 1. Course of the reactions in one-step (a) and two-step processes (b)

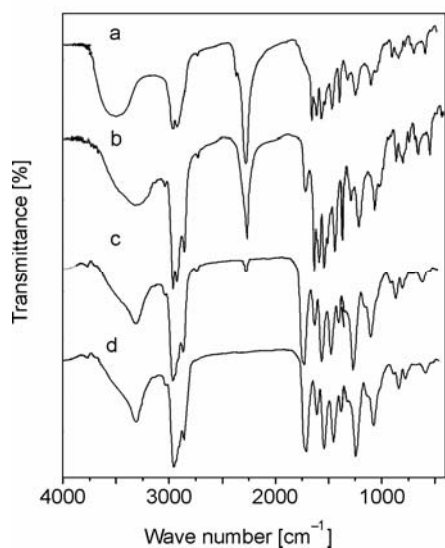


Fig. 1. IR spectra at different intervals of synthesis of NR/1,4-BDO(50/50) by one-step process: a) at the beginning, b) after one hour, c) after three hours, d) final product

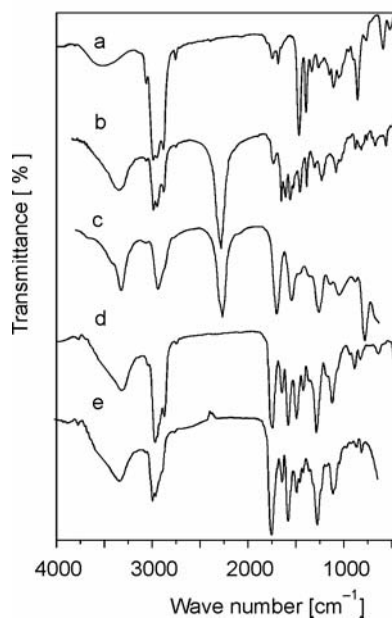
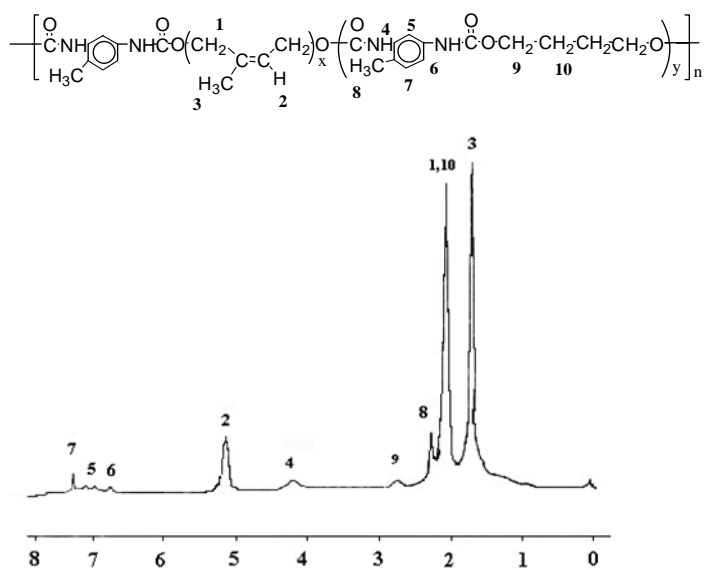
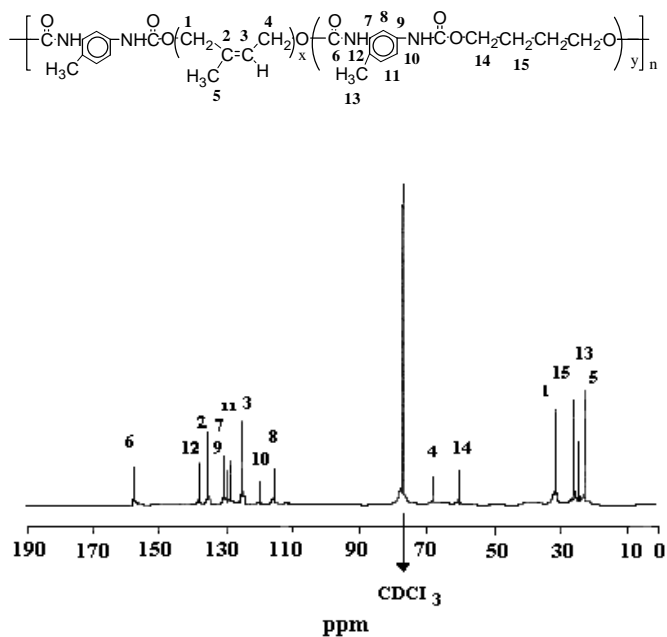


Fig. 2. IR spectra of: a) HTNR, b) NCO endcapped NR, c) PU hard segment based on TDI and 1,4-BDO, d) block copolymer by two-step process, e) etched block copolymer (gel fraction)

Fig. 3.  $^1\text{H-NMR}$  spectrum of NR/1,4-BDO(50/50)-2Fig. 4.  $^{13}\text{C-NMR}$  spectrum of NR/1,4-BDO(50/50)-2

Evidence for this effect is seen in the IR spectra given in Figs. 1 and 2. Various stages in the formation of a typical one-step product are shown in Fig. 1a-d. Very high intensities of the  $-\text{OH}$  and  $-\text{NCO}$  peaks, positioned at  $3470\text{--}3600\text{ cm}^{-1}$  and  $2258\text{ cm}^{-1}$

respectively, shows the presence of excess reactants at the beginning, which decreases after one hour of reaction time with the emergence of a new peak at  $3314\text{ cm}^{-1}$  due to the =NH group (Fig. 1b). The isocyanate peak and broad hydroxyl peak almost disappear after three hours of reaction time, as seen in Fig. 1c, indicating high conversion. The cast product shows (Fig. 1d) the combined features of NR and polyurethane segments. The shoulder peak appearing at  $3420\text{ cm}^{-1}$  in Fig. 2b, d is attributed to the non-hydrogen bonded =NH groups in polyurethane.

The series of reactions leading to the formation of the two-step product is also supported by the IR spectra in Figs. 2a–d. Fig. 2a shows the IR spectrum of liquid NR with a broad hydroxyl band at  $3490\text{--}3580\text{ cm}^{-1}$ . End-capped liquid NR shows the presence of the =NH and isocyanate peaks as in Fig. 2b. When the chain is extended with 1,4-butanediol, this gives the final product with IR features as shown in Fig. 2d. Both the isocyanate peak and hydroxyl peak are absent in this spectrum, indicating their involvement in the reaction. The spectrum of the final product bears all the features of NR and polyurethane components as in the case of the one-step block copolymer. Figure 2c, which is a spectrum of the polyurethane reaction mixture prepared separately by reacting slightly excess TDI and 1,4-BDO, is given for comparison purposes. The proton NMR (Fig. 3) and  $^{13}\text{C}$  NMR (Fig. 4) spectra of a typical two-step product, NR/1,4-BDO(50/50)-2, support the copolymer structure. Peak assignments are shown in the respective figures. The peaks characteristic of hard segments are found to be relatively weak in these spectra. As noted above, block copolymers were found to be insoluble in common solvents and in such cases the NMR solvent,  $\text{CDCl}_3$ , could solvate the NR segments and cause high mobility, whereas the solvation of PU segments becomes difficult owing to the inability of the solvent to break the high intersegmental interaction existing in them. This causes low mobility of the hard segments and renders the respective NMR peaks weak.

A notable feature of the spectral analysis is that no major shift in the absorption frequency of NR and PU segments is observed in the spectra. This indicates that intersegmental interaction between NR and PU segments is absent in the block copolymers and that they are present as separate phases. This is supported by the large difference in the solubility parameter of the polyurethane segments ( $25\text{ (J}\cdot\text{cm}^{-2})^{1/2}$ ) and NR segments ( $16,6\text{ (J}\cdot\text{cm}^{-2})^{1/2}$ ). The closeness of the respective solubility parameters is shown to be a criterion for the miscibility of two components. These observations are viewed in the light of the nonpolar and polar character of NR and polyurethane segments, respectively, which do not mutually interact.

Phase separation in the block copolymer is further evidenced by DSC studies. Curves a and c in Fig. 5, being the thermograms of two typical two-step block copolymers, NR/1,4-BDO(60/40)-2 and NR/1,4-BDO(40/60)-2, respectively, show two different transitions corresponding to the NR and polyurethane segments. This is characteristic of a phase separated product. Moreover, the  $T_g$  values of NR in both cases are the same ( $-63\text{ }^\circ\text{C}$ ), irrespective of the composition of the block copolymers. This indicates that the rubber and polyurethane phases exist without mutual interaction, which otherwise would have lead to shifted  $T_g$  values. Thermograms of another two-

step sample and of all the one-step samples are taken at higher temperature only, since the subambient regions of the thermograms used for reading the value of  $T_g$  for NR is expected to be similar for all samples (due to the structural identity and identical grade of the liquid NR used for synthesis). The polyurethane phase shows only a glass transition, since crystallinity is absent due to the dissymmetry of TDI, which bears isocyanate groups at the 2- and 4- positions, affecting the uniformity of the polyurethane chain. Higher values of  $T_g$  for the polyurethane segments are explained on the basis of their rigidity, which is caused by hydrogen bonding and other interactive forces existing between the urethane groups.

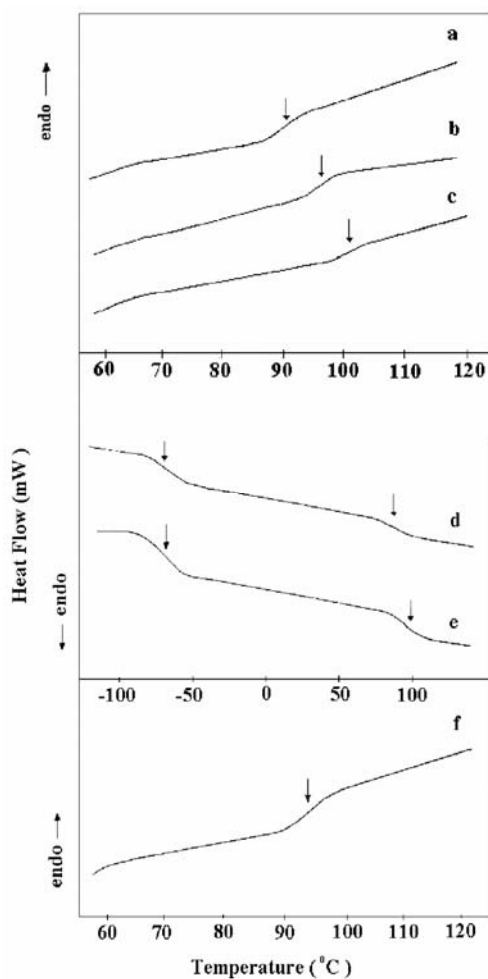


Fig. 5. DSC thermograms of the block copolymers:  
 a) NR/1,4-BDO(60/40)-1 (Perkin-Elmer),  
 b) NR/1,4-BDO(50/50)-1 (Perkin-Elmer),  
 c) NR/1,4-BDO(40/60)-1 (Perkin-Elmer),  
 d) NR/1,4-BDO(60/40)-2 (Mettler),  
 e) NR/1,4-DO(40/60)-2 (Mettler),  
 f) NR/1,4-BDO(50/50)-2 (Perkin-Elmer)

The aromatic ring structures present in the diisocyanate moiety of the hard segment structural units also contribute to segment rigidity. Single hard segment  $T_g$  values are observed in all samples, showing a narrow distribution of hard segment lengths in them. This is expected, since synthesis was carried out in solution, where

polymerization proceeds in a nearly systematic way. Unlike soft segment  $T_g$ , the hard segment  $T_g$  varies with composition as given in Table 2. It increases with hard segment content. This is due to the fact that samples with the higher hard segment content possess longer PU blocks, resulting from the respective OH/NCO ratio. The longer the blocks, the higher the extent of intermolecular forces existing between them, which causes a rise in  $T_g$ .

Table 2. DSC results of the block copolymers

Sample	$T_g$ [°C]	
	Soft segment	Hard segment
NR/1,4-BDO(60/40)-1	–	88.0
NR/1,4-BDO(50/50)-1	–	94.0
NR/1,4-BDO(40/60)-1	–	99.0
NR/1,4-BDO(60/40)-2	–63.0	87.0
NR/1,4-BDO(50/50)-2	–	94.0
NR/1,4-BDO(40/60)-2	–62.0	96.0

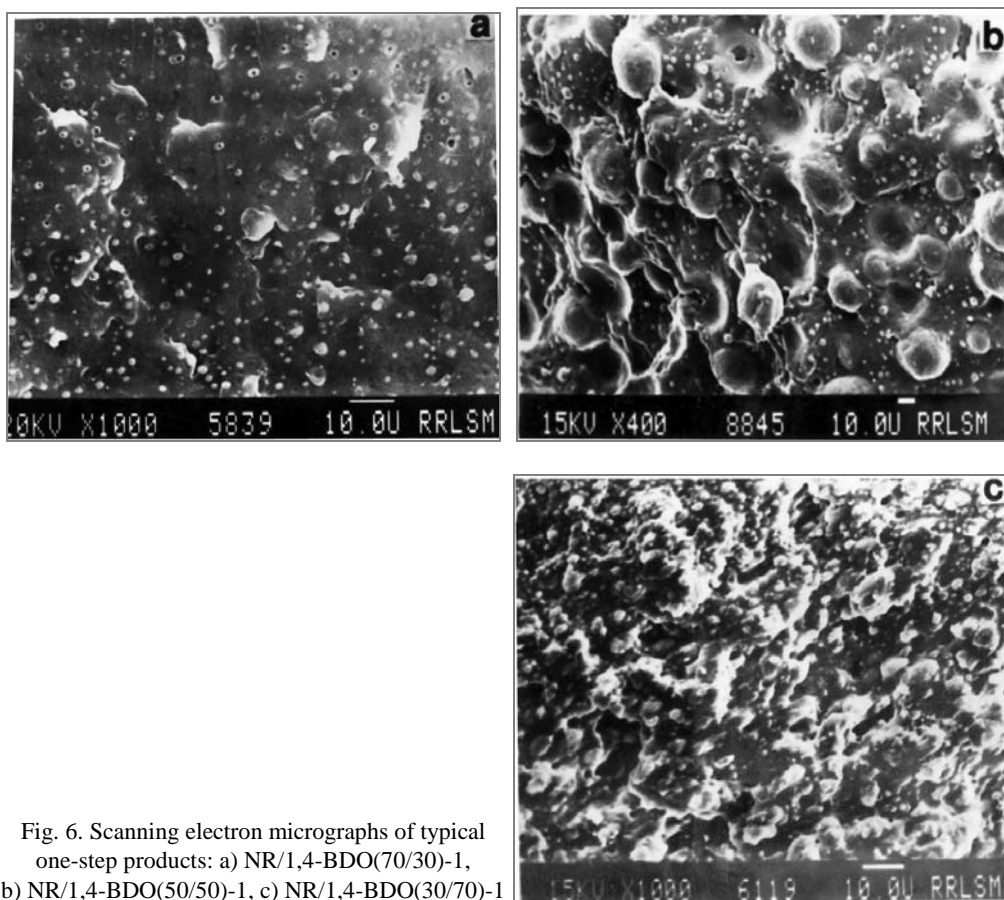


Fig. 6. Scanning electron micrographs of typical one-step products: a) NR/1,4-BDO(70/30)-1, b) NR/1,4-BDO(50/50)-1, c) NR/1,4-BDO(30/70)-1

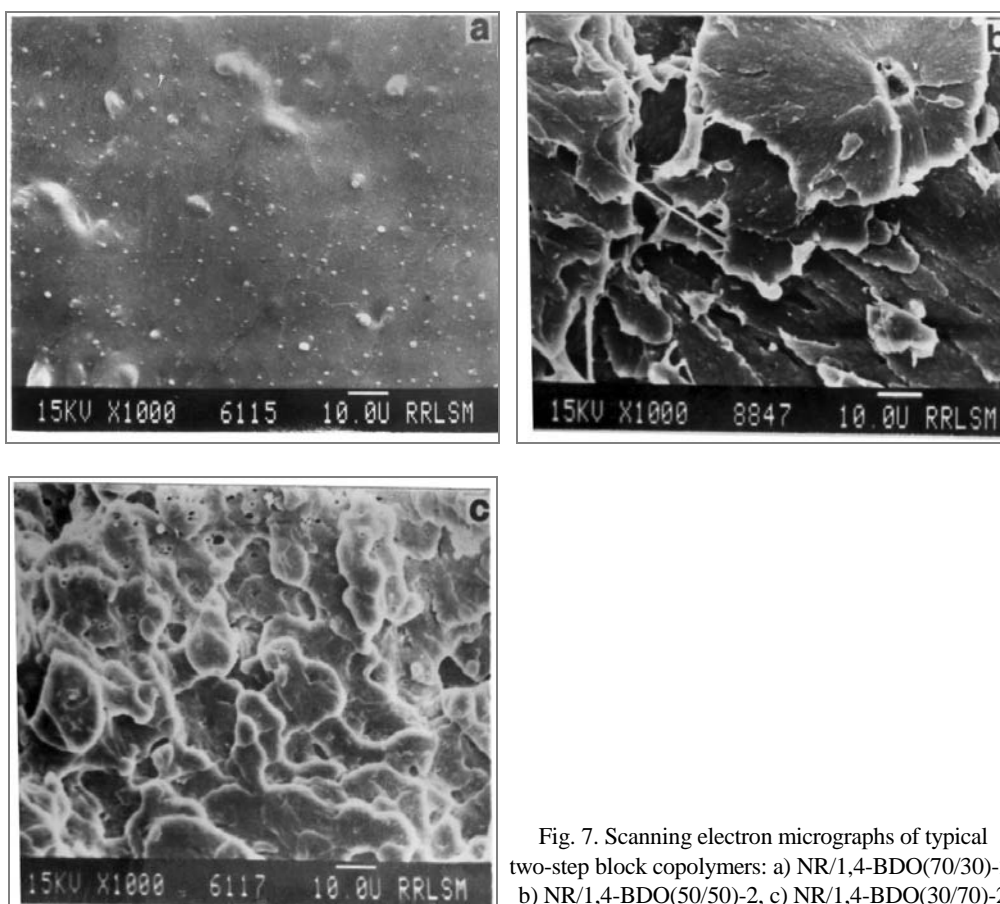


Fig. 7. Scanning electron micrographs of typical two-step block copolymers: a) NR/1,4-BDO(70/30)-2, b) NR/1,4-BDO(50/50)-2, c) NR/1,4-BDO(30/70)-2

Heterophase morphology is further shown by SEM analysis. These micrographs (Figs. 6, 7) exhibit the presence of incompatible phases forced to coexist. Hard segments agglomerate into discrete amorphous phases, which are seen as well-defined boundary surfaces in the SEM micrographs. Their sizes range from 3.75 to 20.66  $\mu\text{m}$ . These are, however, much larger sizes compared to hard domains usually observed in block copolymer morphology, which tend to vary from discrete spherical dispersions of nano size at low hard segment content to regular lamellar distributions at higher hard segment content. Due to extremely small size, hard domains in block copolymers would be visible only in high resolution TEM studies. It was thus inferred that the beads observed in the present case are larger agglomerations of polyurethane homopolymers, which remain unbonded with the rubber chains during synthesis.

Such a possibility was further explored by conducting quantitative etching studies on the NR/1,4-BDO(50/50)-2 sample, so as to separate the unbonded polyurethane fraction. The solvent used for this purpose was N,N'-dimethyl formamide, which is a very good polyurethane solvent. It was found that 25.62% of the total sample weight was extracted. The etched sample (gel fraction) was subjected to IR analysis. A com-

parison of its IR spectrum with that of the unetched original sample shows similar features of NR and PU segments, indicating that both samples have the same structural characteristics. These findings suggest that block copolymerization takes place as envisaged in Scheme 1, but with slightly lower efficiency, so that a part of the PU remains a homopolymer.

Table 3. Variation of bead size and bead density with the polyurethane content in the block copolymers (measured from SEM)

Sample	Weight % of hard segment	Mean domain size [ $\mu\text{m}$ ]	Domain density on surface ( $\times 10^8 \text{ m}^{-2}$ )
NR/1,4-BDO(70/30)-1	33.0	3.75	1.98
NR/1,4-BDO(50/50)-1	51.2	20.66	6.78
NR/1,4-BDO(30/70)-1	70.3	not measurable	not measurable
NR/1,4-BDO(70/30)-2	33.0	4.25	2.01
NR/1,4-BDO(50/50)-2	51.2	not reliable	not reliable
NR/1,4-BDO(30/70)-2	70.3	not measurable	not measurable

The size and population of the random beads observed in the SEM micrograph was tabulated in Table 3. The population is given in terms of bead density, which is the number of beads per square meter on the sample surface. The overall bead size and bead density are found to vary with hard segment content in the sample. For example, in NR/1,4-BDO(70/30)-1, the minor component, i.e., polyurethane, is present as discrete particles of a small size at lower densities in the continuous matrix of NR segments. When hard segment content is increased to 51.217%, as in NR/1,4-BDO(50/50)-1, the hard domain size and domain density increase to a great extent. With further increase of hard segment content to 70.328%, the hard domains tend to coalesce and form a continuous phase. Domain size and density are hence not measurable in this case. The corresponding two-step samples, except NR/1,4-BDO(50/50)-2, give similar results. In the case of NR/1,4-BDO(50/50)-2, the micrograph shows a deformed surface containing torn fragments, which is characteristic of a flexible material. Domains are not visible. This can probably happen if major quantities of the PU component were incorporated into the block copolymer structure. The present samples hence can be considered to be systems consisting of three separate phases, viz., the NR soft phase, the polyurethane hard phase (present in the block copolymer), and the homopolymer polyurethane phase (as beads). However, DSC studies showed only one glass transition corresponding to the polyurethane phase. This may be due to comparable chain lengths of the polyurethane block copolymer phase and the homopolymer phase, which would hence be represented by a single transition in the DSC thermogram.

A two-phase morphology is further supported by thermogravimetric analysis. All samples decomposed in two stages (Figs. 8, 9), indicating the coexistence of two components. The onset of weight loss, the temperature of complete decomposition, the DTG peak temperatures, and the percentage of weight loss in each stage are summarized in Table 4.

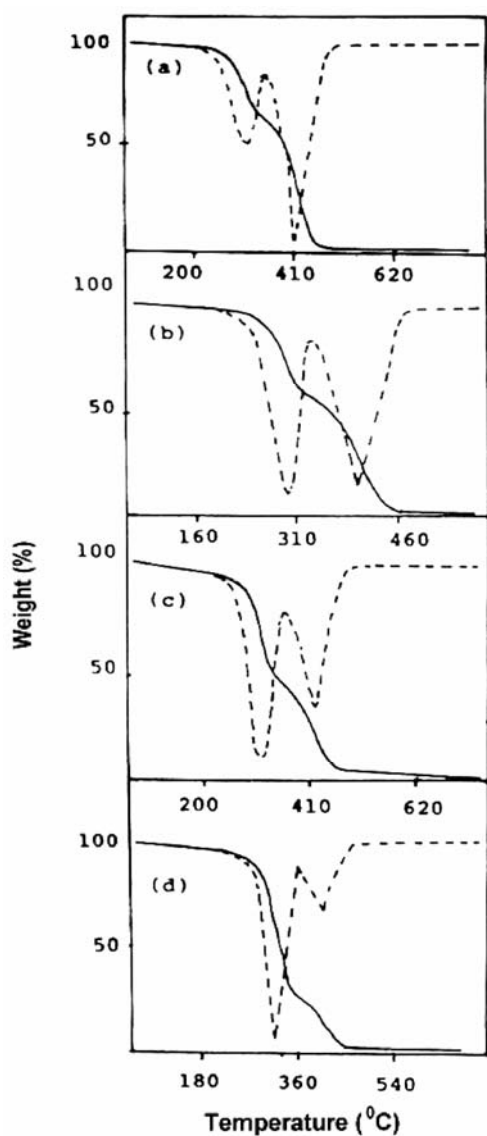


Fig. 8. Thermograms of the one-step block copolymers from TGA analysis:  
 a) NR/1,4-BDO(70/30)-1, b) NR/1,4-BDO(60/40)-1,  
 c) NR/1,4-BDO(50/50)-1, d) NR/1,4-BDO(30/70)-1

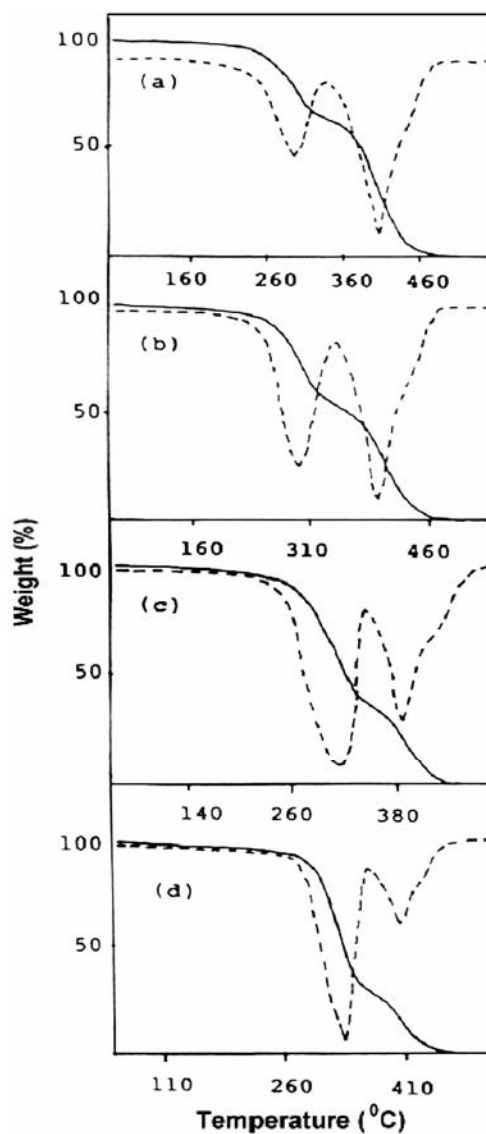


Fig. 9. Thermograms of the two-step block copolymers from TGA analysis:  
 a) NR/1,4-BDO(70/30)-2, b) NR/1,4-BDO(60/40)-2,  
 c) NR/1,4-BDO(40/60)-2, d) NR/1,4-BDO(30/70)-2

The onset of weight loss in the first stage occurs between 240 °C and 290 °C. The percentage of weight loss in this stage increases with increasing hard segment content, which indicates that the first stage of decomposition is due to hard segments. Obviously, the second stage of decomposition is due to the soft segments, since the percentage of weight loss here increases with increasing soft segment content. The first

stage of decomposition is completed in the temperature range 295–340 °C. The second stage of decomposition is rather rapid – it begins around 300 °C and is completed in the range 440–490 °C. A plateau of temperature separating the two stages of decomposition indicates that the two components decompose at different temperatures. Two stage decomposition is a clear indication of the heterophase nature of block copolymers.

Table 4. Phenomenological data of thermal decomposition of the one-step and two-step block copolymers

Sample	Onset of weight loss [°C]		Per cent of weight loss		Peak temperature [°C]	
	Stage 1	Stage 2	Stage 1	Stage 2	Stage 1	Stage 2
NR/1,4-BDO(70/30)-1	244.00	341	36.00	63.00	307.00	410.00
NR/1,4-BDO(60/40)-1	254.00	333	43.00	55.00	316.00	422.00
NR/1,4-BDO(50/50)-1	270.00	352	56.00	42.00	312.00	419.00
NR/1,4-BDO(30/70)-1	280.00	356	72.00	26.00	314.00	408.00
NR/1,4-BDO(70/30)-2	244.00	342	35.00	64.00	296.00	405.00
NR/1,4-BDO(60/40)-2	253.00	355	45.00	54.00	297.00	393.00
NR/1,4-BDO(40/60)-2	252.00	354	61.00	38.00	313.00	387.00
NR/1,4-BDO(30/70)-2	273.00	359	70.00	29.00	322.00	403.00

### 3.1. Activation energy of decomposition

The activation energy of block copolymer decomposition was derived from the TG curves by applying an analytical method proposed by Coats and Redfern [7]. The integral equation used has the form

$$\ln \frac{g(\alpha)}{T^2} = \ln \left[ \frac{AR}{\phi E} \left( 1 - \frac{2RT}{E} \right) \right] - \frac{E}{RT}$$

where  $g(\alpha)$  is the kinetic model function,  $\alpha$  – the decomposed fraction at any temperature  $T$ ,  $\phi$  – the heating rate,  $A$  – a numerical constant, and  $E$  stands for activation energy. The slope of the plot of left hand side against  $1/T$  is a straight line, from which the energy of activation  $E$  was calculated.

All TG data were analyzed using the nine mechanistic equations proposed by Satawa [8] and their kinetic parameters were calculated. It was found that the Mampel equation ( $-\ln(1-\alpha) = kt$ ) best represents the experimental data and gives a proper mechanism of the reaction in all samples, which corresponds to a random nucleation mechanism for thermal decomposition with one nucleus in each domain.

In the one-step samples, the activation energy for the first stage of thermal decomposition increases from 101  $\text{KJ}\cdot\text{mol}^{-1}$  to 136  $\text{KJ}\cdot\text{mol}^{-1}$  as the hard segment content is increased from 30% to 70% (Table 5). An increase in activation energy indicates an

increase in the thermal stability of the hard segments. Thermal stability, however, is a property determined by chemical structure and hard segment content only influences a segment length. Structural factors that vary with hard segment content seem to play a decisive role in this respect.

Table 5. Tensile properties of the block copolymers

Sample	Young's modulus [N/mm <sup>2</sup> ]	Tensile strength [N/mm <sup>2</sup> ]	Elongation at break [%]
NR/1,4-BDO(70/30)-1	3.93	4.06	194
NR/1,4-BDO(60/40)-1	7	7.88	161
NR/1,4-BDO(50/50)-1	20.78	12.01	98
NR/1,4-BDO(40/60)-1	64.43	16.28	65
NR/1,4-BDO(30/70)-1	97.76	29.86	30
NR/1,4-BDO(70/30)-2	11.58	4.91	225
NR/1,4-BDO(60/40)-2	12.97	8.02	177
NR/1,4-BDO(50/50)-2	21.06	14.53	82
NR/1,4-BDO(40/60)-2	69.12	22.20	68
NR/1,4-BDO(30/70)-2	104.92	31.56	39

The allophanate linkage that can form crosslinks in polyurethane segments in the presence of free diisocyanate may be a factor worth considering in this case. Since the quantity of diisocyanate being introduced into the reacting system increases with hard segment content, allophanate formation is enhanced, which in turn leads to a higher level of crosslinking in polyurethane segments (Fig. 11). Such an increase in crosslinking obviously increases the thermal stability of the segments. A similar increase in activation energy with PU content is observed in the two-step samples for the degradation of polyurethane segments. Comparing the one-step and two-step products it is observed that the PU components in both series of products have comparable values of activation energy. This indicates that the polyurethane segments in both the types of products possess similar structural characteristics.

Regarding soft segment degradation, the activation energy for one-step samples is found to decrease with hard segment content. The value is 126 KJ mol<sup>-1</sup> for 30 % PU content, which decreases to 90 KJ mol<sup>-1</sup> for 70 % PU content. On the other hand, the two-step products exhibit an activation energy of soft segment degradation that varies only in a narrow range, irrespective of hard segment content. For example, the value is 180 KJ mol<sup>-1</sup> for 30 % PU content and 190 KJ mol<sup>-1</sup> for 70 % content. It was also found that the activation energy of soft segment degradation differs greatly between one-step and two-step products at all hard segment contents. The two-step samples exhibit much higher values compared to the one-step samples. The direct effect of PU content on the stability of NR is not expected since these are phase separated systems. It seems, however, that NR structure stands modified so as to alter the activation energy for its degradation, depending on the method of synthesis and also with the variation in PU content.

The above observations may be explained based on the occasional multifunctionality of liquid NR. In addition to terminal hydroxyl groups, liquid NR molecules may possess hydroxyl functionality in the molecular chain. This arises by the opening of a few number of epoxy groups, which were inducted into the chain during the depolymerisation process. The multifunctionality of liquid NR leads to the crosslinking of segments during chain extension in the presence of diisocyanate and diols (Fig 10). Crosslinking obviously causes NR segments in the block copolymer to be stable.

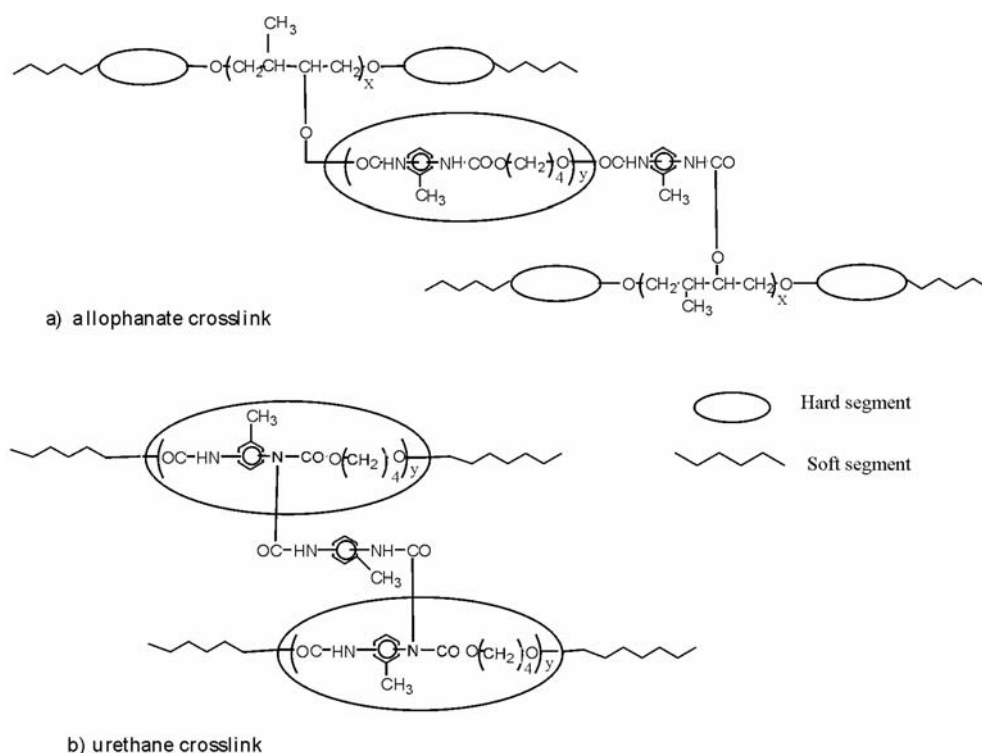


Fig. 10. Schematic representation of crosslinks formed in one-step and two-step block copolymers:  
a) allophanate crosslink in hard segment; b) urethane crosslink in soft segment

In one-step synthesis, diisocyanate is added to a mixture of NR and extender diol. Diisocyanate reacts preferentially with the extender diol in the initial stages of forming the polyurethane segments, since the extender diol is present in large excess compared to NR in the reaction mixture. As the relative concentration of diol decreases, diisocyanate tends to react with the hydroxyl group of NR chains, forming isocyanate endcapped NR molecules. These undergo chain extension with the hydroxyl bearing polyurethane segments. Multifunctionality in NR thus causes chain extension from all centers of hydroxyl occupation, which finally leads to crosslinking. The one-step product with 30 % PU content thus gives a value of  $126 \text{ KJ}\cdot\text{mol}^{-1}$  for the activation energy NR segment degradation. As the PU content increases, however, the activation

energy tends to decrease and finally settles at  $90 \text{ KJ mol}^{-1}$  for 70% PU content. This decrease in the activation energy with increasing PU content for two-step samples can be explained basing on the fact that at higher PU content the reaction mixture contains a large excess of extender diol, so that the preferable reaction is between diisocyanate and the extender diol rather than the less reactive secondary hydroxyl groups in the NR chains. This results in a lower level of crosslinking in the NR soft segments as the hard segment content increases. In such cases, the activation energy for NR degradation decreases.

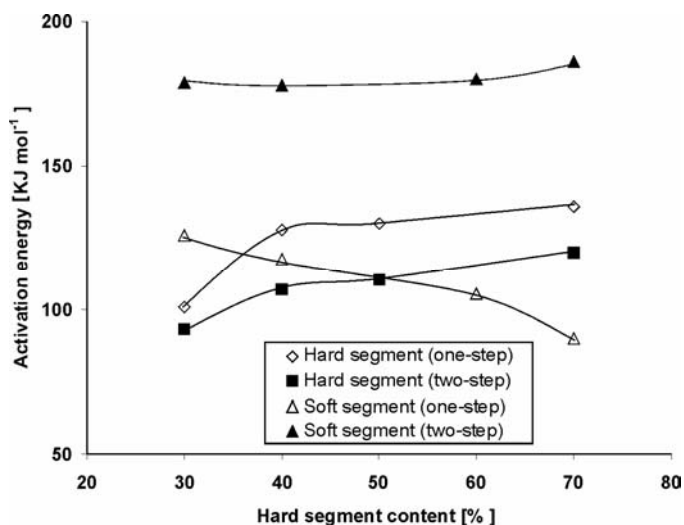


Fig. 11. Change of activation energy for the degradation with hard segments content in one- step and two-step block copolymers

Two-step synthesis, however, involves the introduction of excess isocyanate into NR solution during the initial stages, so that all the hydroxyl multifunctional centres in the NR chain react with  $-\text{NCO}$  groups. This is the case for all two-step syntheses, which means that two-step products should be crosslinked to a similar extent irrespective of PU content and hence the activation energy values remain almost steady as seen in Fig. 11. A higher level of crosslinking in two-step products explains the higher values of activation energy as compared to one-step products.

### 3.2. Stress-strain behaviour

The shapes of stress-strain curves are indicative of the nature of the materials (Fig. 12). Samples with low hard segment content resemble flexible rubber, while samples with higher hard segment content, which exhibit yielding and necking, resemble flexible plastics. A sample with hard segment content of approximately 70 wt. % undergoes a failure at yield point, characteristic of a rigid plastic. An increase in the hard

segment content thus tends to improve the tensile properties of both the one-step and two-step samples. This is due to pseudo crosslinking and reinforcing filler effects offered by hard segments [9]. Changes in the nature of the continuous phase of the material, from predominantly soft to hard with increasing hard segment content, also contribute to the improvement in tensile properties [10]. It has been reported that tensile strength increases suddenly above 60 % hard segment content [11], due to a marked change in domain morphology that results from an inversion of the hard and soft phases in polyurethane elastomers. Materials with intermediate hard segment content exhibit the tensile properties of rigid elastomers. This observation is in accordance with the findings of Chang et al. [12].

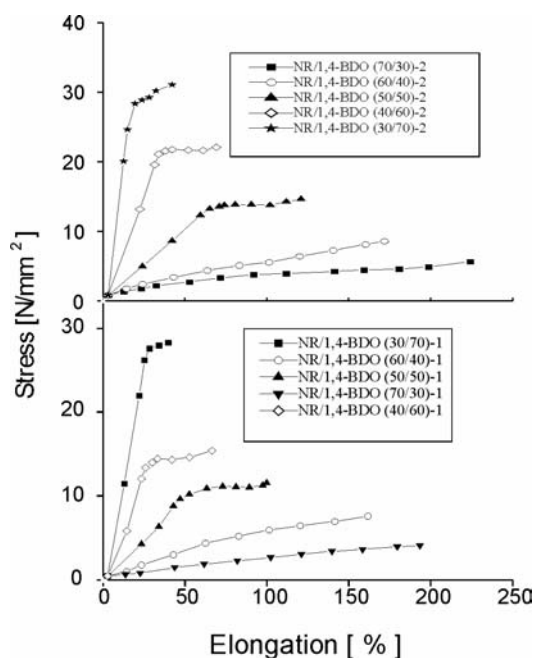


Fig. 12. Stress–strain curves of: a) one-step block copolymers  
b) two-step block copolymers

Two-step materials are found to possess slightly a higher tensile strength, ultimate elongation, and Young's modulus than the one-step products (Table VI). This could be explained basing on the higher level of crosslinking in the NR segments as described in the previous section. This could also be due to more systematic chain extension reactions as compared to one-step synthesis, which would reduce the number of loose NR chain ends in the product and enhance its tensile properties. An increase in both the tensile strength and elongation at break of the two-step samples compared to the respective one-step samples also support this view. Moreover, a systematic chain extension reaction leads to smaller interconnected PU domains, hence two-step products possess a large total surface area of these domains, which are more effective

at stopping catastrophic crack growth through the NR matrix. This view is supported by the findings of Smith [13].

The ultimate properties of these materials, however, are lower compared to those of conventional polyurethane elastomers. This is attributed to the absence of phase mixing, and to the inability of the soft segments to crystallize under strain [14]. The absence of strain-induced crystallinity may be due to the short length of the NR segments in the block copolymer.

The mode of failure as observed in SEM micrographs also supports the stress–strain behaviour of the samples. For example, Fig. 7b shows the presence of ridges of torn fragments on the fracture surface, which is in a highly deformed state. This indicates that the corresponding sample, viz., NR/1,4-BDO(50/50)-2, undergoes fracture by stretching and tearing, which is a characteristic feature of elastomers. In the case of NR/1,4-BDO(30/70)-2, SEM indicates a broken surface with a continuous network of hard phase, which could be formed by the brittle fracture of the sample. Such behaviour is characteristic of a rigid material and such variations in the mechanical nature of samples with increasing PU content have been supported by tensile properties as well. The matrices of the samples as seen in the SEM micrographs contribute basically to the mechanical behaviour. Therefore, an increase in PU content from 30 % to 70 % changes the ductile matrix into a rigid one due to phase inversion.

## 4. Conclusion

Liquid NR formed by the photochemical depolymerisation of NR is found to be useful for the synthesis of newer macromolecular structures such as block copolymers. In the present case, the block copolymers lack solubility, which indicates that they are crosslinked materials. The highly phase separated systems, however, are useful for structure–property relations in block copolymers. Further investigation may lead to the formation of a soluble product, which will extend the utility of the products into other areas such as surfactant etc.

## References

- [1] FRANCIS D.J., RAVINDRAN T., NAYAR M.R.G., 32nd Annual Polyurethane Technical Marketing Conference, San Francisco, October 1–4, 1989, 373.
- [2] PAUL C.J., NAIR M.R.G., *Ind. J. Nat. Rubber Research*, 1&2 (1992), 199.
- [3] PAUL C.J., NAIR M.R.G., NEELAKANTAN N.R., KOSHY P., *Polym. Eng. Sci.*, 3 (1998), 440.
- [4] PAUL C.J., NAIR M.R.G., NEELAKANTAN N.R., KOSHY P., IDAGE B.B., BHELHEKAR A.A., *Polymer* 26 (1998), 6861.
- [5] RAVINDRAN T., NAYAR M.R.G., FRANCIS D.J., *J. Appl. Polym. Sci.*, 42 (1991), 325.
- [6] RAVINDRAN T., NAYAR M.R.G., FRANCIS D.J., *J. Appl. Polym. Sci.*, 35 (1988), 122.
- [7] GUPTA T., ADHIKARI B., *Thermochim. Acta*, 402 (2003), 169.
- [8] SATAVA V., *Thermochim. Acta*, 2 (1971), 423.
- [9] LEE C.Y., KIM J., SUH K.D., *J. Appl. Polym. Sci.*, 78 (2000), 1853.

- [10] GORNA K., POLOWINSKI S., GOGOLEWSKI S., *J. Polym. Sci., A, Polym. Chem.*, 40 (2002), 156.
- [11] PETROVIC Z.S., FERGUSON I. *Prog. Polym. Sci.* 16 (1991), 695.
- [12] CHANG A.L., BRIBER R.B., THOMAS E.L., ZDRAHALA R.J., CRITCHFIELD F.E., *Polymer* 23 (1982), 1060.
- [13] SMITH T.L., *Polym. Eng. Sci.*, 17 (1977), 129.
- [14] SPECKHARD T.A., GIBSON P.E., COOPER S.L., CHANG V.S.C., KENNEDY J.P., *Polymer* 26 (1985), 55.

*Received 16 July 2004*  
*Revised 23 September 2004*

## **Correlation between high-pressure electrical properties of ZrO<sub>2</sub> and its crystallite size**

ANNA N. TREFILOVA<sup>1\*</sup>, ILIA V. KORIONOV<sup>1</sup>, ALEXEY N. BABUSHKIN<sup>1</sup>,  
WITOLD ŁOJKOWSKI<sup>2</sup>, AGNIESZKA OPALIŃSKA<sup>2</sup>

<sup>1</sup>Department of Physics, Ural State University, Lenina 51, Ekaterinburg, Russia

<sup>2</sup>High Pressure Research Center, Polish Academy of Sciences,  
ul. Sokołowska 29/37, 01-142 Warsaw, Poland

A relation between crystallite size and electrical properties of ZrO<sub>2</sub> has been investigated by measurements of high-pressure electrical resistance. The resistance of nanocrystalline praseodymium-doped zirconia powders has been measured in the pressure and temperature ranges between 15 and 50 GPa, and 77 and 400 K, respectively. Around 30–37 GPa the resistances of all samples decrease by 3–4 orders of magnitude. Therefore, the anomalies in the pressure dependence of the resistance and of parameters depending on the concentration, mobility and activation energy of the charge carriers were found at ca. 40–45 GPa. The activation energy of the charge carriers depends on the crystallite size.

*Key words: zirconium dioxide; electrical properties; pressure-induced phase transition; nanocrystalline sample*

### **1. Introduction**

Zirconium dioxide, a major component of the best fuel cell materials [1], exhibits quite interesting properties. Studies on the high pressure behaviour of pure ZrO<sub>2</sub> revealed the presence of successive transformations to two different orthorhombic phases (Ortho-I and Ortho-II) [2]. Ortho-I is a distorted fluorite structure and Ortho-II is a densely packed PbCl<sub>2</sub>-type structure. In his recent work Ohtaka et al. [3] suggest that the monoclinic-to-Ortho-I and Ortho-I-to-Ortho-II phase transitions occur at about 4 GPa and 12 GPa, respectively, for pure ZrO<sub>2</sub> near room temperature. However, the latter (reconstructive) transition is extremely sluggish and the metastability is observed over a wide pressure range.

---

\* Corresponding author, e-mail: Anna.Trefilova@usu.ru.

In this paper, supplementing our earlier publication [4], we report on the results of investigation of a correlation between electrical properties and crystallite size of  $\text{ZrO}_2$  in the pressure range between 15 and 50 GPa and temperature range between 77 and 400 K. Size of crystallites changed from 10 to 500 nm. Our experimental data reveal that the smaller crystallite size, the higher is the transformation pressure.

## 2. Experimental

The d.c. conductivity measurements were carried out in a diamond anvil cell (DAC) with anvils of the “rounded cone-plane” (Verechagin–Yakovlev) type made of synthetic carbonado-type diamonds [5], consisting of dielectric grains of synthetic diamonds in layers of conducting materials. These anvils are relatively good conductors, thus permitting measurement of the resistances of samples placed between the anvils in the DAC by using the anvils as the electrical contacts to the sample. The procedure for the determination of the pressure reached in a DAC of the “rounded cone-plane” type has been described in [6, 7].

Measurements were made with powder samples of  $\text{ZrO}_2$  with various crystallite sizes and with a “bulk material” samples of zirconia containing 5 mole % of  $\text{Y}_2\text{O}_3$ . The crystallite sizes in the “bulk” samples amounted ca. 500 nm. The sample was synthesized by the Daiichi Kigensou Company in Japan (Lot # NEY-5M LO524). Moreover, we used nanocrystalline praseodymium-doped zirconia powders, produced using a microwave driven hydrothermal process under pressures up to 8 GPa. Nanopowders of  $\text{ZrO}_2$  containing 0.5 mole % of Pr were synthesized in the High Pressure Research Center of the Polish Academy of Sciences [8].

## 3. Results and discussion

The pressure dependences of the electrical resistivities of nanocrystalline  $\text{ZrO}_2$  are shown in Fig. 1. At ca. 30–37 GPa, the resistances of all samples decrease by 3–4 orders of magnitude. Based on the fact that this result could be reproduced using different samples and different DACs, we are sure that the effect is not due to a short-circuit between the anvils nor to a dielectric breakdown of the sample. Furthermore, we found that the value of this pressure increases with the decrease of the crystallite size. Further anomalies have been found at ca. 40–45 GPa.

The temperature dependence of the resistance of the nanocrystalline samples at most pressures can be fitted by the equation

$$R = R_0 \exp\left(\frac{E_a}{kT}\right) \quad (1)$$

$E_a$  standing for the activation energy, and  $R_0$  being a parameter depending on the mobility and concentration of the charge carriers.

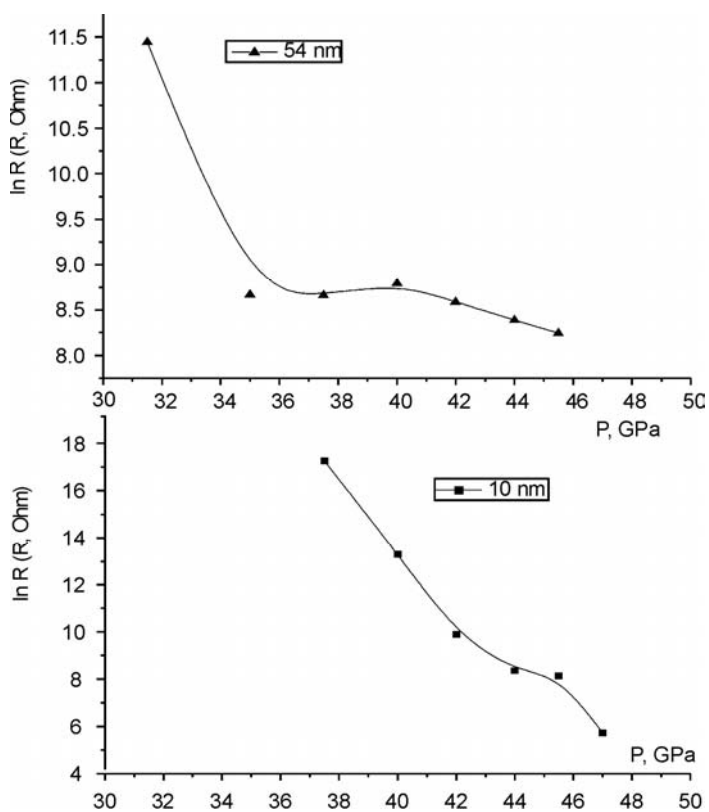


Fig. 1. Pressure dependences of the electrical resistance in nanocrystalline  $ZrO_2$  samples determined for two average crystallite sizes. The measurements were taken at 290 K

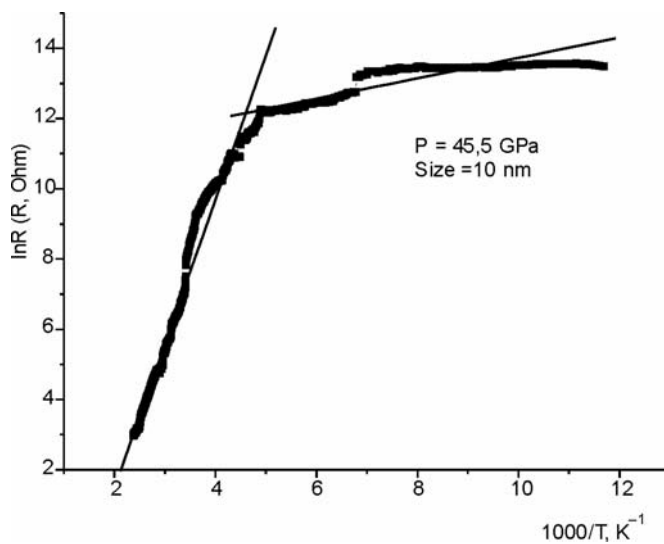


Fig. 2. A typical temperature dependence of resistance in a 10 nm sample

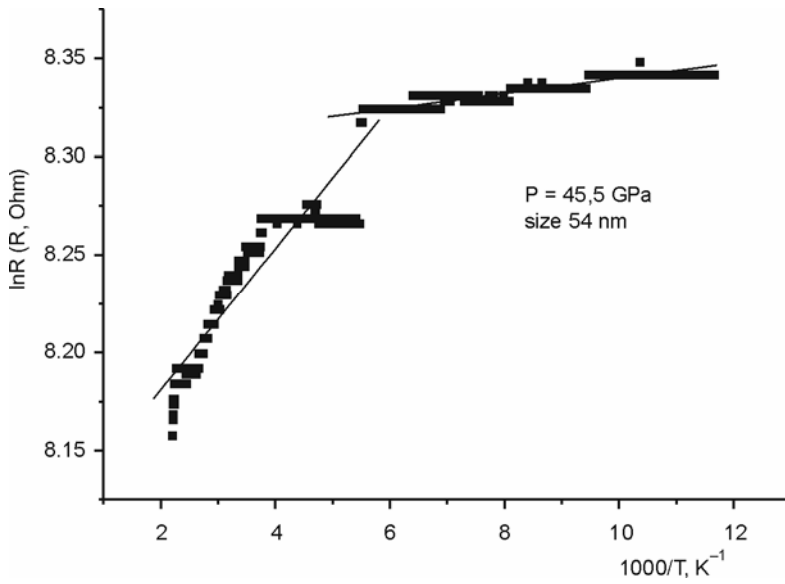


Fig. 3. A typical temperature dependence of resistance in a 54 nm sample

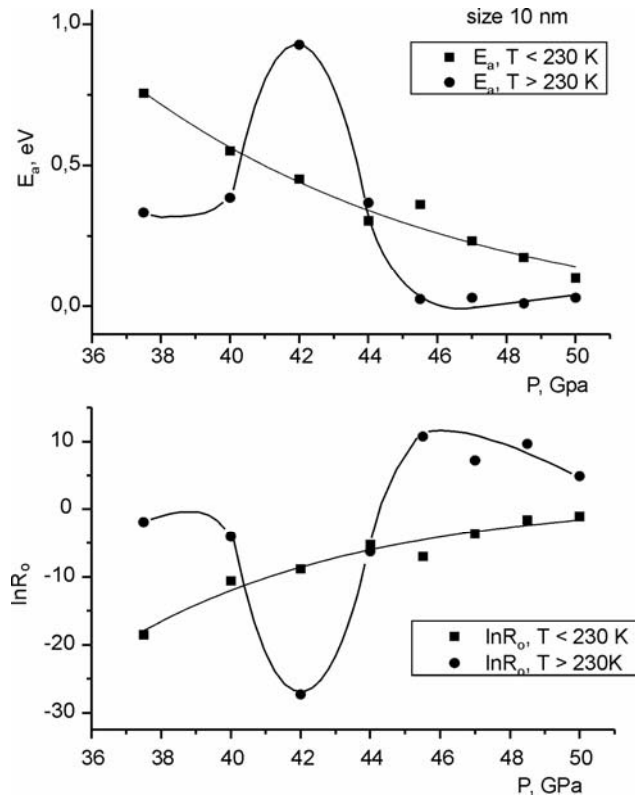


Fig. 4. The pressure dependence of  $E_a$  and  $R_0$  in a 10 nm sample

The temperature dependences of the resistance for samples 10 nm and 54 nm at 45.5 GPa consist of two regions characterized by different slopes (Figs. 2 and 3). In a 10 nm sample the crossover appears at 230 K, whereas in a 54 nm sample – between 230 and 250 K. The temperature dependence determined in a 12 nm sample at 42 GPa consists of three regions: below 230 K, between 230 and 310 K, and above 310 K.

The temperature dependence of the resistance of the bulk material varies qualitatively with the pressure applied. At 40 GPa the dependence consists of two regions, between 80 and 180 K, and between 180 and 400 K, corresponding to two different activation processes described by Eq. (1). Above 47 GPa, however, the dependence exhibits a metal-like character (with the positive temperature coefficient) at temperatures exceeding 320 K.

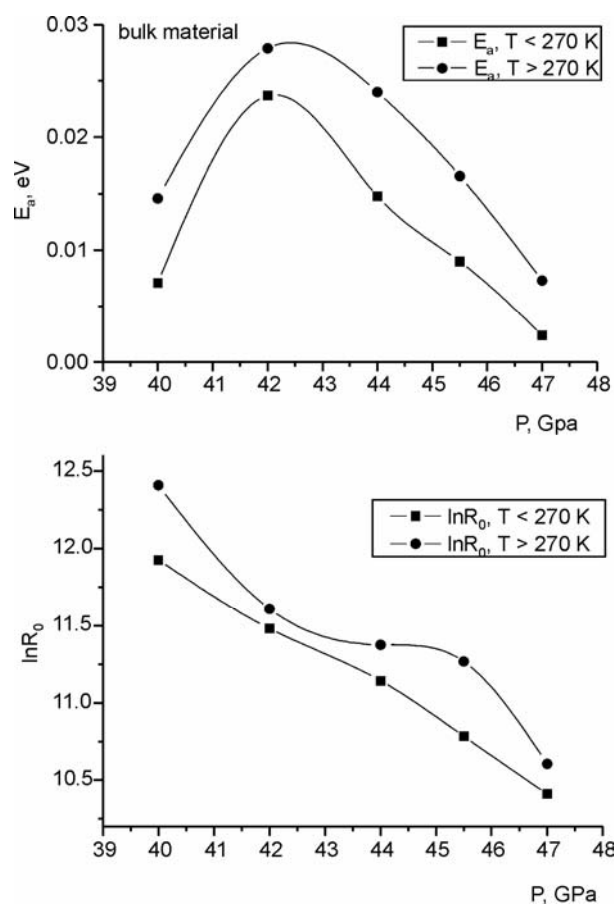


Fig. 5. The pressure dependence of  $E_a$  and  $R_0$  in a bulk sample

Pressure dependences of  $E_a$  and  $R_0$  are shown in Figs 4 and 5. Around 40–44 GPa maxima of the activation energy have been found in all samples, accompanied in some cases by local minima of the pre-exponential factor. This feature might be asso-

ciated with a structural phase transition occurring in  $ZrO_2$  in this pressure range. As  $R_0$  is connected with the concentration and mobility of charge carriers, the decrease of  $R_0$  may be associated with an increase of the mobility and/or the concentration of the charge carriers.

Our results indicate that the activation energy depends on the average size of crystallites: qualitatively,  $E_a$  was found to increase with decreasing crystallite sizes, ranging between 0.01 and 1 eV for a 10 nm sample, and between 0.001 and 0.01 eV for a 56 nm sample, whereas its value for bulk  $ZrO_2$  equals approximately 0.01–0.03 eV. One may speculate that surface effects essentially change the conductivity mechanism of  $ZrO_2$  at high pressures.

Our results provide a first hint that a structural phase transition occurring in  $ZrO_2$  may be connected with changes in the electronic structure but a further work is necessary to corroborate this claim and to determine the nature of the electronic changes.

### References

- [1] WUENSCH B.J., EBERMAN K.W., HEREMANS C., KU E.M., ONNERUD P., YEO E.M.E., HAILE S.M., STALICK J.K., JORGENSEN J.D., *Solid State Ionics*, 129 (2000), 111.
- [2] LEGER, J. M., TOMASZEWSKI P.E., ATOUF A., PEREIRA A.S., *Phys. Rev.*, 47 (1993), 14075.
- [3] OHTAKA O., FUKUI H., KUNISADA T., FUJISAVA T., FUNAKASHI T., UTSUMI W., IRIFUNE T., KURODA K., KIKEGAWA T., *Phys.Rev. B*, 63 (2001), 174108.
- [4] KORIONOV I.V., TREFILOVA A.N., BABUSHKIN A.N., ŁOJKOWSKI W., OPALIŃSKA A., *Mater. Sci.-Poland* 22 (2004), 241.
- [5] VERECHAGIN L.F., YAKOVLEV E.N., STEPANOV T.N., BIBAEV K.H., VINOGRADOV B.V., *Zh. Exp. Theor. Phys. Lett.*, 16 (1972), 240.
- [6] BABUSHKIN A.N., *High Pressure Res.*, 6 (1992), 349.
- [7] BABUSHKIN A.N., KANDRINA Y.A., KOBELEVA O.L., SCHKERIN S.N., VOLKOVA Y.Y., [in:] *Frontiers of High Pressure Research II: Application of High Pressure to Low-Dimensional Novel Electronic Materials*, H.D. Hochheimer, B. Kuchta, P.K. Dorhout, J.L. Yarger. (Eds.), Kluwer, Dordrecht, 2001, p. 131.
- [8] BONDIOLI F., FERRARI A.M., BRACCINI S., LEONELLI C., PELLACANI G.C., OPALINSKA A., CHUDOBA T., GRZANKA E., PALOSZ B., ŁOJKOWSKI W., *Solid State Phenomena*, 94 (2003), 193.

*Received 18 February 2004*

*Revised 5 October 2004*

# **Functions of $\text{Eu}^{3+}$ ions in materials with CdS nanoparticles and oxide matrices**

ANDRZEJ M. KŁONKOWSKI\*, IWONA SZAŁKOWSKA

Faculty of Chemistry, University of Gdańsk,  
ul. Sobieskiego 18, 80-952 Gdańsk, Poland

CdS semiconductor nanoparticles are used to improve the luminescence properties of europium(III)-doped matrices such as silica xerogel and silica nanoparticles, both prepared by a sol-gel method as well as zeolite NaY. The impregnation of CdS nanosized clusters on an  $\text{Eu}^{3+}$ -doped matrix enhances the luminescence of both dopants. Additionally, the luminescence of the materials can be improved by thermal treatment and by changing the  $\text{Eu}^{3+}/\text{CdS}$  molar ratio.  $\text{Eu}^{3+}$  emission spectra show changes in the intensities of the bands at 595 and 612 nm, depending on the structural order of the oxide matrices.

*Key words: luminescent materials; nanoparticles;  $\text{Eu}^{3+}$  ions; oxide matrices; structural order*

## **1. Introduction**

Nanoparticles small enough have a very significant portion of their total atoms on the surface. Therefore, intrinsically different surface chemistry due to unusual surface defects and unusual electronic states affecting surface chemistry might be expected. Due to the range of dimensions involved in nanostructures, the surface-to-volume ratio is high and a significant proportion of the molecules in such systems lie in or close to the region of inhomogeneity associated with particle-medium interfaces. These molecules will have properties (e.g. energy) different from those in the bulk phase. A significant and often dominating contribution comes from molecules in the interfacial region. This is why surface chemistry plays such an important role in

---

\*Corresponding author, e-mail: aklonk@chemik.chem.univ.gda.pl.

nanoparticles and why surface properties become evident when particle size falls below 100 nm [1].

The II–VI semiconductor nanocrystals offer an attractive application. Their emission spectra are very narrow (spectrally pure) and the emission colour is simply tuned by changing their size. As nanocrystal size increases, the energy of the first excited state decreases, qualitatively following a particle-in-a-box behaviour.

This size dependence and the emergence of a discrete electronic structure from a continuum of levels in the valence and conduction bands of the bulk semiconductor result from quantum confinement; hence, semiconducting nanocrystals are referred to as “quantum dots” [2].

In the case of  $\text{Eu}^{3+}$  ions, the main emission lines occur between the  ${}^5\text{D}_0$  level and  ${}^7\text{F}_J$  multiplets. Their narrow emission lines have low intensity, because they are parity and spin forbidden. The oscillator strengths of absorption to the excited states of  $\text{Eu}^{3+}$  ions, as for other rare earth ions, are of the order of magnitude  $10^{-5}$ – $10^{-6}$  [3].

The  ${}^5\text{D}_0 \rightarrow {}^7\text{F}_J$  emission is very suitable for surveying the transition probabilities of sharp spectral features in rare earths. If a rare-earth ion occupies a site with inversion symmetry in a crystal lattice, the optical transitions between  $4f^n$  levels are strictly forbidden as electric-dipole transitions (due to the parity selection rule). They can only occur as magnetic-dipole transitions, which obey the selection rule  $\Delta J = 0, \pm 1$  ( $J = 0$  to  $J = 0$  being forbidden), or as vibronic electric dipole transitions.

If there is no inversion symmetry at the site of a rare-earth ion, the odd crystal field components can mix opposite-parity states into  $4f^n$ -configurational levels. Electric-dipole transitions are now no longer strictly forbidden and appear as weak lines in the spectra, the so-called forced electric-dipole transitions. Some transitions, viz. those with  $\Delta J = 0, \pm 2$ , are hypersensitive to this effect. Even for small deviations from inversion symmetry, they appear dominantly in the spectrum [4].

Hayakawa et al. discussed the interaction between CdS nanoparticles and  $\text{Eu}^{3+}$  ions in silica xerogel as observed by photoluminescence spectroscopy [5–7]. The authors observed that CdS nanocrystals deposited on the surface of  $\text{Eu}^{3+}$ -doped silica xerogel greatly enhanced the luminescence from Eu(II) ions. Reisfeld et al. formed CdS quantum dots in  $\text{ZrO}_2$  films together with Eu(III) and Tb(III) ions [3]. The increased emission intensity of the lanthanide ions was explained by energy transfer resulting from electron-hole recombination in the CdS to the lanthanide.

The matrices in our samples were prepared by a conventional sol-gel method and then immersed in  $\text{Eu}^{3+}$  aqueous solution and a CdS sol. The deposition of CdS nanocrystals on the surface of  $\text{Eu}^{3+}$ -doped  $\text{SiO}_2$  xerogel greatly enhanced the luminescence emission not only from  $\text{Eu}^{3+}$  ions, but also from the CdS nanoparticles themselves. Here we report the enhanced luminescence of both these components, incorporated in such oxide matrices as silica xerogel, silica nanoparticles, and zeolite NaY. Moreover, changes are observed in the relative intensities of emission bands attributed to  ${}^5\text{D}_0 \rightarrow {}^7\text{F}_1$  and  ${}^5\text{D}_0 \rightarrow {}^7\text{F}_2$  hypersensitive transitions, which are related to structural order changes in the matrices.

## 2. Experimental

### 2.1. Sample preparation

Silica xerogel was prepared by a sol-gel process using Si(OCH<sub>3</sub>)<sub>4</sub> (TMOS, Aldrich), distilled water, and methanol (POCh, Poland) [7]. The obtained alcogel was dried at room temperature and then at 120 °C for 3 h. The xerogel was immersed for 1 day in an aqueous solution of EuCl<sub>3</sub>. After that, the material was rinsed with water and dried at 100 °C for 5 h. CdS sol was prepared according to the method described elsewhere [8], viz. 1 cm<sup>3</sup> concentrated (0.1 M) Na<sub>2</sub>S (P.O.Ch, Poland) was injected rapidly into 50 cm<sup>3</sup> stirred 10<sup>-2</sup> M Cd(NO<sub>3</sub>)<sub>2</sub> (POCh, Poland) containing 10<sup>-2</sup> M (NaPO<sub>3</sub>)<sub>3</sub> (POCh, Poland). After immersion in the CdS sol for 1 day, the Eu<sup>3+</sup>-containing silica xerogel with adsorbed CdS particles was washed with water and dried at 100 °C for 5 h [9].

Monodispersed silica nanoparticles were synthesized at 25 °C from the solution containing 0.25 M Si(OC<sub>2</sub>H<sub>5</sub>)<sub>4</sub> (TEOS, Aldrich), 0.5 M NH<sub>3</sub>, and 7.7 M deionized H<sub>2</sub>O in ethanol [10]. The obtained silica particles, with an average size of 392 nm, were (as above) immersed in EuCl<sub>3</sub> solution and then CdS sol. The same impregnation procedure was followed for zeolite NaY (Aldrich), which was also treated as a matrix for Eu<sup>3+</sup> ions and CdS nanoparticles.

To compare the difference in the emission intensities between the samples with and without CdS, and the structural orders in matrices, the same procedure was done for silica xerogel containing only Eu<sup>3+</sup> or CdS, which were designated as control samples. In each case, the Eu<sup>3+</sup> concentration in the impregnation solution was 5 × 10<sup>-5</sup> mole per gram of matrix. The luminescence spectra of the samples consisting of Eu<sup>3+</sup> ions and CdS nanoparticles immobilized in solid matrices were recorded with a Perkin-Elmer LS-50 spectrofluorimeter equipped with a reflection spectra attachment.

## 3. Results

Figure 1 shows the luminescence spectra of silica xerogels doped with Eu<sup>3+</sup> ions (emission spectrum (a)), CdS nanoparticles (emission spectrum (b)), as well as with both Eu<sup>3+</sup> and CdS (two emission spectra (c) and (d), and excitation spectrum (e)). The emission spectrum (a) consists of two bands at 595 and 612 nm, which are attributed to the <sup>5</sup>D<sub>0</sub> → <sup>7</sup>F<sub>1</sub> and <sup>5</sup>D<sub>0</sub> → <sup>7</sup>F<sub>2</sub> transitions in the Eu<sup>3+</sup> ion, respectively [4]. The emission spectrum (b), with a band at 620 nm, is characteristic of CdS. The three-component material comprising the silica xerogel doped with both Eu<sup>3+</sup> and CdS exhibits manifold higher intensity in both the cases simultaneously, viz. Eu<sup>3+</sup> and CdS (see Fig. 1c and d). In the Eu<sup>3+</sup> emission spectrum (Fig. 1c), the ratio of the <sup>5</sup>D<sub>0</sub> → <sup>7</sup>F<sub>2</sub>/<sup>5</sup>D<sub>0</sub> → <sup>7</sup>F<sub>1</sub> band intensities is lower than for the two-component material with Eu<sup>3+</sup> (Fig. 1a). The excitation spectrum of the three-component material consists of two distinct bands: at 394 nm, related to Eu<sup>3+</sup>

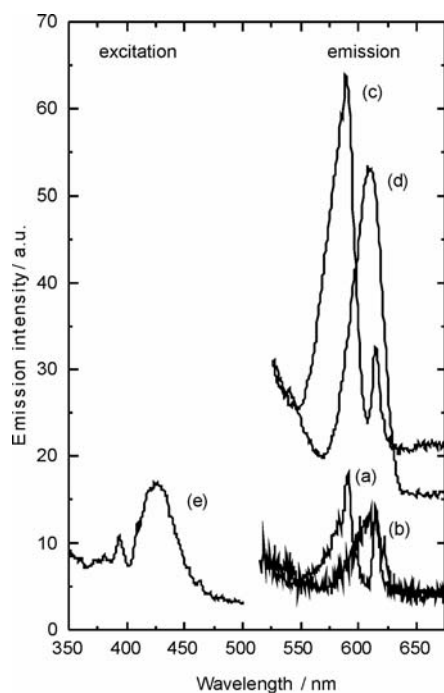


Fig. 1. Emission spectra of: SiO<sub>2</sub> xerogel impregnated with Eu<sup>3+</sup>,  $\lambda_{\text{exc}} = 394$  nm (a), SiO<sub>2</sub> impregnated with CdS sol,  $\lambda_{\text{exc}} = 420$  nm (b) and (d), SiO<sub>2</sub> impregnated with Eu<sup>3+</sup> and CdS,  $\lambda_{\text{exc}} = 394$  and 420 nm (c), excitation spectrum of SiO<sub>2</sub> impregnated with Eu<sup>3+</sup> and CdS,  $\lambda_{\text{em}} = 615$  nm (e)

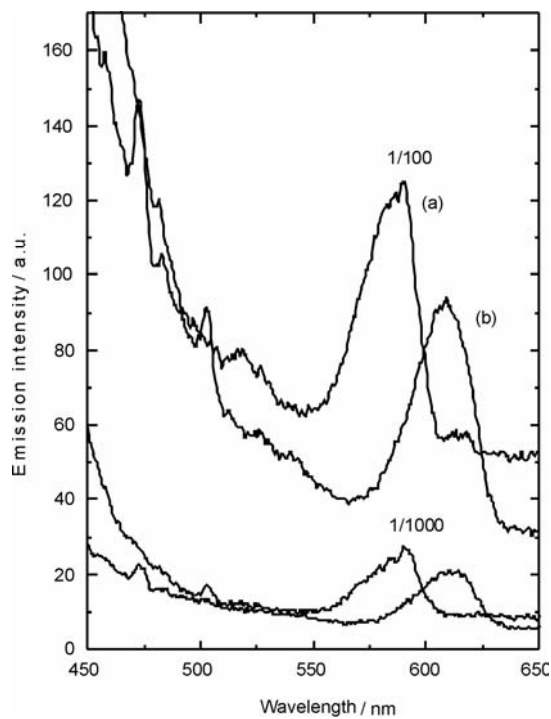


Fig. 2. Emission intensity changes with the Eu<sup>3+</sup>/CdS molar ratio in SiO<sub>2</sub> nanoparticles impregnated with Eu<sup>3+</sup> and CdS: a)  $\lambda_{\text{exc}} = 394$  nm, b)  $\lambda_{\text{exc}} = 420$  nm

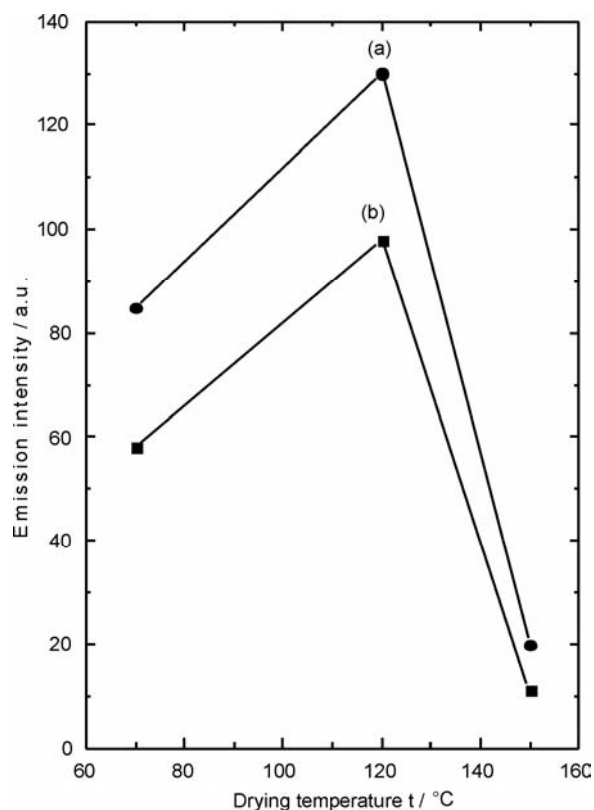


Fig. 3. Emission intensity vs. the drying temperature of SiO<sub>2</sub> xerogel impregnated with Eu<sup>3+</sup> and CdS: a)  $\lambda_{\text{exc}} = 394$  nm, b)  $\lambda_{\text{exc}} = 420$  nm. The lines are drawn as guides for the eye

ions, and at 420 nm, related to CdS nanoparticles (Fig. 1e). In the three-component material (e.g. with SiO<sub>2</sub> nanoparticles as a matrix), the emission intensities of Eu<sup>3+</sup> and CdS depend on the Eu<sup>3+</sup>/CdS molar ratio, i.e. for higher value of this ratio (in the range 1/1000–1/100), the intensities of both spectra increase (Fig. 2). Changes in the emission intensities with the drying temperature of the material are shown in Fig. 3. The intensity reaches a maximum in both cases at 120 °C. In the material dried at a higher temperature (150 °C), the emission intensity dramatically decreases. In Figure 4, the emission spectra of three-component materials with various matrices are compared. Thus, the emission spectra in Fig. 2 are related to the zeolite NaY, silica nanoparticles, and silica xerogel, respectively. In each case, relatively high intensities of both the CdS and Eu<sup>3+</sup> emission spectra are observed, but especially high values are reached for silica nanoparticles. In Fig. 2a, practically only the  $^5\text{D}_0 \rightarrow ^7\text{F}_1$  band is seen in the Eu<sup>3+</sup> spectrum, while in Fig. 2b, besides the  $^5\text{D}_0 \rightarrow ^7\text{F}_1$  band there is also the  $^5\text{D}_0 \rightarrow ^7\text{F}_2$  band with very low intensity. Finally, in Fig. 2c both the bands are present, however the one at a lower wavelength distinctly dominates.

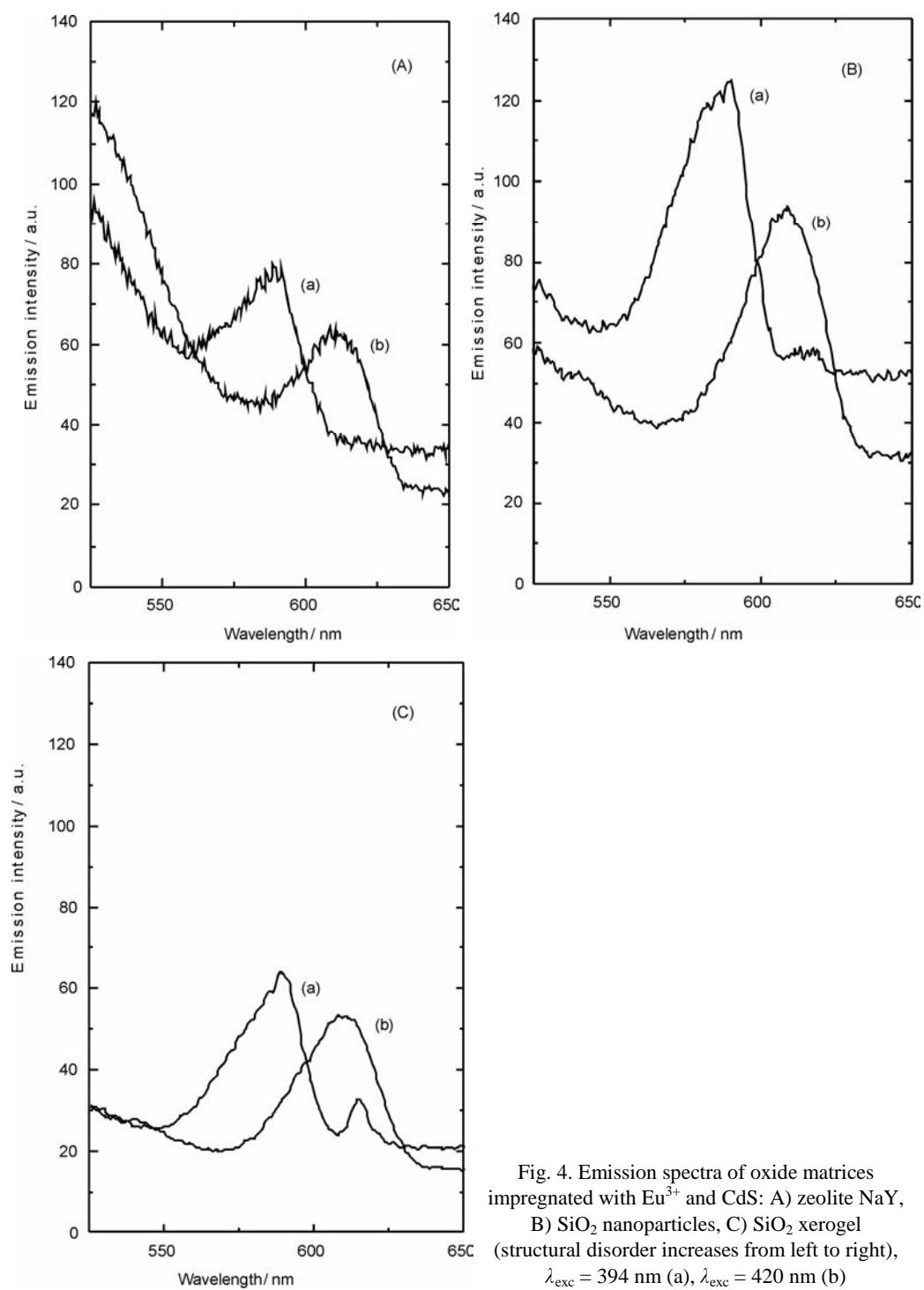


Fig. 4. Emission spectra of oxide matrices impregnated with  $\text{Eu}^{3+}$  and CdS: A) zeolite NaY, B)  $\text{SiO}_2$  nanoparticles, C)  $\text{SiO}_2$  xerogel (structural disorder increases from left to right),  $\lambda_{\text{exc}} = 394 \text{ nm}$  (a),  $\lambda_{\text{exc}} = 420 \text{ nm}$  (b)

## 4. Discussion

CdS nanocrystals have been widely studied because they find several applications in optoelectronics. The most striking feature of these nanosized materials is that their chemical and physical properties differ from those of bulk solids. The reasons explaining this behaviour can be determined by the quantum size effect in nanometer scale materials [11]. Nonradiative energy transfer from a surface level on the CdS particle to the Eu<sup>3+</sup> ion has been thoroughly discussed by Hayakawa, Selvan and Nogami [5].

According to our experimental results, the emission of f-f transitions is enhanced when CdS is present in the Eu<sup>3+</sup>-doped silica xerogel as a II–VI semiconductor and vice versa, the emission of the semiconductor increases in the presence of Eu<sup>3+</sup> ions in the matrix (compare spectra (a) and (c), and (b) and (d) in Fig. 1). It is noteworthy that in both emission actions no CdS → Eu<sup>3+</sup> or Eu<sup>3+</sup> → CdS energy transfer is observed, because Eu<sup>3+</sup> ions and CdS nanoparticles are excited by a  $\lambda_{\text{exc}}$  typical of these particles (394 and 420 nm, respectively). The positions of the CdS spectra (b) and (d) at 620 nm are typical of the bulk semiconductor.

In Eu<sup>3+</sup> spectra, the intensity ratio of the hypersensitive bands ( $^5\text{D}_0 \rightarrow ^7\text{F}_2/^5\text{D}_0 \rightarrow ^7\text{F}_1$ ) decreases when CdS is present (cf. Figs. 1a, c). This means that the presence of nanocrystalline CdS increases the domination of the band characteristic for Eu<sup>3+</sup> ions, which occupy the crystal lattice sites with inversion symmetry, in comparison to the case only Eu<sup>3+</sup> ions exist in the amorphous silica matrix.

When the Eu<sup>3+</sup>/CdS molar ratio increases, luminescent centres of Eu<sup>3+</sup> are formed, and more electrons and holes in CdS nanoparticles can be excited, and consequently radiative recombination in both cases is enhanced (Fig. 2). The simultaneous enhancement of Eu<sup>3+</sup> and CdS emissions reaches a maximum if the sample is dried at 120 °C, as illustrated in Fig. 3. For Eu<sup>3+</sup>, this effect is caused by removing water as a quencher. A higher concentration of active Eu<sup>3+</sup> emission centres probably improves CdS emission intensity. At temperatures above 120 °C, both emission centres are partly deactivated.

Among the studied oxide matrices, the highest luminescence improvement for Eu<sup>3+</sup> and CdS is noted for silica nanoparticles (Fig. 4). Matrices in the materials are ordered according to their structural order: crystalline zeolite (A) > silica nanoparticles (crystallites) (B) > amorphous silica xerogel (C). With increasing disorder, the band intensity attributed to the  $^5\text{D}_0 \rightarrow ^7\text{F}_2$  transition increases. Thus, the Eu<sup>3+</sup> ion might be used as a probe and the intensity ratio of its bands ( $^5\text{D}_0 \rightarrow ^7\text{F}_2/^5\text{D}_0 \rightarrow ^7\text{F}_1$ ) could serve as a measure of the structural order in materials with oxide matrices.

## 5. Conclusions

Luminescent materials with Eu<sup>3+</sup> ions and CdS nanostructures, immobilized on such oxide matrices as silica xerogel, silica nanoparticles, and zeolite NaY by im-

pregnation, exhibit an enhanced emission intensity of both components ( $\text{Eu}^{3+}$  and CdS) when excited by the wavelengths characteristic for the species (394 and 420 nm, respectively).

The emission intensity of both components can be improved by changing the  $\text{Eu}^{3+}/\text{CdS}$  molar ratio in the range 1/1000–1/100 and drying at an elevated temperature (not higher than 120 °C).

The luminescence emission spectra of the  $\text{Eu}^{3+}$  probe ion allow the intensity ratio of the bands  ${}^5\text{D}_0 \rightarrow {}^7\text{F}_2$  and  ${}^5\text{D}_0 \rightarrow {}^7\text{F}_1$  to be treated as a measure of the structural order in doped materials.

#### Acknowledgements

The financial support of this work by the Polish Scientific Research Council (Grant 1235/T09/2001/20) is gratefully acknowledged.

#### References

- [1] EVERETT D.H., *Basic Principles of Colloid Science*, Royal Society of Chemistry, London, 1992, p. 8.
- [2] KIPPENY T., SWAFFORD L.A., ROSENTHAL S.J., *J. Chem. Educ.*, 79 (2002), 1094.
- [3] REISFELD R., GAFT M., SARIDAROV T., PANCZER G., ZELNER M., *Mater. Lett.*, 45 (2000), 154.
- [4] BLASSE G., GRABMAIER B.C., *Luminescent Materials*, Springer-Verlag, Berlin, 1994, p. 41ff.
- [5] HAKAYAMA T., TAMIL SELVAN S., NOGAMI M., *J. Sol-Gel Sci. Tech.*, 19 (2000), 779.
- [6] HAKAYAMA T., TAMIL SELVAN S., NOGAMI M., *J. Luminesc.*, 87–89 (2000), 532.
- [7] BRINKER C.J., SCHERER G.W., *Sol-Gel Science, The Physics and Chemistry of Sol-Gel Processing*, Academic Press, London, 1990.
- [8] TAMIL SELVAN S., HAKAYAMA T., NOGAMI M., *J. Non-Cryst. Solids*, 291 (2001), 137.
- [9] TAMIL SELVAN S., HAYAKAWA T., NOGAMI M., *J. Phys. Chem. B*, 103 (1999), 7064.
- [10] BOGUSH G.H., TRACY M.A., ZUKOSKI C.F. IV, *J. Non-Cryst. Solids*, 104 (1988), 95.
- [11] KLABUNDE K.J., MOHS C., [in:] *Chemistry of Advanced Materials. An Overview*, L.V. Interrante, M.J. Hampden-Smith (Eds.), Wiley, New York 1998, Chap. 7.

*Received 30 August 2004*

*Revised 14 October 2004*

# Formation of nanostructured Tb<sup>3+</sup>-doped yttrium aluminium garnets by the glycol route

PIOTR MAZUR<sup>1\*</sup>, DARIUSZ HRENIAK<sup>1</sup>,  
JANNE NIITTYKOSKI<sup>2</sup>, WIESŁAW STREK<sup>1</sup>, JORMA HÖLSÄ<sup>2</sup>

<sup>1</sup>Institute of Low Temperature and Structure Research, Polish Academy of Sciences,  
P.O. Box 1410, 50-950 Wrocław, Poland

<sup>2</sup>Department of Chemistry, University of Turku, FI-20014 Turku, Finland

Terbium-doped nanocrystalline yttrium aluminium garnet phases, Y<sub>3</sub>Al<sub>5</sub>O<sub>12</sub>:Tb<sup>3+</sup> (YAG:Tb<sup>3+</sup>), were obtained by using rare-earth nitrates as the starting materials, together with citric acid and ethylene glycol according to the Pechini method. Thermogravimetric and differential thermal analysis were used to study the thermal decomposition of the precursor gels and the formation of nanocrystalline YAG:Tb<sup>3+</sup>. An increase in garnet nanocrystallite size from 20 to 40 nm with annealing temperature increasing from 800 to 1160 °C was evidenced with X-ray powder diffraction measurements. The intensity as well as the decay times of both <sup>5</sup>D<sub>3</sub> and <sup>5</sup>D<sub>4</sub> emissions of Y<sub>3</sub>Al<sub>5</sub>O<sub>12</sub>:Tb<sup>3+</sup> were not found to depend on annealing and were thus independent of crystal size.

Key words: *garnet; YAG, nanocrystals; luminescence; terbium*

## 1. Introduction

It is well known that polycrystalline yttrium aluminium garnets, Y<sub>3</sub>Al<sub>5</sub>O<sub>12</sub> (YAG), doped with selected rare earth ions (Tb<sup>3+</sup>, Eu<sup>3+</sup>, Ce<sup>3+</sup>) can be used as efficient phosphors [1–3]. However, the standard synthesis of these materials as single crystals requires temperatures above 1600 °C and intricate conditions during the crystal growth process. Due to these reasons, garnets have been developed for optical applications in other forms, such as micrometric phosphor powders, scintillator ceramics, thin films, and laser ceramics [4–7]. In recent years, a growing number of investigations have been focused on the production of nanocrystalline YAG powders, which have optical properties comparable to YAG powders of micrometer size. For example, the first attempts to construct a solid-state laser based on polycrystalline ceramics were re-

---

\* Corresponding author, e-mail: mazur@int.pan.wroc.pl.

ported some time ago [5]. YAG powders doped with terbium and europium ions are potential candidates for materials in luminescent lamps and display applications [3].

Yttrium aluminium garnets are conventionally manufactured by a solid-state reaction between the rare earth oxides,  $Y_2O_3$  and  $Al_2O_3$  at high temperatures, typically around 1600 °C. In the last decade, several low temperature processes such as co-precipitation [8], the sol-gel method [9, 10], combustion [11–13], and hydrothermal synthesis [14] have been developed to fabricate garnets with fine particle size. The fabrication technology of high-quality nanocrystalline YAG powders, however, is still subject to intense studies since the optical properties of nanocrystals are strongly dependent on the size of individual nanocrystals and conditions of syntheses. Therefore, any information about the nature and formation of crystalline phases is of great importance.

In the present report, the results of studies concerning the formation and properties of  $Tb^{3+}$ -doped yttrium aluminium garnet nanocrystals are revealed. They were obtained by a glycol-route method, also called Pechini's method. Formation was investigated by the TG and DTA methods, which allow the weight loss of the sample to be characterized in detail and additionally gives information about the occurrence of energetic processes [15] during annealing, particularly the decomposition of yttrium nitrate [16] and carbonate [17]. Results of the thermal analysis of the formation of the nanocrystalline YAG: $Tb^{3+}$  phase were compared with those obtained by luminescence methods and X-ray powder diffraction (XRD).

## 2. Experimental

The preparation method of nanocrystalline yttrium aluminium garnets has been reported elsewhere [18, 19]. Briefly, aqueous nitrate solutions of yttrium and terbium were prepared by dissolving high purity  $Y_2O_3$  (99.999 %) and  $Tb_4O_7$  (99.99 %) with ultra-pure  $HNO_3$ . Yttrium nitrate and aluminium chloride (99.9995 %) were then dissolved in stoichiometric amounts in a mixture of aqueous citric acid and ethylene glycol to give a molar ratio of 3:5:50:20. Terbium nitrate was added to the homogeneous solution to give a nominal concentration of terbium vs. yttrium of 2 mole %. The solutions obtained were ultrasonically stirred for two hours. Then they were heated at 80 °C for several hours and dried at 100 °C for seven days in order to obtain gels. Samples of the crushed gel were heat-treated at selected temperatures between 800 and 1160 °C in air in an electric furnace to obtain single phases of yttrium aluminium garnet.

Thermogravimetric curves were recorded in air (flow rate:  $100\text{ cm}^3\cdot\text{min}^{-1}$ ) with a TA Instruments SDT 2960 Simultaneous DTA-TGA thermoanalyser. The sol-gel and solid-state reactions were studied in the temperature range from 25 °C to 1160 °C, with a heating rate of  $5\text{ K}\cdot\text{min}^{-1}$ .  $\alpha\text{-Al}_2O_3$  was used as the DTA reference material. The structure and crystallinity of the samples were evaluated by X-ray powder diffraction with a Stoe powder diffractometer equipped with a position-sensitive detector. Filtered  $CuK_{\alpha 1}$  radiation ( $\lambda = 1.5406\text{ \AA}$ ) and a  $2\theta$  step of 0.02 degrees was

used in the  $2\theta$  range 15–60 degrees. TEM micrographs were recorded with a JEM-3010 (JEOL) electron microscope.

The luminescence spectra of YAG:Tb<sup>3+</sup> between 300 and 900 nm were measured at room temperature with an ISA Jobin-Yvon TRW 1000 monochromator equipped with standard detection as well as data acquisition and treatment systems. All spectra recorded were corrected for the sensitivity of the experimental set-up. The resolution of the spectra was not better than 0.2 nm. The 266 nm line of the 4th harmonic of an Nd:YAG laser was used as the excitation source. Emission lifetimes were measured with a Tektronics TDS 380 oscilloscope and the 308 nm line of a Lambda Physik LPX 100 excimer laser as the excitation source.

### 3. Results and discussion

#### 3.1. DTA-TG analysis

The TG and DTA curves of dried gels (Fig. 1) show that the process of formation of Y<sub>3</sub>Al<sub>5</sub>O<sub>12</sub>:Tb<sup>3+</sup> involves an almost continuous weight loss up to 1000 °C, although most of the loss occurs at rather low temperatures, below 400 °C. The TG curves indicate an overall weight loss of approximately 95%. The weight loss observed in the

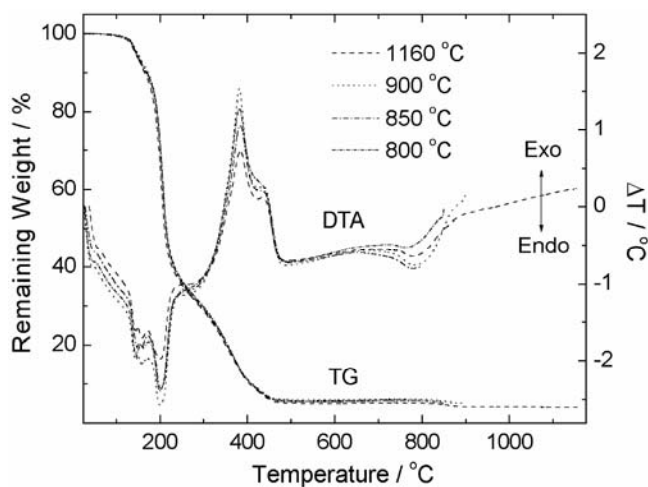


Fig. 1. Thermogravimetric (TG) and differential thermal analysis (DTA) curves of the glycol-route reactions in fabricating Y<sub>3</sub>Al<sub>5</sub>O<sub>12</sub>:Tb<sup>3+</sup> (sample weight: c.a. 10 mg, heating rate: 5 K·min<sup>-1</sup>, airflow rate: 100 cm<sup>3</sup>·min<sup>-1</sup>)

very first part of the TG curve (below 100 °C) is mainly due to the evaporation of organic solvents, since the endothermic signal in the DTA curve is rather weak. The stronger endothermic signal at 150 °C, accompanied by a rather moderate weight loss above 100 and below 180 °C, can be attributed to the removal of water [9], which can

be relatively strongly bound. The next, much stronger weight loss with an endothermic DTA signal in the temperature range of 150–200 °C is due to the removal of NO and NO<sub>2</sub> [12, 16], as a result of the decomposition of nitrates. This is in agreement with low thermal stability of the heavier rare earth (and yttrium) nitrates [20]. Even oxynitrates (RONO<sub>3</sub>) decompose below 500 °C.

The decomposition of organic matter occurs practically simultaneously [2], which is oxidized immediately to CO and CO<sub>2</sub>, causing two very strong exothermic peaks in the DTA curves at 380 and 435 °C. This decomposition is practically over just below 500 °C, though it is possible that some yttrium oxycarbonates may well resist decomposition at higher temperatures, up to 600 °C [21]. Taken into the vigorous decomposition of organic matter and evolution of CO, some carbon might be left in the samples and the total oxidation of organic matter may not be complete. The final, albeit rather weak weight loss observed in the range of 850–900 °C may well be due to the burning of the residual carbon. This reaction should be exothermic, but in the DTA curves a broad endothermic signal is first observed, possibly due to crystallization and the formation of the garnet phase [8, 15]. The exothermic signal of burning carbon may well be masked by this endothermic signal. A sharp DTA signal, however, has been found, typical of the transformation of precursors into a crystalline form of garnet [15]. On the other hand, crystallization is a physical process and should not be accompanied by any weight change. This supports the presence of some residual carbon, as does the observation that in reaction conditions with excess oxygen this weight loss is very small or even not observed, and consequently the DTA signal is weak, too [12]. The amount of residual carbon in the products heated at 800 °C has been determined to be as high as 3% [9], and this amount decreases considerably as a result of heating at temperatures higher than 800 °C.

### 3.2. X-Ray powder diffraction studies

The crystallinity as well as phase purity of Y<sub>3</sub>Al<sub>5</sub>O<sub>12</sub>:Tb<sup>3+</sup> nanocrystalline samples were characterized by X-ray powder diffraction (XRD). All the diffraction reflections observed could be indexed with those assigned to cubic Y<sub>3</sub>Al<sub>5</sub>O<sub>12</sub> [JCPDS#33-40] (Fig. 2). Irrespective of the annealing temperature above 800 °C, the phase purity of the samples was found to be excellent. The width of the reflections, measured as FWHM values, were found to depend on the annealing temperature: the higher the temperature, the sharper were the reflections. This kind of evolution of the FWHM values was to be expected and was used to determine the crystallite size of nanoparticles. The average size of nanoparticles was determined from the broadening of diffraction reflections according to the Scherrer's formula [22]. To obtain true diffraction profiles for various reflections, corrections for instrumental broadening were applied using the FWHM values of Si as a standard. The average size of the nanocrystals was found to be dependent on the annealing temperature, and increased in the temperature range of 800–1160 °C from 20 to 40 nm, respectively. These results are

in good general agreement with TEM images (Fig. 3), which also show that the particles have rather uniform shapes and that the size distribution is not exceedingly large if the rather pronounced tendency to aggregate is omitted.

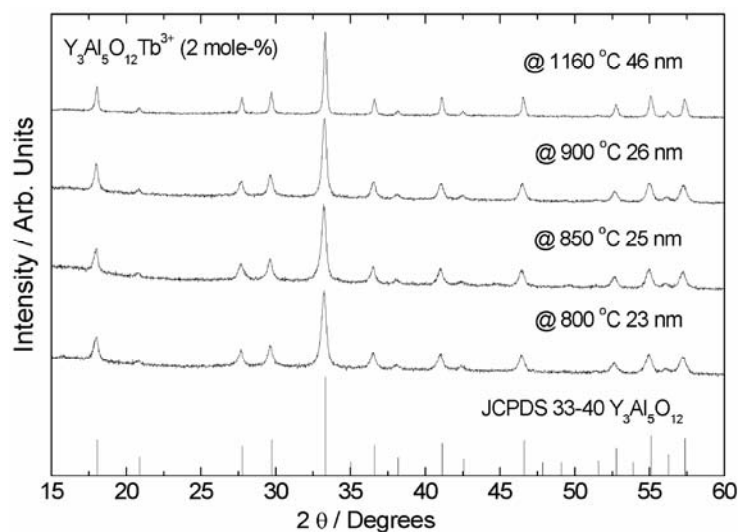


Fig. 2. XRD patterns of the  $Y_3Al_5O_{12}:Tb^{3+}$  (2 mole %) powder samples ( $CuK_{\alpha 1}$  radiation,  $\lambda = 1.5406 \text{ \AA}$ )

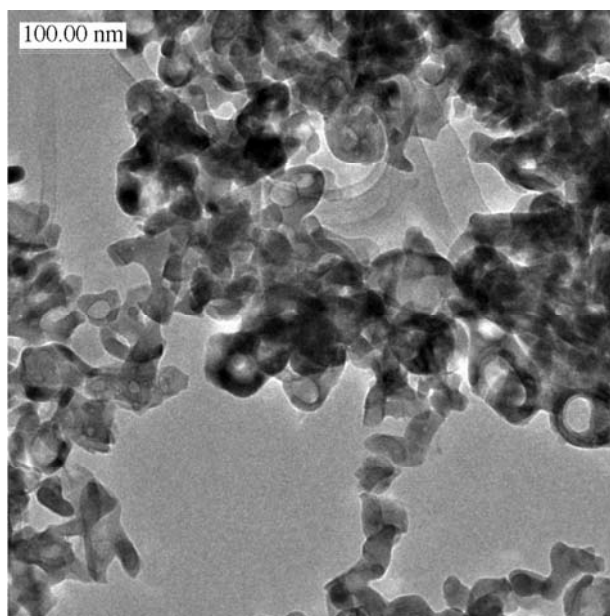


Fig. 3. TEM images of  $Y_3Al_5O_{12}:Tb^{3+}$  (2 mole %) nanocrystals heated at 800 °C

### 3.3. Luminescence Spectra of YAG:Tb<sup>3+</sup>

The emission spectra of YAG:Tb<sup>3+</sup> nanocrystals were measured at room temperature as a function of the annealing temperature (Fig. 4). The spectra consist of characteristic peaks in the UV-blue and blue-green spectral regions, which correspond to the  $^5D_3 \rightarrow ^7F_J$  ( $J = 6-0$ ) and  $^5D_4 \rightarrow ^7F_{J'}$  ( $J' = 6, 5, 4, 3$ ) transitions, respectively. All the observed emission bands of YAG:Tb<sup>3+</sup> nanopowders were found and resolved, even after annealing at 800 °C. This points out that already at this low temperature the samples seem to be well crystallized. It should be noted, however, that since the degeneracy of both emitting levels and terminal ones is rather high, the number of individual transitions between the crystal field levels of each  $^{2S+1}L_J$  is high, too. Accordingly, the use of Tb<sup>3+</sup> luminescence as a structural probe requires low measuring temperatures in contrast to the Eu<sup>3+</sup> ion, the luminescence of which may be used even at room temperature to reliably examine the luminescence characteristics and impurities of samples.

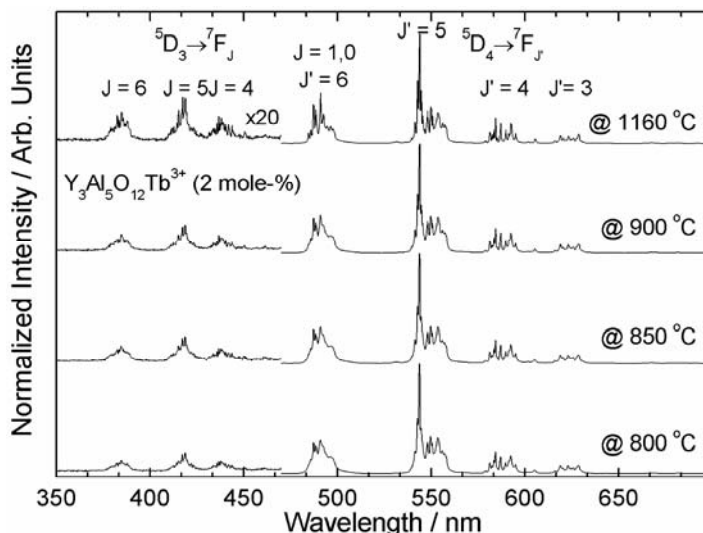


Fig. 4. Luminescence spectra of Y<sub>3</sub>Al<sub>5</sub>O<sub>12</sub>:Tb<sup>3+</sup> (2 mole %) powders derived in glycol-route process

The UV-blue emission of the Tb<sup>3+</sup> ion ( $^5D_3 \rightarrow ^7F_J$ ) was observed to be much weaker compared to blue-green emission ( $^5D_4 \rightarrow ^7F_{J'}$ ) (Fig. 4). The weakness of the blue emission may be rationalized by the concentration quenching associated with the cross-relaxation process ( $^5D_3 \rightarrow ^5D_4$ )  $\leftrightarrow$  ( $^7F_6 \rightarrow ^7F_0$ ), which results in enhanced emission from the  $^5D_4$  level at the expense of  $^5D_3$  emission.

In order to analyse the influence of annealing on the luminescence dynamics and to observe the possible existence or appearance of non-radiative relaxation paths due to crystallite size, the luminescence decays of YAG:Tb<sup>3+</sup> nanocrystallites were recorded at room temperature. Examples of luminescence decay curves, measured for

the blue  ${}^5D_3 \rightarrow {}^7F_5$  (418.7 nm, excitation at 308 nm) and green  ${}^5D_4 \rightarrow {}^7F_5$  (543.6 nm, excitation to the  ${}^7F_6 \rightarrow {}^5D_4$  transition at 484 nm) transitions in  $YAG:Tb^{3+}$  nanocrystallites annealed at 800 °C, are shown in Fig. 5.

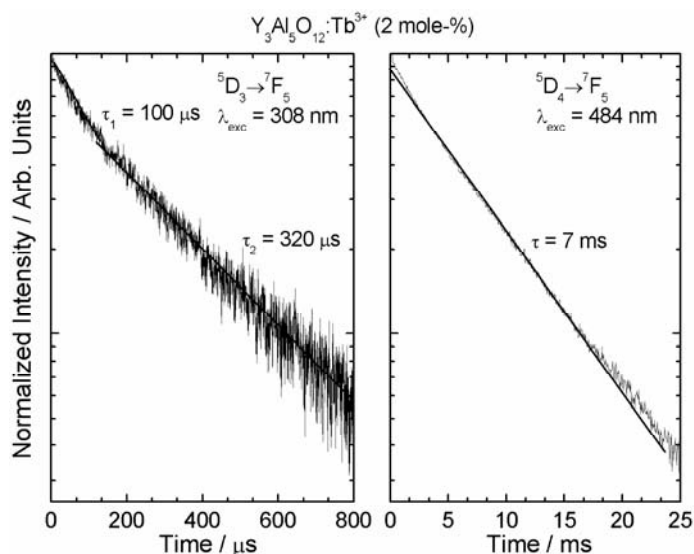


Fig. 5. Luminescence decay curves of the  ${}^5D_3 \rightarrow {}^7F_5$  (left) and  ${}^5D_4 \rightarrow {}^7F_5$  (right) transitions in  $Y_3Al_5O_{12}:Tb^{3+}$  (2 mole %) nanocrystallites

The decay curves for the blue  ${}^5D_3$  emission are composed of two exponential components, a fast component with the decay time of 100  $\mu s$  and a slower one with 320  $\mu s$ . The multicomponent decay time of the  ${}^5D_3$  emission is evidently due to the fact that excitation was not directly to the  ${}^5D_3$  level, but to higher excited levels of the  $4f_8$  electron configuration, or even to the next excited electron configuration,  $4f_75d_1$ . Different excitation paths result in different decay times for the  ${}^5D_3$  emission. The decay curves for the green emission were almost perfectly exponential. The luminescence decay time of  ${}^5D_4 \rightarrow {}^7F_5$  luminescence was determined to be c.a. 7 ms. The  ${}^5D_3$  emission decays observed were much shorter than the  ${}^5D_4$  ones as expected, since emission from the  ${}^5D_3$  level must compete with other processes such as cross-relaxation and multi-phonon de-excitation to the  ${}^5D_4$  level. No significant effect of the annealing temperature and thus crystal size was observed on the measured decay profiles.

#### 4. Conclusions

The formation of  $Y_3Al_5O_{12}:Tb^{3+}$  nanocrystalline powders was analysed by thermogravimetric and differential thermal analyses. It was found that beyond drying, several different processes occurred before the proper formation of nanocrystalline  $YAG:Tb^{3+}$ , being associated with the decomposition of nitrates, (partial) oxidation

and decomposition of organic matter, decomposition of carbonates, and finally the burning of residual carbon. The formation of nanocrystalline YAG:Tb<sup>3+</sup> was achieved already at 780 °C, although the removal of impurities such as carbon demanded a slightly higher annealing temperature. The nanocrystallites obtained demonstrated an increase in crystal size from 20 to 40 nm for annealing taking place at 800 and 1160 °C, respectively. No significant effect of the annealing temperature was observed in the static and dynamic properties of the <sup>5</sup>D<sub>3</sub> and <sup>5</sup>D<sub>4</sub> emissions. The glycol route thus offers a simple and inexpensive method for fabricating good quality YAG:Tb<sup>3+</sup> nanocrystals with luminescence properties comparable to those of microsized crystals.

#### Acknowledgements

The authors thank M. Wolcyrz for the XRD measurements and E. Zawadzak for the TEM graphs. This work was partially supported by the KBN grant PBZ-KBN-095/T08/. J.N. and J.H. acknowledge the financial support from the Academy of Finland (Project No. 204547).

#### References

- [1] SHINOYA S., YEN W.M., *Phosphor Handbook*, CRC Press, Boca Raton, 1998.
- [2] ZHOU Y.H., LIN J., WANG S.B., ZHANG H.J., *Opt. Mater.*, 20 (2002), 13.
- [3] CHOE J.Y., RAVICHANDRAN D., BLOMQUIST S.M., KIRCHNER K.W., FORSYTHE E.W., MORTON D.C., *J. Lumin.*, 93 (2001), 119.
- [4] IKESUE A., FURUSATO I., KAMATA K., *J. Amer. Ceram. Soc.*, 78 (1995), 225.
- [5] IKESUE A., KINOSHITA T., KAMATA K., YOSHIDA K., *J. Amer. Ceram. Soc.*, 78 (1995), 1033.
- [6] LU J., UEDA K., YAGI H., YANAGITANI T., AKIYAMA Y., KAMINSKII A.A., *J. Alloys Comp.*, 341 (2002), 220.
- [7] GRESKOVICH C., CHERNOCH J.P., *J. Appl. Phys.*, 44 (1973), 4599.
- [8] WANG H., GAO L., NIIHARA K., *Mater. Sci. Eng. A*, 288 (2000), 1.
- [9] PILLAI K.T., KAMAT R.V., VAIDYA V.N., SOOD D.D., *Mater. Chem. Phys.*, 44 (1996), 255.
- [10] VAQUEIRO P., LÓPEZ-QUINTELA M.A., *J. Mater. Chem.*, 8 (1998), 161.
- [11] SHIKAO S., JIYE W., *J. Alloys Comp.*, 327 (2001), 82.
- [12] ROY S., WANG L., SIGMUND W., ALDINGER F., *Mater. Lett.*, 39 (1999), 138.
- [13] MCKITTRICK J., SHEA L.E., BACALSKI C.F., BOSZE E.J., *Displays*, 19 (1999), 169.
- [14] INOUE M., OTSU H., KOMINAMI H., INUI T., *J. Alloys Comp.*, 226 (1995), 146.
- [15] PARK C.-H., PARK S.-J., YU B.-Y., BAE H.-S., KIM C.-H., PYUN C.-H., GUANG-YAN H., *J. Mater. Sci. Lett.*, 19 (2000), 335.
- [16] UNFRIED P., *Thermochim. Acta*, 303 (1997), 119.
- [17] MOSCARDINI D'ASSUNÇÃO L., IONASHIRO M., RASERA D.E., GIOLITO I., *Thermochim. Acta*, 219 (1993), 225.
- [18] HRENIAK D., STRĘK W., MAZUR P., PAZIK R., ZĄBKOWSKA-WACŁAWEK M., *Opt. Mater.* 26 (2004), 117.
- [19] HRENIAK D., STRĘK W., MAZUR P., *Mater. Sci.*, 20 (2002), 39.
- [20] WENDLANDT W.W., BEAR J.L., *J. Inorg. Nucl. Chem.*, 12 (1960), 276.
- [21] HÖLSÄ, J., TURKKI, T., *Thermochim. Acta*, 190 (1991), 335.
- [22] KLUG P., ALEXANDER L.E., *X-Ray Diffraction Procedure*, Wiley, New York, 1954, Chapt. 9.

Received 20 April 2004  
Revised 9 November 2004

# **Pre-localized graphite/polyvinyl chloride composites for electromagnetic interference shielding in the X-band frequency range**

V. K. SACHDEV\*, N. K. SRIVASTAVA, KAMLESH KUMAR, R. M. MEHRA

Department of Electronic Science University of Delhi South Campus, New Delhi 110 021, India

The paper reports the development of compression moulded pre-localized graphite/polyvinyl chloride (graphite/PVC) segregated composites with different concentrations of graphite and their application to the shield effectiveness of electromagnetic radiation in the X-band frequency range 8–12 GHz. The incorporation of graphite is related to the formation of conducting channels. It is found that conducting channels are formed above 3 wt. % of graphite. The electrical conductivity is also found to be strongly dependent on the graphite content, and the data are analysed using a percolation model. Variations in SE with graphite loading, due to changes in the conductivity of the composite, have been investigated.

Key words: *polymer composite; conducting filler; shielding efficiency; percolation*

## **1. Introduction**

With the ever-growing applications of advanced electrical and electronic devices emitting electromagnetic radiation, their biological safety becomes of prime importance. Their adverse effect on the human body may well be predicted from their application to roasting in microwave ovens. Moreover, EM pulses can disrupt neighbouring equipment such as computers, or sensitive electronic/electrical measuring instruments. Therefore, it becomes essential to limit and shield all ill effects of EM radiation.

An electromagnetic interference (EMI) shielding material is one that attenuates radiated electromagnetic energy or provides protection by reducing signals to levels at which they no longer adversely affect equipment and can no longer be received by human beings. To reduce the impact of EM radiation, better and more versatile EMI

---

\*Corresponding author, e-mail: vsachdev@eth.net.

shielding materials have always been the topic of investigation and research. Metals have been used for EMI shielding due to their high conductivity. Metals suffer, however, from the inherent disadvantages of corrosion, heavy weight, and poor processibility. Moreover, with the miniaturization of equipment and integration of circuits in limited areas, the possibility of leakage increases as the gaps between circuit units become narrower. Also, the conducting material setting on a circuit for EMI shielding can act as an antenna causing malfunctions in the electronic equipment.

Polymers are lighter in weight, less expensive, corrosion resistant, flexible for complex designs and aesthetically appealing compared to their metallic counterpart. They are electrically insulating and transparent to EM radiations, however, and they are not directly suitable as EMI shielding materials. The easiest way to make them electrically conducting for EMI shielding is to disperse a conductive filler such as black carbon into an insulating polymer matrix [1]. Electroconductive polymer composites can easily be moulded into various complicated shapes even by traditional methods of extrusion and injection moulding. Conductive fillers include metal powders, stainless steel, and carbon and graphite powders [2–4]. Metallic powders generally suffer from oxidation, which deteriorates electrical properties of the composite due to the nonconductive nature of oxide layers.

The segregated distribution of the conductive filler phase in an insulating polymer matrix can impart high electrical conductivity. A comparatively low critical content of conductive filler is needed for a conductive network to form. One way to attain the segregated distribution is to pre-localise of conductive filler phase onto the polymer particles by chemical plating or vacuum coating. Another way is to polymerise a monomer phase and subsequently compact the coated polymer powder by compression moulding around its glass transition temperature and at high pressure. During processing, some of the filler sheaths around polymer particles are expected to break due to compression, permitting polymer particle-to-particle fusion while maintaining a conductive network [5–8]. Such an approach is complicated, however, and industrial production would be expensive. Further, thin brittle conductive layer are very likely to strip off during processing.

The present study deals with the EMI shielding effectiveness (SE) of pre-localized graphite/PVC electroconductive composites. The processing of these composites is cost effective, simpler, and commercially viable [9]. SE, along with the parameter return loss ( $R_L$ ), is investigated for composites with different concentration of graphite over the X-band frequency range of 8–12 GHz. The aim of this work is to design a polymeric composite material for EMI shielding with a smaller amount of conducting filler and retaining desirable mechanical strength.

## 2. Experimental

The matrix polymer used in this work is a commercial grade PVC resin suspension (K 67-01) with a particle size of 105–150  $\mu\text{m}$ , from Reliance Industry Ltd., India. The

density of the compression moulded PVC sample was found to be  $1.12 \text{ g/cm}^3$ . The electrical conducting filler was a graphite powder with particle sizes ranging from 10 to 20  $\mu\text{m}$ , supplied by Graphite India Ltd. The conductivity of graphite with density  $1.75 \text{ g/cm}^3$  is  $1.33 \times 10^4 \text{ S/cm}$ . The higher particle size ratio of PVC resin and graphite ensures a segregated distribution and lower percolation concentration. Composites with low electrical resistivities have been achieved by pre-localising flakes of graphite onto the PVC particles and compacting by compression moulding [9]. Processing and preparation are the same as described in earlier works. The graphite-coated PVC particles were compacted in a  $2.54 \text{ cm}^2$  die by compression moulding at  $78 \text{ }^\circ\text{C}$  and 105 MPa for 15 min. A monotonic increase in microhardness with graphite content, as observed in earlier works, confirms uniform coating on PVC particles and the lack of stripping off while processing. A decrease in hardness with increasing graphite content is assumed to be due to a smaller extent of PVC interparticle fusion during processing, owing to the compaction pressure. This also confirms the uniform coating of PVC particles with graphite. The uniform coating of graphite flakes on PVC particles in a composite sample of 20 wt. % graphite has also been observed in scanning electron microscope (SEM) micrographs [9].

A series of specimens of PVC/graphite conductive composites with graphite contents of 1–20 wt. % were prepared. All these samples were baked at  $120 \text{ }^\circ\text{C}$  and nominal pressure for 15 min. The surface morphologies of these composites were examined by SEM. Variation in conductivity with graphite volume fraction was studied at room temperature. The baked samples with a thickness of  $\sim 0.15 \text{ cm}$  were cut to fit in the cross section of the X-band rectangular wave guide. The size of the sample was  $2.28 \times 1.01 \text{ cm}^2$ . The sample was inserted in the wave guide cell so that it filled the entire cross-section, in order to prevent any leakage of EM energy. Measurements of incident, transmitted, and reflected power were made in the frequency range of 8.0–12.0 GHz.

### 3. Result and discussion

The morphological studies of PVC/graphite conductive composites with different graphite contents using SEM have indicated that networks of graphite conductive channels/paths form due to the presence of graphite particles in the interfacial regions between PVC particles [9]. In the sample with 1 wt. % graphite content, conductive graphite particles are initially apart from each other and found to be increasingly closer in samples with increasing graphite loading (above 3 wt. %). The graphite particles are flakes, while PVC particles are irregular in shape. Aggregates of small particles of graphite are formed between the interfacial regions of the irregular shaped PVC particles. Increasing graphite content leads to larger aggregates of graphite particles. Further increase in graphite content would increase the number of graphite particles touching each other in the composites that form the continuous conductive net-

work, leading to the formation of a conductive mesh structure in the insulating polymer matrix. The increased number of filler particles (graphite) in the conductive mesh of composites leads to better SE by the composites.

Figure 1 illustrates the room temperature electrical conductivity  $\sigma$  of the PVC/graphite composites as a function of graphite volume fraction  $P$ , assuming the density of PVC and graphite to be  $1.12 \text{ g/cm}^3$  and  $1.75 \text{ g/cm}^3$ , respectively. It is seen from the figure that  $\sigma$  is strongly dependent on  $P$  up to  $\sim 0.04$  volume fraction. Such a drastic change in conductivity is related to the dispersion of filler in the polymer matrix, with the formation of a network of graphite conductive channels being evident from SEM images [9]. Critical graphite content may make electron hopping possible, which would result in a sharp increase in conductivity. An abrupt increase in the electrical conductivity is found to occur at  $\sim 0.005_5$  (0.85 wt. %) volume fraction of graphite concentration.

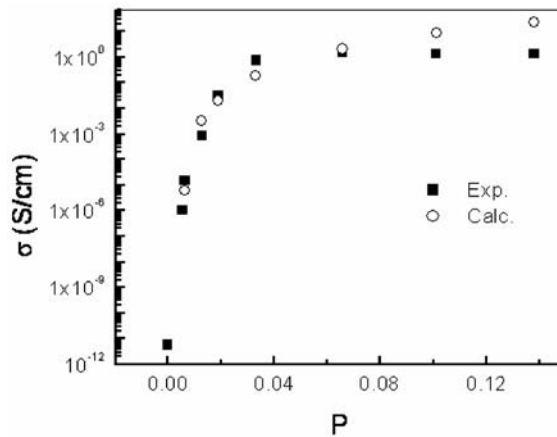


Fig. 1. The conductivity  $\sigma$  as a function of the volume fraction  $P$  of graphite in pre-localized graphite/PVC composites

Such a behaviour of  $\sigma$  with  $P$  is commonly analysed by percolation theory [10, 11]. The expression for  $\sigma$  can be written as

$$\sigma = \sigma_0 (P - P_c)^t \quad (1)$$

where  $\sigma_0$  is the conductivity of filler particles,  $P_c$  is the volume fraction of conductive filler at the percolation threshold, i.e. the volume fraction below which the conductivity falls to a very small value, and  $t$  is the critical index of conductivity. The plot of  $\log \sigma$  vs.  $\log (P - P_c)$  is shown in Fig. 2. The best linear fit has been obtained for  $P_c = 0.005$  ( $\sim 0.78$  wt. % graphite), which is in good agreement with the experimental value of 0.85 wt. % graphite content composite. The values of  $t$  and  $\sigma_0$  as estimated from the slope and intercept are found to be  $3.07 \pm 0.26$  and  $1.13 \times 10^4 \text{ S/cm}$ , respectively. Such a value of  $\sigma_0$  is close to the conductivity of the filler graphite ( $1.33 \times 10^4$

S/cm). It should be mentioned that Kirkpatrick [12] and Straley [13] have obtained values of  $t = 1.5 \pm 0.2$  and  $1.75 \pm 0.1$ , respectively. Wang and Rubner [14], however, have reported the value of  $t = 3.2$  for this system. To test the validity of percolation theory for pre-localized graphite/PVC composites, a comparison between theoretically calculated values using Eq. (1) with the estimated values of  $t$  (3.07) and  $\sigma_0$  ( $1.13 \times 10^4$  S/cm) has been made and is illustrated in Fig. 1. A good agreement is observed, except for composites above 0.066 volume fraction (10 wt. %) of graphite content. The values above 10 wt. % probably fall in region III [15], while the theoretical fitting of this work is assumed to be for region II.

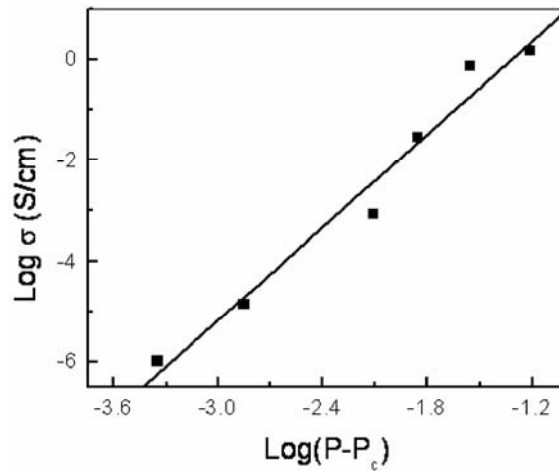


Fig. 2. The conductivity  $\sigma$  as a function of the excessive volume fraction  $P - P_c$  of graphite in pre-localized graphite/PVC composites

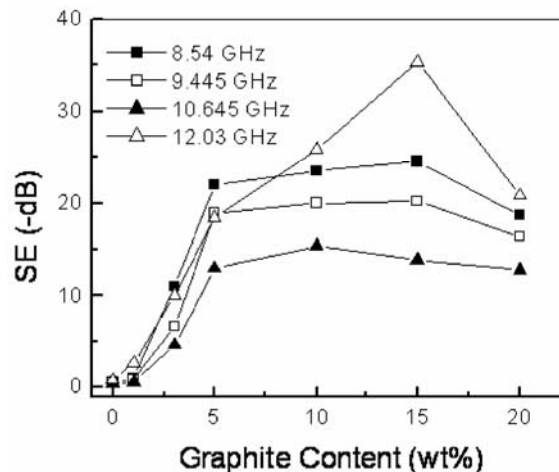


Fig. 3. The variation of shielding effectiveness  $SE$  as a function of graphite content in pre-localized graphite/PVC composites

The variation of shielding effectiveness (SE) for PVC/graphite composites with graphite content of 0 to 20 wt. %, over the frequency range of 8–12 GHz, is shown in Fig. 3. The variations in SE are more or less similar to the changes in conductivity with graphite loading (Fig. 1). It is interesting to note that SE increases sharply up to a graphite loading of 5 wt. % at all the frequencies. For higher graphite loadings, except for 12.03 GHz, SE saturates at 15 wt. % of graphite and starts to decrease with further increase of graphite content. In the case of 12.03 GHz, the system becomes more efficient in shielding at higher loadings up to 15 wt. %, and SE increases up to ~35 dB. The variation of insertion loss ( $R_L$ ) as a function of frequency is shown in Fig. 4.

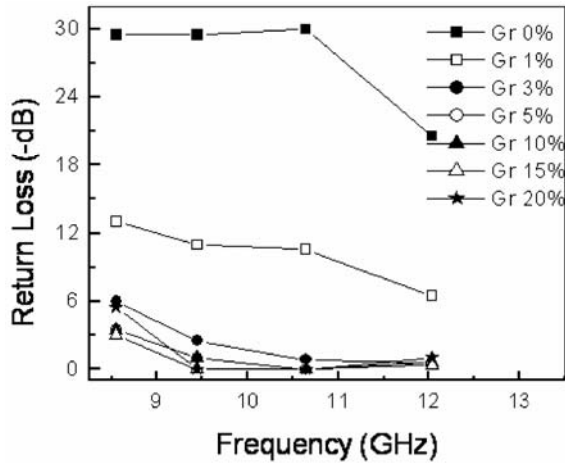


Fig. 4. The Variation of return loss  $R_L$  in pre-localized graphite/PVC composites as a function of frequency in the X-band

It is clear from the figure that composites that have a high value of SE yield a lower value of  $R_L$ . The range of these variations was found to be less than 6 dB over the whole X-band, except for the specimen with 1 wt. % of graphite concentration. The marginal frequency dependence of  $R_L$  may be due to some structural effects, such as the geometrical distribution of the filler and the interaction of electromagnetic waves with graphite.

The variation of SE with graphite loading can be linked to changes in the conductivity of composites with graphite. After a conductive barrier is inserted between a point in space and the source, SE can theoretically be expressed at that point by [16].

$$SE = 10 \lg \left( \frac{P_i}{P_t} \right) = (A + R + B) \text{ dB} \quad (2)$$

where  $P_i$  is the incident power density at a measured point before the shield is in place,  $P_t$  is the transmitted power density at the same point when the shield is in place,  $A$  is the absorption of the shield,  $R$  the reflection at both surfaces, and  $B$  is the multi-

ple internal reflection, which can be either positive or negative and is negligible for  $A > 15$  dB. The return loss due to reflection can be represented as

$$R_L = 10 \lg \left( \frac{P_r}{P_i} \right)_L \quad (3)$$

$P_r$  stands for the reflected power density at the same point.

The value of  $A$  depends on the  $\sigma$  of the sample (relative to copper) as

$$A = 1.32d (\sigma \mu f)^{1/2} \quad (4)$$

where  $\mu$  is the magnetic permeability of the sample relative to vacuum or copper ( $\mu = 1$ ),  $f$  is the frequency of radiation in MHz, and  $d$  is the thickness of the sample in cm. It will be appropriate to say that for effective EMI shielding, the dispersion of the conductive material in the polymer matrix should enhance the conductivity to a large extent since  $SE$  depends on  $\sigma$ , which in turn is a function of the dispersed filler, its size, structure, and distribution in the matrix [17]. The distribution of the filler in the matrix determines the void space between filler aggregates.

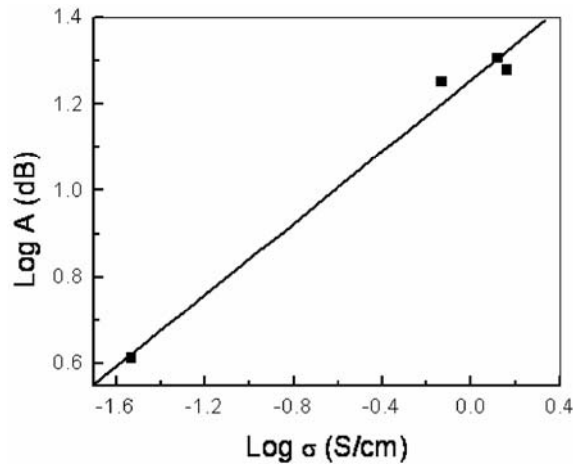


Fig. 5. The variation of the calculated value of  $\log A$  as a function of  $\log \sigma$  at a frequency 9.45 GHz for graphite/PVC composites

By pre-localizing the filler onto the polymer phase [8, 9], one can achieve high electrical conductivity in an insulating polymer with small amounts of electrically conductive filler with better mechanical strength. The segregated distribution of the conductive filler phase with pre-localization ensures a close-packed array throughout the matrix, so that the filler particles are arranged in a manner similar to a very fine conducting mesh that could be used for EMI shielding. The voids in the conductive composites effect absorption and  $R_L$ , owing to their effect on internal reflection. The

frequency dependence of  $SE$  is mainly due to the distribution of the filler in the polymer matrix.

The theoretical validity of Eq. (4), which predicts that absorption is proportional to the square root of conductivity, has been examined for the present investigation. Figure 5 shows the plot ( $\lg A$  vs.  $\lg \sigma$ ) within the X-band frequency range, centred at 9.45 GHz. The value of  $A$  is obtained by putting the data for  $SE$  and  $R_L$  into eq. (2). It is assumed that the contribution of  $B$  to  $SE$  is negligible. The variation of absorption with conductivity is found to be in accordance with Eq. (4), with the slope of  $0.41 \pm 0.03$ . This is close to the theoretical value of 0.5. Using Eq. (1) in (4), the behaviour of absorption as a function of graphite content can also be predicted based on percolation theory.

## 4. Conclusions

Segregated composite systems with graphite pre-localized onto the PVC phase exhibit relatively high conductivity at very low filler loadings. SEM micrographs [9] confirm that graphite particles touch each other at higher graphite concentrations. At all frequencies of the incident radiation,  $SE$  increases and  $R_L$  decreases with the filler loading. Above a critical concentration of graphite,  $SE$  reaches a saturated value. The variation of  $A$  with conductivity is found to be in accordance with the theory for metal fillers within the X-band frequency range centred at 9.45 GHz.  $A$  is directly related to the thickness of the shielding. In the present study, the thickness of the sample was  $\sim 0.15$  cm. By increasing the thickness, an increase in  $SE$  is expected. The shift from low to very high conductivity of the composite (above a critical filler concentration) is well accounted for by the percolation model. The EMI shielding of the polymer composites as a function of graphite content can be predicted by considering the power law in the percolation model.

## Acknowledgements

The authors wish to acknowledge the financial support of UGC, Govt. of India, India. Thanks are due to Graphite India Ltd., Bangalore, India for providing graphite powder and Dr. N. C. Mehra, USIC, University of Delhi, Delhi, India, for the SEM images.

## References

- [1] LUX F., *J. Mater. Sci.*, 24 (1993), 285.
- [2] MARGOLIS J.M., *Conductive Polymers and Plastics*, Chapman & Hall, New York, 1989.
- [3] DELMONTE J., *Metal/Polymer Composites*, Van Nostrand, New York, 1990.
- [4] BIGG D.M., *Metal Filled Polymers*, S. Bhattacharya (Ed.), Marcel Dekker, New York, 1986, pp. 165–226.
- [5] HOCHBERG F., *U. S. Pat. 2, 721, 357* (1955).
- [6] CROSSBY E.G., HORNBECK F.C., *U. K. Pat. 1, 479, 569* (1977).
- [7] NARKIS M., YAKUBOWICZ J., VAXMAN A., MARMUR A., *Polym. Eng. Sci.*, 26 (1986), 139.
- [8] OUYANG M., CHAN C.M., *Polym. Eng. Sci.*, 36 (1996), 2676.

- [9] SACHDEV V.K., MEHRA R.M., MEHRA N.C., *Phys. Stat. Sol. (a)*, 201 (2004), 2089.
- [10] CHEN X.B., DEVAUX J., ISSI J. P., BILLAUD D., *Polym. Eng. Sci.*, 35 (1995), 637.
- [11] FENG J., CHAN C. M., *Polym. Eng. Sci.*, 38 (1998), 1649.
- [12] KIRKPATRICK S., *Rev. Mod. Phys.*, 45 (1973), 574.
- [13] STRALEY J.P., *Phys. Rev. B*, 15 (1977), 5733.
- [14] WANG Y., RUBNER M.F., *Macromolecules*, 25 (1992), 3284.
- [15] NAKAMURA S., SAITO K., SAWA G., KITAGAWA K., *Jpn. J. Appl. Phys.*, 36 (1997), 5163.
- [16] *Handbook of Electromagnetic Compatibility*, R. Perez (Ed.), Academic Press, 1995.
- [17] AHMAD M.S., ABDELAZEES M.K., ZIHLIF A.M., *J. Mater. Sci.*, 24 (1989), 1795.

*Received 21 May 2004*  
*Revised 11 December 2004*

## **Grain refinement in aluminium and the aluminium Al–Cu–Mg–Mn alloy by hydrostatic extrusion**

MAŁGORZATA LEWANDOWSKA<sup>1\*</sup>, HALINA GARBACZ<sup>1</sup>,  
WACŁAW PACHLA<sup>2</sup>, ANDRZEJ MAZUR<sup>2</sup>, KRZYSZTOF J. KURZYDŁOWSKI<sup>1</sup>

<sup>1</sup>Warsaw University of Technology, Faculty of Materials Science and Engineering,  
Wołoska 141, 02-507 Warsaw, Poland

<sup>2</sup>Institute of High Pressure Physics, Polish Academy of Sciences,  
Sokołowska 29/37, 01-142 Warsaw, Poland

Hydrostatic extrusion was used as a method for grain refinement in technically pure aluminium and in an aluminium alloy. Both materials were deformed up to a true strain of ~4. Such a deformation resulted in substantial grain size refinement to below 1  $\mu\text{m}$  in aluminium and below 100 nm in the aluminium alloy. In pure aluminium, microstructure evolution proceeds by a continuous increase in the grain boundary misorientation, without changing the grain size. In the aluminium alloy, which has lower stacking fault energy, grains continuously decrease in size, down to the nanometre scale. As a consequence of such microstructure evolutions, the mechanical properties of pure aluminium remain almost constant within a wide range of strains, whereas the mechanical properties of the aluminium alloy are significantly improved. From the present study, one can conclude that hydrostatic extrusion can offer an alternative way to produce nano-metallic elements made of aluminium alloys for light-weight applications.

*Key words: aluminium, aluminium alloys, ultra-fine grained microstructure, severe plastic deformation, hydrostatic extrusion*

### **1. Introduction**

Ultra-fine grained and nanocrystalline materials arouse great interest due to their attractive properties. In particular, nano-metals exhibit a high strength combined with sufficiently good ductility. The fabrication methods of bulk ultra-fine and nanocrystalline metals can roughly be classified into the three groups: (i) nano-crystallization of amorphous materials, (ii) severe plastic deformation (SPD), and (iii) consolidation

---

\*Corresponding author, e-mail: malew@inmat.pw.edu.pl.

of nano-powders. In the last decade, various SPD methods have been developed to produce a wide range of ultra-fine and nano-scale grained metals and alloys [1–5]. Among these methods, those most frequently reported include equal channel angular pressing (extrusion) (ECAP or ECAE) [6], high-pressure torsion (HPT) [7], accumulative roll bonding (ARB) [8], cyclic extrusion–compression (CEC) [9], repetitive corrugation and straightening [10], cold rolling [11] and hydrostatic extrusion (HE) [12, 13]. Among these methods, HE offers the potential for producing homogeneous, fully dense bulk materials in a variety of forms. Rods, wires of complex cross-sections, and also small tubes can be produced by HE [14]. These are features often unattainable by other SPD techniques. In the present work, HE was used to refine the grains in technically pure aluminium and in an aluminium alloy. Attention was focused on the possibility of obtaining a homogenous nanocrystalline structure in aluminium alloys intended for light-weight constructions.

## 2. Experimental methods

Technically pure 1050 (99,5%) aluminium and a 2017 Al–4Cu–0.5Mg–1Mn aluminium alloy were used in this study. The as-received aluminium was work-hardened and its microstructure contained elongated subgrains of about 1  $\mu\text{m}$  equivalent diameter. The aluminium alloy was solution heat-treated at 505  $^{\circ}\text{C}$  and water quenched to obtain a single-phase material. Its microstructure consisted of nearly equiaxed subgrains, about 2  $\mu\text{m}$  in diameter. The initial microstructures of aluminium and aluminium alloy are shown in Fig. 1.

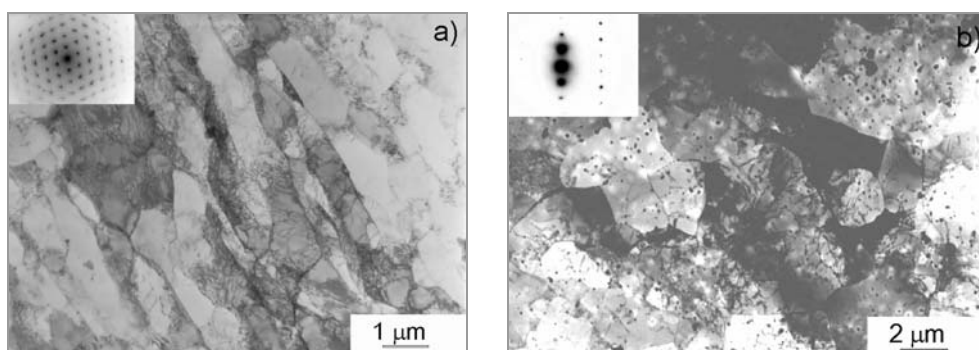


Fig. 1. TEM micrographs of aluminium (a) and Al–Cu–Mg–Mn alloy (b) in their initial state

The rods, 20 mm in diameter, were subject to HE, which resulted in a total cross-section reduction of 44.4. The HE was run in a press, designed and constructed at the Institute of High Pressure Physics, Warsaw. The cross section reduction obtained during a multipass HE operation corresponds to an accumulated true strain of 3.79. The strain rate during HE exceeded  $3.0 \times 10^2 \text{ s}^{-1}$  (for the smallest wire diameters). The extrusion products were cooled with water at the die exit.

The microstructure and mechanical properties of the materials in their initial state and after HE were investigated. The microstructure was evaluated by transmission electron microscopy (TEM). The observations were carried out with thin foils cut perpendicularly to the extrusion direction. The microstructures were also quantitatively described using computer-aided image analysis. Mechanical properties were characterized by microhardness, measured on transverse sections of the rods and wires. Tensile tests were conducted at room temperature at a strain rate of  $8.33 \times 10^{-4} \text{ s}^{-1}$ . Both microstructure and mechanical properties were investigated seven days after the extrusion process.

### 3. Results

TEM images and corresponding selected area electron diffraction (SAED) patterns for an aluminium sample subjected to multipass HE are shown in Figs. 2a, b. After the true strain of 1.39, the microstructure consists of small equiaxed grains (Fig. 2a). Dislocations of high density are visible within the grains. The SAED pattern (the insert in Fig. 2a) is typical of a mosaic structure built-up of grains with small misorientations (diffracted beams are scattered by a few degrees). After the true strain of 3.79, the microstructure changes profoundly (Fig. 2b). Small equiaxed grains are still characteristic features of the microstructure, but the grains are free of dislocations and the diffracted beams visible in the diffraction patterns are scattered into rings. A diffraction image of this kind indicates that the microstructure contains grains separated by both low- and high-angle grain boundaries. Misorientation measurements of the grain boundaries in HE-processed aluminium are in progress.

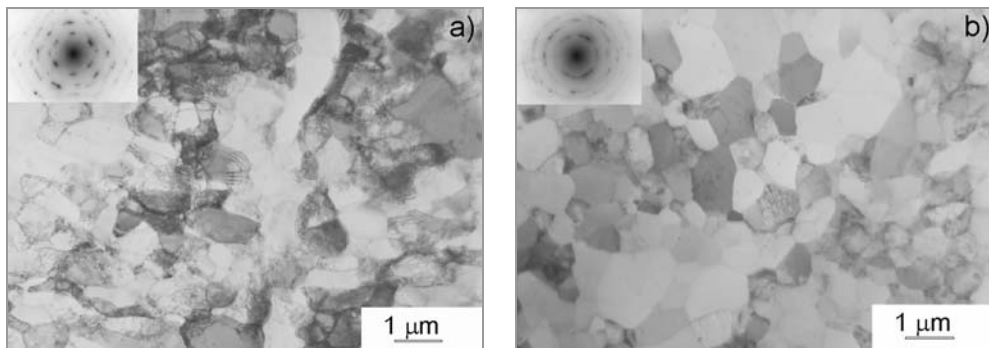


Fig. 2. TEM micrographs and corresponding SAED patterns for aluminium: (a) after HE to a true strain of 1.39, (b) after HE to a cumulative true strain of 3.79

The microstructures of technically pure aluminium processed by HE were also evaluated quantitatively in terms of their grain size and shape. To this end, all types of grain boundaries (with low and high misorientation angles) were taken into account. The size of grains was determined in terms of the mean value of the equivalent diameter  $E(d_{eq})$  and the variation coefficient  $CV$ , defined as the ratio  $E(d_{eq})/SD(d_{eq})$ , where

$SD(d_{eq})$  is the standard deviation of  $d_{eq}$ . The grain elongation factor  $\alpha$ , defined as the ratio of the maximum diameter to the equivalent diameter of a given grain,  $d_{max}/d_{eq}$ , was used to describe the shape of grains. The measured values of  $E(d_{eq})$ ,  $CV(d_{eq})$ , and  $\alpha$  are given in Table 1. It can be seen that, in technically pure aluminium processed by HE, the average grain size does not depend on the accumulated plastic strain. On the other hand, the grain elongation decreases continuously with the imposed strain.

Table 1. Values of microstructural parameters (mean equivalent diameter of grains  $E(d_{eq})$ , variation coefficient  $CV(d_{eq})$ , and grain elongation factor  $\alpha$ ) for aluminium in the initial state and after HE

True strain	$E(d_{eq})$ [ $\mu\text{m}$ ]	$CV(d_{eq})$	$\alpha$	Spread of diffraction spots
0	0.92	0.41	1.48	9°
1.39	0.71	0.37	1.37	15°
2.77	0.68	0.47	1.33	33°
3.79	0.70	0.31	1.30	not measurable

Compared to the microstructure of technically pure aluminium, the microstructure of the aluminium alloy evolves in a different way. After a true strain of 1.39, the TEM observations reveal subgrains with dislocations of high density (Fig. 3a). The subgrain size is smaller and the dislocation density is much higher than those in technically pure aluminium. The SAED patterns exhibit a scatter of the diffracted beams by a few degrees. This suggests that the misorientation angles between the subgrains are small. After the final step of HE, the microstructure consists of small equiaxed grains (see Fig. 3b) with grain boundaries with various (low and high) misorientation angles (see the SAED pattern presented as an insert). Compared to the results for technically pure aluminium, grain refinement in the aluminium alloy is much more effective.

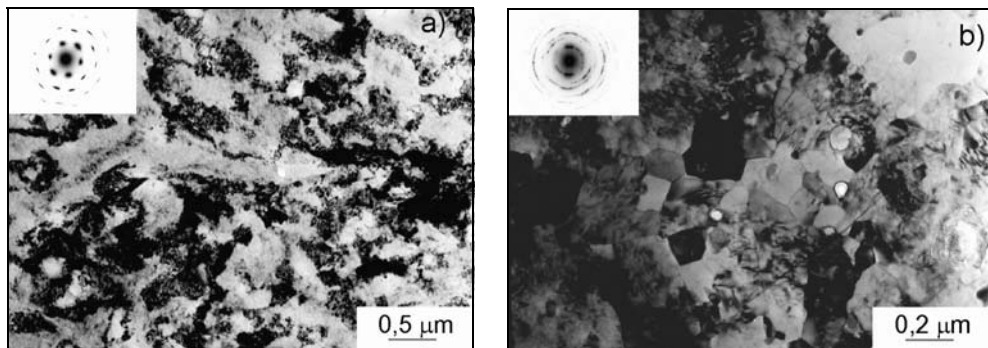


Fig. 3. TEM micrographs and corresponding SAED patterns for Al–Cu–Mg–Mn alloy: (a) after HE to a true strain of 1.39, (b) after HE to a cumulative true strain of 3.79

Grain size measurements in the aluminium alloy processed by HE show that the mean equivalent diameter of the grains sharply decreases with increasing strain, from

a few micrometers in the initial state to about 100 nm after applying a cumulative true strain of 3.79. At the same time, grain elongation remains unchanged and the misorientation between neighbouring grains increases, as seen in the SAED pattern. The microstructural parameters for the aluminium alloy are given in Table 2.

Table 2. Values of microstructural parameters (mean equivalent diameter of grains  $E(d_{eq})$ , variation coefficient  $CV(d_{eq})$ , and grain elongation factor  $\alpha$ ) for aluminium alloy in the initial state and after HE

True strain	$E(d_{eq})$ [ $\mu\text{m}$ ]	$CV(d_{eq})$	$\alpha$	Spread of diffraction spots
0	2.180	0.23	1.38	0°
1.39	~0.500	-	-	15°
2.77	0.170	0.29	1.29	38°
3.79	0.095	0.42	1.3	not measurable

One of the main factors that decide about the performance of engineering materials is the homogeneity of their microstructures. In order to analyse the homogeneity of extruded wires in relation to their mechanical properties, microhardness was measured on transverse-sections. The results of these measurements are given in Fig. 4. In both materials, irrespective of the strain applied, microhardness was evenly distributed across the diameter of wires. The results exhibit a relatively small scatter, with the variation coefficient being smaller than 0.02. No visible gradient of the microhardness distribution at the circumference of the wire or near its axis was observed. This confirms that the materials processed by HE are highly homogeneous in terms of their microstructural features.

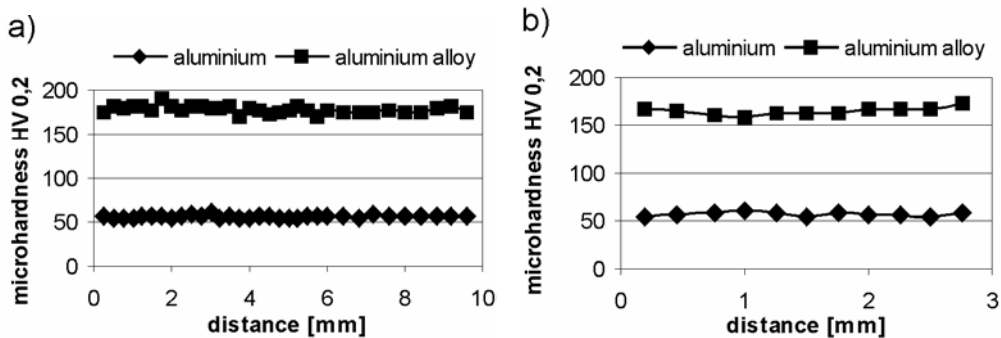


Fig. 4. Microhardness distributions measured on the transverse-sections of hydrostatically extruded rods: (a) to a strain of 1.39 (b) to a cumulative strain of 3.79

In order to determine mechanical properties, static tensile tests were performed at room temperature. The yield stress and elongation for both aluminium and the aluminium alloy are plotted in Fig. 5. In both materials, the yield stress increases with the imposed extrusion strain. The increase in yield stress, however, is greater in the alu-

minium alloy, amounting to 100%. The highest increase in the yield stress occurs after the first pass.

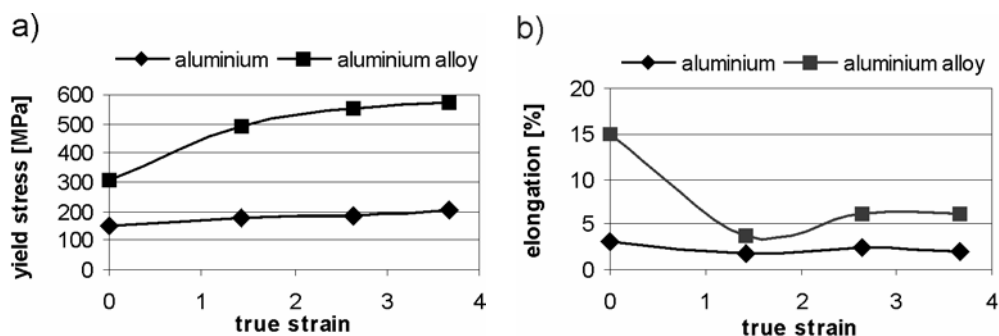


Fig. 5. The yield stress (a) and elongation (b) as functions of the imposed strain during HE of pure aluminium and Al–Cu–Mg–Mn alloy

In subsequent passes, the process saturates and the yield stress approaches a “plateau”. It should be noted that in the aluminium alloy the yield stress achieves the value of 570 MPa, compared to 350 MPa for the same alloy subjected to traditional heat treatment. Here, too, the greatest reduction in elongation is observed after the first extrusion. In the next passes, it remains constant (aluminium) or even increases (aluminium alloy), as seen in Fig. 5b. The change in ductility is more pronounced in the aluminium alloy, where it reaches a useful level of 5% after three passes.

#### 4. Discussion

In literature, various SPD methods have been used for grain refinement in aluminium and its alloys. The reported grain sizes obtained in technically pure aluminium by ECAP vary between 0.5 and 1.5  $\mu\text{m}$  [e.g. 6; 15–16]. As to the influence of the deformation on microstructure, it is commonly observed that ECAP microstructure evolves from subgrain bands (after a single pressing) into a system of high angle boundaries (during subsequent passes) [6]. At high strains, the average grain size is only slightly refined, whereas the average boundary misorientation increases more rapidly [16].

In CEC, the microstructure evolution in technically pure aluminium proceeds in a similar way [9]. The microstructure transforms from a cellblock type into an almost equiaxed one. The spacing between the boundaries that subdivide the structure is almost unaffected by the strain, and the misorientation across these boundaries increases with increasing strain.

The present experiments with HE indicate that the mechanism of microstructure evolution is similar in this case. The misorientation angle of the grain boundaries increases as a function of the accumulated strain, but with grain size remaining almost constant. This type of microstructure evolution has been confirmed by previous re-

sults [12], where a true strain of  $\sim 6.2$  was achieved. Aluminium is a metal with a high stacking fault energy, in which a cross slip occurs very easily and thus, during the consecutive steps of deformation, dislocations can move easily towards the grain boundaries and be absorbed into them. As a result, the grain interiors undergo recovery, while the misorientation angles of the grain boundaries increase. These two processes may take place at a constant grain size, as observed in the present work.

The SPD methods differ in their efficiency of generating high angle boundaries [15]. It has been observed that, in terms of grain boundary misorientations, ECAP with a strain of  $\sim 8$  gives similar results to CEC conducted at a strain of 60. From this point of view, HE seems to be almost as efficient as ECAP. The results of diffracted beam scattering measurements (Table 1) are very similar to those obtained in aluminium processed by ECAP [6].

In literature, microstructure evolution in aluminium alloys subjected to SPD has been studied primarily for ECAP. It has been found that in Al–Mg [17, 18] and Al–Mn [19] alloys grain refinement is greater than that in technically pure aluminium. This was attributed to the lower rate of recovery in aluminium alloys, which results in a smaller final grain size.

In the Al–Cu–Mg–Mn alloy investigated here, the lower recovery rate is especially visible during the first HE pass, where the deformed microstructure is characterized by a high density of the dislocation tangles, and the grain structure is not well established. During consecutive extrusions, dislocations cannot easily move to the grain boundaries, and in order to minimize the stored energy they tend to divide the grains into blocks with different slip system combinations [20]. These blocks can rotate to achieve different final orientations, causing a significant increase of grain boundary misorientations. This is accompanied by a continuous decrease of the final grain size. The mechanism described above can explain the drop in the average grain size down to 95 nm, which leads to a substantial improvement of the mechanical properties of the alloy. It should be noted that the grain size reduction observed in the present work is similar to that reported for Al–1.7 at. Cu subjected to 8 passes of ECAP [21]. This confirms that HE is an effective process, which leads to a similar grain size reduction to that achieved by other SPD methods.

## 5. Conclusions

The following conclusions may be drawn from the results obtained in this study:

- HE can be used for grain refinement in aluminium and aluminium alloys. Grain size below 1  $\mu\text{m}$  in technically pure aluminium and below 100 nm in the aluminium alloy can be obtained at a final strain smaller than 4.
- Due to the high ability of pure aluminium to recover, microstructure evolution proceeds through an increase of grain boundary misorientation without changing grain

size. As a consequence, mechanical properties remain almost constant within a wide range of strains.

- In the aluminium alloy with low stacking fault energy, the grains continuously decrease in size during consecutive extrusions, which leads to a grain size reduction much more effective than that observed in technically pure aluminium. As a consequence, mechanical properties are significantly improved.

- Taking into account the technological features of HE, one can conclude from the present study that this technique offers an alternative way of producing nano-metallic tubes and rods of aluminium alloys intended for light-weight applications.

#### Acknowledgement

This work was supported by the State Committee for Scientific Research (grants No. 4 T08A 04525; 4T08A 02724).

#### References

- [1] VALIEV R.Z., ISLAMGALIEV R.K., ALEXANDROV I.V., *Progr. in Mat. Sci.*, 45 (2000), 103.
- [2] SEGAL V.M., *Mater. Sci. Eng.*, A197 (1995), 157.
- [3] HORITA Z., FUJINAMI T., NEMOTO M., LANGDON T.G., *J. Mat. Proc. Techn.*, 117 (2001), 288.
- [4] ZHILYAEV A.P., LEE S., NURISLAMOVA G.V., VALIEV R.Z., LANGDON T.G., *Scripta Mater.*, 44 (2001), 2753.
- [5] KORZNIKOV A.V., PAKIELA Z., KURZYDŁOWSKI K.J., *Scripta Mater.*, 45 (2001), 309.
- [6] IWAHASHI Y., HORITA Z., NEMOTO M., LANGDON T.G., *Acta Mater.*, 46 (1998), 3317.
- [7] ZHILYAEV A.P., KIM B.-K., NURISLAMOVA G.V., BARO M.D., SZPUNAR J.A., LANGDON T.G., *Scripta Mater.*, 46 (2002), 575.
- [8] SAITO Y., UTSUNOMIYA H., TSUJI N., SAKAI T., *Acta Mater.*, 47 (1999), 579.
- [9] RICHERT M., LIU Q., HANSEN N., *Mat. Sci. Eng.*, A260 (1999), 275.
- [10] HUANG J.Y., ZHU Y.T., JIANG H., LOWE T.C., *Acta Mater.*, 49 (2001), 1497.
- [11] LIU Q., HUANG X., LLOYD D.J., HANSEN N., *Acta Mater.*, 50 (2002), 3789.
- [12] STYCZYŃSKI L., PACHLA W., WOJCIECHOWSKI S., *Metal Sci.*, 16 (1982), 525.
- [13] LEWANDOWSKA M., GARBACZ H., PACHLA W., MAZUR A., KURZYDŁOWSKI K.J., *Solid State Phenomena*, 101–102 (2005), 65.
- [14] *Mechanical Behaviour of Materials Under Pressure*, H. Li Pugh (Ed.), Elsevier, Amsterdam, 1970.
- [15] SUN P.L., YU C.Y., KAO P.W., CHANG C.P., *Scripta Mater.*, 47 (2002), 377.
- [16] CAO W.Q., GODFREY A., LIU Q., *Mat. Sci. Eng.*, A361 (2003), 9.
- [17] HASEGAWA H., KOMURA S., UTSUNOMIYA A., HORITA Z., FURUKAWA M., NEMOTO M., LANGDON T.G., *Mat. Sci. Eng.*, A265 (1999), 188.
- [18] MORRIS D.G., MORRIS M.A., *Acta Mater.*, 50 (2002), 4047.
- [19] CABIBBO M., EVANGELISTA E., LATINI V., NES E., TANGEN S., *Mat. Sci. Forum*, 426–432 (2003), 2673.
- [20] HUGHES D.A., HANSEN N., *Acta Mater.*, 45 (1997), 3871.
- [21] MURAYAMA M., HORITA Z., HONO K., *Acta Mater.*, 49 (2001), 21.

*Received 20 December 2004*

*Revised 26 January 2005*

## **Direct synthesis as a new approach to heteropolynuclear complexes**

VOLODYMYR N. KOKOZAY\*, DENIS V. SHEVCHENKO

Department of Inorganic Chemistry, National Taras Shevchenko University,  
Volodymyrska 64, Kyiv 01033, Ukraine

The idea of direct synthesis of coordination compounds – use of elemental metals or their oxides as starting materials – has been developed into “Salt route”, “Ammonium salt route” and “Direct template synthesis”, methods to synthesize heteropolynuclear complexes. The advantages of this approach in obtaining heterobi-, heterotrimetallic and mixed-anion heteropolynuclear coordination compounds are shown taking complexes of transition metals (Cu, Ni, Co, Mn, Zn, Cd) with aminoalcohols and ethylenediamine ligand as an example. The results of the X-ray crystal structure analysis and magnetic properties of the most interesting complexes are presented.

*Key words: elemental metals; metal oxides; heteropolynuclear complexes; direct synthesis, crystal structure*

### **1. Introduction**

The design and synthesis of novel solid-state architectures using transition metal cations and multifunctional ligands enforcing metal bridging is a prolific domain in the field of coordination and materials chemistry [1]. The number of heteropolynuclear aggregates has increased enormously in recent years [2–4]. Interest in such nanoscale structures is due to a variety of potentially important applications from the areas of single molecule magnetism [5–7], photophysics [8], molecular electronics [9]. Furthermore, structural analysis of nanometer-sized heteropolynuclear molecules can give important insight into the early stages of nucleation [10], which is of relevance to all scientists working in areas such as nanoparticulates.

The distinct philosophies of “designed synthesis” and “self assembly” offer two main approaches to achieving the objective of creating new polynuclear materials with which to extend the range of present working theories. Synthetic difficulties in obtaining elaborate ligands and molecular synthons that can be used as ligands are

---

\* Corresponding author, e-mail: kokozay@univ.kiev.ua.

a critical factor in restricting further studies because of the often tedious, costly and multi-step procedures.

We have previously shown that various metal complexes can be obtained easily through a one-pot reaction of a metal powder or metal oxide with a complex-forming agent in a non-aqueous solution [11]. In this paper, an attempt is undertaken to show prospects of direct synthesis in preparations of heteropolynuclear complexes.

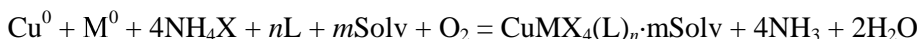
## 2. Heterobimetallic complexes

Developing the direct synthesis methodology we can offer two main routes for the preparation of heterobimetallic complexes. The first one, the so called "Salt route" method has been developed for protonic ligands. It can be illustrated by the reaction scheme to obtain heterobimetallic Cu-containing complexes with aminoalcohols (HL) as ligands:



where  $M = \text{Ni}, \text{Co}, \text{Zn}, \text{Cd}, \text{Pb}$ ;  $X = \text{Cl}, \text{Br}, \text{I}, \text{SCN}, \text{OAc}$ ; Solv – dmf, dmsO,  $\text{CH}_3\text{OH}$ ,  $\text{CH}_3\text{CN}$ .

For the case of aprotic ligands the "Ammonium salt route" method can be used:



where  $\text{M}^0 = \text{Co}, \text{Ni}, \text{Zn}, \text{Cd}$ ;  $\text{MO} = \text{ZnO}, \text{CdO}$ .

At the same time protonic ligands can be successfully used to prepare complexes by "Ammonium salt route" as well:



Some of heterobimetallic complexes obtained by the above mentioned routes [12–19] are shown in Table 1. The complexes with aminoalcohol ligands as a rule are built of polynuclear assemblies with the number of metal atoms that depends on the pair of metals chosen, the nature of aminoalcohol and anion.

Three heterotrinnuclear complexes  $[\text{Cu}_2\text{Zn}(\text{NH}_3)\text{Cl}_3(\text{L}^2)_3]$  (**1**)  $[\text{Cu}_2\text{Zn}(\text{NH}_3)\text{Br}_3(\text{L}^2)_3]$  (**2**) and  $[\text{Cu}_2\text{Zn}(\text{NCS})_3(\text{L}^2)_3] \cdot \text{CH}_3\text{CN}$  (**3**) have been prepared using zerovalent copper, zinc oxide, an ammonium salt and 2-dimethylaminoethanol in air [17]. The overall structural configuration of **1** and **2** are similar. The trinuclear skeletons of **1** (Fig. 1) and **2** consist of a portion of a distorted cube in which alternate corners are non-metal (three oxygens and one chlorine) and metal atoms, and one corner metal site is vacant. The coordination geometry around the terminal, crystallographically independent copper atoms is distorted square pyramidal,  $\text{Cu}(1)\text{N}_2\text{O}_2\text{X}$  and  $\text{Cu}(3)\text{NO}_2\text{X}_2$ ,  $X = \text{Cl}$  (**1**),  $\text{Br}$  (**2**).

Table 1. Some heterobinuclear complexes obtained by direct synthesis [12–24]<sup>1</sup>

Initial system	Complex
Salt route	
Cu <sup>0</sup> -PbX <sub>2</sub> -HL <sup>1</sup> -Solv	CuPbX <sub>2</sub> (L <sup>1</sup> ) <sub>2</sub> ·nSolv X = Cl, Br, I Solv = dmsO, HL <sup>1</sup> ; n = 0; 1
Cu <sup>0</sup> -MX <sub>2</sub> -HL <sup>2</sup> -Solv	Cu <sub>2</sub> MX <sub>3</sub> (L <sup>2</sup> ) <sub>3</sub> ·Solv; M = Co, Pb; X = Cl, I, NCS; Solv = CH <sub>3</sub> CN, dmF, dmsO
Cu <sup>0</sup> -CoX <sub>2</sub> -H <sub>2</sub> L <sup>2</sup> -CH <sub>3</sub> CN	[Cu <sub>2</sub> Co(μ <sub>3</sub> -OH)Br <sub>2</sub> (L <sup>2</sup> ) <sub>3</sub> ] <sub>2</sub> ·2CH <sub>3</sub> CN [Cu <sub>2</sub> Co(μ <sub>3</sub> -OH)I <sub>2</sub> (L <sup>2</sup> ) <sub>3</sub> ] <sub>2</sub> ·4CH <sub>3</sub> CN
Cu <sup>0</sup> -Co(OAc) <sub>2</sub> -H <sub>3</sub> L <sup>4</sup> -Solv	[Cu <sub>2</sub> Co <sup>II</sup> Co <sup>III</sup> (OAc) <sub>4</sub> (H <sub>2</sub> L <sup>4</sup> ) <sub>2</sub> (L <sup>4</sup> ) <sub>2</sub> ] <sub>2</sub> ·2HOAc
Ammonium salt route	
Cu <sup>0</sup> -ZnO-NH <sub>4</sub> X-HL <sup>2</sup> -Solv	Cu <sub>2</sub> Zn(NH <sub>3</sub> ) <sub>n</sub> X <sub>3</sub> (L <sup>2</sup> ) <sub>3</sub> ·mCH <sub>3</sub> CN X = Cl, Br, I, NCS; n = 0; 3, m = 0; 1
Cu <sup>0</sup> -ZnO-NH <sub>4</sub> Br-HL <sup>3</sup> -CH <sub>3</sub> OH	[Cu <sub>2</sub> Zn <sub>2</sub> (NH <sub>3</sub> ) <sub>2</sub> Br <sub>2</sub> (HL <sup>3</sup> ) <sub>4</sub> ]Br <sub>2</sub> ·CH <sub>3</sub> OH
Cu <sup>0</sup> -ZnO-NH <sub>4</sub> X-en-Solv Solv = CH <sub>3</sub> OH, CH <sub>3</sub> CN, dmF, dmsO	[Cu(en) <sub>2</sub> ZnX <sub>4</sub> ] <sub>n</sub> ·Solv X = Cl, Br, I, NCS, OAc Solv = H <sub>2</sub> O, CH <sub>3</sub> CN, dmF, dmsO; n = 0; 0.5; 1
Cu <sup>0</sup> -CdO-NH <sub>4</sub> X-en-Solv Solv = CH <sub>3</sub> OH, CH <sub>3</sub> CN, dmF, dmsO	[Cu(en) <sub>2</sub> CdX <sub>4</sub> ] <sub>n</sub> ·Solv X = Cl, Br, I, Solv = dmF, dmsO; n = 0; 1
Cu <sup>0</sup> -CdO-NH <sub>4</sub> OAc-en-Solv Solv = CH <sub>3</sub> OH, CH <sub>3</sub> CN, dmF, dmsO	[Cu(en) <sub>2</sub> ][Cd <sub>2</sub> (OAc) <sub>6</sub> ]
Cu <sup>0</sup> -CdO-NH <sub>4</sub> NCS-en-CH <sub>3</sub> OH	[{Cu(en) <sub>2</sub> ] <sub>3</sub> Cd(NCS) <sub>6</sub> ](NCS) <sub>2</sub>
Salt route + Ammonium salt route	
Cu <sup>0</sup> -Cd(OAc) <sub>2</sub> -NH <sub>4</sub> X-en-Solv Solv = CH <sub>3</sub> OH, dmF, dmsO	[Cu(en) <sub>2</sub> Cd(OAc) <sub>2</sub> X <sub>2</sub> ] X = Cl, Br
Cu <sup>0</sup> -Cd(OAc) <sub>2</sub> -NH <sub>4</sub> I-en-Solv Solv = dmF, dmsO	[Cu(en) <sub>2</sub> CdI(OAc) <sub>3</sub> ]
Cu <sup>0</sup> -Cd(OAc) <sub>2</sub> -NH <sub>4</sub> NCS-en-Solv Solv = CH <sub>3</sub> OH, CH <sub>3</sub> CN, dmF	[Cu <sub>2</sub> (en) <sub>4</sub> Cd <sub>2</sub> (OAc) <sub>2</sub> (NCS) <sub>6</sub> ]
Cu <sup>0</sup> -Cd(dca) <sub>2</sub> -NH <sub>4</sub> NCS-en-CH <sub>3</sub> OH	[Cu(en) <sub>2</sub> Cd(dca) <sub>2</sub> (NCS) <sub>2</sub> ]
ZnO-NiX <sub>2</sub> -NH <sub>4</sub> X-en-Solv Solv = CH <sub>3</sub> OH, CH <sub>3</sub> CN, dmF, dmsO	[Ni(en) <sub>3</sub> ][ZnX <sub>4</sub> ] <sub>n</sub> ·Solv X = Cl, Br, NCS Solv = CH <sub>3</sub> CN, dmsO; n = 0; 1; 2
CdO-NiX <sub>2</sub> -NH <sub>4</sub> X-en-Solv Solv = CH <sub>3</sub> OH, CH <sub>3</sub> CN, dmF, dmsO	[Ni(en) <sub>3</sub> ][CdX <sub>4</sub> ] <sub>n</sub> ·Solv X = Cl, Br Solv = dmsO; n = 0; 3
CdO-NiBr <sub>2</sub> -NH <sub>4</sub> Br-en-dmF	[Ni(en) <sub>2</sub> (dmF) <sub>2</sub> ][CdBr <sub>4</sub> ]
CdO-Ni(NCS) <sub>2</sub> -NH <sub>4</sub> NCS-en-CH <sub>3</sub> CN	[Ni <sub>2</sub> (en) <sub>4</sub> Cd(NCS) <sub>6</sub> ] <sub>2</sub> ·CH <sub>3</sub> CN

<sup>1</sup>HL<sup>1</sup> - 2-aminoethanol, HL<sup>2</sup> - 2-dimethylaminoethanol, H<sub>2</sub>L<sup>3</sup> - diethanolamine, H<sub>3</sub>L<sup>4</sup> - triethanolamine, dca - N(CN)<sub>2</sub><sup>-</sup>.

Complex [Cu<sub>2</sub>Zn(NCS)<sub>3</sub>(L<sup>2</sup>)<sub>3</sub>]<sub>2</sub>·CH<sub>3</sub>CN has a symmetrical trinuclear core similar to that of **1** and **2** (Fig. 2). The copper atom adopts a square-pyramidal coordination sphere, with a chromophore {CuN<sub>2</sub>O<sub>2</sub>S} in which the axial atom belongs to a thiocyanate group of the neighbouring molecule. Intermolecular association in the structure of **3** occurs through the Cu-S interactions between the S(2) atom of the SCN-group

coordinated to Zn(1) and two copper atoms of the adjacent complex molecule. As a consequence, a polymeric chain assembly is evident along the *c*-axis of the crystal (Fig. 2).

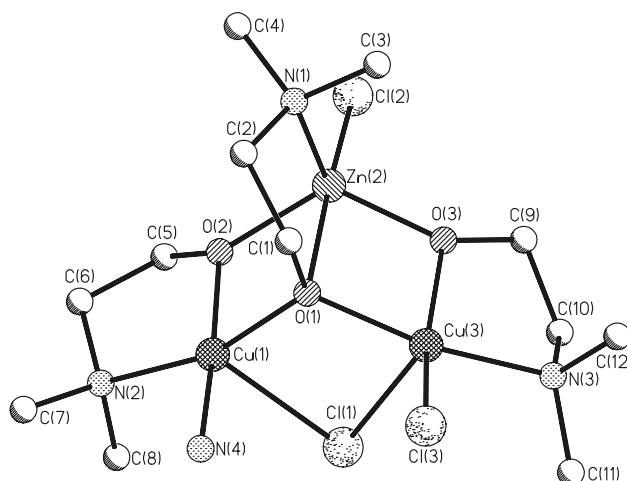


Fig. 1. Molecular structure of  $[\text{Cu}_2\text{Zn}(\text{NH}_3)\text{Cl}_3(\text{L}^2)_3]$ , showing the atom numbering scheme (H atoms omitted for clarity) [17]

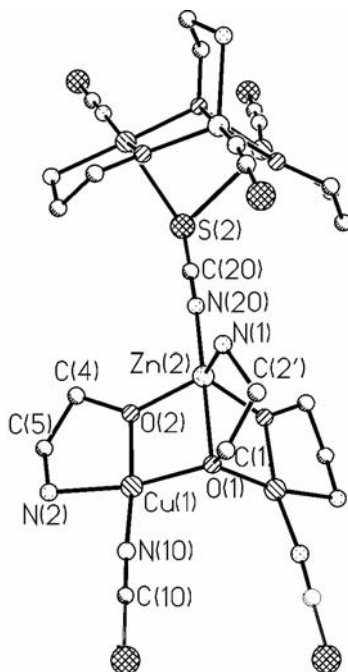


Fig. 2. Molecular structure of  $[\text{Cu}_2\text{Zn}(\text{NCS})_3(\text{L}^2)_3] \cdot \text{CH}_3\text{CN}$  with the atom numbering scheme, showing the intermolecular  $\text{Cu-S}_{\text{NCS}}$  interactions in a polymeric chain (H atoms omitted for clarity) [17]

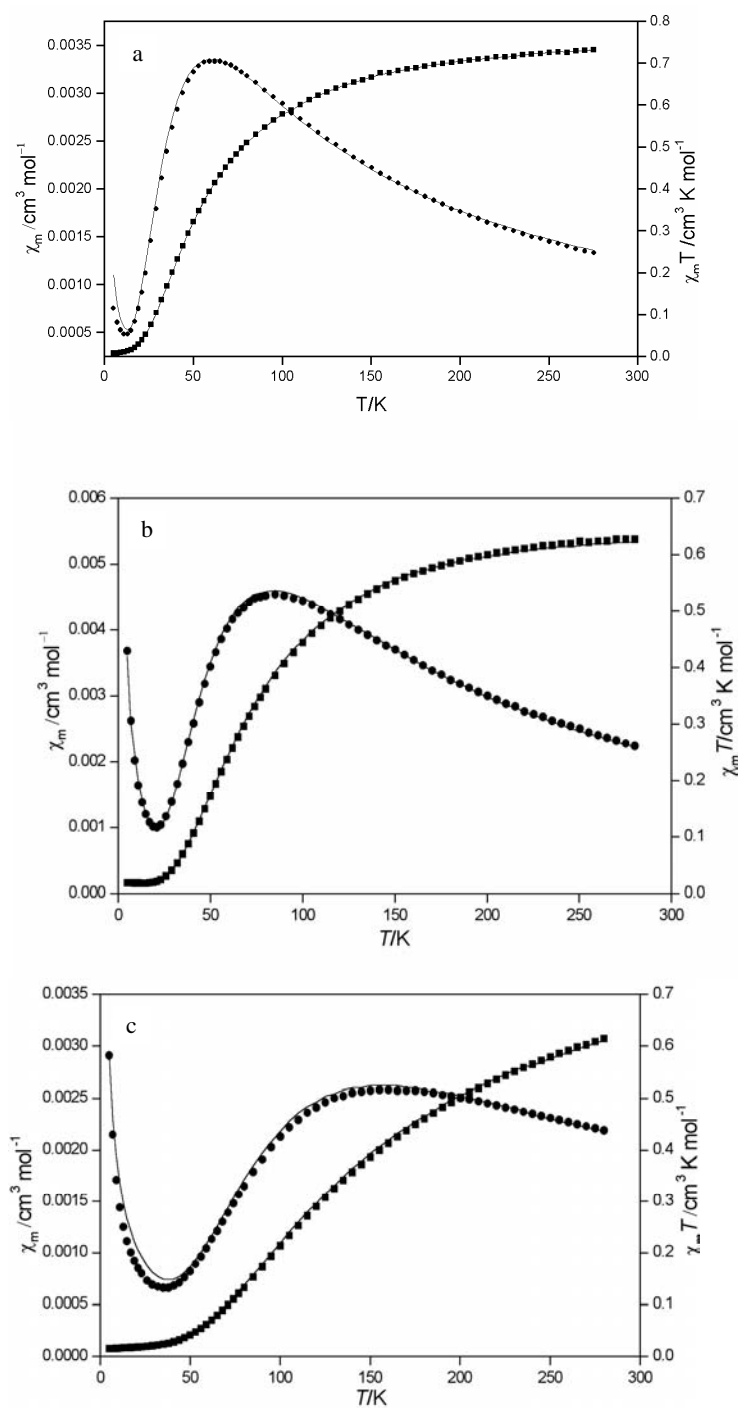


Fig. 3. Plots of  $\chi_m$  (dots) and  $\chi_m T$  (squares) vs.  $T$  for complexes:  $[\text{Cu}_2\text{Zn}(\text{NH}_3)\text{Cl}_3(\text{L}^2)_3]$  (a),  $[\text{Cu}_2\text{Zn}(\text{NH}_3)\text{Br}_3(\text{L}^2)_3]$  (b) and  $[\text{Cu}_2\text{Zn}(\text{NCS})_3(\text{L}^2)_3] \cdot \text{CH}_3\text{CN}$  (c) [17]

The temperature dependence of the molar magnetic susceptibility of **1**, **2** and **3** measured as solids in the range of 5–280 K is shown in Fig. 3. At room temperature, the  $\chi_m T$  values of 0.74, 0.63 and 0.61 cm<sup>3</sup>·K·mol<sup>-1</sup> ( $\mu_{\text{eff.}} = 2.42, 2.24$  and  $2.22\mu_B$ ) for **1**, **2** and **3**, respectively, are in agreement with the presence of two weakly coupled  $S = 1/2$  centres. On lowering the temperature, the value of  $\chi_m T$  decreases, reaching the value of 0.01–0.02 cm<sup>3</sup>·K·mol<sup>-1</sup> at 5 K for all the three complexes. This behaviour is typical of an antiferromagnetic exchange interaction between the copper(II) ions in the compounds. The best data fits (solid lines in Fig. 3) reveals that the order of antiferromagnetic interactions is **1** ( $2J = -68$  cm<sup>-1</sup>) < **2** ( $2J = -96$  cm<sup>-1</sup>) < **3** ( $2J = -178$  cm<sup>-1</sup>) [17]. Somewhat surprisingly, this trend is in contrast to the increase in Cu...Cu distance from **1** to **3**, but correlates nicely with the Cu–O–Cu angle in the complexes: 112.7(2) < 114.4(3) < 119.5(5)°.

The heterobimetallic complex [Cu<sub>2</sub>Zn<sub>2</sub>(NH<sub>3</sub>)<sub>2</sub>Br<sub>2</sub>(HL<sup>3</sup>)<sub>4</sub>]Br<sub>2</sub>·CH<sub>3</sub>OH (**4**) has been prepared in the reaction of zerovalent copper with zinc oxide in air-exposed solution containing ammonium bromide and diethanolamine [18]. The structure of **4** is built of the tetranuclear metallomacrocyclic cation [Cu<sub>2</sub>Zn<sub>2</sub>(NH<sub>3</sub>)<sub>2</sub>Br<sub>2</sub>(HL<sup>3</sup>)<sub>4</sub>]<sup>2+</sup>, bromide anions and methanol molecules in the crystal lattice. The four metal atoms are linked together by bridging oxygen atoms of the four diethanolamine groups to form a rhombus with the edge lengths being 3.4274(6) (Cu...Zn') and 3.4422(7) (Cu...Zn) Å (Fig. 4). The cations are further stabilized by intramolecular O–H...O and N–H...O hydrogen bonds. The intermolecular hydrogen bonding that involves OH and NH groups of the ligands and uncoordinated Br<sup>-</sup> anions links the metallomacrocycles together to form an extended three-dimensional network.

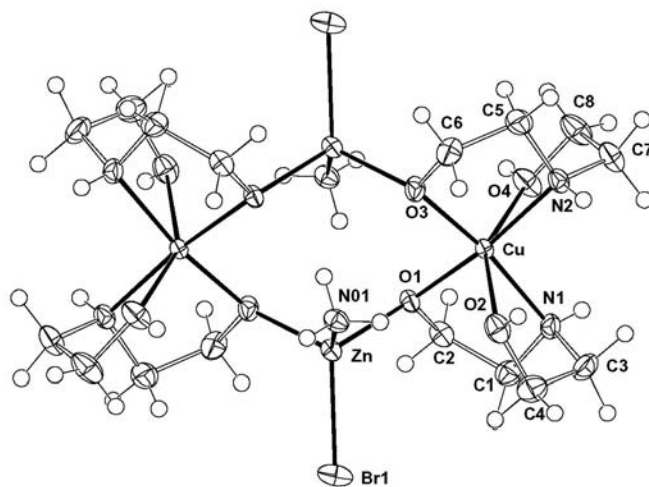


Fig. 4. Molecular structure of the heterometallomacrocyclic cation of [Cu<sub>2</sub>Zn<sub>2</sub>(NH<sub>3</sub>)<sub>2</sub>Br<sub>2</sub>(HL<sup>3</sup>)<sub>4</sub>]Br<sub>2</sub>·CH<sub>3</sub>OH with the 50% probability ellipsoids shown [18]

The magnetic susceptibility per half of the molecule of **4** shown in Fig. 5 increases with decreasing temperature to reach a maximum at ca. 30 K and then decreases with further temperature lowering. This behaviour is typical of an antiferromagnetic spin exchange operating in the  $\text{Cu}_2\text{Zn}_2$  units of ( $J = 35.0 \text{ cm}^{-1}$ ) [18].

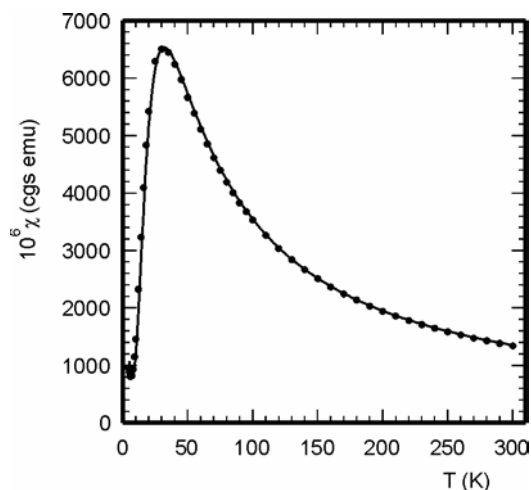


Fig. 5. Magnetic susceptibility per 1/2 mole vs.  $T$  for complex  $[\text{Cu}_2\text{Zn}_2(\text{NH}_3)_2\text{Br}_2(\text{HL}^3)_4]\text{Br}_2\cdot\text{CH}_3\text{OH}$  [18]

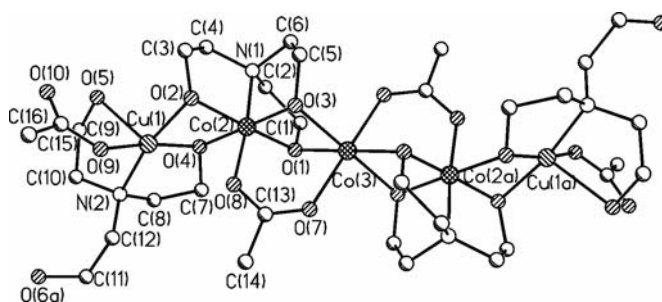


Fig. 6. Structure of pentanuclear unit in  $[\text{Cu}_2\text{Co}^{\text{II}}\text{Co}^{\text{III}}_2(\text{OAc})_4(\text{H}_2\text{L}^4)_2(\text{L}^4)_2]\cdot 2\text{HOAc}$  [16]

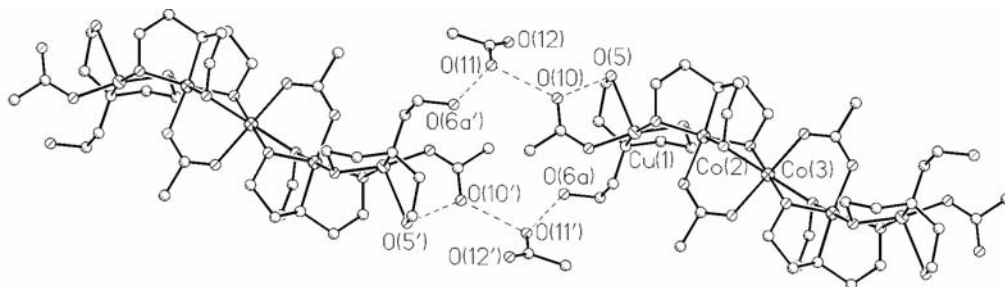


Fig. 7. View of  $[\text{Cu}_2\text{Co}^{\text{II}}\text{Co}^{\text{III}}_2(\text{OAc})_4(\text{H}_2\text{L}^4)_2(\text{L}^4)_2]\cdot 2\text{HOAc}$  showing the hydrogen-bonded network involving the non-coordinating acetic acid molecules [16]

Reaction of zerovalent copper with cobalt(II) acetate and triethanolamine in dmf solution in air yields the unique mixed-valence complex  $[\text{Cu}_2\text{Co}^{\text{II}}\text{Co}^{\text{III}}_2(\text{OAc})_4(\text{H}_2\text{L}^4)_2(\text{L}^4)_2]\cdot 2\text{HOAc}$  (**5**) [16]. The complex consists of the pentanuclear unit  $[\text{Cu}_2\text{CoCo}_2(\text{OAc})_4(\text{H}_2\text{L}^4)_2(\text{L}^4)_2]$ , which has an inversion centre (Fig. 6) and two molecules of acetic acid in the crystal lattice. The five metal ions are linked together by eight oxygen atoms of the four triethanolamine ligands and by two acetate groups with metal–metal separations being 2.823(2) and 2.964(1) Å for Cu(1)...Co(2) and Co(2)...Co(3), respectively. The divalent cobalt atom, Co(3), is located at the centre of inversion, and its coordination geometry can be best described as a slightly distorted octahedron. The geometry at the trivalent cobalt atoms, Co(2) and Co(2a), is distorted octahedral. The atom Cu(1) is five-coordinate with square-pyramidal geometry. Two non-coordinating acetic acid molecules are connected to the pentanuclear unit *via* hydrogen bonds. The intermolecular hydrogen bonding links the pentanuclear units together and results in the formation of an extended one-dimensional structure (Fig. 7).

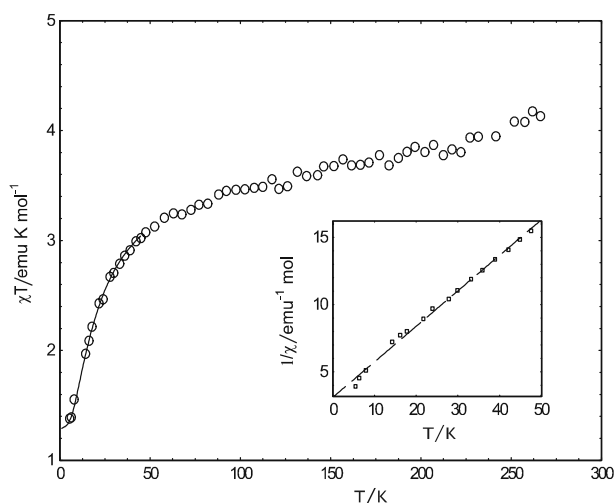


Fig. 8.  $\chi_m T$  vs.  $T$  curve for  $[\text{Cu}_2\text{Co}^{\text{II}}\text{Co}^{\text{III}}_2(\text{OAc})_4(\text{H}_2\text{L}^4)_2(\text{L}^4)_2]\cdot 2\text{HOAc}$  [16]

At room temperature the value of  $\chi_m T$  ( $4.1 \text{ emu}\cdot\text{K}\cdot\text{mol}^{-1}$ ) (Fig. 8) is in agreement with the presence of two uncorrelated  $S = 1/2$  centres and one  $S = 3/2$  centre with largely unquenched angular orbital momentum. Magnetic measurements showed a marked decrease of the  $\chi_m T$  value at low temperature, indicative of antiferromagnetic interactions between magnetic centres. A fit was attempted assuming an effective  $S = 1/2$  ground state for Co(II) and Ising-type anisotropy, considering only intramolecular interactions. The obtained value for  $J_z = 36 \text{ cm}^{-1}$  must originate from the efficient role of the diamagnetic Co(III) in the transmitting the interaction between Cu(II) and Co(II) below 40 K [16].

The reaction of acetonitrile solutions of  $\text{CoX}_2\cdot 2\text{H}_2\text{O}$  ( $X = \text{Br}, \text{I}$ ) and 2-dimethylaminoethanol with copper powder in the air leads to the formation hexanuclear com-

plexes  $[\text{Cu}_2\text{Co}(\mu_3\text{-OH})\text{Br}_2(\text{L}^2)_3]_2 \cdot 2\text{CH}_3\text{CN}$  (**6**) and  $[\text{Cu}_2\text{Co}(\mu_3\text{-OH})\text{I}_2(\text{L}^2)_3]_2 \cdot 4\text{CH}_3\text{CN}$  (**7**) [15]. In the structure of **6** and **7** (Fig. 9) two symmetry-related  $\text{Cu}_2\text{Co}$  units are linked by amino alkoxo bridges to form a hexanuclear molecule with intermetallic distances ranging from 3.102(2)–3.260(2) ( $\text{Cu}\dots\text{Co}$ ) to 3.287(3)–3.931(2) Å ( $\text{Cu}\dots\text{Cu}$ ). The triangular planes formed by two copper and one cobalt atoms are capped by a  $\mu_3\text{-OH}$  group that adopts an asymmetric bonding mode with two shorter distances (mean 1.962(9) Å) to the copper atoms and longer one to the cobalt centre (mean 2.293(10) Å). The two copper centres have distinct chemical environments but both adopt a distorted square-pyramidal coordination. The two copper square pyramids are tilted toward each other as a result of the bridging function of the axial halide atom. Five-coordination of the cobalt atom is completed by three oxygen atoms, one nitrogen atom and the  $\mu_3\text{-hydroxide}$  in an elongated trigonal bipyramidal geometry.

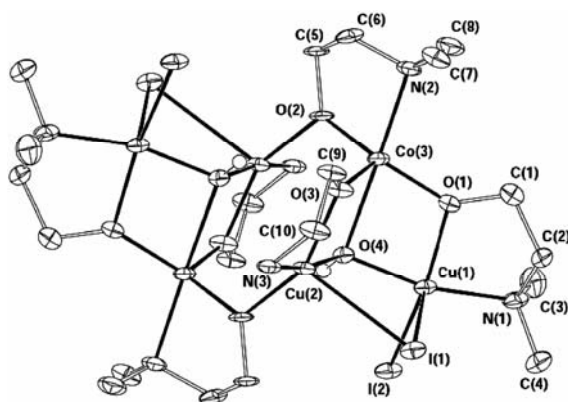


Fig. 9. ORTEP plot of  $[\text{Cu}_2\text{Co}(\mu_3\text{-OH})\text{I}_2(\text{L}^2)_3]_2 \cdot 4\text{CH}_3\text{CN}$  with the atom numbering scheme [15]

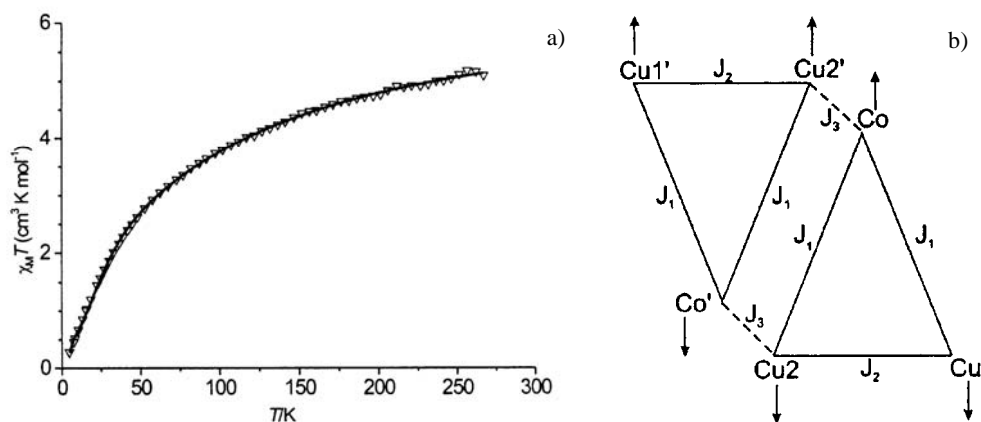


Fig. 10.  $\chi_m T$  vs.  $T$  curve for  $[\text{Cu}_2\text{Co}(\mu_3\text{-OH})\text{I}_2(\text{L}^2)_3]_2 \cdot 4\text{CH}_3\text{CN}$  (a) and exchange coupling pattern with the scheme of the spin topology (b) [15]

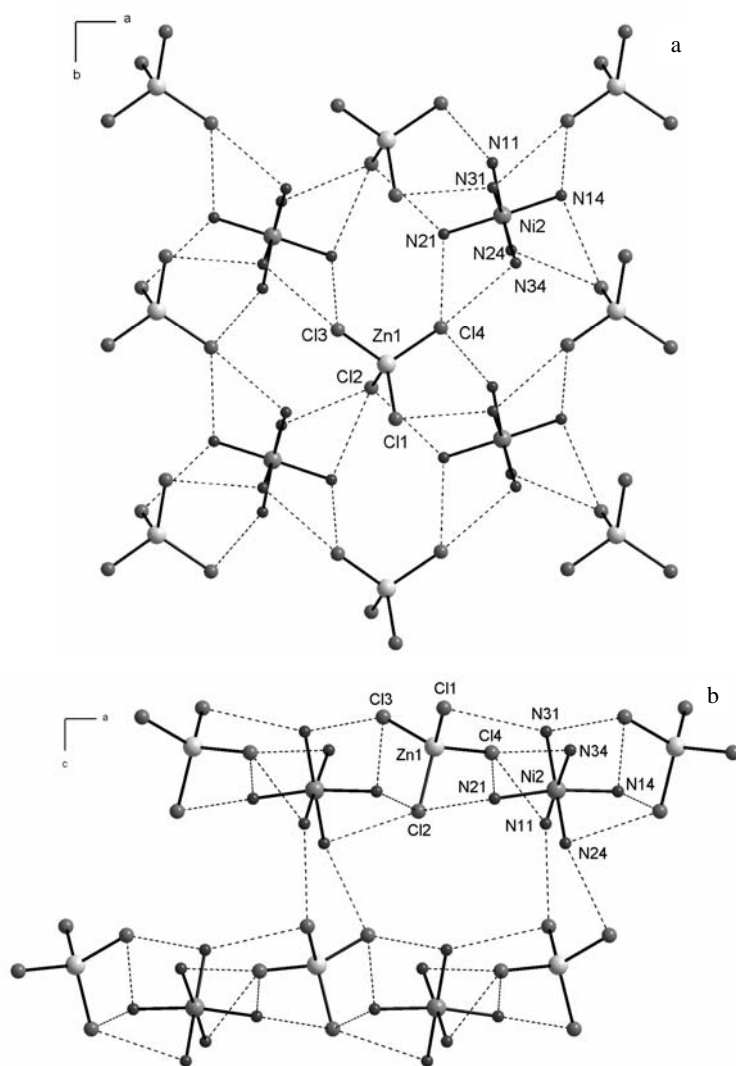


Fig. 11. View of a fragment of the 2D layer projected onto the  $ab$  plane (a) and a packing diagram of the sheets (b) of  $[\text{Ni}(\text{en})_3][\text{ZnCl}_4]$  [19]

The magnetic susceptibility data for **7** have been quantitatively analysed in the 5–280 K temperature range (Fig. 10) on the assumption of isotropic coupling between the magnetic centres as the ground electronic state of the trigonal bipyramidal  $\text{Co}(\text{II})$  centre is orbitally non-degenerate. Variable-temperature magnetic susceptibility study gave satisfactory fits to the observed susceptibility considering **7** as a combination of two trinuclear entities. An antiferromagnetic spin exchange operates in the  $\text{Cu}_2\text{Co}$  unit ( $J_{\text{CuCu}} = 48.7(9)$ ;  $J_{\text{CuCo}} = 86.2(1.3) \text{ cm}^{-1}$ ) while a weak ferromagnetic coupling is active between Cu and Co atoms from different trinuclear entities ( $J_{\text{CuCo}'} = -8.0(4) \text{ cm}^{-1}$ ) [15].

A bridging mode is not typical of ethylenediamine. Therefore the replacement of aminoalcohol with en results in the dramatic change of the structure of heteropolynuclear complexes. The anions overtake bridging functions and a role of hydrogen bonds becomes more important. The increase of inter-metal distances prevents from exchange interactions.

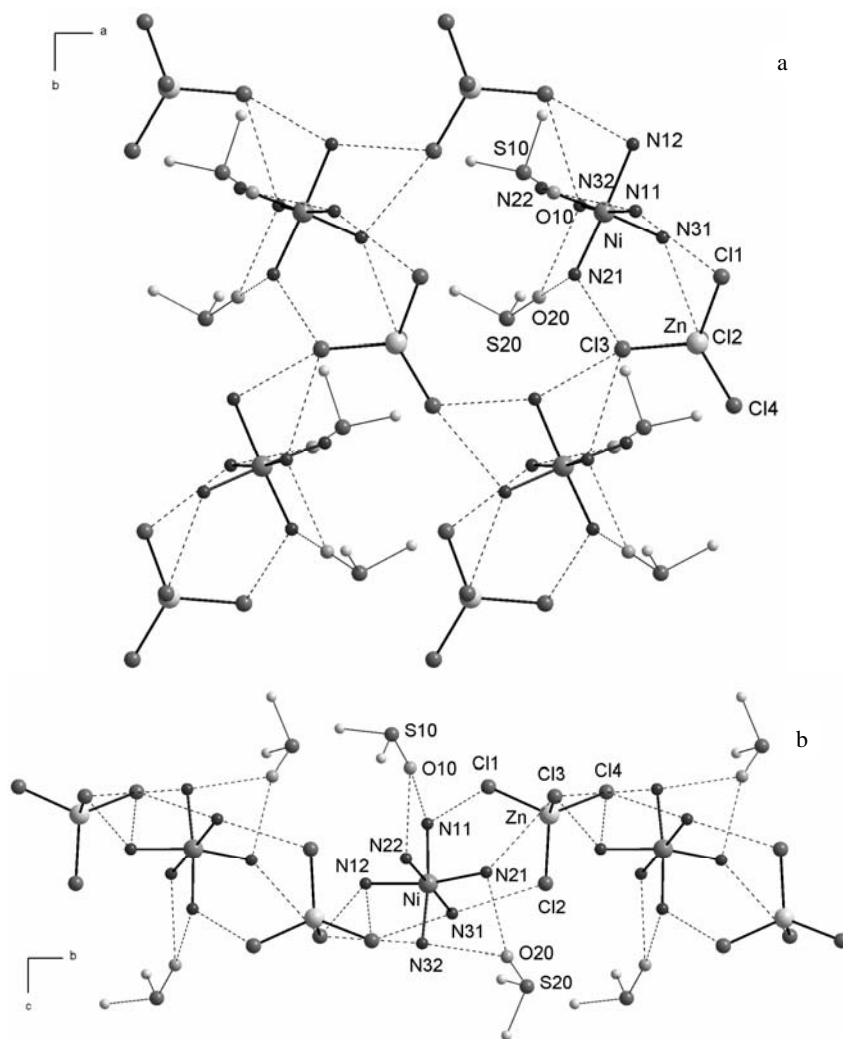


Fig. 12. H-bonding motifs generating infinite 2D sheets in  $[\text{Ni}(\text{en})_3][\text{ZnCl}_4] \cdot 2\text{dmsO}$  (a) and a view of the complex projecting onto the  $cb$  plane (b) [19]

Heterobimetallic complexes  $[\text{Ni}(\text{en})_3][\text{ZnCl}_4]$  (**8**),  $[\text{Ni}(\text{en})_3][\text{ZnCl}_4] \cdot 2\text{dmsO}$  (**9**) and  $[\text{Ni}(\text{en})_3][\text{Zn}(\text{NCS})_4] \cdot \text{CH}_3\text{CN}$  (**10**) have been synthesized in the open-air reaction of zinc oxide, nickel chloride (or nickel powder),  $\text{NH}_4\text{X}$  ( $\text{X} = \text{Cl}, \text{NCS}$ ) and ethylenediamine in non-aqueous solvents [19]. Complex **8** consists of  $[\text{Ni}(\text{en})_3]^{2+}$  and

$[\text{ZnCl}_4]^{2-}$  ions that form a three-dimensional network by means of H-bonds (Fig. 11). Between the anion and cation, a lot of intermolecular  $\text{N-H}\cdots\text{Cl}$  interactions, which indicate weak extensive hydrogen bonding, are found and one  $[\text{Ni}(\text{en})_3]^{2+}$  unit is hydrogen bonded to five different anions (four in the 2D layer and one between adjacent sheets).

Compound **9** made of the same building blocks ( $[\text{Ni}(\text{en})_3]^{2+}$  cations and  $[\text{ZnCl}_4]^{2-}$  anions) also contains two molecules of dimethylsulfoxide, the presence of which causes considerable changes in the crystal architecture (Fig. 12). The plentiful array of hydrogen bonds, that occur as in all described complexes, strengthen the structure, but in contrast to **8**, the  $[\text{Ni}(\text{en})_3]^{2+}$  unit is hydrogen-bonded to only three different  $[\text{ZnCl}_4]^{2-}$  anions instead of five different  $[\text{ZnCl}_4]^{2-}$  anions (as in the case in **8**) being additionally H-bonded to two dmso molecules. All the chlorine atoms are linked by means of H-bonds with amino groups of the ethylenediamine of the cations, and one of them is 3-coordinated by H(N) atoms, one 2-coordinated and two unbranched. These listed hydrogen bonds are stabilized the two-dimensional sheets of **9**, which are slightly undulating in comparison with **8**, but further interlayer H-bonds are now not possible due to the presence of the dmso solvent molecules [19].

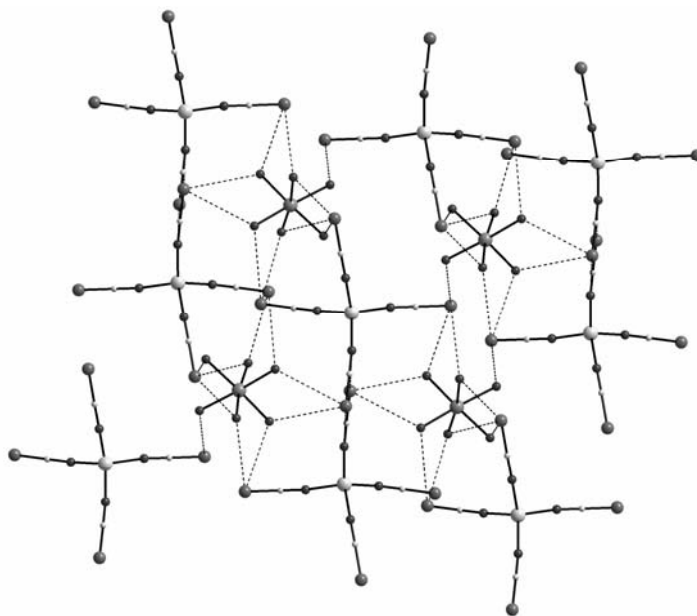


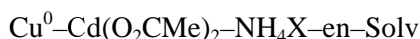
Fig. 13. Packing diagram of  $[\text{Ni}(\text{en})_3][\text{Zn}(\text{NCS})_4]\cdot\text{CH}_3\text{CN}$  projected onto the  $ac$  plane showing a 3D network generated by hydrogen bonds [19]

The compound  $[\text{Ni}(\text{en})_3][\text{Zn}(\text{NCS})_4]\cdot\text{CH}_3\text{CN}$  consists of the  $[\text{Ni}(\text{en})_3]^{2+}$  cations and  $[\text{Zn}(\text{NCS})_4]^{2-}$  anions, the presence of which facilitate formation of a three-dimensional architecture based on numerous  $\text{N-H}\cdots\text{S}$  hydrogen bonds (Fig. 13). The geometrical parameters of the  $[\text{Ni}(\text{en})_3]^{2+}$  unit are similar to those found in **8** and **9**. The crystal

structure of **10** is reinforced by several hydrogen bonds and the  $[\text{Ni}(\text{en})_3]^{2+}$  unit is H-bonded to five different  $[\text{Zn}(\text{NCS})_4]^{2-}$  anions and a molecule of  $\text{CH}_3\text{CN}$ . All four S atoms joined with  $\text{NH}_2$  groups of  $[\text{Ni}(\text{en})_3]^{2+}$  cations using hydrogen bonds, and two of them are 3-coordinated by H(N) atoms and two – 2-coordinated [19]. Such an essential influence of the nature of the anion on the nuclearity and coordination topology can be used for the regulative change of the structure of the heteropolynuclear complex by the synthesis of compounds with a necessary combination of anions. The possibility of the synthesis of heteropolynuclear complexes with a certain set of anions of different nature can be achieved with the combination of “Salt” and “Ammonium salt” methods of direct synthesis:



Moreover, such a combination makes it possible to prepare mixed-metal mixed-anion complexes in “one pot”. Thus, to prepare mixed-anion heterobimetallic coordination polymers  $[\text{Cu}(\text{en})_2\text{Cd}(\mu\text{-Cl})(\mu\text{-O}_2\text{CMe})\text{Cl}(\text{O}_2\text{CMe})]_n$  (11),  $[\text{Cu}(\text{en})_2\text{CdI}_{1.64}(\text{O}_2\text{CMe})_{2.36}]_n$  (12),  $[\text{Cu}_2(\text{en})_4\text{Cd}_2(\text{NCS})_2(\text{NCS})_4(\text{O}_2\text{CMe})_2]_n$  (13) the following systems have been used [20]:



where X = Cl, Br, I, NCS; Solv = dmf, dmsO,  $\text{CH}_3\text{OH}$ ,  $\text{CH}_3\text{CN}$ .

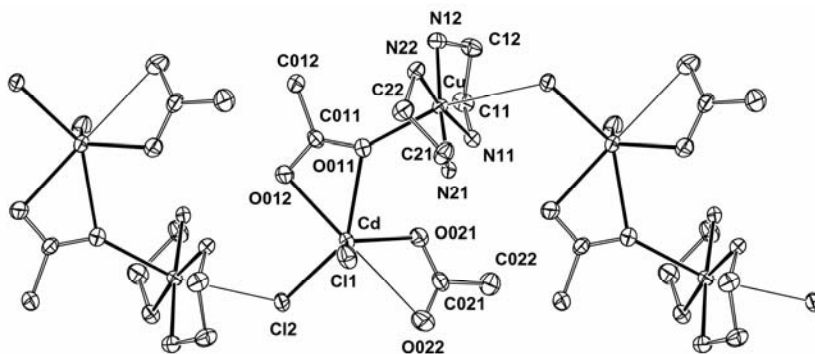


Fig. 14. The one-dimensional helical chain in the compound  $[\text{Cu}(\text{en})_2\text{Cd}(\mu\text{-Cl})(\mu\text{-O}_2\text{CMe})\text{Cl}(\text{O}_2\text{CMe})]_n$  with the numbering scheme [20]

The structure of compound **11** consists of an infinite one-dimensional helical chain comprised of cationic  $\text{Cu}(\text{en})_2^{2+}$  and mixed-ligand anionic  $\text{Cd}(\mu\text{-Cl})(\mu\text{-O}_2\text{CMe})\text{Cl}(\text{O}_2\text{CMe})^{2-}$  building blocks, linking together through one bridging chlorine atom and an oxygen atom of the chelating (and also bridging) bidentate acetate ligand (Fig. 14). The Cd atom in **11** is six-coordinate; the coordination sphere consisting two acetate groups, one of which is weakly bidentate, the other one being bidentate [through O(011) and O(012)] and bridging unidentate [through O(011)]. Each of

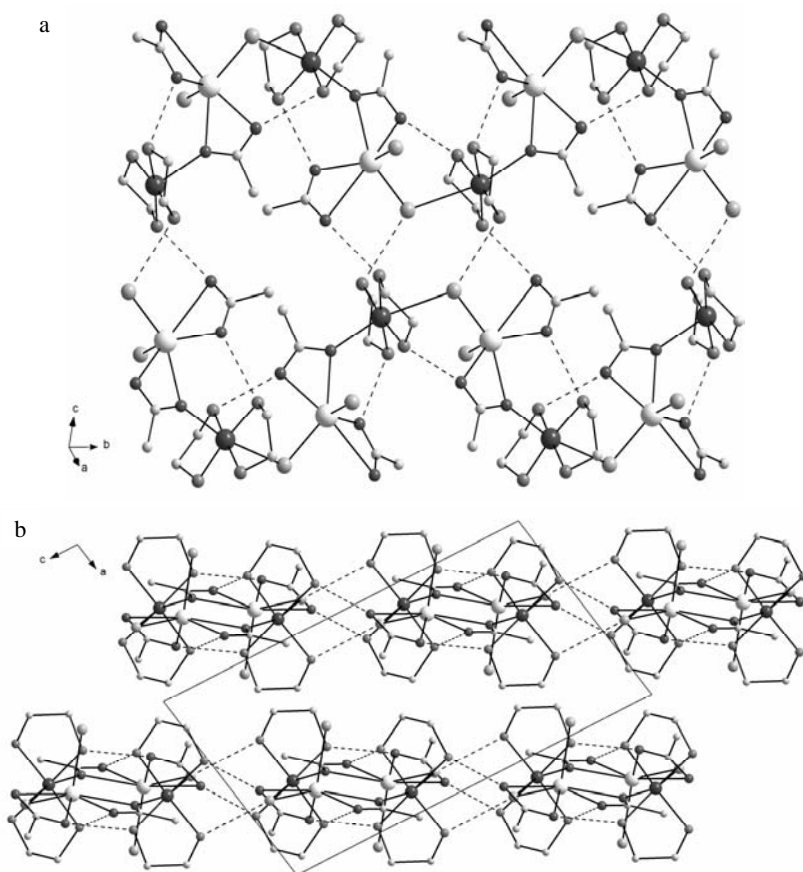


Fig. 15. Fragment of the 2D sheet (a) and a view of the layer arrangement (b) in the structure of  $[\text{Cu}(\text{en})_2\text{Cd}(\mu\text{-Cl})(\mu\text{-O}_2\text{CMe})\text{Cl}(\text{O}_2\text{CMe})]_n$  [20]

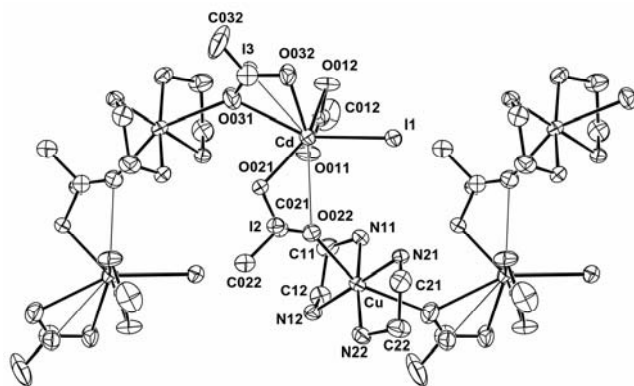


Fig. 16. Perspective view of a helical chain in complex  $[\text{Cu}(\text{en})_2\text{CdI}_{1.64}(\text{O}_2\text{CMe})_{2.36}]_n$  together with the atom numbering [20]

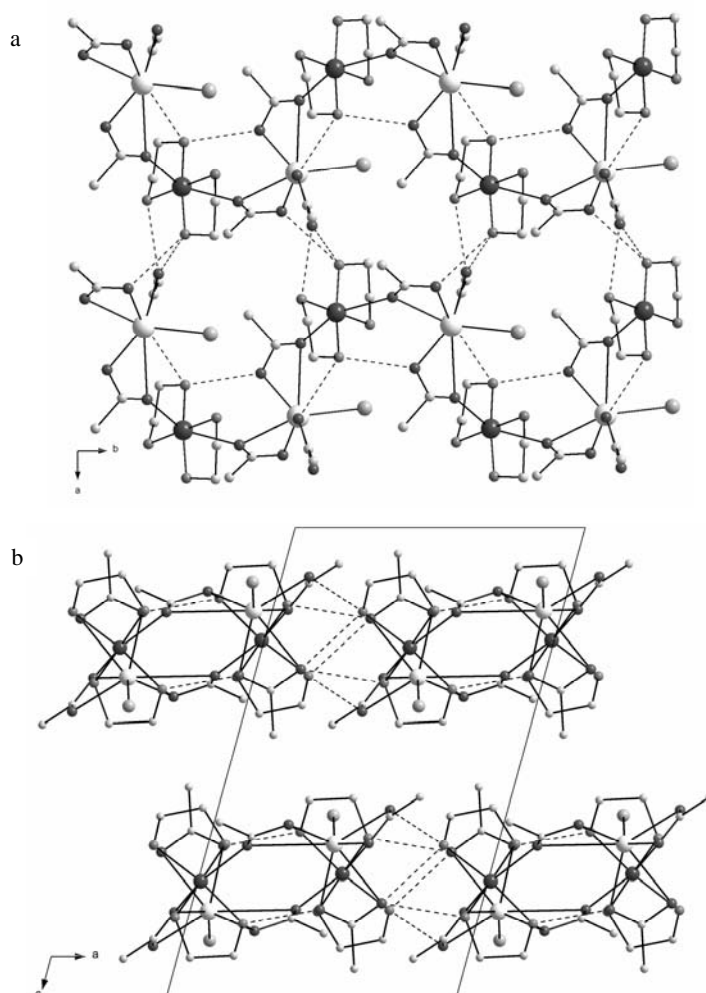


Fig. 17. View of a fragment of the 2D layer (a) and a packing diagram of the polymeric sheets (b) in complex  $[\text{Cu}(\text{en})_2\text{CdI}_{1.64}(\text{O}_2\text{CMe})_{2.36}]_n$  [20]

the Cd(II) is further coordinated by one terminal and one bridging chlorine atom to form a  $\text{CdO}_4\text{Cl}_2$  distorted octahedron. The chains of  $\text{Cu}-\text{Cl}(2)-\text{Cd}-\text{O}(011)$  atoms reveal a helical shape. Two sets of H-bonds assemble the chains, related by the crystallographic planes into a two-dimensional structure (Fig. 15) [20]. The complex **12** is basically 1D helical chain structure formed by  $\text{Cu}(\text{en})_2^{2+}$  units and  $\text{Cd}(\mu-\text{O}_2\text{CMe})_2\text{I}(\text{O}_2\text{CMe})^{2-}$  building blocks, which are joined through oxygen atom from a weakly bidentate chelate acetate ligand and also through the oxygen atoms of the other acetate group which is bridging unidentate and bidentate (Fig. 16). However both bridging acetate sites are also partially occupied by iodide ions. Thus as well as bridging  $\text{Cd}(\mu-\text{O}_2\text{CMe})_2\text{I}(\text{O}_2\text{CMe})^{2-}$  units, there is also a minor component of  $\text{Cd}(\mu-\text{O}_2\text{CMe})(\mu-\text{I})\text{I}(\text{O}_2\text{CMe})^{2-}$ . There may also be some  $\text{Cu}(\text{en})_2\text{Cd}(\mu-\text{I})_2\text{I}(\text{O}_2\text{CMe})^{2-}$  corresponding the

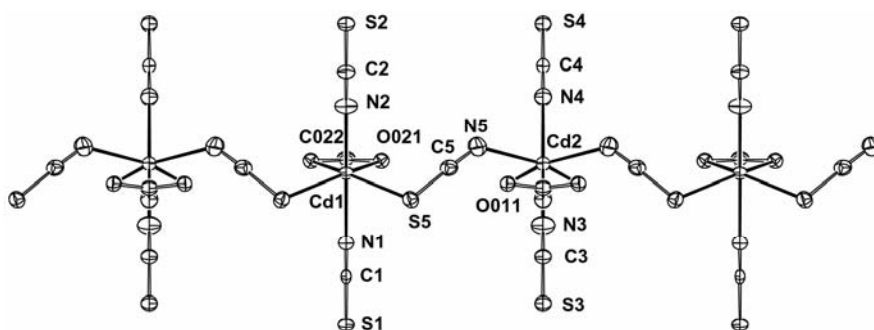


Fig. 18. View of the anionic chain motif of complex  $[\text{Cu}_2(\text{en})_4\text{Cd}_2(\text{NCS})_2(\text{NCS})_4(\text{O}_2\text{CMe})_2]_n$  together with the atom numbering scheme [20]

replacement of both bridging acetates. In **12** only one nitrogen atom from  $\text{NH}_2$  group of en takes part in the intrachain hydrogen bonding with oxygen atoms of the acetate ligands, in contrast with two  $\text{N}_{\text{en}}$  atoms that participated in H-bonding in **11**. Furthermore, only one type of H-bonding interactions, those involving a hydrogen atom of an  $\text{NH}_2$  group of en and an oxygen atom of a bidentate acetate group, facilitates the formation of 2D sheets (Fig. 17) [20].

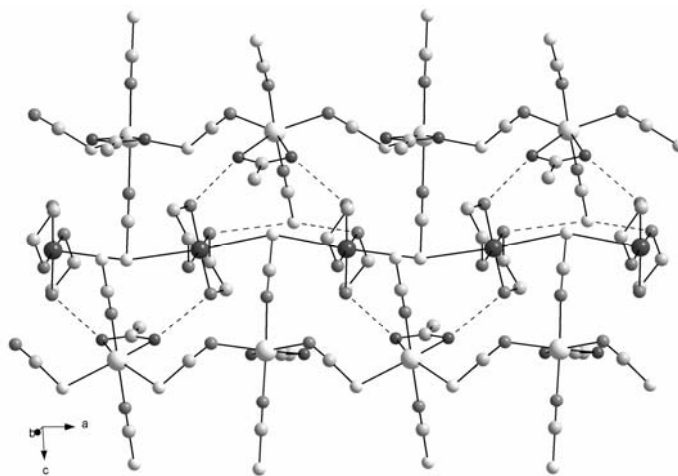


Fig. 19. Perspective view of a sheet in complex  $[\text{Cu}_2(\text{en})_4\text{Cd}_2(\text{NCS})_2(\text{NCS})_4(\text{O}_2\text{CMe})_2]_n$  [20]

X-Ray analysis reveals a two-dimensional wave-like polymeric network for complex **13**, the crystal structure of which consists of 1D anionic chains of  $\text{Cd}_2(\text{NCS})_6(\text{O}_2\text{CMe})_2^{4-}$  and  $\text{Cu}(\text{en})_2^{2+}$  units. The view of the 1D anionic chain motif together with the atom numbering scheme is presented in Fig. 18, while Fig. 19 shows the perspective view of a 2D sheet. Both copper(II) and cadmium(II) atoms are joined through  $-\text{Cu}-\text{SCN}-\text{Cd}-$  linkages. The polymeric anion contains two crystallographically independent cadmium atoms, Cd(1) and Cd(2), both of which are six-coordinate with

$\text{CdS}_2\text{N}_2\text{O}_2$  and  $\text{CdN}_4\text{O}_2$  distorted octahedral geometries, respectively. Both Cd(II) atoms are coordinated by one chelating bidentate acetate group, one terminal thiocyanate ligand, one  $\mu_{1,3}$ -NCS group, which connect the copper(II) and cadmium(II) atoms in the 2D layer, and another two  $\mu_{1,3}$ -NCS groups which serve bridges between the metal centres. The polymeric mixed-anion  $-\text{NCS}-\text{Cd}(\text{NCS})_2(\text{O}_2\text{CMe})-\text{SCN}-\text{Cd}(\text{NCS})_2(\text{O}_2\text{CMe})-\text{NCS}-$  chains are almost linear. The resulting 2D sheets consist of 18-membered  $[\text{Cd}_3(\mu_{1,3}-\text{NCS})_4\text{Cu}_2\text{S}_{\text{NCS}}]$  rings folded in a wave-like manner (Fig. 19) [20].

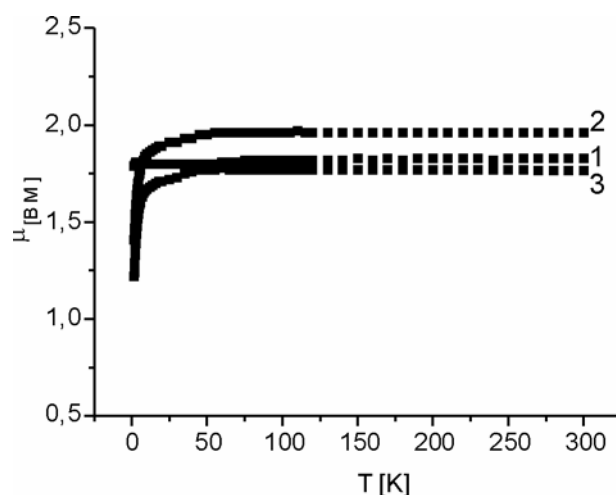


Fig. 20. Temperature dependences of the effective magnetic moment for  $[\text{Cu}(\text{en})_2\text{Cd}(\mu\text{-Cl})(\mu\text{-O}_2\text{CMe})\text{Cl}(\text{O}_2\text{CMe})]_n$ , (1)  $[\text{Cu}(\text{en})_2\text{CdI}_{1.64}(\text{O}_2\text{CMe})_{2.36}]_n$  (2) and  $[\text{Cu}_2(\text{en})_4\text{Cd}_2(\text{NCS})_2(\text{NCS})_4(\text{O}_2\text{CMe})_2]_n$  (3) [20]

Magnetic data for **11–13** are shown in Fig. 20 as  $\mu_{\text{eff}}$  vs.  $T$  plots, which indicate that in all cases the magnetic behaviour is in general paramagnetic, although at the lowest temperatures a characteristic decrease of  $\mu_{\text{eff}}$  for **11** and **13** is observed. The Weiss temperatures, calculated on the basis of inverse dependence of molar magnetic susceptibilities on temperature,  $\theta = -1.037$ ,  $-0.191$  and  $-0.99224$  for **11**, **12** and **13** respectively, suggest weak antiferromagnetic interactions, probably due to Cu–Cu contacts, intrachain at a distance of  $8.183(1)$  Å for **11** and interchain at a distance of  $6.165(2)$  Å for **13** [20]. The room-temperature magnetic moment for each copper atom, ca.  $1.8\mu_B$ , is in the normal range for isolated  $S = 1/2$  ions.

### 3. Heterotrimetallic complexes

As the reaction systems employed have been so productive in generating new heterobimetallic complex an attempt was undertaken to use the approach developed to obtain heterotrimetallic complexes (Table 2).

Table 2. Heterotrimetallic complexes obtained by direct synthesis [25, 26]

Initial system	Complex
$\text{Cu}^0\text{-CoCl}_2\text{-NiCl}_2\text{-HL}^2\text{-CH}_3\text{OH}$	$\text{Cu}_2\text{Ni}_2\text{Co}^{\text{II}}\text{Cl}_5(\text{L}^2)_5$ $\text{Cu}_2\text{Ni}_2\text{Co}^{\text{II}}\text{Cl}_4(\text{L}^2)_6$
$\text{Cu}^0\text{-CdCl}_2\text{-NiCl}_2\text{-HL}^2\text{-Solv}$ Solv = $\text{CH}_3\text{OH}$ , $\text{CH}_3\text{CN}$	$\text{Cu}_2\text{Ni}_2\text{Cd}_2\text{Cl}_6(\text{L}^2)_6 \cdot 2\text{H}_2\text{O}$
$\text{Cu}^0\text{-CoX}_2\text{-ZnO-NH}_4\text{X-HL}^2\text{-CH}_3\text{OH}$ X = OAc, NCS	$\text{CuCo}^{\text{III}}\text{Zn}(\text{L}^2)_4(\text{NCS})_2\text{OAc}$
$\text{Cu}^0\text{-CoX}_2\text{-NiX}_2\text{-H}_2\text{L}^3\text{-CH}_3\text{OH}$ X = Cl, Br, OAc, NCS, HCOO, $\text{NO}_3$	$[\text{Ni}(\text{H}_2\text{L}^3)_2][\text{CuCo}^{\text{III}}(\text{L}^3)_2(\text{H}_2\text{L}^3)(\text{NCS})]_2\text{X}_2$ X = NCS, HCOO, $\text{NO}_3$ $[\text{Ni}(\text{H}_2\text{L}^3)_2][\text{CuCo}^{\text{III}}(\text{L}^3)_2(\text{H}_2\text{L}^3)(\text{NCS})]_2\text{X}_2 \cdot 2\text{H}_2\text{O}$ X = Cl, Br
$\text{Cu}^0\text{-CoX}_2\text{-CdX}_2\text{-H}_2\text{L}^3\text{-CH}_3\text{OH}$ X = Cl, Br, NCS	$[\text{CuCo}^{\text{III}}\text{Cd}(\text{H}_2\text{L}^3)_2(\text{L}^3)_2(\text{NCS})\text{X}_2] \cdot \text{CH}_3\text{OH}$ X = Cl, Br
$\text{Cu}^0\text{-CoCl}_2\text{-ZnCl}_2\text{-H}_2\text{L}^3\text{-CH}_3\text{OH}$	$[\text{Zn}_2\text{CuCo}^{\text{III}}(\text{L}^3)_3\text{Cl}_3(\text{CH}_3\text{OH})] \cdot \text{CH}_3\text{OH}$

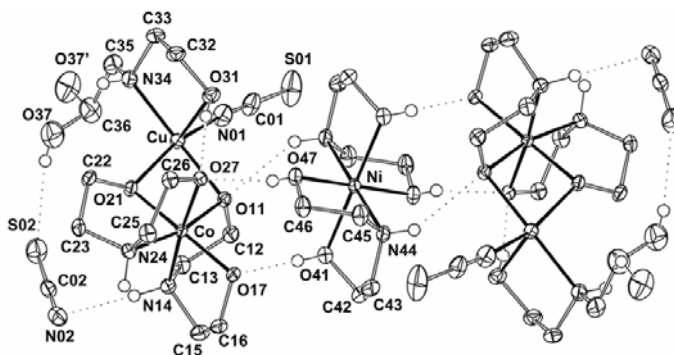


Fig. 21. The structure of the pentanuclear aggregate  $\{[\text{Ni}(\text{H}_2\text{L}^3)_2][\text{CoCu}(\text{L}^3)_2(\text{H}_2\text{L}^3)(\text{NCS})]_2\}^{2+}$  in  $[\text{Ni}(\text{H}_2\text{L}^3)_2][\text{CoCu}(\text{L}^3)_2(\text{H}_2\text{L}^3)(\text{NCS})]_2(\text{NCS})_2$  and  $[\text{Ni}(\text{H}_2\text{L}^3)_2][\text{CuCo}(\text{L}^3)_2(\text{H}_2\text{L}^3)(\text{NCS})]_2\text{Br}_2 \cdot 2\text{H}_2\text{O}$  with the numbering scheme [25]

Three novel heterotrimetallic complexes  $[\text{Ni}(\text{H}_2\text{L}^3)_2][\text{CoCu}(\text{L}^3)_2(\text{H}_2\text{L}^3)(\text{NCS})]_2(\text{NCS})_2$  (**14**),  $[\text{Ni}(\text{H}_2\text{L}^3)_2][\text{CuCo}(\text{L}^3)_2(\text{H}_2\text{L}^3)(\text{NCS})]_2\text{Br}_2 \cdot 2\text{H}_2\text{O}$  (**15**) and  $[\text{CuCoCd}(\text{H}_2\text{L}^3)_2(\text{L}^3)_2(\text{NCS})\text{Br}_2] \cdot \text{CH}_3\text{OH}$  (**16**) have been prepared using zerovalent copper, cobalt thiocyanate, nickel thiocyanate (**14**), nickel bromide (**15**) or cadmium bromide (**16**) and methanol solutions of diethanolamine in air. The overall structural configurations of isomorphous **14** and **15** [25] are similar with the uncoordinated  $\text{NCS}^-$  group in **14** replaced by disordered  $\text{Br}^-$  anion and water molecule in **15**. The molecular diagram and numbering scheme of **14** is shown in Fig. 21 which illustrates the general geometry of the two compounds. The most prominent feature of the structures of **14** and **15** is the formation of the “pentanuclear” aggregate  $\{[\text{Ni}(\text{H}_2\text{L}^3)_2][\text{CoCu}(\text{L}^3)_2(\text{H}_2\text{L}^3)(\text{NCS})]_2\}^{2+}$  made up of two neutral  $[\text{CoCu}(\text{L}^3)_2(\text{H}_2\text{L}^3)(\text{NCS})]$  units and the cation  $[\text{Ni}(\text{H}_2\text{L}^3)_2]^{2+}$ , previously unknown. The Ni cation is on a crystallographic inversion centre, the Cu/Co moieties are situated on general positions. The presence of the molecular inversion

centre requires all five metal atoms to lie in the same plane. In the Cu–Co–Cu–Co parallelogram centred on Ni the bridged Cu...Co separations are of approximately 2.924 while other metal–metal distances vary from 4.640 to 5.328 Å.

The divalent nickel ion adopts a slightly distorted octahedral environment by interacting with two oxygen and two nitrogen atoms in the equatorial plane and two axially disposed oxygen atoms from two  $\text{H}_2\text{L}^3$  ligands.

The metal atoms within  $[\text{CoCu}(\text{L}^3)_2(\text{H}_2\text{L}^3)(\text{NCS})]$  units are bridged by two oxygen atoms of two diethanolamine ligands. The copper(II) atom has distorted square-pyramidal coordination to a  $\text{NO}_3\text{N}_{\text{NCS}}$  donor set. Each  $[\text{CoCu}(\text{L}^3)_2(\text{H}_2\text{L}^3)(\text{NCS})]$  unit is linked to the central Ni complex by two strong  $\text{O}-\text{H}\cdots\text{O}^-$  and one weaker  $\text{N}-\text{H}\cdots\text{O}^-$  charge-assisted hydrogen bonds, this arrangement producing eight-membered H-bonded rings (Fig. 21). Additional intermolecular association in the lattice occurs through the hydrogen bonding of the  $\text{N}-\text{H}\cdots\text{N}$ ,  $\text{N}-\text{H}\cdots\text{S}$ ,  $\text{O}-\text{H}\cdots\text{S}$  and  $\text{N}-\text{H}\cdots\text{Br}$  types involving thiocyanate groups (**14**) and bromide anions (**15**) to form 3-D frameworks (Fig. 22).

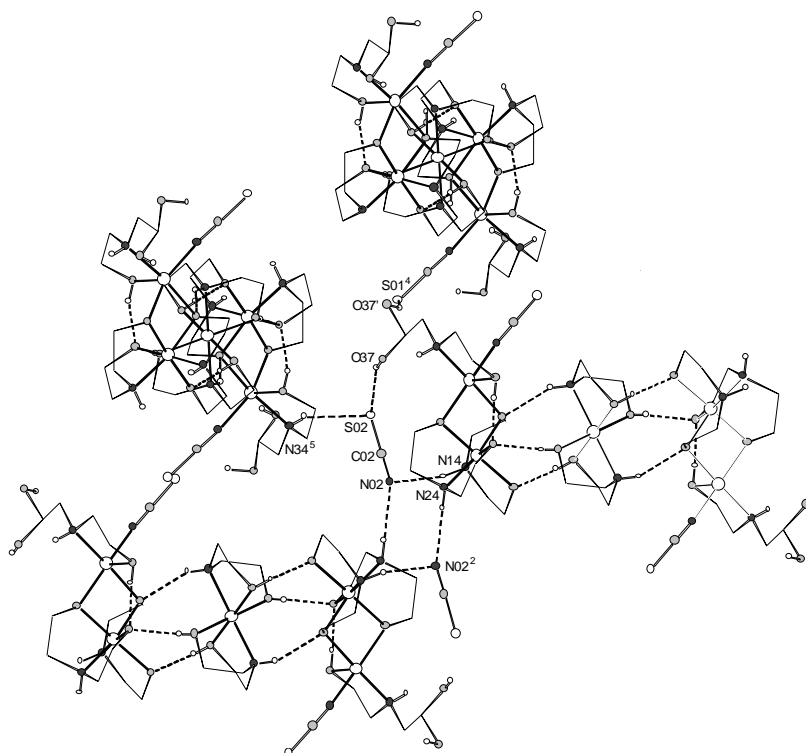


Fig. 22. View of  $[\text{Ni}(\text{H}_2\text{L}^3)_2][\text{CoCu}(\text{L}^3)_2(\text{H}_2\text{L}^3)(\text{NCS})_2(\text{NCS})_2]$  showing the hydrogen bonding network involving the uncoordinated thiocyanate anions [25]

X-ray crystallographic analysis of  $[\text{CuCoCd}(\text{H}_2\text{L}^3)_2(\text{L}^3)_2(\text{NCS})\text{Br}_2]\cdot\text{CH}_3\text{OH}$  (**16**) [25] reveals an asymmetric three-metal atom core with metal atoms in a triangular array

(Fig. 23). With  $\text{Cd}^{2+}$  a different structure is obtained – the  $[\text{CoCu}(\text{L}^3)_2(\text{H}_2\text{L}^3)(\text{NCS})]$  unit is now linked to Cd centre through coordination of oxygen atoms of  $\text{L}^3$  groups on the Co atom to form a discrete heterotrimetallic molecular species. The structural properties of the Cu/Co moiety are similar to those in **14** and **15** with Co atom being six-coordinate and Cu atom displaying a distorted square-pyramidal coordination. The geometry of the cadmium atom can be described as distorted octahedral with donor atoms of diethanolamine ligands and bromine atom.

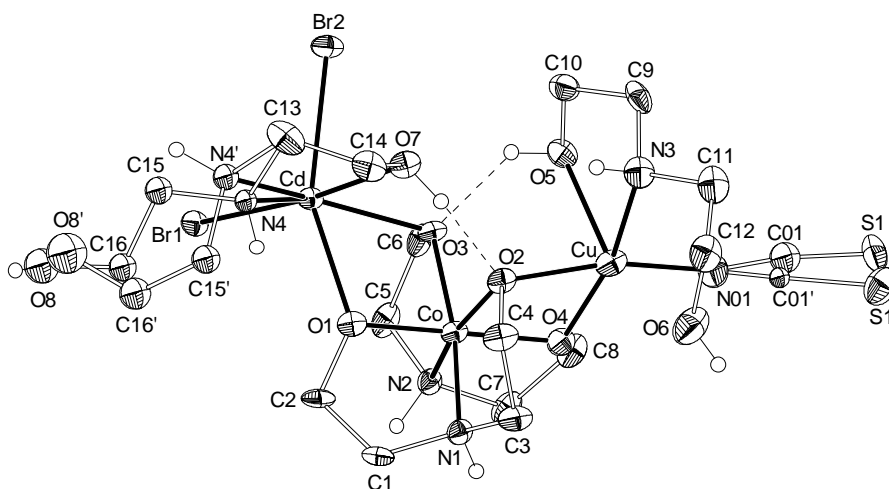


Fig. 23. Molecular structure of  $[\text{CuCoCd}(\text{H}_2\text{L}^3)_2(\text{L}^3)_2(\text{NCS})\text{Br}_2] \cdot \text{CH}_3\text{OH}$  with the numbering scheme [25]

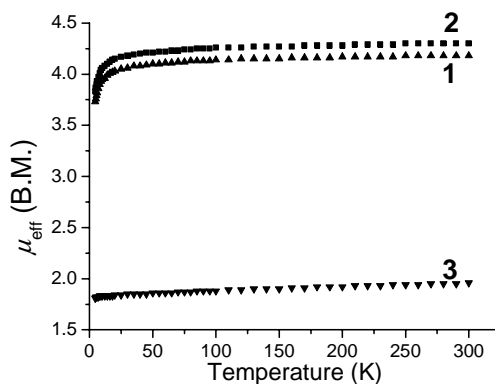


Fig. 24. Temperature dependences of the effective magnetic moment for  $[\text{Ni}(\text{H}_2\text{L}^3)_2][\text{CoCu}(\text{L}^3)_2(\text{H}_2\text{L}^3)(\text{NCS})_2(\text{NCS})_2]$  (1),  $[\text{Ni}(\text{H}_2\text{L}^3)_2][\text{CuCo}(\text{L}^3)_2(\text{H}_2\text{L}^3)(\text{NCS})_2]\text{Br}_2 \cdot 2\text{H}_2\text{O}$  (2) and  $[\text{CuCoCd}(\text{H}_2\text{L}^3)_2(\text{L}^3)_2(\text{NCS})\text{Br}_2] \cdot \text{CH}_3\text{OH}$  (3) [25]

Experimental magnetic data for **14–16** are displayed in Fig. 24 as  $\mu_{\text{eff}}$  vs.  $T$  plots. These show that in all cases the magnetic behaviour is paramagnetic [25]. On the as-

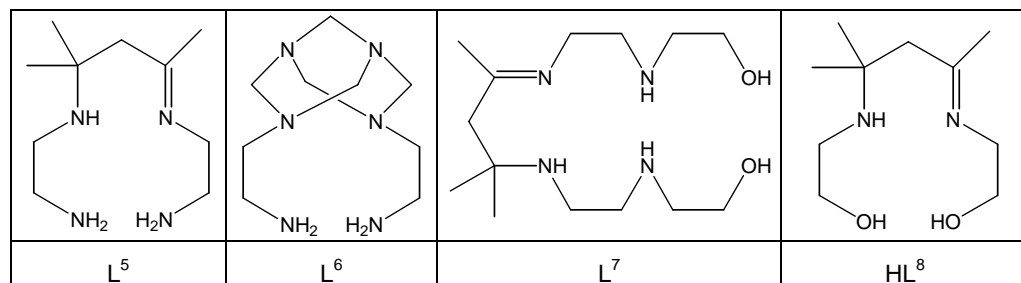
sumption that the  $\text{Co}^{3+}$  ions are diamagnetic, the room-temperature magnetic moment for **16**, 1.95 B.M., is typical of isolated  $S = 1/2$  ions. The  $\mu_{\text{eff}}$  values (per mole of complex) of the  $\{\text{Cu}_2\text{Co}_2\text{Ni}\}$  complexes **14** and **15** are 4.18 and 4.3 B.M., respectively. Those are similar to the calculated value of 4.03 B.M. for a high spin  $\text{Cu}_2^{\text{II}}\text{Ni}^{\text{II}}$  combination in which the constituent metals have typical  $\mu_{\text{eff}}$  values of 1.9 and 3.0 B.M.

#### 4. Direct template synthesis

Various solvents have been used to develop techniques of direct synthesis of heterobimetallic ethylenediamine complexes. Condensation of acetone with ethylenediamine resulted in the open-chain ligand, becoming the beginning of a new synthetic approach to heteropolynuclear complexes that we called "Direct template synthesis" (Table 3).

Table 3. Heterobimetallic complexes obtained by direct template synthesis [27, 28]

Initial system	Complex
$\text{Cu}^0\text{-M}^0\text{-en}\cdot n\text{HX}\text{-(CH}_3\text{)}_2\text{CO - Solv}$ $\text{M}^0 = \text{Zn, Mn}$ $\text{Ni}^0\text{-M}^0\text{-en}\cdot n\text{HX}\text{-(CH}_3\text{)}_2\text{CO - Solv}$ $\text{M}^0 = \text{Zn, Mn}$ $\text{X} = \text{Cl, Br, NCS}$ $\text{Solv} = \text{dmf, dmsO, CH}_3\text{OH, CH}_3\text{CN}$	$[\text{CuL}^5\text{XZnX}_3]$ $\text{X} = \text{Cl, Br, NCS}$ $[\text{CuL}^5][\text{MnCl}_4]$ $[\text{NiL}^5][\text{ZnX}_4]$ $\text{X} = \text{Cl, Br, NCS}$ $[\text{NiL}^5][\text{MnX}_4]$ $\text{X} = \text{Cl, NCS}$
$\text{Co}^0\text{-ZnO-en}\cdot 2\text{HCl}\text{-(CH}_3\text{)}_2\text{CO-dmf}$	$[\text{Co}^{\text{III}}\text{L}^5\text{Cl}_2][\text{ZnCl}_3(\text{dmf})]$
$\text{Ni}^0\text{-K}_3[\text{Cr}(\text{NCS})_6]\text{-en}\cdot 2\text{HCl}\text{-(CH}_3\text{)}_2\text{CO-CH}_3\text{CN}$	$[(\text{NiL}^5)_6(\text{Cr}(\text{NCS})_6)_3][\text{Cr}(\text{NCS})_6]$
$\text{Ni}^0\text{-ZnO-en}\cdot 2\text{HX-NH}_4\text{X-CH}_2\text{O-Solv}$ $\text{X} = \text{Cl, Br}$ $\text{Solv} = \text{dmf, dmsO}$	$[\text{NiL}^6][\text{ZnX}_4]$
$\text{M}^0(1)\text{-M}^0(2)\text{-amine}\cdot n\text{HCl}\text{-(CH}_3\text{)}_2\text{CO-Solv}$ $\text{M}^0(1) = \text{Ni, Cu; M}^0(2) = \text{Zn, Mn}$ $\text{Amine} = \text{N-(2-hydroxyethyl)-ethylenediamine, 2-aminoethanol}$ $\text{Solv} = \text{dmf, dmsO, CH}_3\text{OH, CH}_3\text{CN}$	$[\text{M}(1)\text{L}^7][\text{M}(2)\text{Cl}_4]$ $[\text{CuL}^8\text{ZnCl}_3]_2$



Complexes  $[\text{CuL}^5\text{Zn}(\text{NCS})_4]$  (**17**) and  $[\text{NiL}^5][\text{Zn}(\text{NCS})_4]$  (**18**) [27] have similar compositions and also similar crystal architecture. The  $\text{M}(\text{L}^5)^{2+}$  and  $\text{Zn}(\text{NCS})_4^{2-}$  ions can be seen as the main building blocks in both structures. In the case of **17** they are associated via the semi-coordinate  $\text{Cu}\dots\text{S}$  bond of 2.9 Å in a more robust “molecular” building block,  $[\text{Cu}(\text{L}^5)\text{-}\mu\text{-SCNZn}(\text{NCS})_3]$  (Fig. 25). The building blocks  $\text{M}(\text{L}^5)^{2+}$  and  $\text{Zn}(\text{NCS})_4^{2-}$  are arranged in such a way that infinite helical chains form along the  $a$ -axis. The cations  $\text{Cu}(\text{L}^5)^{2+}$  and  $\text{Ni}(\text{L}^5)^{2+}$  are weakly bonded to the anionic chains through  $\text{N-H}\dots\text{S}$  hydrogen bonds and the semi-coordinate  $\text{Cu}\dots\text{S}$  bond of 2.9 Å in the case of **18**.

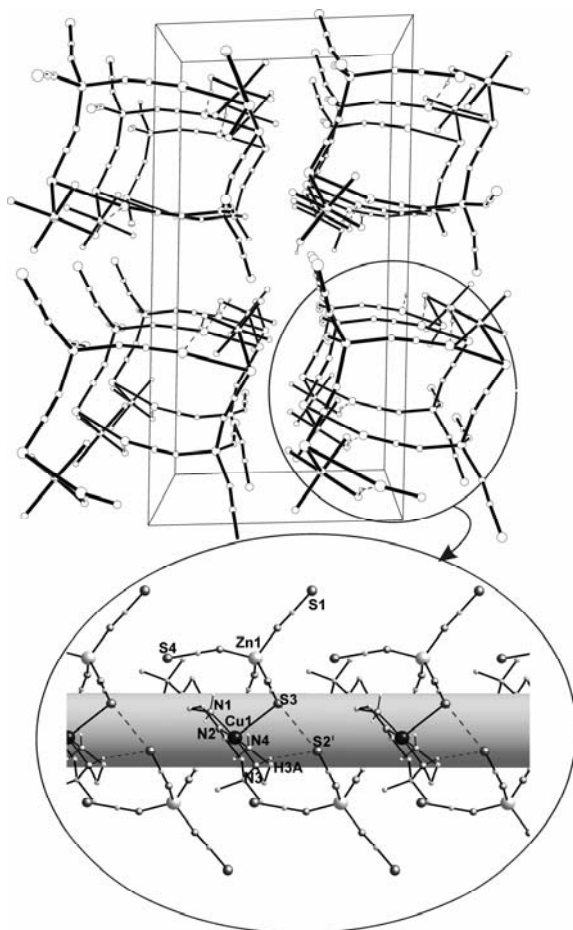


Fig. 25. Packing of helices in the crystal of  $[\text{CuL}^5\text{Zn}(\text{NCS})_4]$  [27]

The nickel atom in  $[\text{NiL}^6][\text{ZnCl}_4]$  (**19**) [27] (Fig. 26) has a square-planar environment being coordinated to four nitrogen atoms of the two ethylenediamine moieties of the ligand. The five-membered metal-chelate ring has the gauche conformation, and

the two six-membered rings have a chair conformation. The cations linked together via the N–H...N bond of 3.1 Å and 174° to form cationic chains. Those are further connected by  $[\text{ZnCl}_4]^{2-}$  anions through the set of the linear Zn–Cl...H–N and cyclic Zn–Cl...H<sub>2</sub>N motifs into a 2D net (Fig. 26).

The main structural blocks in the crystal of  $[\text{Cu}(\text{L}^7)][\text{MnCl}_4]$  (**20**) are  $[\text{Cu}(\text{L}^7)]^{2+}$  cations and  $[\text{MnCl}_4]^{2-}$  anions (Fig. 27). The coordination environment of Cu(II) atom is formed by six (4N + 2O) donor atoms of  $\text{L}^7$ . The geometry of  $[\text{MnCl}_4]^{2-}$  is near tetrahedral, the average Cl–Mn–Cl bond angle being 109.5°. Hydrogen bonding seems to play an important role in the formation of the crystal lattice of **20**, taking into account the potential capacity of  $[\text{Cu}(\text{L}^7)]^{2+}$  to act as a hydrogen donor and  $[\text{MnCl}_4]^{2-}$  anion to act as a hydrogen acceptor. All of the five protons and all the chlorine atoms from the anion are involved in the N–H...Cl and O–H...Cl bonds (Fig. 27) [28].

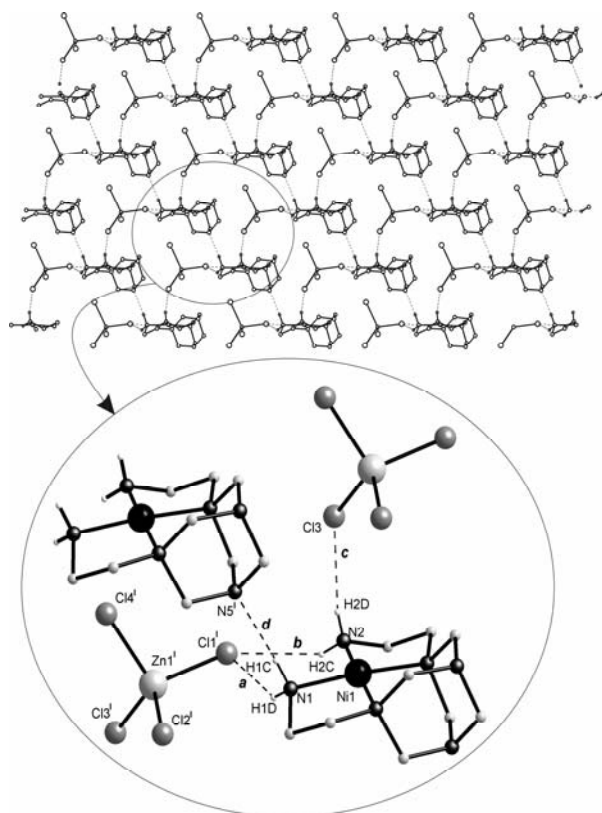


Fig. 26. The hydrogen bonded sheet of  $[\text{NiL}^6][\text{ZnCl}_4]$  and its motif [27]

In contrast to the above mentioned compounds  $[\text{Cu}(\text{L}^8)\text{ZnCl}_3]_2$  (**21**) [27] possesses a molecular (0D) framework (Fig. 28). Each molecule is a centrosymmetric dimer in which two  $[\text{Cu}(\text{L}^8)\text{ZnCl}_3]$  halves can be distinguished. These halves are bound by long range, or semi-coordinate, Cu–Cl(1) bonds (2.728(2) Å) forming an eight-membered

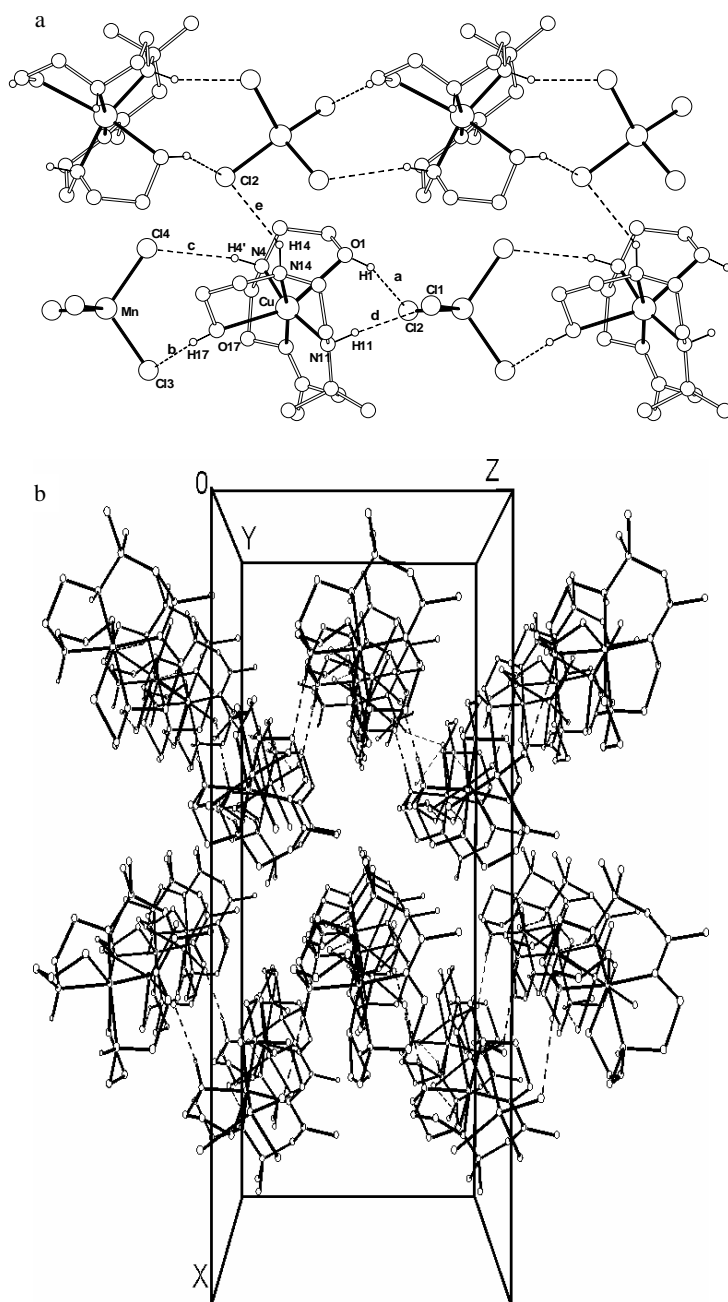


Fig. 27. Fragment of the layer in  $[\text{CuL}_7][\text{MnCl}_4]$  with indication of H-bonds (a) and packing of the layers along the  $b$  axis (b) [28]

metallocycle based on a tetranuclear  $\text{Zn}_2\text{Cu}_2$  skeleton with alternating metal and O/Cl atoms. The square-pyramidal coordination geometry around the copper centre is cre-

ated by 2N and 2O donor atoms from the monodeprotonated ( $L^8$ )<sup>-</sup> ligand in the basal plane and chlorine atom Cl(1) occupying the axial position. The zinc atom (with  $ZnCl_3O$  chromophore) adopts a very distorted tetrahedral symmetry. An interesting feature of the structure is the existence of two strong intramolecular H-bonds between neutral and deprotonated OH groups of  $L^8$  (with the O...O distance of ca. 2.5 Å) which form an additional 8-membered ring joining copper atoms inside the dimer molecule.

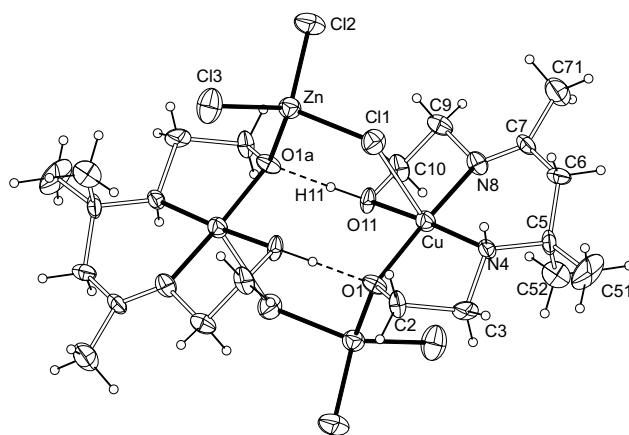


Fig. 28. Molecular structure of  $[CuL^8ZnCl_3]_2$  with the numbering scheme [27]

A large amount of compounds that can participate in condensation reactions promises new advances in the field of direct template synthesis.

## 5. Conclusion

This paper describes novel synthetic routes to heteropolynuclear complexes developed using simple starting materials and relatively mild reaction conditions. Well-known classic acidoligands – carbonate and nitrate – have been of much interest recently as building blocks for the construction of coordination polymers. For example, carbonate group can act even as a  $\mu_6$ -bridge [29]. Heteropolynuclear complexes with these anions have to form in conditions of direct synthesis as well, for example, in the systems:



It is hoped that this synthetic approach will be profitable in obtaining novel heteropolynuclear complexes with various nuclearity and dimensionalities.

### Acknowledgement

The work was supported in part by INTAS (Project N 03-51-4532).

## References

- [1] RAO C.N.R., SRINIVASAN N., VAIDHYANATHAN R., *Angew. Chem. Int. Ed.*, 43 (2004), 1466.
- [2] BRAUNSTEIN P., ORO L.A., RAITHBY P.R., *Metal Clusters in Chemistry*, Wiley-VCH, Weinheim, 1999.
- [3] WINPENNY R.E.P. *Comment. Inorg. Chem.*, 20 (1999), 233.
- [4] BRECHIN E.K., COXALL R.A., PARKIN A., PERSONS S., TASKER P.A., WINPENNY R.E.P., *Angew. Chem. Int. Ed.*, 27 (2001), 2700.
- [5] LIPPARD S.L., *Angew. Chem. Int. Ed.*, 27 (1988), 344.
- [6] PERSONS S., WINPENNY R.E.P., *Acc. Chem. Res.*, 30 (1997), 89.
- [7] GATTESCHI D., SESSOLI R., CORNIA A., *Chem. Commun.*, (2000), 725.
- [8] MCCLENAGHAN N.D., LOISEAU F., PUNTORIERO F., SERRONI S., CAMPAGNA S., *Chem. Commun.*, (2001), 2634.
- [9] GROSS-LANNERT R., KAIM W., OLBRICH-DEUSSNER B., *Inorg. Chem.*, 29 (1990), 5046.
- [10] MICKLITZ M., MCKEE V., RARDIN R.L., PENCE L.E., PAPAETHYMIU G.C., BOTT S.G., LIPPARD S.L., *J. Am. Chem. Soc.*, 116 (1994), 8061.
- [11] SKOPENKO V.V., KOKOZAY V.N., VASSILYEVA O.YU., PAVLENKO V.A., [in:] *Direct Synthesis of Coordination and Organometallic Compounds*, A.D.Garnovskii, B.I.Kharissov (Eds.), *Oxidative Dissolution of Metals and Metal Oxides in a Liquid Phase*, Elsevier, Amsterdam, 1999.
- [12] VASSILYEVA O.YU., KOVBASYUK L.A., KOKOZAY V.N., LINERT W., *Z. Kristallogr. NCS*, 213 (1998), 437.
- [13] VASSILYEVA O.YU., KOKOZAY V.N., ZHUKOVA N.I., KOVBASYUK L.A., *Polyhedron*, 16 (1997), 263.
- [14] KOVBASYUK L.A., VASSILYEVA O.YU., KOKOZAY V.N., LINERT W., REEDIJK J., SKELTON B.W., OLIVER A.G., *J. Chem. Soc., Dalton Trans.*, (1998), 2735.
- [15] MAKHANKOVA V.G., VASSILYEVA O.YU., KOKOZAY V.N., SKELTON B.W., SORACE L., GATTESCHI D., *J. Chem. Soc., Dalton Trans.*, (2002), 4253.
- [16] MAKHANKOVA V.G., VASSILYEVA O.YU., KOKOZAY V.N., SKELTON B.W., REEDIJK J., VAN ALBADA G.A., SORACE L., GATTESCHI D., *New J. Chem.*, 25 (2001), 685.
- [17] VINOGRADOVA E.A., VASSILYEVA O.YU., KOKOZAY V.N., SQUATTRITO P.J., REEDIJK J., VAN ALBADA G.A., LINERT W., TIWARY S.K., RAITHBY P.R., *New J. Chem.*, 25 (2001), 949.
- [18] KOKOZAY V.N., VASSILYEVA O.YU., BUYAYLO E.A., SKELTON B.W., JEZIERSKA J., OZAROWSKI A., BRUNEL L.C., in preparation.
- [19] KOKOZAY V.N., NESTEROVA O.V., PETRUSENKO S.R., SKELTON B.W., BJERNEMOSE J.K., RAITHBY P.R., *Inorg. Chim. Acta*, accepted.
- [20] KOKOZAY V.N., PETRUSENKO S.R., NESTEROVA O.V., LIPETSKAYA A.V., SKELTON B.W., JEZIERSKA J., *Polyhedron*, accepted.
- [21] PRYMA O.V., PETRUSENKO S.R., KOKOZAY V.N., SKELTON B.W., SHISHKIN O.V., TEPLYTSKA T.S., *Eur. J. Inorg. Chem.*, (2003), 1426.
- [22] PRYMA O.V., PETRUSENKO S.R., KOKOZAY V.N., SHISHKIN O.V., ZHIGALKO M.V., *Inorg. Chem. Commun.*, 6 (2003), 896.
- [23] PRYMA O.V., PETRUSENKO S.R., KOKOZAY V.N., SHISHKIN O.V., ZHIGALKO M.V., *Z. Naturforsch. B*, 58 (2003), 1117.
- [24] PRYMA O.V., PETRUSENKO S.R., KOKOZAY V.N., SKELTON B.W., *Inorg. Chem. Commun.*, 7 (2004), 450.
- [25] NESTEROV D.S., MAKHANKOVA V.G., VASSILYEVA O.YU., KOKOZAY V.N., KOVBASYUK L.A., SKELTON B.W., JEZIERSKA J., *Inorg. Chem.*, 43 (2004), 7868.
- [26] NESTEROV D.S., KOKOZAY V.N., MAKHANKOVA V.G., SKELTON B.W., in preparation.
- [27] SHEVCHENKO D.V., PETRUSENKO S.R., KOKOZAY V.N., ZHUBATYUK R.I., ZHIGALKO M.V., SHISHKIN O.V., SKELTON B.W., RAITHBY P.R., in preparation.
- [28] SHEVCHENKO D.V., PETRUSENKO S.R., KOKOZAY V.N., SKELTON B.W., *J. Coord. Chem.*, 57 (2004), 1287.
- [29] ROHMER M.M., BERNARD M., *J. Chem. Soc., Dalton Trans.*, (2003), 3587.

*Received 16 December 2004*

*Revised 9 March 2005*